CMMoST 2021

6TH INTERNATIONAL CONFERENCE ON

Mechanical Models in Structural Engineering

01 – 03 December 2021

Escuela de Ingenierías Industriales
Universidad de Valladolid

Full Papers

UNIVERSIDAD DE GRANADA

UNIVERSIDAD D SEVILLA

Universidad de Valladolid

6^{th} International Conference on Mechanical Models in Structural Engineering

CMMOST 2021

Valladolid, December 2021

Editors

Antolín Lorenzana Ibán

Luisa María Gil Martín

Enrique Hernández Montes

Margarita Cámara Pérez

Víctor Compán Cardiel

Andrés Sáez Pérez

Coordination and design

Álvaro Magdaleno González

Escuela de Ingenierías Industriales. Universidad de Valladolid
Paseo del Cauce 59, 47009 Valladolid (Spain)
cmmost21@uva.es

ISBN: 978-84-09-39323-7

CMMOST 2021. Full Papers is licensed under CC BY–NC–ND 4.0
© 2022 Universidad de Valladolid

Without written permission of the editors and the authors it is forbidden to reproduce or adapt in any form or by any means any part of this publication. Requests for obtaining the right to reproduce or utilize parts of this publication should be addressed to the editors.

UNIVERSIDAD DE GRANADA

UNIVERSIDAD D SEVILLA

Universidad de Valladolid

SPONSORS


ITAP


Ayuntamiento de
Valladolid

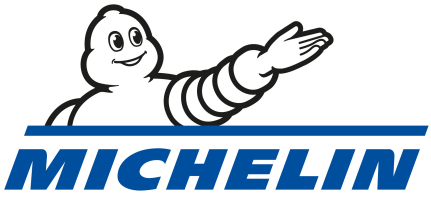
MICHELIN


CARTIF


Spanish Group
IABSE


media madera
ingenieros consultores


Colegio Oficial de
Ingenieros Industriales
de Madrid


acoustic
camera

CONTENTS

ORGANIZATION

Organizers

Antolín Lorenzana Ibán	Universidad de Valladolid
Luisa María Gil Martín	Universidad de Granada
Enrique Hernández Montes	Universidad de Granada
Margarita Cámara Pérez	Universidad de Sevilla
Víctor Compán Cardiel	Universidad de Sevilla
Andrés Sáez Pérez	Universidad de Sevilla

Local committee

Álvaro Magdaleno González	Universidad de Valladolid
Jesús Fernández Vizán	Universidad de Valladolid
Mariano Cacho Pérez	Universidad de Valladolid
José María García Terán	Universidad de Valladolid
Elena Pérez Vázquez	Universidad de Valladolid

Conference Secretariat

Álvaro Magdaleno González	Universidad de Valladolid
Natividad Cabreros Martínez	Universidad de Valladolid
Ismael Martín Villa	Universidad de Valladolid

Scientific committee

Manuel Aenlle López	Universidad de Oviedo, Spain
Francisco Javier Baeza de los Santos	Universidad de Alicante, Spain
Aitor Baldomir García	Universidade da Coruña, Spain
Manuel T. Braz Cesar	Instituto Politécnico de Bragança, Portugal
Juan Francisco Carbonell Márquez	Universidad de Málaga, Spain
Federico Carlos Buroni Cuneo	Universidad de Sevilla, Spain
Germán Castillo López	Universidad de Málaga, Spain
Manuel Chiachío Ruano	Universidad de Granada, Spain
Juan Chiachío Ruano	Universidad de Granada, Spain
Manuel Alejandro Fernández Ruiz	Universidad de Cádiz, Spain
Dora Foti	Politecnico di Bari, Italy
Alberto Fraile de Lerma	Universidad Politécnica de Madrid, Spain
Pietro Gambarova	Politecnico di Milano, Italy
Marta García Diéguez	Universidad de Oviedo, Spain
Enrique García Macías	Universidad de Granada, Spain
Jaime García Palacios	Universidad Politécnica de Madrid, Spain
Felipe García Sánchez	Universidad de Málaga, Spain
José María Goicolea Ruigómez	Universidad Politécnica de Madrid, Spain
María Dolores Gómez Pulido	Universidad Politécnica de Madrid, Spain
Salvador Ivorra Chorro	Universidad de Alicante, Spain
Lourdes Jalón Ramírez	Universidad de Granada, Spain
Tomislav Jarak	University of Zagreb, Croatia
Javier Fernando Jiménez Alonso	Universidad de Sevilla, Spain
María Jesús Lamela Rey	Universidad de Oviedo, Spain
Fouzia Larbi Chaht	Ecole Nationale Polytechnique d'Oran, Algeria
Stefano Miccoli	Politecnico di Milano, Italy
Olga Mijuskovic	University of Montenegro, Montenegro
Carlos Moutinho	Universidade do Porto, Portugal
Iván Muñoz Díaz	Universidad Politécnica de Madrid, Spain
Pablo Pachón García	Universidad de Sevilla, Spain
Michele Palermo	Università di Bologna, Italy
Stavroula J. Pantazopoulou	York University, Canada
Emiliano Pereira González	Universidad de Alcalá, Spain
Jorge Pérez Aracil	Universidad Politécnica de Madrid, Spain
Paul Reynolds	University of Exeter, United Kingdom
Luis Rodríguez de Tembleque	Universidad de Sevilla, Spain
Mario E. Rodríguez Rodríguez	Universidad Nacional Autónoma de México
Biljana Scepanovic	University of Montenegro, Montenegro
Stefano Silvestri	Università di Bologna, Italy
José Manuel Soria Herrera	Universidad Politécnica de Madrid, Spain
Alberto Taliercio	Politecnico di Milano, Italy
Tomaso Trombetti	Università di Bologna, Italy
Dimitrios Vamvatsikos	National Technical University of Athens, Greece

PREFACE

Valladolid, December 2021

CMMoST 2021 is the 6th edition of the Thematic Conference on Mechanical Models in Structural Engineering that is being held from 1 to 3 December in Valladolid (Spain). This series of conferences started in 2011 and progressed successfully over the decade. Previous editions were held in Granada (2011 and 2013), Sevilla (2015), Madrid (2017) and Alicante (2019). This series constitutes an excellent opportunity to present research projects and results and also share experiences in the field of mechanical modeling in structural engineering. CMMoST is aimed at both researchers and professionals dedicated to the development and application of mechanical models in structural engineering.

In this edition, 54 contributions are programmed in 14 sessions, including 2 plenary lecture sessions and 12 oral sessions. The presentations come from 5 countries apart from Spain and 14 will be contributed by predoctoral researchers. Since its beginning, CMMoST has maintained its international scope, but also tries to encourage the young local researchers, making it easier for them to make their presentations in Spanish. Because of this, two official languages are permitted: English and Spanish.

Supported by the participants and local sponsors, CMMoST 2021 proposes an attractive social program that includes a reception at the Escuela de Ingenierías Industriales (School of Industrial Engineering), a tour around the city center of Valladolid, a wine experience at the Wine Museum in the nearby village of Peñafiel and a gala dinner to taste dishes of the local, traditional cuisine.

Finally, the Organization Committee of CMMoST 2021 is very thankful to the authors for their valuable contributions, to the chairmen for their help and the Conference Secretariat for their dedication to the tedious administrative tasks. To all of you, thank you very much.

PLENARY SPEAKERS

Francisco Martínez Cutillas

Civil Engineer (Universidad Politécnica de Madrid, UPM, 1987) and PhD in Engineering (UPM, 1993), he has been professor of Mechanics and Structures at the ETSI de Caminos, Canales y Puertos of UPM since 1996, combining academic activities with his professional activity in the company Principia. He works mainly in the area of structural mechanics, specializing in the risk of cracks in reinforced concrete structures, damage and constitutive modeling of structural materials. His studies in nonlinear dynamics, impact, seismic effects, large dynamic deformations, explosions and metal forming are also noteworthy.

Enrique Hernández Montes

Civil Engineer (University of Granada, 1992) and PhD in Civil Engineering (University of Granada, 1995), he has been professor in Mechanics and Structures at the ETSI de Caminos of Granada since 2007. In addition to his academic activities and several research stays as a visiting professor at the universities of Illinois Urbana-Champaign, Milan and Santa Clara, he has worked as a structural specialist in companies (Prointec S.A., Global Quality Steel) and has been involved in multiple projects of bridges and reinforced concrete cavity walls and piles. He has proposed the EB-PA method (energy-based push-over analysis, included in the North American standard FEMA-440) and has published more than 100 papers. He is also the inventor of several patents (asymmetric piles) and the author of specialized books in structural technology.

Full Papers

Scalable and low-cost MEMS-based Structural Health Monitoring System

Izquierdo, Alberto[1]; Villacorta, Juan J.[1]; del Val, Lara[2]; and Magdaleno, Álvaro[2]

ABSTRACT

This paper presents a scalable low-cost Structural Health Monitoring (SHM) system based on multiple myRIO platforms and digital MEMS (Micro Electro-Mechanical Systems) triaxial accelerometers. The system acquires the accelerations and also computes the corresponding frequency response functions for the subsequent modal analysis. This proposed SHM system was first validated using only a single board with some accelerometers on a timber beam. And after that, a larger system composed by several slave boards connected and synchronized to a master one was deployed on a timber platform to estimate its modal properties. In both scenarios, the obtained results were compared with measured by a conventional SHM system based on piezoelectric accelerometers. After carrying out these validation tests, a high correlation can be appreciated in the behaviour of both systems, concluding that the proposed system is sufficiently accurate and sensitive for operative purposes, and significantly more affordable than a traditional one.

Keywords: Scalable, low-cost, SHM, MEMS accelerometers, Experimental Modal Analysis

1. INTRODUCTION

During the last decades, the concern about the preservation of structures and infrastructures has been constantly increasing, but the high number of historical buildings and civil structures that need to be monitored makes it a complicated and barely affordable problem. The need for cost-effective systems capable of detecting and recording the dynamical response of large and relevant structures is undeniable. Non-destructive techniques (NDT) and those which are little or non-invasive for the structure under study are the most interesting procedures to assess the state of potentially damaged buildings. The application of such techniques helps the companies and governments to foresee maintenance works, which imply important economical savings and environmental care.

Among these techniques, those based on monitoring the dynamical response of the structure have attracted much interest during the last few years [1], as they are robust and harmless for the structure under test. With a set of well-placed sensors, a series of time signals can be collected from the structure and processed to estimate its modal or physical properties. The evolution of these properties over time can be helpful to assess the actual state of a structure and locate the potential damage it may suffer [2,3]. For these techniques, the sensors need to be permanently installed on the structure to be truly effective, continuously recording the structural response, transferring the recorded data to a remote

[1] *Signal Theory and Communications and Telematics Engineering Department. University of Valladolid (SPAIN). E-mail addresses: alberto.izquierdo@uva.es (Corresponding author), juavil@tel.uva.es*

[2] *Industrial Engineering School. University of Valladolid (SPAIN). E-mail addresses: lvalpue@eii.uva.es, alvaro.magdaleno@uva.es*

server and providing trustfully information about its current state [1,4–6]. But nowadays, this is a hard challenge that commercial structural health monitoring (SHM) systems are not fully prepared to undertake, as only few of them are conceived to work continuously. Additionally, commercially available SHM systems has another important restraint: its cost.

Due to their versatility, durability and reduced cost, accelerometers are mainly used to perform continuous monitoring of the dynamical structural response [7]. This type of sensor is intended to measure the acceleration response of a certain point of the structure in one, two or three directions, in order to estimate the modal properties of the structure: natural frequencies, damping ratios and mode shapes [8]. There exist a variety of types of accelerometers used in SHM systems, being the ones based on piezoelectric crystals and those embedded in Micro Electro-Mechanical Systems (MEMS) the most spread ones [9-11]. Piezoelectric sensors produce higher quality measurements than MEMS sensors, but at a significant higher cost.

SHM systems must comprise not only sensors but also a suitable data logger for acquiring data from them and processing the registered signals. Such integrated systems remain a challenge, and there are very few commercially available systems at a great cost [12,13]. To overcome this, the use of digital platforms integrating microprocessors and field-programmable gate arrays (FPGA) are proposed. Synchronous acquisition is attended by the FPGA while the processor operates with the previously registered signals.

This work shows a low-cost SHM system based on the use of wireless networks to monitor buildings, together with the use of MEMS accelerometers. A scalable, modular and reconfigurable system architecture, which includes modules of acquisition, processing and analysis for a SHM system, has been developed. This system can record multiple channels at high acquisition rates, like some other expensive commercial datalogger systems, and then, sequentially, process and evaluate the recorded information. It must be remarked that these abilities are not included jointly in standard commercial systems. In order to validate the developed system, one test with one monitoring device was carried out on a timber structure and, in order to verify the synchronization procedure of the system, a second test with three synchronized devices deployed on a medium-sized structure were performed. In both tests, both structures were simultaneously instrumented by using the proposed system and a standard commercial reference system, based on piezoelectric accelerometers and the SIRIUS® datalogger from Dewesoft®[14], specifically designed for this type of analysis.

The manuscript is organized as follows. Section 2 is devoted to show the low-cost device. Section 3 presents the structures, the sensor set-ups, the recording configuration and the subsequent analysis details used in the validation tests, as well as the main results that were obtained. Finally, Section 5 presents the main conclusions and remarks.

2. SYSTEM DESCRIPTION

The main objective of the designed low-cost system is to allow the monitoring of different structures using digital MEMS accelerometers. Taking this objective into account, the system must be scalable, allowing the number of used accelerometers to be varied, and reconfigurable, so that the location of the sensors could be changed to adapt the set-up to the structure to be measured. Besides, the system must also be distributed, consisting of a set of autonomous modules connected wirelessly. Each of the

modules must be able to acquire and process data from a set of sensors by exchanging synchronization information with the other modules and with the control module. The final structural properties, computed from the registered signals, will help to decide about the structural integrity.

Thinking about the system requirements, it will be useful that the system should be able to:

- Generate proper input signals to command the excitation devices (for example, an inertial shaker with different patterns: noise, tones, frequency sweeps, etc.)
- Acquire and integrate information from other sensors (load cells, temperature, humidity, etc.), both analogue and digital.
- Have the possibility of autonomous operation with recording in a cloud database.

2.1. System Architecture

The system architecture that has been defined selected is shown in Fig. 1. The system is formed by the sensors, the adaptation units, called the Back-end units (BE-U), the Processing unit (P-U) and the control unit, called the Front-end unit (FE-U).

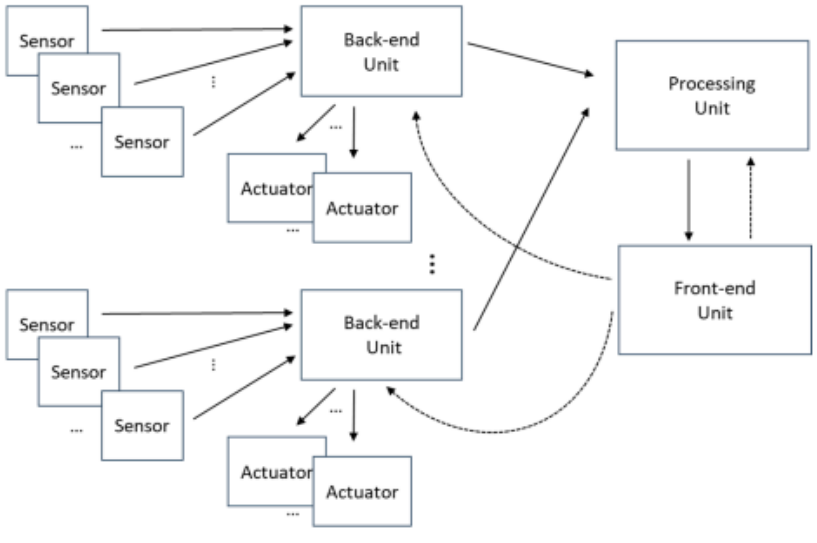

Figure 1. *System architecture.*

The system's sensors, mainly accelerometers, are divided into groups and managed by a set of BE-Us, which configure and read the data provided by each sensor. The system's actuators, such as shakers or pneumatic hammers, are also associated to a back-end unit, which will generate and transfer the actuation signals to the device. The sensor data obtained by the BE-Us are transferred to the P-U, that pre-processes the signals in the time domain (filtering, decimation, etc.) and calculates the FRFs and stores the processing results in a cloud-based database. Finally, the FE-U oversees the measurement and calculation process, establishes the intervals in which the measurements are made and configures the rest of the elements of the system. The FE-U also interacts with the user, allowing the visualization of the measurements and the obtained results.

2.2. Sensor Description

The selected accelerometer was the ADXL355 digital MEMS accelerometer, developed by Analog Devices [15], which is shown in Fig. 2a. These accelerometers measure vibrations with high resolution and very low noise to allow the early detection of structural failures, using wireless sensor networks. Their low power consumption allows for extended product use by prolonging the time between battery changes.

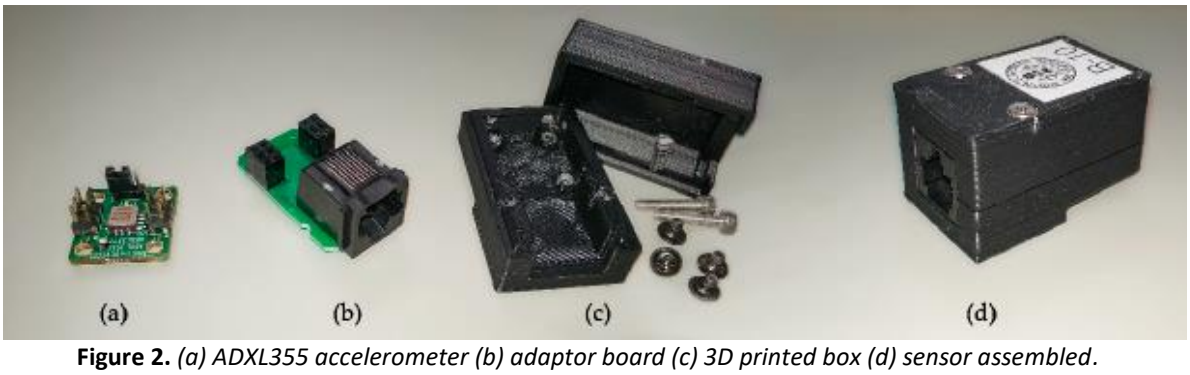

Figure 2. *(a) ADXL355 accelerometer (b) adaptor board (c) 3D printed box (d) sensor assembled*.

The ADXL355 is a low power 3-axis accelerometer with selectable measurement ranges between ±2 g, ±4 g, and ±8 g. It integrates a 20 bits sigma-delta ADC (Analog to Digital Converter) per axis, corresponding with 3.9 µg/LSB (least significant bit), 7.8 µg/LSB and 15.6 µg/LSB mV/g sensitivities, with respect to the defined measurement ranges. It also has a noise density of 25 µg/√Hz, and a bandwidth up to 1500 Hz.

A small adaptor board has been developed to join the sensor to a RJ45 connector, as can be observed in Figure 2b. The whole set has been encapsulated in a little box that has been 3D printed (Figure 2c). This box provides mechanical integrity to the sensor and provides an anchoring mechanism to the structure to be measured. Figure 2d shows the final sensor encapsulated in the box.

2.3. Back-End Unit (BE-U)

Due to its flexibility in the control of the inputs and outputs and its high capacity to parallelize, a FPGA is the most suitable hardware to implement the BE-U. To avoid the complexity and high development time related with this approach, a myRIO platform [16] has been selected as the base for the BE-U. This platform is oriented to sensors with nonstandard acquisition procedures, allowing low-level programming of the acquisition routines using the LabVIEW graphical programming language. Specifically, the myRIO platform is an embedded hardware based on a Xilinx Zynq 7010 chip, which incorporates a FPGA, a dual-core ARM® (Advanced RISC Machine) Cortex™-A9 processor and two MXP ports, all this enclosed in a small box (136 mm x 89 mm x 25 mm).

Both MXP ports with 16 digital input/output (I/O) lines of the FPGA have been used to connect the myRIO platform to the ADXL355 sensors, using a self-developed MXP-to-RJ45 adaptor board with 3 RJ45 connectors, as can be observed in Fig. 3. As each of these sensors needs 5 I/O lines, up to 6 sensors can be attached to a myRIO without multiplexing I/O lines. As far as the FPGA has 40 digital I/O lines, up to 16 sensors could be connected to a single myRIO if needed.

Figure 3. *MyRIO device with two adapter boards and an accelerometer.*

The FPGA also has 2 AD inputs, which have been used to acquire analog data from other devices (like analog accelerometers or a load cell), synchronously with the digital data from the ADXL355 sensors, and 2 DA outputs, which have been employed to generate excitation signals to be used as the source to shakers or other type of modal exciters. And the ARM processor is equipped with 256 MB of DDR3 RAM (Double Data Rate 3 Random-Access Memory), 512 MB of built-in storage space, USB Host port, and Wi-Fi interface.

If several myRIO platforms are included in the system, a synchronization mechanism will be used to ensure that the data from all the accelerometers is acquired simultaneously. In this situation, one of the myRIO devices, as the master, will generate a synchronize signal, which will be used by the rest of the myRIOs (slaves) to start the acquisition synchronously.

2.4. Processing and Front-End Units (P-U and FE-U)

On the one hand, a PC is usually used to implement both the P-U and the FE-U, while one or several myRIO devices work as BE-Us. In this configuration, the PC would perform two main functions:

- As a FE-U, the PC manages all the myRIO platforms connected to the system, using a Wi-Fi interface. The PC sends the configuration of the accelerometer sensors attached to each myRIO device, controls when the acquisition starts and when it stops, and receives the acquired data from the accelerometers for further processing. In addition, the PC shows a user interface that allows changing the system parameters and visualizing the results of the modal analysis of the structure.
- As a P-U, the PC could execute additional algorithms to perform the modal analysis, evaluate structural changes or generate early warning signals, among others.

On the other hand, the ARM processor of the myRIO platform could also be used to implement the PU, the FE-U, and also the BE-U, simultaneously, defining a stand-alone system.

3. SYSTEM VALIDATION

As it was mention in the Introduction, the proposed system has been validated with two tests, comparing its performance with a standard commercial reference system and high-end piezo-electric accelerometers, placed side-by-side with the digital MEMS accelerometers on the test structures. The Dewesoft platform has been selected as this reference system in both validation tests. Dewesoft platform is composed of:

- A DS-SIRIUS DAQ [14] device, specifically a DS-SIRIUS-8xACC-8xAO with 8 input and 8 output channels. DS-SIRIUS is a dual-core 24-bit data logger with an anti-aliasing filter on each channel with up to 200 kS/s sampling rate and 160 dB of dynamic range in the time and frequency domains. It is intended for IEPE (Integrated Electronics Piezo-Electric) sensors and supplies a configurable voltage (up to 10 V) and current (between 4 and 8 mA). The power consumption per channel is 1W.
- Six KS76C.100 [17] accelerometers, which are intended for standard applications in laboratory and industry, for vibrations between 0.5 and 70 kHz, and require a current supply ranging between 2 and 20 mA. Its acceleration range is ±60 g with a sensitivity of 100 ± 5 mV/g and 3 µg/√Hz noise density value.
- DewesoftX data acquisition software.

Table 1 shows the most relevant characteristics of the reference and the proposed systems.

Table 1. Main characteristics of the proposed and reference system

Characteristic	Reference System	Proposed System
Range	±60 g	±2 g, ±4 g and ±8 g
Digital sensitivity	11.9 µg/LSB	3.9, 7.8 and 15.6 µg/LSB
Noise density	3 µg/√Hz	25 µg/√Hz
Maximum sample frequency	200 kHz	4 kHz
Bits per simple	24	20
Maximum accelerometer channels	8 uni-axial	6 tri-axial
Cost (1 device + 6 accel. system configuration)	9050 €	928 €
(3-devices + 12 accel. system configuration)	11600 €	2436 €

3.1. Validation tests layouts

3.1.1. One-device system configuration

To carry out these first tests, a sawn timber beam of Scots pine (Pinus sylvestris L.) with a nominal section of 90 mm x 140 mm and a length of 5000 mm was used. This timber beam was placed on a wooden support, placed also on a steel frame. It lies in a horizontal position (140 mm) with a separation between supports of 4500 mm, as can be observed on Fig. 4. It is instrumented with 5 pairs of accelerometers (each one with a KS76C.100 and a ADXL355) evenly distributed on the timber beam (750 mm of separation), at the positions marked as E1 to E5 on Fig. 4. The beam is excited with an electromechanical shaker placed at 1500 mm from the right support, and with another pair of accelerometers placed on its moving mass (labelled as D in Fig. 4) to record the input force. In the test

layout shown in Fig. 4, the timber beam is marked with an A, the myRIO device with a B, and the shaker with a C.

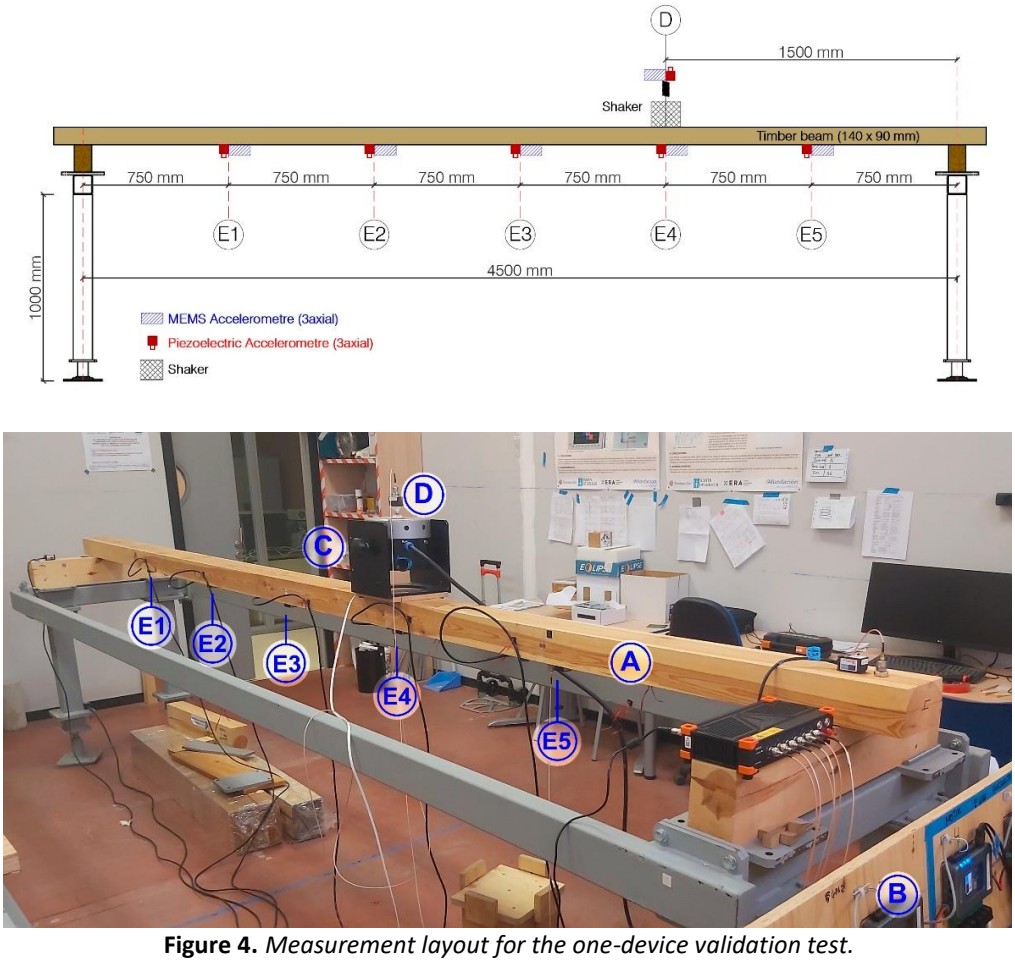

Figure 4. *Measurement layout for the one-device validation test.*

As can be observed in the system configuration for these first tests, which is shown in Fig. 5, the myRIO device obtained the acquire acceleration signals from the six MEMS accelerometers, and also controlled the shaker with a sinusoidal sweep signal with constant amplitude, a frequency range between 3 and 50 Hz and a duration of 3 min for the sweep. In these tests, both systems (proposed and reference) performed the acquisition simultaneously for approximately 8 min, which corresponded to almost 3 cycles of excitation.

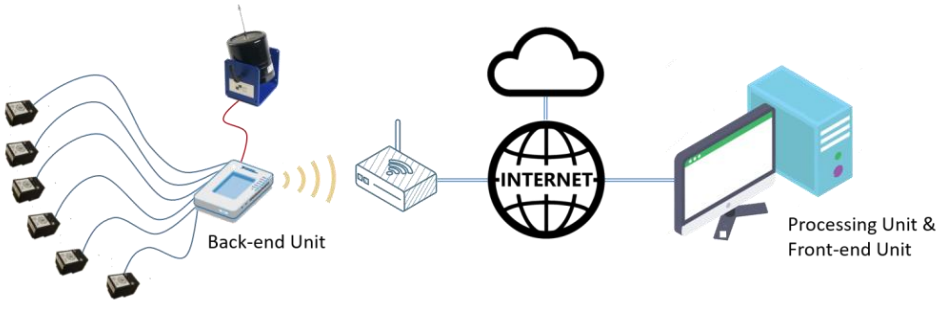

Figure 5. *System configuration for the one-device validation test.*

3.1.2. Multi-device system configuration

In order to validate a multi-device distributed system as a tool to estimate or identify the modal properties of a structure, both systems (proposed and reference) were installed on a timber platform of 1 m width, composed of 10 tightly attached timber beams (made of GLULAM 24 h) with a total length of 13.5 m, a height of 140 mm and a width of 100 mm each, as it is shown in Fig. 6. The platform is simply supported at its both ends, and two sets of three springs (each one with an elastic constant of approximately 6600 N/m) are located at the middle section, compensating the self-weight deflection. Ten pairs of accelerometers of each type (piezoelectric and MEMS) are placed on the structure drawing a 5 × 2 grid, as shown in Fig. 6. In addition, to induce a controlled force on the structure, an electromechanical shaker is placed on it, as can be observed in Fig. 6, in order to excite as many modes as possible in the frequency range of interest. Due to this, two more pairs of accelerometers are required: one pair is placed on the moving mass of the shaker and another pair is located on its frame, rigidly attached to the structure and defining the driving point.

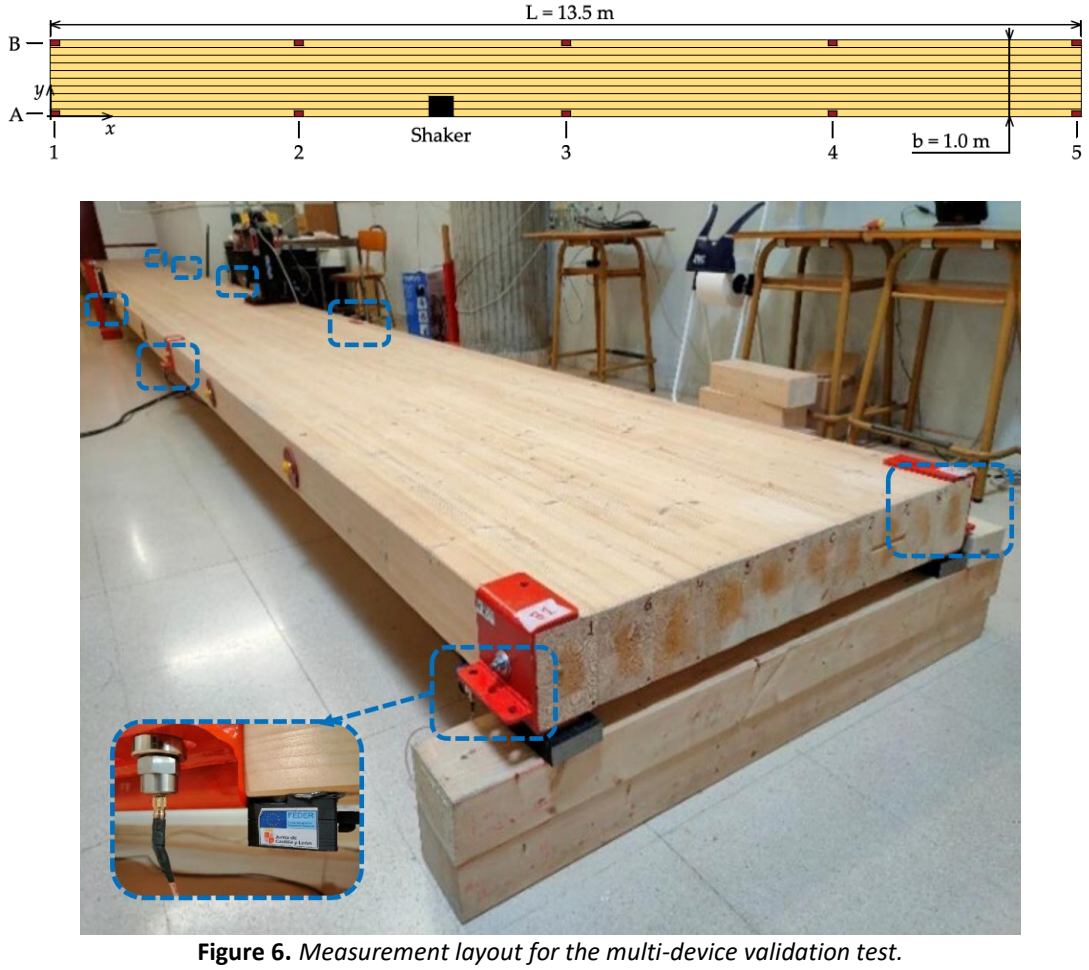

Figure 6. *Measurement layout for the multi-device validation test.*

As can be observed in the proposed system configuration for these second tests shown in Fig. 7, the shaker is controlled by one BE-U, generating a random noise with frequency components between 0 and 100 Hz. This BE-U, also records the signals acquired by the two MEMS accelerometers placed on the shaker, and two BE-Us more record the response of the ten MEMS accelerometers installed on the structure. All the BE-Us defined in the configuration record information at 4000 S/s during 660 s.

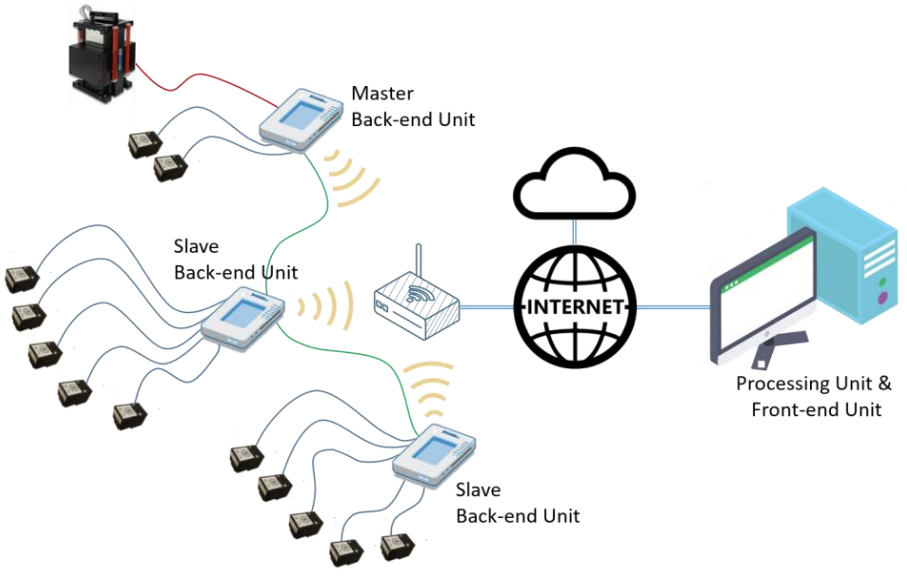

Figure 7. *System configuration for the multi-device validation test.*

3.2. Validation results

3.2.1. One-device system results

The objective of the first set of tests was the validation of the accuracy of the proposed system. So, in order to achieve this objective, the response of the timber beam was analyzed in both time and frequency domains.

In order to compare the proposed system with the reference one in the time domain, the acquired signals of each system have been recorded, preprocessed with a low-pass FIR filter (1 kHz cut-off frequency, 106 coefficients, and Kaiser window with 0.005 ripple) and aligned to match the starting time. As one example, Fig. 8 shows the excitation signals registered with both systems by the accelerometers placed under the shaker (position E4 in Fig. 4). As it is usual when the response of a structure subjected to sinusoidal excitation is obtained, high amplitudes reveal the coincidence of the input frequency with the resonance frequencies of the structure, while low amplitudes correspond to frequencies to which the structure is less sensitive. The comparison of the measurements of the sensors shows a great similarity in the data provided by both systems with minor variations, that can be caused by the different location along the beam. Due to the volume that the accelerometers themselves occupy; it is impossible to place them in exactly the same geometric position, and it was decided to carry out the measurements simultaneously with both systems, to ensure that the conditions under which the tests were carried out were the same. The cross-correlation between these corresponding acquired pair of signals has been analyzed, resulting in a correlation coefficient of 0.9985.

The signals obtained by each of the six pairs of accelerometers were processed by each corresponding system to calculate the FRFs of the test structure by using a 32,768 points (8.192 s at 4000 samples/second) Blackman window, leading to a frequency resolution of 0.366 Hz. In the case of the proposed system, the FRFs where calculated using a custom LabVIEW software. Fig. 9 shows the comparison of the FRFs obtained by each system in the range of interest.

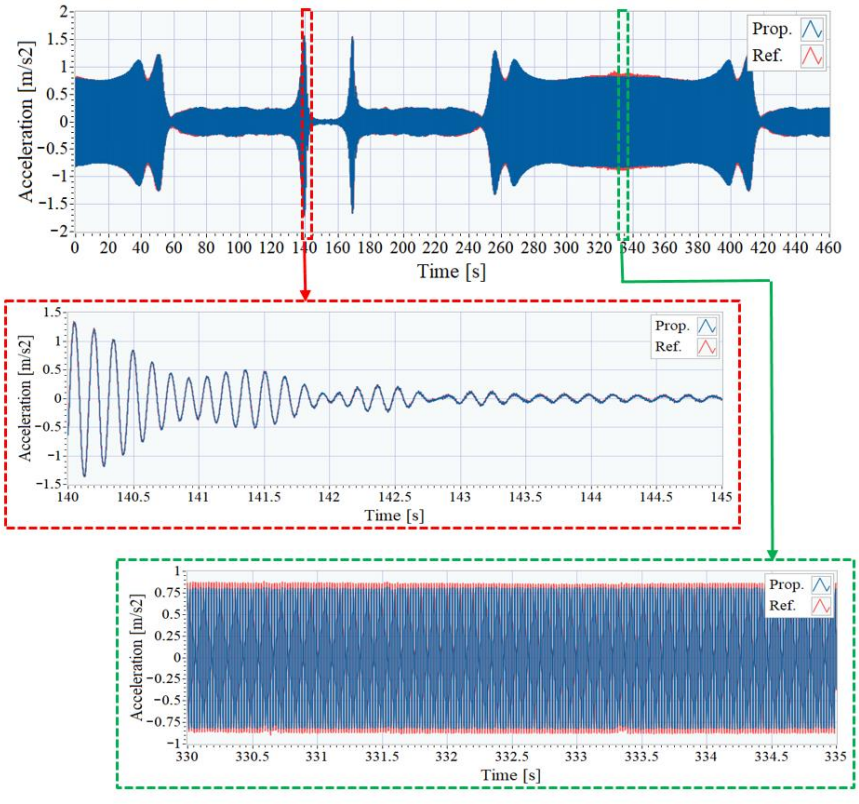

Figure 8. *Time signals of accelerometers at position E4.*

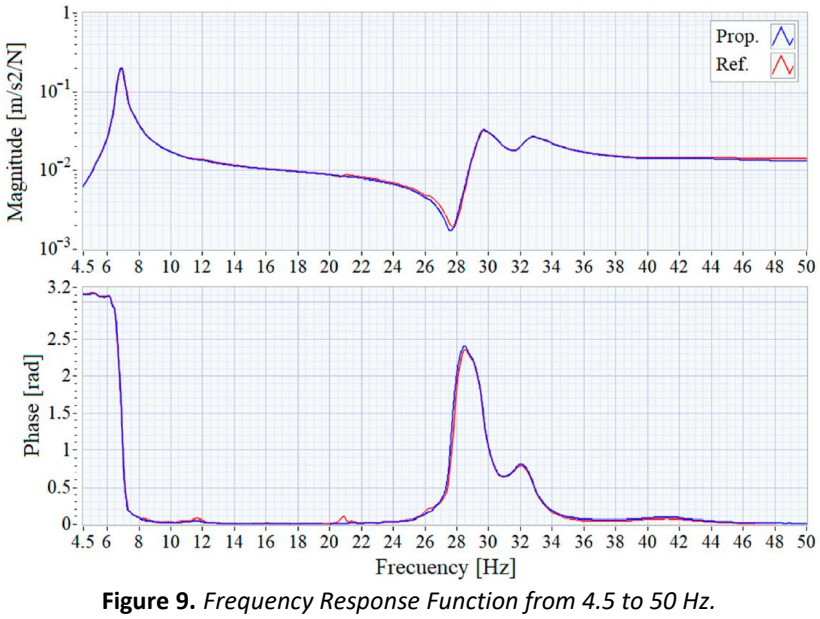

Figure 9. *Frequency Response Function from 4.5 to 50 Hz.*

As can be observed, the small discrepancies observed in the time domain recordings result in minimal changes in the frequency domain responses, validating of the proposed system for modal analysis of structures. In both FRFs, a main resonance peak around 6.9 Hz can be clearly distinguished. These FRF graphs show that the results obtained with the two systems are almost identical, being the cost

associated to the proposed system for this test configuration, ten times lower than the cost of the reference system, as it is detailed in Table 1. This cost difference could be even higher if the cost of the proposed system is compared to brands in the upper segment of the market or if it is considered that each accelerometer of the proposed system is triaxial, when the reference ones are uniaxial.

3.2.2. Multi-device system results

The objective of the second set of tests was the validation of the use of the proposed system in an experimental modal identification of a structure more complex than a timber beam. In this case, several myRIO devices needed to be employed to acquire the acceleration signals associated to the vibrating structure. So, for this new configuration, the synchronization of the proposed system if it is formed by several myRIO devices needed to be validated.

As the first step in these new validation tests, the synchronization between the BE-Us was assessed to verify that the acquisition was properly performed. Thus, three myRIO devices were used, the same number that were going to be used in the second part of these validation tests. One of them acted as Master BE-U and the other two were the Slaves BE-Us, each one connected by a 1 m long synchronization cable to the Master unit. In this previous test, a delay between the synchronization clock and the BE-U acquisition clocks of about 50 ns was measured. This delay was partly due to the propagation delay through the synchronization cable, and also included a fixed delay due to the clock regeneration algorithm. Conversely, it was observed that all the sampling clocks, reconstructed by each BE-U, were almost in phase, with a delay between them below 10 ns. Additionally, some synchronization tests using 10 m-long cables were carried out. In this case, the delay between the synchronization clocks was no greater than 55 ns. Considering that the maximum sampling period was 250 µs, due to the sampling frequency being 4 kHz, it could be concluded that the data acquired using the distributed system was synchronous enough for the purposes intended in this new validation tests, which was the experimental modal identification of a timber platform.

Once that it was confirmed that the synchronization between the BE-Us was reliable, the experimental modal identification of the timber platform was carried out. As the first step, the FRFs of the structure were estimated separately by each system by using the recordings of the corresponding pair of 12 accelerometers, using the estimated force induced by the shaker as the input to the system and the remaining 11 accelerometers signals as the outputs of the system, leading to a total of 11 FRFs. To perform the FRFs computation, the time signals are segmented with a Hanning window of 120 s length (480,000 samples), leading to a frequency resolution of 0.0167 Hz. The computed FRFs associated to the side A of the structure (Fig. 6 above picture) are shown in Fig. 10. Subtle differences can be appreciated between both sets of FRFs, which are mainly due to slight misplacements of the sensors that compose each co-located pair (see Fig. 6, below picture). However, these differences are not significant in the surroundings of main peaks of the magnitude plots, which are representative of the structural dynamic behavior.

After estimating the FRFs, they were processed in order to estimate the properties of a set of modes: natural frequency, damping ratio and mode shape, using the Frequency Domain Parameter Identification algorithm (FDPI) [18,19]. The identified modal properties were then compared to the ones obtained after processing the FRFs issued by the reference system with a more robust and powerful method [20].

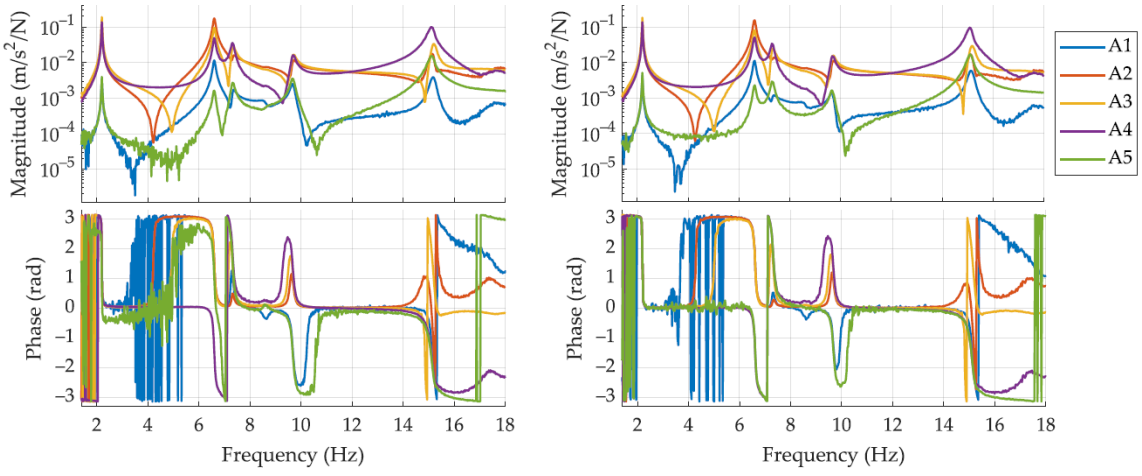

Figure 10. *FRFs corresponding to points A1 to A5 estimated by means of the reference system (left) and the proposed system (right).*

The identified natural frequencies and damping ratios are shown in Table 2. The values obtained with the proposed system and the FDPI algorithm were compared to the ones obtained with the reference system and the reference algorithm by means of the relative error, whose expression is shown in Equation (1) and where the symbol x may stand for the natural frequency or the damping ratio. As can be observed, in order to compute this relative error, the estimates provided by the reference system (RF) were taken as the trustfully ones and the properties obtained by means of the proposed system (FDPI) ware compared against them. Moreover, the identified mode shapes were compared through the known as Modal Assurance Criterion (MAC) [20], and they are also shown in Table 2 and in Fig. 11.

$$\epsilon = 100 \cdot \frac{x_{FDPI} - x_{RF}}{x_{RF}} \tag{1}$$

Table 2. Estimated modal properties.

Mode	Natural Frequency (Hz)			Damping Ration (%)			MAC
	RF	FDPI	Error (%)	RF	FDPI	Error (%)	
1	2.198	2.190	-0.377	0.389	0.436	11.90	0.999
2	6.602	6.600	-0.049	0.709	0.744	4.91	0.997
3	7.324	7.361	0.508	0.910	1.050	15.40	0.981
4	9.685	9.669	-0.165	0.802	0.812	1.35	0.995
5	15.070	15.050	-0.135	0.931	0.779	-16.30	0.994
6	24.150	24.140	-0.037	0.684	0.674	-1.55	0.942
7	26.790	26.710	-0.032	1.100	1.080	-2.10	0.973
8	28.230	28.060	-0.599	1.080	1.200	10.60	0.953
9	39.560	39.130	-1.080	0.977	1.020	4.80	0.989

As it is shown in Table 2, there is a high correspondence between the modal properties estimated by using the proposed system and the ones estimated by using the reference one. The relative error

between both sets of natural frequencies, is under 1.1% in all cases, being the difference smaller than the frequency resolution (0.0167 Hz) in some of them. Damping ratios show higher error values, greater than 15% in a pair of cases. This may be due to this magnitude is always affected by higher uncertainty levels, and it usually evidences more variability. For this reason, the results obtained here are considered to be within the normal bounds. The MAC column shows the success in estimating the mode shapes, as this value increases towards 1 when two modes shapes are similar.

A more complete comparison by calculating the MAC value associated to the mode shapes of different mode number was carried out. These MAC values are expected to be significantly lower to 1 if the mode shapes are different enough. The complete comparison is shown in the MAC matrix in Fig. 11. In this case, the white colour corresponds to a null MAC value, whereas the solid black colour indicates a MAC value that equals 1. Intermediate values are represented with yellow, orange and red colours in ascending order. It can be observed that the main diagonal is mostly black, according to the values in the last column of Table 2, whereas the values outside the main diagonal are mostly yellow and white, evidencing, as expected, the lack of similarities between the rest of pairs of mode shapes.

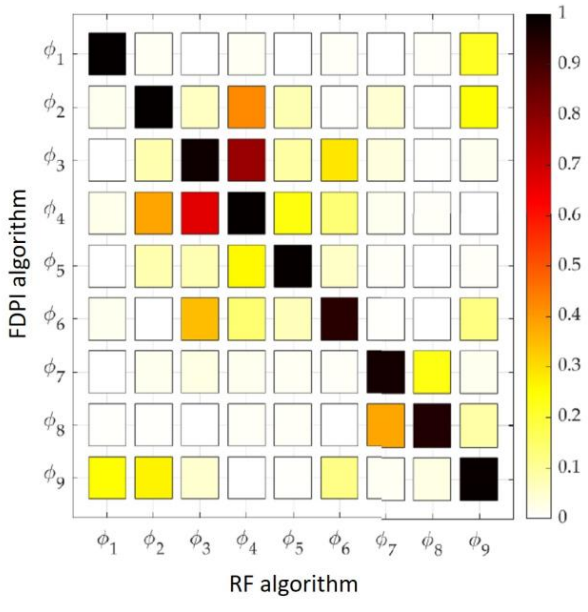

Figure 11. *MAC matrix of the mode shapes estimated through the RF and the FDPI algorithms.*

4. CONCLUSIONS

This paper presents a low-cost system for monitoring the structural health (SHM) based on MEMS sensors. The architecture consists of back-end units devoted to recording the signals collected by the MEMS accelerometers, as well as generating the excitation signals. The processing units are in charge of pre-processing the signals in the time domain, calculating the FRFs and, finally, performing the modal analysis of the structure. The whole process is controlled by the front-end units.

The proposed architecture based on these modules provides a scalable, reconfigurable and low-cost system compared to commercial systems based on analog sensors and acquisition systems with high-performance analog-digital converters. Validation tests has been carried out, based on one or several units based on a myRIO platform together with some digital MEMS accelerometers, placed on different

timber structures, and connected in order to synchronously acquire data from all sensors. The obtained results have validated that the proposed low-cost system is able to synchronously measure data useful to accurately perform the complete modal analysis of a structure.

ACKNOWLEDGEMENTS

This research was funded by the Junta de Castilla y León, co-financed by the European Union through the European Regional Development Fund (ref. VA095P17 and VA228P20). Additionally, the partial support through the RTI2018-098425 project, Spanish Government, is acknowledged.

REFERENCES

[1] Ye, X.W.; Jin, T.; Yun, C.B. (2019). A review on deep learning-based structural health monitoring of civil infrastructures. *Smart Structures and Systems, 24, 567-585*.

[2] Farrar, C.R.; Doebling, S.W.; Nix, D.A. (2001). Vibration–based structural damage identification. *Philosophical Transactions of the Royal Society A: Mathematical, Physical and Engineering Sciences, 359, 131-149*.

[3] Mahammad, A.H.; Kamrul, H.; Ker, P.J. (2018). A review on sensors and systems in structural health monitoring: Current issues and challenges. *Smart Structures and Systems, 2, 509-525*.

[4] Farrar, C.; Worden, K. (2006). An introduction to structural health monitoring. *Philosophical Transactions of the Royal Society A: Mathematichal, Physical and Engineering Sciences, 365, 303-315*.

[5] Matos, J.C.E. et al. (2009). Health Monitoring System (HMS) for structural assessment. *Smart Structures and Systems, 5, 223–240*.

[6] Soria, J.M. et al. (2016). Vibration monitoring of a steel-plated stress-ribbon footbridge: Uncertainties in the modal estimation. *Journal of Bridge Engineering, 21, C5015002*.

[7] Girolami, A.; Brunelli, D.; Benini, L. Low-cost and distributed health monitoring system for critical buildings. In 2017 IEEE Workshop on Environmental, Energy, and Structural Monitoring Systems (pp. 1-6). New York: Institute of Electrical and Electronics Engineers (IEEE).

[8] Salawu, O. (1997). Detection of structural damage through changes in frequency: A review. *Engineering Structures, 19, 718-723*.

[9] Ribeiro, R.R.; Lameiras, R.D.M. (2019). Evaluation of low-cost MEMS accelerometers for SHM: Frequency and damping identification of civil structures. *Latin American Journal of Solids and Structures, 16*.

[10] Acar, C.; Shkel, A.M. (2003). Experimental evaluation and comparative analysis of commercial variable-capacitance MEMS accelerometers. *Journal of Micromechanics and Microengineering, 13, 634-645*.

[11] Zhu, L. et al. (2018) Development of a High-Sensitivity Wireless Accelerometer for Structural Health Monitoring. *Sensors, 18, 262*.

[12] Tan, T.D.; Anh, N.T.; Anh, G.Q. Low-cost Structural Health Monitoring scheme using MEMS-based accelerometers. In 2011 Second International Conference on Intelligent Systems, Modelling and Simulation (pp. 217–220).

[13] Rosal, J.E.C.; Caya, M.V.C. Development of Triaxial MEMS Digital Accelerometer on Structural Health Monitoring System for Midrise Structures. In 2018 IEEE 10th International Conference on Humanoid, Nanotechnology, Information Technology, Communication and Control, Environment and Management (pp. 1–5).

[14] DS-SIRIUS Data-Logger. https://dewesoft.com/products/daq-systems/sirius

[15] ADXL355 3-Axis MEMS Accelerometer. https://www.analog.com/media/en/technical-documentation/datasheets/adxl354_355.pdf

[16] myRIO Platform. https://www.ni.com/pdf/manuals/376047c.pdf

[17] KS76C.100 IEPE Accelerometers. https://mmf.de/standard_accelerometers.htm

[18] Böswald, M. et al. A review of experimental modal analysis methods with respect to their applicability to test data of large aircraft structures. In 2006 International Conference on Noise and Vibration Engineering (pp. 2461-2482).

[19] Lembregts, F.; Leuridan, J.; Van Brussel, H. (1990) Frequency domain direct parameter identification for modal analysis: State space formulation. *Mechanical Systems and Signal Processing, 4, 65-75*.

[20] Maia, N.; Silva, J. (1997). Theoretical and Experimental Modal Analysis; Engineering Dynamics Series; Research Studies Press: Baldock, UK.

Evaluation of vibration transmission of L-shaped plates using finite element analysis

Jesús Magdaleno[1], Enrique Segovia[2], Jesús Carbajo[3], Jaime Ramis[4], M. Ángeles Martín[5]

ABSTRACT

In this paper, velocity level difference through L-shaped plates is studied using finite element analysis (FEA). Validation is performed using experimental measurements and comparing different finite elements models. The velocity level difference between the source and receiving plate is used to study how vibration flows for third-octave frequency bands, within the frequency range 40-3150 Hz. The influence of different types of geometry, material properties, meshes, types of excitations and the incorporation of an elastic layer, simulating a floating floor, were studied. The use of finite elements models with 2D elements proved to be adequate and a good approximation was obtained from both experimental and finite element analysis results.

Keywords: L-shaped plates, vibroacoustic, finite element analysis, vibration.

1. INTRODUCTION

The study of vibration transmission and energy flow between coupled plates improves the predictive models of structure-borne sound transmission. This is of interest in many fields of application, e.g., in automotive, aeronautic, marine, and building industries [1].

The Finite Element Method (FEM) is increasingly used to build predictive models. It is also used to validate analytical and numerical methods, although verification and validation of FEM models are necessary [2]. This is not sufficiently documented in many cases.

Simmons [3] used FEM to calculate the vibrational energies of plates forming L- and H-structures at discrete frequencies between 10 and 2000 Hz, where one plate is excited by a point force and power is transmitted through the junction to other plates. The kinetic energy on a plate was derived from the measured or the calculated displacements at n evenly distributed points to compare experimental, FEM and SEA (Statistical Energy Analysis) results. The FEM gave very good estimates in general.

An analytical model of the bending wave transmission between semi-infinite thin plates connected by a hinge or by an elastic interlayer is studied in [4], with different elastic interlayers in a T–junction. In

[1] *School of Industrial Engineering, University of Valladolid (SPAIN). magdal@uva.es (Corresponding author).*
[2] *Department of Physics, System Engineering and Signal Theory, University of Alicante (SPAIN).*
[3] *Research Institute for Integrated Coastal Zone Management-IGIC, Polytechnic University of Valencia (SPAIN).*
[4] *Department of Physics, System Engineering and Signal Theory, University of Alicante (SPAIN). jramis@ua.es.*
[5] *School of Industrial Engineering, University of Valladolid (SPAIN).*

this work, a two-dimensional finite element model is used to calculate a correction factor for stiffness. Steel and Craik [5] used a finite element model to overcome SEA limitations at low frequencies and study the coupling loss factor (CLF) for walls in buildings more accurately. In [6] the FEM is combined with a Statistical Energy Analysis-like (SEAL) for derivation of energy flow between two thin plates. A thin L-shaped plate is investigated using a commercial FE code. Mace and Shorter [7] used energy flow models from finite element analysis, with harmonic excitation, in a system comprising three coupled plates. Traditional SEA predictions were inaccurate in this case. In [8], a power flow density vector of L-shaped plates is used adopting a substructure approach, comparing results with those obtained with the FEM. Hopkins [9] [10] studied an L-junction and a T-junction, with agreement between both FEM and data measured with SEA at high frequencies. Monte Carlo methods were used to evaluate the uncertainty in the material properties and dimensions. Results from the numerical experiments are used for calculating the change in the coupling parameters and their use in SEA and the vibration reduction index in European standard EN 12354 [11].

A benchmarking exercise is presented in [12] for SEA analysis of semi-infinite, isotropic, thin and flat plates. The transmission coefficient is determined by considering a wave to be incident on the junction formed by the intersection of several semi-infinite plates. To facilitate exactitude assessment and help to boost the designer's confidence in simulation, Bochniak and Cieslik [13] introduced uncertainty considerations in vibration energy flow analysis. They used the structural intensity pattern, which presents a vectorial nature of vibrational energy flow in structures, and FEM was used for obtaining harmonic response solution. In [14] the verification of the results obtained was performed on FEM and genetic algorithms were applied to the evaluation of the fundamental frequency of stiffened plates.

Clasen and Langer [15] analysed the influence of various damping mechanisms on the transmission of sound in buildings, using FEM models, studying different constructive configurations. They analysed the influence of damping on the joints of walls, introducing a spring-damper system in several small-scale models. Du et al. [16] studied uniform elastic boundary restraints in two elastically coupled rectangular plates with an analytical method, validating the results with FEM models. The FEM is used in [17] to obtain a numerical evaluation of the vibration reduction index in structural joints, comparing results with those evaluated using the EN 12354 [11], and allowing the calculation of an adaptation term that makes both approaches converge. Comparison with results obtained by empirical formulas reveals that results from the standard's calculation cannot accurately reproduce the expected behaviour, and thus indicate that alternative complementary calculation procedures are required. The behaviour of a structural joint in terms of vibration transmission is complex, depends strongly on the frequency, and should be evaluated for each structural reality. The prediction of vibration transmission across networks of coupled beams using a bending wave only model and a bending and longitudinal wave model is studied in [18], by application of SEA and advanced SEA to structure-borne sound transmission. SEA is used with coupling loss factors determined from wave theory and is compared with numerical experiments from FEM. 2D and 3D FEM models of an acoustic laboratory were used in [19], and the results were verified with experimental measurements, to study airborne sound properties of composite structural insulated panels. The 2D results obtained a good agreement with experimental results.

In [20] the vibration problems of various types of coupled plates are solved using an improved Fourier series method. The method was validated with results obtained by the finite element analysis. In addition, numerical results (FEM) are presented in [21] to validate the correctness of an improved Fourier series method used to analyse the vibration of moderately thick coupled rectangular plates with general elastic boundary supports and arbitrary coupling conditions.

Poblet-Puig and Guigou-Carter [22] used spectral finite elements for parametric analysis of the vibration reduction index of heavy junctions oriented to flanking transmissions and EN-12354 prediction method. A parametric analysis of the vibration reduction index was performed for several junction types, observing the influence of several parameters such as damping, junction dimensions and the mass ratio. Hopkins et al. [23] also used the vibration reduction index and developed new regression curves by numerical experiments with FEM, SFEM and wave theory. The junctions considered were formed from heavyweight walls and floors and the new relationships were implemented in the prediction models improving the agreement between the measured and predicted airborne and impact sound insulation.

One of the difficulties that arise when computational methods are used is the need for methods to evaluate the reliability and accuracy of their results. In the field of FEM application in the transmission of sound in buildings, this fact was evidenced by [2]. They indicate that the reliability of the FEM depends heavily on the way the model is defined and include validation through experimental measures in a study of low-frequency dwellings.

In one of the first works on FEM application in structural sound transmission, Simmons [3] points towards the need to verify that the commercial program used produces valid results, since there are no published previous cases of usage in the frequency range of interest. To do this, he compares simple cases for which the analytical solution is known, or for which experimental results exist, with the results of the program. Concerning the dynamic analyses, Wilson [24] indicates that to reduce errors caused by model approximations, many different analyses are necessary, and unsurprisingly there are 20 of them. In each analysis, different calculation models, loadings and/or boundary conditions are used.

Verification and validation are the main methods and procedures used to assess reliability, limitations, weaknesses, and uncertainties of computational simulations. In [25] examples are found of typical situations in which errors are commented and techniques are proposed for verifying and validating. A more detailed process can be found in [26], [27] and [28].

The accuracy in FEM depends on the size of the mesh, element quality, etc. In [29] a smoothed finite-element/boundary-element coupling procedure (SFEM/BEM) is extended to analyse the structural-acoustic problem to improve accuracy.

In this paper we aim at analysing the vibroacoustic response obtained by FEM models in the case of L-linked plates, using the commercial FE package I-DEAS. The difference in velocity level between the excited element and the non-excited element, $D_{\mathrm{v,ij}}$, will be used as an indicator of vibration transmission. This parameter is also used by other authors [9] [1] [22]. The experimental model will be made using stone with concrete-like properties. The influence of the thickness of the connected plates, different characteristics of the material, meshes and the incorporation of two samples of

elastic layers, similar to floating floors, will be studied. The results will be validated and calibrated using experimental measures and comparing different FEM calculation models. Third-octave frequency bands within the frequency range 40-3150 Hz will be studied.

2. METHODOLOGICAL APPROACH

2.1. Background theory

Vibration transmission at junctions where building elements connect is related to the vibration reduction index (K_{ij}), [30] [31] [11], and is normalized to obtain invariant magnitude.

$$K_{\mathrm{ij}} = \frac{D_{\mathrm{v,ij}} + D_{\mathrm{v,ji}}}{2} + 10\log\frac{L_{\mathrm{ij}}}{\sqrt{a_{\mathrm{i}} a_{\mathrm{j}}}} \tag{1}$$

where $D_{\mathrm{v,ij}}$ is the velocity level difference between source element i and receiver element j, L_{ij} is the junction length between elements i and j, and a_i is the equivalent absorption length given by

$$a_{\mathrm{i}} = \frac{2{,}2\,\pi^2\,S_{\mathrm{i}}}{c_o\;T_{\mathrm{s,i}}}\sqrt{\frac{f_{ref}}{f}} \tag{2}$$

in which S_{i} is the area, c_o is the speed of sound in air, $T_{\mathrm{s,i}}$ is the structural reverberation time, f_{ref} is a reference frequency (f_{ref} =1000 Hz) and f is the frequency.

This vibration transmission model is based on a simplified SEA theory of power transmission, where only bending waves are taken into consideration, and the number of subsystems considered are reduced to first order transmissions only [32]. In [32] [33] [34] [35] a review of prediction models, included in building acoustics regulations, can be found along with the advances that have been made and detected needs for improvement. It is possible to obtain the value of K_{ij} using velocity level measurements (L_{v}), as well as the structural reverberation time (T_{s}) of the two elements [31].

Initially, the parameter to be determined based on the velocities is the average velocity level L_{v}. For stationary, structural or aerial excitation, the spatial average is calculated using

$$L_{\mathrm{v}} = 10 \cdot \log\frac{v_1^2 + v_2^2 + \cdots + v_n^2}{n \cdot v_0^2} \quad dB \tag{3}$$

where $v_1^2 + v_2^2 + \cdots + v_n^2$ are the mean square velocities at n different positions on the element, in m/s, and v_0 the reference velocity ($v_0 = 1 \times 10^9$ m/s). As from L_{v} the difference in velocity level $D_{\mathrm{v,ij}}$ is determined using

$$D_{\mathrm{v,ij}} = L_{\mathrm{v,i}} - L_{\mathrm{v,j}} \tag{4}$$

The comparison between the experimental measurements and the FEM models will be done by means of $D_{\mathrm{v,ij}}$, to avoid the influence of structural reverberation time on the calculations. This parameter is also used by other authors [9] [1] [22]. Energy measurement by using velocity measurement points is used in [36] [37], where the number and position of these points are chosen at random and without any precise criterion. This type of approach gives satisfactory results for high

frequencies, but large variations appear at low frequencies. It is not intended to compare the results with those predicted by the SEA, but a similar methodology is used.

2.2. Experimental study

Two cases of perpendicular plate joints were studied. The first joint was formed by two thick plates with a thickness of 60 mm and dimensions of 560 × 530 mm for the horizontal plate and 640 × 530 mm for the vertical plate (Fig. 1). The second joint consisted of a thick horizontal plate with a thickness of 60 mm and dimensions of 545 × 530 mm and another thin vertical plate with a thickness of 30 mm and dimensions of 640 × 530 mm. All measurements had a tolerance range of ± 1 mm. Washers were attached every 50 mm following a matrix pattern to facilitate data collection (Fig. 1). The response was measured in each of the washers.

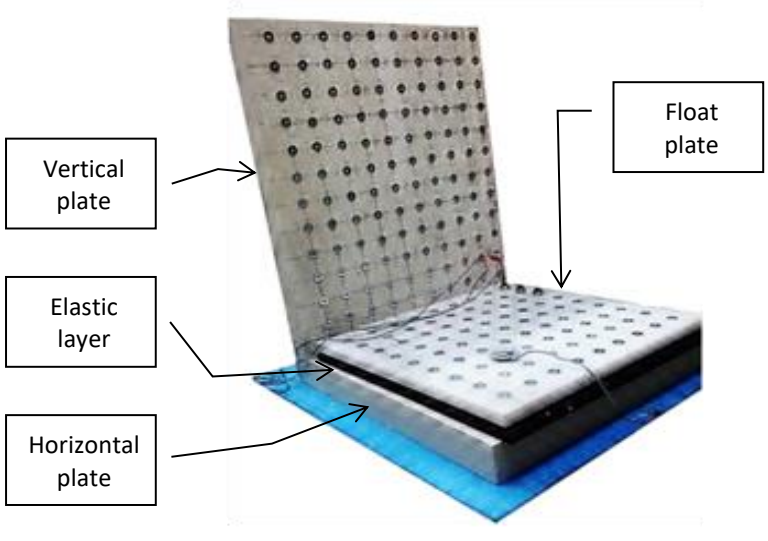

Figure 1. *Geometry of the joint connecting thick plates and floating plate.*

Material used for the plates was a type of stone, called Bateig. Its physical properties are similar to those of concrete, and are described in *Table 1* [38]. Some of the properties of the material were used to calibrate FEM analysis results.

Table 1. Nominal properties of Bateig stone (Bateig32).

Young's modulus (E)	32 GPa
Poisson's ratio (ν)	0.23
Density (ρ)	2315 Kg/m^3
Structural damping coefficient	0.01
Sound speed (c)	3718 m/s

In the study that included an elastic layer, a marble plate was used as a floating plate, with a thickness of 20 mm, a density of 2656 kg/m3, a Young's modulus of 80 GPa and a Poisson's ratio of 0.3. The properties of the elastic layers are detailed in *Table 2*.

Experimental measurements were made by placing the sample on a material that allowed movements from the supporting surface (Fig. 1). The excitation was produced by an electrodynamic type of

actuator, similar to that used in Distributed Mode Loudspeakers (DML). The input signal was a Maximum Length Sequence (MLS) [39]. An NI PCI-6120 data acquisition card was used. The excitation occurred in the same three points as the FEM model (Fig. 3a).

Table 2. Properties of the elastic layers.

Elastic layer	Thickness mm	Density (ρ) Kg/m^3	Dynamic stiffness (s') MN/m^3	Structural damping coefficient
Elastic layer 1	12.5	697.63	5.34	0.17
Elastic layer 2	30	94.83	13.93	0.077

The measurement was carried out simultaneously at three different points, with three accelerometers. The measure points corresponded to the washers attached to the surface (Fig. 1). There were 81 points in the excited horizontal plate and 108 points in the unexcited vertical plate. Signals were registered using the LabWIEW platform with a sampling rate of 96 kS/s and processed using MATLAB.

2.3. FEM model

FEM models with 2D elements were used and the average surface of the plates was taken as reference. These plates were meshed with 8-node shell elements, called "Thin Shell - Parabolic Quadrilateral", with six degrees of freedom per node (three translational and three rotational). This element was based on Mindlin's thick plate equations, which included movement due to shear stress. The formulation is described in [40] [41]. The maximum element size used was 50 mm, so at least 33 elements per wavelength were used for the maximum frequency of interest in this study (2250 Hz). Specifications of meshes used in the models without elastic layers are detailed in *Table 3*.

Table 3. FEM mesh without elastic layer used in the numerical simulations.

	Model	
	Coarse mesh	Fine mesh
Element size (mm)	50	25
Number of Elements	264	1008
Number of Nodes	863	3163

To model the elastic layer of the floating floors, spring-type elements were used (Fig. 2). These elements were massless, translational node to node, and with structural damping coefficient. Spring stiffness was calculated based on the dynamic stiffness of the elastic layer, multiplied by the surface of the elastic layer and divided by the number of springs [42]. For the coarse mesh, 408 springs had a rigidity of 9590 N/m for elastic layer 1 and a stiffness of 3675 N/m for elastic layer 2.

In accordance with the experimental measurements and calculations made of own frequencies, an unconstrained system was used as the most appropriate model, with no movement restriction.

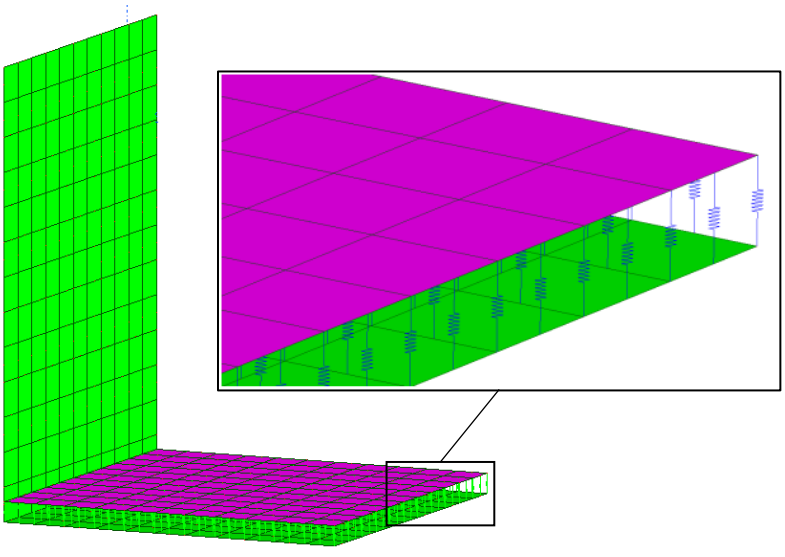

Figure 2. *Models with elastic layer. Mesh for the plates and for the elastic layer.*

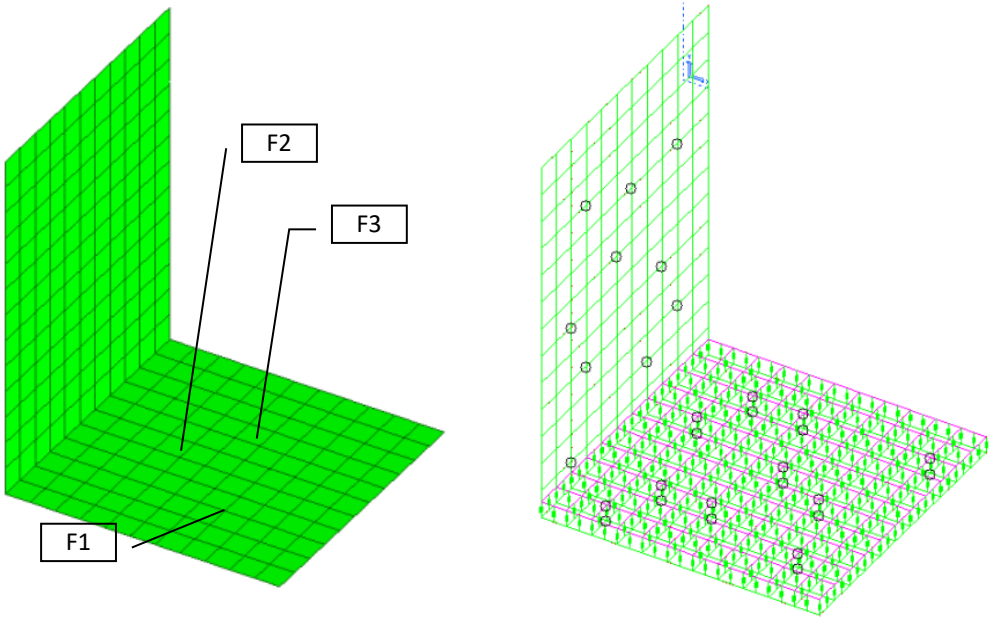

a) Excitation points b) Measurements points

Figure 3. *Excitation and measurements points in FEM models.*

Two types of excitations were used in the FEM models to analyse which of them best simulates the experimental method. The first type simulates transient excitation through a perpendicular impact to the surface, recording the response for 5 s in the models without an elastic layer and 10 s in models with the elastic layer, because of longer system response duration. The impact characteristics were determined so that the response had a similar amplitude to that obtained in the experiments. The second type of excitation simulated a stationary excitation by a series of impacts at a given point, with a frequency of 10 Hz, simulating a tapping machine (TM) [43]. The responses of both types of

excitations were calculated when applied to three points at similar positions to those used experimentally (Fig. 3a).

Since our objective was to determine velocities at different points, a modal analysis was made to determine own frequencies and own modes. Using the modal overlapping method, the response to the excitation was evaluated. Subsequently, the velocities obtained were processed to calculate speed levels and speed level differences.

3. VALIDATION AND CALIBRATION

FEM models must be validated and calibrated to obtain more reliable and accurate results. To do so, we evaluated the differences between several models, in addition to the differences with the experimental measures. The models of plates without elastic layers, i.e., without a floating plate, were validated and calibrated first. To do this, the results of own frequencies, average quadratic velocity, speed level and speed level difference were used. To start with, results obtained with the excitation at one point were used and the results with the excitations in other points were compared later to evaluate the predictive capacity of the model. We also evaluated the use of 10 velocity measurement points, instead of the dot matrix that was used in the experimental measurements. Some of the material's properties were used to calibrate the results of FEM analyses [44] [45]. For this, modifications in Young's modulus and in the density of the material were studied.

In the case of thick plate junction, mean square velocity results of the excited plate of the fine and coarse mesh models using a Young's modulus of 25 MPa show similar results to the experimental ones (Fig. 4). Therefore, this value of the Young's modulus and the coarse mesh seemed to be adequate for this case. The results of the mean square velocity in the FEM models, taking 10 velocity measurement points (Fig. 3b), were similar to those obtained using the same measurement points as those used in the experimental process (Fig. 4). Furthermore, speed level results differed by less than 2 dB from the 630 Hz band, when 10 measurement points were used, differences being somewhat greater at lower frequencies. Taking advantage of these similar results, the following analyses will use 10 velocity measurement points in FEM models, unless otherwise indicated.

Regarding the influence of the number of elements in FEM models, the maximum difference in own frequencies was 1.65% in mode 42 (3479 Hz), with differences smaller than 0.8% below 1753 Hz (mode 16). As for the differences between the experimental model and the FEM models, the maximum difference was 4.2%. The results on velocity levels in FEM models of thick plate junctions without elastic layer differed by less than 3 dB in most cases, having a similar frequency distribution in both plates, so a smaller difference was expected when the speed difference between plates was evaluated. Therefore, this confirmed the coarse mesh appeared to be of sufficient size and a more detailed convergence analysis was not considered necessary, although calculations were also performed for the thin mesh to check the effect of number of elements in the speed level difference.

An additional check was done based on the results of the speed level difference between the excited plate and the non-excited plate, to obtain an estimate of energy transmission. The response was related to similar frequency in the experimental results and in the FEM models (Fig. 5). Values of the FEM models were quite close to each other, at approximately 1 dB. Differences between the FEM models and the experimental results were around 4 dB.

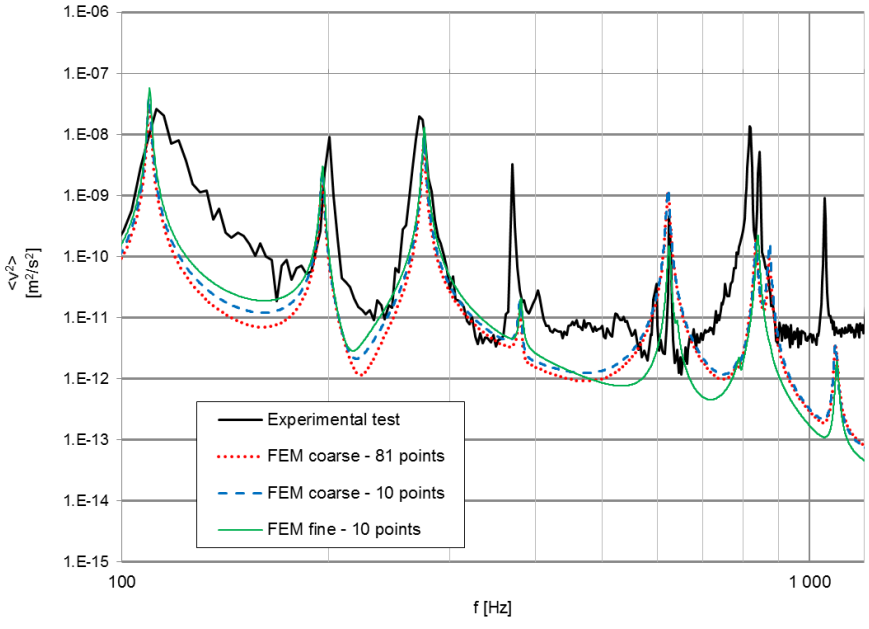

Figure 4. *Mean square velocity in the horizontal plate of the joint with thick plates without elastic layer. E=25 MPa. (<v²> - mean square velocity, f - frequency).*

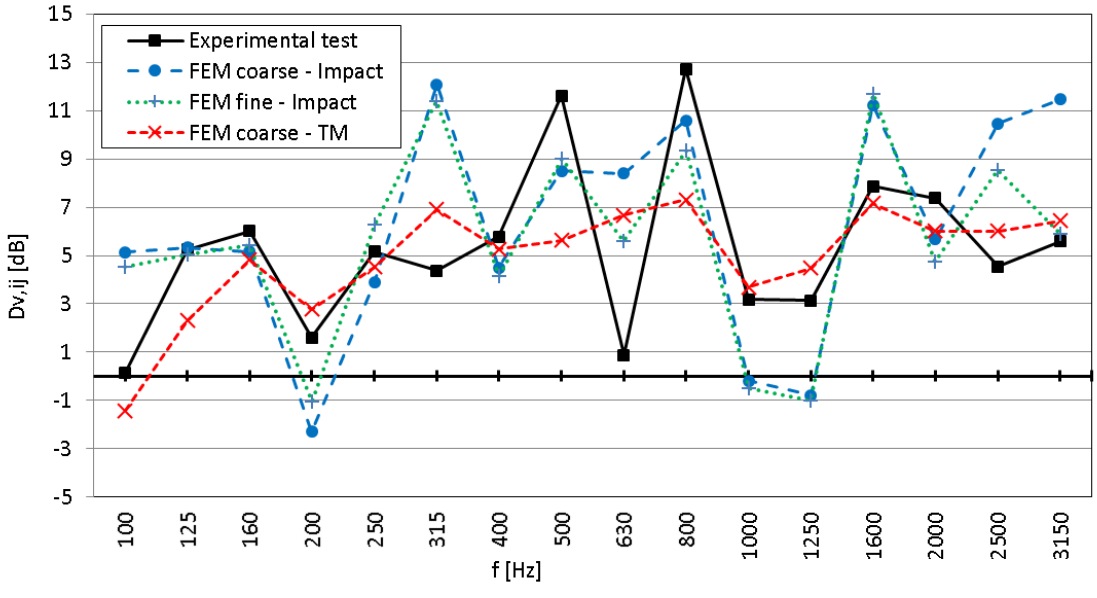

Figure 5. *Velocity level difference at the junction of thick plates with an elastic layer. Different meshes and excitation types ($D_{v,ij}$ - velocity level difference, f - frequency).*

The precision obtained seems acceptable compared to other studies. For example, [46] found standard deviations in Dv, between 2 dB and 10 dB in masonry walls, with an average of around 4 dB. These differences were greater at low frequencies.

To evaluate the predictive capacity of the model, responses of the thick plate model with excitations at other points were analysed, and a similar response was observed. A quantitative assessment will be given later when the results are presented.

Based on these studies, we can consider that the coarse mesh FEM model, material with E = 25 MPa and 10 points measures, achieved an accuracy that was adequate to describe junction behaviour of two thick plates without an elastic layer. Following a similar procedure, the most suitable model for thick plate-thin plate junctions, was the one using coarse mesh, material with E = 32 MPa and 10 points measures, as modal behaviour was better adjusted at low frequencies. The influence on the final results of the speed level difference will be evaluated later.

In elastic layer models, modal behaviour was more complex. A similar evolution of the mean square velocity values was observed in the experimental values and in the FEM models up until 1000 Hz, although comparisons were difficult due to the complexity of the response. The differences between own frequencies of the calculation models and those obtained experimentally were also observed by [42], with notable variations due to the difference in behaviour of the reduced mass in relation to the springs simulating the floating floor.

4. RESULTS AND DISCUSSION

Results on velocity level difference, $D_{\mathrm{v,ij}}$, in joints without an elastic layer, between thick plates joints and between thick plate-thin plate joints, are shown in Fig. 6. Three cases are represented: Experimental test, FEM model with tapping machine type excitation and FEM model with impact type excitation. For each case, the average results at three excitation points and with maximum and minimum values are shown, for third-octave frequency bands. A similar frequency relationship is observed in the experimental results and FEM models. Maximum and minimum values usually showed big differences compared to the mean value in both the experimental measurements and in the numerical calculations, especially in some frequency bands.

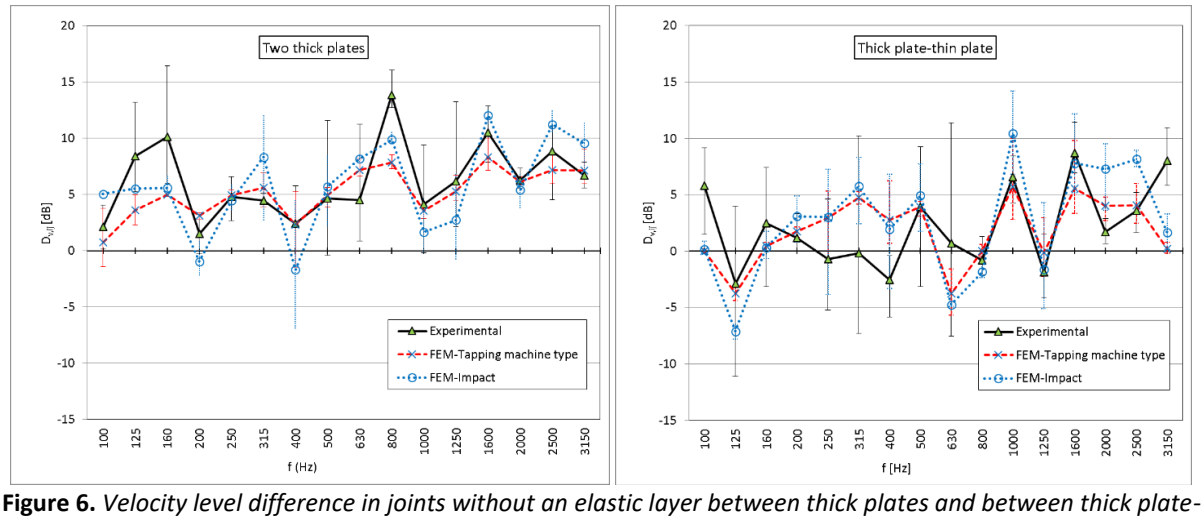

Figure 6. *Velocity level difference in joints without an elastic layer between thick plates and between thick plate-thin plate, impact type and tapping machine type excitation. Average of three excitation points and maximum and minimum values. ($D_{v,ij}$ - velocity level difference, f - frequency).*

In order to evaluate the predictive capacity of the FEM model without an elastic layer, calibrated with the F1 excitation, the weighted normalized impact sound pressure level, $L_{\mathrm{n,w}}$, according to EN ISO 717-2 [47] are shown in Fig. 7. In the case of the junction of thick plates without an elastic layer, almost all results showed differences smaller than 2 dB. The average experimental result was 14.7 dB and the average result for the FEM model and impact type excitation was 15.7 dB. In the case of

joining the thick and thin plates with no elastic layer, almost all the results, in the experimental measurements and in the FEM model, did not differ by more than 2 dB, being the average value 11.7 dB for the experimental measurements and 12.7 dB for the thick FEM model and impact type excitation.

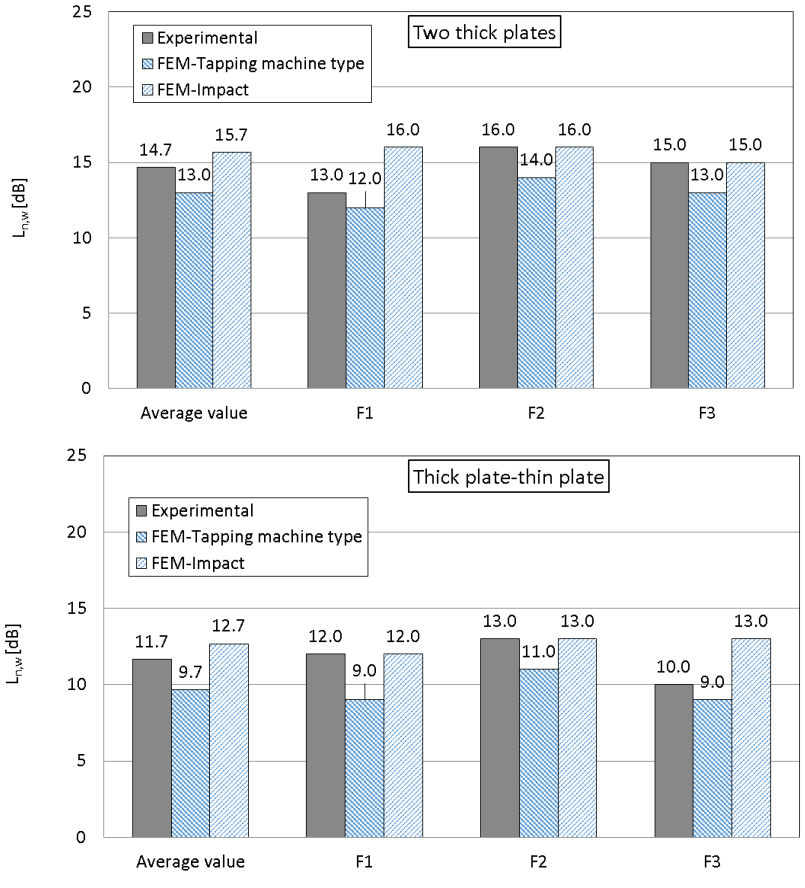

Figure 7. *Weighted normalized impact sound pressure level: average and values in the three excitation points. ($L_{n,w}$ - weighted normalized impact sound pressure level).*

For models with an elastic layer and floating floor, the results of the speed level difference, in the cases of thick plates and elastic layers, averaged and with maximum and minimum values, are shown in Fig. 8a and Fig. 8b. A similar relationship with frequency is observed in the experimental results and FEM models, using tapping machine type excitation to cover the desired frequency range.

Results of velocity level difference, in the case of thick and thin plate junction, averaged and with maximum and minimum values, are shown in Fig. 8c and Fig. 8d. A similar relationship with frequency is observed in experimental results and in FEM models, with somewhat lower values in the FEM model than in the experimental ones in the case of elastic layer 2.

In order to evaluate the predictive capacity of the FEM model with an elastic layer, values of the averaged frequency velocity level difference according to [47] in the case of thick plate junctions where a floating plate is used on the elastic layer, are shown in Fig. 9. The average result in experimental and FEM measurements showed a difference of around 1 dB, all values being comprised between 55 dB and 57 dB.

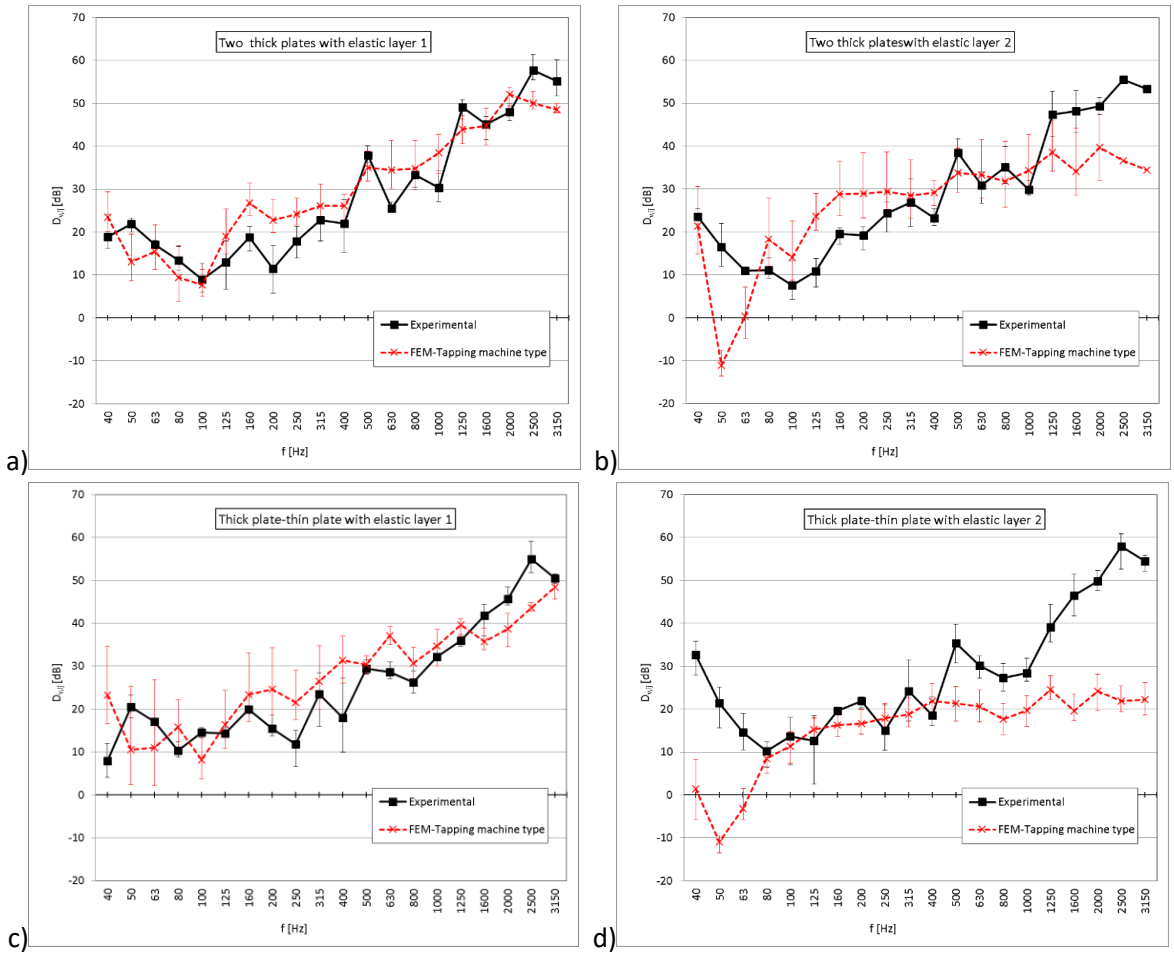

Figure 8. *Velocity level difference: two thick plates and a thick plate-thin plate. Elastic layer 1 and 2. Average of three excitations and maximum and minimum values. ($D_{v,ij}$ - velocity level difference, f – frequency).*

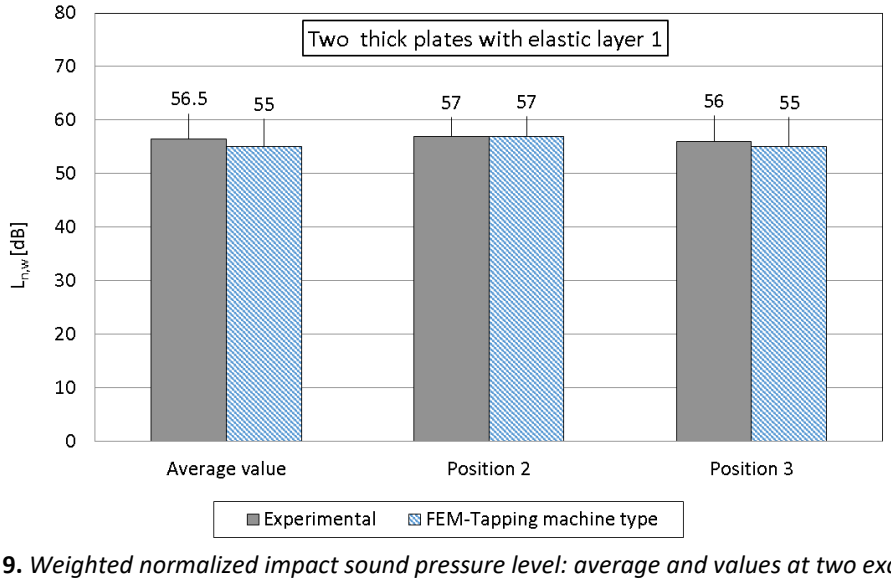

Figure 9. *Weighted normalized impact sound pressure level: average and values at two excitation points. ($L_{n,w}$ - weighted normalized impact sound pressure level).*

The values of the weighted normalized impact sound pressure level according to [47], for the different types of joints, are shown in Fig. 10. The experimental mean values and the FEM mean values, for joints without an elastic layer, differ by less than 2 dB. For elastic-layer joints, the difference between the mean values is between 1 dB and 14.3 dB, though in three out of four cases it was not greater than 7 dB.

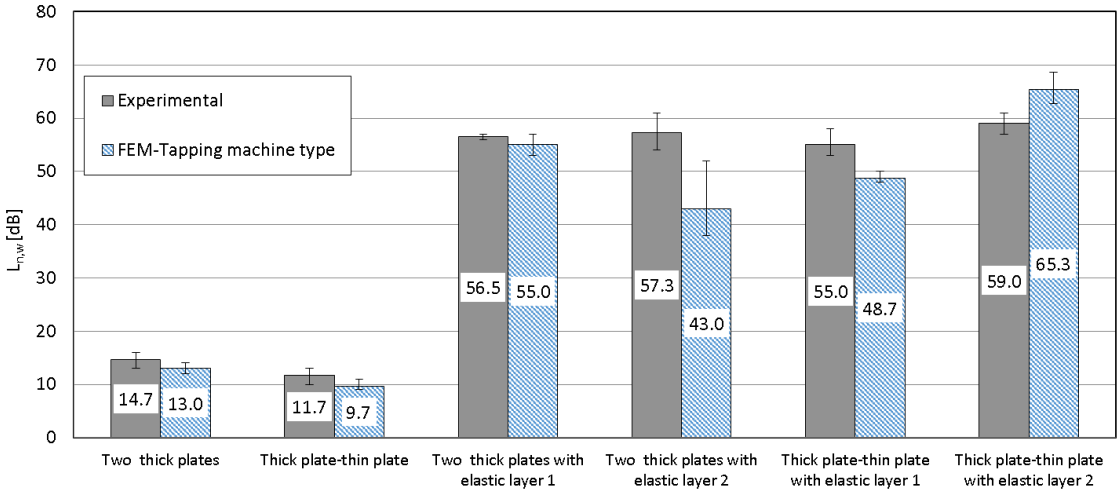

Figure 10. *Weighted normalized impact sound pressure level: average and maximum and minimum values. ($L_{n,w}$ - weighted normalized impact sound pressure level).*

5. CONCLUSIONS

The validation and calibration process allowed to make the adopted FEM model more reliable, by evaluating the differences with experimental measures and other FEM models. In this way, the most appropriate model and variability order of FEM models were determined based on the variable mesh size.

The use of randomly selected 10 points for measuring velocity produced satisfactory results in FEM models. The use of tapping machine type excitation enables to cover the desired frequency range.

The $D_{\mathrm{v,ij}}$ results for the models without an elastic layer showed a similar relationship with frequency in the experimental results and FEM models. The values averaged according to [47] showed similar results. In larger models, where the SEA can be applied with greater precision, it is expected that the FEM results achieve a better approximation to the experimental results.

In the elastic layer models 1 and 2, $D_{\mathrm{v,ij}}$ results had a similar relationship with frequency in the experimental results and in the FEM models. For the values averaged according to [47], experimental results and results of FEM models showed differences smaller than 7 dB in three of the four cases.

Worthy of note is that, even though the modal behaviour was complex in elastic layer models, and it was not possible to calibrate own frequencies very accurately, experimental and calculated results of the velocity level difference were fairly close. Therefore, it is recommended to validate FEM models using $D_{\mathrm{v,ij}}$.

As a result, FEM 2D models were developed and validated, obtaining results that were similar to those obtained through experimental measurements. This is a step forward in the use of virtual models in vibroacoustic study.

REFERENCES

[1] Hopkins, C. (2009). Experimental statistical energy analysis of coupled plates with wave conversion at the junction. Journal of Sound and Vibration, 322(1–2), 155–166. https://doi.org/http://dx.doi.org/10.1016/j.jsv.2008.10.025.

[2] Maluski, S. P. S., & Gibbs, B. M. (2000). Application of a finite-element model to low-frequency sound insulation in dwellings. The Journal of the Acoustical Society of America, 108(4), 1741–1751.

[3] Simmons, C. (1991). Structure-borne sound transmission through plate junctions and estimates of sea coupling loss factors using the finite element method. Journal of Sound and Vibration, 144(2), 215–227. https://doi.org/http://dx.doi.org/10.1016/0022-460X(91)90745-6.

[4] Mees, P., & Vermeir, O. (1993). Structure-Borne Sound Transmission at Elastically Connected Plates. Journal of Sound and Vibration, 166(1), 55–76. Retrieved from http://www.scopus.com/inward/record.url?eid=2-s2.0-0027912155&partnerID=40&md5=aa4c9d03e41a69fd5923f52476f05321.

[5] Steel, J. A., & Craik, R. J. M. (1994). Statistical Energy Analysis Of Structure-borne Sound Transmission By Finite Element Methods. Journal of Sound and Vibration, 178(4), 553–561. https://doi.org/http://dx.doi.org/10.1006/jsvi.1994.1503.

[6] Fredo, C. R. (1997). A SEA-like approach for the derivation of energy flow coefficients with a finite element model. Journal of Sound and Vibration, 199(4), 645–666. https://doi.org/http://dx.doi.org/10.1006/jsvi.1996.0634.

[7] Mace, B. R., & Shorter, P. J. (2000). Energy flow models from finite element analysis. Journal of Sound and Vibration, 233(3), 369–389. https://doi.org/http://dx.doi.org/10.1006/jsvi.1999.2812.

[8] Wang, Z. H., Xing, J. T., & Price, W. G. (2002). An investigation of power flow characteristics of L-shaped plates adopting a substructure approach. Journal of Sound and Vibration, 250(4), 627–648. https://doi.org/http://dx.doi.org/10.1006/jsvi.2001.3956.

[9] Hopkins, C. (2003a). Vibration transmission between coupled plates using finite element methods and statistical energy analysis. Part 1: Comparison of measured and predicted data for masonry walls with and without apertures. Applied Acoustics, 64(10), 955–973. https://doi.org/10.1016/S0003-682X(03)00062-8.

[10] Hopkins, C. (2003b). Vibration transmission between coupled plates using finite element methods and statistical energy analysis. Part 2: The effect of window apertures in masonry flanking walls. Applied Acoustics, 64(10), 975–997. https://doi.org/10.1016/S0003-682X(03)00063-X.

[11] EN 12354-1:2000. (2000). Building acoustics – Estimation of acoustic performance of buildings from the performance of elements. Part 1: Airborne sound insulation between rooms.

[12] Craik, R. J. M., Bosmans, I., Cabos, C., Heron, K. H., Sarradj, E., Steel, J. A., & Vermeir, G. (2004). Structural transmission at line junctions: a benchmarking exercise. Journal of Sound and Vibration, 272(3–5), 1086–1096. https://doi.org/http://dx.doi.org/10.1016/j.jsv.2003.07.011.

[13] Bochniak, W., & Cieslik, J. (2005). Uncertainty in vibration energy flow analysis. Archives of Acoustics, 30(4), 451–463. Retrieved from http://www.scopus.com/inward/record.url?eid=2-s2.0-30344435332&partnerID=40&md5=bd6e5db27fa4b674031166a4b43dba5c.

[14] Iwaniec, M. (2006). Application of genetic algorithms to the evaluation of the fundamental frequency of stiffened plates. Archives of Acoustics, 31(3), 335–346. Retrieved from http://www.scopus.com/inward/record.url?eid=2-s2.0-33748804957&partnerID=40&md5=e5382b04b868b6599160efa9449d541b.

[15] Clasen, D., & Langer, S. (2007). Finite element approach for flanking transmission in building acoustics. Building Acoustics, 14(1), 1–14. Retrieved from http://www.scopus.com/inward/record.url?eid=2-s2.0-80054806668&partnerID=40&md5=c864e8498a38f29ff9c2100ba855ea95.

[16] Du, J., Li, W. L., Liu, Z., Yang, T., & Jin, G. (2011). Free vibration of two elastically coupled rectangular plates with uniform elastic boundary restraints. Journal of Sound and Vibration, 330(4), 788–804. https://doi.org/http://dx.doi.org/10.1016/j.jsv.2010.08.044.

[17] Ramis, J., Segovia, E., Alba, J., Carbajo, J., & Godinho, L. (2012). Numerical evaluation of the vibration reduction index for structural joints. Archives of Acoustics, 37(2), 189–197.

[18] Wang, X., & Hopkins, C. (2014). Application of SEA and Advanced SEA to structure-borne sound transmission on a rectangular beam framework. In 21st International Congress on Sound and Vibration (pp. 13–17).

[19] Wawrzynowicz, A., Krzaczek, M., & Tejchman, J. (2014). Experiments and FE analyses on airborne sound properties of composite structural insulated panels. Archives of Acoustics, 39(3), 351–364. Retrieved from http://www.scopus.com/inward/record.url?eid=2-s2.0-84926616910&partnerID=40&md5=a665d43279a9029cf631a0e2be6af75d.

[20] Shi, S., Jin, G., & Chen, M. (2014). The modeling and free vibration analysis of coupled plates of various types. In D. C. D. L. M. T. B. N. Davy J. Burgess M. (Ed.), INTERNOISE 2014 - 43rd International Congress on Noise Control Engineering: Improving the World Through Noise Control. Australian Acoustical Society. Retrieved from https://www.scopus.com/inward/record.uri?eid=2-s2.0-84923625032&partnerID=40&md5=3251e2b43dc7fdd3e6352063467e2b2a.

[21] Wang, J.-F. (2014). Vibration Analysis of Moderately Thick Coupled Rectangular Plates. Proceedings of the 2014 International Conference on Mechanics and Civil Engineering, 7, 272–276. Retrieved from %3CGo.

[22] Poblet-Puig, J., & Guigou-Carter, C. (2015). Using spectral finite elements for parametric analysis of the vibration reduction index of heavy junctions oriented to flanking transmissions and EN-12354 prediction method. Applied Acoustics, 99(0), 8–23. https://doi.org/http://dx.doi.org/10.1016/j.apacoust.2015.03.025.

[23] Hopkins, C., Crispin, C., Poblet-Puig, J., & Guigou-Carter, C. (2016). Regression curves for vibration transmission across junctions of heavyweight walls and floors based on finite element methods

and wave theory. Applied Acoustics, 113, 7–21. https://doi.org/http://dx.doi.org/10.1016/j.apacoust.2016.06.002.

[24] Wilson, E. L. (2002). Three-dimensional static and dynamic analysis of structures: a physical approach with emphasis on earthquake engineering (Vol. 3). Berkeley: Computers and structures.

[25] Carson II, J. S. (2002). Model verification and validation. In Winter Simulation Conference Proceedings (Vol. 1, pp. 52–58). Retrieved from http://www.scopus.com/inward/record.url?eid=2-s2.0-0036928328&partnerID=40&md5=cb1f4e42e649d4ed80612216ebc1f0f9.

[26] Thacker, B. H., Doebling, S. W., Hemez, F. M., Anderson, M. C., Pepin, J. E., & Rodriguez, E. A. (2004). Concepts of model verification and validation. Los Alamos National Lab., Los Alamos, NM (US).

[27] Babuska, I., & Oden, J. T. (2004). Verification and validation in computational engineering and science: Basic concepts. Computer Methods in Applied Mechanics and Engineering, 193(36–38), 4057–4066. Retrieved from http://www.scopus.com/inward/record.url?eid=2-s2.0-4344712048&partnerID=40&md5=6e3e07950e831b8d7eddbfbe84c57f2c.

[28] Oberkampf, W. L., & Trucano, T. G. (2008). Verification and validation benchmarks. Nuclear Engineering and Design, 238(3), 716–743. https://doi.org/10.1016/j.nucengdes.2007.02.032.

[29] Tian, W., Yao, L., & Li, L. (2017). A Coupled Smoothed Finite Element-Boundary Element Method for Structural-Acoustic Analysis of Shell. Archives of Acoustics, 42(1), 49–59. https://doi.org/10.1515/aoa-2017-0006.

[30] Gerretsen, E. (1994). European developments in prediction models for building acoustics. Acta Acustica, 2(3), 205–214.

[31] EN ISO 10848-1:2006. (2006). Acoustics – Laboratory measurement of the flanking transmission of airborne and impact sound between adjoining rooms – Part 1: Frame document.

[32] Gerretsen, E., & Nightingale, T. R. T. (1999). Prediction models in building acoustics: Introduction to the special session at Forum Acusticum 1999 in Berlin. Building Acoustics, 6(3), 151–158. Retrieved from http://www.scopus.com/inward/record.url?eid=2-s2.0-84864689913&partnerID=40&md5=ea66a868876b8869384a94bffa00c0ad.

[33] Gerretsen, E. (2005). Development and use of prediction models in building acoustics as in EN 12354. In Forum Acusticum Budapest 2005: 4th European Congress on Acustics (pp. 1893–1899). Retrieved from http://www.scopus.com/inward/record.url?eid=2-s2.0-84864625499&partnerID=40&md5=a1b57ec07e02607cbd6df6eaf44b5cd9.

[34] Gerretsen, E. (2008). Prediction models for building performance - European need and world wide use. In Proceedings - European Conference on Noise Control (pp. 1663–1667). Retrieved from http://www.scopus.com/inward/record.url?eid=2-s2.0-84874891657&partnerID=40&md5=c4b9fba935edc3428ba3acce2c1a2860.

[35] Gerretsen, E. (2009). The development of the EN 12354 series: 1989-2009. In 8th European Conference on Noise Control 2009, EURONOISE 2009 - Proceedings of the Institute of Acoustics (Vol. 31). Retrieved from http://www.scopus.com/inward/record.url?eid=2-s2.0-84864701500&partnerID=40&md5=1a6f34a2097f36b734856411262f9324.

[36] Guyader, J. L., Boisson, C., & Lesueur, C. (1982). Energy transmission in finite coupled plates, part I: Theory. Journal of Sound and Vibration, 81(1), 81–92. https://doi.org/http://dx.doi.org/10.1016/0022-460X(82)90178-X.

[37] Boisson, C., Guyader, J. L., Millot, P., & Lesueur, C. (1982). Energy transmission in finite coupled plates, part II: Application to an L shaped structure. Journal of Sound and Vibration, 81(1), 93–105. https://doi.org/http://dx.doi.org/10.1016/0022-460X(82)90179-1.

[38] Torres, J., Cárdenas, W., Carbajo, J., Segovia, E., & Ramis, J. (2012). Estudio de la radiación en vigas utilizando la técnicas de medición de holografía de campo cercano. In VIII Congreso Ibero-americano de acústica.

[39] Molina, P., Torres, J., Segovia, E., & Ramis, J. (2014). Estudio de la transmisión de las vibraciones usando modelos a tamaño reducido. In Tecniacústica 2014. Murcia.

[40] Huang, H. C., & Hinton, E. (1986). A new nine node degenerated shell element with enhanced membrane and shear interpolation. International Journal for Numerical Methods in Engineering, 22(1), 73–92.

[41] Hughes, T. J. R., & Hinton, E. (1986). Finite element methods for plate and shell structures (Vol. 1). Pineridge Press International.

[42] Cho, T. (2013). Vibro-acoustic characteristics of floating floor system: The influence of frequency-matched resonance on low frequency impact sound. Journal of Sound and Vibration, 332(1), 33–42. https://doi.org/http://dx.doi.org/10.1016/j.jsv.2012.07.047.

[43] Magdaleno, J. (2015). Simulación numérica de la transmisión indirecta estructural y de la transmisión del ruido de impactos en edificios. Universidad de Valladolid. Retrieved from http://uvadoc.uva.es/handle/10324/16297.

[44] Mottershead, J. E., & Friswell, M. I. (1993). Model updating in structural dynamics: A survey. Journal of Sound and Vibration, 167(2), 347–375. Retrieved from http://www.scopus.com/inward/record.url?eid=2-s2.0-0027683685&partnerID=40&md5=060277b5c9f8bc0ac38fc3dd61bf18bf.

[45] Mottershead, J. E., Link, M., & Friswell, M. I. (2011). The sensitivity method in finite element model updating: A tutorial. Mechanical Systems and Signal Processing, 25(7), 2275–2296. https://doi.org/http://dx.doi.org/10.1016/j.ymssp.2010.10.012.

[46] Hopkins, C. (2007). Sound insulation. Elsevier / Butterworth-Heinemann. Retrieved from http://almena.uva.es/search~S1*spi?/tsound+insulation/tsound+insulation/1,1,1,B/frameset&FF=tsound+insulation&1,1,?save=b1634652.

[47] EN ISO 717-2:2013. (2013). Acoustics – Rating of sound insulation in buildings and of building elements – Part 2: Impact sound insulation.

Damage detection in slender structures based on a hybrid system of supervised learning algorithms and model updating to analyze raw dynamic data

Peláez, César[1]; Magdaleno, Álvaro[2]; Lorenzana, Antolín[3]

ABSTRACT

Artificial intelligence techniques applied to the Structural health Monitoring have grown significantly in recent years due to their ability to detect damage at an early stage, reducing maintenance costs and ensuring the comfort and safety to users.

The goal of this paper is the development of a hybrid system that combines the use of supervised learning algorithms (Artificial Neural Networks) with model updating, in order to detect, locate, and estimate the severity of structural damage. The hybrid approach allows to generate training data for the supervised learning algorithms from the structure model avoiding the need of experimental data from both damaged and undamaged structure scenarios. In addition, the system is intended to work in real time, therefore large data processing or parameter extraction has been avoided and raw dynamic data is analyzed instead.

The developed system has been implemented and experimentally validated on a laboratory scale structure.

Keywords: Damage detection, Hybrid system, Artificial Neural Network, Vibration-based method

1. INTRODUCTION

Structural alteration can be caused by many factors, such as design and constructive problems, operational conditions, severe natural events, natural aging, etc. In most cases, modifications in structures may be associated with damage, and when damaged, the material and geometric characteristics of a structural component change, affecting the stiffness and stability of the structure.

Conventional damage assessment methods, which depend on periodic visual inspection of structures are not efficient especially for complex structures as they require highly-trained labour and easy access to the monitored structural members. Therefore, a significant amount of research has been conducted to develop automated local and global structural health monitoring techniques [1]. Structural Health Monitoring (SHM) allows detecting the presence of damage at an early stage, thus reducing maintenance costs and ensuring more comfort and safety to the users.

[1] *Universidad de Valladolid (Spain). cesar.pelaez@uva.es (Corresponding author)*
[2] *Universidad de Valladolid (Spain). alvaro.magdaleno@uva.es*
[3] *Universidad de Valladolid (Spain). ali@eii.uva.es*

Vibration-based damage detection methods are used to assess the overall performance of the monitored structure by translating its vibration response measured by a network of accelerometers into meaningful indices reflecting the actual condition of the structure [2]. Within these vibration-based techniques, either a parametric (model-based) approach can be adopted, which consist in identifying the structure model at a certain status and comparing it with the model of the undamaged structure in order to identify and locate the modifications suffered, or a non-parametric (data-based) approach, which employs statistical means to identify the damage directly from the measured signals.

Computational learning methods are considered useful tools for solving structural damage assessment problems. These algorithms work as classifiers that try to identify damage levels using as input data characteristics extracted from dynamic responses. There have been numerous parametric and non-parametric structural damage detection methods based on machine learning techniques proposed in the literature. Among parametric methods, the most common classifiers are multi-layer feedforward artificial neural networks (ANNs) [6-12]. On the other hand, several nonparametric and machine learning based damage detection methods that use a wide range of signal processing techniques have been also used for feature extraction. These techniques include simple statistical measures [4,13], principal component analysis [14-16], wavelet transform [17] or the use of the raw dynamic data as the method input [2]. Also, different classifiers have been used in nonparametric algorithms such as ANNs [16,17], singular value decomposition [18] and support vector machine [19]. Previous studies have shown that nonparametric methods are able to distinguish damage cases that cannot be easily attributed to changes in modal parameters [20].

One of the problems of data-driven techniques lies in the need of available data from both the damaged and undamaged structure, which is not always feasible in real structures. To prevent this, the approach adopted in this paper has consisted in the implementation of a hybrid system for the identification of damage in a structure, with the aim of locating this damage and identifying the type of damage suffered and its severity. In this way, the model of the structure is used to generate data from the undamaged and damaged cases and this data is fed to a machine learning algorithm capable of classifying the structure's status based on the temporary acceleration signals.

Artificial neural networks will be used in this paper as classification algorithms. These are adaptive systems that maps input-outputs through non-linear functions. It operates by the interconnection of neurons placed in different layers. Each neuron has two adaptable parameters (weight and bias) which are optimized in the training phase. They are supervised learning systems, so it requires to be trained with data in which both input and output are known.

Therefore, the main objective of the proposed methodology in this paper resides in being able of identifying the location and severity of any structural damage in real time by processing the raw vibration signals acquired by a network of accelerometers, avoiding any feature extraction which will limit the identification time. The hybrid approach consists in, once the structure model has been obtained from a modal identification, it is used to generate training data of the damaged and undamaged structure scenarios. Then, two artificial neural networks are used, the first one to locate the presence of damage based on the temporal acceleration signals. And, once the floor or floors where the modification has occurred is defined, specific training data is generated to identify the severity of the damage suffered.

This document continues with a brief description of the case study of this paper in Section 2. Section 3 presents the proposed hybrid algorithm for damage detection. The experimental validation performed, along with the description of the tests carried out and the results and performance evaluation both in a simulation environment and on a laboratory scale structure are provided in Section 4. Finally, some discussions and conclusions, together with suggestions for future work, are given in section 5.

2. CASE STUDY

The proposed methodology has been implemented in a laboratory-scale structure consisting of a 4-story shear building. Figure 1 presents a picture of the structure together with a scheme of the associated concentrated mass model. It consists of 2 mm thick and 10 cm wide aluminium panels separated by 30 cm and 10x1x30 cm methacrylate plates that function as the base of each of the floors. These plates are supported into the aluminium panels with aluminium joint bars and steel screws on which the magnets that hold the accelerometers are placed. The natural frequencies of the base structure are found at 0.89, 2.78, 4.39 and 7.45 Hz. The building is a configurable structure where it is possible to specify both the floor number and the physical properties of each floor (mass and stiffness). In the studied case, damage is defined exclusively as a modification in the structure's mass, in a manner that makes it easy to associate the floor on which the modification has occurred. M45 nuts weighing 190.5g (Figure 2.a) have been used to alter the mass of each floor of the building in a discrete manner. The vibrational response of each of the floors has been monitored using a set of piezoelectric accelerometers (Figure 2.b). Similarly, two means were used to induce energy on the structure, first, in order to excite it with a known input, a Mutronic load cell (Figure 2.c) with a capacity of up to 500 kg and a sensitivity of 2mV/V was used. On the other hand, when developing a SHM system it is important to be able to detect modifications and damages in the structures without interacting with them, i.e., only by measuring their ambient response. To simulate this, a fan as shown in Figure 2.d has been used to transmit forces to the building in a random and uncontrolled manner.

a) *Concentrated mass model* *b) Picture of lab-scale structure*

Figure 1. *4-story shear building.*

a) M45 Nuts (added mass)

b) Piezoelectric accelerometer

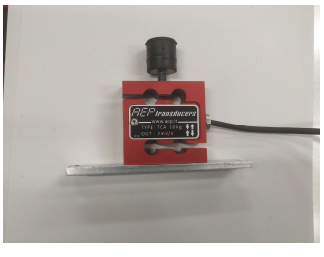

c) Concentrated mass model

d) Fan used as structure exciter

Figure 2. *Instrumentation*

Two tests have been conducted, in the first one the aim was to detect and localize the floor in which the mass has been modified. This modification consisted of the addition of two nuts (380.1 g) in one or more plants. The second test was intended not only to detect the location of the damage but also to determine its severity. The structure alterations consisted of adding from 1 to 4 nuts on one or more floors. The two tests have been validated both by simulation and experimental measurements.

3. PROPOSED HYBRID METHODOLOGY

This section describes the methodology used in the proposed hybrid algorithm for structural damage detection. Figure 3 shows the flow diagram followed by the developed algorithm. In the following paragraphs, each of the stages of the method are described.

Test 1 will only extend up to the diagnostic phase of the first neural network, while the second test will use a second neural network trained with data generated based on the first network's output. This two-phase approach [2] has been selected in order to avoid the need of using large databases storing information from all possible damage scenarios. For a 4-story building with 4 damage levels the total number of possible combinations reaches 625 cases (4^4), and this number will grow significantly when working with complex structures or with continuous rather than discrete damage levels, making the single neural network approach impractical due to computational time and storage requirements.

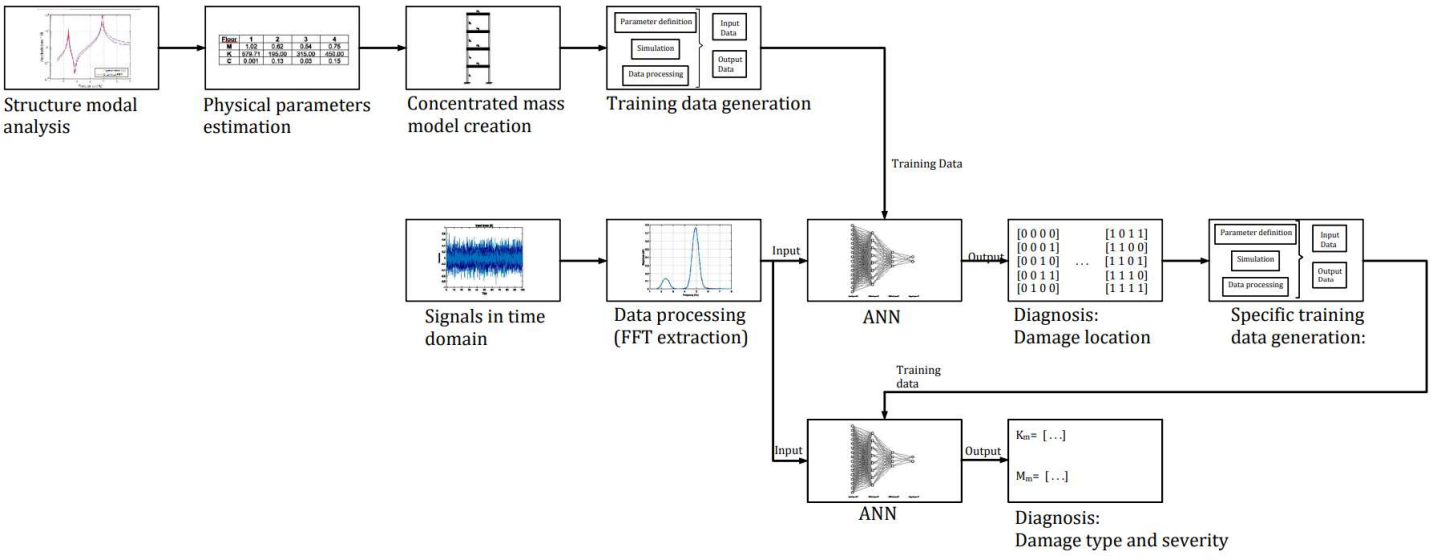

Figure 3. *Flow diagram of the proposed method*

3.1. Experimental modal analysis

The dynamics of the studied structure are identified through an experimental modal analysis (EMA), where the frequency response functions (FRF) are obtained. An impact modal analysis technique has been used, where energy is induced in the structure using a load cell and its response is measured by a set of piezoelectric accelerometers placed on each floor. Data acquisition was carried out using a Dewesoft data acquisition card, with a sampling frequency of 400 Hz.

The acquired data have been postprocessed using Matlab software to estimate the experimental FRFs by executing the *tfestimate* function, selecting a rectangular window with a size of 32768 points. Figure 4 shows the FRFs obtained, representing the system accelerance between 0 and 10 Hz.

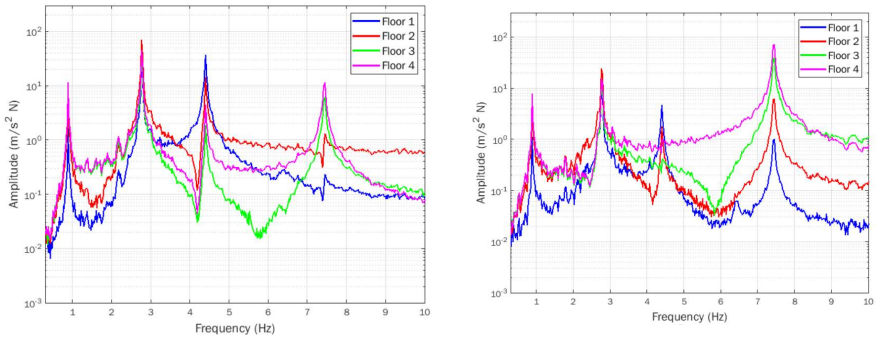

a) Impact on second floor *b) Impact on third floor*

Figure 4. *Experimental Frequency Response Functions*

3.2. Physical parameters extraction and concentrated mass model determination

The physical parameters of the structure (mass, stiffness and damping matrices) have been extracted using a curve fitting algorithm in such a way that the error between the experimental and analytical FRFs is minimized.

With the aim of determining the analytical frequency response functions of the system, its state space representation was used (Eq. 1), where the input of the system f(t) corresponds to a vector containing information about the force applied at each floor of the structure, and the output y(t) corresponds to a vector with the accelerations experienced at each floor, x(t) denotes the vector formed by the state variables of the system, selected to correlate with the position and velocity of each floor of the structure (Eq. 2).

$$\dot{x}(t) = A_{ss}x(t) + B_{ss}f(t) \tag{1}$$

$$y(t) = C_{ss}x(t) + D_{ss}f(t)$$

$$x_1(t) = \begin{pmatrix} u_1(t) \\ u_2(t) \\ u_3(t) \\ u_4(t) \end{pmatrix} \tag{2}$$

$$x_2(t) = \begin{pmatrix} \dot{u}_1(t) \\ \dot{u}_2(t) \\ \dot{u}_3(t) \\ \dot{u}_4(t) \end{pmatrix}$$

The matrices A_{ss}, B_{ss}, C_{ss} and D_{ss} are chosen to satisfy the equation of motion of the structure according to its physical properties (Eq. 3) (where M, C, K represent the mass, stiffness and damping matrices, respectively (Eq. 4)). Hence, they are expressed according to the equations presented in (Eq. 5).

$$M\ddot{u} + C\dot{u} + Ku = f(t) \tag{3}$$

$$M = \begin{bmatrix} m_1 & 0 & 0 & 0 \\ 0 & m_2 & 0 & 0 \\ 0 & 0 & m_3 & 0 \\ 0 & 0 & 0 & m_4 \end{bmatrix} \tag{4}$$

$$K = \begin{bmatrix} k_1 + k_2 & -k_2 & 0 & 0 \\ -k_2 & k_1 + k_2 & -k_3 & 0 \\ 0 & -k_3 & k_2 + k_3 & -k_4 \\ 0 & 0 & -k_4 & k_3 + k_4 \end{bmatrix}$$

$$C = \begin{bmatrix} c_1 + c_2 & -c_2 & 0 & 0 \\ -c_2 & c_1 + c_2 & -c_3 & 0 \\ 0 & -c_3 & c_2 + c_3 & -c_4 \\ 0 & 0 & -c_4 & c_3 + c_4 \end{bmatrix}$$

$$A_{ss} = \begin{bmatrix} 0 & I \\ -M^{-1}K & -M^{-1}C \end{bmatrix} \tag{5}$$

$$B_{ss} = \begin{bmatrix} 0 \\ M^{-1} \end{bmatrix}$$

$$C_{ss} = [-M^{-1}K \quad -M^{-1}C]$$

$$D_{ss} = [M^{-1}]$$

For obtaining the analytical FRFs, the Matlab function *ss* is used to create the state space model, and the *freqresp* function is then applied on the model created. Following this process, the 12 physical parameters were optimized by applying *lsqnonlin* function, whose fitness function consisted in minimizing the error between the real and imaginary parts of the FRFs for the experimental system and the one obtained with the parameters of each iteration.

The physical parameters obtained are expressed in Table 1 for the original structure without any added mass. In addition, Figure 5 shows the comparison between both experimental and analytical frequency response functions.

Table 1. Obtained physical parameters

Physical parameters	Test 1
m_1	1.10 Kg
m_2	1.70 Kg
m_3	1.54 Kg
m_4	0.81 Kg
k_1	583.9 N/m
k_2	202.7 N/m
k_3	264.9 N/m
k_4	1122.1 N/m
c_1	0.0001 Ns/m
c_2	0.0911 Ns/m
c_3	0.0772 Ns/m
c_4	0.1153 Ns/m

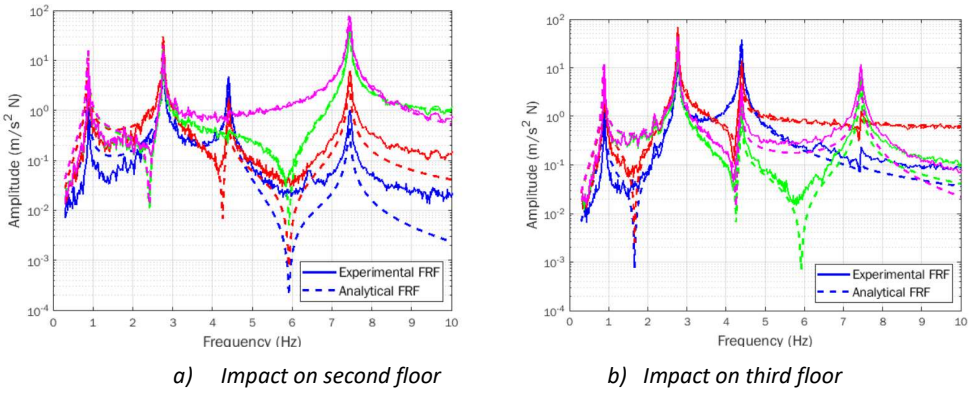

a) Impact on second floor *b) Impact on third floor*

Figure 5. *Comparison between experimental and modelled Frequency Response Functions*

3.3. Training data generation and processing

Training data is generated by following the algorithm described in Figure 6. First, the different alterations of the physical properties in the undamaged structure model are defined, in a way that the system is trained with all the potential scenarios. Next, the way of inducing energy into the structure is determined, this is a key aspect of the proposed method, since one of the assets of this algorithm resides in the capability of classifying experimentally measured scenarios without the need of previously acquiring experimental training data. Besides, another significant feature of the method is based on the use of dynamic raw data for damage detection. Consequently, it becomes crucial that the vibrational data generated by simulation correlates and resembles as closely as possible to the experimental data that will be used to validate the system, so it is important to define the way in which the system receives the excitation, since the temporal dynamic response will differ greatly if the system is excited in distinct ways (noise, sine, chirp, step, ...), or in different floors, amplitudes or frequencies.

The next step is to run the simulation with the physical variations and the defined input. The Matlab function *lsim* has been used for this purpose, setting the simulation time and the sampling frequency in 4 minutes and 1000 Hz, respectively. All the time signals sets used in this work, both in simulation and experimentally, will have this structure, meaning that these 4 vectors (1 per floor) of 240000 points (240 seg x 1000 points per second) will be the information that defines a damage scenario and from which the system must predict the structure's status, being the inputs to the black box algorithm.

These four generated signals will be submitted to a processing treatment that will consist of dividing each signal into sets of 2000 points, containing information of two-seconds intervals. After that, two approaches have been considered, the first one consists in normalizing these temporal data sets between -1 and 1, whereas the second one consists in first passing the data to the frequency domain by computing the FFT (Fast Fourier Transform) of these segments between 0.2 and 10 Hz with a resolution of 0.01 Hz and then normalizing them between 0 and 1. The efficiency of the algorithm for both approaches is evaluated in the following sections. Figure 7 compares data after time and frequency domain processing.

The next step will be to merge the four signals associated with each floor into a single vector, which will be the one feeding the neural network in the training phase, previously, since being a supervised learning system, it will be necessary to associate to each dataset the corresponding neural network output. The outputs will take the form of a matrix of 1 row and 4 columns where, for the neural network responsible of detecting the damage location, each element can take a value of 1 or 0 to indicate whether or not there is any modification in that floor, respectively. In the case of the neural network responsible of predicting the severity of the damage, the associated output will consist of the same matrix where each element will be a positive or negative integer indicating the amount of mass (expressed in number of nuts) added in that floor.

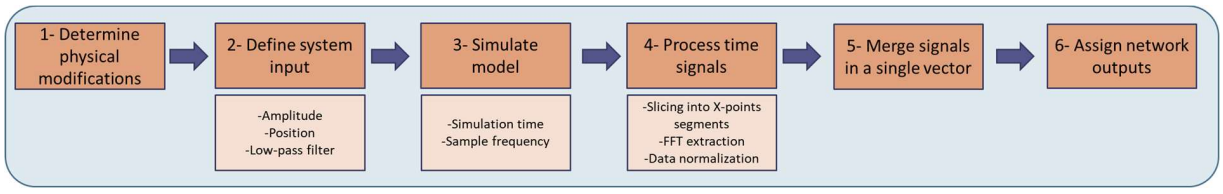

Figure 6. Flow diagram training data generation and processing

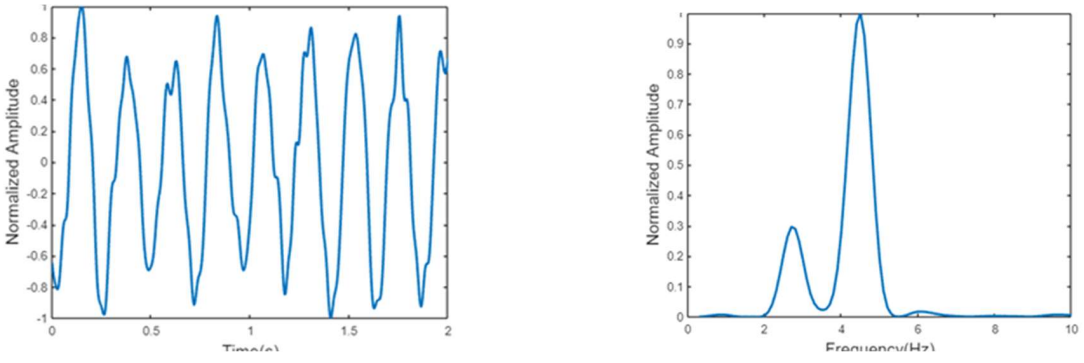

a) Input after time domain processing *b) Input after frequency domain processing*

Figure 7. *Comparison between time and frequency domain data processing.*

3.4. ANN design and training

Neural networks are adaptive systems that have been successfully used for solving various problems that cover high degrees of nonlinearity. Among the many possible ANN architectures, a Multiplayer Perceptron (MLP) has been employed to design the implemented neural network. The MLP consists in a feedforward topology composed of an input layer, one or more hidden layer and an output layer, which performs the input-output mapping through nonlinear functions. Neurons are interconnected and each connection has two associated adaptable parameters, weight and bias, adjusted by the backpropagation algorithm. The backpropagation transmits the error obtained in the output layer to the other layers and then updates the weights related to each MLP connection. The neurons take into account all connection contributions and produce an output that is a non-linear function of the sum of its inputs, aiming to minimize the error between the desired results and the network output. This iterative process is known as the training phase and stops when a specific criterion is achieved. After that, at the testing phase, the ANN model has to be able to generalize and recognize other inputs not seen during the training procedure [21].

The neural network used in the algorithm is a MLP with two hidden layers. It has been implemented in Matlab using the *feedforwardnet* function. Since MLP neural networks behave as a universal approximator, the use of two hidden layers is enough to guarantee the convergence of any regression problem. Moreover, it should be noted that there is no unanimous criterion in the literature to select the optimal value of layers or neurons per layers, instead these parameters are usually determined empirically. After some tests, the number of neurons for each hidden layer has been defined as 64 and 32, respectively. The remaining parameters established in the creation of the artificial neural network can be consulted in Table 2. A diagram of the implemented neural network can be seen in Figure 8.

Table 2. Implemented neural networks parameters

ANN Parameter	Value
Training ratio	70%
Validation ratio	15%
Test ratio	15%
Training function	Resilient Backpropagation
Perform function	MSE
Limit training epochs	10000
Limit training time	30000
Training goal	0.01
Training minimum step	1e-6
Training maximum fails	500
Training minimum gradient	1e-100
Activation/Transfer function	Log-sigmoid

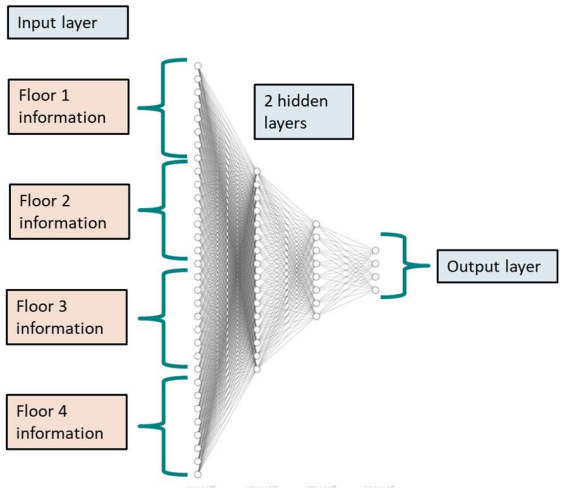

Figure 8. *Diagram of the implemented neural network.*

3.5. Output processing and diagnosis

Finally, the processing of the network output in order to obtain a diagnosis of the structure's status will consist of averaging the outputs of each segment corresponding to the same scenario. Since for each studied scenario a 4 minutes time signal (Black box input) is acquired at a sampling frequency of 1000 Hz (240000 points) and this signal is then divided into sets of 2000 points, which are introduced as neural network input, 120 outputs will be obtained (240000/2000) for each structure status, thus the output associated with a particular scenario will correspond to the average of the outputs of each set, this average will be rounded to 0 or 1 in the case of the network in charge of detecting the presence of damage, and to the nearest integer in the case of the network in charge of guessing the number of nuts added or removed, thereby establishing the diagnosis for each network.

4. VALIDATION AND RESULTS

4.1. Test 1. Detection of damage locations

In this first test the objective is set as the detection of damage presence and its location in the structure. Damage is defined as the addition of an extra mass on one or more floors. Additional mass in all cases has been remained fixed and known (2 nuts, 390 grams).

Once the system model has been obtained after experimentally performing a modal analysis on the structure, the training data is generated by simulation using the Matlab *lsim* function. The occurrence of damage is reflected by inserting the mass addition of known value (390 g) in the discrete mass model, so that there will be 16 possible scenarios with all combinations of mass location in each of the 4 floors.

The system input is defined as a normally distributed random signal of mean 0 N and variance 5N, generated with the *randn* function and applied equally on the 4 floors. These input signals are passed through a low pass filter with a 10 Hz cutoff frequency before being fed into the system. The model for each scenario is executed for a time of 4 minutes at a sampling frequency of 1000 Hz, these signals are then processed as mentioned in the previous section using two approaches, one in the time domain and the other in the frequency domain. Finally, each dataset is associated with the corresponding neural network output (from [0 0 0 0 0] for the scenario corresponding to the undamaged structure to [1 1 1 1 1] for the scenario corresponding to adding mass on all floors). After that, the artificial neural network is created and trained with the parameters defined in Table 2, resulting in the training, validation and test errors shown in Figure 9 for both processing approaches in temporal and frequency domain.

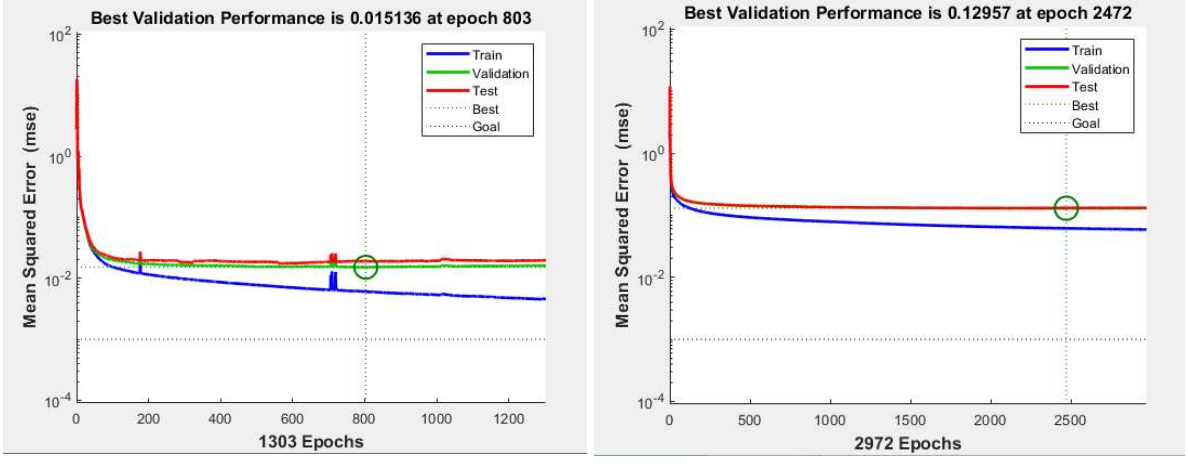

a) Frequency domain processing *b) Time domain processing*

Figure 9. Training results for Test 1 for frequency and time domain processing

Test 1. Simulation validation

The systems are then validated by simulation proceeding with the generation of 4-minute signals for each of the 16 scenarios, these signals are obtained similarly to the training data but with the addition of 5%, 10% and 20% of white noise, and also keeping a noise level of 5% but modifying the input variance (2.5, 0.5 and 10 N) and the added mass (190 and 760 g) in order to assess the reliability and robustness of the system. The signals are processed and fed to the artificial neural network, whose output is post-processed and interpreted as discussed in section 3.2.. Thus, 16 validations have been performed (8 for each type of processing). The neural network outputs for one of these validations are shown in Table 3; since the system has only two possible states for each floor (0=undamaged, 1=damaged) all network outputs above 0.5 will be interpreted as presence of damage in that floor. The red color indicates the prediction of damage in the corresponding floor while the green color indicates that the floor remains undamaged.

Table 3. ANN outputs when inputting signals with 5% noise and frequency domain processing

Damage Case	Story			
	1	2	3	4
1: [0 0 0 0]	-0.0105	0.0784	-0.0052	0.0047
2: [0 0 0 **1**]	0.0144	0.0444	0.0142	**1.0024**
3: [0 0 **1** 0]	0.0108	0.0673	**0.9543**	0.0042
4: [0 0 **1 1**]	0.0116	0.0551	**0.9754**	**1.0118**
5: [0 **1** 0 0]	0.0174	**0.9461**	0.0712	0.0013
6: [0 **1** 0 **1**]	0.0061	**0.8999**	0.0174	**0.9847**
7: [0 **1 1** 0]	0.0121	**0.9900**	**0.9663**	0.0029
8: [0 **1 1 1**]	0.0034	**0.9852**	**0.9831**	**0.9960**
9: [**1** 0 0 0]	**1.0067**	0.0365	0.0306	0.0177
10: [**1** 0 0 **1**]	**0.9928**	0.0426	-0.0041	**0.9983**
11: [**1** 0 **1** 0]	**0.9975**	0.0853	**0.9362**	0.0093
12: [**1** 0 **1 1**]	**0.9847**	0.0434	**0.9911**	**0.9986**
13: [**1 1** 0 0]	**0.9949**	**0.9969**	0.0444	0.0119
14: [**1 1** 0 **1**]	**0.9836**	**0.9799**	0.0137	**1.0002**
15: [**1 1 1** 0]	**0.9907**	**0.9821**	**0.9342**	0.0158
16: [**1 1 1 1**]	**0.9933**	**0.9727**	**0.9741**	**1.0033**

The success rate is computed as the number of correctly predicted floor states relative to the number of evaluated floor states (4x the number of assessed scenarios). Table 4 shows the performance of the systems with different processing for the different conditions evaluated. It can be seen that both systems predict all floor states successfully for all scenarios except for those in which the mass added in the validation is different from that added in the training data, emphasizing the importance of training the system with similar cases to those which will be encountered in the real structure

Table 4. Success rate for both processing approaches

Noise level	Processing	
	Time domain	Frequency domain
5% noise level	100%	100%
10% noise level	100%	100%
20% noise level	100%	100%
2.5 N input variance	100%	100%
0.5 N input variance	100%	100%
10 N input variance	100%	100%
½ added mass (190 g)	65.6%	71.9%
2x added mass (760 g)	87.5%	90.6%

Test 1. Experimental validation

Next, the experimental validation is performed, 10 validation scenarios out of the 16 possible cases have been selected. For each of them, signals of 4 minutes duration at a sampling frequency of 1000Hz have been acquired with the piezoelectric accelerometers placed in each floor. Data have been acquired with the Dewesoft data acquisition system. The structure has been excited with a fan so that the force exerted is unknown. Signals are processed and fed to the ANN, obtaining the outputs shown in Tables 5 and 6. Verifying that for both processing approaches all experimental scenarios are properly predicted with a success rate of 100%.

Table 5. ANN experimental validation outputs with frequency domain processing

Damage Case	Story			
	1	2	3	4
1: [0 0 0 0]	0.0412	0.0651	0.2366	0.0400
2: [**1** 0 0 0]	**0.9608**	0.0089	0.1738	0.1248
3: [0 **1** 0 0]	0.1038	**0.6466**	0.3117	0.3711
4: [0 0 **1** 0]	0.0964	0.2510	**0.6668**	0.2452
5: [0 0 0 **1**]	0.1120	0.1786	0.2935	**0.9926**
6: [**1** 0 **1** 0]	**0.9693**	0.1838	**0.8452**	0.1581
7: [0 **1** **1** 0]	0.0560	**0.8329**	**0.8072**	0.2794
8: [0 **1** 0 **1**]	0.0508	**0.9281**	0.3221	0.9946
9: [0 **1** **1** **1**]	0.1981	**0.9226**	**0.8167**	**0.9789**
10: [**1** **1** **1** **1**]	**1.0072**	**0.9760**	**0.8982**	**1.0019**

Table 6. ANN experimental validation outputs with time domain processing

Damage Case	Story			
	1	2	3	4
1: [0 0 0 0]	0.0699	0.2147	0.3270	0.3582
2: [**1** 0 0 0]	**0.6943**	0.3012	0.3744	0.3539
3: [0 **1** 0 0]	0.2733	**0.5307**	0.4302	0.4536
4: [0 0 **1** 0]	0.1526	0.3657	**0.5547**	0.4037
5: [0 0 0 **1**]	0.3345	0.2963	0.3680	**0.8204**
6: [**1** 0 **1** 0]	**0.7402**	0.3264	**0.5980**	0.3196
7: [0 **1 1** 0]	0.2388	**0.6952**	**0.6365**	0.4155
8: [0 **1** 0 **1**]	0.2239	**0.7384**	0.4291	0.8983
9: [0 **1 1 1**]	0.3129	**0.7959**	**0.6716**	**0.8548**
10: [**1 1 1 1**]	**0.8908**	**0.8060**	**0.6159**	**0.8378**

4.2. Test 2. Detection of damage locations and severities

The second test will aim not only to detect the presence of damage and its location, but also to predict its severity. For this purpose, 4 levels of damage have been defined, consisting of adding from 1 to 4 nuts in the different floors of the structure, for a total of 625 (4^4) possible combinations (1, 16, 96, 256 and 256 when 0, 1, 2, 3 and 4 floors are damaged). The hybrid methodology with two neural networks described in section 3 has been applied.

First, the training data of the first neural network is generated; this network must classify the structure states among the 16 possible scenarios of mass location. In order to balance the training data, 256 simulations of the model are performed for each of the 16 scenarios, since for the case of mass in the 4 floors with 4 possible levels of damage this will be the number of possible combinations, thus in the remaining cases (0, 1, 2 and 3 damaged floors), where the number of possible combinations will be 1, 4, 16 and 64, respectively, cases are repeated until 256 model simulations are executed for each mass location scenario.

4-minute signals are generated from these 4096 (256x16) scenarios. In this case, only the frequency domain processing is considered, since it reduces the dimension of the input data (when working with FFTs between 0.2 and 10 Hz with a resolution of 0.1 Hz, each neural network input has a length of 396 points (99 for each floor), while with the time domain processing the length of each input was 8000 points (2000 per floor)), significantly reducing the storage requirement.

Neural network is created with the specifications described in Table 2 and trained with this generated data. When assessing a structure state, training data for the second network is generated based on the output returned by the first neural network, so that for states with 0, 1, 2, 3 or 4 damaged floors the second network must classify among 1, 4, 16, 64 and 256 possible scenarios, respectively, thereby, data

will be generated by entering these possible scenarios in the model, and simulating and processing the corresponding 4-minute signals.

Test 2. Simulation validation

Next, the system validation is performed by simulation, generating again 4-minute acceleration signals for each of the 625 possible scenarios, adding in this case a white noise level of 5%. These signals are fed into the black box algorithm and the performance of this system is studied in Table 7. For clarity it has been avoided to show the outputs of each of the 625 cases.

It can be observed that the system successfully detects and locates 100% of the validation scenarios, and is able to predict the damage severity (expressed in the number of nuts added in each floor) in 92% of the cases. In addition, when discussing damage severity prediction, it is important to consider not only the number of predicted nuts, but to contextualize this information with the amount of added mass since when working with continuous rather than discrete damage levels, this will be more significant. In this regards, the average error of predicted added mass with respect to the added mass has been calculated, obtaining a mean error of 39.8 grams, which can be considered very acceptable.

Table 7. Success rate for Test 2: simulation validation

	Number of scenarios	Succes rate	
		ANN 1	ANN2
Undamaged	1	100%	100%
1 Floor damaged	16	100%	89.06%
2 Floor damaged	96	100%	90.89%
3 Floor damaged	256	100%	90.82%
4 Floor damaged	256	100%	93.85%
Total	625	100%	92.04%

Test 2. Experimental validation

Finally, the experimental validation consisted of experimentally acquiring signals corresponding to 21 different scenarios, and introducing these signals into the developed algorithm.

Tables 8 and 9 show the outputs of the first and second neural networks for each damage case. And Table 10 shows the success rates for the different validation scenarios. It can be observed that the system successfully predicts the location of the damage in all cases. It is also clearly seen how the success rate in predicting the severity of the damage decreases as the number of damaged floors increases, since the classification task becomes more complex when having more scenarios to take into account. Even so, the system performance is still reasonably satisfactory and the mean error in the prediction of the added mass is 64 grams.

Table 8. ANN1 experimental validation outputs

Damage Case	Story			
	1	2	3	4
1: [0 0 0 0]	0.0671	0.2276	0.3291	0.0633
2: [**1** 0 0 0]	**0.6230**	0.2859	0.3933	0.0647
3: [0 **1** 0 0]	0.0681	**0.8975**	0.4593	0.0938
4: [0 0 **1** 0]	0.0782	0.3673	**0.9507**	0.2075
5: [0 0 0 **1**]	0.0901	0.3300	0.4706	**1.0118**
6: [**1** 0 0 **1**]	**0.9880**	0.2144	0.2749	**0.8306**
7: [0 **1** 0 **1**]	0.3125	**0.9485**	0.4008	**0.9909**
8: [**1 1 1** 0]	**0.9925**	**0.7365**	**0.9360**	0.1694
9: [**1** 0 **1 1**]	**0.9819**	0.3932	**0.9273**	**1.0028**
10: [**1 1 1 1**]	**0.9657**	**0.8881**	**0.8501**	**0.9861**
11: [**1 1 1 1**]	**0.9863**	**0.8677**	**0.8610**	**0.9530**
12: [**1 1 1 1**]	**0.9912**	**0.9575**	**0.8610**	**0.9633**
13: [**1 1 1 1**]	**0.9396**	**0.9388**	**0.9047**	**0.9654**
14: [**1 1 1 1**]	**1.0110**	**0.9769**	**0.8182**	**0.9990**
15: [**1 1** 0 **1**]	**0.9919**	**0.8933**	0.3206	**0.9716**
16: [**1 1 1 1**]	**1.0101**	**0.8752**	**0.8950**	**0.9824**
17: [**1 1** 0 **1**]	**0.9984**	**0.9139**	0.3954	**0.9735**
18: [**1 1 1 1**]	**1.0080**	**0.9375**	**0.8943**	**0.9891**
19: [0 0 **1 1**]	0.1274	0.3396	**0.9556**	**1.0031**
20: [0 **1 1 1**]	0.2225	**0.9103**	**0.9274**	**0.8854**
21: [**1 1** 0 **1**]	**0.9471**	**0.9515**	0.3788	**0.9925**

Table 9. ANN2 experimental validation outputs

Damage Case	Story			
	1	**2**	**3**	**4**
1: [0 0 0 0]	0	0	0	0
2: [1 0 0 0]	1.4439	0	0	0
3: [0 2 0 0]	0	2.3724	0	0
4: [0 0 3 0]	0	0	2.6851	0
5: [0 0 0 4]	0	0	0	3.5153
6: [3 0 0 1]	1.6566	0	0	2.1594
7: [0 4 0 3]	0	4.0887	0	3.2204
8: [2 1 3 0]	1.6098	1.7439	3.5970	0
9: [3 0 2 2]	2.2082	0	3.3572	2.4736
10: [1 2 3 3]	1.0504	3.2162	3.6227	3.4468
11: [2 2 2 2]	1.9596	2.4662	2.7036	2.7800
12: [3 2 2 2]	2.5931	2.4793	2.6176	2.2805
13: [1 2 2 2]	1.1269	2.4793	2.8648	2.3456
14: [2 4 2 2]	2.0019	3.8312	3.1169	2.5563
15: [2 2 0 2]	1.5686	2.3243	0	2.2158
16: [2 2 2 3]	1.9892	2.7906	2.8317	3.3434
17: [4 2 0 2]	2.8800	2.6089	0	2.1750
18: [2 3 2 3]	2.0428	3.4567	3.0506	3.0423
19: [0 0 2 2]	0	0	3.1066	2.3580
20: [0 2 3 1]	0	2.3574	3.0700	1.6969
21: [1 4 0 3]	1.300	4.0962	0	3.3853

Table 10. Success rate for Test 2: simulation validation

	Number of scenarios	**Succes rate**	
		ANN 1	**ANN2**
Undamaged	1	100%	100%
1 Floor damaged	4	100%	100%
2 Floor damaged	3	100%	75%
3 Floor damaged	6	100%	70.83%
4 Floor damaged	7	100%	60.71%
Total	21	100%	75%

5. CONCLUDING REMARKS

A system capable of detecting damage in a structure has been developed by applying machine learning and automatic learning methodology. The objectives of the developed paper can be mainly summarized as the following three.

Firstly, the aim was to develop a black box algorithm that could detect damage in a structure, locating this damage and predicting its severity. This has been achieved and has been implemented experimentally on a laboratory-scale structure, achieving 100% efficiency in the detection and localization of the damage, as well as 75% in the prediction of its severity, with an average error of 64 grams in the prediction of added mass (corresponding to damage in the studied structure).

Another important feature of the developed algorithm is that it allows to establish a diagnosis of a structure state without the need for complex processing of the measured data. The predictions are made on the basis of experimentally obtained 4-minute acceleration signals. Thus, the developed system could be used for real-time damage detection when implemented on hardware that supports it.

Finally, one of the limitations of SHM systems based on supervised learning algorithms described in the literature lies in the need of training data from the undamaged and damaged structure. This is not feasible in real structures, hence the approach adopted in this paper has consisted in the development of a hybrid system in which the training data is generated by simulating the structure model obtained by performing an experimental modal analysis on it.

The next steps of this work will consist of being able to detect the location and severity of different types of damage and classifying them. For example, differentiating between changes in mass and stiffness and predicting the severity of each.

In addition, this methodology will be applied to more complex structures and will be implemented on hardware that allows real-time damage detection.

ACKNOWLEDGEMENTS

This research was partially funded by the Ministerio de Economía y Competitividad, Spanish Government, through the research project number RTI2018-098425

REFERENCES

[1] *Anton S.R., Inman D.J., Park G., (2009) Reference-free damage detection using instantaneous baseline measurements. AIAA J. 47 (2009) 1952-1964.*
[2] *Abdeljaber O. et al., (2016) Real-time vibration-based structural damage detection using one-dimensional convolutional neural networks. Journal of Sound and Vibration (2016).*
[3] *Alves V., et al., (2015). Structural modification assessment using supervised learning methods applied to vibration data. Engineering Structures, 99, 439-448.*

[4] *Finotti R.P., et al., (2018). An SHM approach using machine learning and statistical indicators extracted from raw dynamic measurements. Latin American Journal of Solid and Structures, 2019, 16(2), e165.*

[5] *Doebling S.W, Farrar C.R., Prime M.B., Shevirz D., (1998) A review of damage identification methods that examines changes in dynamic properties. Shock and Vibration Digest, 30(2), 91-105.*

[6] *S.J.S. Hakim, H. Abdul Razak, S.A. Ravanfar, Fault diagnosis on beam-like structures from modal parameters using artificial neural networks, Measurement 76 (2015) 45–61.*

[7] *C. Ng, Application of Bayesian-designed artificial neural networks in Phase II structural health monitoring benchmark studies, Aust. J. Struct. Eng. 15 (2014). 27–37.*

[8] *L.D. Goh, N. Bakhary, A.A. Rahman, B.H. Ahmad, Prediction of unmeasured mode shape using artificial neural network for damage detection, J. Teknol. (Sci. Eng.) 61 (2013) 57–66.*

[9] *M. Mehrjoo, N. Khaji, H. Moharrami, A. Bahreininejad, Damage detection of truss bridge joints using artificial neural networks, Expert Syst. Appl. 35 (2008) 1122–1131.*

[10] *M. Betti, L. Facchini, P. Biagini, Damage detection on a three-storey steel frame using artificial neural networks and genetic algorithms, Meccanica 50 (2014) 875–886.*

[11]*P.M. Pawar, K. Venkatesulu Reddy, R. Ganguli, Damage detection in beams using spatial fourier analysis and neural networks, J. Intell. Mater. Syst. Struct. 18 (2006) 347–359.*

[12]*K. V. Yuen, H.F. Lam. On the complexity of artificial neural networks for smart structures monitoring. Engineering Structures 28 (2006) 977–984*

[13]*P. Chun, H. Yamashita, S. Furukawa, Bridge damage severity quantification using multipoint acceleration measurement and artificial neural networks, Shock Vib. 2015 (2015).*

[14]*U. Dackermann, J. Li, B. Samali, Dynamic-based damage identification using neural network ensembles and damage index method, Adv. Struct. Eng. 13 (2010) 1001–1016.*

[15]*U. Dackermann, W.A. Smith, R.B. Randall, Damage identification based on response-only measurements using cepstrum analysis and artificial neural networks, Struct. Health Monit. 13 (2014) 430–444.*

[16]*R.P. Bandara, T.H.T. Chan, D.P. Thambiratnam, The three-stage artificial neural network method for damage assessment of building structures, Austr. J. Struct. Eng. 14 (2013).*

[17]*Y.-Y. Liu, Y.-F. Ju, C.-D. Duan, X.-F. Zhao, Structure damage diagnosis using neural network and feature fusion, Eng. Appl. Artif. Intell. 24 (2011) 87–92.*

[18]*E. Figueiredo, G. Park, C.R. Farrar, K. Worden, J. Figueiras, Machine learning algorithms for damage detection under operational and environmental variability, Struct. Health Monit. 10 (2011) 559–572.*

[19]*A. Santos, E. Figueiredo, M.F.M. Silva, C.S. Sales, J.C.W.A. Costa, Machine learning algorithms for damage detection: kernel-based approaches, J. Sound Vib. 363 (2016) 584–599.*

[20]*M. Gul, F. Catbas, Damage assessment with ambient vibration data using a novel time series analysis methodology, J. Struct. Eng. 137 (2010) 1518–1526.*

[21]*N.R. Euliano, J.C. Proncipe, W.C. Lefebvre. Neuroal and adaptive systems: fundamentals through simulations. John Wiley & Sons (2020).*

Estimation of short-term deflection in RC beams using effective moments of inertia

Gil-Martín, Luisa María[1]; Fernández-Ruíz, M. Alejandro[2] ; Carbonell-Márquez, Juan Francisco[3]; Hernández-Montes, Enrique[4]

ABSTRACT

International practice codes for the design of RC structures use linear elastic formulation to calculate deflections by double integration of curvatures along the length of the element. If the member is cracked, different formulae of interpolation between uncracked and fully cracked states have been proposed in order to account for the concrete tension stiffening effect. American and Canadian codes consider an interpolation formula in order to achieve an equivalent moment of inertia, whereas Eurocode 2 makes use of a mechanic-based approach. Based on the formulation given by Eurocode 2 an equivalent inertia is achieved, resulting in a straightforward process to compute deflections. A comparison of the short-term deflections obtained from both procedures is carried out, concluding that both the Branson´s approximation and the procedure of Eurocode 2 are very similar when deflections are relevant. Two detailed experimental campaigns are analyzed to support these conclusions.

Keywords: Equivalent inertia; immediate deflection; tension stiffening.

Nomenclature

b	Width of the rectangular cross-section of concrete
d	Effective depth of the cross-section
E_s	Modulus of elasticity of steel
E_c	Modulus of elasticity of concrete
I	Moment of inertia of the section
I_{cr}	Moment of inertia of the cracked section transformed to concrete
I_e	Effective moment of inertia for calculation of deflection
I_g	Moment of inertia of the gross section
I_{uncr}	Moment of inertia of the uncracked section transformed to concrete
L	Length of beam span
M_{cr}	Cracking moment
δ	Deflection at mid-span of a simply supported beam subjected to a uniformly distributed load
δ_{cr}	Deflection at mid-span of a simply supported beam subjected to a uniformly distributed load associated to Mcr.
n	Steel to concrete moduli of elasticity ratio

[1] *Department of Structural Mechanics. University of Granada (SPAIN). mlgil@ugr.es (Corresponding author)*
[2] *Department of Industrial and Civil Engineering. University of Cádiz (SPAIN). manuelalejandro.fernandez@gm.uca.es*
[3] *Department of Mechanics. Universidad de Córdoba (SPAIN). jcarbonell@uco.es*
[4] *Department of Structural Mechanics, University of Granada (SPAIN). emontes@ugr.es*

ϕ Curvature of the section
ρ Tension reinforcement ratio

1. INTRODUCTION

One of the serviceability limit states that a reinforced concrete (RC) structure needs to fulfil is the deflection control. Deformations beyond a certain limit given by standard codes must not occur. In this regard, Eurocode 2 (EC2) [1] presents similar limitations to the ACI-318-19 [2] and CSA-A23.3-19 [3]. In EC2 [1], the deflection of a beam, slab or cantilever, computed under quasi permanent loads, is limited to *L/250* for total deflection and L/500 for deflection after, *L* being the span between supports. As a serviceability limit state, the study of deformations is carried out without magnification of loads and therefore, the study of deformations is conducted based on linear elasticity.

Members in RC structures are usually divided into two types of zones or regions: B regions, where plane section hypothesis can be applied, and D regions, where this is applied. When dealing with deformations of an RC member in the linear range, deformation in the D regions are usually neglected, that is, the nodes are considered to be rigid in the linear elastic range. Therefore, the deformation of the member is mainly due to the deformation of the B regions and the study of deflections is done by means of a differential equation that connects the curvature with the deflection of an elastic beam under flexure:

$$y''(x) = \frac{d^2 y(x)}{dx^2} \approx \phi(x) = \frac{M(x)}{EI} \tag{1}$$

where x is the coordinate along an axis that coincides with the longitudinal axis of the member, y(x) is the deformed shape of the element due to the bending moment distribution M(x), ϕ(x) is the curvature of the section placed at x, E is the modulus of elasticity of the material and I is the moment of inertia of the section. In Eq. (1) it is assumed that deflections are small enough and that the beam theory is applicable.

When dealing with RC structures, it is common to assume properties of sections transformed to concrete and $E=E_c$. However, an important issue arises when employing Eq. (1) to compute deflections: what is the moment of inertia *I* to be used in calculations? If the bending moment along the member is lower than the cracking moment, $M(x) \leq M_{cr}$, the moment of inertia *I* to be used would be that which corresponds to the transformed uncracked section, I_{uncr}. Conversely, if along a portion of the RC member $M(x) > M_{cr}$ then some sections of the member within that length would be cracked and their moment of inertia would be I_{cr}. The mean contribution of concrete in tension in the cracked areas (where $M(x) > M_{cr}$) is known as the tension-stiffening effect, which indicates the capability of concrete between cracks to carry the tensile stress through the concrete-rebar interaction, contributing to the tensile stiffness of RC structures [4,5]. Therefore, an intermediate value of *I* between I_{cr} and I_{uncr} needs to be used to calculate short-term deflections.

The present work provides a discussion on the value of *I* to be introduced in Eq. (1) in order to get an accurate computation of the short-term deflection of an RC member. In order to do so, the method based on the effective moment of inertia proposed by Branson [6] is compared with the one proposed by EC2 [1]. The comparison is applied to two experimental campaigns available in literature.

2. SHORT-TERM DEFLECTIONS BASED ON THE BRANSON´S EFFECTIVE MOMENT OF INERTIA

ACI-318 deals with calculation of immediate deflections and states that they should be computed by means of linear elastic methods, i.e. Eq.(1), taking into account the effects of cracking and reinforcement on member stiffness. ACI-318-14 [7] proposed the employment of an effective moment of inertia, I_e, developed by Branson [6], to estimate short-term deflections:

$$I_e = \left(\frac{M_{cr}}{M_a}\right)^3 I_g + \left[1 - \left(\frac{M_{cr}}{M_a}\right)^3\right] I_{cr} \leq I_g \tag{2}$$

This expression for the effective moment of inertia is also adopted by the Canadian Standard CSA-A23.3-19 [3].

In Eq.(2) M_a is the maximum moment in a member at stage deflection is calculated and I_g is the moment of inertia of the gross section. It should be noted that Eq.(2) considers I_e as a weighted average value of I_{cr} and I_g. In the former expression, it has been assumed that: $I_{uncr} = I_g$, which is true in most cases except for heavily reinforced sections. This is proved valid in [8].

Eq. (2) does not account for shrinkage or any other effect related to time because factors influencing long-term effects are not included. Another important factor that should be noted is that I_e given by Eq. (2) is taken constant along the RC member, that is, it is an average stiffness over the entire span.

Regarding this issue, ACI-318 §24.2.3.7 states that when dealing with prismatic beams, I_e can be taken as the value obtained with Eq. (2) evaluated at the mid-span for simple and continuous spans, and at the support for cantilever beams. Commentary R24.2.3.7 states in this regard that the mid-span stiffness has the dominant effect on deflections of the member, accounting for cracking.

Finally, once the effective inertia is computed, the deflection is obtained by twofold integration of Eq. (1).

3. EC2 METHOD TO COMPUTE SHORT-TERM DEFLECTIONS

Deflections in a cracked RC member are also computed in EC2 [1] using the linear elastic equation Eq. (1). In this case, following the well-known CEB report number 158 [9], the EC2 §7.4.3 interpolates the curvature of a section in the cracked portions of an RC member, ϕ, between two different states: state I, ϕ_I, in which the section is assumed to be uncracked and concrete is supposed to withstand any value of tension without limit, and state II, ϕ_{II}, in which the section is fully cracked:

$$\phi = (1-\zeta)\phi_I + \zeta\phi_{II} \quad \text{being} \quad \zeta = 1 - \beta\left(\frac{\sigma_{sr}}{\sigma_s}\right)^2 \tag{3}$$

σ_{sr} being the tensile stress in the reinforcement calculated on the basis of a cracked section under the loading conditions causing first cracking and σ_r the tensile stress under which the curvature is computed ($\sigma_s \geq \sigma_{sr}$). As short term loads are under consideration, the parameter β that takes into account the duration of loads is equal to 1, and as deflections due to flexure are to be computed, σ_{sr}/σ_r can be replaced by M_{cr}/M, M being the bending moment applied to the section where the curvature is calculated and M_{cr} the cracking moment. Assuming that reinforcement is not constant along the length of the member and taking into account that curvatures in states I and II can be written as:

$$\phi_I = \frac{M}{E_c I_{uncr}} \tag{4}$$

$$\phi_{II} = \frac{M}{E_c I_{cr}}$$

the curvature of a section placed at x is given by:

$$\phi(x) = \left(\frac{M_{cr}(x)}{M(x)}\right)^2 \frac{M(x)}{E_c I_{uncr}(x)} + \left[1 - \left(\frac{M_{cr}(x)}{M(x)}\right)^2\right] \frac{M(x)}{E_c I_{cr}(x)} \geq \frac{M(x)}{E_c I_{uncr}(x)} \tag{5}$$

EC2 [1] § 7.4.3 (7) states that the most rigorous computation of deflections will imply the twofold integration of Eq. (5) along the length of the RC member.

Moreover, EC2 [1] adds that acceptable solutions for deflection can be obtained as:

$$y(x) = \left(\frac{M_{cr}(x)}{M(x)}\right)^2 y_I(x) + \left[1 - \left(\frac{M_{cr}(x)}{M(x)}\right)^2\right] y_{II}(x) \tag{6}$$

with $y_I(x)$ and $y_{II}(x)$ as the deflections assuming the whole member is in the uncracked state and considering all the sections of the member fully cracked, respectively.

$$\begin{aligned} y_I(x) &= \iint_x \phi_I(\chi)\, d\chi = \iint_x \frac{M(\chi)}{E_c I_{uncr}(\chi)}\, d\chi \\ y_{II}(x) &= \iint_x \phi_{II}(\chi)\, d\chi = \iint_x \frac{M(\chi)}{E_c I_{cr}(\chi)}\, d\chi \end{aligned} \tag{7}$$

4. EFFECTIVE MOMENT OF INERTIA BASED ON EC2 FORMULATION

Whether the most rigorous method integrating the interpolation of the curvature of each section along the member or the simpler method interpolating the uncracked and cracked deflections, the EC2 [1] approach turns out to appear more complex than the ACI-318 method. However, an equivalent effective moment of inertia to be introduced in Eq. (1) can be deducted from the formulation of EC2 [1] as follow.

As stated above, curvature $\phi(x)$ can be written as:

$$\phi(x) = \frac{M(x)}{E_c I(x)} = \left(\frac{M_{cr}(x)}{M(x)}\right)^2 \frac{M(x)}{E_c I_{uncr}(x)} + \left[1 - \left(\frac{M_{cr}(x)}{M(x)}\right)^2\right] \frac{M(x)}{E_c I_{cr}(x)} \tag{8}$$

The former expression can be simplified yielding:

$$\frac{1}{I(x)} = \left(\frac{M_{cr}(x)}{M(x)}\right)^2 \frac{1}{I_{uncr}(x)} + \left[1 - \left(\frac{M_{cr}(x)}{M(x)}\right)^2\right] \frac{1}{I_{cr}(x)} \tag{9}$$

Accounting the commentary R24.2.3.7 of ACI-318that, for continuous prismatic members, mid-span stiffness has the dominant effect on deflections:

$$\frac{1}{I_e}=\frac{1}{I(x)}\bigg|_{x=L/2}=\left(\frac{M_{cr}(x)}{M(x)}\right)^2\frac{1}{I_{uncr}(x)}+\left[1-\left(\frac{M_{cr}(x)}{M(x)}\right)^2\right]\frac{1}{I_{cr}(x)}\bigg|_{x=L/2} \tag{10}$$

And, therefore, effective moment of inertia, I_e, is given by:

$$I_e=\frac{I_{cr}}{1-\left(1-\frac{I_{cr}}{I_g}\right)\left(\frac{M_{cr}}{M}\right)^2} \tag{11}$$

all the parameters implicit in Eq. (11) being evaluated at mid-span (x=L/2). In Eq.(11), the moment of inertia of the uncracked section transformed to concrete, I_{uncr}, has been replaced by the moment of inertia of the gross section, I_g, just as in the Branson´s equation, Eq.(2).

Effective moment of inertia given by Eq.(11) is the one proposed by Bischoff [8], which has been proved to have sufficient accuracy for a wide range of reinforcement ratios. In order to overcome the underestimation of the deflections given by the Branson´s equation (Eq. (2)) in the case of members with low reinforcement ratios, the last version of the ACI-318-19 [2] has adopted the effective moment of inertia approximation proposed by Bischoff [8] but considering two-thirds of the full value of the cracking moment specified [10,11].:

$$I_e=\begin{cases} I_g & if \quad M_a\le 2/3M_{cr} \\ \dfrac{I_{cr}}{1-\left(\frac{2/3M_{cr}}{M_a}\right)^2\left(1-\frac{I_{cr}}{I_g}\right)} & if \quad M_a>2/3M_{cr} \end{cases} \tag{12}$$

So, once I_e is computed from Eq. (11), the deflection is obtained by twofold integration of Eq. (1).

Eq. (11) is applicable only when dealing with immediate deflections since none of the parameters implicit in it includes any shrinkage or creep effects. In this regard, an equation similar to Eq. (11) is also given in [12], Eq. (3.29), but the parameter β, of duration of loads, is explicitly considered in it even for the calculation of instantaneous deflection, in order to account for the shrinkage which could occur before the first loading. A serious concern may arise in this consideration since the available data of β in the literature barely allow for this subtlety.

As was already mentioned, the effective moments of inertia, I_e, proposed by Branson [6] in Eq. (2) is overestimated for low values of reinforcement ratios [8,12]. According to [8], non-reasonable values of I_e are obtained for $I_g/I_{cr}>3$ which corresponds to reinforcement ratios $\rho<0.01$, or when $\rho<0.005$ according to [12] (see Figure A.1). This fact is also pointed out in [13].

Since short-term deflections are underestimated for lightly reinforced concrete members, an upper limit on I_e given by Eq. (2) and Eq. (9) is imposed in [12]:

$$I_e\le\begin{cases} I_{uncr} & \text{if} \quad I_g/I_{cr}<3 \\ 0.6I_{uncr} & \text{if} \quad I_g/I_{cr}\ge 3 \end{cases} \tag{13}$$

5. DISCUSSION: COMPARISON OF EFFECTIVE MOMENTS OF INERTIA PROPOSED BY BRANSON [6] AND BISCHOFF [8]

In order to better understand the differences between effective moments of inertia, I_e, proposed by Branson [6] (CSA-A23.3-19 [3]) and Bischoff [8] (EC2 [1] and ACI-318-19 [2]) and the influence of the reinforcement ratio in those differences, Figure 1.a and 1.b show the value of I_e, normalized by I_g, in terms of the ratio applied bending moment to cracking moment, M_{cr}/M, computed according to Eqs. (2) and (11), CSA-A23.3-19 [3] and EC2 [1] respectively, for different values of the ratio I_g/I_{cr}. Figue 1.c and 1.d show the differences of Eqs.(2) and (11), also normalized by I_g.

Values of I_g/I_{cr} in the range of the parametric study carried out by Branson [6] have been considered. Figure 1.a and 1.b correspond to $I_g/I_{cr} < 3$ and $I_g/I_{cr} \geq 3$, respectively. The limitation proposed by [12] and given in Eq.(13) has been represented with a horizontal gray line in Figure 1.b and dashed lines in Figure 1.c. Since, for a given ratio $I_g/I_{cr} \geq 3$, the corresponding value of M_{cr}/M in which the limitation in Eq.(13) is reached is different when comparing Eq. (2) and Eq. (11), an average value has been adopted when plotting the dashed lines in Figure 1.d.

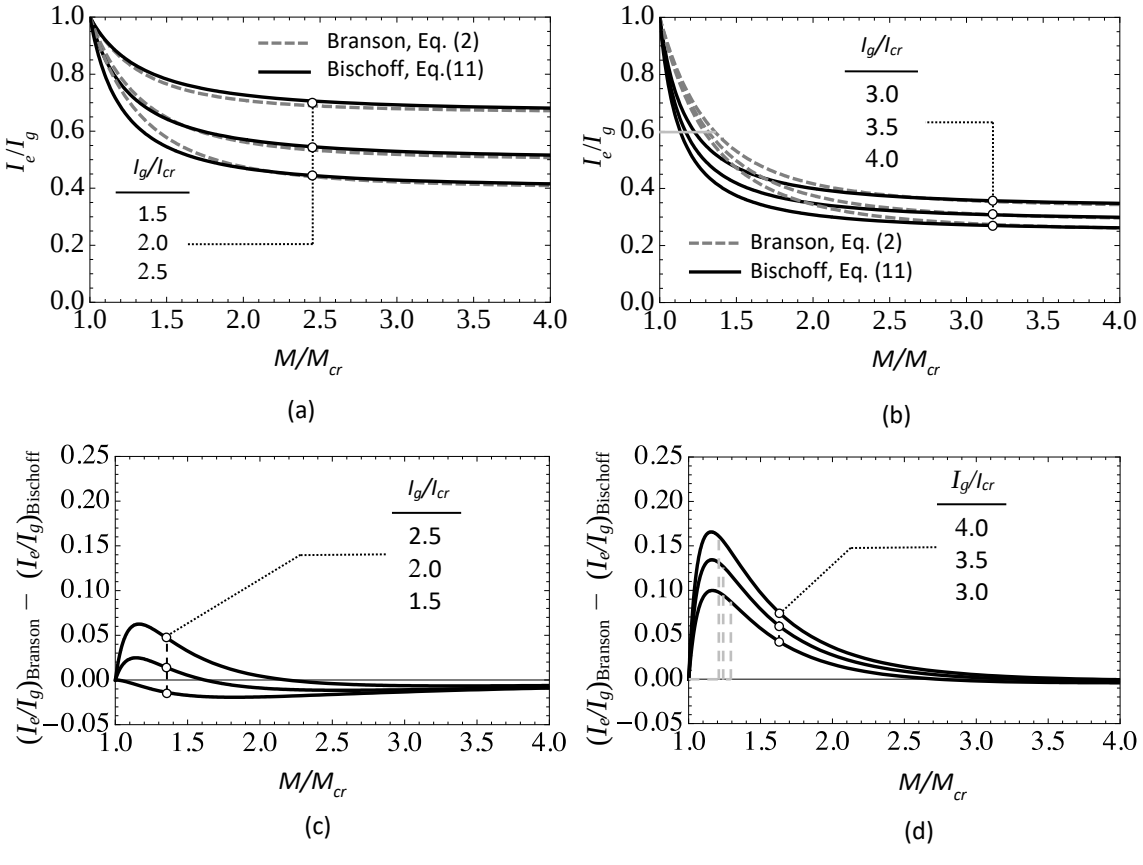

Figure 1. *Comparison between effective moment of inertia, I_e, computed by means of Branson's formula, Eq. (2), and formula obtained from EC2, Eq. (11) in terms of the ratio M/ M_{cr}: (a) values of I_e normalized by I_g for $I_g/I_{cr} < 3$, (b) values of I_e normalized by I_g for $I_g/I_{cr} \geq 3$, (c) difference between I_e computed by means of Eq. (2) and Eq. (9), again normalized by I_g for $I_g/I_{cr} < 3$ and (d) difference between I_e computed by means of Eq. (2) and Eq. (9), again normalized by I_g for $I_g/I_{cr} \geq 3$.*

In light of Figure 1, it can be concluded that, for rectangular RC cross sections with only tension reinforcement, in cases of ratios $I_g/I_{cr}< 3$ (that for $n=6$, with $f_c' = 35$ MPa, corresponding approximately to $\rho \geq 0.5\%$, see Appendix) the differences between equivalent moment of inertia computed according to Branson [6], Eq. (2), and according to EC2 [1], Bischoff´s expression given by Eq. (11), are under 5% I_g. In particular for $M \geq 1.5M_{cr}$ both values of the equivalent moment of inertia can be considered equal. This corresponds to the range of reasonable accuracy of the Branson equation according to [8] and [12].

Furthermore, regardless of the ratio I_g/I_{cr}, if the moment applied at mid-span of the member, M, is 2.5 times the cracking moment, M_{cr}, i.e. $M/M_{cr}=2.5$, the values of the equivalent inertia calculated from Eqs. (2) and (11) are almost the same.

Eq. (2) and Eq. (11) can be used to directly compute short-term deflections as a function of M/M_{cr} and I_g/I_{cr}. Let us consider a simply supported beam subjected to a uniformly distributed load. The deflection at mid-span can be calculated from the elastic formulae: $\delta = \frac{5M\,l^2}{48E_cI_e}$. In Figures 2.a and 2.b the moment-deflection curves normalized by the cracking value obtained from Branson and Bischoff expressions have been represented (Eq. (2) and Eq. (11), respectively) for different values of I_g/I_{cr}.

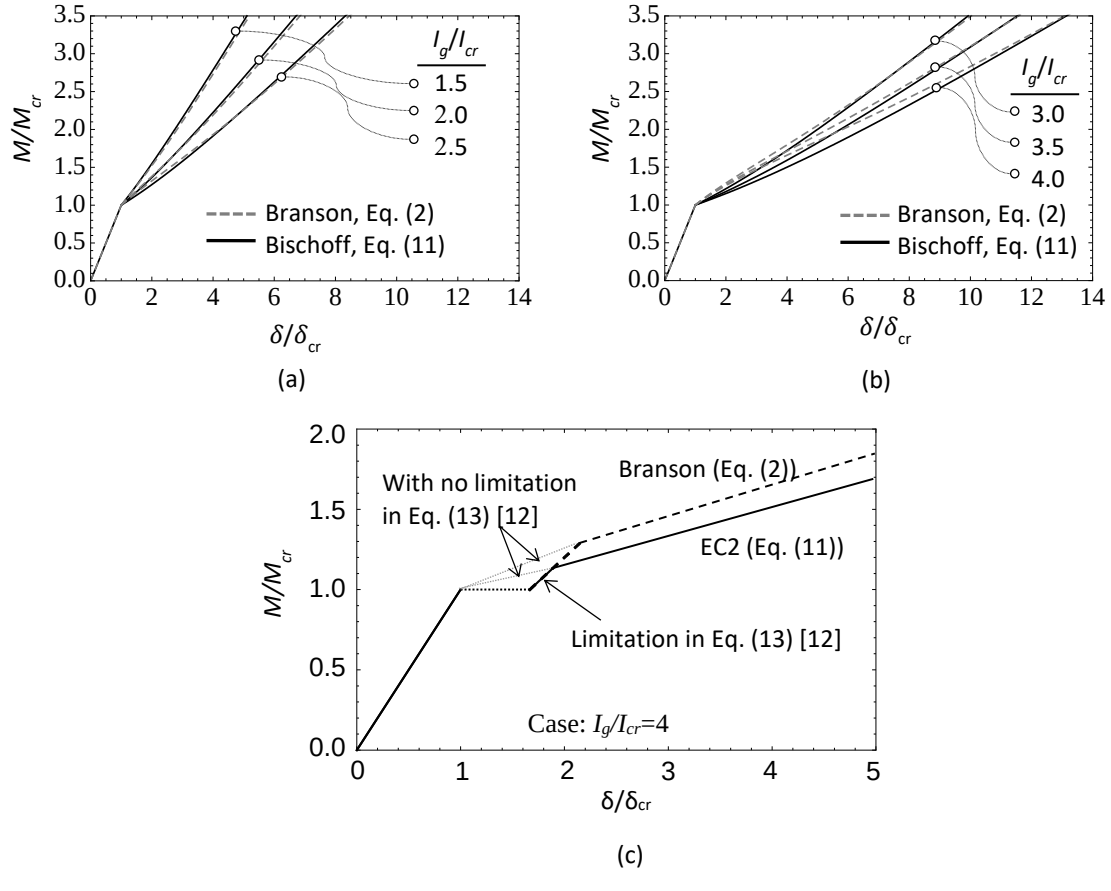

Figure 2. *Generalized moment-deflection curves for the deflection at mid-span of a simply supported beam subjected to a uniformly distributed load for different values of I_g/I_{cr} computed using Eq. (2) (Branson formula) and Eq. (11) (Bischoff formula*): (a) $I_g/I_{cr}<3$. (b) $I_g/I_{cr} \geq 3$. (c) Effect of the limitation in Eq. (13) [12] in the moment-deflection curve for $I_g/I_{cr}=4$.

As it can be also seen in Figure 1, Figures 2.a and 2.b show that the bigger differences between both regulations in relation with the short-term deflection are in the range $1< M/M_{cr} < 2.5$. If the upper limit of the effective moment of inertia for beams with $I_g/I_{cr} \geq 3$ *given in* Eq. (13) is imposed (see Figure 2.c, which corresponds to $I_g/I_{cr} = 4$), then the moment-deflection curve is forced to present a discontinuity at $M=M_{cr}$ (dotted horizontal line in Figure 2.c).

6. EXPERIMENTAL CAMPAIGNS

The accuracy of the expressions of I_e given by Eq. (2) and Eq. (11) has been investigated based on experimental results available in literature. The reinforced concrete test beams considered in this study are simply supported beams subjected to uniformly distributed load. The experimental value of I_e was determined from the measured deflections using the elastic deflection formula:

$$I_{exp} = \frac{5M\ L^2}{48E_c\delta_{exp}} \tag{14}$$

where L is the length of beam span, E_c the instantaneous modulus of elasticity of concrete and δ_{exp} the experimental deflection measured at mid-span.

6.1. Campaign 1

In Al-Zaid et al. [14] three identical pairs of reinforced concrete beams with rectangular cross sections were tested under different loading conditions. The gross and the moment of inertia at cracking of the beams were $I_g=1.33\cdot10^8$ mm^4 and $I_{cr}=3.8\cdot10^7$ mm^4, respectively. Specimens B1-U and B2-U have been considered here. In Table 1, measured values of the short-term deflection at mid-span for different values of the bending moment and the corresponding experimental effective moment of inertia from Eq. (14) have been summarized. The experimental deflection δ in Table 1 is the average value of both identically loaded specimens. Theoretical values of I_e from Eq. (2) and Eq. (11) and the ratios I_{exp}/I_e (equal to $\delta_{exp}/\delta_{EC2}$ or $\delta_{exp}/\delta_{ACI318}$) are also summarized in Table 1.

Table 1. Test results of beams B1-U and B2-U tested in Al-Zaid et al. [14]

Beam designation	M/M_{cr}	δ_{exp} mm	I_{exp} *10^5 mm^4	I_e from Eq. (2) *10^5 mm^4	I_{exp}/I_e $\delta_{exp}/\delta_{ACI318}$ Eq. (2)	I_e from Eq. (11) *10^5 mm^4	I_{exp}/I_e $\delta_{exp}/\delta_{EC2}$ Eq. (11)
B1-U and B2-U	1,11	1,3	986,1	1077,07	0,92	905,43	1,09
	1,23	1,7	839,9	892,31	0,94	720,52	1,17
	1,36	2,1	734,7	758,99	0,97	619,47	1,19
	1,48	2,5	673,2	674,08	1,00	564,15	1,19
	1,60	2,9	628,7	612,75	1,03	527,26	1,19
	1,73	3,3	589,6	564,12	1,05	499,28	1,18
	1,98	4,1	543,4	502,81	1,08	464,76	1,17
	2,22	5,0	503,6	467,13	1,08	444,49	1,13
	2,47	5,9	475,4	443,26	1,07	430,45	1,10
	2,72	6,7	458,5	427,37	1,07	420,65	1,09
	2,96	7,6	445,8	416,76	1,07	413,77	1,08
	3,21	8,4	436,2	408,82	1,07	408,33	1,07
	3,46	9,2	428,3	403,02	1,06	404,14	1,06
	3,70	10,1	417,8	398,82	1,05	400,94	1,04

Figure 3 shows the evolution of I_e as a function of the ratio M/M_{cr}. In the case of the two specimens considered, I_g/I_{cr} = 3.87 (>3), so the upper limit of I_e proposed in [12] has also been considered (dotted lines in Figure 3**¡Error! No se encuentra el origen de la referencia.**). It can be seen that I_e obtained from Eq. (2) without the limitation proposed in Eq. (13) [12] shows a good agreement with the experimental results in the whole range of M/M_{cr}. The Branson formula [6] leads to values of I_e slightly overestimated in the range of smaller M/M_{cr} ($M/M_{cr}<1.5$). Values of I_e from Eq. (11) are always kept considerably below the experimental ones, leading to greater deflections that those given by the experiments especially for bending moment in the range $1< M/M_{cr} < 1.5$. From Figure 3, it is evident that the upper limit imposed in [12] to I_e (Eq. (13) only affects the curve for bending moments slightly higher than the cracking moment (dashed lines in Figure 3), leading to an excessive reduction of the tension stiffening effect. Besides, for higher load levels ($M/M_{cr}>2.5$) all the curves in Figure 3 tend asymptotically to the moment of inertia at cracking, I_{cr}.

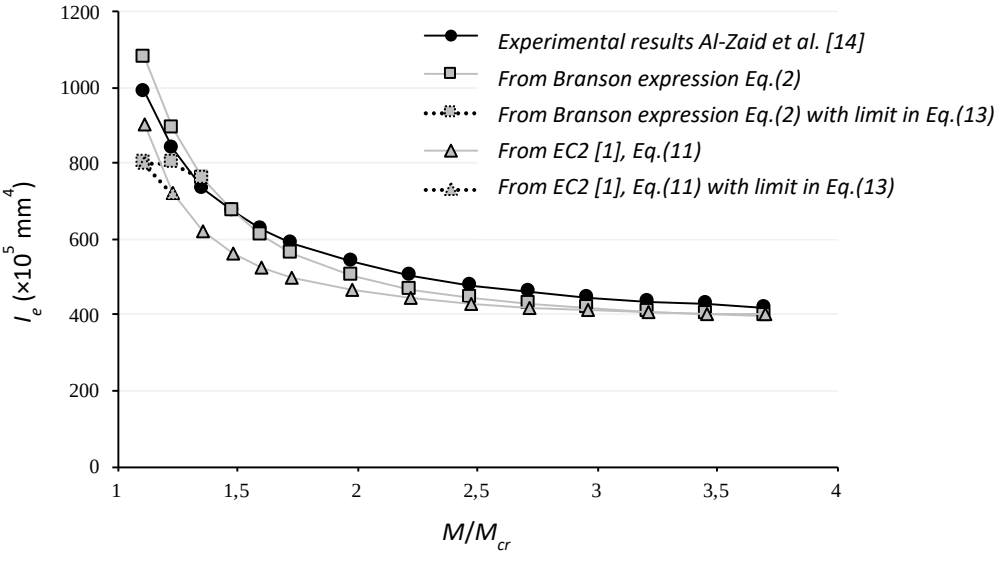

Figure 3. *Comparison of the experimental and estimated values of the effective moment of inertia, I_e, of simply supported beam with rectangular cross sections and subjected to uniformly distributed load (tested by Al-Zaid et al. [10]) as a function of M/M_{cr}.*

6.2. Campaign 2

In this second campaign, twelve pairs of reinforced concrete beams tested in Washa and Fluck [15] are studied. All the specimens are simply supported beam with rectangular cross sections and were tested under uniformly distributed loads. For this campaign, the authors only could get one result M-δ for each tested specimen. The results of the experimental campaign are summarized in Table 2.

Table 2. Test results of the reinforced concrete beams tested in Washa and Fluck [15]

Beam designation	I_g *10^5 mm^4	I_{cr} *10^5 mm^4	M/M_{cr}	δ_{exp} mm	I_{exp} *10^5 mm^4	I_e from Eq. (2) *10^5 mm^4	I_{exp}/I_e $\delta_{exp}/\delta_{ACI318}$ Eq. (2)	I_e from Eq. (11) *10^5 mm^4	I_{exp}/I_e $\delta_{exp}/\delta_{EC2}$ Eq. (11)
A1, A4	4795	3039	2,44	13,5	3405	3160,03	1,08	3238,36	1,05
A2, A5	4795	2872	2,44	15,8	2909	3004,54	0,97	3079,61	0,94
A3, A6	4795	2764	2,44	17,0	2693	2903,98	0,93	297s5,89	0,90
B1, B4	1066	420	2,27	23,4	558	475,03	1,17	475,83	1,17
B2, B5	1066	416	2,27	24,9	520	471,37	1,10	471,68	1,10
B3, B6	1066	408	2,27	26,4	491	464,05	1,06	463,37	1,06
C1, C4	520	296	2,50	40,1	308	310,34	0,99	317,91	0,97
C2, C5	520	285	2,50	43,4	286	300,04	0,95	307,21	0,93
C3, C6	520	274	2,50	47,8	260	289,74	0,90	296,44	0,88
D1, D4	520	296	2,38	11,9	394	312,60	1,26	320,34	1,23
D2, D5	520	285	2,38	14,2	331	302,41	1,09	309,69	1,07
D3, D6	520	274	2,38	17,8	264	292,23	0,90	298,95	0,88

All the beams in Washa and Fluck [15] verified that $I_g / I_{cr} < 3$, so the upper limit proposed in [12] does not have to be applied. Results in Table 2 confirm that the maximum differences between experimental and estimated values of the effective moment of inertia, I_{exp} and I_e, correspond to specimens B and D, for which the ratios M/M_{cr} are 2.27 and 2.38, respectively. However, for bigger ratios, such as specimens A and C (with M/M_{cr} equal to 2.44 and 2.5, respectively), experimental and calculated values of I_e are almost identical.

In Figure 4, the experimental values of I_e computed from the tests carried out in [15] are plotted against the computed values using both Eq. (2) and Eq. (11).

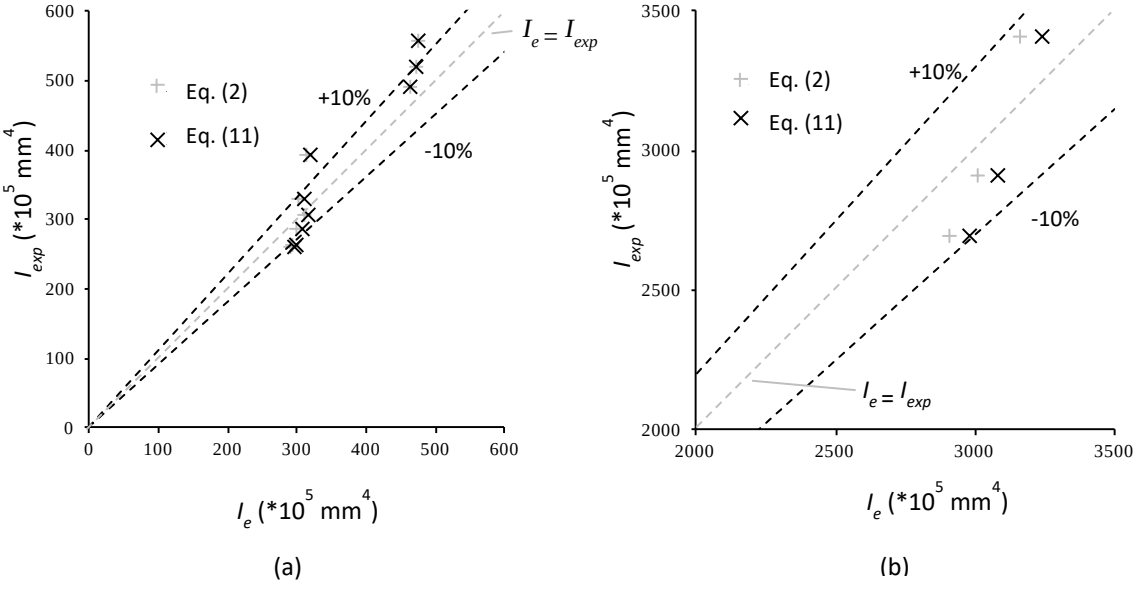

Figure 4. *Comparison of experimental values of moment of inertia I_{exp} [15] with the values of I_e obtained from Eq.(2) and Eq.(11).*

As can be seen in Figure 4, the majority of the data points lie within the $\pm$ 10% limits represented with dashed lines in this figure, which gives an idea of the degree of precision of the expressions proposed by both expressions, Branson [6] and Bischoff [8].

7. CONCLUSIONS

Design codes of RC structures allow for the calculation of the short-term deflection of the members by using linear elastic formulation. According to American code ACI-318, the short-term deflections in a cracked prismatic member are obtained from twofold integration of curvatures using an effective moment of inertia, supposed constant over the entire span. This effective moment of inertia is a weighted average value of the moments of inertia of the gross section and the cracked section transformed to concrete.

EC2 proposes a mechanical-based method which interpolates between the uncracked and the fully cracked states, leading to almost identical effective moment of inertia than the ACI-318-19.

The most widespread used expressions of the effective moment of inertia have been studied and the accuracy of both formulations to calculate the short-term deflections was evaluated based on experimental data found in the literature.

The preceding discussion shows how the effective moments of inertia given by Branson [6] and Bischoff [8] (EC2 [1]) lead to similar values of the short-term deflections for values of the ratio M/M_{cr} greater than 2.5. The most important discrepancy between the values of I_e proposed by both regulations occurs in the range M/M_{cr} between 1 and 2.5 and light reinforcement ratios ($\rho < 0.5\%$), these differences being less than 15%. For M/M_{cr} greater than 2.5 the difference between both codes is negligible. In the case of reinforcement ratios greater than 1% the difference is also negligible.

APPENDIX

Let us consider a rectangular cross section reinforced against a bending moment producing tension at the bottom of the section, b being its width and d the distance between compression fiber to centroid of longitudinal tension reinforcement, A_s. If $\rho = \frac{A_s}{bd}$ is the reinforcement ratio and $n = \frac{E_s}{E_c}$, the ratio between depth of the neutral fiber assuming cracked section, x_{cr}, and d can be written as:

$$\frac{x_{cr}}{d} = -\rho n + \sqrt{(\rho n)^2 + 2\rho n} \tag{A.1}$$

The moment of inertia of the gross section can be expressed as:

$$I_g = \frac{1}{12} b d^3 \tag{A.2}$$

Furthermore, the moment of inertia of the cracked section transformed to concrete is:

$$I_{cr} = \frac{1}{3} b x_{cr}^3 + n A_s (d - x_{cr})^2 \tag{A.3}$$

Combining Eqs. (A.2) and (A.3), the ratio I_g / I_{cr} can be obtained. Figure A.1.

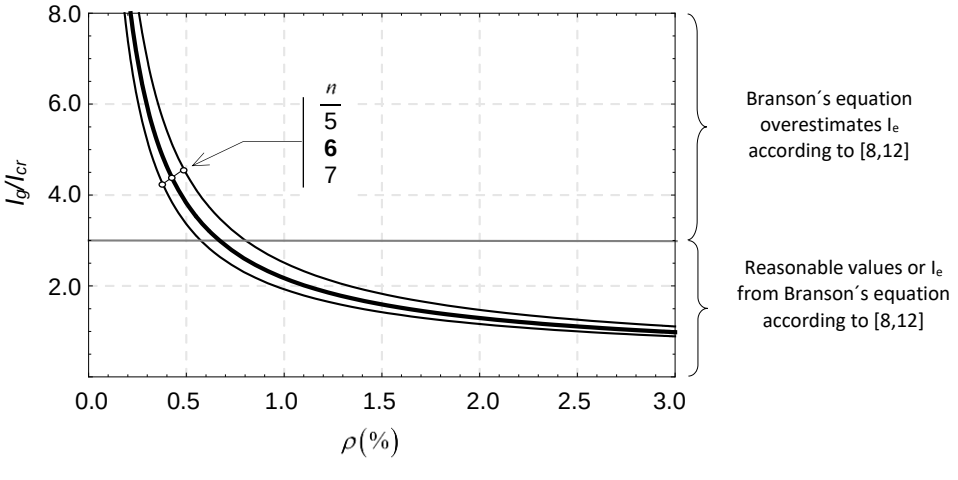

Figure A.1. *Values of the ratio I_g / I_{cr} in terms of the reinforcement ratio ρ and n.*

REFERENCES

[1] European Committee for Standardization. Eurocode 2: Design of concrete structures - Part 1–1: General rules and rules for buildings UNE-EN 1992-1-1. Brussels: European Committee for Standardization; 2013.

[2] ACI Commitee 318. 318-08: Building Code Requirements for Structural Concrete and Commentary. Detroit: American Concrete Institute, ACI; 2019.

[3] CSA A23.3: Design of concrete structures. Canadian code. Ontario, Canada. 2019.

[4] Xu L-Y, Nie X, Zhou M, Tao M-X. Whole-process crack width prediction of reinforced concrete structures considering bonding deterioration. Eng Struct 2017;142:240–54. doi:10.1016/j.engstruct.2017.03.060.

[5] Carbonell-Márquez JF, Gil-Martín LM, Fernández-Ruíz MA, Hernández-Montes E. Effective area in tension stiffening of reinforced concrete piles subjected to flexure according to Eurocode 2. Eng Struct 2014;76:62–74. doi:10.1016/j.engstruct.2014.06.041.

[6] Branson D. Instantaneous and time-dependent deflections of simple and continuous reinforced concrete beams. Auburn AL: State of Alabama Highway Dept. Bureau of Research and Development; 1965.

[7] ACI Commitee 318. 318-08: Building Code Requirements for Structural Concrete and Commentary. Detroit: American Concrete Institute, ACI; 2014.

[8] Bischoff PH. Reevaluation of Deflection Prediction for Concrete Beams Reinforced with Steel and Fiber Reinforced Polymer Bars. J Struct Eng 2005;131:752. doi:10.1061/(ASCE)0733-9445(2005)131:5(752).

[9] CEB. CEB Design Manual on Cracking and Deformations, Bulletin d'information 158. Paris: Comite Euro-International du Beton; 1985.

[10] Scanlon, A. & Bischoff, P. H. (2008). Shrinkage restraint and loading history effects on deflections of flexural members. ACI Structural Journal, 105(4), 498-506.

[11] Bischoff, P. H. & Scanlon, A. (2007). Effective moment of inertia for calculating deflections of concrete members containing steel reinforcement and fiber-reinforced polymer reinforcement. ACI Structural Journal, 104(1), 68-75.

[12] Gilbert RI, Ranzi G. Time-Dependent Behaviour of Concrete Structures. New York: Spon Press; 2011.

[13] Gribniak V, Cervenka V, Kaklauskas G. Deflection prediction of reinforced concrete beams by design codes and computer simulation. Eng Struct 2013;56:2175–86. doi:10.1016/j.engstruct.2013.08.045.

[14] Al-Zaid RZ, Al-Shaikh AH, Abu-Hussein MM. Effect of loading type on the effective moment of

inertia of reinforced concrete beams. ACI Struct J 1991;88:184–90.

[15] Washa GW, Fluck PG. Effect of compressive reinforcement on the plastic flow of reinforced concrete beams. ACI J Proc 1952;49:89–108.

AVOIDING FAILURE PROPAGATION IN STEEL TRUSS BRIDGES: A CASE STUDY

Buitrago, Manuel[1]; Bertolesi, Elisa[2]; Caredda, Giacomo[3]; Orrù, Martina[3]; Porcu, M. Cristina[3]; Adam, Jose M.[1,4]

ABSTRACT

This study aimed to experimentally and computationally analyse the robustness of riveted steel bridges based on truss-type structures and to define practical recommendations for early detection of local failures before they cause progressive structural collapse. This paper describes a unique case of a 21m full-scale bridge span tested under laboratory conditions with an extensive monitoring system to evaluate structural behaviour and robustness as damage or failure progressed in its elements. A computational analysis was also included to examine other possible causes not included in the experiment. The results proved the structural redundancy of this type of truss structure based on different Alternative Load Paths (ALPs) and gave rise to a series of practical structural health recommendations to identify early failures and avoid progressive or sudden bridge collapse. The study carried out and the recommendations it produced are now being applied in three similar bridge case studies.

Keywords: Robustness, Truss-like Structures, Railway Bridges, Finite Element Modelling, Structural Health Monitoring.

1. INTRODUCTION

Bridges over the Firth of Tay (Scotland, 1879), the Birz river (Switzerland, 1891), the Peene river (Germany, 1900), in Quebec (Canada, 1907), the Seongsu bridge (South Korea, 1994), the I-35 bridge in Minneapolis (USA, 2007), the Chauras bridge (India, 2012) or the I-5 Skagit River in Washington (USA, 2013), are some historic and recent examples of disproportionate collapse of truss-like railway and road bridges with a huge number of deaths and injuries and economic losses [1–4]. A study carried out in the USA [5] identified the failure of more than 500 bridges over a period of 11 years (1989-2000), 21.3% of which were associated with steel truss-like bridges, thus demonstrating the high occurrence (an average of 9.7 bridges of this type per year in the USA) and vulnerability of this type of structure. Natural disasters, impacts, overloads, structural and design deficiencies, construction and supervision mistakes, or the lack of maintenance or inspection are the main causes of these collapses. Something in common is that a local failure triggered a progressive collapse of the whole structure or of a large part of it.

[1] *ICITECH, Universitat Politècnica de València, Camino de Vera s/n, 46022 Valencia, Spain*
[2] *Department of Civil and Environmental Engineering, Brunel University London, UB8 3PH Uxbridge, UK*
[3] *Department of Civil and Environmental Engineering and Architecture, University of Cagliari, Piazza d'Armi, 09123 Cagliari, Italy.*
[4] *CALSENS, Camino de Vera s/n, 46022 Valencia, Spain. E-mail address: joadmar@upv.es (corresponding author).*

Bridge structures are expected to withstand loads defined in codes (e.g. gravity, wind, snow, etc.); however, these structures may be subjected to extreme events (also called low-probability/high-consequence events) such as hurricanes, tsunamis, explosions, vehicle impacts, fires, human errors, terrorist attacks [6,7]; or to be exposed to several degradation actions such as corrosion [8] or fatigue [9]. These events can cause the sudden loss of local elements and trigger a cascading failure of the bridge, known as progressive bridge collapse [10].

Progressive structural collapse is now a hot topic subjected to widespread theoretical and experimental studies on buildings [11–17]. In bridges, the studies focused basically on the numerical or analytical assessment of robustness (e.g. Ghali and Tadros [6], Wang and Zhou [18], Jiang et al. [19]) or the analysis of real cases (e.g. Starossek [10], Bontempi [20], Deng et al. [1]), including truss bridges [21–29] with an unique experimental test [29]. In truss bridges, from a theoretical viewpoint [21,23,27], it has been shown that a failure in any element can trigger partial or total bridge collapse, so that there is a need for further studies to analyze the real behavior of these bridges to serve as the basis of future theoretical and numerical developments.

This paper describes the research team's unique opportunity to study a full-scale steel-riveted truss bridge with the triple aim of: 1) an experimental analysis of its robustness, 2) an extensive parametric computational analysis, and 3) establish practical recommendations for early detection of local failures, which can also set off a progressive collapse. The study was both ambitious and novel and permitted an advance in two areas, including i) the analysis of robustness in the local failure of some elements and ii) structural health monitoring to prevent progressive collapse.

To comply with these aims, after this section a brief description of the bridge is given in Section 2 and the experimental study is described in Section 3. The parametric computational study is discussed in Section 4 and the knowledge obtained from the experimental and computational studies was used as the basis for a series of recommendations for early detection of local failures in elements (Section 5). Conclusions are given in Section 6.

2. DESCRIPTION OF THE BRIDGE

The railway bridge studied was built between 1913 and 1915 and so was more than 100 years old. Its structure was formed by a series of Pratt type trusses connected by riveted joints. It also had a series of horizontal and vertical braces in the form of St. Andrew's crosses, and longitudinal and transverse beams to locally distribute train loads to the Pratt trusses. The heights of the metal piers varied up to 23.6m, and it had two isostatic spans at each end (span length ranged from 21.1m to 21.5m) with a continuous beam in the two central spans (42.0m each). All the supports were hinged with free rotations. One support in each span also had free longitudinal displacement as a roller (A1 for span 1, P1 for span 2, P2 for span 3, P4 for span 4, P5 for span 5 and A2 for span 6). Fig. 1 gives the principal bridge dimensions and a view of a train passing over it. A more in-depth description of the bridge can be found in Bertolesi et al. [30] and Buitrago et al. [31].

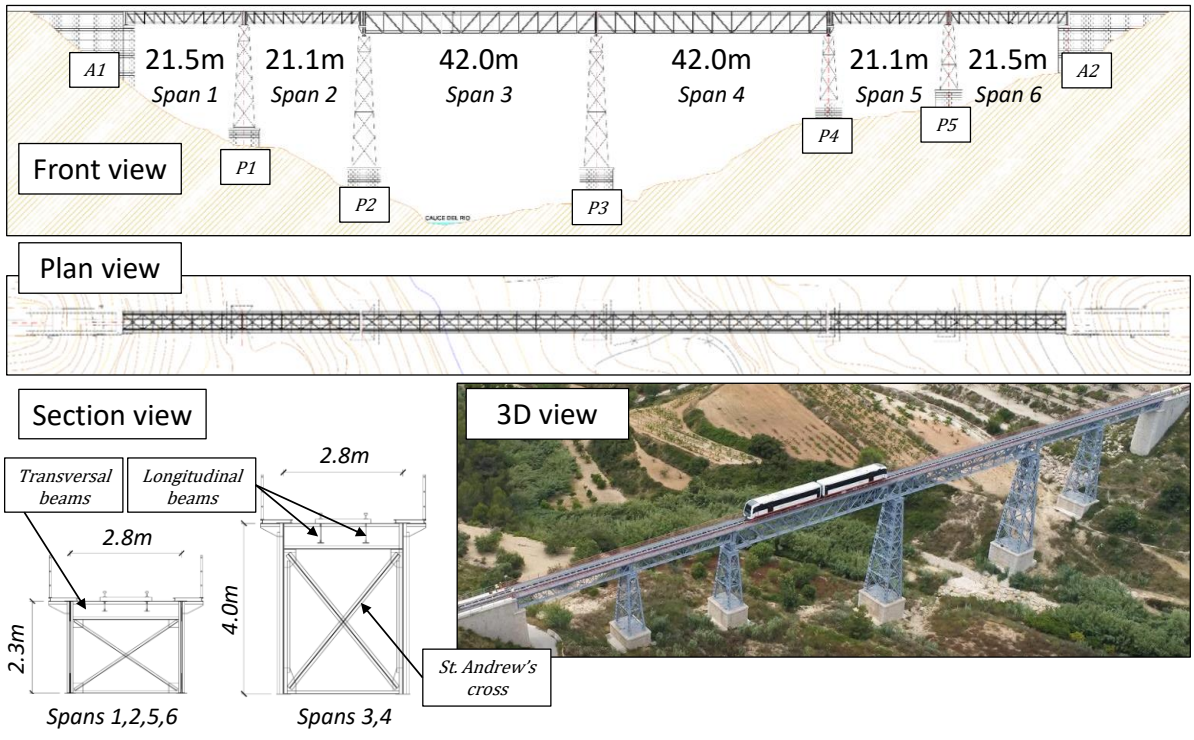

Figure 1. *Geometry of the bridge and general views.*

3. LABORATORY INVESTIGATIONS

The laboratory study was carried out on one of the isostatic spans (Span 2 or 5 in Fig. 1) of a twin of the bridge shown in Fig. 1 with the same geometry and year of construction as the one analysed here and had been in service for the same length of time. The span under consideration had the same characteristics as spans 2 or 5 shown in Fig. 1. Fig. 2 illustrates the complex process of transporting the bridge to the ICITECH laboratories

Figure 2. *Positioning of the bridge into the ICITECH laboratories.*

The 21.1m span had the same support conditions as the originals, with free rotations at both sides and longitudinal displacements on one side only. The hydraulic jack with a maximum load capacity of 1300kN used to test the bridge was installed with the help of a reaction frame at the centre of the span which was anchored to the laboratory's reaction slab. The load applied by the jack was shared between 4 points by a system of metal girders to avoid high load concentrations. The test setup and details of the load distribution system can be seen in Fig. 3.

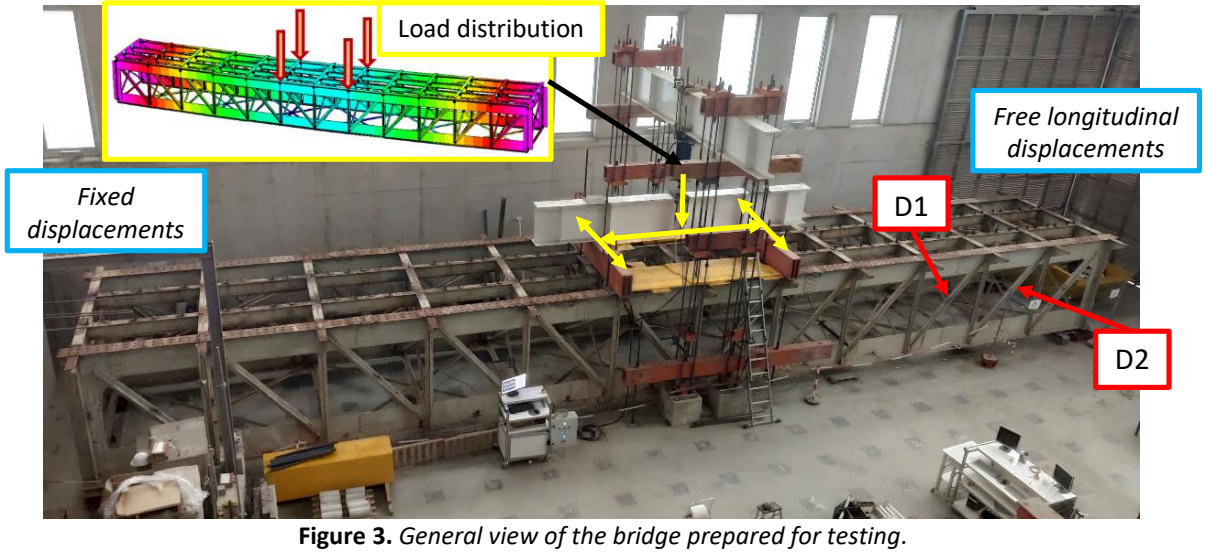

Figure 3. *General view of the bridge prepared for testing.*

In the present experimental study, the scenario-independent approach was selected to analyse structural robustness after a series of damage to D1 and D2 diagonal elements (see Fig. 3) and study the structural behaviour after activating Alternative Load Paths (ALPs). Each diagonal cross-section was composed of four L-profiles. The series of damage for each diagonal included a cutting of a quarter and a half of an L profile (F/2 and F, respectively), and of complete L profiles progressively (1L, 2L, 3L) until the cutting of a complete diagonal (D). Then, the second diagonal followed the same series of damage until achieving the cutting of diagonals D1 and D2. The monitoring equipment consisted of 40 strain gauges, 8 LVDTs and 2 fibre optic accelerometers (see a more in-depth description in [31]).

After the series of damage to D1 and D2, some interesting results were found on:

- Strain data results: high bending stresses are induced at the level of upper and lower chords, and also at columns, although the original structure is only working and prepared for axial stresses and residual bending moments.
- Deflections: Fig. 4 shows the deformed shape of the damaged and the undamaged Pratt truss (damaged and undamaged plane, respectively) during the series of damage. The behaviour of both trusses is markedly different. Deflections measured on the undamaged truss were not affected by the damage sequence with a maximum vertical deflection at mid-span slightly over 25mm. However, deflections on the damaged plane were strongly affected by the damage sequence, starting with the same deflection (25mm) and ending with 40mm deflection at mid-span. Measuring deflections on the damaged plane can thus be considered an effective way of interpreting damage by registering significant changes in both the

maximum value and deformed shape, which was greater on the right (position X between 10.6m and 21.1m).

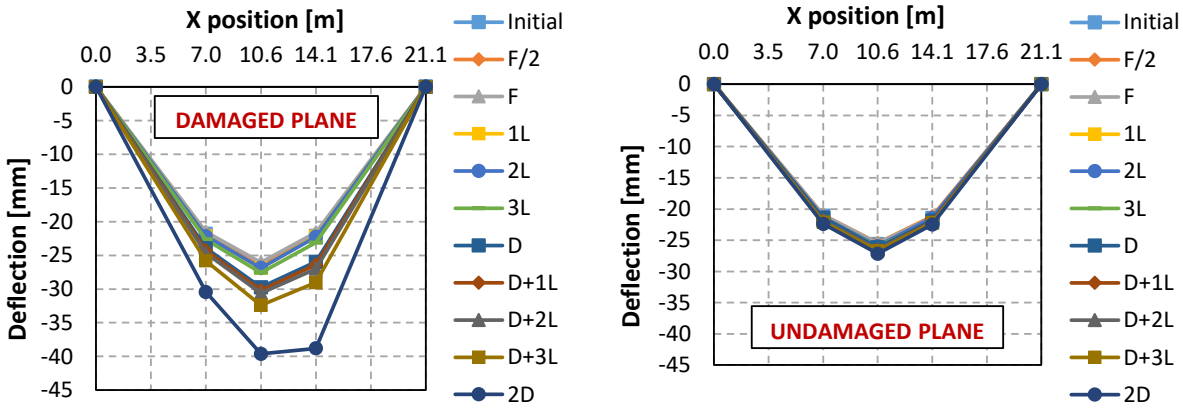

(a) Damaged plane (b) Undamaged plane

Figure 4. *Evolution of deflections during the series of damage.*

- Vibrational modes: the first frequency corresponding to the vertical vibration mode falls as damage is increased but it is only significant when damage is severe.

In this case the structure, which originally worked basically under axial forces, made use of the structural redundancy of the joints to adapt to the failure of diagonals, as the joints were able to resist high bending moments. Thanks to this ability, when the diagonals failed, the structural behaviour of the affected zone changed from Pratt truss to Vierendeel behaviour (same structure but without diagonals), in which the capacity of the joints to resist bending moments is crucial. When a structure like the span under study has no diagonals, the structure is known as a Vierendeel beam, and the load transmission to the foundations is only possible with the help of the moment-resisting capacity of joints. The moments registered in the vertical columns and top and bottom chords confirm this hypothesis.

4. PARAMETRIC COMPUTATIONAL ANALYSIS

This section presents a parametric computational analysis of the bridge comprising different damage scenarios (DSs) and analysing the structural response of the bridge. In this way, more elements than only diagonals are assessed, and the robustness of the structure can be determined. Those DSs considered are: (i) Upper Transversal beam – UT; (ii) Upper Stringer or longitudinal beam – US; (iii) Lower Chord – LC; (iv) Upper Chord – UC; and (v) vertical Column – C. The Finite Element (FE) model is constructed using ABAQUS Software [32], with a high accuracy degree, using solid elements, the real geometry of the bridge and the real material properties. In addition, as traffic loads, the real traffic on the lane was considered in different static load steps calculations to analyse the robustness of the structure under real loading conditions.

A summary of the results can be found on Figs. 5-9.

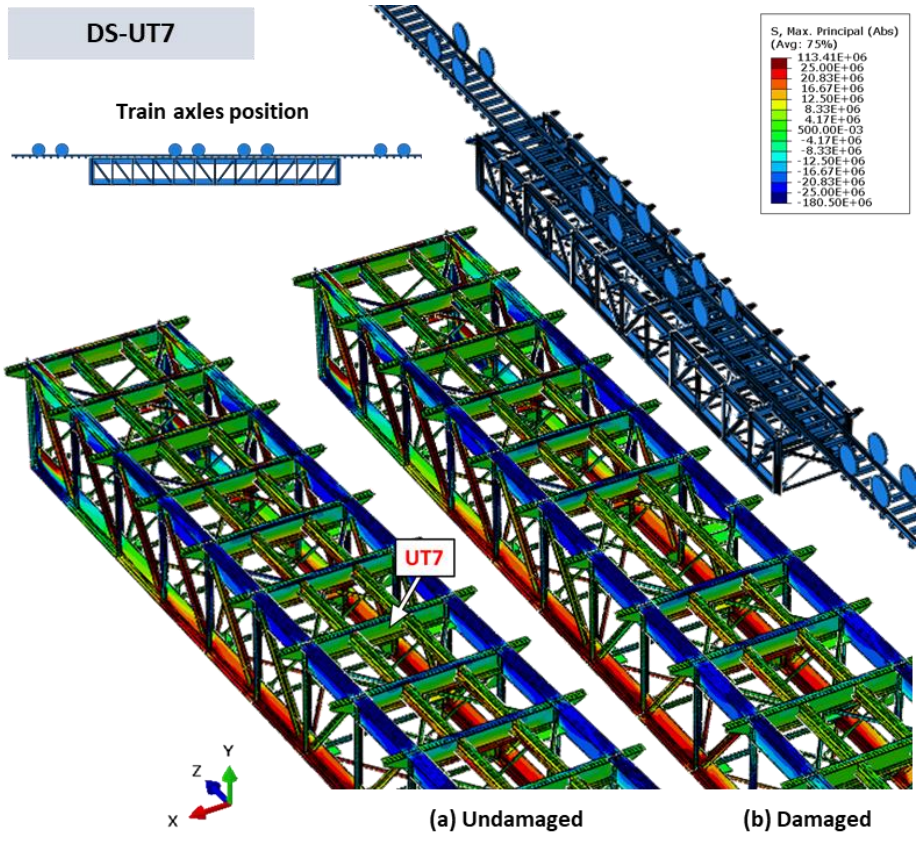

Figure 5. *Principal stress contour maps for the original and the damaged structure with the removal of an UT. Units in Pa.*

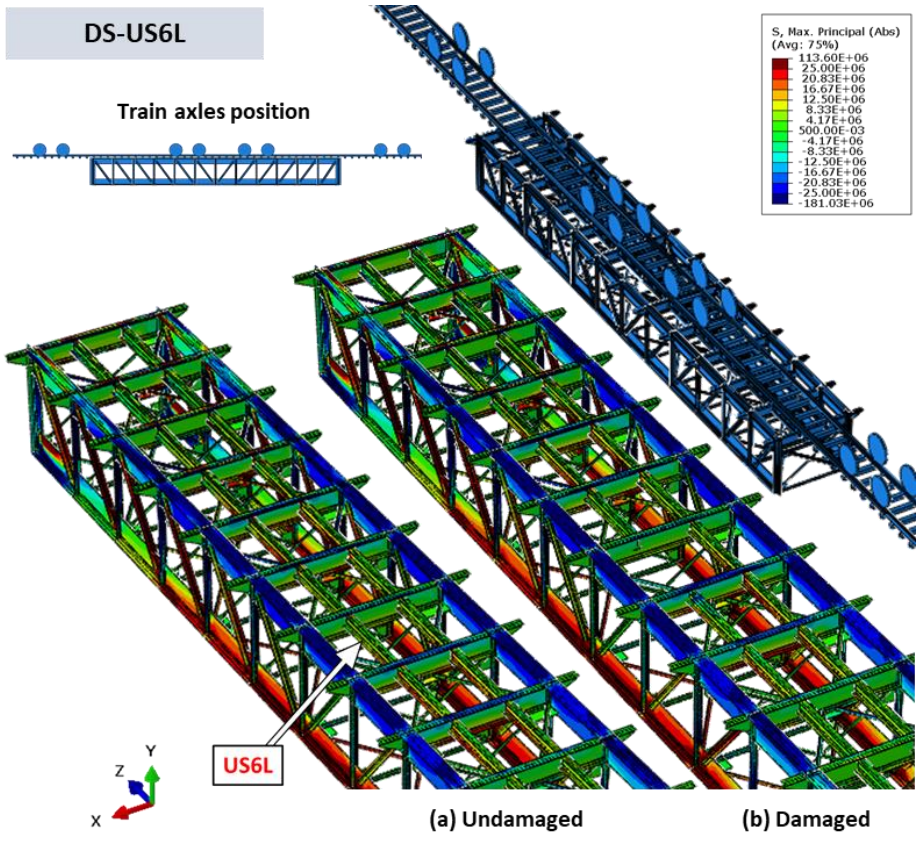

Figure 6. *Principal stress contour maps for the original and the damaged structure with the removal of an US. Units in Pa.*

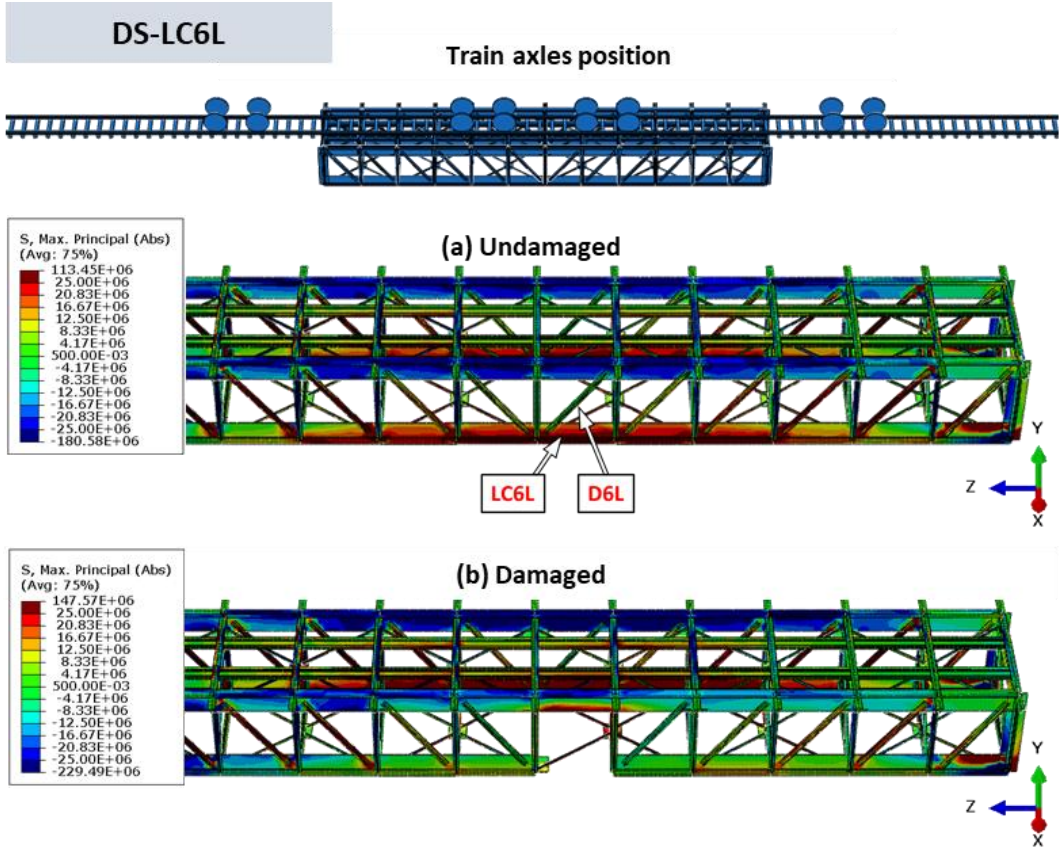

Figure 7. *Principal stress contour maps for the original and the damaged structure with the removal of a LC. Units in Pa.*

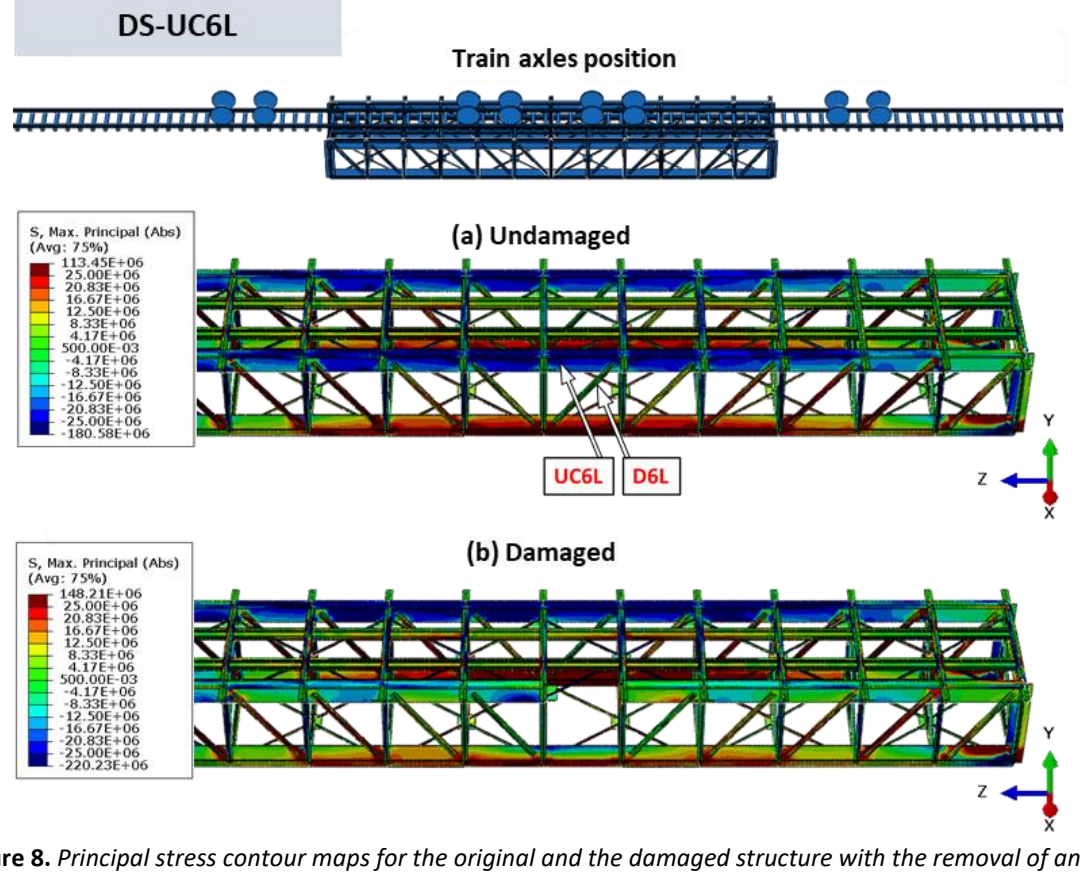

Figure 8. *Principal stress contour maps for the original and the damaged structure with the removal of an UC. Units in Pa.*

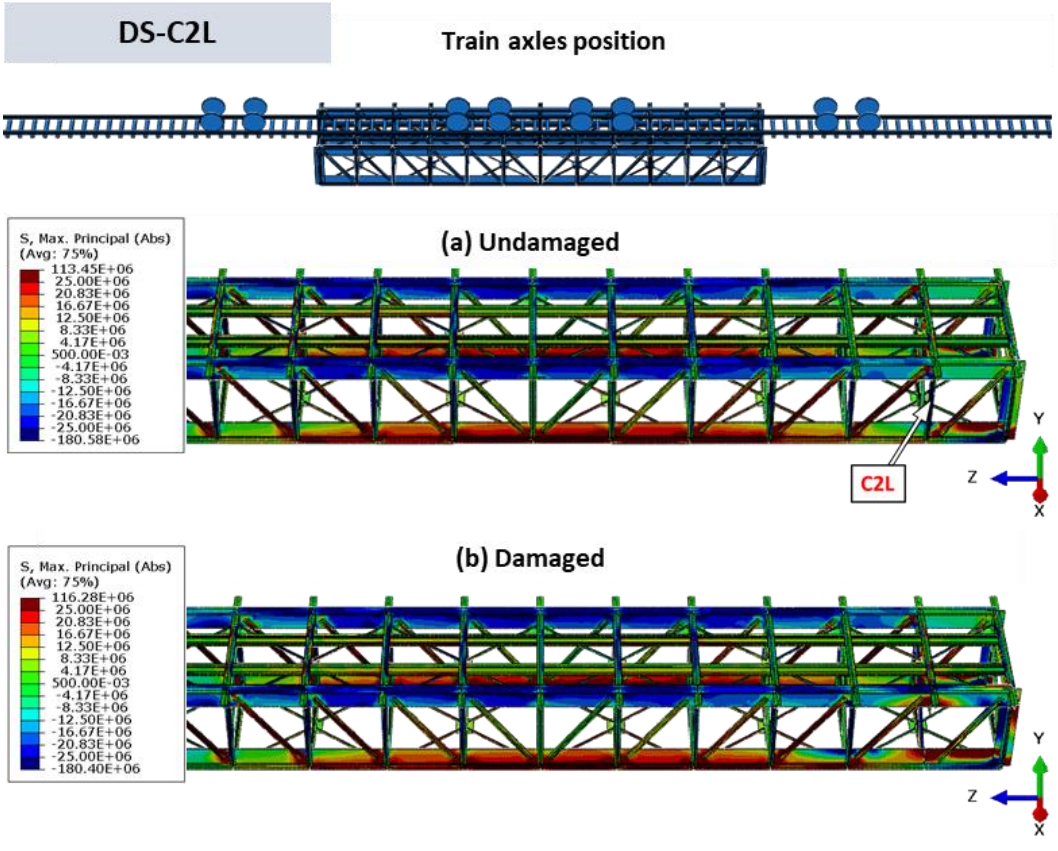

Figure 9. *Principal stress contour maps for the original and the damaged structure with the removal of a C. Units in Pa.*

Any structure is robust if, after a local failure, it is able to activate Alternative Load Paths (ALPs) efficiently, without compromising the safety of the structure. In the case discussed in this study, for all DSs, efficient ALPs are activated and the structure is able to resist and adapt to the new conditions. However, there are significant differences between each of the situations that trigger the activation of different ALPs. Table 1 presents a summary of the main ALPs that have been efficiently activated for each of the DSs analyzed.

As for the primary elements, in DS-UT7, the failure of a transverse beam required a notable change in the way loads were transmitted, requiring, in the new situation, the stringers (and to a lesser extent the rails) to support greater loads with a span length equal to two times the original span length. The DS-US6L has been even more critical, as it has required the contribution of the rails as a last line of defense to redistribute local load to the secondary elements.

In the DSs of the secondary elements, the case of the DS-LC6L caused the main activation of two ALPs simultaneously. On the one hand, the failure of a lower chord required a change of the structural behavior of the upper chord, mainly from compression stresses to bending stresses. On the other hand, simultaneously, the failure of the lower chord has triggered a load transmission towards the right side, raising the stress levels of the elements that have allowed this transmission (e.g. lower horizontal bracing) and the Pratt-truss elements of the other side. This, however, is not happening in the DS-UC6L, where only the load transmission to the right side was the main ALP. In this last case (i.e. DS-UC6L) the elements that have allowed the load transmission from the one side to the other (e.g. transverse beam and stringers, upper horizontal bracing) are much stronger than in the case of the

DS-LC6L, thus causing this ALP to be the predominant one and the lower chord did not show important bending stresses.

Finally, in DS-C2L, the failure of one column required that the nodes, at the positions of the upper and lower chords, were able to absorb bending stresses.

Table 1. Main active ALPs after each DS.

	DS	Failure description	Alternative Load Paths
Primary Elements	DS-UT7	Transversal beam	Stringers working with a double span; slight contribution of rails
	DS-US6L	Stringer or longitudinal beam	Contribution of rails
Secondary Elements	DS-LC6L	Lower Chord	(i) Bending of the upper chord (ii) Load transmission to the other Pratt truss
	DS-UC6L	Upper Chord	Load transmission to the other Pratt truss
	DS-C2L	Column	Bending of joints

5. PRACTICAL RECOMMENDATIONS FOR STRUCTURAL HEALTH MONITORING

Firstly, strain gauges should be installed at the centre of gravity and the centre of the elements to measure axial loads in truss structures (theoretically, elements are only subjected to axial loads in truss structures). However, other sensor locations are recommended to detect early failures, such as away from the section's centre of gravity and closer to the joints instead of at the centre. Table 2 gives a summary of all this information with recommendations for conventional monitoring and early failure detection of the different elements.

Table 2. Location of strain sensors.

Element	General purpose	Early failure detection	
		General position	Additional details. To be measured in case of failure
Chords	Section: Centre of gravity	Section: far from the center of gravity	Compression and tension increments in the top and bottom chords, respectively
Diagonals	Position: Centre of the length of the element	Position: close to a joint	Tension increments
Vertical columns			Compression increments. In general, in the point of the element closer to the center of the bay

Secondly, it is also recommended to monitor deflections by any of the different methods, for example topography or LVDTs. As in conventional monitoring, it is generally enough to measure deflection at one point at mid-span, although early failure detection may require monitoring deflection at other points. Full monitoring can be carried out by measuring deflection at two points at mid-span and at a

quarter and three quarters the length of the span (4 extra points). This is important to identify the site of the failure.

6. CONCLUSIONS

This paper described an experimental and computational study of the robustness of a steel riveted truss bridge on getting the opportunity to lab-test a full-scale bridge span. From this test and the subsequent numerical analysis, the following conclusions could be obtained:

- The structure, theoretically with truss-type behaviour, had structural redundancy based on the joints' capacity to absorb bending moments that increase with the level of damage.
- The structure was able to find effective alternative load paths (ALPs) and changed its original function to be able to withstand the new distribution of the loads. These ALPs were limited by the structural load levels until some of the elements initiated plastic behaviour.
- A set of practical recommendations were made for structural health monitoring with the aim of identifying early failures. These recommendations were provided for different parameters (strains, deflections), and the type, location and number of sensors for a structure with both a basic and an ambitious monitoring system.

In future work, a further validation of these practical recommendations will be made with the data analysis of three real case studies on different railway bridges in which an ambitious monitoring system with more than 400 sensors was installed.

ACKNOWLEDGEMENTS

We would like to express our gratitude to the FGV (Ferrocarrils de la Generalitat Valenciana) and FCC Construcción S.A., CHM Obras e Infraestructuras S.A., Contratas y Ventas S.A. and CALSENS S.L. for giving us the opportunity to test a bridge at the ICITECH facilities, also to Juan Antonio García Cerezo, of FGV, for his invaluable cooperation and recommendations.

REFERENCES

[1] Deng L, Wang W, Yu Y. (2016). State-of-the-Art Review on the Causes and Mechanisms of Bridge Collapse. *J Perform Constr Facil,* 30:04015005.

[2] Biezma MV, Schanack F. (2007). Collapse of Steel Bridges. *J Perform Constr Facil,* 21:398–405.

[3] National Transportation Safety Board. Collapse of the I-5 Skagit River Bridge Following a Strike by an Oversize Combination Vehicle in Mount Vernon, Washington May 23, 2013. Washington D.C.: 2014.

[4] Birajdar HS, Maiti PR, Singh PK. (2014). Failure of Chauras bridge. *Eng Fail Anal*, 45:339–46.

[5] Wardhana K, Hadipriono FC. (2003). Analysis of Recent Bridge Failures in the United States. *J Perform Constr Facil,* 17:144–50.

[6] Ghali A, Tadros G. (1997), Bridge progressive collapse vulnerability. *J Struct Eng,* 123:227–31.

[7] Cha EJ, Ellingwood BR. (2012). Risk-averse decision-making for civil infrastructure exposed to low-probability, high-consequence events. *Reliab Eng Syst Saf,* 104:27–35.

[8] Colajanni P, Recupero A, Ricciardi G, Spinella N. (2016). Failure by corrosion in PC bridges: a

case history of a viaduct in Italy. *Int J Struct Integr,* 7:181–93.

[9] Zhuang M, Miao C. (2020). Fatigue reliability assessment for hangers of a special-shaped CFST arch bridge. *Structures*, 28:235–50.

[10] Starossek U. (2009). Avoiding disproportionate collapse of major bridges. *Struct Eng Int*, 19:289–97.

[11] Adam JM, Parisi F, Sagaseta J, Lu X. (2018). Research and practice on progressive collapse and robustness of building structures in the 21st century. *Eng Struct,* 173:122–49.

[12] Adam JM, Buitrago M, Bertolesi E, Sagaseta J, Moragues JJ. (2020). Dynamic performance of a real-scale reinforced concrete building test under corner-column failure scenario. *Eng Struct,* 210:110414.

[13] Alshaikh IMH, Bakar BHA, Alwesabi EAH, Akil HM. (2020). Experimental investigation of the progressive collapse of reinforced concrete structures: An overview. *Structures,* 25:881–900.

[14] Fu Q, Tan K-H. (2019). Numerical study on steel-concrete composite floor systems under corner column removal scenario. *Structures*.

[15] Mucedero G, Brunesi E, Parisi F. (2020). Nonlinear material modelling for fibre-based progressive collapse analysis of RC framed buildings. *Eng Fail Anal,* 118:104901.

[16] Bao Y, Main JA, Noh S-Y. (2017). Evaluation of Structural Robustness against Column Loss: Methodology and Application to RC Frame Buildings. *J Struct Eng,* 143:04017066.

[17] Eren N, Brunesi E, Nascimbene R. (2019). Influence of masonry infills on the progressive collapse resistance of reinforced concrete framed buildings. *Eng Struct,* 178:375–94.

[18] Wang MR, Zhou ZJ. (2012). Progressive collapse and structural robustness of bridges. *Appl Mech Mater,* 193–194:1021–4.

[19] Jiang H, Wang J, Chorzepa MG, Zhao J. (2017). Numerical investigation of progressive collapse of a multispan continuous bridge subjected to vessel collision. *J Bridg Eng*, 22:04017008.

[20] Bontempi F. (2019). Elementary concepts of structural robustness of bridges and viaducts. *J Civ Struct Heal Monit,* 9:703–17.

[21] Miyachi K, Nakamura S, Manda A. (2012). Progressive collapse analysis of steel truss bridges and evaluation of ductility. *J Constr Steel Res*, 78:192–200.

[22] Garavaglia E, Sgambi L, Basso N. (2012). Selective maintenance strategies applied to a bridge deteriorating steel truss. *Bridg. Maintenance, Safety, Manag. Resil. Sustain. - Proc. Sixth Int. Conf. Bridg. Maintenance, Saf. Manag*., p. 1764–70.

[23] Khuyen HT, Iwasaki E. (2016). An approximate method of dynamic amplification factor for alternate load path in redundancy and progressive collapse linear static analysis for steel truss bridges. *Case Stud Struct Eng,* 6:53–62.

[24] Olmati P, Brando F, Gkoumas K. (2013). Robustness assessment of a steel truss bridge. *Struct. Congr., Reston, VA: American Society of Civil Engineers*; p. 250–61.

[25] Trong Khuyen H, Eiji I. (2017). Linear redundancy analysis method considering plastic region for steel truss bridges. *J Bridg Eng,* 22:05016011.

[26] Garavaglia E, Sgambi L. (2016). Selective maintenance planning of a steel truss bridge based on the Markovian approach. *Eng Struct*, 125:532–45.

[27] Ma X, Han B. (2011). Analysis and mitigation of progressive collapse for steel truss girders. *Second Int. Conf. Mech. Autom. Control Eng., IEEE*; p. 1931–4.

[28] Olmati P, Gkoumas K, Brando F, Cao L. (2013). Consequence-based robustness assessment of

a steel truss bridge. *Struct. Congr., Techno-Press*; p. 250–61.

[29] Azizinamini A. (2002). Full scale testing of old steel truss bridge. *J Constr Steel Res,* 58:843–58.

[30] Bertolesi E, Buitrago M, Adam JM, Calderón PA. (2021). Fatigue Assessment of Steel Riveted Railway Bridges: Full-Scale Tests and Analytical Approach. *J Constr Steel Res,* 182:106664.

[31] Buitrago M, Bertolesi E, Calderón PA, Adam JM. (2021). Robustness of steel truss bridges: laboratory testing of a full-scale 21-metre bridge span. *Structures*, 29:691–700.

[32] ABAQUS. Abaqus, Theory manual 2019.

The Octahedron family as a source of tensegrity structures: study of the equilibrium configurations considering different force:length ratios

Fernández-Ruiz, Manuel Alejandro[1]; Hernández-Montes, Enrique[2]; Gil-Martín, Luisa María[3]

ABSTRACT

A tensegrity family is a group of tensegrity structures that share a common connectivity pattern. In the case that just two values of the force density or force:length ratio are adopted (one for cables and another for struts), the members of the octahedron family are: the octahedron, the expanded octahedron and the double-expanded octahedron. In this work a higher number of possible force:length ratio values have been considered in order to find new members of the family. The values of the force:length ratios which satisfy the super-stability conditions have been computed analytically. New super-stable tensegrity forms of the octahedron family have been obtained. Results show that all of them are members of the octahedron family having as folded forms all the lower members of the family.

Keywords: Tensegrity; Octahedron family; Analytical form-finding; Force density method.

1. INTRODUCTION

Tensegrity structures are pre-stressed pin-jointed self-equilibrated structures composed by compression and tension members (called struts and cables respectively). They were first introduced by Fuller [1] and they have attracted the attention of researchers in the last years due to their lightweight, controllability, deployability and ingenious forms. Due to this, tensegrity structures have been applied in a wide diversity of fields as civil engineering [2], aerospace [3], biology [4] and robotic [5].

Self-equilibrium is one of the key aspects in the design of tensegrity structures. This is because the geometrical configuration and the prestress state of the members of the tensegrity are interdependent between each other. The process of determining a geometrical configuration and a suitable prestress state of the members of a tensegrity that leads to an equilibrium shape is called form-finding. Tibert and Pellegrino [6] presented a review of form-finding methods of tensegrity structures. The Force Density Method (FDM) proposed in [7,8] is one of the most used form-finding methods of tensegrity structures. The FDM is based on the concept of force density or force:length ratio q, defined as the ratio between the axial force and the length of each member of the tensegrity, which is is considered as an input of the form-finding problem.

[1] *Department of Industrial and Civil Engineering. University of Cádiz (SPAIN). manuelalejandro.fernandez@uca.es (Corresponding author)*
[2] *Department of Structural Mechanics, University of Granada (SPAIN). emontes@ugr.es*
[3] *Department of Structural Mechanics. University of Granada (SPAIN). mlgil@ugr.es*

In general, two categories of form-finding methods can be defined: numerical and analytical. In the literature there are some numerical form-finding methods [9–12]. This type of form-finding methods are used to obtain the equilibrium configuration of complex tensegrity structures with a high number of members or with lack of symmetry. On the other hand, analytical methods are employed in the case of tensegrity structures with a lower number of members and with a high order of symmetry. Examples of them can be found in [13–16].

Another key aspect in the design of tensegrity structures is the stability. A tensegrity is super-stable if it is always stable for any level of self-stress and materials properties considered [17,18]. The super-stability of a tensegrity is a robust criterion for this type of structures. The analytical form-finding method proposed in [13,14] leads to super-stable tensegrity structures.

The concepts of full and folded forms of tensegrity structures were introduced in [13]. Full forms are tensegrity structures in which all the nodes have different coordinates in the space. On the other hand, folded forms are tensegrity structures where some nodes share the same position in the space. A tensegrity family is a group of tensegrity structures that share a common connectivity pattern [14]. A tensegrity belongs to a family if it has as folded forms all the lower members of the family. In Fernández-Ruiz et al. [14] the Octahedron family was presented, considering only two different values of q: q_c for cables and q_b for struts or bars.

In this work the octahedron family is presented as a source of tensegrity forms. New super-stable tensegrity forms are derived from the connectivity pattern of the Octahedron family considering a higher number of different force:length ratio values.

2. EQUILIBRIUM EQUATIONS AND SUPER-STABILITY OF TENSEGRITY STRUCTURES

The FDM method proposed by Schek [8] was originally conceived as a form-finding method for general networks. However, it can be applied to tensegrity structures. The connectivity of a tensegrity composed by m members and n nodes is defined by the connectivity matrix $\mathbf{C}$ ($\in\Re^{m\times n}$). Matrix $\mathbf{C}$ is constructed in the following way: if a general member j connects nodes i and k (with $i < k$), the ith and kth elements of the jth row of $\mathbf{C}$ are set to 1 and -1 respectively. The force:length ratio of each member is collected in the diagonal matrix $\mathbf{Q}$ ($\in\Re^{m\times m}$). Finally, the force density matrix is defined as $\mathbf{D} = \mathbf{C}^T\mathbf{Q}\mathbf{C}$ ($\in\Re^{m\times m}$). The symbol $[]^T$ represents the transpose operation. The equilibrium equations of a general tensegrity can be formulated as:

$$\begin{aligned} \mathbf{D}\,\mathbf{x} &= 0 \\ \mathbf{D}\,\mathbf{y} &= 0 \\ \mathbf{D}\,\mathbf{z} &= 0 \end{aligned} \qquad (1)$$

In Eq. (1) $\mathbf{x}$, $\mathbf{y}$ and $\mathbf{z}$ ($\in\Re^n$) are the nodal coordinate vectors in x, y and z directions of the space.

A tensegrity structure of dimension d has a force density matrix $\mathbf{D}$ with a rank deficiency of at least d+1 [10,13]. This condition is generally called the non-degeneracy condition. In Hernández-Montes et

al. [13] this condition is achieved imposing that the characteristic polynomial of **D** (see Eq. (2))has *d*+1 zero roots.

$$p(\lambda) = \lambda^n + a_{n-1}\lambda^{n-1} + \cdots + a_1\lambda + a_0 \quad (2)$$

By doing so, the three coefficients a_3, a_2 and a_1 (which are expressed in terms of the different force:length ratio values considered for all the members of the tensegrity) are set to zero, forming a system of equations (see Eq. (3)). By construction of **D** in the case of tensegrity structures, a_0 is always equal to 0 [13].

$$\begin{aligned} a_3(q_1, \dots, q_m) &= 0 \\ a_2(q_1, \dots, q_m) &= 0 \\ a_1(q_1, \dots, q_m) &= 0 \end{aligned} \quad (3)$$

Regarding the stability of the resultant tensegrity, the super-stability conditions for a tensegrity structure are the following [14,19]:

1. The rank deficiency of the force density matrix **D** is exactly *d* + 1.
2. The force density matrix **D** is positive semi-definite.
3. The rank of the matrix **G** is (d^2 + *d*)/2. A deeper explanation about matrix **G** can be seen in [19].

A more detailed description of the analytical form-finding procedure used in this work can be seen in [13,14].

3. THE OCTAHEDRON FAMILY

The octahedron family is composed by three members: the octahedron, the expanded octahedron and the double-expanded octahedron [14]. The first member of the family is the octahedron (see Figure 1.a), which is composed by 15 members (12 cables and 3 struts) and 6 nodes. The expanded octahedron (see Figure 1.b) is the second member of the family, and it has 30 members (24 cables and 6 struts) and 12 nodes. Both tensegrities are well-known tensegrity forms present in numerous works in the literature. The expanded octahedron is the expansion of the octahedron (as it is indicated by its name), in such a way that each node, cable and strut of the octahedron is duplicated during the expansion process. Based on the expansion from the octahedron to the expanded octahedron, Fernández-Ruiz et al. [14] obtained the double-expanded octahedron, the third component of the octahedron family (see Figure 1.c). This new tensegrity form is composed by 60 members (48 cables and 12 struts) and 24 nodes. All the components of the octahedron family are formed by the combination of rhombic cells.

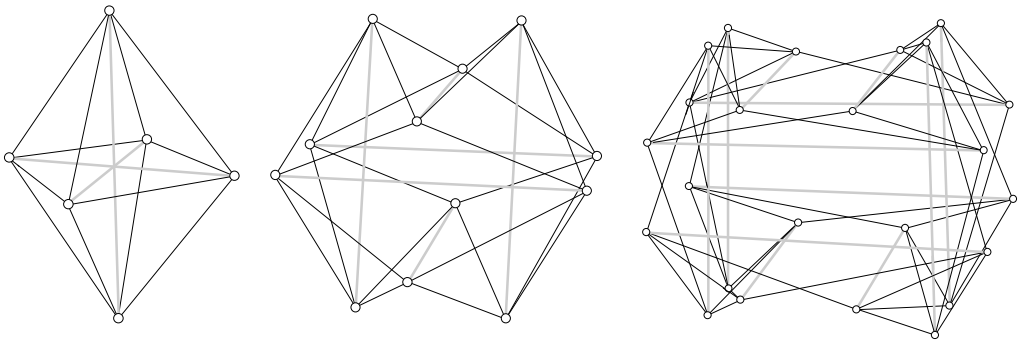

(a) (b) (c)

Figure 1. *Octahedron family: (a) octahedron, (b) expanded octahedron and (c) double-expanded octahedron. Black lines correspond to cables and grey lines to struts. Adapted from* [20].

It is interesting to remark that in the case of the three members of the octahedron family [14] represented in Figure 1 only two different q values were considered: q_c for cables and q_b for bars or struts (black and grey lines respectively in Figure 1). New tensegrity forms can be derived from the Octahedron family based on its connectivity pattern, either by the definition of a higher member through an expansion process or by introducing a higher number of different force:length ratio values for cables and struts.

4. OCTAHEDRON FAMILY. NEW SUPER-STABLE TENSEGRITY FORMS

As commented before, all the cables and struts of the tensegrities of the Octahedron family in Figure 1 have the same value of q. Nevertheless, new super-stable tensegrity forms that belongs to the Octahedron family can be obtained considering a higher number of q values.

4.1. Octahedron

A plane connection graph is a graphical representation of the connectivity between the nodes of a tensegrity [14]. Figure 2 shows the plane connection graph of the octahedron which has been defined based on the connectivity rules of the octahedron family defined in [14]. The connectivity matrix $\mathbf{C} \in \Re^{15\times 6}$ of the octahedron can be constructed using the plane connection graph shown in Figure 2.

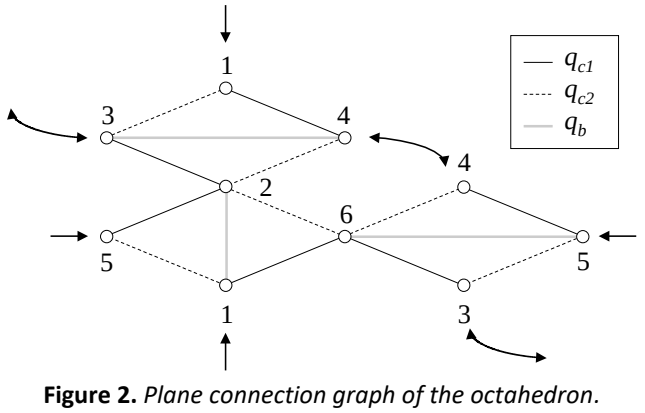

Figure 2. *Plane connection graph of the octahedron.*

Now three different values of force:length ratio are going to be considered: q_{c1} for type-1 cables (continuous black lines in Figure 2), q_{c2} for type-2 cables (dashed black lines in Figure 2) and q_b for struts (grey lines in Figure 2). Then the characteristic polynomial p(λ) of the resulting matrix $\mathbf{D}\in\Re^{15\times6}$ is computed and the non-degeneracy condition in 3D shown in Eq. (3) is imposed. Two independent normalized force:length ratios taken as $Q_1 = -q_{c1}/q_b > 0$ and $Q_2 = -q_{c2}/q_b > 0$ are considered as in [16]. As it has been already explained in Section 2, the system of equations $a_1(Q_1, Q_2) = a_2(Q_1, Q_2) = a_3(Q_1, Q_2) = 0$ implies that matrix **D** has a rank deficiency of at least 4. The solutions of the above system of equations are: $\{q_b = 0\}$ (not considered), $\{Q_1, = -1/2; Q_2 = 1/2\}$ (not possible because Q_1 is < 0), $\{Q_1 = 1; Q_2 = -1\}$ (not possible because Q_2 is < 0) and $\{Q_1 = 1/2; Q_2 = 1/2\}$. So, the only possible solution is $Q_1 = Q_2 = 1/2$, which coincides with the unique solution proposed in [14] (that is, $q_{c1} = q_{c2} = -2\ q_b$). This solution leads to the octahedron [14] (see Figure 1.a), which is a super-stable tensegrity form.

4.2. Expanded octahedron

Figure 3 shows the plane connection graph of the expanded octahedron. It can be clearly seen that the expanded octahedron has twice the number of rhombic cells of the previous member of the family (the octahedron, see Figure 2). Consequently, the expanded octahedron has twice the number of nodes, cables and struts in comparison with the octahedron. The connectivity matrix $\mathbf{C}\in\Re^{30\times12}$ of the expanded octahedron is defined based on the plane connection graph (see Figure 3).

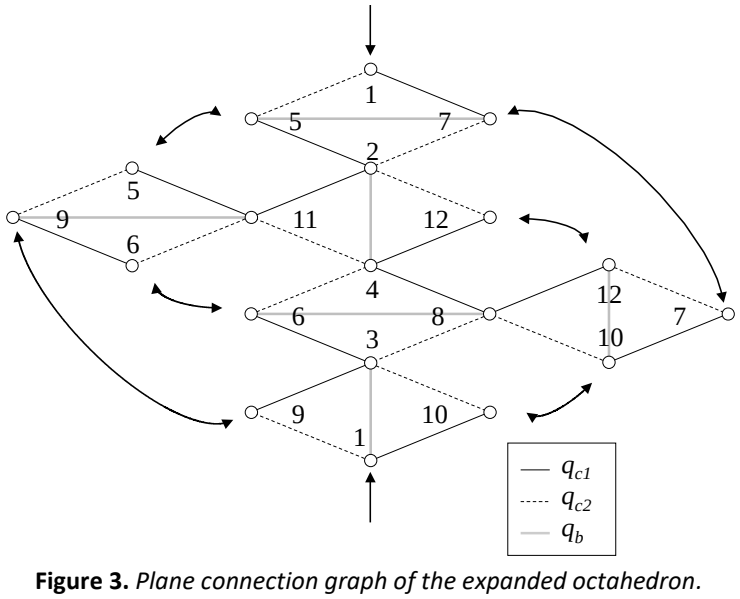

Figure 3. *Plane connection graph of the expanded octahedron.*

Let us consider again three different values of q: q_{c1} for type-1 cables, q_{c2} for type-2 cables and q_b for struts (continuous black lines, dashed black lines and grey lines in Figure 3 respectively), resulting in $\mathbf{Q}\in\Re^{30\times30}$. The characteristic polynomial p(λ) of the resulting matrix $\mathbf{D}\in\Re^{12\times12}$ is calculated and the system of equations $a_1(Q_1, Q_2) = a_2(Q_1, Q_2) = a_3(Q_1, Q_2) = 0$ solved. The solutions of the system are: $\{q_b = 0\}$ (not considered), $\{Q_1 = 0; Q_2 = 0\}$ (not considered), $\{Q_1 = 1/2; Q_2 = 1/2\}$ and the values shown in Eqs. (4) and (5).

$$Q_2 = \frac{-1 + 4Q_1 - 3{Q_1}^2 - \sqrt{1 - 2Q_1 + {Q_1}^2 - 6{Q_1}^3 + 9{Q_1}^4}}{3(-1 + 2Q_1)} \tag{4}$$

$$Q_2 = \frac{-1 + 4Q_1 - 3{Q_1}^2 + \sqrt{1 - 2Q_1 + {Q_1}^2 - 6{Q_1}^3 + 9{Q_1}^4}}{3(-1 + 2Q_1)} \tag{5}$$

The solution $Q_1 = Q_2 = 1/2$ coincides with the solution obtained in the previous subsection. This solution corresponds to the octahedron (see Figure 1.a) but now with two nodes sharing the same position of the space (that is, duplicated nodes). This proves that the octahedron is the folded form of the expanded octahedron [14].

The self-equilibrated configurations of the expanded octahedron considering three different q values are the ones collected in the previous solutions. However, it has to be pointed out that only some of them satisfy the super-stability conditions defined in Section 2. Henceforth, the super-stability of the solutions is studied. Figure 4.a shows the Q_1 - Q_2 curves corresponding to Eqs. (4) and (5). Firstly, the condition $q_b < 0$, $q_{c1} > 0$ and $q_{c2} > 0$ must be fulfilled (which corresponds with $Q_1 > 0$ and $Q_2 > 0$ as stated above). Thus, curve 1 of Eq. (5) and the part of the curve of Eq. (4) which is not in the region $Q_1 > 0$ and $Q_2 > 0$ must be excluded from the study. Secondly, condition (1) for the super-stability of tensegrity structures requires that the force density matrix **D** must have exactly four zero-eigenvalues. This condition is fulfilled for all the Q_1 - Q_2 pairs of values defined by Eqs. (4) and (5) in the region $Q_1 > 0$ and $Q_2 > 0$ and for the solution $Q_1 = Q_2 = 1/2$. Thirdly, condition (2) of super-stability requires that matrix **D** should be positive semi-definite. This condition is not fulfilled by the solution $Q_1 = Q_2 = 1/2$ which has some negative eigenvalues, so it is excluded of the super-stability analysis (this has been represented by a small white circle in Figure 4.a). Figure 4.b shows the minimum eigenvalue of matrix **D** obtained from the region $Q_1 > 0$ and $Q_2 > 0$ of the curve corresponding to Eq. (4) (i.e., in the range $0 < Q_1 < 2/3$). It can be seen in Figure 4.b that there is always a negative eigenvalue of **D** in this region and consequently, Eq. (4) is excluded from the study. On the other hand, the matrix **D** corresponding to the values of curve 2 of Eq. (5) is always positive semi-definite. Finally, condition (3) requires that the geometry matrix **G** (defined in [19]) should have a rank of 6 in the case of a three-dimensional tensegrity. The tensegrities defined by curve 2 of Eq. (5) in Figure 4.a have a geometrical matrix **G** with a rank of six. Consequently, all the solutions defined by curve 2 of Eq. (5) fulfill all the super-stability conditions given in Section 2 and they are super-stable tensegrity structures. This analysis of the super-stability of the expanded octahedron considering three different q values coincides with the analysis of the stability of rhombic truncated tetrahedral tensegrities carried out in [16]. The significant difference is that the same results have been achieved from two different paths: topology in the case of the present paper and geometry in the case of Zhang et al. [16].

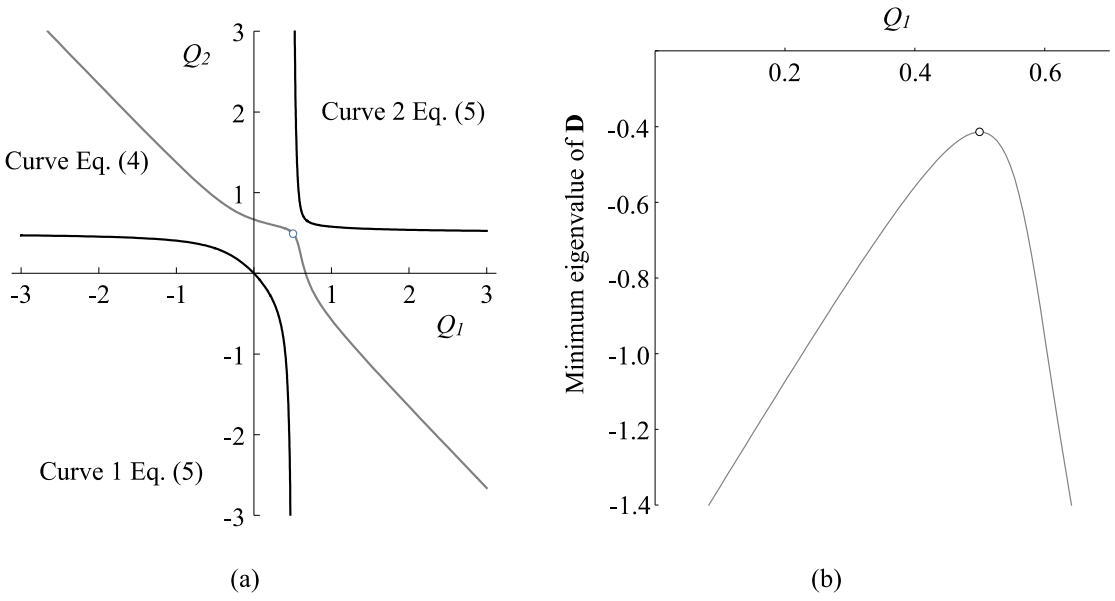

Figure 4. *(a) Q_1 - Q_2 self-equilibrium curves of the expanded octahedron (Eqs. (4) and (5)) and (b) minimum eigenvalue of* **D** *for the Q_1 - Q_2 curve of Eq. (4) in the region $Q_1 > 0$ and $Q_2 > 0$..*

The expanded octahedron has the same q value for all the cables being $q_{c1} = q_{c2} = -2/3\ q_b$ [14]. If the condition $Q_1 = Q_2$ is introduced in Eq. (5) two solutions are obtained: $Q_1 = Q_2 = 0$ and $Q_1 = Q_2 = 2/3$ (which coincides with $q_{c1} = q_{c2} = -2/3\ q_b$, expanded octahedron, see Figure 5.b). The rest of the tensegrity forms defined by curve 2 of Eq. (5) can be considered as part of the octahedron family because all of them share a common connectivity pattern. Thus, the expanded octahedron is a second member of the family together with the solutions corresponding to curve 2 of Eq. (5), see Figure 4.a. Examples of these tensegrity structures are shown in Figure 5. It can be seen that the tensegrities shown in Figure 5.a and 5.c (based on the connectivity pattern of the octahedron family) resembles a truncated tetrahedron. In fact, the well-known expanded octahedron is a rhombic truncated tetrahedral tensegrity with $Q_1 = Q_2$ [16].

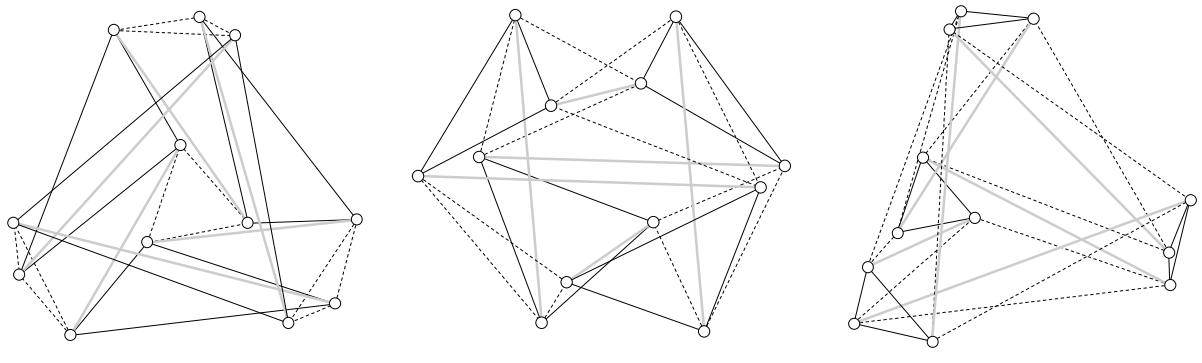

(a) $Q_1 = 3/5$; $Q_2 = 0.82$; $q_b = -1$ (b) $Q_1 = 2/3$; $Q_2 = 2/3$; $q_b = -1$ (c) $Q_1 = 1$; $Q_2 = 0.58$; $q_b = -1$

Figure 5. *Equilibrium shapes obtained from the plane connection graph shown in Figure 3 considering different values of* q. *(a) $Q_1 = 3/5$ & $Q_2 = 0.82$ (Eq. (5)) & $q_b = -1$, (b) expanded octahedron $Q_1 = 2/3$ & $Q_2 = 2/3$ (Eq. (5)) & $q_b = -1$ and (c) $Q_1 = 1$ & $Q_2 = 0.58$ (Eq. (5)) & $q_b = -1$. Black continuous and dashed lines and grey lines correspond to q_{c1}, q_{c2} and q_b respectively in accordance with Figure 3*

4.3. Double-expanded octahedron

The double-expanded octahedron is a new tensegrity structure introduced in [14]. This tensegrity was defined applying the connectivity pattern of the octahedron family [14], instead of using geometrical interpretations based on truncated regular polyhedrons as other authors did [16,21,22]. The plane connection graph of the double-expanded octahedron is shown in Figure 6. This tensegrity has twice the number of rhombic cells of the expanded octahedron (see Figure 3) and four times the number of rhombic cells of the octahedron (see Figure 2). The number of nodes, cables and struts follows the same proportionality rule. The connectivity matrix $\mathbf{C}\in\Re^{60\times24}$ of the double-expanded octahedron is defined based on the plane connection graph displayed in Figure 6.

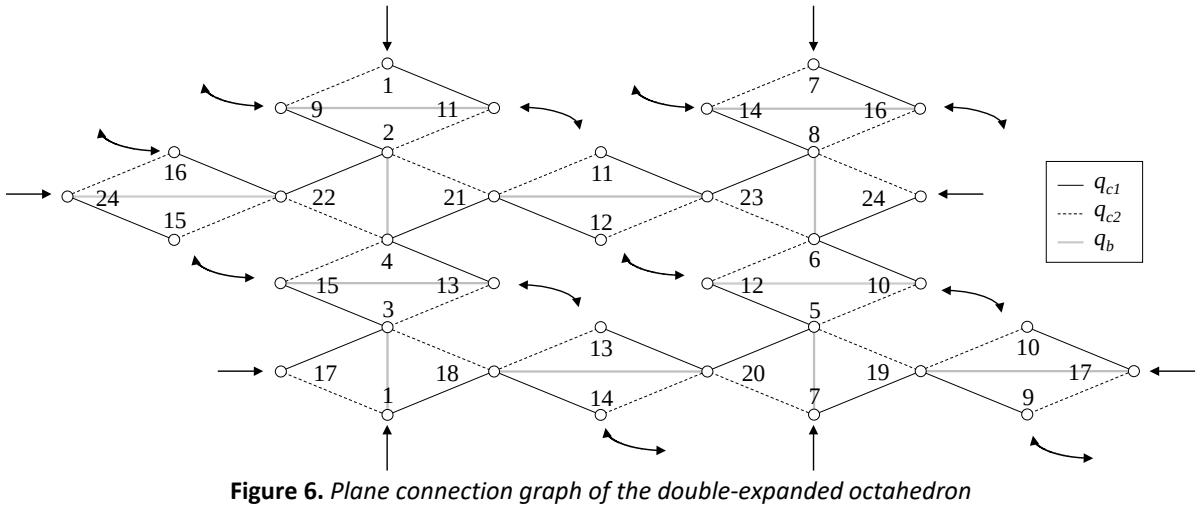

Figure 6. *Plane connection graph of the double-expanded octahedron*

As in the previous cases, three different values of q are considered: q_{c1} for type-1 cables, q_{c2} for type-2 cables and q_b for struts (continuous black lines, dashed black lines and grey lines in Figure 6 respectively), resulting in $\mathbf{Q}\in\Re^{60\times24}$. Once the characteristic polynomial p(λ) of $\mathbf{D}\in\Re^{24\times24}$ is calculated and the system of equations $a_1(Q_1, Q_2) = a_2(Q_1, Q_2) = a_3(Q_1, Q_2) = 0$ solved, the following solutions are obtained: $\{q_b = 0\}$ (not considered), $\{Q_1 = -Q_2\}$ (not possible because both Q_1 and Q_2 have to be positive), $\{Q_1 = -1/2;\ Q_2 = 1/2\}$ (not possible because Q_1 is < 0), $\{Q_1 = 2/3;\ Q_2 = 0\}$ (not considered because $Q_2 = 0$), $\{Q_1 = 1;\ Q_2 = -1\}$ (not possible because Q_2 is < 0), $\{Q_1 = 1/3;\ Q_2 = 1\}$, $\{Q_1 = 1/2;\ Q_2 = 1/2\}$ and the expressions shown in Eqs. (4), (5), (6) and (7).

$$Q_2 = \frac{1}{4}\left(3 - 6Q_1 - \sqrt{3}\sqrt{3 - 4Q_1 + 12{Q_1}^2}\right) \tag{6}$$

$$Q_2 = \frac{1}{4}\left(3 - 6Q_1 + \sqrt{3}\sqrt{3 - 4Q_1 + 12{Q_1}^2}\right) \tag{7}$$

From now on the super-stability condition for each one of the tensegrities corresponding to the obtained solutions is analyzed. The solution $\{Q_1 = 1/2;\ Q_2 = 1/2\}$ corresponds to the octahedron with

all its members and nodes quadruplicated (folded form). Analogously the solutions given by Eqs. (4) and (5) correspond to the expanded octahedron but in this case with all its members and nodes duplicated (folded form). Because all the self-equilibrium configurations of the previous members of the family are present as folded forms of the double-expanded octahedron, it can be concluded that all of them are members of a same tensegrity family.

Figure 7.a shows the Q_1 - Q_2 curves defined by Eqs. (4), (5), (6) and (7). Firstly, it is necessary to check that Q_1 and $Q_2 > 0$. Based on this condition, curve 1 of Eq. (5), the curve of Eq. (6) and the part of the curves of Eq. (4) and Eq. (7) which are not in the region $Q_1 > 0$ and $Q_2 > 0$ have been excluded from the study. Regarding condition (1) of super-stability, solutions $\{Q_1 = Q_2 = 1/2\}$ and $\{Q_1 = 1/3;\ Q_2 = 1\}$ have more than 4 zero-eigenvalues and consequently they have also been excluded because of the super-stability requirement. Regarding the condition (2) of super-stability, matrix **D** should be positive semi-definite. Figure 7.b shows the minimum eigenvalue of **D** corresponding to the Q_1 - Q_2 curves of Eqs. (4), (5) and (7). As in the case of the expanded octahedron, matrix **D** corresponding to the solutions given in Eq. (4) which fulfill $Q_1 > 0$ and $Q_2 > 0$ has negative eigenvalues. Consequently, the equilibrium configurations obtained from Eq. (4) are not considered in this work. The same occurs with the regions $Q_1 > 0.6$ of Eq. (5) and $Q_1 < 0.6$ of Eq. (7) (see Figure 7.b), so all the corresponding equilibrium configurations have been discarded. Consequently, the only regions which lead to positive semi-definiteness of matrix **D** are: $0.5 < Q_1 < 0.6$ of Eq. (5) and $Q_1 > 0.6$ of Eq. (7). It can be verified that both regions fulfill condition (3) of super-stability. Consequently, tensegrity structures whose force:length ratios satisfy Eq. (5) in the range $0.5 < Q_1 < 0.6$ or Eq. (7) in the range $Q_1 > 0.6$ are super-stable.

It is interesting to note that results shown in Figures 4.b and 7.b have been obtained numerically whereas in the paper a symbolic analysis has been carried out.

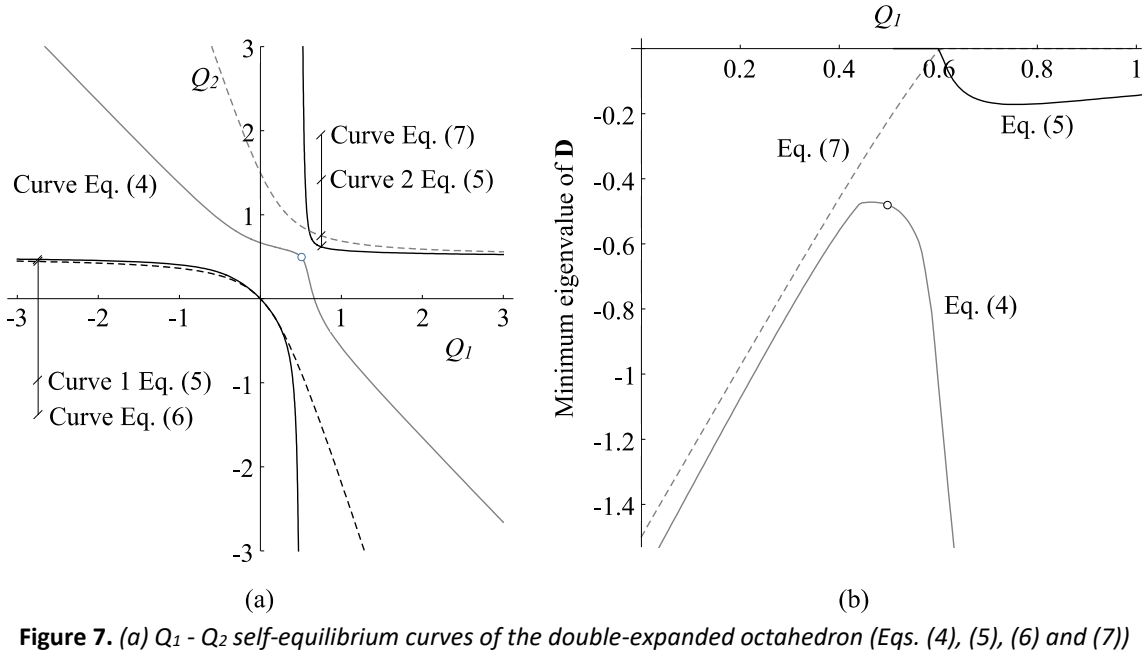

Figure 7. *(a) Q_1 - Q_2 self-equilibrium curves of the double-expanded octahedron (Eqs. (4), (5), (6) and (7)) and (b) minimum eigenvalue of **D** for the Q_1-Q_2 curve of Eqs. (4), (5) and (7) when both $Q_1 > 0$ and $Q_2 > 0$ are fulfilled.*

Results above show that folded and full forms solutions are collected in different curves. The curve corresponding to Eq. (7) corresponds to full forms whereas Eqs. (4) and (5) and the solution {Q_1 = 1/2; Q_2 = 1/2} correspond to folded forms (expanded octahedron and octahedron, respectively). From the previous study, it can be concluded that the only super-stable folded forms of the octahedron family so far are the ones obtained from Eq. (5) in the region 0.5 < Q_1 < 0.6. On the other hand, the equilibrium configurations obtained from Eq. (7) with Q_1 > 0.6 lead to super-stable full forms.

The double-expanded octahedron has the same q value for all the cables in such a way that q_{c1} = q_{c2} = -3/4 q_b [14]. If the condition Q_1 = Q_2 is introduced in Eq. (7) two solutions are obtained: Q_1 = Q_2 = 0 and Q_1 = Q_2 = 3/4 (which coincides with q_{c1} = q_{c2} = -3/4 q_b, i.e. double-expanded octahedron, see Figure 8.a). New super-stable tensegrity forms can be obtained introducing different Q_1 - Q_2 pairs of values according to Eq. (7) with Q_1 > 0.6 (see Figure 8.b and 8.c).

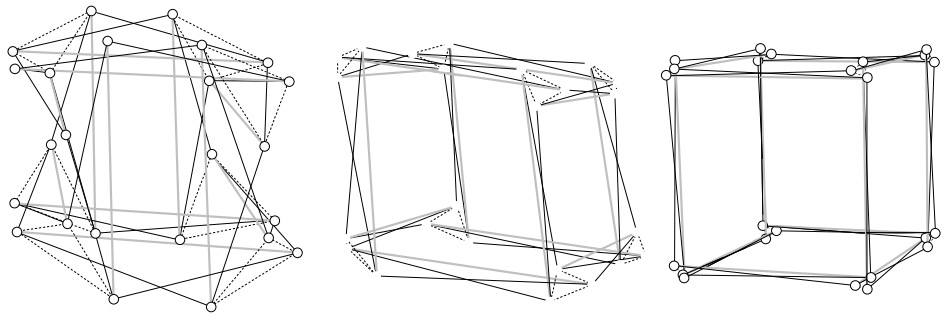

(a) Q_1 = 3/4; Q_2 = 3/4 q_b = -1 | (b) Q_1 = 2; Q_2 = 0.59 q_b = -1 | (c) Q_1 = 5; Q_2 = 0.53 q_b = -1

Figure 8. *Equilibrium shapes obtained from the plane connection graph shown in Figure 6 considering different values of q. (a) Double-expanded octahedron Q_1 = 3/4 & Q_2 = 3/4 (Eq. (7)) & q_b = -1, (b) Q_1 = 2 & Q_2 = 0.59 (Eq. (7)) & q_b = -1 and (c) Q_1 = 5 & Q_2 = 0.53 (Eq. (7)) & q_b = -1. Black continuous and dashed lines and grey lines correspond to q_{c1}, q_{c2} and q_b respectively in accordance with Figure 6.*

It can be clearly seen that, as the value of Q_1 in Eq. (7) increases, the resultant tensegrity resembles more a truncated cube. So, as the expanded octahedron can be geometrically obtained from a truncated tetrahedron [16], the double expanded octahedron can be geometrically obtained from a truncated cube.

5. CONCLUSIONS

The Octahedron family has been presented as a new source of tensegrity structures. In the case that only two force:length ratio values are considered (i.e. one for cables and another one for struts) three members of the family are obtained: the octahedron, the expanded octahedron and the double-expanded octahedron. The topology of these tensegrity structures is stablished following a certain connectivity pattern, which is common for the whole family. In this work a higher number of possible q values has been considered. In particular, two types of cables are identified, with different q values. The system of equations resulting from the form-finding problem has been solved analytically and

new super-stable tensegrity forms have been obtained. All the tensegrity structures studied in this work belongs to the Octahedron family because they have as folded forms all the inferior members of the family.

REFERENCES

[1] R.B. Fuller, Synergetics - explorations in the geometry of thinking, Macmillan, London, UK, 1975.

[2] B. Adam, I.F.C. Smith, Active tensegrity: A control framework for an adaptive civil-engineering structure, Comput. Struct. 86 (2008) 2215–2223. doi:10.1016/j.compstruc.2008.05.006.

[3] A.G. Tibert, S. Pellegrino, Deployable Tensegrity Reflectors for Small Satellites, J. Spacecr. Rockets. 39 (2002) 701–709. doi:10.2514/2.3867.

[4] D.E. Ingber, The Architecture of Life, Sci. Am. 278 (1998) 48–57.

[5] A. Graells Rovira, J.M. Mirats Tur, Control and simulation of a tensegrity-based mobile robot, Rob. Auton. Syst. 57 (2009) 526–535. doi:10.1016/j.robot.2008.10.010.

[6] A.G. Tibert, S. Pellegrino, Review of Form-Finding Methods for Tensegrity Structures, Int. J. Sp. Struct. 18 (2003) 209–223. doi:10.1260/026635103322987940.

[7] K. Linkwitz, H.J. Schek, Einige Bemerkungen zur Berechnung von vorgespannten Seilnetzkonstruktionen, Ingenieur-Archiv. 40 (1971) 145–158. doi:10.1007/BF00532146.

[8] H.J. Schek, The force density method for form-finding and computation of general networks, Comput. Methods Appl. Mech. Eng. 3 (1974) 115–134. doi:10.1016/0045-7825(74)90045-0.

[9] H.C. Tran, J. Lee, Advanced form-finding of tensegrity structures, Comput. Struct. 88 (2010) 237–246. doi:10.1016/j.compstruc.2009.10.006.

[10] J.Y. Zhang, M. Ohsaki, Adaptive force density method for form-finding problem of tensegrity structures, Int. J. Solids Struct. 43 (2006) 5658–5673. doi:10.1016/j.ijsolstr.2005.10.011.

[11] G.G. Estrada, H.-J. Bungartz, C. Mohrdieck, Numerical form-finding of tensegrity structures, Int. J. Solids Struct. 43 (2006) 6855–6868.

[12] J. Cai, J. Feng, Form-finding of tensegrity structures using an optimization method, Eng. Struct. 104 (2015) 126–132. doi:10.1016/j.engstruct.2015.09.028.

[13] E. Hernández-Montes, M.A. Fernández-Ruiz, L.M. Gil-Martín, L. Merino, P. Jara, Full and folded forms: a compact review of the formulation of tensegrity structures, Math. Mech. Solids. 23 (2018) 944–949. doi:10.1177/1081286517697372.

[14] M.A. Fernández-Ruiz, E. Hernández-Montes, J.F. Carbonell-Márquez, L.M. Gil-Martín, Octahedron family: The double-expanded octahedron tensegrity, Int. J. Solids Struct. 165 (2019) 1–13. doi:10.1016/j.ijsolstr.2019.01.017.

[15] N. Vassart, R. Motro, Multiparameted form-finding method: application to tensegrity systems, Int. J. Sp. Struct. 14 (1999) 89–104.

[16] L.Y. Zhang, Y. Li, Y.P. Cao, X.Q. Feng, A unified solution for self-equilibrium and super-stability of rhombic truncated regular polyhedral tensegrities, Int. J. Solids Struct. 50 (2013) 234–245. doi:10.1016/j.ijsolstr.2012.09.024.

[17] R. Connelly, Tensegrity structures. Why are they stable?, in: M.F. Thorpe, P.M. Duxbury (Eds.), Rigidity Theory Appl., Kluwer Academic / Plenum Publishers, 1998: pp. 47–54.

[18] J.Y. Zhang, M. Ohsaki, Stability conditions for tensegrity structures, Int. J. Solids Struct. 44 (2007) 3875–3886. doi:10.1016/j.ijsolstr.2006.10.027.

[19] J.Y. Zhang, M. Ohsaki, Tensegrity Structures. Form, Stability, and Symmetry, Springer, 2015.

[20] M.A. Fernández-Ruiz, E. Hernández-Montes, L.M. Gil-Martín, The Octahedron family as a source of tensegrity families: The X-Octahedron family, Int. J. Solids Struct. 208–209 (2021) 1–12. doi:10.1016/j.ijsolstr.2020.10.019.

[21] J.Y. Zhang, M. Ohsaki, Self-equilibrium and stability of regular truncated tetrahedral tensegrity structures, J. Mech. Phys. Solids. 60 (2012) 1757–1770. doi:10.1016/j.jmps.2012.06.001.

[22] L.Y. Zhang, Y. Li, Y.P. Cao, X.Q. Feng, H. Gao, Self-equilibrium and super-stability of truncated regular polyhedral tensegrity structures: A unified analytical solution, Proc. R. Soc. A Math. Phys. Eng. Sci. 468 (2012) 3323–3347. doi:10.1098/rspa.2012.0260.

Mechanical behavior of demountable and reusable joints with welded studs

García-García, Ismael[1]; López-Colina, Carlos[2]; Serrano-López, Miguel Ángel[3]; C-Wang, Yong[4]

ABSTRACT

The use of demountable structures has some advantages as the flexibility to change location, the reuse or positive environmental and economic effects [1]. However, the use of hollow structural sections in beam-to-column demountable joints is not widely extended due to difficulties executing and modelling the joint. The impossibility of access to the inner part of the tube leads to a difficulty of executing bolted joints. Furthermore, the Eurocode 3-1.8 which is focussed on design of joints, does not include design equations to obtain the stiffness and resistance of beam-to-column joints formed by hollow columns and open-section beams. In this paper, the stiffness and resistance of six different configurations of beam-to-column joints with threaded welded studs are studied. Initially, the mechanical properties of the studs welded to hollow columns are assessed. Then, the six specimens were tested until failure and classified by its rotational stiffness, following the Eurocode 3 [2] proposal for stiffness boundaries. Finally, two component-based models were proposed to obtain the initial stiffness of the joints.

Keywords: demountable joints; welded studs; joint characterization.

1. INTRODUCTION

The use of demountable buildings can be one of the potential chances to achieve sustainable construction [1]. The advantages of the method allow energy and materials savings, due to the possibility of reuse and recycling. However, the design of demountable beam–to-column joints with a hollow-section as a column is more difficult than in open-section columns due to the impossibility to access to the inner part of the tube. Some authors [3–5] have proposed a beam-to-column demountable joint that consists of a hollow-section column to which threaded studs are welded so that accessing the inside is not necessary. To assembly the joint, a pair of intermediate pieces are needed. These pieces consist of drilled angle cleats bolted to both flanges of the open-section beam, i.e., the angle cleats are bolted to the beam flanges by using standard bolts while at the same time they are bolted to the tubular column by using the threaded welded studs, as can be seen in Figure 1.

[1] *Department of Construction and Manufacturing Engineering. University of Oviedo (Spain). garciaismael@uniovi.es.(Corresponding author)*
[2] *Department of Construction and Manufacturing Engineering. University of Oviedo (Spain). lopezpcarlos@uniovi.es.*
[3] *Department of Construction and Manufacturing Engineering. University of Oviedo (Spain). serrano@uniovi.es.*
[4] *School of Mechanical, Aerospace and Civil Engineering. The University of Manchester. (United Kingdom). yong.wang@manchester.ac.uk.*

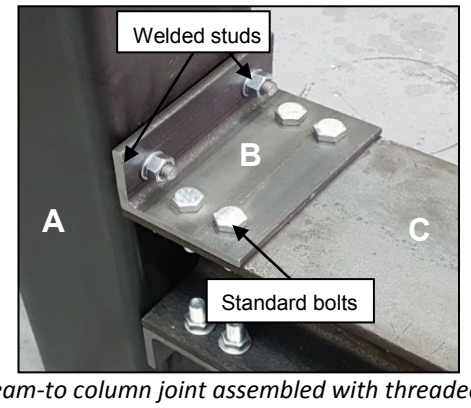

Figure 1. *Example of the beam-to column joint assembled with threaded welded studs. A: hollow-section column. B: angle cleat. C: open-section beam.*

Furthermore, Eurocode 3-1.8 focussed on design of joints does not include design equations to obtain the stiffness and resistance of beam-to-column joints formed by hollow columns and open-section beams. Therefore, the design of steel structures with this kind of connections requires carrying out numerical simulations or experimental test to obtain the mechanical properties of the joints.

In this paper, the stiffness and resistance of six beam-to-column joints assembled with threaded welded studs are studied. Initially, the mechanical properties of 8MnSi7 studs (commercially designed as K800) welded to SHS columns are assessed. The mechanical properties of the different regions of welded studs were estimated in two different ways: by using Small Punch Test (SPT) [6] and by using the relationships between hardness and yield stress proposed by Fujita and Kuki [7] and the relations between hardness and strength proposed by Murphy and Arbtin´s [8]. The properties of the base material of the studs and columns were used to estimate their failure and the moment resistance of the joint.

2. EXPERIMENTAL PROGRAM

2.1. Welded studs characterization

In this research, K800 grade studs were welded to two different thicknesses hollow-section columns in order to obtain the mechanical properties of the welded joint. The threaded studs were RD (reduced diameter) type and they were welded to 8 mm and 10 mm thicknesses hollow-section columns made of S355-J2H steel. The welding was carried out with the INOTOP 1704 drawn arc stud welding machine by Köco, setting up the following welding parameters: current 1150 A, welding time 650 ms and 2.2 mm lift.

Once welded, the specimens were cut and seven samples of 10 × 10 × 0.5 mm were extracted from different positions of the welded joint, according to Figure 2. From 1 to 5 the samples were extracted perpendicularly to the stud axis, while from 6 to 7 the samples were extracted perpendicularly to the tube rolling direction. The extracted samples were used to carry out small punch test, while the adjacent areas of that samples were used to carry out hardness measurements.

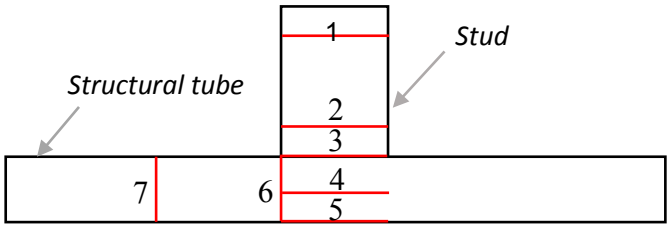

Figure 2. *Sketch of the welding joint. From 1 to 7, positions of the extracted samples.*

The small specimens were tested by using SPT, obtaining a loading - displacement curve. From that curve, the mechanical properties of each sample was estimated, by using the T.E Garcia et al. [6] approaches. Figure 3a shows the test and Figure 3b shows the load vs displacement obtained curve from one of the specimens. The process to obtain the main parameters P_y, P_m and d_m using the t/10 offset criterion are also represented, where P_y is the load at the intersection between the SPT curve and a parallel line to the initial slope with an offset of t/10, t is the sample thickness, P_m is the maximum load value and d_m is the punch displacement corresponding to this maximum load. Furthermore, Vickers hardness tests using a load of 31.12 kg were carried out for determining the resistance to indentation. Hardness tests were used to relate the hardness number with the yield stress and ultimate strength of the material, according to the equations proposed by Fujita and Kuki [7].

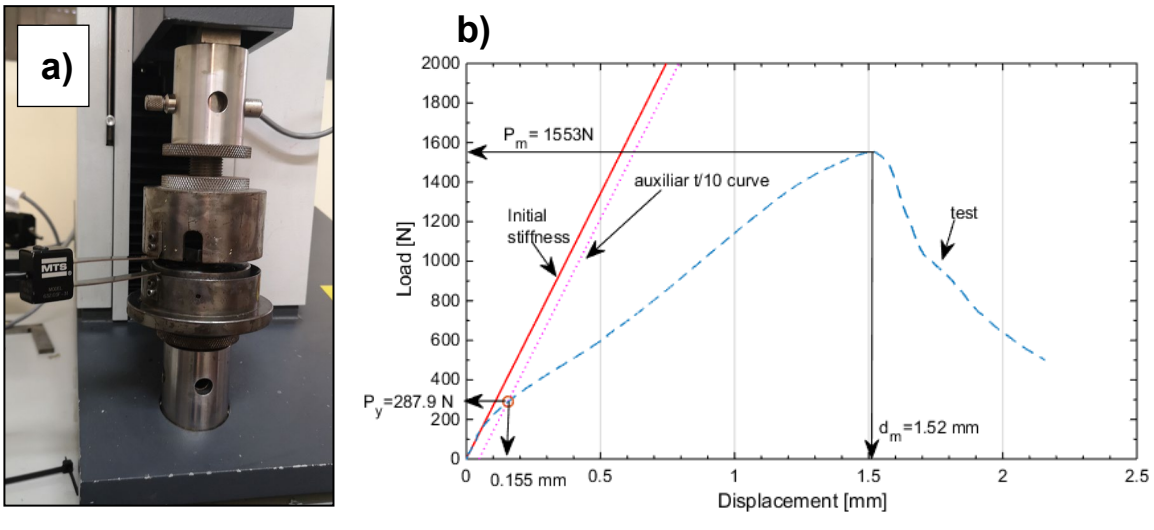

Figure 3. *Testing the SPT samples a) electromechanical tensile testing machine with the SPT testing device. b) Example of the load vs displacement curve and main parameters obtained.*

The estimations of the yield stress and ultimate strength are shown in table 1 and table 2. Table 1 shows for each zone the mechanical properties of K800 grade studs welded to the 8 mm thickness tube, obtained by means of SPT and through HV. Alike, Table 2 shows for each zone the mechanical properties of the 10 mm tube thickness.

Table 1. Mechanical properties of K800 welded studs welded to 8 mm tube thickness.

	SPT		HV	
Zone	**f_y [MPa]**	**f_u [MPa]**	**f_y [MPa]**	**f_u [MPa]**
1	672.4	647.2	690.5	795.4
2	674.4	769.0	682.3	787.8
3	574.5	746.4	748.6	848.4
4	402.1	533.9	523.8	643.1
5	392.3	499.6	390.5	521.2
6	315.1	461.7	420.3	548.4
7	347.5	482.7	353.7	487.6

Table 2. Mechanical properties of K800 welded studs welded to 10 mm tube thickness.

	SPT		HV	
Zone	**f_y [MPa]**	**f_u [MPa]**	**f_y [MPa]**	**f_u [MPa]**
1	529.3	647.8	692.0	960.3
2	594.3	612.9	659.7	912.8
3	600.7	829.1	817.8	1145.1
4	397.4	471	404.9	538.5
5	401.8	474.7	428.0	572.4
6	373.8	456	401.5	533.5
7	295.5	454.9	427.7	571.9

The study of the seven zones allowed estimating the mechanical properties on the weld, the Heat Affected Zones (HAZ), and the base metal. According to previous studies carried out by the autors [9], in wich a comparison with standard tensile tests was done, the approaches proposed by Murphy and Arbtin showed a better good agreement, with the estimations being on the safe side.

2.2. Beam to column full-scale tested specimens

The K800 tested studs in section 2 were used to assembly 6 beam to column joints. The type of joint tested was a column connected to a beam in one side by using two angle cleats, as it is shown in figure 1. The profiles used to create these different beam-to-column configurations together with the length of the beam are shown in table 3. The joints were tested under a monotonic load until failure. The moment of the joint was calculated multiplying the vertical load by the length of the beam. The rotation of the joint was measured by using a digital image correlation system. The results of the experimental stiffness $S_{j,ini,EXP}$ were obtained through the initial slope in the moment vs rotation curve and they are shown in table 5. The moments at break $M_{Rj,EXP}$ and the observed failure modes are also given in table 5. These specimens were designed to have their weakest component in the welded studs.

2.3. A component model to obtain the initial stiffness

Two component-based approaches were also compared with the experimental results of stiffness. The components were mainly considered following the recommendations in EC3 for flange cleated joints between open profiles. They are presented in table 4. In these component-models the stiffness of the

bolts in shear and bearing was considered infinite because they were prestressed and, therefore, they disappear from the calculation. The table presents the references used as sources for the equations.

The Model 1 used the equations for the stiffness of components presented in EC3-1-8. These were developed and tested for of I or H columns and Model 1 tried to directly adapt them to RHS columns. However, in the case of components considering the column web, the formulae were multiplied by 2 trying to adapt them to the two lateral faces. It is worth noting that the EC3-1-8 does not consider the column flange in bending for the compression zone since the centred position of the column web in conventional connections between open sections makes it unnecessary. However, the behaviour of the front face of tubular columns in the compression area is expected to be different. Therefore, the same equation for the front face in bending was used two times in this assessment, one considering the tension zone and another for the compression zone.

Table 3. Beam to column tested joints

Name	Column	Beam	Length [mm]	Steel	Studs	Bolts
SMS1	SHS200.6	HEB200	786.7	S275 JR	M16 K800	M16 10.9
SMS2	SHS200.8	HEB200	789.1	S355 J2H	M16 K800	M16 10.9
SMS3	SHS200.10	HEB200	787.2	S355 J2H	M16 K800	M16 10.9
SMS4	SHS200.6	IPE300	786.6	S275 JR	M16 K800	M16 10.9
SMS5	SHS200.8	IPE300	789.2	S355 J2H	M16 K800	M16 10.9
SMS6	SHS200.10	IPE300	786.8	S355 J2H	M16 K800	M16 10.9

The model 2 is the one proposed by the authors. It combines the Eurocode stiffnesses in some components with proposals for the most specific components regarding the RHS column. These proposals are:

- A semi-empirical simple equation for both the stiffness of the column lateral faces under compression and tension that was proposed and tested by López-Colina et al. (2019) for welded connections between open beams and RHS columns [10]. It was obtained by changing the exponent and coefficient of a simple equation for the stiffness of column webs by Aribert et al. [11].
- A semi-empirical adaptation of the stiffness of an infinitely long cantilever plate for the front face in bending. It was initially tested by Lozano (2019) for the stiffness of welded connections between open beams and RHS columns [12]. This stiffness has been considered for both the component in the compression zone and in the tension zone. It includes a factor, depending on the width ratio, that was experimentally and numerically calibrated. The width ratio β considered in this factor is different for the compression and the tension zone. In the compression zone it is the cleat width (equal to the beam width in our case) divided by the column width, and in the tension zone β is the distance between studs divided by the column width.

The assembly equation of both models is shown in Equation 1. It follows the EC3-1-8 method for flange cleated joints involving the following parameters: E is the Young's modulus, z is the lever arm taken as the distance from the compression centre (mid-plane of the compressed angle cleat flange) to the studs under tension, and the k_i are the stiffness coefficients (see table 4).

$$S_{j,ini} = \frac{Ez^2}{\frac{1}{k_1}+\frac{1}{k_2}+\frac{1}{k_3}+\frac{1}{k_{4,c}}+\frac{1}{k_{4,t}}+\frac{1}{k_6}+\frac{1}{k_{10}}} \quad (1)$$

Table 5 shows the experimental results of initial stiffnesses and the results of the component-based models 1 and 2. The proposed model 2 gives good agreement with the experimental values, with a mean absolute percentage error (MAPE) of 24,94% for Model 1 and 8,28% for Model 2. The maximum deviation of Model 1 is -52,81%, representing the negative value an unconservative prediction, like all the others given by this approach. The maximum deviation of Model 2 is 15,74%, being a slightly conservative prediction, like all the others given by this approach.

Table 4. Components considered in Model 1 (adaptation of EC3-1-8) and Model 2 (proposal).

	EC3 components (I-H sections)	**Components with RHS column**	**Model 1 (EC3-1-8) [2]**	**Model 2 (Proposal)**
k_1	Column web in shear	Lateral faces in shear	[2]	[2]
k_2	Column web (compression)	Lateral faces (compression)	[2] **(×2)**	[10]
k_3	Column web (tensión)	Lateral faces (tensión)	[2] **(×2)**	[10]
$k_{4,c}$	**×**	Front face in bending (compression)	**(=$k_{4,t}$)** [2]	[12]
$k_{4,t}$	Column flange in bending	Front face in bending (tension)	[2]	[12]
k_6	Flange cleat in bending	Flange cleat in bending	[2]	[2]
k_{10}	Bolts in tension	Studs in tension	[2]	[2]

(×2) means that the EC3-1-8 equation for column webs was used, but by 2 (2 lateral faces of the RHS)

These connections were classified according to their stiffness by taking into account a span of 6 m. This agrees with very common beam-depth/span ratios in buildings (20 for IPE and 30 for HEB). All joints could be classified as semi-rigid. This is because their stiffnesses fall over the limits for pinned joints (956 kNm/rad for SMS1 SMS2 and SMS3 and 1340 kNm/rad for SMS4, SMS5 and SMS6) and they are under the limits for rigid joints in non-sway frames (15303 kNm/rad for SMS1 SMS2 and SMS3 and 21445 kNm/rad for SMS4, SMS5 and SMS6).

Table 5. Beam to column tested joints. Results of the experimental tests.

Joint	**$S_{j,ini,EXP}$ [kNm/rad]**	**Model 1 $S_{j,ini,M1}$ [kNm/rad]**	**Model 2 $S_{j,ini,M2}$ [kNm/rad]**	**Observed failure mode**	**$M_{Rj,EXP}$ [kNm]**	**M_{Rj} from the stud analytical failure [kNm]**	**Analytical failure mode**
SMS1	1973	3015	1964	Punching shear	22.14	24.81	Punching shear
SMS2	2801	3638	2747	Studs (T+V)	34.71	32.94	Studs (T+V)
SMS3	3671	3886	3257	Studs (T+V)	31.65	27.58	Studs (T+V)
SMS4	2050	2820	1938	Punching shear	30.37	34.72	Punching shear
SMS5	3795	4379	3198	Studs (T+V)	40.99	42.62	Studs (T+V)
SMS6	4945	5348	4212	Studs (T+V)	41.34	35.65	Studs (T+V)

The ultimate failure modes of the joints in the experimental tests were obtained in the welded studs in all cases (punching shear or stud failure). This is what was expected since the testing programme was prepared with this purpose. However, in real connections it would be preferable to increase the stud diameter (until 20 mm) in order to get a higher ductility and to classify these connections as "partial strength joints".

The analytical resistance of the joint was obtained from the resistance of the studs. The stud resistance due to the combination of shear and tension was calculated according to the equations proposed by EC3, considering a safety factor equal to 1. The ultimate strength approaches proposed by Murphy and Arbtin´s were used in the calculations due to the better agreement previously found by the authors [9]. The fracture in the tests was observed in the zone 4, so the results of this zone were used in the calculations. In the case of the SMS1 and SMS4 specimens, which are welded to 6 mm tube thickness, no experimental data were available, so the results of the 8 mm thickness were used in calculations.

The stud punching shear resistance was calculated according to the EC3 and by using the yield limit obtained in standard tensile tests on coupons taken from the SHS columns. The failure mode of the studs was calculated as the minimum resistance between tension combined with shear and punching shear. The analytical moment of rotation and the analytical failure mode is shown in table 5. As it can be seen, the analytical equations reproduce the failure mode correctly. Which respect to the moment resistance, MRj the differences are less than 15%, being the MAPE 10,36%, but in some cases the results are not in the safe side considering a safety factor equal to 1 obtaining a until a -14,31% deviation (the negative value means an unconservative prediction).

3. CONCLUSIONS

In this paper the mechanical properties of the K800 studs welded to S355J2H columns are studied. The mechanical properties were obtained in different points of the welding through a correlation with the Vickers hardness and by means of the Small Punch Test (SPT). In this paper, the approaches proposed by Murphy and Arbtin´s was used in the calculations due to a previously better agreement found by the authors [9].

Six structural steel demountable flange cleated joints between open beams and SHS columns were designed with welded studs to be assembled and disassembled easily, allowing for reuse and contributing to sustainable construction. The joints were assembled using the previously tested K800 studs. The behaviour of these joints was tested and classified according to EC3 [2]. According to the rotational stiffness classification proposed by Eurocode 3, the six joints can be classified as semi-rigid in buildings with common beam spans.

Two component-based models were compared with the test results. The first one directly adopted the EC3-1-8 stiffness coefficients for open profiles with minimal adaptations. The second one proposed specific stiffness coefficients for the lateral and front faces of the hollow column in the compression and tension zone.

The results showed that the stiffnesses of the components involving the front face and the lateral faces of the tubular columns in the compression and tension zones cannot be directly obtained from the existing equations in EC3-1-8 for the column web. The proposed model (Model 2) obtains a good approach by adopting two simple equations for the stiffness of the lateral and front faces in the compression and tension zone. It can be improved in the future with other results from numerical parametric studies or new experimental tests by varying the dimensions of the specimens.

Another essential point that arises from the study of these joints is that, excepting when the compressed cleat has a similar width to the column one, the flexural stiffness of the front face should be considered not only in the tension zone, but also in the compression one.

The failure of the studied joints was dominated by the failure of the studs. The failure was due to punching shear in the specimens formed by tubes with 6mm thickness and due to a shear and tension combination in the rest of the analysed cases. The analytical failure of the studs due to tension and shear was estimated using the equations proposed in EC3, being the differences less than 15%. Which respect to the analytical failure mode, the equations reproduce the failure mode correctly.

ACKNOWLEDGEMENTS

The economic support given by the Spanish Ministry of Education through the project BIA2017-83467-P, PRE2018-084273 and by the CIDECT through project 5CF is gratefully appreciated.

REFERENCES

[1] Boedianto, J.C., & Walraven, P. (2000). Optimizing the environmental impact of demountable building. *In Proceedings of the RILEM/CIB/ISO international symposium on integrated life-cycle design of materials and structures* (pp. 135–141).

[2] EN 1993-1-8:2005 - *Eurocode 3: Design of steel structures* - Part 1-8: Design of joints, Eurocode 3, 2005.

[3] Maquoi, R., Naveau, X., & Rondal, J., (1984). Beam-column welded stud connections. *Journal of Constructional Steel Research*. doi: 10.1016/0143-974X(84)90032-4.

[4] Vandegans, D. (1996). Use of Threaded Studs in Joints between I-Beam and RHS-Column. In *Istanbul Colloquium on Semi-Rigid Connections*, Zürich, Switzerland (pp. 53–62).

[5] Serrano, M.A., López-Colina, C., Wang, Y.C., Lozano, M., García, I., & Gayarre, F.L. (2021). An experimental study of I beam-RHS column demountable joints with welded studs. *Journal of Constructional Steel Research*, vol. 182, p. 106651, doi: 10.1016/j.jcsr.2021.106651.

[6] García, T.E., Rodríguez, C., Belzunce, F.J., & Suárez, C. (2014). Estimation of the mechanical properties of metallic materials by means of the small punch test. *Journal of Alloys and Compounds*, vol. 582, (pp. 708–717), doi: 10.1016/J.JALLCOM.2013.08.009.

[7] Fujita, M.; Kuki, K. (2016). An Evaluation of Mechanical Properties with the Hardness of Building Steel Structural Members for Reuse by NDT. *Metals* 2016, vol. 6, p. 247.

[8] Murphy, G., Arbtin, E. (1953). *Correlation of Vickers Hardness Number, Modulus of Elasticity, and the Yield Strength for Ductile Metals; Ames Laboratory ISC Technical Reports*. *50*; Iowa City: University of Iowa, IA, USA.

[9] García, I., Serrano, M. A., López-Colina, C., Gayarre, F. L., & Suárez, J. M. (2021). Approaches to the Mechanical Properties of Threaded Studs Welded to RHS Columns. *Materials*, 14(6), 1429.

[10] López-Colina, C. Serrano, M.A., Lozano, M., Gayarre, F.L., Suárez, J.M. & Wilkinson, T. (2019). Characterization of the main component of equal width welded I-beam-to-RHS-column connections. *Steel and Composite Structures*, vol. 32, No. 3 (pp. 337-346). doi: 10.12989/scs.2019.32.3.337.

[11] Aribert, J.M., Lachal, A., Moheissen, M. (1992). Modelling and experimental investigation of plastic resistance and local buckling of H or I steel sections submitted to concentrated or partially distributed loading. Contact Loading and Local Effects in Thin-walled Plated and Shell Structures. International Union of Theoretical and Applied Mechanics. Berlin. Springer. (pp. 101-110). doi: 10.1007/978-3-662-02822-3_13.

[12] Lozano, M. (2019). The component method applied to welded beam-to-column joints between open profiles and structural tube. PhD thesis (in Spanish). University of Oviedo. Spain.

Progressive collapse assessment of precast reinforced concrete structures using the Applied Element Method (AEM)

Nirvan Makoond[1]; Manuel Buitrago[2]; Jose Adam[3]

ABSTRACT

Progressive collapse can be defined as the process by which initial local damage sets in motion a chain of failures, which can sometimes lead to disproportionate or total collapse. It is a phenomenon that can often be triggered by abnormal loading caused by extreme events, which all types of buildings may be exposed to. Despite the fact that precast concrete structures, which are being increasingly used, can be particularly vulnerable to progressive collapse, there have been relatively few studies on the robustness of this structural typology compared to cast-in-place and steel-composite structures. Numerical models calibrated based on experimental results are one of the most promising tools for better understanding the response of precast concrete structures to accidental actions since they allow them to be studied under a wide variety of loading scenarios. This paper presents the modelling strategy and results employed for predicting the behaviour of a precast concrete test structure under different column removal scenarios using the applied element method. These results have been used to plan the monitoring strategy and loading scheme for experimental tests on an actual two-storey 15 m x 12 m structure that will be built and monitored during the sudden removal of 3 different columns.

Keywords: Robustness; Extreme events; Precast concrete; Column removal; Applied Element Method

1. INTRODUCTION

The progressive collapse of structures has attracted considerable research interest in recent years [1]. Understood as the process by which initial local damage propagates to cause a chain of failures that can lead to disproportionate or total collapse, it is a phenomenon that can often be triggered by abnormal loading caused by extreme events, which all types of buildings may be exposed to. There exist several known occurrences of progressive collapse which have led to grave negative consequences for society such as the Ronan Point collapse in London (1968), the collapse of the Twin Towers of the World Trade Center in New York (2001), and that of the Hard Rock Hotel in New Orleans (2019).

Precast concrete components are being increasingly used in construction due to significant advantages in terms of cost-effectiveness, quality assurance and durability. However, the specific features of this structural typology make them particularly vulnerable to extreme events since they

[1] *ICITECH. Universitat Politècnica de València (SPAIN). ncmakoon@upv.es*
[2] *ICITECH. Universitat Politècnica de València (SPAIN). mabuimo1@upv.es*
[3] *ICITECH. Universitat Politècnica de València (SPAIN). joadmar@upv.es (Corresponding author)*

consist of distinct elements connected together and therefore exhibit clear lines of weakness at the joints [2]. Despite this apparent vulnerability, there have been very few studies on the progressive collapse resistance of precast concrete structures when compared to research on cast-in-place and steel-composite structures. In fact, to the best of the authors' knowledge, although there have been a number of experimental tests on real-scale building structures involving the sudden removal of columns [3–7], no such tests have ever been performed on precast concrete structures.

Numerical models calibrated based on experimental results are one of the most promising tools for better understanding the response of precast concrete structures to accidental actions since they allow them to be studied under a wide variety of loading scenarios. However, the obtention of accurate results with respect to the response of critical parts (joints) using conventional models based on the Finite Element Method (FEM) presents several important challenges. Primordially, it requires very detailed and tedious modelling of the joints which may in turn require the definition of parameters that cannot be easily determined experimentally.

A numerical modelling technique that emerged in the late 1990s and known as the Applied Element Method (AEM) [8] presents several advantages for studying the progressive collapse behaviour of precast concrete structures. It has been demonstrated through several examples that this method is able to accurately model structural collapse behaviour through all stages of loading including elastic response, crack initiation and propagation in brittle materials, reinforcement yielding, element separation, and even collision. This is achieved through an efficient formulation which employs small rigid elements connected by normal and shear springs distributed on their faces.

This paper presents the preliminary results of AEM simulations of a real-scale two-storey precast concrete test structure that will be specifically built and tested in order to better understand the progressive collapse resistance of this structural typology. The experimental program of the real-scale structure involves three individual tests, each intended to simulate the removal of a specific edge or corner column as shown in Figure 1.

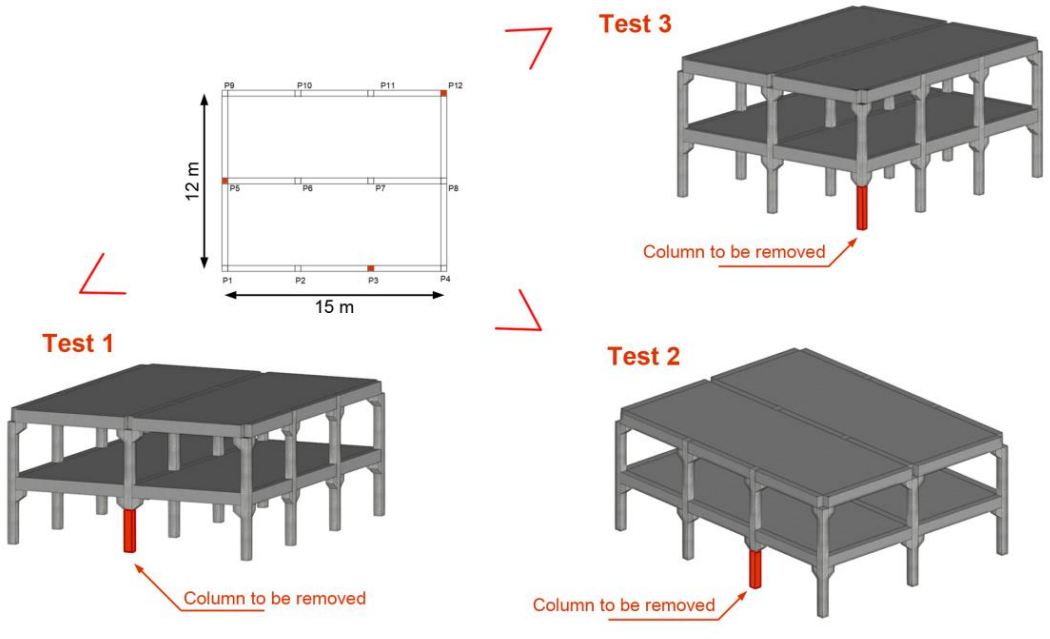

Figure 1. *Column removal scenarios to be investigated during real-scale experimental program.*

Naturally, such an experimental campaign involves high costs and can also involve a considerable amount of risk. As such, it is very important to perform predictive modelling using a validated methodology prior to performing the tests. Results from this endeavour can then be used to design loading schemes and monitoring strategies that will allow:

- The most important Alternative Load Paths (ALPs) to be studied in detail.
- The effectiveness of recommendations from the latest relevant guidelines to be evaluated.

After providing a very brief overview of some fundamental concepts of the AEM, validation study cases chosen from literature and involving experimental tests on different sub-assemblages are presented. A comparison of experimental and simulation results is given, highlighting specific aspects which are important for accurate predictive modelling of precast structures using the AEM. The numerical model of the real-scale precast concrete test structure is then described before presenting the initial simulation results. The monitoring plans designed for the actual experimental tests are then revealed before summarising the main conclusions that can be made at this stage of the research.

2. VALIDATION CASE STUDIES

Unlike solid finite elements, which can deform and change shape, the AEM employs rigid elements connected by distributed normal and shear springs present on each element face. Each rigid element is represented by only six degrees of freedom at its centre. This makes the method much more computationally efficient when compared to FEM (a typical solid 8-node element is represented by 24 degrees of freedom). In addition, the fact that the distributed springs can fail and separate means that the method can be used for modelling all stages of structural response up to failure.

All AEM simulations forming part of this research have been performed using the Extreme Loading for Structures (ELS) software package [9]. As mentioned in the introduction, although a calibration process is planned following the experimental campaign, the prior simulation results are very important for planning the loading schemes and monitoring strategies for the actual test themselves. As such, it is very important to perform a validation exercise involving the simulation of experimental tests whose results have been presented in the scientific literature. Comparison of the experimental and simulation results will not only allow a reasonable level of confidence to be established on the predicted behaviour of the test building but will also allow reasonable estimates of unknown input parameters to be derived. Such parameters include those controlling the behaviour of the interface between precast elements.

The chosen study cases are briefly presented in this section along with comparisons of the most important results.

2.1. Pushdown tests on reinforced concrete sub-assemblages

The first study case chosen for validation purposes refers to pushdown tests performed by Qian et al. on reinforced concrete beam-column sub-assemblages subjected to the loss of a middle column [10]. The test setup used for all specimens is shown in Figure 2. Each test involved the following 4 stages:

(i) The side columns of the sub-assemblage were constrained as shown in Figure 2 and a hydraulic jack placed below the middle column protruded upwards acting as a vertical restraint on the column.

(ii) Metal plates were hung from the beams of the sub-assemblage as shown in Figure 2 to simulate the design service load.

(iii) The stroke of the jack below the middle column was gradually retracted, simulating a slow release of the axial force in the middle column.

(iv) After the lower jack was completely detached and removed, the upper jack began to apply an additional downward force on the middle column until failure.

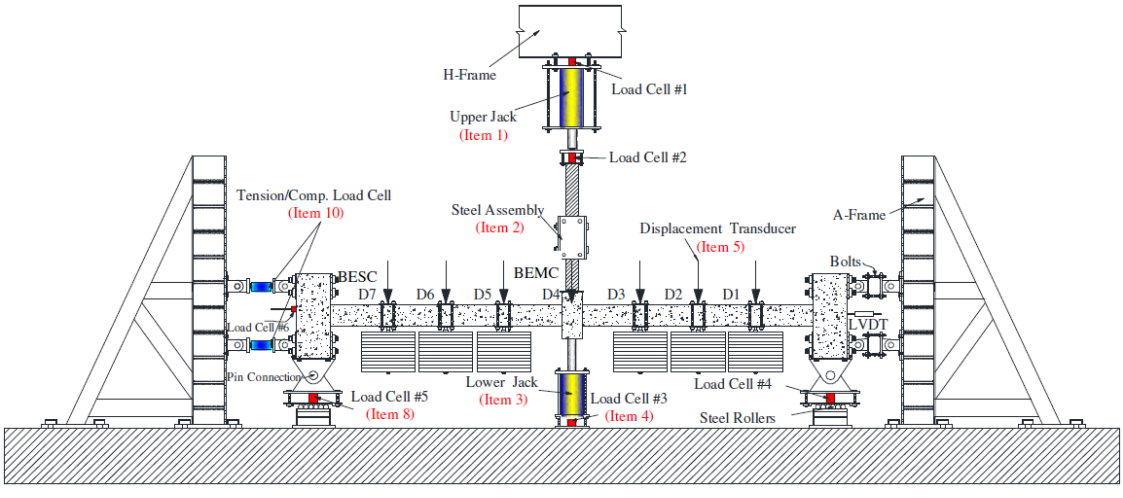

Figure 2. *Setup and instrumentation layout used for tests performed by Qian et al. Image taken from [10].*

In particular, two specimens were chosen for validation purposes. Both specimens consisted of two beams with a clear span of 3300 mm. However, one of the specimens was made of posttensioned concrete, tensioned using unbonded posttensioning strands (UPS) placed according to the parabolic profile shown in Figure 3(a). The other specimen served as a control specimen and the remaining reinforcement besides the UPS were therefore identical in both specimens.

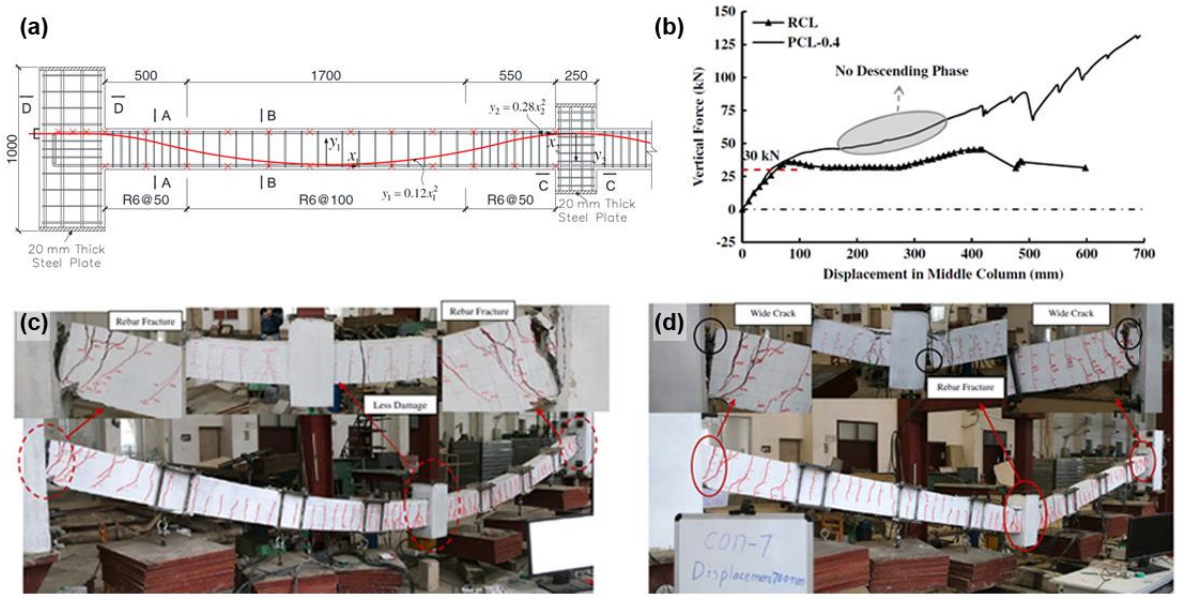

Figure 3. *(a) Dimensions and reinforcement details of the specimens chosen for validation; (b) Experimental load-displacement curve for reinforced concrete sub-assemblages with (PCL) and without (RCL) unbonded posttensioning strands; (c) Observed damage at failure for control specimen; (d) Observed damage at failure for posttensioned specimen. All images taken from [10].*

It is clear that the addition of the UPS significantly changed the progressive collapse behaviour of the reinforced concrete sub-assemblage, both in terms of load capacity and failure mode. As shown in Figure 3(b), far higher vertical forces were required to push down the posttensioned specimen as could be expected. With respect to the failure mode, it can be observed that more damage is concentrated towards the beam ends near the side columns in the control specimen (see Figure 3(c)) whereas more damage is concentrated at the beam ends near the middle column in the posttensioned specimen (see Figure 3(d)). For each of the specimens, it was observed that rebar fracture occurs in these areas of high damage concentration before complete failure.

The predicted load-displacement curve from the AEM simulations for the control specimen is shown in Figure 4 while that of the posttensioned specimen is shown in Figure 6. In both cases, they are shown together with the experimental curves presented in [10] to facilitate comparison. It should be noted that the load-displacement curves were shifted upward by 30 kN in [10] to facilitate the comparison between the two cases and to include the axial load release stage in the comparison. Both these curves were shifted back down in the figures shown in this paper to allow a direct comparison with the simulation results. The failure modes predicted by the AEM simulations are also depicted for both cases in Figures 5 and 7.

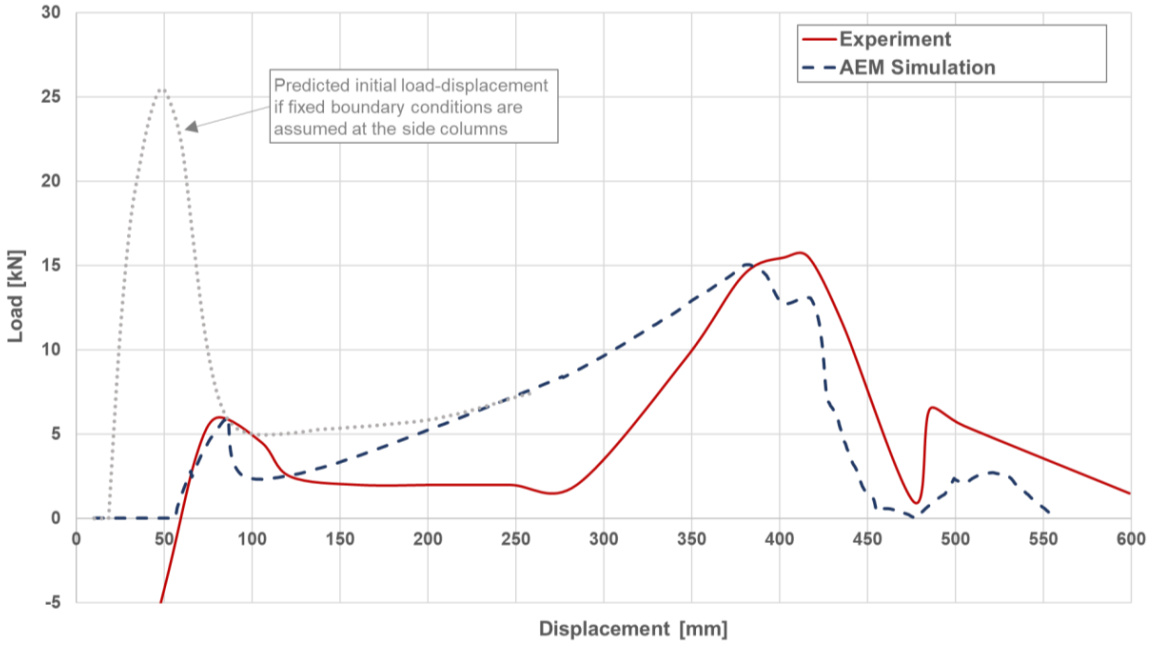

Figure 4. *Comparison of experimental and simulation load-displacement for control specimen.*

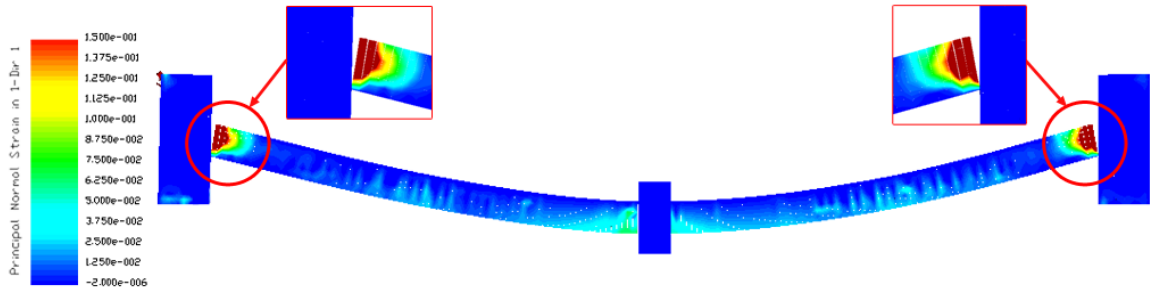

Figure 5. *Failure mode predicted by numerical model for control specimen.*

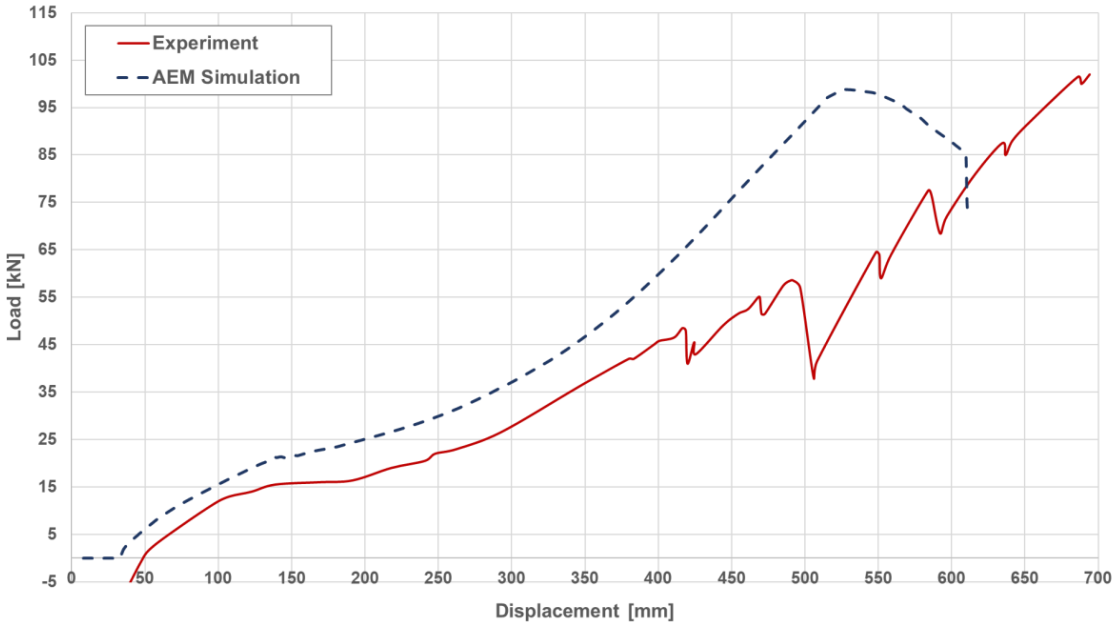

Figure 6. *Comparison of experimental and simulation load-displacement for posttensioned specimen.*

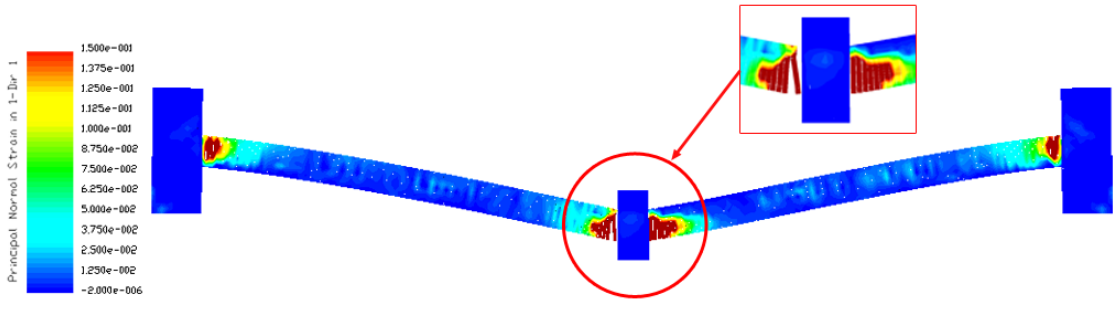

Figure 7. *Failure mode predicted by numerical model for posttensioned specimen.*

For both the control and posttensioned specimens, it is clear to see that the numerical models are able to properly predict the different stages of the response of the sub-assemblages up to failure, including the catenary tensile action of the beams. The load capacities of the structures are well estimated for both cases and the failure modes predicted are very much consistent with those observed during the experiments.

For this case, it was found that adequate calibration of the post-yield ductility characteristics of the reinforcement was particularly important. In addition, it was found that boundary conditions can play a very important role when calibrating the response of sub-assemblages. This was particularly challenging to achieve in this case as lateral load cells were used as part of the constraint system during the actual experiment. These impose a stiffness rather than a true fixed condition. As such, accurate modelling of the boundary conditions would in fact involve modelling the bracing used and imposing a lateral stiffness rather than a constraint. Since this is not an option in the latest version of ELS (version 8), an equivalent modelling procedure was employed involving different analysis stages during which the number of constrained elements were gradually reduced. Keeping fixed boundary conditions results in a substantially different load-displacement curve, particularly at lower displacements, as shown in Figure 4. This result reveals a key shortcoming of developing conclusions on progressive collapse response based on tests on sub-assemblages as it shows that such

experiments actually rely on strong assumptions on the boundary conditions imposed on part of a structure. These conditions may differ significantly in a real complete structural system, particularly under accidental loading conditions. As such, this result highlights the importance of performing tests on full-scale complete structures to better understand their resistance to progressive collapse.

2.2. Dynamic load tests on cast-in-place and precast sub-assemblages

The second study case chosen for validation purposes refers to the dynamic tests performed by Zhou et al. [11] on two specimens, a cast-in-place reinforced concrete sub-assemblage and a precast concrete one. The test setup for each specimen is shown in Figure 2. Each test specimen underwent a series of dynamic tests during which the sudden removal of the middle column was simulated using the quick-release device shown in Figure 8. The load in the steel baskets supported by the beams was increased for every subsequent test in the series until the specimens failed. The precast concrete sub-assemblage failed during the 4th load test, whereas the cast-in-place one failed unexpectedly after 20 minutes under the sustained load of the 6th test.

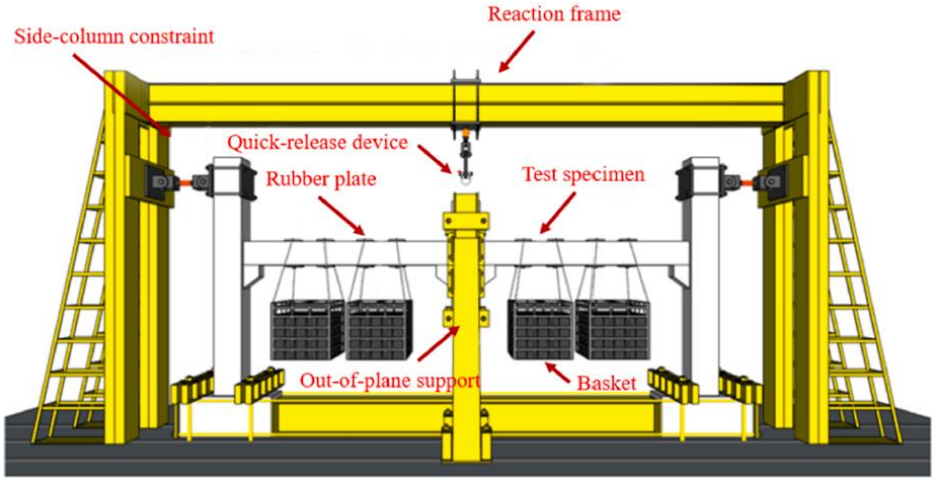

Figure 8. *Setup used by Zhou et al. for performing dynamic tests on cast-in-place and precast reinforced concrete sub-assemblages. Image taken from [11].*

Two numerical models of the different test specimens were created, using solid elements to model the concrete elements and springs to model the reinforcements. The geometry and reinforcement details were accurately reproduced according to the details reported in [11]. The material properties reported in the same reference also served as the main basis for the material models employed for the simulations. However, for the case of the precast sub-assemblage, the structure's response was largely governed by the interface between the corbels and the precast beam and the dowel that runs through it. Following a calibration procedure, it was found that accurate results could be obtained by using an effectively friction-only interface with no tensile or shear strength and with a very low shear stiffness. A friction coefficient of 0.4 was used for the interface between precast concrete elements and one of 0.1 was used between metal plates and concrete. The elastic modulus of these interfaces was set to that of the concrete material. Additionally, in order to account for very localized deformations that occurred during the tests at the interface between corbel and beam, the shear modulus of the dowel bar material had to be reduced significantly.

For the simulation of each load test, the weight of the steel baskets and their contents were considered simply by imposing lumped masses on the beams at the approximate locations where they

were hung. Each test simulation involved two stages: a static calculation stage during which the vertical displacement of the middle column was constrained and a dynamic calculation stage of at least 1 s involving the sudden release of this constraint. The self-weight and additional mass were imposed during the first step. Discretizing the dynamic calculation stage into time steps that are relatively small compared to the natural period was found to be of the utmost importance for obtaining accurate results.

A comparison of the most significant simulation and experimental results are given in Figure 9 and Tables 1 and 2, while observed and predicted failure modes are compared in Figures 10, 11 and 12.

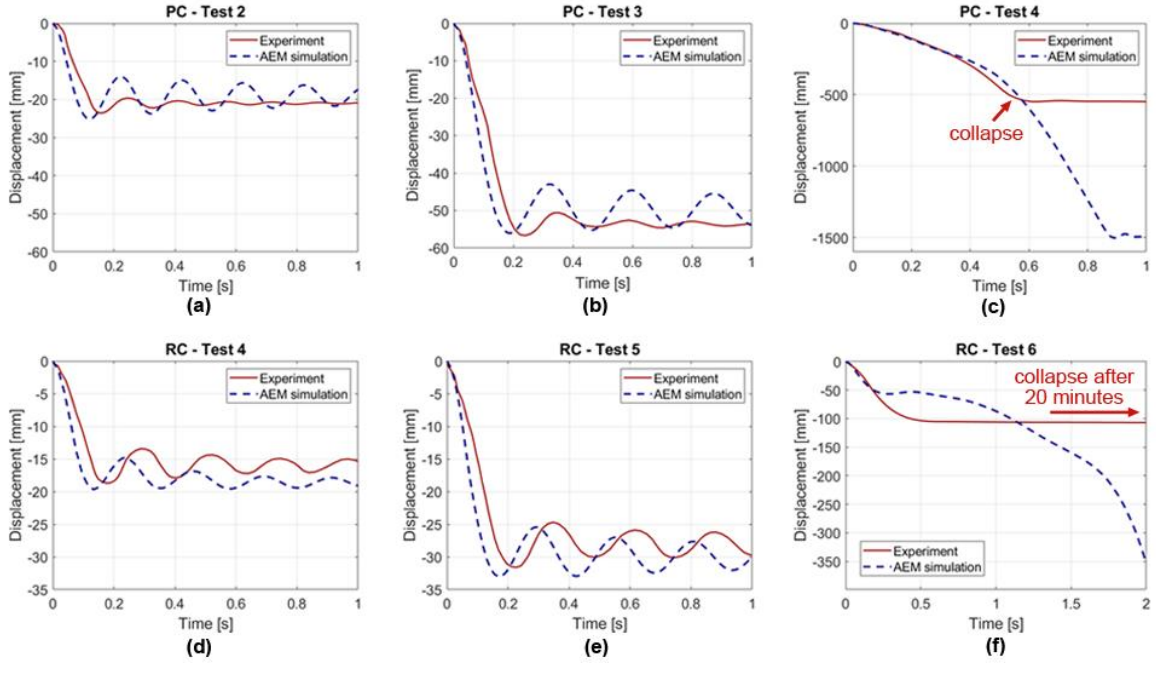

Figure 9. *Comparison of experimental and predicted dynamic response for different test specimens. The test during which the specimen failed and the two tests prior to it are shown for both the precast concrete (PC) and cast-in-place concrete (RC) sub-assemblages.*

In general, it can be said that the AEM models were able to accurately reproduce the experimentally observed differences between the cast-in-place and precast concrete sub-assemblages in terms of displacement magnitude, dynamic response and failure mode. For both specimens, the AEM simulation was able to correctly predict the load stage at which failure occurs. However, it must be said that the predicted dynamic response at failure for the cast-in-place specimen differs significantly from that observed during the test. Specifically, the onset of failure begins much earlier under the load of the 6th test in the simulation as shown in Figure 9(f).

Table 1. Comparison of experimental and simulation results for the precast concrete sub-assemblage.

PC	Peak deflection of middle column [mm]			Natural period [s]			Response time [s]		
	Test	AEM Model	Diff. [%]	Test	AEM Model	Diff. [%]	Test	AEM Model	Diff. [%]
Test 1	**-11.1**	-8.7	22%	**0.10**	0.12	-19%	**0.076**	0.070	8%
Test 2	**-24.1**	-25.1	-4%	**0.16**	0.18	-15%	**0.131**	0.120	8%
Test 3	**-58.1**	-56.5	3%	**0.22**	0.25	-13%	**0.207**	0.190	8%

Table 2. Comparison of experimental and simulation results for the cast-in-place sub-assemblage.

RC	Peak deflection of middle column [mm]			Natural period [s]			Response time [s]		
	Test	AEM Model	Diff. [%]	Test	AEM Model	Diff. [%]	Test	AEM Model	Diff. [%]
Test 1	**-2.2**	-2.3	-5%	**0.09**	0.08	11%	**-***	0.04	-
Test 2	**-6.6**	-6.9	-5%	**0.14**	0.13	4%	**0.094**	0.08	15%
Test 3	**-11.8**	-12.4	-5%	**0.19**	0.17	10%	**0.115**	0.11	4%
Test 4	**-19.2**	-18.7	3%	**0.23**	0.21	7%	**0.150**	0.13	13%
Test 5	**-32.3**	-33.0	-2%	**0.26**	0.24	9%	**0.194**	0.169	13%

* The comparison with the experimental response time is not performed for the 1st test since, as stated in [11], the dynamic response was not significant during this test.

In fact, the differences between measured and predicted natural periods after the loss of the middle-column support can also be considered as being rather high (up to 19% in one particular case). Nevertheless, this can most likely be attributed to the fact that the steel baskets with weights in them were simply modelled as lumped masses. As shown in Figures 10 and 11, these baskets are free to swing and collide and can definitely influence the true dynamic behaviour of the system.

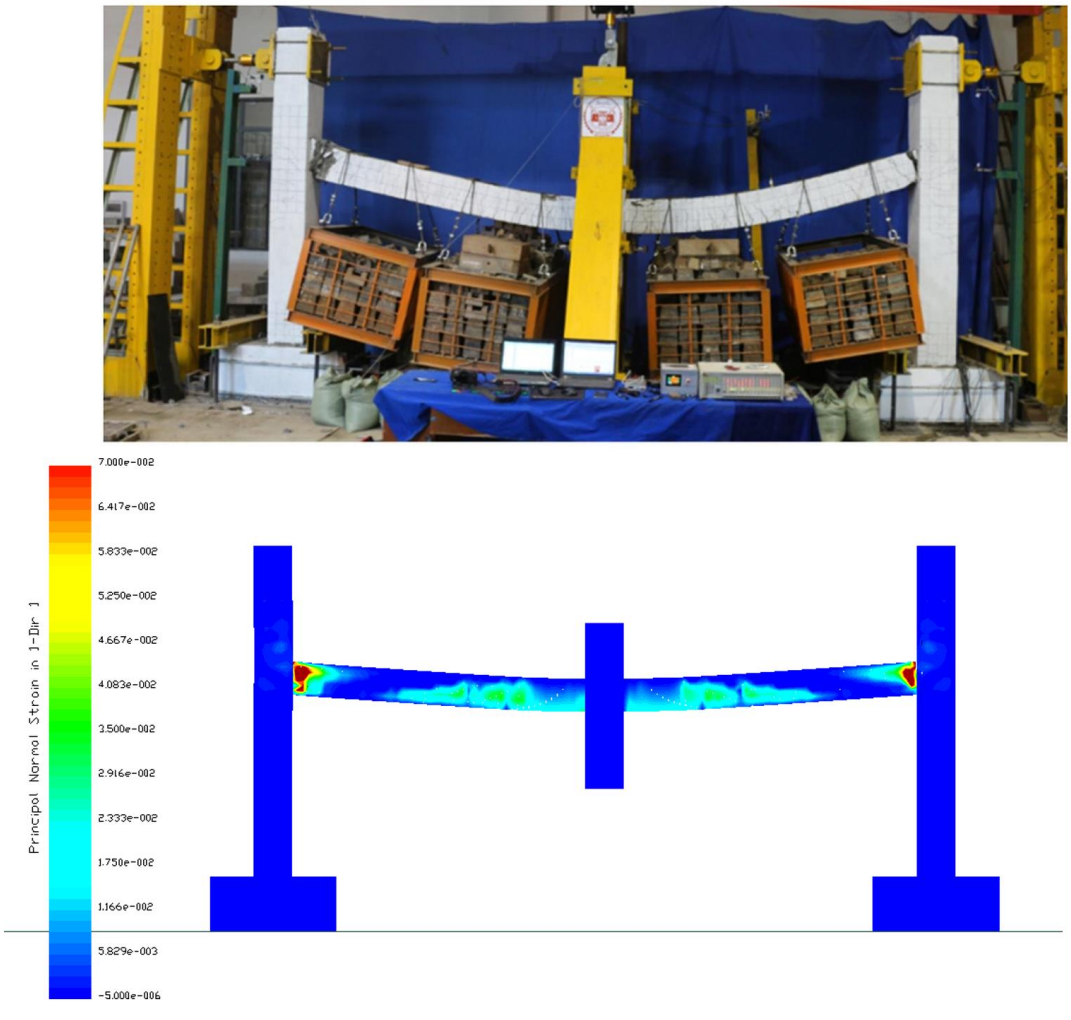

Figure 10. *Comparison between experimentally observed and predicted failure mode during 6th load test for cast-in-place sub-assemblage. Picture of actual test taken from [11].*

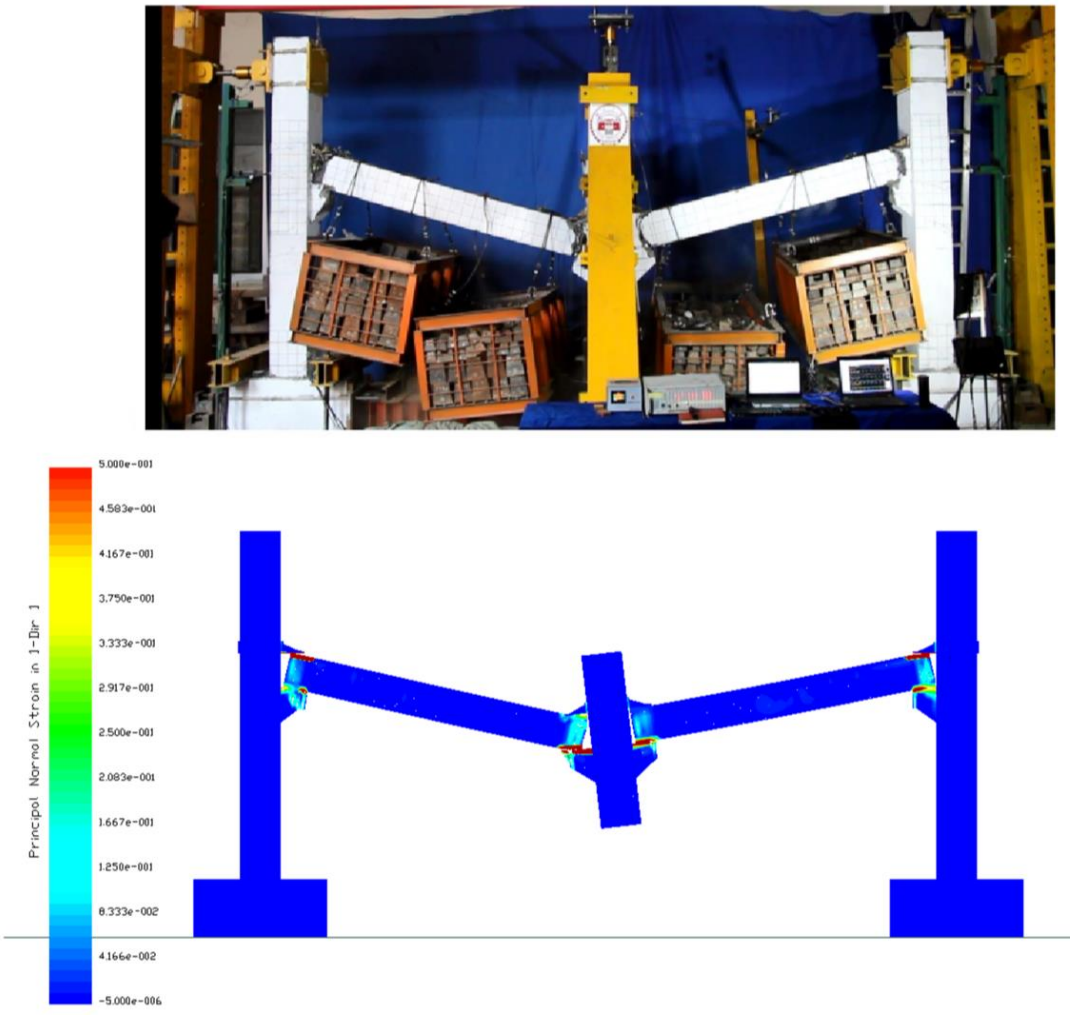

Figure 11. *Comparison between experimentally observed and predicted failure mode during the 4th load test for the precast concrete sub-assemblage. Picture of actual test taken from [11].*

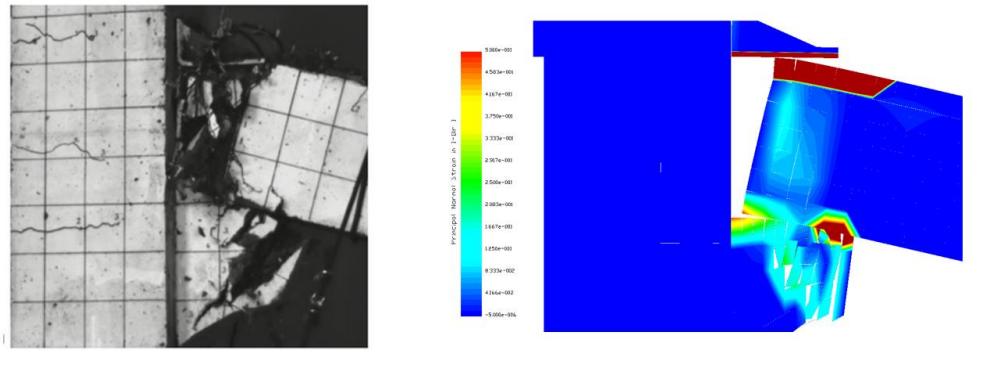

Figure 12. *Close-up comparison showing corbel-beam joint at failure during the experiment and the AEM simulation. Picture of actual test taken from [11].*

Given the good agreement between AEM simulations and the measured response of the precast concrete sub-assemblage, the calibrated properties of the interface between corbel and beam were employed for modelling the interface between precast concrete elements for simulations of the test building described in subsequent sections. The calibration results were also used to modify the material of the dowel bars connecting corbels and beams, and for setting an appropriate time step for dynamic analyses.

3. TEST BUILDING & AEM SIMULATION

The design of the precast concrete building to be purposely built for research purposes involves an assembly of the following typical precast elements:

- Columns with corbels.
- Beams.
- Prestressed hollow-core slabs.

Besides the reinforcement present in the precast elements, the design also includes dowel bars connecting the corbels and the beam, a number of reinforcements intended to improve the connection between different structural elements, tie reinforcements, and a mesh covering each floor in the topping that is to be cast in-situ (see Figure 13).

The structure was designed in accordance with the Spanish building code for concrete structures [12] and following specific robustness considerations described in the Eurocodes (EN 1990 [13], EN 1991-1-7 [14], EN 1992-1 [15]) and in the guides published by the International Federation for Structural Concrete (*fib*) [2] and the Institution of Structural Engineers [16].

As can be seen in Figure 1 and Figure 13, one side of the frame structure of the building spans 3 bays while the other spans 2 bays. Each floor is supported by edge beams surrounding the entire perimeter of the building and an interior beam running parallel to the longer side. Each beam is supported at both ends over the corbels.

3.1. Model geometry

The geometry of the precast concrete building including every specific rebar was reproduced with great detail according to the design specifications that will be used for construction. The resulting model geometry is shown in Figure 13, while details of some of the most important reinforcements are shown in Figure 14. Additionally, in order to be able to appropriately model the discontinuous behaviour between precast elements, different interfaces were defined between the beams and corbels and between the topping and the rest of elements as shown in Figure 15.

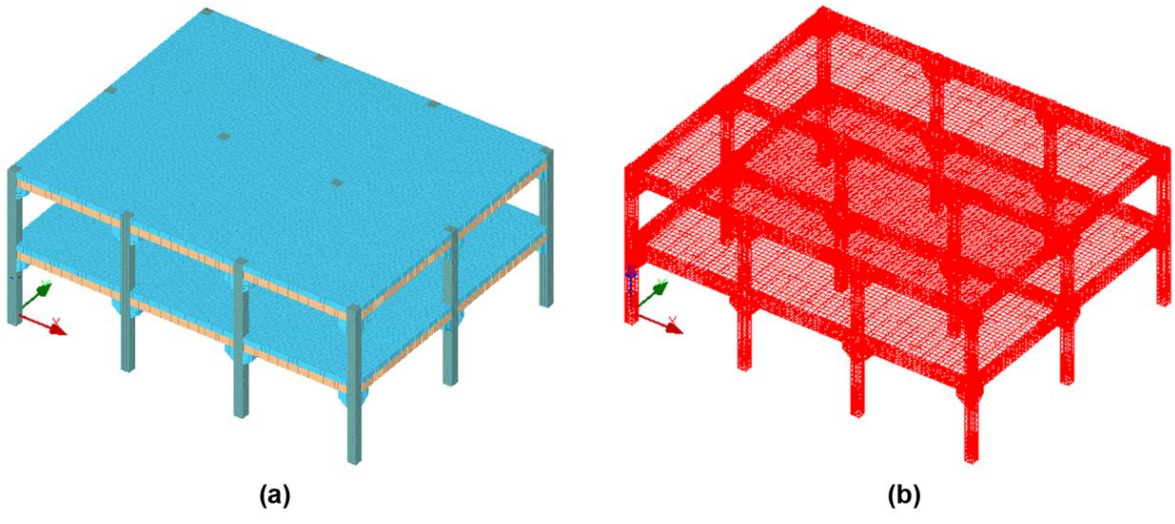

Figure 13. *(a) Model geometry. (b) All reinforcement details modelled as springs.*

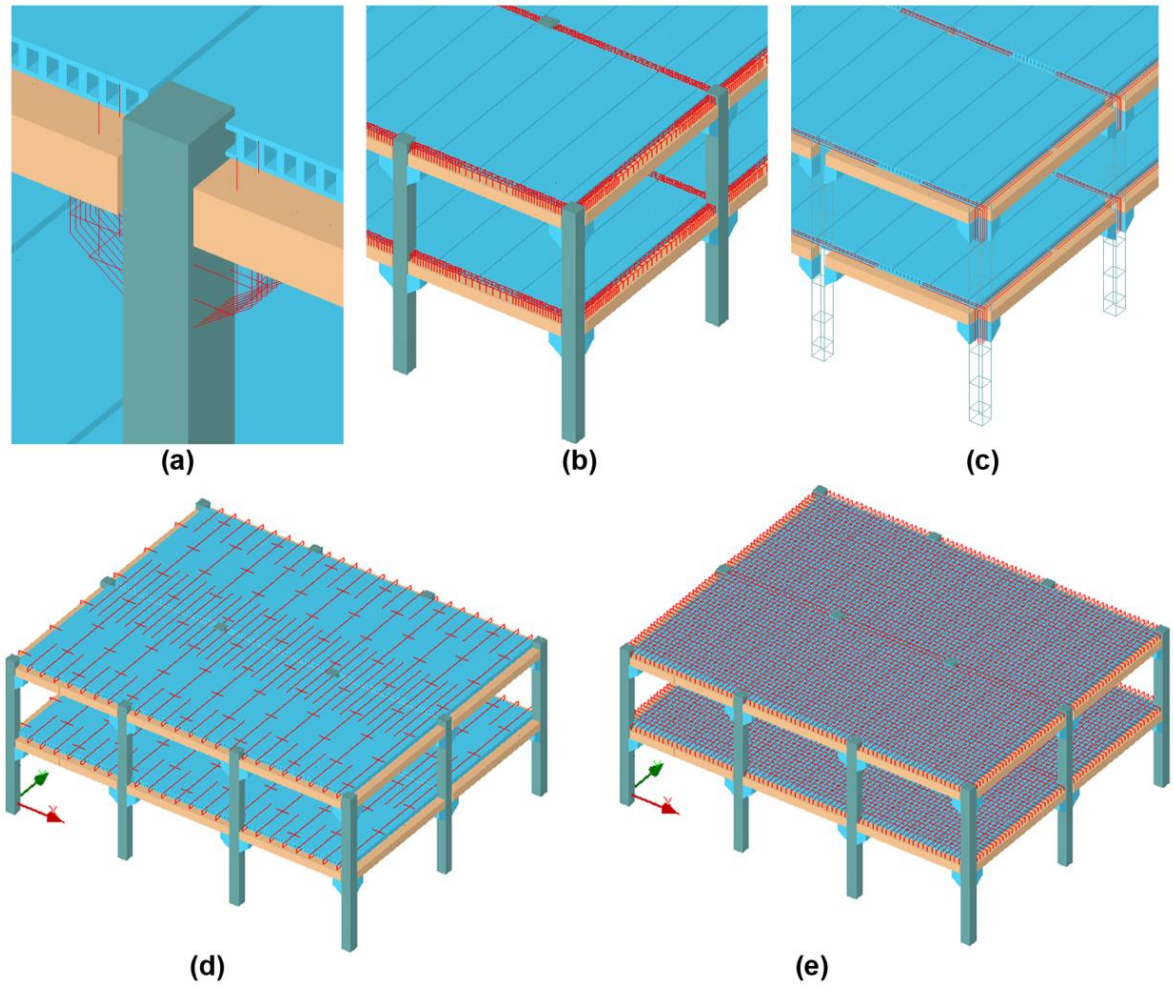

Figure 14. *(a) Corbel reinforcement and dowels passing through the precast beams; (b) Stirrups stemming out of precast beams and additional longitudinal reinforcement; (c) tie reinforcement; (d) Reinforcement between hollow-core slabs; (e) Mesh in topping.*

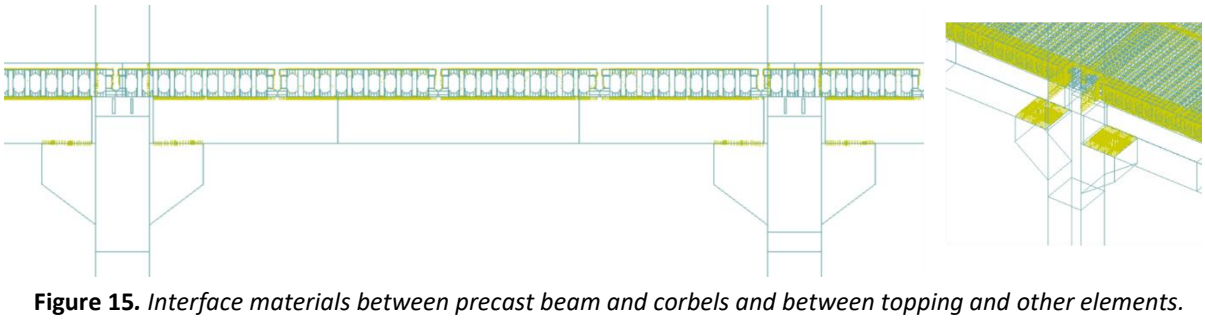

Figure 15. *Interface materials between precast beam and corbels and between topping and other elements.*

3.2. Material parameters

The material properties assigned to concrete and steel elements or springs were based on the material grades established during design and on information available in either the Spanish building code [12] or in the relevant Eurocode [15]. These estimates will be improved following an extensive material testing campaign that will be carried out during the construction phase. The estimates for the most basic material properties used for concrete and steel in the prior simulations are summarised in Table 3 and Table 4.

Table 3. Concrete material properties.

Structural element	Material designation	γ [kN/m³]	E [GPa]	ν	f_c [MPa]	f_t [MPa]
Precast elements & topping	**HA - 30**	24	33	0.2	30	2.9
Hollow-core slabs	**HA - 45**		36		45	3.8

Table 4. Steel material properties.

Designation	γ [kg/m³]	E [GPa]	ν	Yield Strength [MPa]	Tensile strength [MPa]	Ultimate strain
B 500 SD	7850	200	0.3	500	550	0.17

As previously mentioned, the material properties assigned to the interface between corbels and beam was established from the calibration described in Section 3.2. Although it is possible that the topping will be able to establish a greater level of adhesion with other elements, the same interface properties employed between corbels and beams has been used for most of the prior simulations in order to obtain conservative estimates of the expected behaviour. Nevertheless, some simulations have still been performed considering a greater level of adhesion between the topping and other elements in order to better understand the effect this could have on the global behaviour. This is discussed in greater detail in Section 3.4.

3.3. Loading, boundary conditions and simulation of column removal scenarios

As mentioned in the introduction, three different tests simulating the sudden loss of different columns are planned. Each column will be removed and restored back to its original position after the tests using a specifically designed hinged metallic pillar such as the ones used for the tests described in [7]. As shown in Figure 1, two of the tests involve the removal of edge columns while the final test involves the sudden loss of a corner column. The edge column to be removed during the first test is in the middle of a façade which is parallel to the direction along which the hollow-core slabs are placed. Contrarily, the edge column that will be removed during the second test is part of an exterior frame which is perpendicular to the direction of the slabs.

For each of the aforementioned 3 scenarios, a uniformly distributed load of 4 kN/m^2 on the first and second floor topping in all bays adjacent to the column to be removed was imposed using equivalent lumped masses at the centre of elements. This uniformly distributed load represents the minimum value of variable action that needs to be considered for accidental design situations according to [14]. Once these lumped masses were defined, the simulations could be performed. Each simulation consisted of the following 2 stages:

- A static load stage during which the response of the intact structure was evaluated under the effect of its self-weight and the additional uniformly distributed load.

- A dynamic load stage during which one of the first-floor columns was suddenly demolished according to the planned removal location of the test scenario. The dynamic response of the structure after the removal was simulated for at least 2 s.

3.4. Simulation results

The predicted dynamic response after sudden column loss for each test scenario is shown in Figure 16. For each test, the time and magnitude of the first peak deflection are summarised in Table 5.

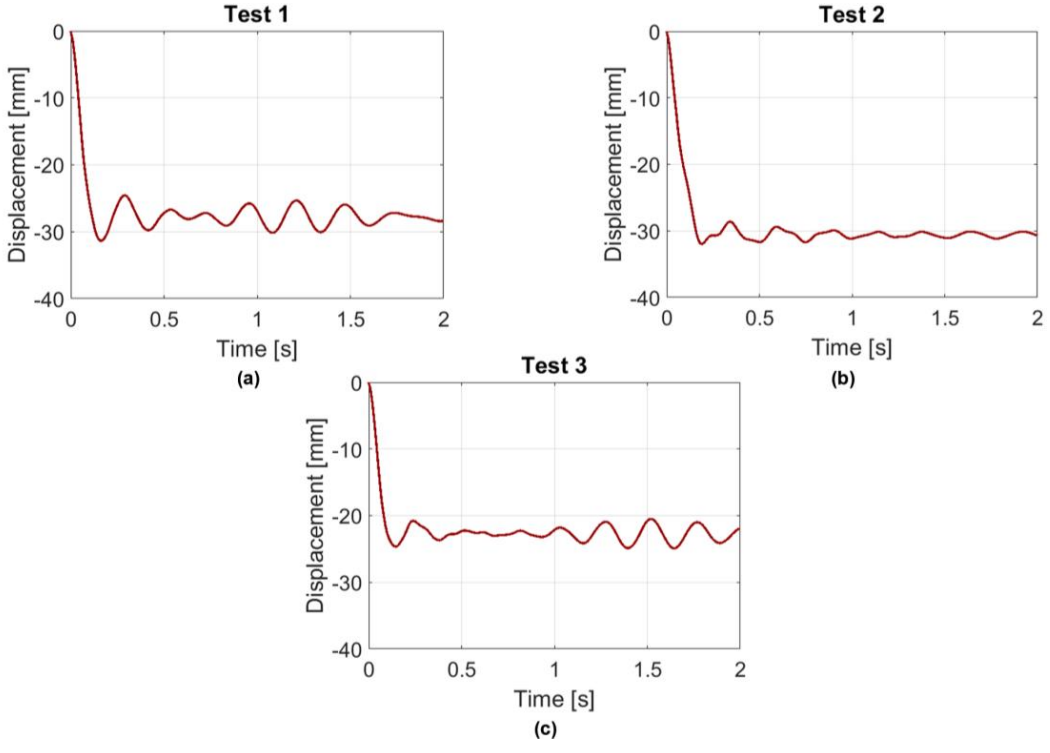

Figure 16. *Predicted dynamic response after the sudden loss of the column according to the scenario reproduced in: (a) Test 1, (b) Test 2 and (c) Test 3.*

Table 5. Summary of predicted peak deflection and response time for the 3 test scenarios.

	Peak deflection of middle column [mm]	**Response time [s]**
Test 1	-31.4	0.16
Test 2	-32.0	0.19
Test 3	-24.6	0.15

Further simulations under the effect of higher uniformly distributed loads predict that the most critical case is that of Test 2, involving the sudden loss of an edge column in a frame perpendicular to the orientation of the hollow-core slabs. For this case, it turns out that the adhesion between the topping and the hollow-core slabs can be a rather significant parameter when predicting the structural response under the effect of loads higher than 4 kN/m^2. Detailed analysis of the results reveal that this is because this adhesion can play an important role in determining how the reinforcements shown in Figure 17(b), which are effectively placed in the topping, act on the hollow-core slabs. In fact, under the effect of a uniformly distributed load of 5 kN/m^2, if there is no adhesion between topping and hollow-core slabs, the reinforcements effectively hold back the topping as the column is removed while allowing the hollow-core slabs to slide in the opposite direction as shown in Figure 17(c). In order to investigate what level of adhesion needs to be specified as an input in order for the deflection to stabilise under the effect of a distributed load of 5 kN/m^2, a small parametric study was performed. As shown in Figure 17(a), specifying a tensile and shear strength at these

interfaces equivalent to 25% of the concrete tensile and shear strength resulted in the simulation predicting a displacement that stabilised within a 1 s analysis window under the effect of a distributed load of 5 kN/m^2.

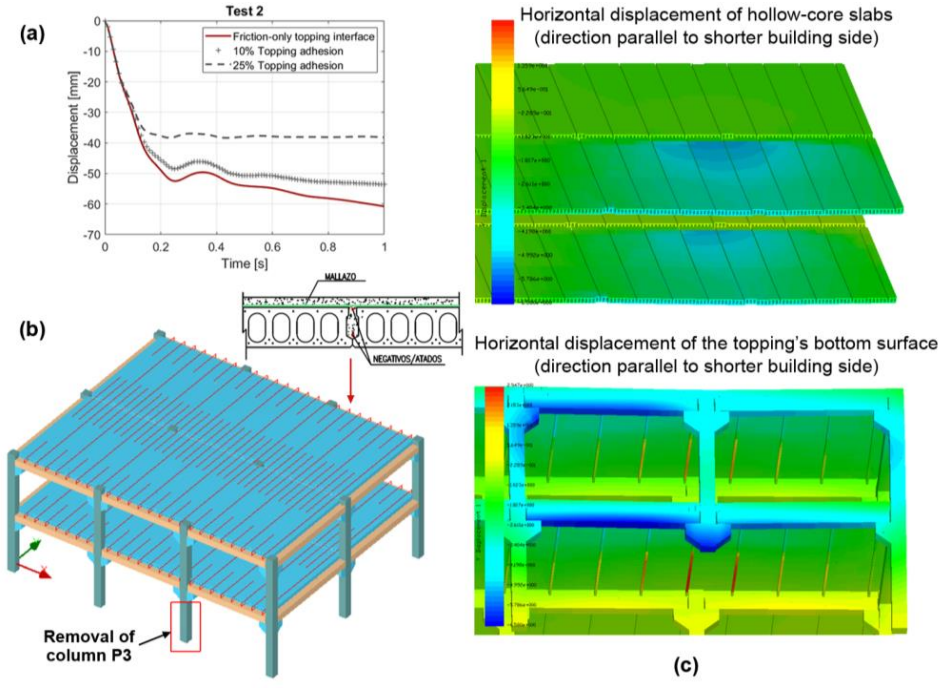

Figure 17. *(a) Predicted dynamic response after the sudden loss of the column according to the scenario of Test 2 but under the influence of a uniformly distributed load of 5 kN/m^2. (b)Some of the reinforcements placed parallel to the shorter side of the building. (c) Evidence that the hollow-core slabs and the topping are sliding over each other as they are moving in opposing directions.*

The peak displacements and the response times summarized in Table 5 can prove to be very important when choosing the types of sensors and instruments that will be used for monitoring the structure during the tests. For instance, it is of vital importance to choose displacement sensors that have a measurement range able to capture the predicted magnitude and to use a sampling frequency able to accurately capture the dynamic response.

In order to decide where strains and horizontal displacements should be monitored, it can be very advantageous to analyse the alternative load paths predicted by the simulations. These can be visualised by observing the evolution of the principal strains of different elements during the simulations. The principal strains predicted at the end of the dynamic simulations for the three test scenarios are shown in Figures 18, 19 and 20.

In addition to the above-mentioned parameters, natural vibration frequencies and mode shapes can also be very useful to ensure that model calibration has been performed accurately following the tests. However, accurately identifying these vibration characteristics usually also require some prior knowledge about them. Given that a detailed numerical model has already been created in this case, the natural vibration frequencies (or periods) as well as the mode shapes can be computed for any state of the structure during the simulations. This is achieved by performing conventional eigenvalue analysis using the stiffness and mass matrices corresponding to a particular state of the structure during the simulations. As expected given the regularity of the structure, the eigenvalue analysis predicts that the first mode of vibration of the undamaged structure refers to the building swaying

back and forth in the direction parallel to the building's shorter side. Although the predicted modes of vibration after column removal do retain a significant displacement component in this direction for all three tests, the mode tends to adopt more of a torsional character which differs depending on which column is removed. The predicted natural periods of vibration after sudden column loss are summarised in Table 6.

Table 6. Summary of predicted natural periods of vibration after column removal for the 3 test scenarios.

	1st Natural period (T_1) [s]	**% change in T_1 from undamaged structure**
Undamaged structure	**0.23**	-
Test 1	0.30	32%
Test 2	0.28	24%
Test 3	0.27	19%

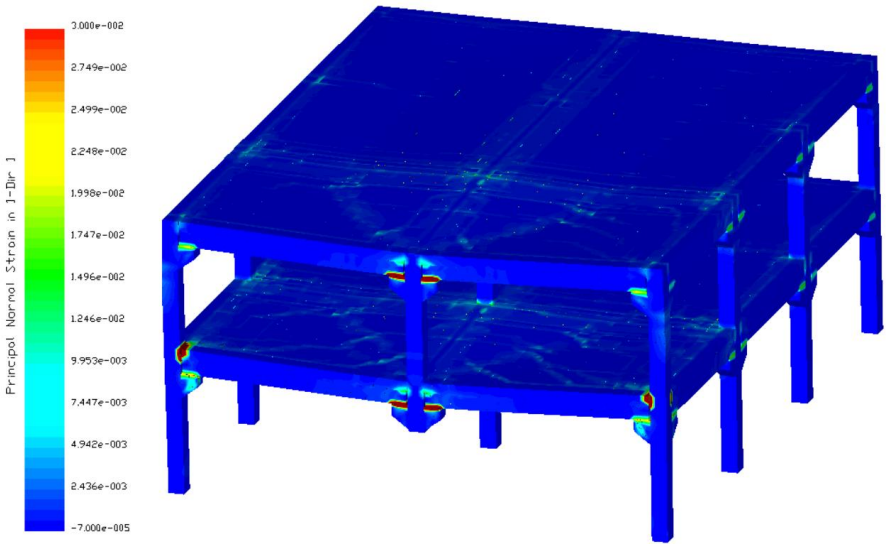

Figure 18. *Principal strain and deformed shape (×5) predicted at the end of the simulation of Test 1.*

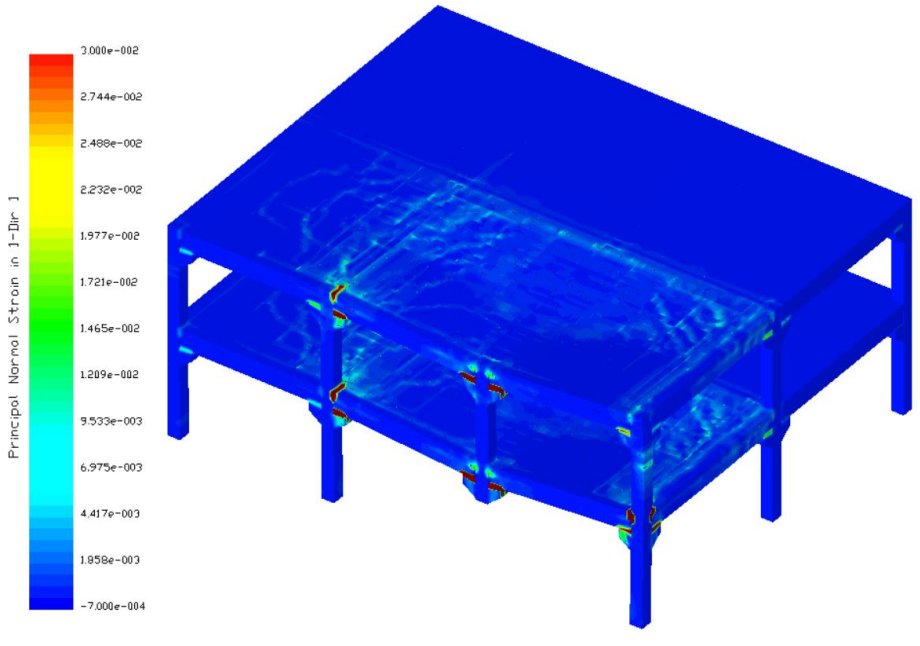

Figure 19. *Principal strain and deformed shape (×5) predicted at the end of the simulation of Test 2.*

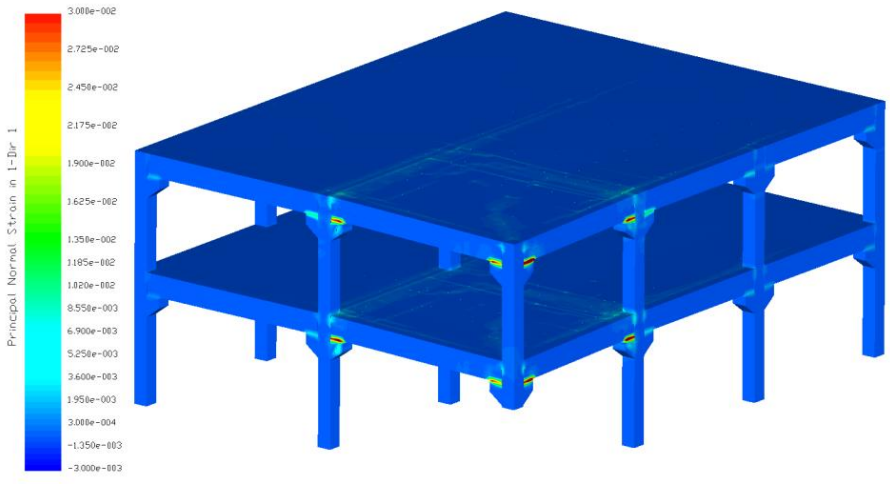

Figure 20. *Principal strain and deformed shape (×5) predicted at the end of the simulation of Test 3.*

4. CONCLUSIONS

To conclude, it can be said that the preliminary simulations of the planned column removal tests on a real-scale structure have allowed the identification of the most critical reinforcements and elements to monitor. In addition, results have allowed the magnitude of key behaviour parameters to be estimated which enables the design of an appropriate monitoring strategy to ensure successful research outcomes.

The numerical simulations have also helped to identify possible sources of uncertainty which can influence structural behaviour. For instance, it was found that the actual adhesion between topping and precast hollowcore slabs can play an important role under the effect of higher loads for one of the test cases in particular.

Finally, the preliminary simulations suggest that specific reinforcements introduced in the design to improve continuity definitely appear to be effective since they help to successfully activate alternative load paths and contain the displacements after the sudden loss of a column to relatively low values under the effect of design loads.

ACKNOWLEDGEMENTS

The authors would like to acknowledge the funding received from the Ministry of Science and Innovation of Spain through the PREBUST project (ref: BIA2017-88322-R). The authors would also like to express their gratitude to the Generalitat Valenciana/Fons Social Europeu [APOSTD/2019/101] for funding received under a postdoctoral program. In addition, the help and support provided by Ayman El-Fouly (Applied Science International) for performing simulations in ELS is also gratefully acknowledged. Finally, thanks also go to Satyadhrik Sharma (Hopper Engineering and Consultancy) for numerous fruitful conversations on numerical modelling in ELS.

REFERENCES

[1] J.M. Adam, F. Parisi, J. Sagaseta, X. Lu, Research and practice on progressive collapse and robustness of building structures in the 21st century, Engineering Structures. 173 (2018) 122–149. https://doi.org/10.1016/j.engstruct.2018.06.082.

[2] A. Van Acker, C. Chastre, A. Cholewicky, B. Crisp, V. Lúcio, K.S. Elliott, B. Engström, A. Gasperi, A. Suikka, S. Tsoukantas, J. Vambersky, J. Vantomme, fib Bulletin 63. Design of precast concrete structures against accidental actions, Fédération internacionale du béton (fib), Lausanne, 2012. http://www.fib-international.org/design-of-precast-concrete-structures-against-accidental-actions.

[3] M. Sasani, M. Bazan, S. Sagiroglu, Experimental and Analytical Progressive Collapse Evaluation of Actual Reinforced Concrete Structure, ACI Structural Journal. 104 (2007) 731–739. https://doi.org/10.14359/18955.

[4] B.I. Song, K.A. Giriunas, H. Sezen, Progressive collapse testing and analysis of a steel frame building, Journal of Constructional Steel Research. 94 (2014) 76–83. https://doi.org/10.1016/J.JCSR.2013.11.002.

[5] Y. Xiao, S. Kunnath, F.W. Li, Y.B. Zhao, H.S. Lew, Y. Bao, Collapse test of three-story half-scale reinforced concrete frame building, ACI Structural Journal. 112 (2015) 429–438. https://doi.org/10.14359/51687746.

[6] M. Bermejo, A.P. Santos, J.M. Goicolea, Development of practical finite element models for collapse of reinforced concrete structures and experimental validation, Shock and Vibration. 2017 (2017). https://doi.org/10.1155/2017/4636381.

[7] J.M. Adam, M. Buitrago, E. Bertolesi, J. Sagaseta, J.J. Moragues, Dynamic performance of a real-scale reinforced concrete building test under a corner-column failure scenario, Engineering Structures. 210 (2020) 110414. https://doi.org/10.1016/j.engstruct.2020.110414.

[8] K. MEGURO, H. TAGEL-DIN, APPLIED ELEMENT METHOD FOR STRUCTURAL ANALYSIS, Doboku Gakkai Ronbunshu. 2000 (2000) 31–45. https://doi.org/10.2208/jscej.2000.647_31.

[9] Applied Science International, Extreme Loading for Structures, (n.d.). https://www.extremeloading.com/ (accessed September 27, 2021).

[10] K. Qian, Y. Liu, T. Yang, B. Li, Progressive Collapse Resistance of Posttensioned Concrete Beam-Column Subassemblages with Unbonded Posttensioning Strands, Journal of Structural Engineering. 144 (2018) 04017182. https://doi.org/10.1061/(ASCE)ST.1943-541X.0001940.

[11] Y. Zhou, X. Hu, Y. Pei, H.-J. Hwang, T. Chen, W. Yi, L. Deng, Dynamic load test on progressive collapse resistance of fully assembled precast concrete frame structures, Engineering Structures. 214 (2020) 110675. https://doi.org/10.1016/j.engstruct.2020.110675.

[12] Ministerio de Fomento, Instrucción de Hormigón Estructural (EHE-08), (2008).

[13] European Committee for Standardization (CEN), EN 1990:2002: Eurocode 0 - Basis of structural design, (2002).

[14] European Committee for Standardization (CEN), EN1991-1-7:2006: Eurocode 1 - Actions on structures - Part 1-7: General actions - accidental actions., (2006).

[15] European Committee for Standardization (CEN), EN1992-1-1:2004: Eurocode 2 - Design of concrete structures - Part 1-1 : General rules and rules for buildings, (2004).

[16] The Institution of Structural Engineers, Practical guide to structural robustness and disproportionate collapse in buildings, (2010).

ANALYSIS OF SPHERICAL SHELL STRUCTURES USING THREE-DIMENSIONAL FINITE ELEMENTS FORMULATED IN GENERAL CURVILINEAR COORDINATES

J.M. Martínez Valle[1]

[1]*Departament of Mechanics. University of Córdoba (Spain). jmvalle@uco.es*

ABSTRACT

Shell structures are structures of great beauty that have been present for many centuries in our architecture and civil works. The calculation of this type of structures is complex and we only have analytical solutions to the problem for certain types of loading, boundary conditions and specific geometries. In addition, in general, to obtain solutions of this type we assume that they work in a membrane state, a true hypothesis for well-designed shells, but a little refined one to study certain areas of the shell structure, such as the changes in cross-sections, proximity to the supports or to the concentrated (punctual) loads etc. where the appearance of the flexure phenomena becomes unavoidable. In this work, we propose the study of spherical shells by means of the three-dimensional finite element of 20 nodes but formulated in spherical coordinates. The author's experience with this type of elements is very positive both in terms of computational cost and for the non-appearance of shear or membrane locking for thin thicknesses, with an adequate treatment of this element. Good Results are also shown in this paper.

Keywords: Shell structures, finite elements, general curvilinear coordinates.

1. INTRODUCCION

El Método de los Elementos Finitos (M.E.F.) surgió como respuesta a problemas de ingeniería gobernados por ecuaciones diferenciales complicas cuyas soluciones analíticas eran difíciles o no posibles de obtener y ante el espectacular avance de la ingeniería informática que permitía resolver grandes sistemas de ecuaciones lineales en un plazo de tiempo razonable, [1].

Los elementos finitos utilizados para estudiar estructuras laminares se pueden dividir básicamente en tres grupos: elementos de sólido degenerado, [2], elementos basados en teorías de láminas, y elementos finitos tridimensionales. Los primeros en utilizarse para láminas fueron los dos primeros mientras que los elementos finitos tridimensionales reaparecieron en la década de los 90. Todos estos elementos sufren de problemas de convergencia de la solución a la real (como todos los métodos numéricos) en determinados casos. Por ejemplo, un elemento lámina con deformación por corte y aplicado a láminas delgadas sufre del denominado bloqueo (locking) por cortante. Además existen los denominados bloqueos de membrana (esfuerzos de membrana predominantes), bloqueo trapezoidal (solo para elementos tridimensionales)) y bloqueo de curvatura.

Para intentar resolver este tipo de problemas han aparecido distintos métodos para aliviar esta sobrerigidización de los elementos. Técnicas de integración reducida, deformaciones impuestas y mejoradas, [3] y [4], o principios variacionales multicampo como el principio de Hellinger Reissner o el

de Hu Washizu son y han sido muy frecuentes en el desarrollo de elementos fiables. Un buen artículo donde se repasan las distintas variedades de elementos finitos así como las distintas mejoras para evitar el fenómeno del bloqueo, es [5].

Los elementos finitos tridimensionales de alto orden alivian la intensidad de este tipo de problemas a cambio de un mayor esfuerzo de computación. La enorme capacidad de los ordenadores actuales hace de este tipo de elementos una opción interesante para el estudio del comportamiento de láminas.

En este trabajo, presentamos una versión modificada del elemento finito de 20 nodos desarrollándolo completamente en coordenadas curvilíneas y concretamente para láminas de geometría esférica. Las relaciones deformación- desplazamiento se construyen teniendo en cuenta las ecuaciones lineales en sistemas curvilineos de la elasticidad tridimensional y expresándolas en sus componentes físicas.

Pese a un mayor esfuerzo inicial de computación debido a las complicadas relaciones deformación – desplazamiento resultantes, la versatilidad del nuevo elemento es superior a la de su homologo cartesiano y porta una descripción precisa de la superficie media.

2. GEOMETRÍA DE LÁMINAS

El estudio de las estructuras laminares se caracteriza en parte por el buen conocimiento de una superficie de referencia que suele ser la superficie media, [6].

Suponemos que para cada tipología estructural de lámina específica podemos tomar un sistema de coordenadas curvilíneas ortogonales, es decir que la base natural asociada, que así mismo suponemos normalizada, es ortogonal asociada a esta superficie de referencia. Por ejemplo para láminas cilíndricas las coordenadas polares.

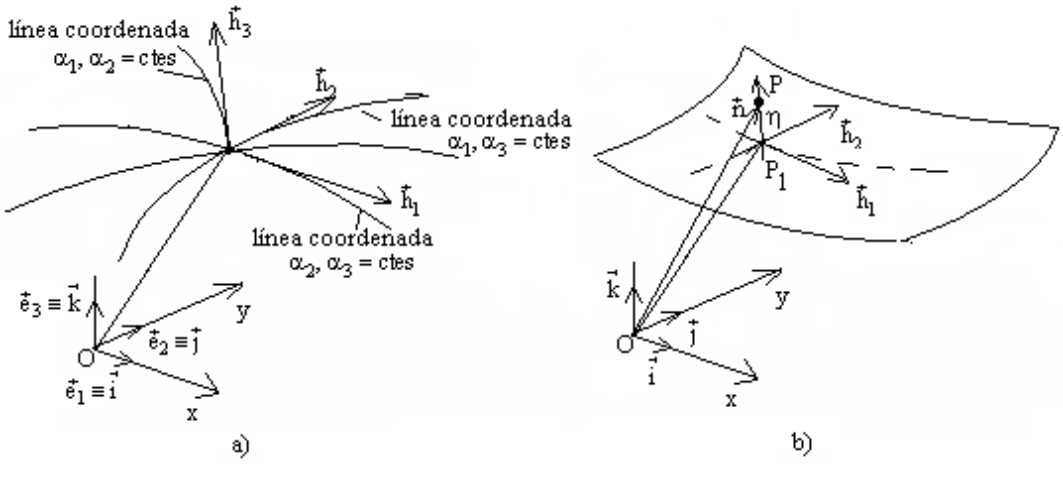

Figura 1. *Sistema de referencia sobre la superficie media. Líneas coordenadas y vectores tangentes.*

En otros casos como el de láminas en pendiente suave definidas sobre planta rectangular, en que las curvas que resultan de la intersección de la superficie con planos y=constante y x=constante respectivamente son cuasi ortogonales, y en los que suponemos conocida la ecuación de la superficie media de la lámina en la forma $z = z(x, y)$, si tomamos un punto P_1 sobre ella y la coordenada sobre la normal a la superficie (ver Fig. 1 a) y b)), la posición de un punto P vendrá dada por

$$\overrightarrow{OP} = \overrightarrow{OP_1} + \eta\vec{n}, \tag{1}$$

donde $\vec{n}$ es el vector normal y η es la coordenada según este vector. Los vectores naturales en los puntos de la superficie los denominamos $\vec{h}_1$. En función de ellos los vectores naturales en P valen

$$\frac{\partial\overrightarrow{\mathrm{OP}}}{\partial\alpha_1} = \vec{h}_1 + \eta\frac{\partial\vec{\mathrm{n}}}{\partial\alpha_1}, \tag{2}$$

y como $\frac{\partial\vec{\mathrm{n}}}{\partial\alpha_i} = -\frac{1}{\rho_i}\vec{h}_i$, siendo ρ_i los radios de curvatura, tenemos

$$\frac{\partial\overrightarrow{\mathrm{OP}}}{\partial\alpha_1} = \vec{h}_i\left(1 - \frac{\eta}{\rho_i}\right). \tag{3}$$

Las componentes del tensor métrico en P, $g_{ii} = 1$si i=j y $g_{ij} = 0$ si i es distinto de j, en función del valor que alcanza en los puntos de la superficie, valen

$$g_{ii} = (g_{ii})_P = \frac{\partial\overrightarrow{\mathrm{OP}}}{\partial\alpha_i}\cdot\frac{\partial\overrightarrow{\mathrm{OP}}}{\partial\alpha_i} = \left(1 - \frac{\eta}{\rho_i}\right)^2\cdot\left(\vec{h}_i\cdot\vec{h}_i\right) = \left(1 - \frac{\eta}{\rho_i}\right)^2\cdot(g_{ii})_{sup}. \tag{4}$$

Y por tanto

$$\sqrt{g_{ii}} = \left(1 - \frac{\eta}{\rho_i}\right)\cdot\sqrt{(g_{ii})_{sup}}. \tag{5}$$

donde ρ_i son los radios de curvatura de la superficie de referencia de estudio. Si tomamos α_1≡x, α_2≡y y α_3≡η, con lo que los radios de curvatura ρ_1 y ρ_2 vendrán dados por

$$\frac{1}{\rho_1} = \frac{z_{,xx}}{\left(1 + z_{,x}{}^2\right)^{\frac{3}{2}}}$$

$$\frac{1}{\rho_2} = \frac{z_{,yy}}{\left(1 + z_{,y}{}^2\right)^{\frac{3}{2}}} \tag{6}$$

Y si llamamos $p = \frac{\partial z}{\partial x}$, $q = \frac{\partial z}{\partial y}$, $r = \frac{\partial^2 z}{\partial x^2}$, $s = \frac{\partial^2 z}{\partial x\partial y}$, $t = \frac{\partial^2 z}{\partial y^2}$, los vectores naturales sobre la superficie en P_1, de vector de posición $\overrightarrow{OP_1} = x\vec{\imath} + y\vec{\jmath} + z(x,y)\vec{k}$, son

$$\vec{h}_1 = \vec{\imath} + p\vec{k}$$

$$\vec{h}_2 = \vec{\imath} + q\vec{k}\ . \tag{7}$$

Las derivadas de las componentes del tensor métrico que valen

$$\frac{\partial\sqrt{g_{ii}}}{\partial\alpha_k}=\frac{1}{\sqrt{g_{ii}}}\left(\frac{\partial\vec{h}_i}{\partial\alpha_k}\cdot\vec{h}_i\right) \tag{8}$$

Que tras particularizar resultan

$$\begin{gathered}\frac{\partial\sqrt{g_{11}}}{\partial\alpha_1}=\frac{\partial}{\partial\alpha_1}\left(\left(1-\frac{\eta}{\rho_1}\right)\cdot\sqrt{(g_{11})_{sup}}\right)=\left(1-\frac{\eta}{\rho_1}\right)\cdot\frac{rp}{\sqrt{1+p^2}}\\ \frac{\partial\sqrt{g_{11}}}{\partial\alpha_3}=\frac{\partial}{\partial\eta}\left(\left(1-\frac{\eta}{\rho_1}\right)\cdot\sqrt{(g_{11})_{sup}}\right)=\sqrt{(g_{11})_{sup}}\frac{\partial}{\partial\eta}\left(1-\frac{\eta}{\rho_1}\right)=-\sqrt{1+p^2}\cdot\frac{1}{\rho_1}\end{gathered} \tag{9}$$

Pero en general $\frac{\eta}{\rho_1}\ll 1$ y podemos prescindir del primero frente al segundo, por lo que nos queda

$$\begin{gathered}\frac{\partial\sqrt{g_{11}}}{\partial\alpha_1}=\frac{rp}{\sqrt{1+p^2}}\\ \frac{\partial\sqrt{g_{11}}}{\partial\alpha_2}=\frac{sp}{\sqrt{1+p^2}}\end{gathered} \tag{10}$$

Procediendo de igual manera para las derivadas de g_{22} obtenemos:

$$\begin{gathered}\frac{\partial\sqrt{g_{22}}}{\partial\alpha_1}=\frac{tq}{\sqrt{1+q^2}}\\ \frac{\partial\sqrt{g_{22}}}{\partial\alpha_2}=\frac{sq}{\sqrt{1+q^2}}\end{gathered} \tag{11}$$

$$\frac{\partial\sqrt{g_{22}}}{\partial\alpha_3}=\frac{\partial}{\partial\eta}\left(\left(1-\frac{\eta}{\rho_2}\right)\cdot\sqrt{(g_{22})_{sup}}\right)=\sqrt{(g_{22})_{sup}}\frac{\partial}{\partial\eta}\left(1-\frac{\eta}{\rho_2}\right)=-\sqrt{1+q^2}\cdot\frac{1}{\rho_2}$$

Las derivadas g_{33} así mismo valen

$$\frac{\partial\sqrt{a_{33}}}{\partial\alpha_1}=0,\frac{\partial\sqrt{a_{33}}}{\partial\alpha_2}=0,\frac{\partial\sqrt{a_{33}}}{\partial\eta}=0 \tag{12}$$

Estas expresiones nos van a ser de gran utilidad para la formulación de la matriz de rigidez de nuestro elemento finito en coordenadas curvilíneas.

3. GEOMETRÍA DE LA LÁMINA ESFERICA

Para láminas esféricas, la relación entre los vectores unitarios del sistema cartesiano y el tangente a la superficie de referencia es,

$$\begin{bmatrix} \vec{t}_r = \dfrac{\vec{h}_r}{|\vec{h}_r|} \\ \vec{t}_\vartheta = \dfrac{\vec{h}_\vartheta}{|\vec{h}_\vartheta|} \\ \vec{t}_\varphi = \dfrac{\vec{h}_\varphi}{|\vec{h}_\varphi|} \end{bmatrix} = \begin{bmatrix} \cos\varphi\cos\vartheta & \cos\varphi\sin\vartheta & \sin\varphi \\ -\sin\vartheta & \cos\vartheta & 0 \\ -\sin\varphi\cos\vartheta & -\sin\varphi\sin\vartheta & \cos\varphi \end{bmatrix} \begin{bmatrix} \vec{i} \\ \vec{j} \\ \vec{k} \end{bmatrix} = C \begin{bmatrix} \vec{i} \\ \vec{j} \\ \vec{k} \end{bmatrix} \tag{13}$$

donde $\{\vec{t}_r \quad \vec{t}_\vartheta \quad \vec{t}_\varphi\}$ son los vectores tangentes.

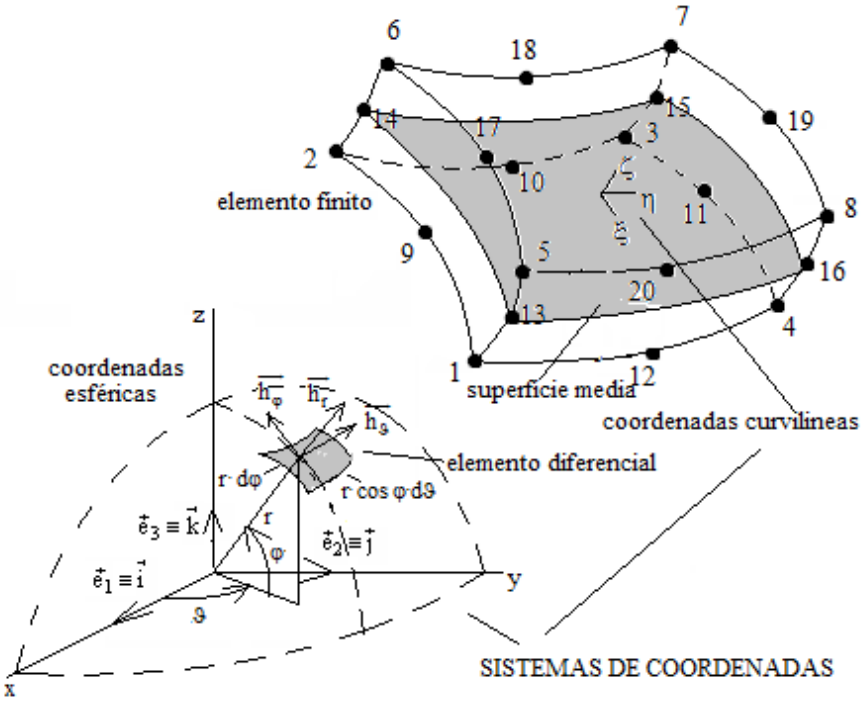

Figura 2. *Elemento finito de 20 nodos. Sistema de referencia cartesiano, representación del sistema isoparamétrico* $\{\zeta \quad \eta \quad \xi\}$ *y particularización para el sistema de referencia esférico.*

En la Fig. 2. podemos ver una representación del elemento finito a formular, y los correspondientes sistemas de referencia que utilizamos a lo largo del trabajo.

4. DEFORMACIONES EN COORDENADAS CURVILINEAS ORTOGONALES Y MATRIZ DE RIGIDEZ

Con carácter general, las deformaciones en régimen lineal en coordenadas curvilíneas vienen dadas por, [7]

$$\varepsilon_{\alpha_i} = \frac{\partial}{\partial \alpha_i}\left(\frac{v_i}{\sqrt{g_{ii}}}\right) + \frac{v_n}{\sqrt{g_{nn} g_{ii}}} \frac{\partial \sqrt{g_{ii}}}{\partial \alpha_n} \tag{14}$$

Si tenemos en cuenta las ecuaciones del epígrafe anterior donde calculábamos las derivadas de las componentes del tensor métrico, podemos expresar las deformaciones en función de parámetros conocidos.

Para posteriores cálculos nos interesa expresar esta última ecuación en forma matricial, para lo cual primero sustituimos el tensor métrico del espacio laminar g_{ij} por el de la superficie media a_{ij} que es lo que el que solemos trabajar usualmente.

$$\{\varepsilon^o\} = \begin{Bmatrix} \varepsilon_1^0 \\ \varepsilon_2^0 \\ \varepsilon_3^0 \\ \gamma_{12}^0 \\ \gamma_{23}^0 \\ \gamma_{13}^0 \end{Bmatrix} = \begin{Bmatrix} \frac{1}{\sqrt{a_{11}}}\frac{\partial u_1}{\partial \alpha_1} + \frac{u_2}{\sqrt{a_{11}a_{22}}}\frac{\partial \sqrt{a_{11}}}{\partial \alpha_2} + \frac{u_3}{\sqrt{a_{33}a_{11}}}\frac{\partial \sqrt{a_{11}}}{\partial \alpha_3} \\ \frac{1}{\sqrt{a_{22}}}\frac{\partial u_2}{\partial \alpha_2} + \frac{u_1}{\sqrt{a_{11}a_{22}}}\frac{\partial \sqrt{a_{22}}}{\partial \alpha_1} + \frac{u_3}{\sqrt{a_{33}a_{22}}}\frac{\partial \sqrt{a_{22}}}{\partial \alpha_3} \\ \frac{1}{\sqrt{a_{33}}}\frac{\partial u_3}{\partial \alpha_3} + \frac{u_1}{\sqrt{a_{11}a_{33}}}\frac{\partial \sqrt{a_{33}}}{\partial \alpha_1} + \frac{u_2}{\sqrt{a_{33}a_{22}}}\frac{\partial \sqrt{a_{33}}}{\partial \alpha_2} \\ \frac{1}{\sqrt{a_{22}}}\frac{\partial u_1}{\partial \alpha_2} - \frac{u_1}{\sqrt{a_{11}a_{22}}}\frac{\partial \sqrt{a_{11}}}{\partial \alpha_2} + \frac{1}{\sqrt{a_{11}}}\frac{\partial u_2}{\partial \alpha_1} - \frac{u_2}{\sqrt{a_{11}a_{22}}}\frac{\partial \sqrt{a_{22}}}{\partial \alpha_1} \\ \frac{1}{\sqrt{a_{33}}}\frac{\partial u_2}{\partial \alpha_3} - \frac{u_2}{\sqrt{a_{33}a_{22}}}\frac{\partial \sqrt{a_{22}}}{\partial \alpha_3} + \frac{1}{\sqrt{a_{22}}}\frac{\partial u_3}{\partial \alpha_2} - \frac{u_3}{\sqrt{a_{33}a_{22}}}\frac{\partial \sqrt{a_{33}}}{\partial \alpha_2} \\ \frac{1}{\sqrt{a_{33}}}\frac{\partial u_1}{\partial \alpha_3} - \frac{u_1}{\sqrt{a_{11}a_{33}}}\frac{\partial \sqrt{a_{11}}}{\partial \alpha_3} + \frac{1}{\sqrt{a_{11}}}\frac{\partial u_3}{\partial \alpha_1} - \frac{u_3}{\sqrt{a_{11}a_{33}}}\frac{\partial \sqrt{a_{33}}}{\partial \alpha_1} \end{Bmatrix} = \tag{15}$$

$$\begin{Bmatrix} 0 & \frac{\partial \sqrt{a_{11}}}{\partial \alpha_2} & \frac{1}{\sqrt{a_{11}a_{33}}}\frac{\partial \sqrt{a_{11}}}{\partial \alpha_3} \\ \frac{\partial \sqrt{a_{22}}}{\partial \alpha_1} & 0 & \frac{1}{\sqrt{a_{33}a_{22}}}\frac{\partial \sqrt{a_{22}}}{\partial \alpha_3} \\ \frac{\partial \sqrt{a_{33}}}{\partial \alpha_1} & \frac{\partial \sqrt{a_{33}}}{\partial \alpha_2} & 0 \\ -\frac{\partial \sqrt{a_{11}}}{\partial \alpha_2} & -\frac{\partial \sqrt{a_{22}}}{\partial \alpha_1} & 0 \\ 0 & -\frac{1}{\sqrt{a_{33}a_{22}}}\frac{\partial \sqrt{a_{22}}}{\partial \alpha_3} & 0 \\ -\frac{1}{\sqrt{a_{11}a_{33}}}\frac{\partial \sqrt{a_{11}}}{\partial \alpha_3} & 0 & 0 \end{Bmatrix} \begin{Bmatrix} u^1 \\ u^2 \\ u^3 \end{Bmatrix} + \begin{Bmatrix} \frac{1}{\sqrt{a_{11}}} & 0 & 0 & 0 & 0 & 0 & 0 & 0 & 0 \\ 0 & 0 & 0 & 0 & \frac{1}{\sqrt{a_{22}}} & 0 & 0 & 0 & 0 \\ 0 & 0 & 0 & 0 & 0 & 0 & 0 & 0 & \frac{1}{\sqrt{a_{33}}} \\ 0 & \frac{1}{\sqrt{a_{22}}} & 0 & \frac{1}{\sqrt{a_{11}}} & 0 & 0 & 0 & 0 & 0 \\ 0 & 0 & 0 & 0 & 0 & \frac{1}{\sqrt{a_{33}}} & 0 & \frac{1}{\sqrt{a_{22}}} & 0 \\ 0 & 0 & \frac{1}{\sqrt{a_{33}}} & 0 & 0 & 0 & \frac{1}{\sqrt{a_{11}}} & 0 & 0 \end{Bmatrix} \begin{Bmatrix} u^1_{,\alpha 1} \\ u^1_{,\alpha 2} \\ u^1_{,\alpha 3} \\ u^2_{,\alpha 1} \\ u^2_{,\alpha 2} \\ u^2_{,\alpha 3} \\ u^3_{,\alpha 1} \\ u^3_{,\alpha 2} \\ u^3_{,\alpha 3} \end{Bmatrix}$$

Para el caso concreto de láminas esféricas, tenemos,

$$\{\varepsilon_0\} = \begin{Bmatrix} \varepsilon_r \\ \varepsilon_\theta \\ \varepsilon_\varphi \\ \gamma_{r\theta} \\ \gamma_{\theta\varphi} \\ \gamma_{r\varphi} \end{Bmatrix} = \begin{Bmatrix} \frac{\partial u_r}{\partial r} \\ \frac{u_r}{r} + \frac{1}{r}\frac{\partial u_\theta}{\partial \theta} - \frac{u_\varphi \tan\varphi}{r} \\ \frac{u_r}{r} + \frac{1}{r}\frac{\partial u_\varphi}{\partial \varphi} \\ \frac{1}{r\cos\varphi}\frac{\partial u_r}{\partial \theta} + \frac{\partial u_\theta}{\partial r} - \frac{u_\theta}{r} \\ \frac{u_\theta \tan\varphi}{r} + \frac{1}{r}\frac{\partial u_\theta}{\partial \varphi} + \frac{1}{\cos\varphi}\frac{\partial u_\varphi}{\partial \theta} \\ -\frac{u_\varphi}{r} + \frac{1}{r}\frac{\partial u_r}{\partial \varphi} + \frac{\partial u_\varphi}{\partial r} \end{Bmatrix} = \begin{Bmatrix} 0 & 0 & 0 \\ \frac{1}{r} & 0 & -\frac{\tan\varphi}{r} \\ \frac{1}{r} & 0 & 0 \\ 0 & -\frac{1}{r} & 0 \\ 0 & \frac{\tan\varphi}{r} & 0 \\ 0 & 0 & -\frac{1}{r} \end{Bmatrix} \begin{Bmatrix} u_r \\ u_\theta \\ u_\varphi \end{Bmatrix} + \tag{16}$$

$$+\begin{Bmatrix} 1 & 0 & 0 & 0 & 0 & 0 & 0 & 0 & 0 \\ 0 & 0 & 0 & 0 & \frac{1}{r} & 0 & 0 & 0 & 0 \\ 0 & 0 & 0 & 0 & 0 & 0 & 0 & 0 & \frac{1}{r} \\ 0 & 1 & 0 & \frac{1}{r\cos\varphi} & 0 & 0 & 0 & 0 & 0 \\ 0 & 0 & 0 & 0 & 0 & \frac{1}{\cos\varphi} & 0 & \frac{1}{r} & 0 \\ 0 & 0 & 1 & 0 & 0 & 0 & \frac{1}{r} & 0 & 0 \end{Bmatrix} \begin{Bmatrix} u_{r,r} \\ u_{\theta,r} \\ u_{\varphi,r} \\ u_{r,\theta} \\ u_{\theta,\theta} \\ u_{\varphi,\theta} \\ u_{r,\varphi} \\ u_{\theta,\varphi} \\ u_{\varphi,\varphi} \end{Bmatrix} = [A_1] \begin{Bmatrix} u_r \\ u_\theta \\ u_\varphi \end{Bmatrix} + [A_2] \begin{Bmatrix} u_{r,r} \\ u_{\theta,r} \\ u_{\varphi,r} \\ u_{r,\theta} \\ u_{\theta,\theta} \\ u_{\varphi,\theta} \\ u_{r,\varphi} \\ u_{\theta,\varphi} \\ u_{\varphi,\varphi} \end{Bmatrix}$$

E interpolando adecuadamente, esta última expresión la podemos escribir de una forma más compacta como,

$$\{\varepsilon_0\} = [A_1][N]_{3,60} \begin{Bmatrix} u_{r1} \\ u_{\theta1} \\ u_{\varphi1} \\ u_{r2} \\ u_{\theta2} \\ u_{\varphi2} \\ \vdots \\ \vdots \\ u_{r20} \\ u_{\theta20} \\ u_{\varphi20} \end{Bmatrix} + [A_2][N]_{9,60}(u_r^i)_{60,1} \begin{Bmatrix} u_{r1} \\ u_{\theta1} \\ u_{\varphi1} \\ u_{r2} \\ u_{\theta2} \\ u_{\varphi2} \\ \vdots \\ \vdots \\ u_{r20} \\ u_{\theta20} \\ u_{\varphi20} \end{Bmatrix} \tag{17}$$

De esta forma, las deformaciones y el operador *B* que interviene en nuestra matriz de rigidez, lo podemos escribir,

$$\{\varepsilon_o\} = B_o \cdot D_{ele} \tag{18}$$

Siendo

$$B_o = [A_1]_{6*3} \cdot [N]_{3*60} + [A_2]_{6*9} \cdot N_{9,60} \tag{19}$$

De manera que la matriz de rigidez está totalmente definida considerando las relaciones constitutivas habituales para un material elástico. Un desarrollo similar al actual, pero para otras geometrías, lo podemos encontrar en [8].

5. RESULTADOS

Vamos a estudiar, con el elemento hexaédrico isoparamétrico de 20 nodos formulado en coordenadas esféricas, el caso de la cúpula esférica (cerrada) de radio R=10 m, simplemente apoyada (en la que para eliminar el movimiento de sólido rígido de la cúpula se coacciona el movimiento según el paralelo en el plano de apoyo), de espesor t=0.09 m, coeficiente de Poisson $\mu = 0.3$, E=21.000.000 kN/m^2 y $\alpha = \frac{\pi}{2}$ Vamos a calcular los esfuerzos y las expresiones generales de los corrimientos, y en particular el corrimiento vertical del punto situado sobre el eje de revolución y el corrimiento horizontal en el apoyo, cuando está sometida a una presión radial distribuida por unidad de superficie de P=1620 kN/m^2.

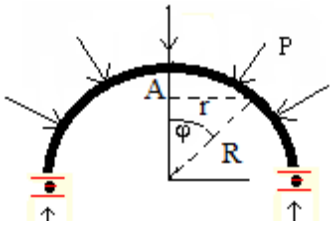

Figura 3. *Cúpula esférica sometida a presión radial. Parámetros de cálculo.*

Los valores de los **esfuerzos de membrana,** según la teoría elemental de la elasticidad son,

$$N_\varphi = N_\vartheta = -\frac{R \cdot P}{2} = -8100 \text{ kN/m}$$

Y el corrimiento según la normal a la superficie esférica vale

$$w = \frac{R^2 \cdot P}{2} \cdot \frac{1-\mu^2}{E \cdot t}(1-\mu) = 0.0273\text{m}$$

Estudiamos la lámina mediante el M.E.F con el elemento hexaédrico de 20 nodos (formulación en coordenadas esféricas), adoptando una subdivisión de 30 elementos según el meridiano, 24 según el paralelo de apoyo y 1 elemento según el espesor, con las condiciones de contorno especificadas. Los resultados obtenidos se muestran en las siguientes figuras, Fig.4.

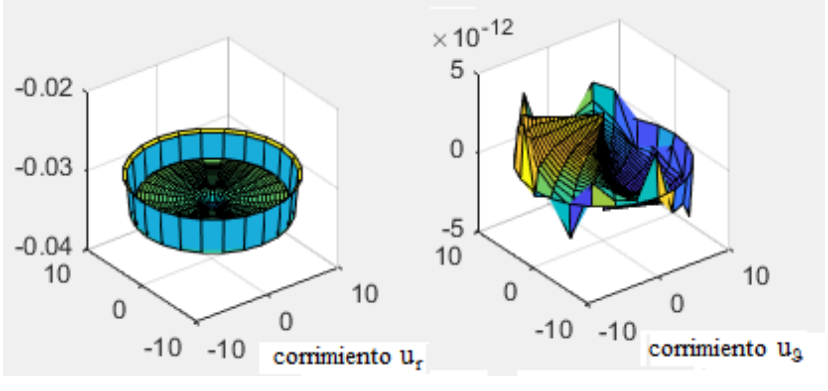

Figura 4. *Representación gráfica de los corrimientos.*

Como podemos ver, al corrimiento u_φ los resultados que se obtienen son valores casi nulos en todos los puntos de la lámina; valores que son totalmente acordes con la teoría. El corrimiento vertical difiere en 2,7 % del valor teórico.

Por lo que respecta a los esfuerzos de membrana, los valores que se obtienen para todos los puntos de la lámina cumplen, con pequeñas diferencias, que en ningún punto alcanzan el 3%. Los resultados los vemos en las gráficas siguientes, Fig.5.

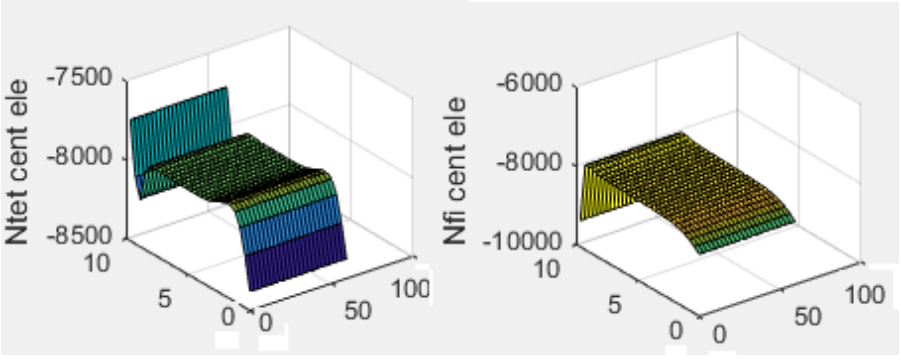

Figura 5. *Representación gráfica de los esfuerzos.*

En un segundo ejemplo, proponemos la misma geometría anterior pero sometida a una sobrecarga vertical de volumen uniforme de 18000 kN/m^3, es decir una fuerza distribuida por unidad de superficie de P=1620 kN/m2 (Nota: queremos resaltar la importancia de la sobrecarga adoptada de cien veces el peso propio, que hemos escogido para que los corrimientos tengan cierta entidad).

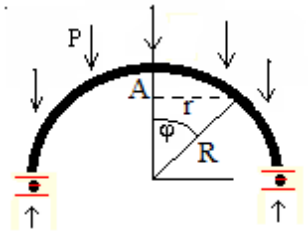

Figura 6. *Cúpula esférica sometida a sobrecarga vertical.*

En este caso, los valores teóricos de los esfuerzos de membrana proporcionados por la teoría de la elasticidad son,

$$N_\varphi = R\cdot P\cdot\frac{(\cos\varphi - 1)}{\text{sen}^2\varphi};\ N_\vartheta = P\cdot R\cdot\frac{1-\cos^3\varphi}{\text{sen}^2\varphi}$$

Y el corrimiento según la normal a la superficie esférica vale,

$$w = \text{ctg}\varphi\cdot u\ -R^2\cdot P\cdot\frac{1-\mu^2}{E\cdot t}\left(\frac{1+\mu}{1+\cos\varphi}-\cos\varphi\right)$$

Estudiamos de nuevo este caso, con nuestro elemento de 20 nodos formulado en coordenadas esféricas con la misma subdivisión que en el ejemplo anterior.
En la siguiente figura se representan de nuevo los corrimientos,

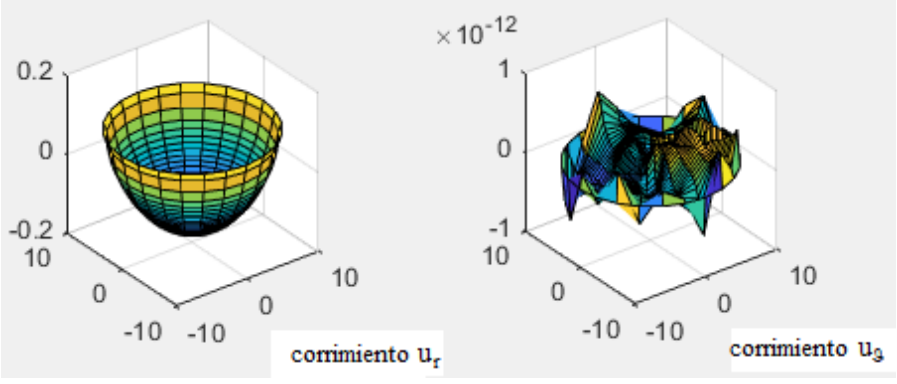

Figura 7. *Representación gráfica de los corrimientos.*

El valor del corrimiento en la clave y los apoyos son, respectivamente, -0.1690 y 0.0871 (en donde el signo negativo indica que el corrimiento es hacia el centro de curvatura y el signo positivo lo contrario). Los resultados obtenidos son totalmente acordes con los valores teóricos, relativos al cálculo en estado de membrana, y las diferencias, *debidas a la presencia de las pequeñas flexiones derivadas de los pequeños cambios en la curvatura*, están en torno al 2 %. *Estas pequeñas flexiones hacen que los resultados ahora obtenidos sean más exactos que los obtenidos en el estado de membrana.*
Conclusiones similares al ejemplo anterior se pueden inferir en cuanto a los esfuerzos para este ejemplo.
Respecto a la convergencia del método numérico propuesto, comentar que con un refinamiento de malla de 60*48 elementos los errores respecto a la solución teórica son en torno al 1%.

3. CONCLUSIONES

En este trabajo hemos presentado un nuevo elemento finito tridimensional formulado en coordenadas curvilíneas y concretado para láminas esféricas. El elemento finito en cuestión es una versión modificada del elemento finito serendípito clásico de 20 nodos pero formulado en un sistema de referencia curvilíneo, tangente a la superficie media de la lámina.

Pese al mayor esfuerzo inicial de computación debido a las complicadas relaciones deformación-desplazamiento, necesarias para evaluar la matriz de rigidez, el nuevo elemento aporta una descripción precisa de la geometría de la lámina y por tanto es adaptable a cualquier geometría.

Al tener 20 nodos el elemento, los problemas de bloqueo de la matriz de rigidez para espesores delgados no son significativos a la vista de los resultados obtenidos.

Extensiones del trabajo a fenómenos elastoplásticos, plásticos o estudios de grandes deformaciones se harán en próximas entregas.

AGRADECIMIENTOS

A la Universidad de Córdoba y al Prof. Dr. José Miguel Martínez Jiménez, director del dpto. de mecánica hasta el año 2011.

REFERENCIAS

[1] Zienkiewicz, O. C., and Taylor, L.R. (2000). El Método de los Elementos Finitos. Mecánica de Sólidos. McGraw-Hill.

[2] Ahmad, S., Irons, B., and Zienkiewicz, O.C. (1970). Analysis of thick and thin shell structures by curved finite elements. *Int. J. Numer. Meth. Engrg.,* 419-451.

[3] Hauptmann, R., and Schweizerhof, K. (1998). A systematic development of solid-shell element formulations for linear and nonlinear analyses employing only displacement degrees of freedom. *International Journal for Numerical Methods in Engineering,* 42:49–70.

[4] Alves de Sousa, R., Cardoso, R., Valente, R., Yoon, J., Gracio, J., and Jorge, R.(2006). A new one-point quadrature enhanced assumed strain (EAS) solid-shell element with multiple integration points along thickness—part II: nonlinear applications. *Int J Numer Methods Eng,* 67:160–188.

[5] Yang, H., Saigal, S., Masud, A., and Kapania, R. (2004). A survey of recent shell finite elements. *International Journal for Numerical Methods in Engineering*, 47:101–127.

[6] Itskov M. (2009). Tensor Algebra and Tensor Analysis for Engineers: With Applications to Continuum Mechanics. Springer.

[7] Rekach, V. G., (1978). Manual of the theory of Elasticity. Mir Moscú.

[8] Martínez Valle J.M. (2014). Formulación del elemento finito serendípito de 20 nodos para la modelización y simulación dinámica de placas y láminas (Doctoral Thesis). Cordoba: Servicio de Publicaciones de la Universidad de Córdoba (España).

Modelling variable pedestrian dynamic loading factors induced on rigid surfaces

Marta García-Diéguez[1]; Jose Luis Zapico-Valle[2]

ABSTRACT

This paper presents a stochastic model of walking force featuring variable walking speed on step-by-step basis as the key input modelling parameter. This is a notable difference from traditional deterministic and periodic models where the key modelling parameter is the average pacing rate in a walking trial. Starting from the previously developed models of variable walking speed and spatiotemporal parameters in a walking trial, this study derived a complementary model of variable dynamic load factors (DLFs) corresponding to the first five harmonics and subharmonics of the walking force. The mean and the coefficient of variation of DLFs are described as the product of two factors. The first one is modelled as a second-order polynomial and is the deterministic part and the second is a random part defined by a Beta distribution.

Keywords: pedestrian load, dynamic load factors, vibration serviceability, rigid surfaces, load modelling.

1. INTRODUCTION

Vibration serviceability assessment is crucial for design pedestrian structures, such as footbridges and floors. A quality models of pedestrian-induced loading is important to obtain reliably predict vibrations at the design stage [1] [2].

This study addresses the dynamic load factors (DLFs) of the first five dominant harmonics and subharmonics, thus covers the frequency range between 0.5 and 12 Hz. Also, the study focusses on vibration response dominated by only one force harmonic or subharmonic. Under this condition, the relative phase of the (sub)harmonics has negligible effect on the response.

The present study builds on the previously derived models of variable walking speed, step length and footfall intervals. More detailed descriptions of the models and experimental setups can be found elsewhere [3,4]. A force records from fifty test subjects (25 males and 25 females) were used to develop this model and the previous ones.

[1] *Department of Construction and Manufacturing Engineering. University of Oviedo (SPAIN). garciadmarta@uniovi.es (Corresponding author)*

[2] *Department of Construction and Manufacturing Engineering. University of Oviedo (SPAIN). jzapico@uniovi.es*

2. MODELLING DLF

Each experimental ground reaction force (GRF) signal was normalised to body weight and cut into segments corresponding to both step and stride intervals. Each segment corresponding to a step interval was run through the fast Fourier transform (FFT) algorithm to extract the amplitudes (i.e. DLFs) of the first five dominant harmonics. More details about amplitudes identification can be found in [4]. Moreover, the FFT is applied to the stride segments to get DLFs of the first five subharmonics. Hereafter, DLFs will be labelled $DLF_i^{(j)}$. The subscript indicates the step number in a sequence of N steps. The superscript $j = 1, \dots, 5$ stands for the order of harmonics while $j = 0.5, \dots, 4.5$ stands for the order of subharmonics.

An example of a $DLF_i^{(j)}$ sequence across successive steps is depicted in Fig. 1 for the second Fourier harmonic ($j = 2$). Based on a visual inspection, all other harmonics and subharmonics across all walking trials in the experiments show a similar random character. $DLF_i^{(j)}$ can be broken down into two components: an average value $\overline{DLF}^{(j)}$ and random deviations $\widetilde{DLF}_i^{(j)}$ i.e.

$$DLF_i^{(j)} = \overline{DLF}^{(j)} + \widetilde{DLF}_i^{(j)}. \quad (1)$$

$\overline{DLF}^{(j)}$ are not correlated with pedestrian weight, which in line with findings reported elsewhere [5]. Also, variations $\widetilde{DLF}_i^{(j)}$ are not correlated either with variations of other (sub)harmonics and the corresponding variations of the footfall intervals. This means that $DLF_i^{(j)}$ can be studied independently from footfall intervals and other harmonics.

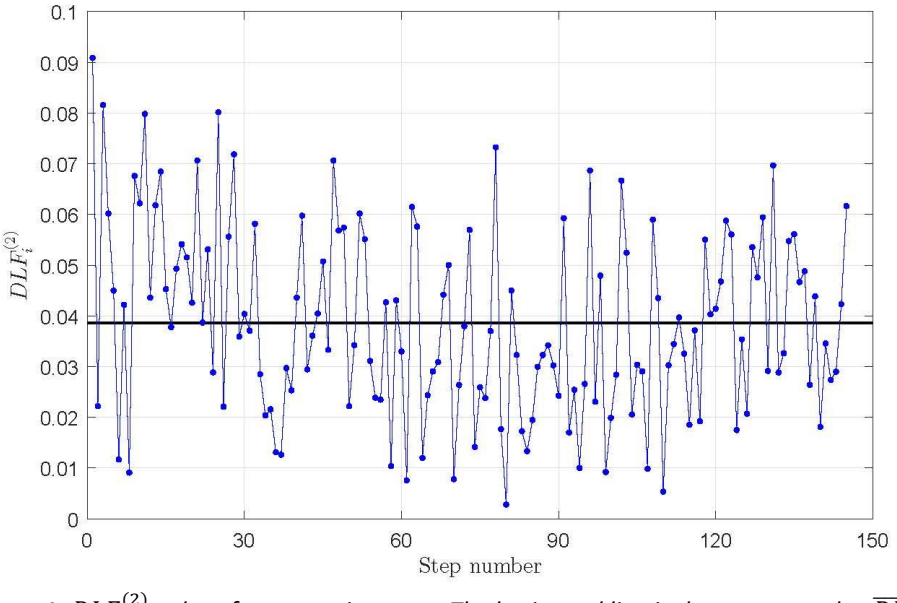

Figure 1. *$DLF_i^{(2)}$ values for successive steps. The horizontal line is the average value $\overline{DLF}^{(j)}$.*

Fig. 2 shows the lack of interconnection between successive $\widetilde{DLF}_i^{(j)}$ values which means that the current value of $\widetilde{DLF}_i^{(j)}$ in step i is independent from the values made in a few previous steps. Therefore, the variations can be considered a random process. The coefficient of variation is an easy way to quantify it:

$$CoV^{(j)} = \frac{S_{DLF}^{(j)}}{\overline{DLF}^{(j)}}, \tag{2}$$

where $S_{DLF}^{(j)}$ is a standard deviation of $DLF_i^{(j)}$.

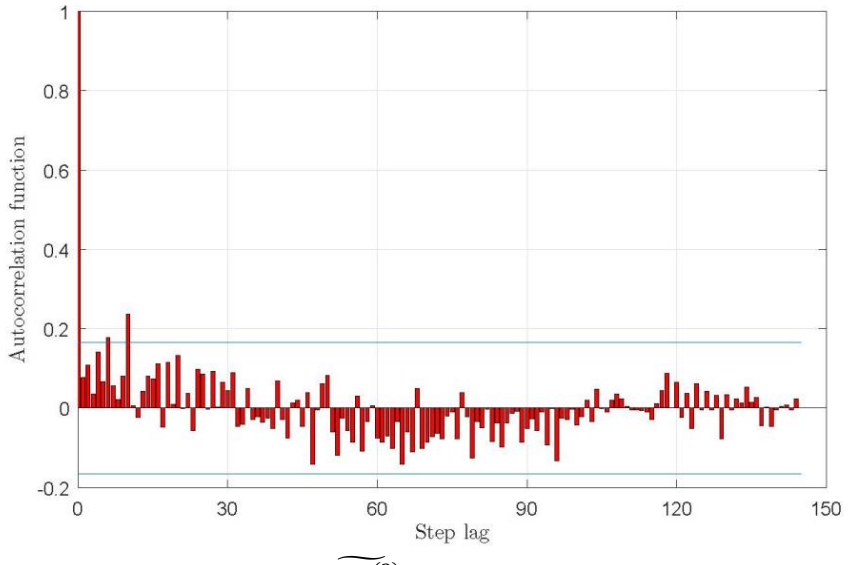

Figure 2. *Autocorrelation function of $\widetilde{DLF_i^{(2)}}$, corresponding to the data presented in Fig. 1. The horizontal line are a 95% confidence interval..*

$DLF_i^{(j)}$ values are in the range [0,1] and they fit well a Beta distribution $B(a,b)$ shown in Fig. 3. Parameters a and b of the Beta distribution can be obtained from its mean μ and variance σ^2 [6]:

$$a = \frac{\mu^2\,(1-\mu)}{\sigma^2} - \mu, \qquad b = a\,\frac{1-\mu}{\mu} \tag{3}$$

In a trial, μ and σ^2 can be approximated from its average $\overline{DLF}^{(j)}$ and $CoV^{(j)}$ as:

$$\mu \cong \overline{DLF}^{(j)}, \qquad \sigma^2 \cong \left(\overline{DLF}^{(j)} \cdot CoV^{(j)}\right)^2. \tag{4}$$

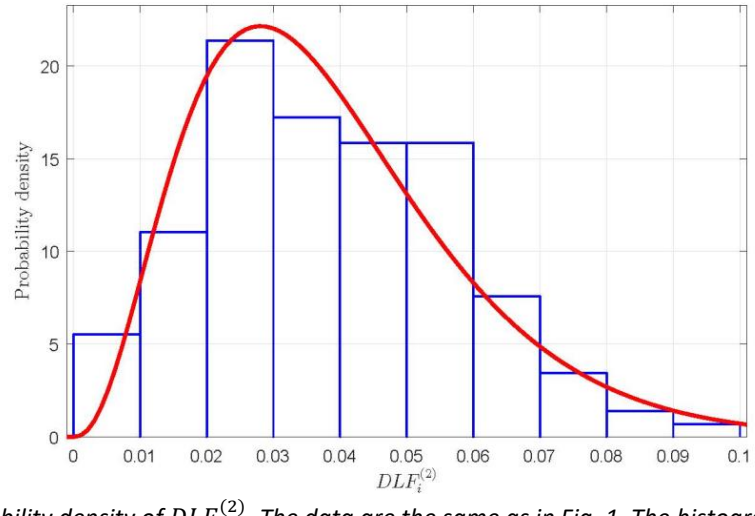

Figure 3. *Probability density of $DLF_i^{(2)}$. The data are the same as in Fig. 1. The histogram is derived from the experimental data, while the line is the fitted Beta distribution.*

To conclude, the sequence $DLF_i^{(j)}$ in a walking trial can be considered a random process described by a Beta distribution which parameters can be approximated using the average $\overline{DLF}^{(j)}$ and $CoV^{(j)}$ calculated from DLF data extracted from a measured GRF trial. Therefore, adequate mathematical descriptions of the average and CoV are crucial to generate reliably a synthetic sequence of DLFs.

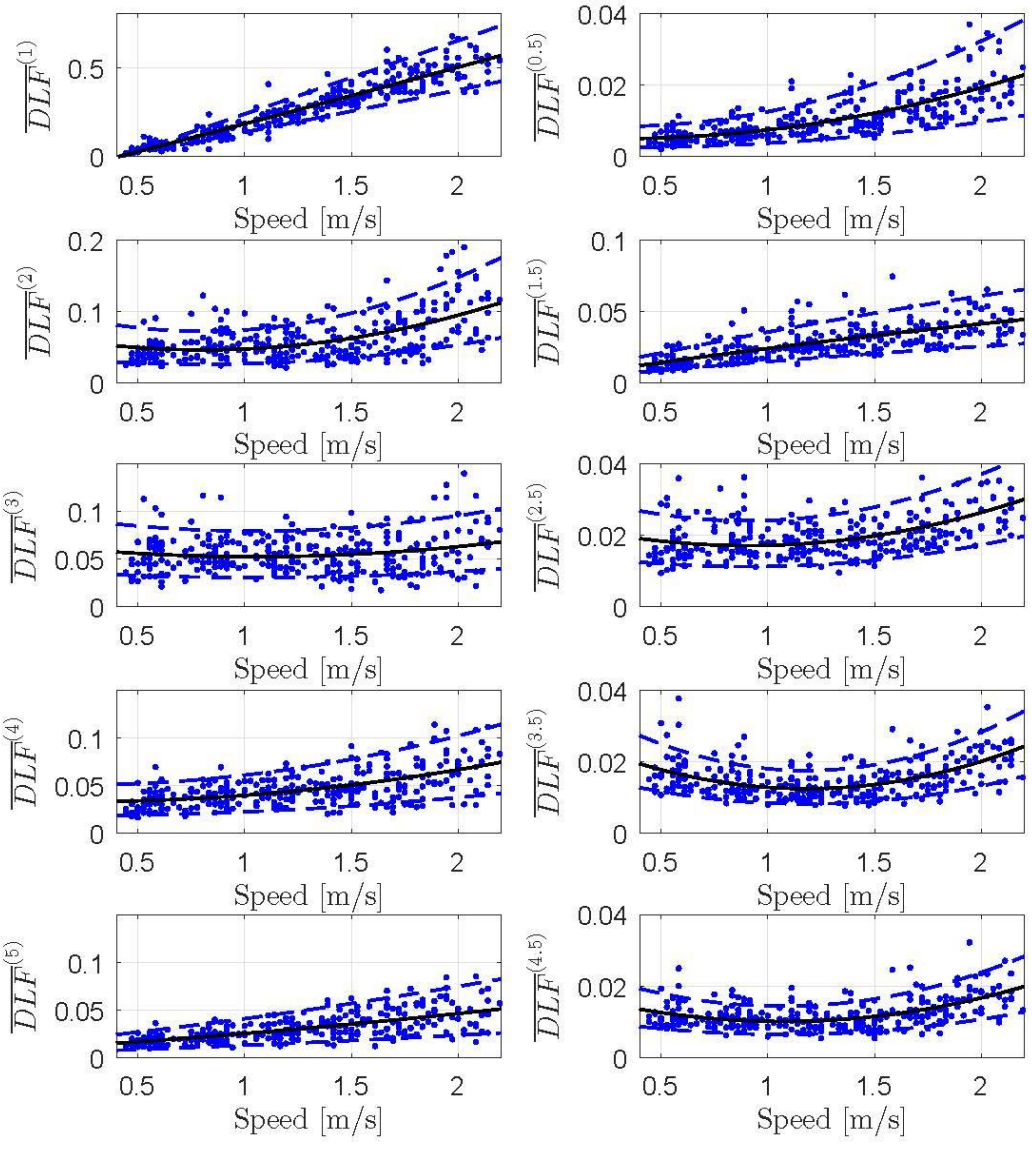

Figure 4. *$\overline{DLF}^{(j)}$ vs. walking speed. The dots represent the data, the solid lines the quadratic fit and the discontinuous lines the 95% confidence intervals.*

Fig. 4 shows a relationship between the average values from each walking trial and the constant walking speed, v. First of all, a visual inspection of the graphs shows an interpedestrian variability of

the data. Moreover, all the graphs show apparently increasing trend of the $\overline{DLF}^{(j)}$ values as pedestrian walk faster. Although the trend becomes flatter for the higher (sub)harmonics, all the data can be described by the following formulation:

$$\overline{DLF}^{(j)} = \overline{DLF_d}^{(j)} \cdot 10 \cdot \overline{DLF_r}^{(j)}, \quad (5)$$

The first factor $\overline{DLF_d}^{(j)}$ represents a deterministic component of $\overline{DLF_i}^{(j)}$, while the second factor $\overline{DLF_r}^{(j)}$ is a random variable which accounts for the interpedestrian variability. The deterministic factor describes the increasing trend between average DLF and v, which can be mathematically modelled as a second-order polynomial:

$$\overline{DLF_d}^{(j)} = c_9^{(j)} \cdot v^2 + c_{10}^{(j)} \cdot v + c_{11}^{(j)}. \quad (5)$$

The values of the coefficients $c_9^{(j)}$, $c_{10}^{(j)}$ and $c_{11}^{(j)}$ were obtained by fitting the polynomial to the data shown in Fig. 4 and are reported in Table 1. The fits and 95% confidence intervals are shown in Fig. 4 together with the experimental data.

Table 1. Parameter values of $\overline{DLF^{(j)}}$ model.

(Sub) harmonic order (j)	c_9	c_{10}	c_{11}	c_{12}	c_{13}
0.5	0.0049	-0.0028	0.0055	10.06	89.29
1	0.0037	0.3064	-0.1263	45.51	407.69
1.5	-0.0017	0.0222	0.0035	18.85	168.56
2	0.0341	-0.0551	0.0685	13.78	123.17
2.5	0.0077	-0.0140	0.0236	24.55	220.83
3	0.0118	-0.0246	0.0657	15.93	143.33
3.5	0.0114	-0.0270	0.0284	24.35	219.03
4	0.0103	-0.0039	0.0333	14.24	128.88
4.5	0.0077	-0.0164	0.0188	22.00	198.18
5	0.0024	0.0138	0.0089	10.66	96.85

The random factor $\overline{DLF_r}^{(j)}$ was calculated after substituting Eq. (5) into Eq. (4):

$$\overline{DLF_r}^{(j)} = \frac{\overline{DLF}^{(j)}}{10 \cdot \left(c_9^{(j)} \cdot v^2 + c_{10}^{(j)} \cdot v + c_{11}^{(j)}\right)}. \quad (6)$$

Eventually, the value of $\overline{DLF_r}^{(j)}$ representative of each pedestrian was estimated as the average value of the related six experiments. The constant 10 in Eq. (4) limits values of the random factor to the range [0,1]. Thus, the values fit well Beta distribution $B(c_{12}, c_{13})$. The values of the parameters c_{12} and c_{13} listed in Table 1 were obtained using the maximum likelihood method [6].

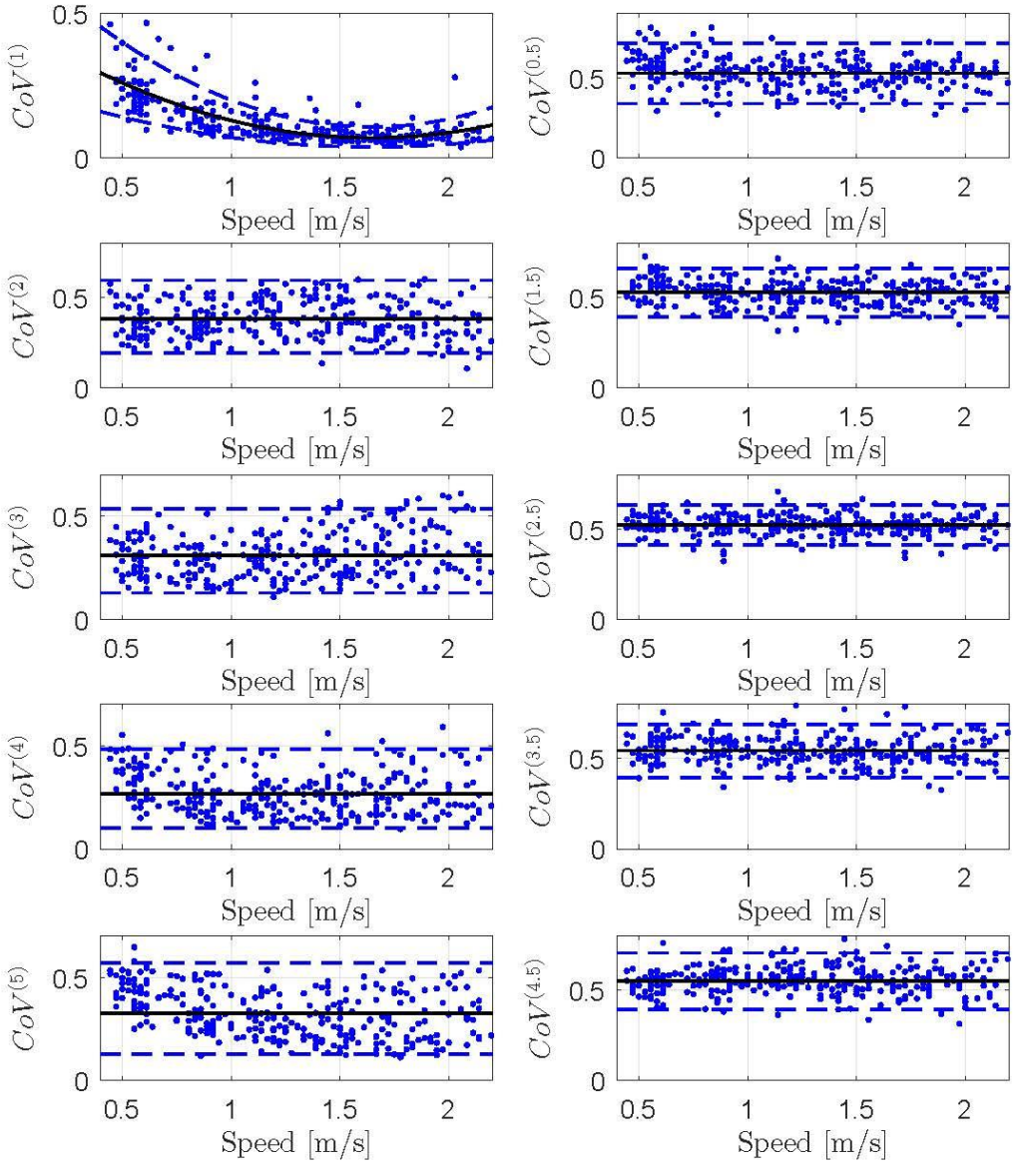

Figure 5. *$CoV^{(j)}$ vs walking speed. The dots represent the data, the solid lines the quadratic fit and the discontinuous lines the 95% confidence intervals.*

The calculated $CoVs$ of the DLF values are shown in Fig. 5. Apart from the first harmonic, the data show no apparent trend as walking speed increases. Therefore, they can be assumed uniformly distributed across the measured range of speeds. For the first harmonic, the data form a concave pattern with the minimum at the speed of approximately $1.7\ m/s^2$. This can be interpreted as the preferred walking speed at which the body energy expenditure is minimised [2]. The value is within the range reported in the relevant studies on energetic cost of walking [7].

Similar to the average values of $\overline{DLF}^{(j)}$, also $CoV^{(j)}$ can be described as the product of a deterministic factor $CoV_d^{(j)}$ and a random factor $CoV_r^{(j)}$:

$$CoV^{(j)} = CoV_d^{(j)} \cdot 10 \cdot CoV_r^{(j)}. \quad (7)$$

The deterministic part can be modelled as a second-order polynomial:

$$CoV_d{}^{(j)} = c_{14}^{(j)} \cdot v^2 + c_{15}^{(j)} \cdot v + c_{16}^{(j)}. \quad (8)$$

The values of the coefficients $c_{14}^{(j)}$, $c_{15}^{(j)}$ and $c_{16}^{(j)}$ are reported in Table 2. Note that $c_{14}^{(j)}$ and $c_{15}^{(j)}$ are zero for all harmonics except the first, which means that the corresponding fit becomes just a constant flat line $CoV_d^{(j)} = c_{16}^{(j)}$.

Table 2. Parameter values of $CoV^{(J)}$ model.

(Sub) harmonic order (j)	c_9	c_{10}	c_{11}	c_{12}	c_{13}
0.5	0	0	0.1000	13.53	12.10
1	0.1450	-0.4773	0.4625	13.35	121.81
1.5	0	0	0.1000	27.33	24.54
2	0	0	0.1000	7.90	12.82
2.5	0	0	0.1000	39.65	36.29
3	0	0	0.1000	5.73	12.67
3.5	0	0	0.1000	23.24	19.41
4	0	0	0.1000	5.04	13.73
4.5	0	0	0.1000	20.53	16.62
5	0	0	0.1000	5.12	10.56

The random part, $CoV_r^{(j)}$, is obtained by dividing the actual $CoV^{(j)}$ values by the deterministic part and the constant 10:

$$CoV_r{}^{(j)} = \frac{CoV^{(j)}}{10 \cdot \left(c_{14}^{(j)} \cdot v^2 + c_{15}^{(j)} \cdot v + c_{16}^{(j)}\right)}. \quad (9)$$

Similar to $\overline{DLF_r}^{(j)}$, the value of $CoV_r^{(j)}$ corresponding to each pedestrian was estimated as the average value of the related six experiments. It was found that $CoV_r^{(j)}$ values fit well a Beta distribution, $B(c_{17}, c_{18})$. The values of the parameters c_{17} and c_{18} are determined by the maximum likelihood method [6] and are reported in Table 2. The fits and the corresponding 95% confidence intervals are shown in Fig. 5 together with the experimental data.

As a summary of the synthetic generation of DLF values, an algorithm is described here. For a given sequence of variable footfall speeds in a walking trial, v_i, explained in [3], the corresponding sequence of variable $DLF_i^{(j)}$ values is generated as follows:

1. Calculate the deterministic part of $\overline{DLF}^{(j)}$, $\overline{DLF_{di}}^{(j)} = c_9^{(j)} \cdot v^2 + c_{10}^{(j)} \cdot v + c_{11}^{(j)}$.
2. Sample $\overline{DLF_r}^{(j)}$ from $B(c_{12}, c_{13})$.
3. Calculate the adaptive values for successive steps/strides, $\overline{DLF_i}^{(j)} = \overline{DLF_d}^{(j)} \cdot 10 \cdot \overline{DLF_r}^{(j)}$.

4. Calculate de deterministic factor of $CoV_i^{(j)}$, $CoV_{di}{}^{(j)} = c_{14}^{(j)} \cdot v^2 + c_{15}^{(j)} \cdot v + c_{16}^{(j)}$.
5. Sample $CoV_r^{(j)}$ from $B(c_{17}, c_{18})$.
6. Calculate $CoV^{(j)}$ for successive steps/strides, $CoV_i^{(j)} = CoV_{di}^{(j)} \cdot 10 \cdot CoV_r^{(j)}$.
7. Compute mean and variance for each step/stride, $\mu_i^{(j)} \cong \overline{DLF}^{(j)}$, $\left(\sigma_i^{(j)}\right)^2 \cong \left(\overline{DLF_i}^{(j)} \cdot CoV_i^{(j)}\right)^2$.
8. Calculate parameters a_i and b_i of $DLF_i^{(j)}$ distribution of the (sub)harmonics in each (stride) step, $a_i^{(j)} = \frac{\left(\mu_i^{(j)}\right)^2\left(1-\mu_i^{(j)}\right)}{\left(\sigma_i^{(j)}\right)^2} - \mu_i^{(j)}$, $b_i^{(j)} = a_i^{(j)}\frac{1-\mu_i^{(j)}}{\mu_i^{(j)}}$.
9. Generate $DLF_i^{(j)}$ sequence by sampling from $B\left(a_i^{(j)}, b_i^{(j)}\right)$.

The first three steps of the algorithm create artificial DLF values which variation is reduced to the inter-pedestrian variability. The remaining steps add the intra-pedestrian variability, so such DLFs account for the actual top level of variability of the GRF amplitudes.

3. MODEL ASSESSMENT

Amplitudes and trends of the synthetic DLFs generated as elaborated in the previous section will be compared in with the DLFs reported elsewhere [8], [9].

Fig. 6 shows widely popular deterministic DLF models of the first four walking harmonics derived by Kerr using single footfall GRFs recorded by a force plate [8]. Kerr fitted a third order polynomial curve to DLFs of the first harmonic as a function of walking frequency. DLF values of the other three higher order harmonics were found independent from the walking frequency, thus modelled as constants. Fig. 6 also shows synthetic DLF data from this study corresponding to the Kerr's models. They include only deterministic components of DLFs described by Eq. (5). As the equation features walking speeds, the corresponding walking frequencies were determined by the power law f_s=1/c_3·v^(1-c_4) and using the mean values of parameters c_3 and c_4 [4].

The first harmonic graph shows the same growing trend of DLFs as walking frequencies increase up to 2.3 Hz. The two curves run in parallel with a small offset of approximately 0.05. However, the present model is still within Kerr's 95% confidence interval. Above 2.3 Hz, the DLFs follow two opposite trends. Kerr's model suggests decreasing while the present model shows increasing DLF amplitudes with further increments of walking frequency. Nevertheless, Kerr himself noted that his results above 2.2 Hz are likely to be untrue due to a great level of data scarcity. For the higher harmonics, unlike Kerr's flat lines the present model features a light increasing trend in DLF values as the pedestrians increase walking frequency. Again, the apparent differences are for pacing rates higher than approximately 2.3 Hz. Considering different experimental setups and the large scatter in the data points in both studies, the models generate fairly close results. The present study derived the DLFs from continuously measured treadmill walking including many successive footfalls per a walking trial rather than just a single footfall as collected by Kerr. Moreover, the present study added a higher statistical rigor to the modelling by using around 30,000 data points, which is thirty times higher than in the Kerr's study.

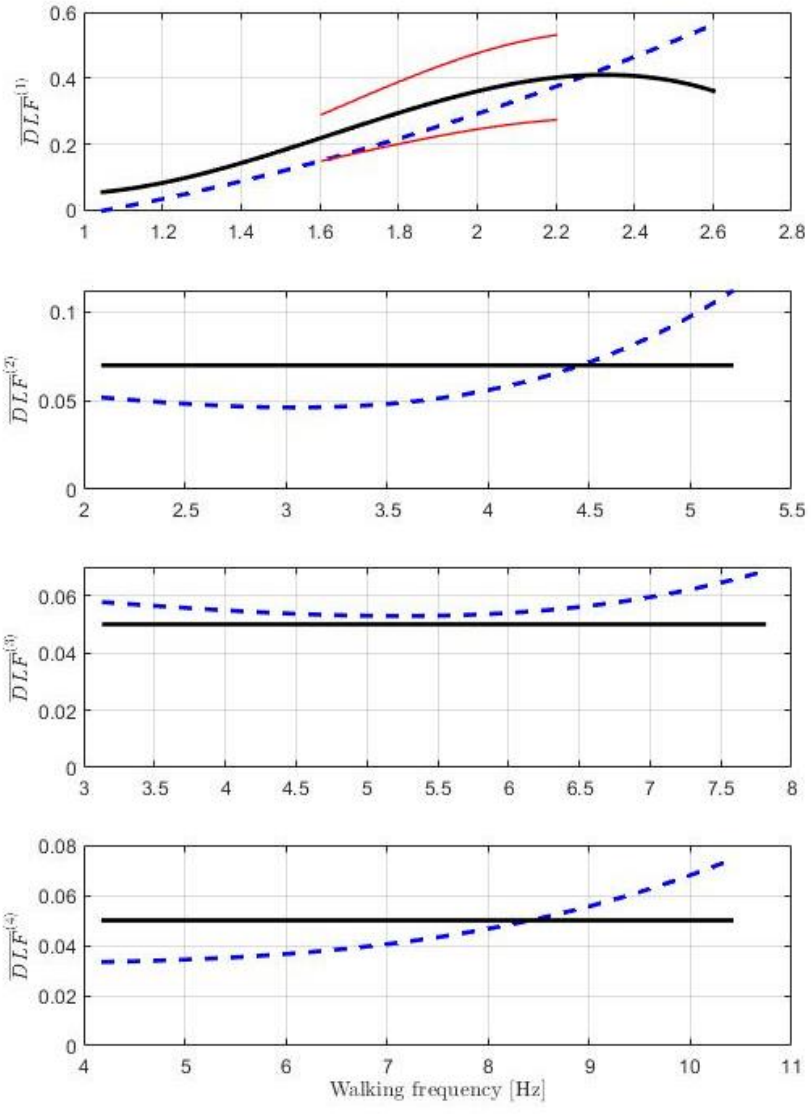

Figure 6. $\overline{DLF}^{(j)}$ *vs. walking speed. Solid lines: Kerr's study. Bold line: averages. Fine line: 95% confidence interval. Dashed lines: present study.*

DLFs derived from continuously measured force time histories as in this study are rare and limited. The values for the first five harmonics extracted by Kumar et al [9] from treadmill force records generated by 12 test subjects (9 males and 3 females) at University of Sheffield are shown in Fig. 7. The average value of the $\overline{DLF}^{(j)}$ from the present study together with their 95% confidence interval are added for comparison. Overall, the match is apparently closer than in case of the Kerr's model (Fig.6). Increasing trends in DLF values are similar for all harmonics and most of the Sheffield data are within the confidence intervals. The best match is for the first harmonic, while some Sheffield DLFs are below the lower confidence border for the higher harmonics. However, more data points are needed to provide a more conclusive comparison. The reader should also bear in mind that the Sheffield experiments measured ethnically more diverse population of test subjects, while the present study data included predominantly Spanish Caucasians.

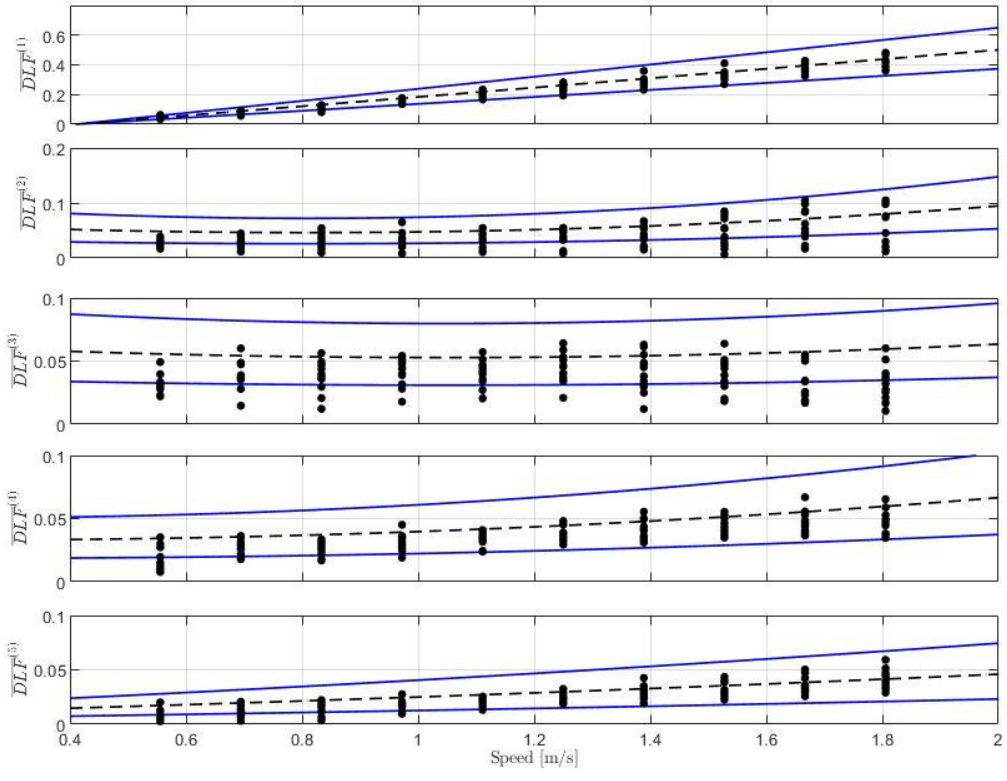

Figure 7. $\overline{DLF}^{(j)}$ *vs. walking speed. Dashed lines represent average values, while solid lines are 95% confidence intervals. Dots are the results in Kumar et al.*

4. CONCLUSIONS

The key novelty of the model presented here and the previous ones developed by the authors is that it creates stochastic walking force signal where all modelling parameters are function of variable walking speed on the step-by-step basis. This is a radical difference from traditionally used deterministic models which generate periodic force time histories and where the modelling parameters are function of the average pacing rate in a walking trial. Walking speed rather than pacing rate is a more natural choice of the input variable as human nervous system adopts speed of successive steps to the surrounding environment and different circumstances. Moreover, crowded situations are the most relevant loading scenarios where the speed of individual pedestrians is more or less controlled by the crowd flow and the crowd density.

Based on the previously developed models describing inter- and intra-pedestrian variability of walking speed and spatiotemporal parameters in walking trial, the present study delivered a complementary model of variable DLFs corresponding to the first five harmonics and subharmonics of the walking force. Although Kerr studied the first four harmonics only based on single footfall data [8], his deterministic DLF values are in line with the corresponding DLF values derived in the present study from continuously measured force time histories. Both the mean and CoV of DLFs are described as the products of two factors. The first represents the deterministic dependence on the step speed and is

modelled as a second-order polynomial. The second factor stands for the random inter-pedestrian variability of the DLFs and it is defined by a Beta distribution. Finally, all the relevant models could be integrated in a comprehensive model of artificial walking force signals where both pacing rate and force amplitudes vary on the step-by-step basis as functions of the variable step speed.

ACKNOWLEDGEMENTS

The authors would like to thank all the voluntaries for their generous help to collect the experimental data used in the model development. The financial support provided by the Spanish Ministry of Economy and Competitiveness through project PGC2018-096670-B-100 is specially acknowledged.

REFERENCES

[1] Zivanovic, S., Pavic, A., Reynolds, P., (2005). Vibration serviceability of footbridges under human-induced excitation: a literature review. Journal of Sound and Vibration 279 pp 1-74.

[2] Racic, V. & Brownjohn, J.M.W., (2009). Experimental identification and analytical modelling of human walking forces: Literature review. Journal of Sound and Vibration 326 pp 1-49.

[3] García-Diéguez, M. & Zapico-Valle, J.L., (2019). Statistical modelling of spatiotemporal variability of overground walking. Mechanical Systems and Signal Processing 129 pp 186-200.

[4] García-Diéguez, M. & Zapico-Valle, J.L., (2017). Statistical Modeling of the Relationships between Spatiotemporal Parameters of Human Walking and Their Variability. Journal of Structural Engineering 143(12).

[5] Racic, V. & Brownjohn, J.M.W., (2011). Stochastic model of near-periodic vertical loads due to humnas walking. Advances Engineering Informatics 25 pp 259-275.

[6] Rohatgi, V.K. & Ehsanes Saleh A.K.Md. (2011) An introduction to probability and statistics. John Wiley & Sons.

[7] Rose, J. & Gamble, J.G. (1994) Human walking. Williams & Wilkins 2nd edition. Baltimore.

[8] Kerr, S.C. (1998) Human induced loading on staircases - PhD Thesis, University College London. Mechanical Engineering Department, London, UK.

[9] Kumar, P., Kumar, A., Racic, V., Erlicher S. (2018) Modelling vertical human walking forces using self-sustained oscillator. Mechanical Systems and Signal Processing 99 pp 345-363.

ULTRA-HIGH PERFORMANCE CONCRETE (UHPC) WITH SUBSTITUTION OF CEMENTITIOUS MATRIX BY WASTE

Rubio-Cintas Maria Dolores[1], Parrón-Rubio Maria Eugenia[2], Perez-Garcia Francisca[3]., Garcia-Manrique Jose Manuel[4], Gonzalez-Herrera Antonio[5]

[1] *Departamento de Ingeniería Industrial e Ingeniería Civil. Escuela Politécnica Superior de Algeciras, Universidad de Cádiz. (ESPAÑA). mariadolores.rubio@uca.es (Corresponding author)*
[2] *Departamento de Ingeniería Industrial e Ingeniería Civil. Escuela Politécnica Superior de Algeciras, Universidad de Cádiz. (ESPAÑA). mariaeugenia.parron@uca.es*
[3] *Departamento de Ingeniería Civil, Materiales y Fabricación. Universidad de Málaga. (ESPAÑA). perez@uma.es*
[4] *Departamento de Ingeniería Civil, Materiales y Fabricación. Universidad de Málaga. (ESPAÑA). josegmo@uma.es*
[5] *Departamento de Ingeniería Civil, Materiales y Fabricación. Universidad de Málaga. (ESPAÑA). agh.uma.es@gmail.com*

Corresponding author: mariadolores.rubio@uca.es

ABSTRACT

The Campo of Gibraltar is one of the most significant industrial regions in Andalucia, generating a significant amount of solid waste that is later taken to landfills. Some of them can be recover in the cementitious matrix manufacture and then reuse and valorize in the civil construction sector. This research is focused on give them a new possibility of handling in Ultra-High Performance Concrete (UHPC) in several application as the rehabilitation of the system maritime, improving and strengthening the port work, as well as the consolidation of the industrial infrastructure of the area or on the maritime land coastline. The efficiency of concrete structures necessarily leads to an improvement in their overall performance not only from a structural point of view but also from a sustainability point of view. The proposed concrete model has the quality of being supported by simple and well-known laws for each of its components. Three different dosages were carried out, an initial standard, the replacement of 10% of petroleum cracking catalysts (FCC) and a third where 5% of FCC and blast furnace slag were replaced by cement.

***Keywords**: Ultra-High Performance Concrete, waste, GGBFS, mechanical properties*

1. INTRODUCCIÓN

Los residuos sólidos que se generan hoy en día son uno de los problemas más importantes que el ser humano debe de resolver. Siendo los industriales, por sus diferentes contenidos en materiales peligrosos, los más abundantes, fundamentalmente en zonas donde hay industrial, conllevan consigo el depósito de los mismos en vertederos especiales para evitar el lixiviado de los metales.

Una posibilidad para la reutilización de este tipo de residuos es introducirlos en matrices cementosas, formando parte de la misma, por la sustitución de alguna de las materias primas incluso del propio cemento. La mezcla resultante debe poseer unas características mecánicas y un comportamiento adecuado para su uso en la ingeniería civil. Realizando una selección de residuos, el número de ellos que terminaría en el vertedero se vería considerablemente reducido, ya que tratado y seleccionado en plantas adecuadamente, se utilizaría como una materia prima, para usarse inmediatamente. El objetivo, además de cerrar el ciclo de vida de un material de desecho, consigue un importante ahorro energético ya que se utilizaría directamente previa tamización del mismo para encontrar la correcta granulometría que se precisa para el desarrollo del hormigón. Al no ser necesario volver a procesarlo ni compactarlo sustituye directamente a materias primas (áridos) o cemento en función del tipo de residuo a sustituir, disminuyendo tanto la huella de carbono como la huella hídrica en el proceso productivo del hormigón[1–4].

Por otro lado, el hormigón de muy alta resistencia (UHPC) es un hormigón relativamente caro por los componentes que forman su matriz ya que los áridos de los que está formado son silicios. La sustitución de parte de sus componentes por residuos valorizados cuyas características sean similares a estos materiales tanto en sus dimensiones como en su composición química abarata el producto y a su vez contribuyendo con el medio ambiente[2,5–7]

En este artículo se realizan ensayos de sustitución de cemento por FCC (catalizadores de residuos del petróleo) y escorias de alto horno. La sustitución de diferentes componentes en matrices cementosas hoy en día está avalada por muchas publicaciones en la que la sustitución en el hormigón da resultados óptimos[8].

2. MATERIALES

El cemento que se utilizó fue Cemento Portland Ordinario (OPC) CEM I 52,5 R con una densidad relativa de 3,1 g/cm^3.

Las escorias del alto horno en ese trabajo fueron por cortesía de Estabisol S.A. (Asturias). Es un polvo fino de 60 µm cuya composición química se obtuvo por fluorescencia de rayos X (XRF). Los FCC fueron proporcionados por una empresa petrolífera. La composición química de cada componente se muestra en la tabla 1.

Tabla 1. Composición química de las escorias de alto horno

Escorias de alto horno		**FCC**	
CaO	47.14	Al_2O_3	51.507
SiO_2	32.3	SiO_2	44.396
Al_2O_3	10.7	K_2O	0.002
MgO	7.64	CaO	0.0019
SO_3	1.52	Fe_2O_3	0.505
TiO_2	0.699	MnO	0.002

K_2O	0.448	NiO	0.123
MnO	0.419	La_2O_3	2.194
Fe_2O_3	0.29	ZnO	0.015
SrO	0.115	TiO_2	0.198
Na_2O	0.08	SO_3	0.289
ZrO_2	0.0386	SrO	0.004
NiO	0.035		
Cr_2O_3	0.011		

En los áridos finos utilizados son de arena silícea (0- 0.5mm) y gruesa (0,6 - 1,2 mm). La distribución del tamaño de grano de la arena fina y gruesa se muestran en la figura 2

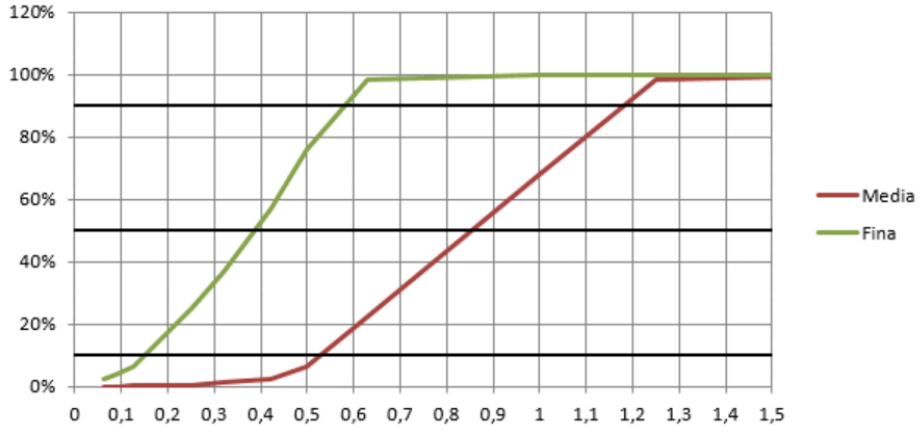

Figura 1. *Tamaño de los áridos que atraviesan el tamiz.*

El humo de sílice empleado fue proporcionado por Sika (Sika Fume S-92-D) con un tamaño medio de partícula de 0.1 µm. La harina de sílice tenía un diámetro medio de partícula de 6.5 µm y fue suministrado por Sibelco.

Las fibras de acero empleadas fueron 13 mm de largo con un diámetro de 0.2 mm.

Finalmente, se utilizó un aditivo reductor de agua (WRA) suministrado por Sika (Viscocrete 225) con el objetivo de cumplir con los requisitos de trabajabilidad (1,4% por peso total).

En ensayos anteriores se estudiaron diferentes tipos de dosificaciones siempre partiendo de una dosificación sin adición, para tener una comparativa del mismo. Se utilizaron en la sustitución de cemento residuos de catalizadores del craqueo del petróleo (FCC) y escorias de alto horno.

La designación y dosificación que se utilizo fue la siguiente:

Table 2. Dosificación del material

Propiedades	**UHO (kg/m^3)**	**UHF (kg/m^3)**	**UHG (kg/m^3)**
Cemento	800	720	720
FCC	-	80	40
Escoria blanca	-	-	40
Arena fina	565	302	302
Arena gruesa	565	565	565
Humo de sílice	175	175	175
Harína de sílice	225	225	225
Fibras de acero	160	160	160
Agua	19,27	19,27	19,27
Aditivo	35	35	35
w/b	0.19	0.19	0.19

Correspondiendo UH0 con hormigón de control UHF una sustitución del 5% FCC y 5% de FCC y 5% de escoria de alto horno.

Una breve descripción del proceso sería: una vez obtenida la mezcla se procede a la fabricación del hormigón. Las dosificaciones son muy exhaustivas ya que una pequeña variación puede llevar a la no compactación del material dada la sensibilidad en la trasformación de su fase solida a autocompactante. Este paso conlleva el estudio de la relación agua cemento no puede superar 0,2, al realizar sustitución de cemento por escoria es muy importante tener esta parte en consideración mediante las pruebas previas para que no supere este valor. Una vez obtenido el hormigón se introdujeron en probetas de 10x10x10 cm y posteriormente en una cámara de curado para que no sufra retracción durante su fraguado, para lo que es importante tener las mismas condiciones de humedad y temperatura.

3. RESULTADOS Y DISCUSIÓN

3.1. Resistencia a compresión

La resistencia a compresión de las mezclas se realizó a diferentes edades como muestra la figura 2. Para su estudio se rompieron entre 2 y 3 probetas por ensayo.

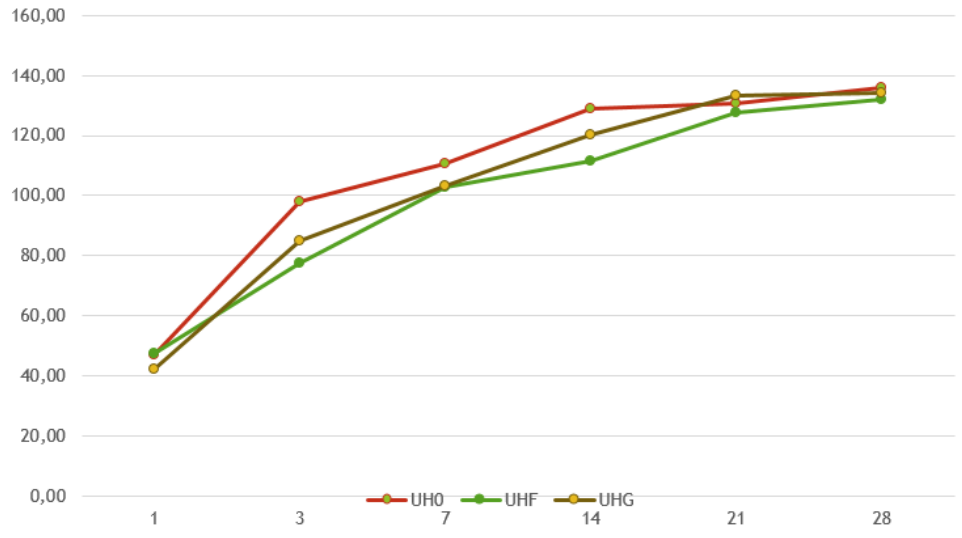

Figure 2. *Resistencia a compresión a diferentes edades*

Se observa que en las mezclas de hormigón a 1 día es relativamente mínima entre el hormigón de control y las adiciones. Con respecto a las ganancias se observa que UHF tiene casi un 1% de aumento de resistencia con respecto a UH0 lo que nos indica que el coeficiente de retracción que se puede provocar en el inicio del secado es prácticamente nulo. De igual manera en UHG hay una disminución del 10% con respecto al de control. En trabajos realizados con escorias de alto horno, donde se utilizan las escorias no alcanzan hasta prácticamente 28 días la misma capacidad resistente o superior[2,9,10]. Se ve que las curvas aumentan con respecto del paso del tiempo y a dicha edad el comportamiento de la mezcla UHF no experimenta una gran diferencia con respecto al hormigón de control. Por el contrario, sí se observa que hay casi un 2% de incremento en la mezcla escoria de alto horno. El aumento de la resistencia a compresión por FCC y escorias de alto horno, es decir, la mezcla UHG va obteniendo ganancia conforme va pasando el tiempo. Esto puede ser debido que el agua en la mezcla es menor que la cantidad necesaria para una hidratación completa, y una porción de dicha mezcla se hidrata para producir silicato cálcico hidratado (CSH), sirviendo las partículas tanto de GGBFS como las FCC como rellenos en la matriz de hormigón. La conclusión que se puede extraer es que el reemplazo parcial del cemento por GGBFS reduce la resistencia a edad temprana, pero aumenta a edades más avanzadas. La ganancia de fuerza en edades tardías como se comentó anteriormente se atribuye a las propiedades pucelánicas de GGBFS.

3.2. Resistencia a Flexión

La evolución de la resistencia a la flexotracción se muestra en la figura 3. Se ve afectada por el aumento de la escoria de alto horno con un remplazo de un 5% en masa del cemento. La resistencia a la flexotracción permanece estable con el remplazo de los FCC con un remplazo total de un 10% en masa del cemento, es decir, no hay variación en el comportamiento resistente de la misma, mientras que aumenta al rededor del 11% cuando se hace un remplazo de la masa del cemento a un 5% de los FCC y 5% de los GGBFS.

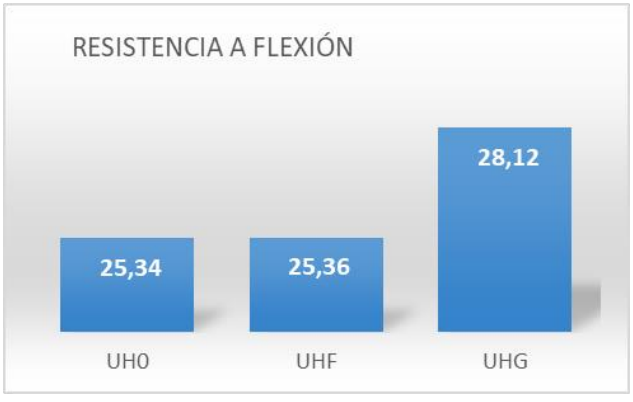

Figure 3. *Resistencia a tracción a 28 días*

Por lo que se puede concluir que las utilizaciones de los FCC no disminuyen la resistencia a flexión del hormigón y que mezclados con la GGBFS aumentan esta resistencia alrededor de un 11% con respecto al hormigón de referencia. Estos residuos serían aptos para la utilización en hormigones como remplazo en parte del cemento y así poder reducir la cantidad de cemento y por ende la emisión nociva que las producciones de este generan en su creación[11,12].

3.3. Módulo de elasticidad

El ensayo tiene como objetivo determinar el módulo de Young de la secante en los distintos hormigones planteados en este trabajo. La medición se ha realizado sobre 3 probetas diferentes de cada tipo de hormigón endurecido, pero siempre fabricadas con la misma mezcla.

Las probetas utilizadas en el ensayo tienen geometría cilíndrica Ø15x30 cm y todas ellas han sido curadas bajo agua a 20°±2°C. La determinación del parámetro indicado se ha realizado a los 28 días de edad.

Figure 4. *Ensayo del módulo elástico*

Para la realización de los ensayos se han seguido las especificaciones establecidas en la norma UNE-EN 12390-13:2014, método B.

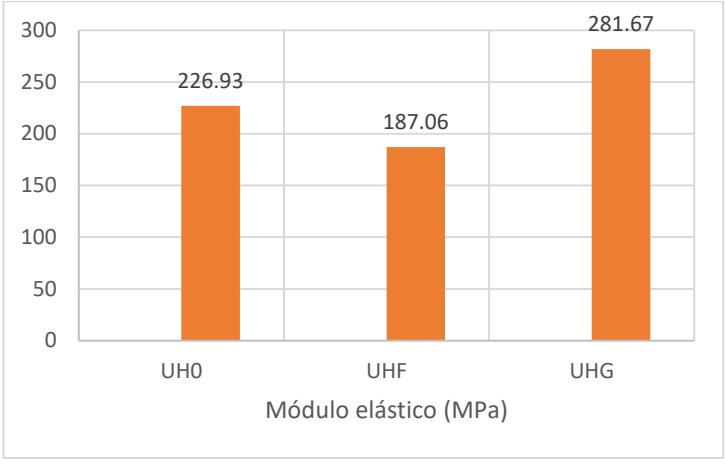

Figure 5. *Módulo elástico experimental*

El módulo de elasticidad se ajusta bien a los datos experimentales. Se observa que el modelo UHG aumenta con respecto a las otras dos mezclas alrededor de un 24,2% con respecto a la de control. Por el contrario, disminuye en UHF alrededor de un 17,3%, observándose que la adición de escorias de alto horno aumenta la capacidad resistente y por tanto el módulo de elasticidad con respecto a la dosificación de los FCC.

4. CONCLUSIONES

En este artículo se ha estudiado la influencia de la sustitución parcial de cemento por diferentes residuos (FCC, Escorias de alto horno) en HMAR. Se estudiaron 3 mezclas diferentes incluidas la de control donde estos residuos fueron reemplazados parcialmente por cemento. Las características mecánicas de todas las mezclas se evaluaron en una campaña experimental intensiva. Las siguientes conclusiones de la investigación experimental que se presentan a continuación:

1. La sustitución de FCC en la mezcla UHF tiene una disminución prácticamente irrelevante del 1% con respecto UH0 con lo que es óptima la utilización de este residuo como reducción de cemento.

2. Las propiedades mecánicas de la mezcla UHG reduce la resistencia a compresión en edades tempranas. Sin embargo, aumenta a edades posteriores. Esto se puede atribuir a las propiedades pucelánicas de la escoria granulada de alto horno.

3. La resistencia a flexión permanece constante en las mezclas UHF, por el contrario, en las UHG aumentan alrededor de 11% dicha capacidad resistente.

4. En el estudio del módulo elástico aumenta alrededor de un 24,2% El UHG con respecto al de control

5. BIBLIOGRAFÍA

[1] G. Wang, Y. Wang, Z. Gao, Use of steel slag as a granular material: volume expansion prediction and usability criteria, J. Hazard. Mater. 184 (2010) 555–560. https://doi.org/https://doi.org/10.1016/j.jhazmat.2010.08.071.

[2] M.E. Parron-Rubio, F. Perez-Garcia, A. Gonzalez-Herrera, M.J. Oliveira, M.D. Rubio-Cintas, Slag

Substitution as a Cementing Material in Concrete: Mechanical, Physical and Environmental Properties, Materials (Basel). 12 (2019) 2845. https://doi.org/10.3390/ma12182845.

[3] M.D. Rubio-Cintas, M.A. Fernandez-Ruiz, F. Perez-García, M.E. Parron-Rubio, Effect of the addition of electric arc furnace dust on the mechanical properties and carbonation performance of concrete, Eur. J. Environ. Civ. Eng. (2020). https://doi.org/10.1080/19648189.2020.1767697.

[4] S. Demirhan, G. Yildirim, Q.S. Banyhussan, K. Koca, O. Anil, R.T. Erdem, M. Sahmaran, Impact behaviour of nanomodified deflection-hardening fibre-reinforced concretes, Mag. Concr. Res. (2019). https://doi.org/https://doi.org/10.1680/jmacr.18.00541.

[5] J. Xie, J. Wang, R. Rao, C. Wang, C. Fang, Effects of combined usage of GGBS and fly ash on workability and mechanical properties of alkali activated geopolymer concrete with recycled aggregate, Compos. Part B Eng. 164 (2019) 179–190. https://doi.org/10.1016/j.compositesb.2018.11.067.

[6] S. Pyo, K. Wille, S. El-Tawil, A.E. Naaman, Strain rate dependent properties of ultra high performance fiber reinforced concrete (UHP-FRC) under tension, Cem. Concr. Compos. 56 (2015) 15–24.

[7] M.D. Rubio-Cintas, M.E. Parron-Rubio, F. Perez-Garcia, A.B. Ribeiro, M.J. Oliveira, Influence of steel slag type on concrete shrinkage, Sustain. 13 (2021) 1–13. https://doi.org/10.3390/su13010214.

[8] E. Gómez, El papel del catalizador usado de Craqueo Catalítico (FCC) como material puzolánico en el proceso de corrosión de armaduras de hormigón, (2007).

[9] C. Duran Atiş, C. Bilim, Wet and dry cured compressive strength of concrete containing ground granulated blast-furnace slag, Build. Environ. 42 (2007) 3060–3065. https://doi.org/10.1016/j.buildenv.2006.07.027.

[10] G. Laforest, J. Duchesne, Stabilization of electric arc furnace dust by the use of cementitious materials: Ionic competition and long-term leachability, (2006). https://doi.org/10.1016/j.cemconres.2006.05.012.

[11] D.Y. Yoo, N. Banthia, Mechanical properties of ultra-high-performance fiber-reinforced concrete: A review, Cem. Concr. Compos. 73 (2016) 267–280. https://doi.org/10.1016/j.cemconcomp.2016.08.001.

[12] B. Mobasher, A. Li, Y. Yao, A. Arora, N. Neithalath, Characterization of toughening mechanisms in UHPC through image correlation and inverse analysis of flexural results, Cem. Concr. Compos. 122 (2021) 104157. https://doi.org/10.1016/J.CEMCONCOMP.2021.104157.

COST-EFFICIENT MODELING FOR ESTIMATING THE ELASTIC PROPERTIES OF FIBER-REINFORCED COMPOSITES

García Merino, José Carlos[1]; Calvo Jurado, Carmen[2]; Rodríguez de Tembleque, Luis[3]; Sáez Pérez, Andrés[4]; García Macías , Enrique[5]

ABSTRACT

This paper presents the application of polynomial chaos expansion (PCE) as a surrogate model to perform stochastic homogenization of fiber-reinforced composites. The surrogate model is built to bypass the computationally intense numerical homogenisation of the elastic properties of 3D representative volume elements (RVEs) under periodic boundary conditions. With the aim of keeping minimal the computational burden involved in the PCE, an adaptive sparse expansion is implemented to automatically identify the optimal combination of orthogonal bases within a desired range of model orders. The developed surrogate model is used to estimate the probability distribution functions of the effective elastic moduli of epoxy doped with fully aligned carbon fibers (CFs). The presented numerical results and discussion demonstrate the ability of the proposed approach to perform uncertainty propagation analyses with minimum computational effort, offering vast possibilities for the stochastic design of macroscopic composite structural elements.

Keywords: Surrogate modelling, Composites, Homogenization, RVE, Numerical homogenization.

1. INTRODUCTION

Owing to the enormous potential of polymer nano/micro-composites for the design of high performance and multifunctional structures, their implementation in aircraft, aerospace, automotive and construction industries has undergone a sustainable growth in recent years [1]. Prominent examples of this trend are the Boeing 787 and Airbus 350 transport aircrafts, in which composites contribute over 50% of the total structural mass. Fueled by the progressive cheapening of their production along with recent advances in the development of carbon-based nano-modified composites and additive manufacturing, the global composite market is projected to reach USD 160.54 billion by 2027 at a compound annual growth rate (CAGR) of 7.6% between the period 2020-2027 [2].

The implementation of such composites into engineering systems implies a higher level of complexity in the design, requiring a further analysis of the constituent materials and their interaction. The

[1]*Departamento de Matemáticas, Universidad de Extremadura (Spain). jcgarcia@unex.es (Corresponding author)*
[2]*Departamento de Matemáticas, Universidad de Extremadura (Spain). ccalvo@unex.es*
[3]*ETSI, Universidad de Sevilla (Spain). luisroteso@us.es*
[4]*ETSI, Universidad de Sevilla (Spain). andres@us.es*
[5]*ETSI de Caminos, Canales y Puertos, Universidad de Granada (Spain). enriquegm@ugr.es*

material properties of these composites depend upon many factors such as the volume fraction, filler orientation, distribution, and geometry of the fillers, as well as their interaction with the host matrix material. A wide variety of homogenization techniques has been proposed in the literature, ranging from analytical mean-field homogenization approaches to numerical techniques, using finite element (FE) and boundary element methods, atomistic-based continuum mechanics, molecular dynamics simulations, Fast Fourier Transform techniques, just to mention a few [3][4]. Approaches using the FE method for the virtual testing of representative volume elements (RVEs) under periodic boundary conditions have become particularly popular due to their flexibility to model a large variety of microstructures. Such approaches allow to accurately represent the actual geometry of the inclusions, and the number of assumptions and simplifications of the underlying microstructure is kept minimal. Nevertheless, the mesh densities required to accurately represent the microstructure usually imply considerable computational burdens, limiting their applicability when modelling the response of full-scale macro-structural systems. This is particularly limiting when aiming to implement stochastic design strategies, which typically require an elevated number of model evaluations.

In order to tackle these limitations, this work proposes the use of adaptive sparse PCE as a computationally efficient surrogate model to bypass the estimates from the numerical homogenization of 3D RVEs of epoxy composites doped with fully aligned CFs under periodic boundary conditions. With the purpose of keeping minimal the computational burden involved in the surrogate model, an adaptive sparse expansion based upon the least angle regression (LAR) algorithm is implemented to automatically identify the optimal combination of orthogonal bases within a certain range of candidate model orders. The numerical results and discussion of this preliminary work demonstrate the effectiveness of the developed approach to perform uncertainty propagation analyses with minimum computational demands and times.

The remainder of this work is organised as follows. Section 2 presents the theoretical fundamentals, including the numerical homogenisation approach and the proposed surrogate model in Sections 2.1, and 2.2, respectively. Section 3 presents the numerical results and discussion, and Section 4 concludes the work.

2. THEORETICAL BACKGROUND

2.1. Numerical homogenisation

Several strategies can be followed for the numerical homogenization of composite materials. The simplest one consists in the use of periodic unit cells [5], containing a canonical arrangement of inclusions which are assumed to replicate periodically throughout the composite material. The mesh density required to discretize such RVEs is limited and so is the computational burden involved in the homogenization. Nevertheless, most composite materials present a certain degree of randomness in the dispersion of the doping fillers, being necessary to implement more computationally intense 3D random RVEs [6]. In this work, we implement a general cubic $l_1 \mathrm{x} l_2 \mathrm{x} l_3$ 3D prismatic model (see Fig. 1) which allows the intersection of fillers with the cell boundaries. For the construction and analysis of the material microstructure, a combination of scripts generated in MATLAB environment and in the

commercial FE code ANSYS are used. Specifically, the adopted methodology for defining the geometry of the RVE involves the following four steps:

1. Generate center coordinates $(x, y, z = l_3)$, construct a circle with the diameter of the fibers, and extrude it along the *z*-axis. The centers are allowed to fall outside of the cell.
2. Check if the fiber cuts any of the cell's surfaces. If so, symmetric fillers, -one, three or seven, depending if the original one cuts one, two or three cell's faces, respectively- are generated in order to impose periodicity.
3. Check if all the fillers generated in the previous step intersect the previous existing ones. If not, the proposal fiber is accepted, otherwise return to step 1.
4. Repeat until the desired filler volume fraction is achieved.

Once the geometry is set up, it is discretized in ANSYS using 4-nodes linear tetrahedral solid elements (SOLID285). An example of one the generated RVEs is shown in Fig. 1, including the fibers (a), matrix phase (b), and the corresponding mesh (c).

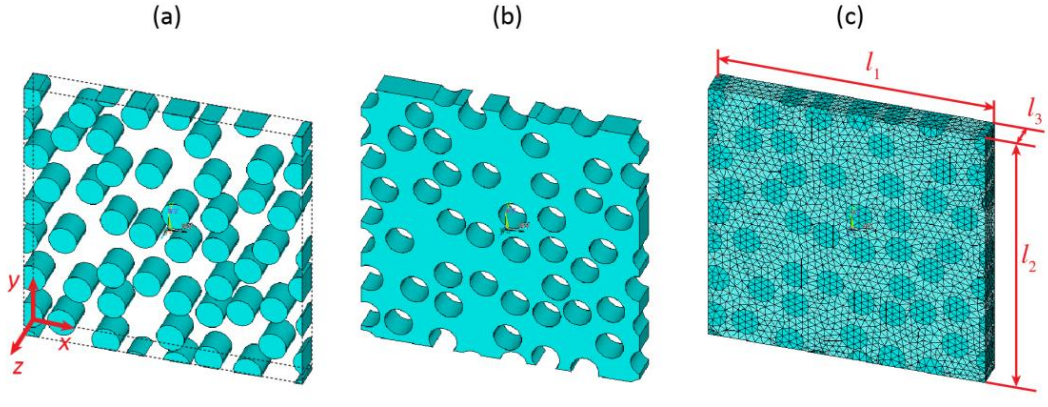

Figure 1. *Example of a RVE with a side length of 100x100x10 μm and doped with 35% volume fraction of carbon fillers (a) and mesh (17112 nodes) (b).*

To compute the effective properties of the composites, it is assumed that the material can be defined as the periodic replication of the previously defined RVE as shown in Fig. 2 (a). Therefore, to determine the effective elastic properties of one single isolated RVE, periodic boundary conditions must be applied. The volume of the RVE is V and the general periodic boundary conditions applied on its faces are given by [7]:

$$u_i = \hat{\varepsilon}_{ij} x_j + v_i, \tag{1}$$

where $\hat{\varepsilon}_{ij}$ denotes the volume average strains, v_i represents the local periodic part of the displacement components u_i on the boundary surfaces, and indexes i and j denote the global Cartesian directions. The latter displacement components are generally unknown and depend upon the applied loading, although they take the same values at every two homologous points on opposite faces of V.

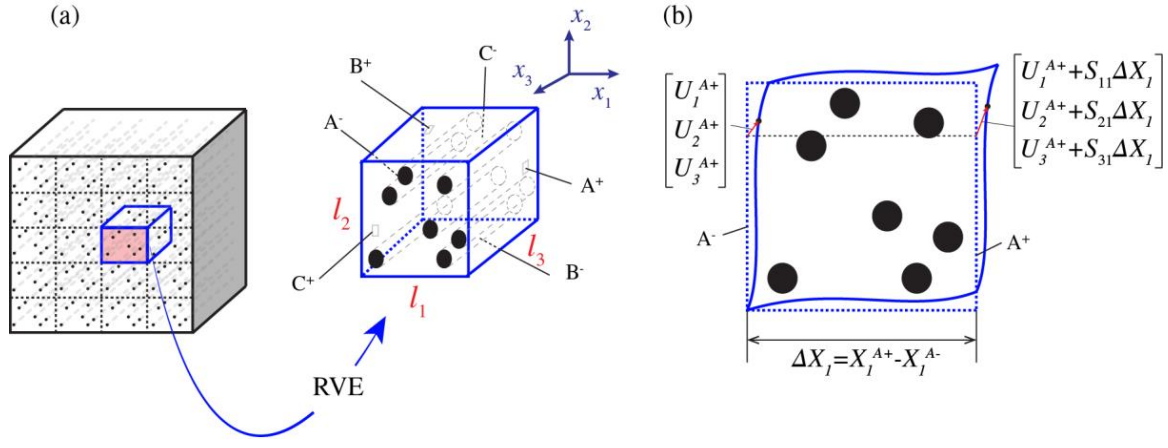

Figure 2. *Schematic representation of a periodic composite and definition of the RVE (a). Periodic boundary conditions for a pair of nodes located on the opposite surfaces A^- and A^+ (b).*

The volume average stresses $\hat{\sigma}_{ij}$ and strains $\hat{\varepsilon}_{ij}$ in the RVE can be computed as:

$$\hat{\sigma}_{ij} = \frac{1}{V}\int_V \sigma_{ij}\mathrm{d}V\,, \hat{\varepsilon}_{ij} = \frac{1}{V}\int_V \varepsilon_{ij}\mathrm{d}V, \tag{2}$$

with V being the volume of the RVE. Then, the ij-th component of the elastic tensor can be directly estimated as $C_{ij}^* = \hat{\sigma}_{ij}/\hat{\varepsilon}_{ij}$. Since, in general, the elastic tensor of an anisotropic material can be written following Voigt's notation as a symmetric 6x6 matrix as:

$$\begin{pmatrix}\sigma_1\\ \sigma_2\\ \sigma_3\\ \sigma_4\\ \sigma_5\\ \sigma_6\end{pmatrix} = \begin{pmatrix} C_{11}^* & C_{12}^* & C_{13}^* & 0 & 0 & 0\\ & C_{22}^* & C_{23}^* & 0 & 0 & 0\\ & & C_{33}^* & 0 & 0 & 0\\ & & & C_{44}^* & 0 & 0\\ & & & & C_{55}^* & 0\\ & & & & & C_{66}^* \end{pmatrix}\begin{pmatrix}\varepsilon_1\\ \varepsilon_2\\ \varepsilon_3\\ \varepsilon_4\\ \varepsilon_5\\ \varepsilon_6\end{pmatrix}, \tag{3}$$

or, alternatively, in terms of the compliance matrix $\boldsymbol{S}^*$ as:

$$\begin{pmatrix}\varepsilon_1\\ \varepsilon_2\\ \varepsilon_3\\ \varepsilon_4\\ \varepsilon_5\\ \varepsilon_6\end{pmatrix} = \begin{pmatrix} S_{11}^* & S_{12}^* & S_{13}^* & 0 & 0 & 0\\ & S_{22}^* & S_{23}^* & 0 & 0 & 0\\ & & S_{33}^* & 0 & 0 & 0\\ & & & S_{44}^* & 0 & 0\\ & & & & S_{55}^* & 0\\ & & & & & S_{66}^* \end{pmatrix}\begin{pmatrix}\sigma_1\\ \sigma_2\\ \sigma_3\\ \sigma_4\\ \sigma_5\\ \sigma_6\end{pmatrix}, \tag{4}$$

a total of six virtual tests with boundary conditions detailed in Table 1 are required to fully characterize the homogenized tensor $\boldsymbol{C}^*$ (3 pure dilations and 3 pure distortions). The periodic boundary conditions have been implemented in ANSYS by coupling the displacements of opposite nodes and opposite boundaries. For each pair of displacement components at two corresponding nodes with identical in-plane coordinates (within a certain tolerance) on two opposite cell faces, the constraint conditions from Table 1 are imposed. As an example, Fig. 2 shows the constraint equations to be defined for a pair of nodes located on the opposite surfaces A^- and A^+. Interested readers may find further information on the computational implementation of periodic boundary conditions in reference [7].

Once computed, the engineering constants in the case of a general orthotropic material can be obtained in terms of S_{ij} as:

$$E_{11}^* = \frac{1}{S_{11}^*}, E_{22}^* = \frac{1}{S_{22}^*}, E_{33}^* = \frac{1}{S_{33}^*}, v_{12}^* = -\frac{S_{12}^*}{S_{11}^*}, v_{13}^* = -\frac{S_{13}^*}{S_{11}^*}, v_{23}^* = -\frac{S_{23}^*}{S_{33}^*}, \quad (5)$$

$$G_{23}^* = \frac{2}{S_{44}^*}, G_{22}^* = \frac{2}{S_{55}^*}, G_{33}^* = \frac{2}{S_{66}^*}. \quad (6)$$

Table 1. Periodic boundary conditions

Virtual tests	**Along x**	**Along y**	**Along z**
Virtual test 1 *Extension along x*	$x = 0, U_1 = 0,$ $x = L_1, U_1 = L_1$	$y = 0, y = L_1, U_2 = 0$	$z = 0, z = L_3,$ $U_3 = 0$
Virtual test 2 *Extension along y*	$x = 0, x = L_1,$ $U_1 = 0$	$y = 0, U_2 = 0$ $y = L_2, U_2 = L_2$	$z = 0, z = L_3,$ $U_3 = 0$
Virtual test 3 *Extension along z*	$x = 0, x = L_1,$ $U_1 = 0$	$y = 0, y = L_2,$ $U_2 = 0$	$z = 0, U_3 = 0$ $z = L_3, U_3 = L_3$
Virtual test 4 *Distortion on x-z*	$x = 0, x = L_1,$ $U_1 = 0$	$y = 0, y = L_2,$ $U_1 = U_3 = 0$	$z = 0, U_2 = 0,$ $z = L_3, U_2 = L_3$
Virtual test 5 *Distortion on x-y*	$x = 0, x = L_1,$ $U_2 = U_3 = 0$	$y = 0, y = L_2,$ $U_2 = 0$	$z = 0, U_1 = 0$ $z = L_3, U_1 = L_3$
Virtual test 6 *Distortion on y-z*	$x = 0, x = L_1,$ $U_2 = U_3 = 0$	$y = 0, U_1 = 0$ $y = L_2, U_1 = L_1$	$z = 0, z = L_3,$ $U_3 = 0$

In the particular case of transversely isotropic materials with *x-y* as the plane of isotropy (like it is the case of a RVE made of an isotropic matrix material doped with a sufficient number of transversely isotropic fillers aligned in the *z*-axis), the components $\boldsymbol{S}^*$ in Eq. (4) simplify to:

$$\begin{pmatrix} \varepsilon_1 \\ \varepsilon_2 \\ \varepsilon_3 \\ \varepsilon_4 \\ \varepsilon_5 \\ \varepsilon_6 \end{pmatrix} = \begin{pmatrix} \frac{1}{E_\perp} & -\frac{v_\perp}{E_\perp} & -\frac{v_{\parallel\perp}}{E_\parallel} & 0 & 0 & 0 \\ & \frac{1}{E_\perp} & -\frac{v_{\parallel\perp}}{E_\parallel} & 0 & 0 & 0 \\ & & \frac{1}{E_\parallel} & 0 & 0 & 0 \\ & & & \frac{1}{2G_{\parallel\perp}} & 0 & 0 \\ & & & & \frac{1}{2G_{\parallel\perp}} & 0 \\ & & & & & \frac{1+v_\perp}{E_\perp} \end{pmatrix} \begin{pmatrix} \sigma_1 \\ \sigma_2 \\ \sigma_3 \\ \sigma_4 \\ \sigma_5 \\ \sigma_6 \end{pmatrix}, \quad (7)$$

which is fully characterized by five independent constants, namely the longitudinal $E_{\|}$ and transverse Young's moduli $E_{\perp}$, the Poisson's ratios $v_{\perp}$ and $v_{\|\perp}$ in and outside of the plane of isotropy, and the shear modulus $G_{\|\perp}$ outside of the plane of isotropy.

2.2. PCE surrogate modelling

Assuming the microstructural properties of interest as independent random variables arranged in a vector $\boldsymbol{x} \in \mathcal{R}^M$, the PCE representation of the effective properties *y* obtained from the numerical homogenization of a RVE $M(\boldsymbol{x})$ is defined as an expansion of *y* onto an orthogonal multivariable polynomial basis as [9]:

$$y = M(\boldsymbol{x}) = \sum_{\boldsymbol{\alpha} \in \mathbb{N}^M} a_{\boldsymbol{\alpha}} \Psi_{\boldsymbol{\alpha}}(\boldsymbol{x}), \tag{8}$$

with $a_{\boldsymbol{\alpha}}$ being unknown deterministic coefficients, and $\Psi_{\boldsymbol{\alpha}}$ are multivariate polynomials built up by a family of orthogonal polynomials as:

$$\Psi_{\boldsymbol{\alpha}}(\boldsymbol{x}) = \prod_{i=1}^{M} \Psi_{\alpha i}^{(i)}(x_i)\,, \tag{9}$$

where the multidimensional index notation $\boldsymbol{\alpha} = [\alpha_1, \dots, \alpha_M]$ is adopted. A variety of families of orthogonal polynomials has been proposed in the literature, being the Legendre and Hermite polynomials reported in Table 2 the most commonly used ones for uniformly and normally distributed input variables, respectively.

Table 2. Orthogonal polynomial bases used in PCE.

Statistical distribution	Orthogonal polynomials
Gaussian $\mathcal{N}(0,1)$	Hermite polynomials: $H_n(x) = (-1)^n e^{\frac{x^2}{2}} \frac{d^n}{dx^n} e^{\frac{-x^2}{2}}$
Uniform $\mathcal{U}(-1,1)$	Legendre polynomials: $P_n(x) = \frac{1}{2^n} \sum_{k=0}^{n} \binom{n}{k}^2 (x+1)^{n-k}(x-1)^k$

In practical applications, the PC expansion in Eq. (8) must be truncated after P terms. A classical approach consists of retaining all those polynomials $\Psi_{\boldsymbol{\alpha}}$ with total degree up to p, that is $0 \leq |\boldsymbol{\alpha}| \leq p$, with $|\boldsymbol{\alpha}| = \sum_{i=1}^{M} \alpha_i$. On this basis, the PCE can be written in matrix form as:

$$y = M(\boldsymbol{x}) = \sum_{0 \leq |\boldsymbol{\alpha}| \leq p} a_{\boldsymbol{\alpha}} \Psi_{\boldsymbol{\alpha}}(\boldsymbol{x}) = \boldsymbol{a}^{\mathrm{T}} \boldsymbol{\Psi}(\boldsymbol{x}). \tag{10}$$

The PCE coefficients can be estimated by least squares regression on a set of *N* realizations of the input variables, also referred to as the experimental design (ED). This is accomplished by sampling a training set T covering the parameter design space:

$$T = \left\{\mathbf{x}^{(1)}, \dots, \mathbf{x}^{(N)}\right\} \subset D, \tag{11}$$

which can be obtained by means of the Latin Hypercube (LH) Sampling [8] procedure. Then, the expansion coefficients can be obtained by minimizing the expectation of the least squares errors as:

$$\boldsymbol{a} = \arg\min_{\boldsymbol{a}\in\mathcal{A}} \frac{1}{N}\sum_{i=1}^{N}\left(M\left(\boldsymbol{x}^{(i)}\right) - \sum_{\boldsymbol{\alpha}\in\mathbb{N}^M} \boldsymbol{a}_{\boldsymbol{\alpha}}\Psi_{\boldsymbol{\alpha}}(\boldsymbol{x}^{(i)})\right)^2, \tag{12}$$

with $\mathcal{A}$ the total number of PC terms or cardinality of the expansion:

$$\mathrm{card}\mathcal{A} = \binom{M+p}{p} = \frac{(M+p)!}{M!\,p!}. \tag{13}$$

The computational cost involved in the fitting of the PCE using the classical truncation scheme in Eq. (12) may be very high if the number of input variables M or the polynomial degree p are considerably large. To alleviate this computational burden, an alternative hyperbolic truncation scheme was proposed by Blatman and Sudret [9] in terms of a q-norm, $0 < q < 1$, as:

$$\|\boldsymbol{\alpha}\|_q = \left(\sum_{i=1}^{M}\alpha_i^q\right)^{\frac{1}{q}}, \tag{14}$$

in such a way that a truncated PCE can be obtained by selecting a finite set of indices $\boldsymbol{\alpha}$ with q-norm less than or equal to p:

$$\mathcal{A}^q = \{\boldsymbol{\alpha}\in\mathbb{N}^M : \|\boldsymbol{\alpha}\| \le p\}. \tag{15}$$

Such a truncation scheme may remain computationally expensive, especially when dealing with large-dimensional and highly non-linear problems. This motivates the use of sparse linear regression methods such as the least-angle regression (LAR) algorithm to further reduce the computational burden. LAR is an efficient algorithm for model selection of sparse linear models. In this context, LAR provides a collection of PC expansions incorporating an increasing number of basis polynomials, from 1 to P= $\mathrm{card}\mathcal{A}^q$. Finally, a cross validation procedure is implemented for selecting the best model. In this work, the Bayesian Information Criterion [BIC] has been implemented [10]. Interested readers may find further details on the implementation of the LAR algorithm in reference [11].

3. NUMERICAL RESULTS AND DISCUSSION

In this section, numerical results and discussion are presented regarding the uncertainty propagation analysis of epoxy composites doped with fully aligned CFs. The material properties used in the analyses presented hereafter are collected in Table 3.

Table 3. Material properties of epoxy/CF composites taken from reference [12].

Epoxy polymer		**Carbon fibers (CF)**	
Young's modulus [GPa]	2.03	E_{11} [GPa]	250.00
Poisson's ratio [-]	0.40	$E_{22} = E_{33}$ [GPa]	22.40
		υ_{12} [-]	0.35
		υ_{31} [-]	0.30
		G_{23} [GPa]	22.10
		Radius [μm]	10.00

3.1. Convergence analysis of the RVE's size and mesh density

In order to assess the quality of the numerical RVE, two important features need to be carefully assessed: the size of the RVE and the mesh density. The size of the RVE must be large enough to ensure that it statistically represents the composite material as a whole. Such a condition can be evaluated by analysing the convergence of the numerical estimates of the effective elastic properties for increasing RVE's dimensions. To do so, the cell's dimensions in the plane perpendicular to the fibers have been progressively increased, while keeping constant its width to height ratio $l_1 = l_2$ and its thickness as $l_3 = l_1/10$. The analysis has been conducted for a volume fraction of 35%, which is the maximum concentration considered in this study. On this basis, five different RVEs containing 15, 24, 38, 56, and 81 fibers have been obtained. The convergence analyses of the longitudinal and transverse Young's moduli are shown in Figs. 3 (a) and (c), respectively. It is noted in these figures that convergence is approximately achieved for a RVE containing 58 fibers (100 x 100 x 10 μm). It is also noted that some discrepancies are found between the elastic moduli E_{22} and E_{33}, which should be equal in the case of a perfect transversely isotropic material. These differences are partly due to limitations in the mesh discretization and the randomness in the filler distribution. Once the RVE's size has been defined, the convergence of the mesh density has been evaluated for nine increasing discretizations, including 2663, 3427, 8211, 19846, 57241, 146171, 390976, and 1190731 nodes. The results of this convergence analysis are presented in Figs. 3 (b) and (d) in terms of longitudinal and transverse moduli, respectively. It is observed in this figure that convergence is approximately achieved at the fourth discretization density (19846 nodes). As a conservative solution, the seventh discretization has been selected (390976 nodes) and kept constant in the subsequent analyses. It is also noted that the previously observed discrepancies between the transverse elastic moduli are minimized as the mesh density increases, although some residual differences remain due to the randomness in the filler distribution.

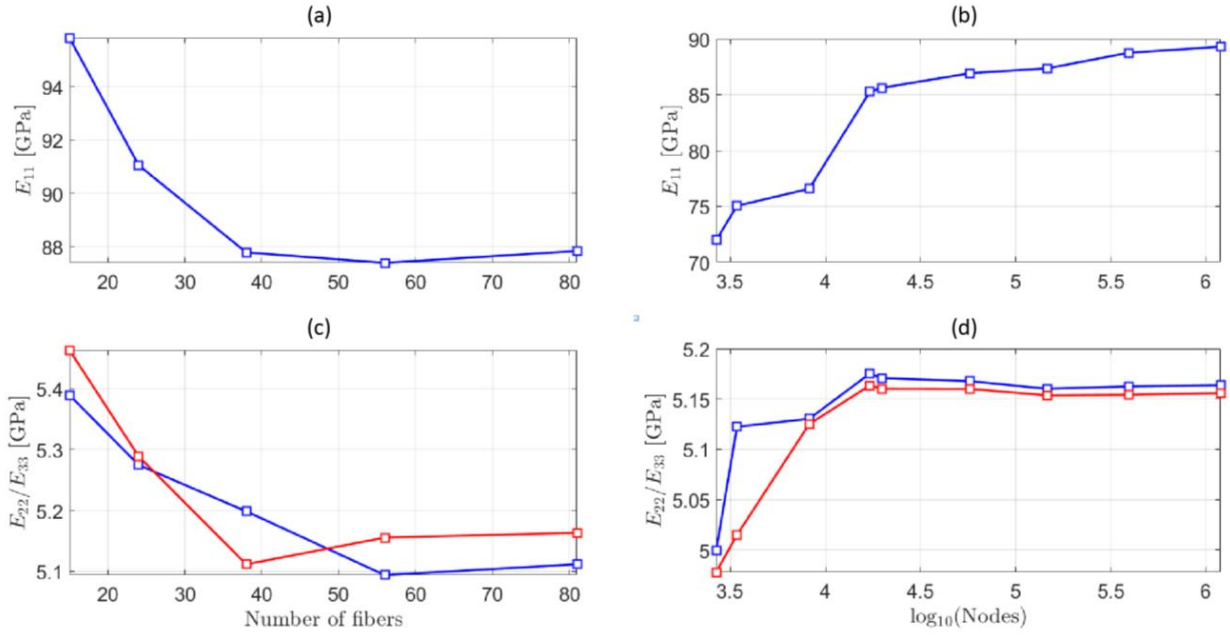

Figure 3. *Convergence analysis of the size of the RVEs (a,c) and mesh density (b,c) for a RVE of dimensions 100 x 100 x 10 µm (58 fibers).*

3.2. PCE expansion

Following the theoretical framework introduced in 2.2, a PCE meta-model has been constructed using 70 training points and validated with 30 independent points. Specifically, two PCE expansions have been constructed to reproduce the longitudinal and transverse Young's moduli, with model orders ranging from 2 to 3. The variables included in the model are the Young's modulus of epoxy, the filler volume fraction, and the longitudinal and transverse elastic moduli of carbon fibers with the statistical properties reported in Table 4. The standard deviations of the elastic properties of the epoxy matrix and the CFs have been obtained by imposing that the 99.5% (3σ) confidence levels correspond to 10% the mean values of the distributions.

Table 4. Considered statistical distributions of the material parameters.

Variable	Distribution
Young's modulus of epoxy	Gaussian $\mathcal{N}(2.03\ ,0.0677)$
Longitudinal modulus of CF	Gaussian $\mathcal{N}(250\ ,8.3333)$
Transverse modulus of CF	Gaussian $\mathcal{N}(22.4,0.7466)$
Filler volume fraction	Uniform $\mathcal{U}(0,0.4)$

To evaluate the accuracy of the surrogate model, the coefficient of determination R^2 is considered as:

$$R^2 = 1 - \frac{\sum_{i=1}^{K}\left(\hat{y}^{(i)} - y^{(i)}\right)^2}{\sum_{i=1}^{K}(\bar{y} - y^{(i)})^2}, \tag{16}$$

where $\hat{y}^{(i)}$ stand for the predictions of the PC expansion and K the number of model evaluations. The comparison of the estimates of the longitudinal and transverse Young's moduli of epoxy/carbon fibers by the surrogate model and the FE homogenization for the validation dataset is furnished in Fig. 4. The low scatter of the points around the diagonal lines and the coefficients of determination which are very close to 1 corroborate that the surrogate models are formed with accuracy. It is important to remark that the computational time involved in the numerical homogenisation amounts to about 15 minutes, while the surrogate model requires less than a millisecond.

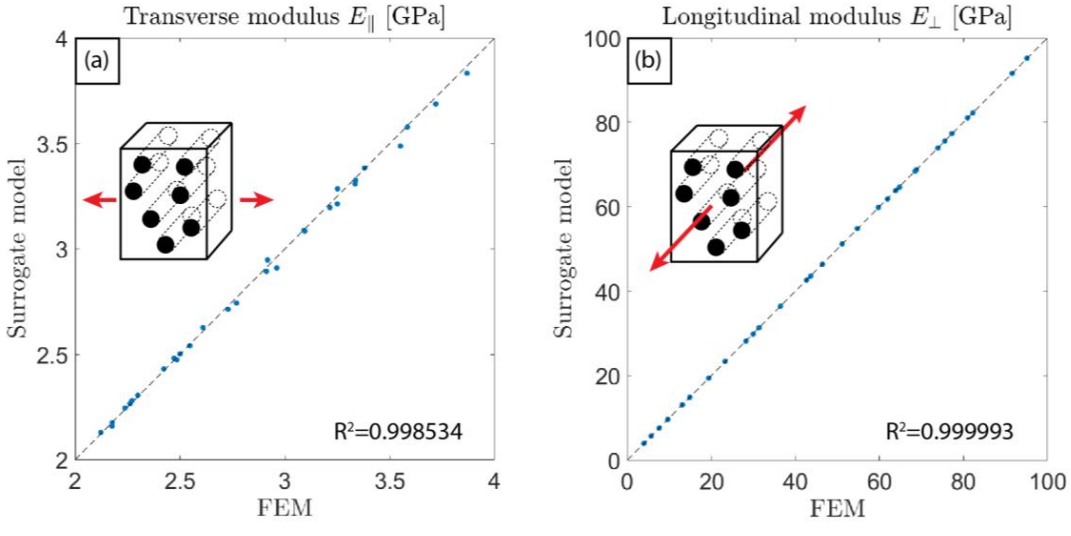

Figure 4. *Comparison of the numerical estimates by FEM and the predictions of the PCE expansion in terms of transverse (a) and longitudinal elastic moduli (b) obtained for the evaluation dataset.*

3.3. Uncertainty propagation analysis

The previously constructed surrogate models are used herein to analyse the propagation of uncertainties in the microstructural properties of epoxy/CF composites upon the effective elastic properties. To do so, a data population of 25000 individuals has been drawn by direct Monte Carlo sampling of the statistical distributions previously reported in Table 4. Then, the effective elastic moduli of the composites have been obtained by direct evaluations of the surrogate model, and the resulting estimates have been analysed in frequentist terms. Such a dense sampling population is required to accurately identify the statistical distributions of the effective elastic moduli. While these analyses using the forward numerical model would be simply unfeasible, the complete simulations took less than 1 second thanks to the computational efficiency of the built surrogate models. The resulting probability distribution functions (PDFs) of the effective transverse $E_{\perp}$ and longitudinal $E_{\|}$ Young's moduli of epoxy doped with 30% CF are reported in Figs. 5 and 6, respectively. It is in noted in Fig. 5 that the effective transverse modulus is dominated by the elastic modulus of the matrix phase, while almost no effect is observed for variations in the elastic moduli of the fibers. Instead, the effective longitudinal modulus in Fig. 6 is largely dominated by the longitudinal modulus of CF. Also, some slight influence is observed for variations in the elastic modulus of the matrix phase.

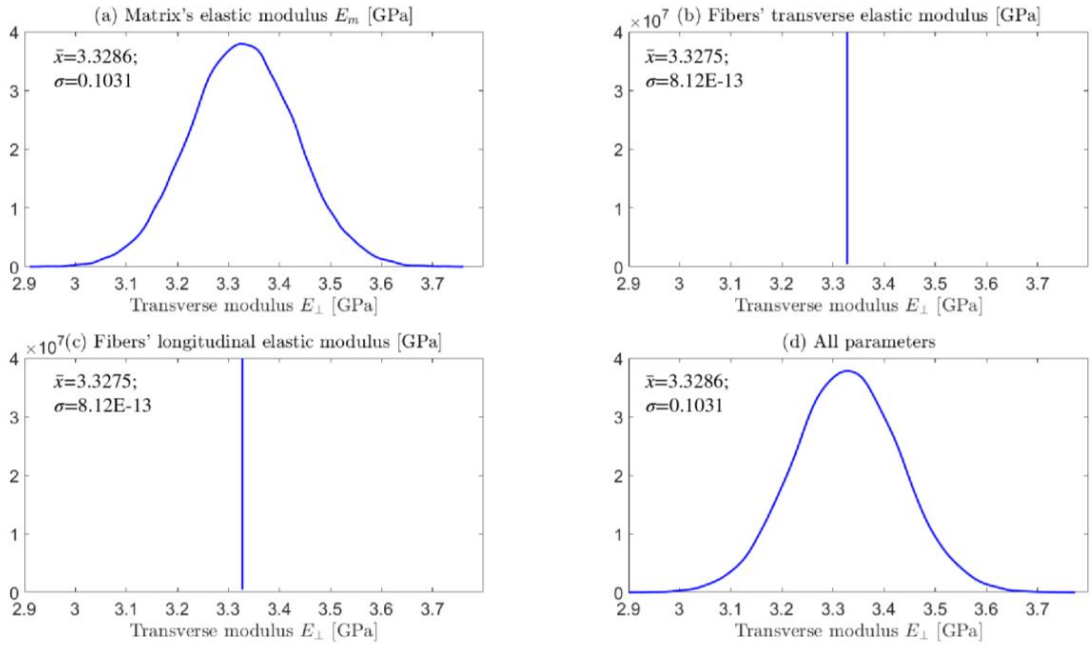

Figure 5. *Probability density functions of the transverse elastic moduli $E_\perp$ of epoxy doped with 30% CFs considering uncertainties in the matrix Young's modulus (a), in the fibers' elastic modulus (b), in the fibers' longitudinal modulus (c), and simultaneous uncertainties in all the parameters (d).*

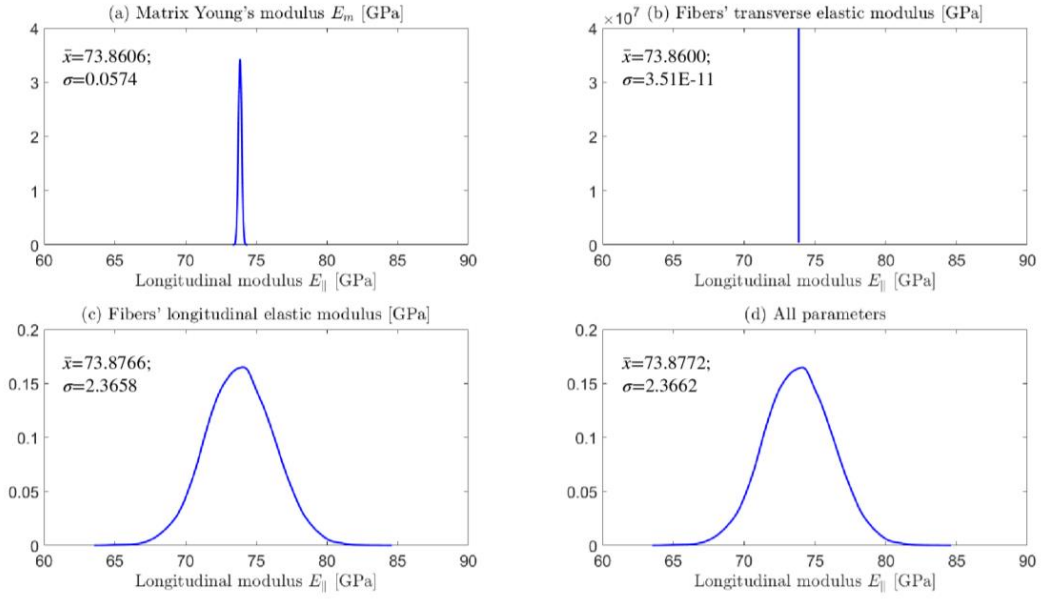

Figure 6. *Probability density functions of the longitudinal elastic moduli $E_\parallel$ of epoxy doped with 30% CFs considering uncertainties in the matrix Young's modulus (a), in the fibers' elastic modulus (b), in the fibers' longitudinal modulus (c), and simultaneous uncertainties in all the parameters (d).*

In order to highlight the potentials of the proposed surrogate model for advanced stochastic design of composite materials, Fig. 7 reports the estimated PDFs of the effective longitudinal and transverse elastic moduli of epoxy/CF composites versus the filler volume fraction. In this figure, dashed red lines indicate the 95% confidence level. Interestingly, it is noted that the uncertainty in the longitudinal elastic modulus raises as the filler volume fraction increases, while the uncertainty in the transverse modulus remains almost constant.

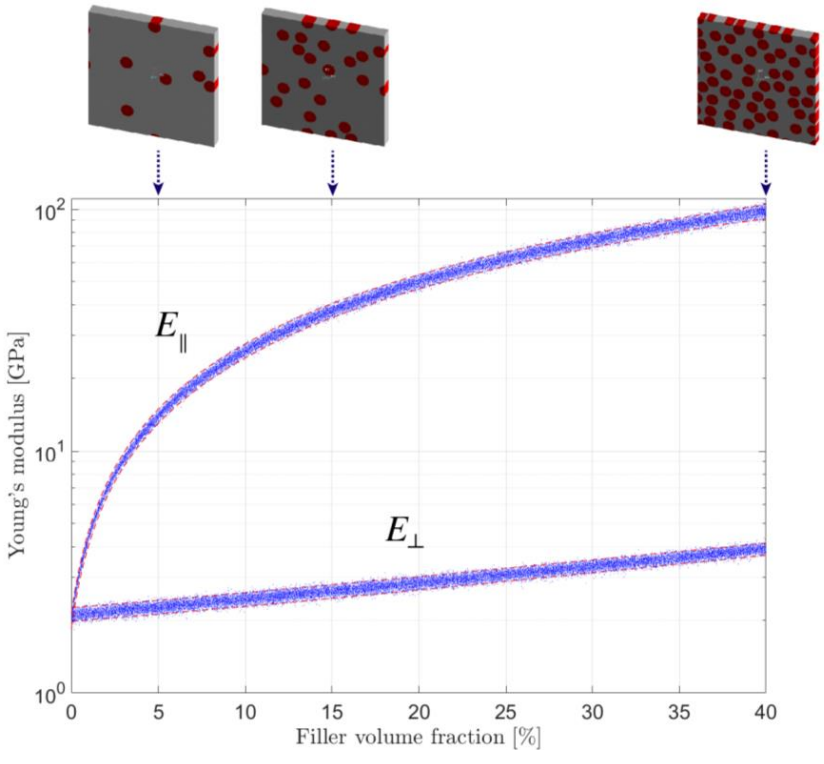

Figure 7. *Stochastic prediction of the elastic moduli of epoxy/CF composites versus the filler volume fraction.*

4. CONCLUSIONS

This paper has presented a computationally efficient surrogate model based upon adaptive sparse PCE to bypass the estimates from the numerical homogenization of epoxy composites doped with fully aligned CFs. The surrogate models have been trained by a DE made of direct evaluations of a FE homogenisation of 3D RVEs under periodic boundary conditions. The independency of the numerical results from the RVE's dimensions and its mesh discretization has been appraised by convergence analyses. Afterwards, statistical distributions of the micromechanical parameters of interest have been pre-defined, namely the elastic modulus of epoxy, the filler volume fraction, and the longitudinal and transverse elastic moduli of CF. Then, the design space has been uniformly sampled by LH and direct Monte Carlo evaluations of the numerical forward model have been used to conform a training and a validation dataset. This database has been used to train PCE meta-models of the effective and longitudinal elastic moduli of epoxy/CF composites, and their accuracy has been assessed in statistical terms by comparing their approximation of the validation dataset. Finally, the built surrogate models have been used to estimate the PDFs of the effective elastic moduli of epoxy/CF composites for a large variety of filler volume fractions. The computational burden involved in these analyses have proved almost negligible, being possible to implement the proposed approach for a variety of composite materials such as functionally graded materials or full-scale structural elements with heterogeneous filler dispersions. Furthermore, the proposed approach may also find important applications in other computationally intensive analyses such as stochastic optimization.

ACKNOWLEDGEMENTS

This work was supported by the Consejería de Economía, Conocimiento, Empresas y Universidades de la Junta de Andalucía (Spain) through the research project P18-RT-3128.

REFERENCES

[1] Oladele, I. O., Omotosho, T. F., & Adediran, A. A. (2020). Polymer-Based Composites: An Indispensable Material for Present and Future Applications. International Journal of Polymer Science, 2020.

[2] Composites Market Size – Share & Trends Analysis Report by Product (Carbon, Glass), by Resin (Thermosetting, Thermoplastics), by Manufacturing Process, by End Use, and Segment Forecasts, 2020-2027. Grand View Research, 2020.

[3] Klusemann, B., & Svendsen, B. J. T. M. (2010). Homogenization methods for multi-phase elastic composites: Comparisons and benchmarks. Technische Mechanik-European Journal of Engineering Mechanics, 30(4), 374-386.

[4] Guo, Q., Yao, W., Li, W., & Gupta, N. (2020). Constitutive models for the structural analysis of composite materials for the finite element analysis: A review of recent practices. Composite Structures, 113267.

[5] Reddy AC. Two dimensional (2D) RVE-Based Modeling of Interphase Separation and Particle Fracture in Graphite/5050 Particle Reinforced Composites. In: ; 2002: 179–183.

[6] Ahmadi Moghaddam H. A Stochastic Finite Element Analysis Framework for the Multiple Physical Modeling of Filler Modified Polymers. PhD thesis. University of Alberta, 2021.

[7] Berger, H., Kari, S., Gabbert, U., Rodríguez-Ramos, R., Bravo-Castillero, J., & Guinovart-Díaz, R. (2005). A comprehensive numerical homogenisation technique for calculating effective coefficients of uniaxial piezoelectric fibre composites. Materials Science and Engineering: A, 412(1-2), 53-60.

[8] McKay, M. D., Beckman, R. J., & Conover, W. J. (2000). A comparison of three methods for selecting values of input variables in the analysis of output from a computer code. Technometrics, 42(1), 55-61.

[9] Blatman, G., & Sudret, B. (2011). Adaptive sparse polynomial chaos expansion based on least angle regression. Journal of computational Physics, 230(6), 2345-2367.

[10] Gideon, S. (1978). Estimating the dimension of a model. The annals of statistics, 6(2), 461-464.

[11] Efron, B., Hastie, T., Johnstone, I., & Tibshirani, R. (2004). Least angle regression. The Annals of statistics, 32(2), 407-499.

[12] Hu, Z., & Karki, R. (2015). Prediction of mechanical properties of three-dimensional fabric composites reinforced by transversely isotropic carbon fibers. Journal of Composite Materials, 49(12), 1513-1524.

6th International Conference on Mechanical Models in Structural Engineering
CMMoST 2021
01-03 DIC 2021 Valladolid SPAIN

Dynamic response of a footbridge when used for a group of synchronized walkers

Cacho-Pérez M[1], Iglesias-Pordomingo A[2], Magdaleno A[3] , Lorenzana A[4]

ITAP, University of Valladolid, Paseo del Cauce 59, 47011 Valladolid, Spain

ABSTRACT

This work studies the dynamic response of a stress-ribbon pedestrian footbridge in service. A simple model is proposed, consisting of an inclined elastic 2D cable. The objective is to have a dynamic structural model to check pedestrian traffic, for instance, or the model established by the Eurocode to limit the state of vibrations or other disturbances.

Experimental acceleration records are available at a number of footbridge locations and information is analysed to extract the modal parameters used by the numerical model in dynamic simulations.

Keywords: dynamic load models, serviceability, dynamic simulations, vibrations, modal parameters

1 INTRODUCTION

A stress ribbon is a structure in which the structural elements (cables or plates) work in traction. This structural element is located in the platform below the deck where pedestrians walk. The structure adapts its geometry to the undergoing oads so the deformation describes as a catenary between the supports.

Although the tensile stresses add rigidity to the structure, the bridge is slender and tends to vibrate, leading to an interesting modal and dynamic study, as sometimes the service conditions are compromised.

The Pedro Gómez Bosque footbridge in Valladolid is a stress ribbon structure with a span of length $L = 85\,m$. The model once updated is compared with the available experimental data, and is applied to the traffic of a group of pedestrians.

The stress ribbon structural typology was first introduced by the German engineer U. Finsterwalder in the 1960s[1, 2, 3, 4, 5]. L. Viera designed the first road infrastructure in 1963, resulting in the La Barra bridge, a three-span stress ribbon ($30+90+30$) in Uruguay. After that, several footbridges were erected in Europe (Karlstreg and Lignon-Loex in Swizerland in 1971, Rosenstein in Germany in 1977, etc.) and Japan (Osaka in 1969, Hayahinomine in 1977, etc.). J. Strasky popularized this typology with multiple works in the Czech Republic in the 1980s. Footbridges supported by cables [6, 7, 8] exceed $100\,m$ in length, but it is the one designed by J. Manterola in 2011, studied in this work, which holds the record for the distance between supports. The cross section of the structural steel plate is $3.6\,m$ wide and $30\,mm$ thick. A number of 110 precast concrete slabs $5.2\,m$ long, $0.75\,m$ wide and $120\,mm$ thick, are situated on the steel band. The structure is completed with rubber flooring and stainless steel and glass

[1]cacho@eii.uva.es (Corresponding author)
[2]alvaro.iglesias@uva.es
[3]alvaro.magdaleno@uva.es
[4]ali@eii.uva.es

handrails. The initial tension on the steel band was adjusted so that the design displacement was limited to $L/50$.

The objective of this work is to present a suitable dynamic model through Matlab/Simulink for this structure and verify its applicability in predicting the dynamic response.

The article has been organized as follows: after this brief introduction the methodology is presented, then the numerical results obtained are included, and finally the main conclusions and contributions of the work are summarized.

Figure 1: Pedro Gómez Bosque Stress-ribbon footbridge under study

2 EXPERIMENTAL RESULTS

This section summarizes the design of the tests carried out on the Pedro Gómez Bosque footbridge: the configuration is common to all tests in terms of the position of the accelerometers. The only important changes that were made between configurations correspond to the positions of the shaker, which can be found in any of its positions $Pi\,(i = 1, \ldots, 4)$, see table 2. All channels have a second order Butterworth low-pass filter with a cutoff frequency of $1000\,Hz$ applied at all times.

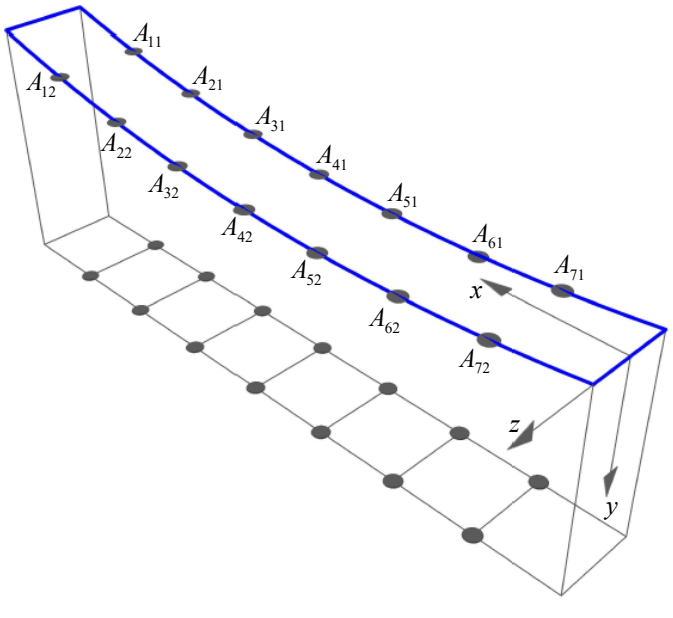

Figure 2: Location of accelerometers

The shaker solicitation consists of a continuous sweep between 0.3 and $2.6\,Hz$ for $300\,s$ and an amplitude of $4\,V$ for the linear motor and a total duration of approximately 10 minutes.

The records have been exported to plain text, for easier processing. The way in which these files are structured is described as follows: in all the files, in addition to the time vector (t, in seconds), all the channels of that test are stored. Accelerometer channels are indicated by the name of the accelerometer (A11, ..., A72, Shaker). The details of their location are indicated in figure 2. A sampling rate of $4000\,S/s$ is considered. Accelerometers are vertically oriented. The accelerometer signals are in (m/s^2) and the force exerted by the shaker on the structure in (N), so they are accelerations with units $1/kg$ (for calculation purposes, the shaker is considered to have $40\,kg$ of moving mass).

The footbridge is $85\,m$ long and has a width (z axis) of $5.2\,m$. The "downstream" side of the structure is considered $z = -2.6\,m$. Accelerometers A11, A21, A31, A41, A51, A61 and A71 are downstream. The coordinate $z = 2.6\,m$ is the "upstream" side and the accelerometers A12, A22, A32, A42, A52, A62 and A72 are arranged, paired with the downstream ones. The position of each accelerometer is indicated in figure 2 and summarized in tables 2 and 1.

Accelerometer	x (m)	z (m)	Accelerometer	x (m)	z (m)
A11	74.4	-2.6	A12	74.4	2.6
A21	63.8	-2.6	A22	63.8	2.6
A31	53.1	-2.6	A32	53.1	2.6
A41	42.5	-2.6	A42	42.5	2.6
A51	31.9	-2.6	A52	31.9	2.6
A61	21.3	-2.6	A62	21.3	2.6
A71	10.6	-2.6	A72	10.6	2.6

Table 1: Position of accelerometers

Pi	x (m)	z (m)	accelerometer
P1	74.4 m	-2.6 m	A11
P2	63.8 m	-2.6 m	A21
P3	53.1 m	-2.6 m	A31
P4	42.51 m	-2.6 m	A41

Table 2: Shaker positions

From the acceleration records of the fourteen available accelerometers, the dynamic system is identified in the state space using the Subspace Stochastic Identification (SSI) [13] technique, which allows the proper frequencies and damping factors to be estimated, as well as the vertical/transverse vibration modes associated with each frequency, see figure 3.

The acceleration record at position A1 due to the transit of six synchronized pedestrians at a rate frequency of $f_s = 2.0\,Hz$ is included in figure 4. The maximum acceleration is ($a_{max} = 0.335\,m/s^2$) and the RMS value ($RMS = 0.0788\,m/s^2$).

The torsion effect has been eliminated by combining the response of the accelerometers in pairs, for example, $A1 = (A11 + A12)/2$, and the acceleration register is indicated in figure 4.

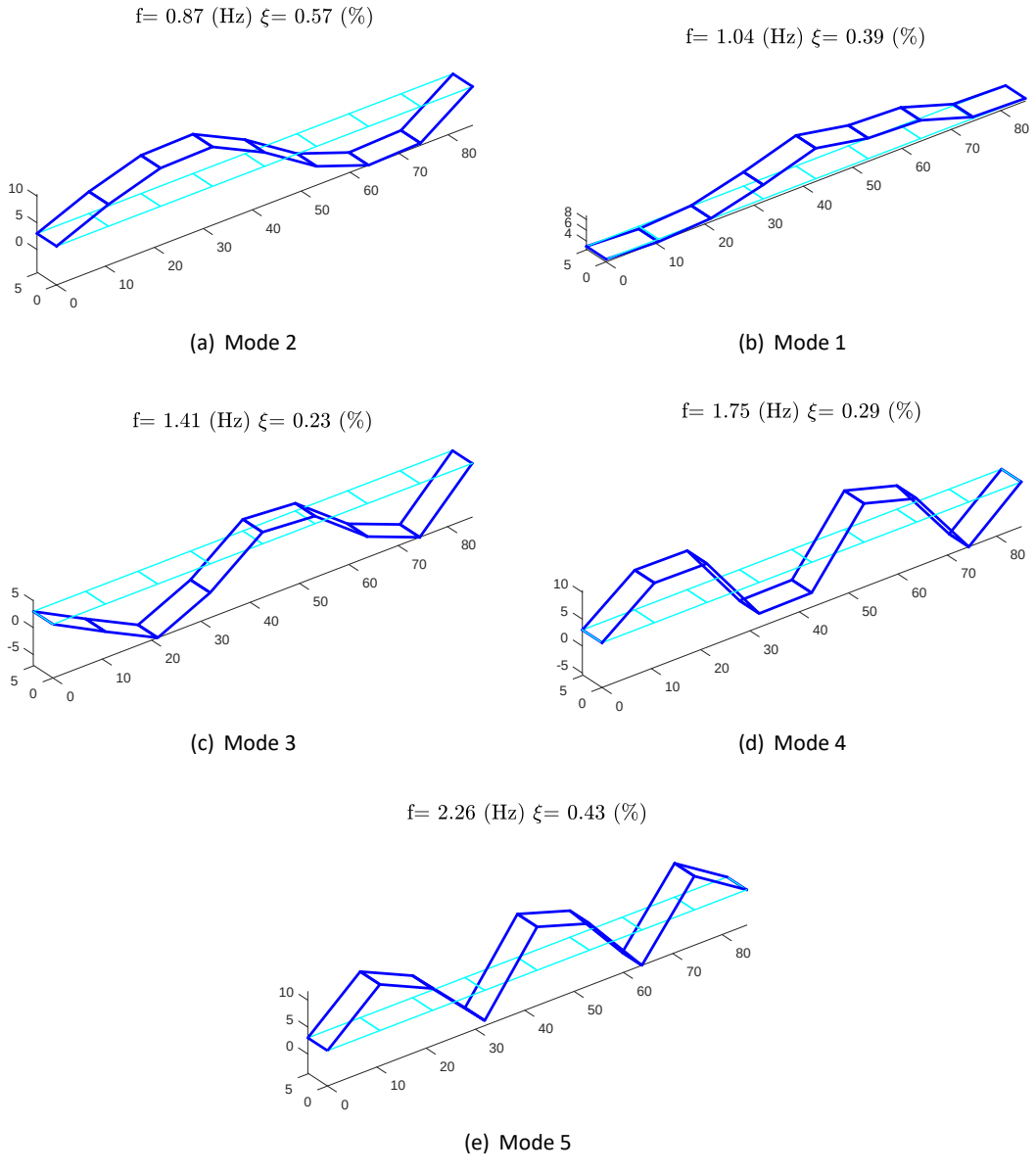

(a) Mode 2

(b) Mode 1

(c) Mode 3

(d) Mode 4

(e) Mode 5

Figure 3: Vertical vibration modes shapes. Experimental

3 METHODOLOGY

This section summarizes: first, the static, modal analysis and dynamic of the inclined elastic cable; and second, the mechanical model of a pedestrian group that transits the footbridge.

3.1 Static

The simplified static analysis proposed assumes a cable of area A and modulus of elasticity E that works as a flexible element which can only withstand normal stresses. Static deformation in hypotheses of small displacements will approximately coincide with a parabola curve, and will depend on the applied load (q) and the value of the horizontal force (H), see figure 5.

$$y_0(x) = \frac{q}{2H}x(L-x) - \frac{h}{L}x \tag{1}$$

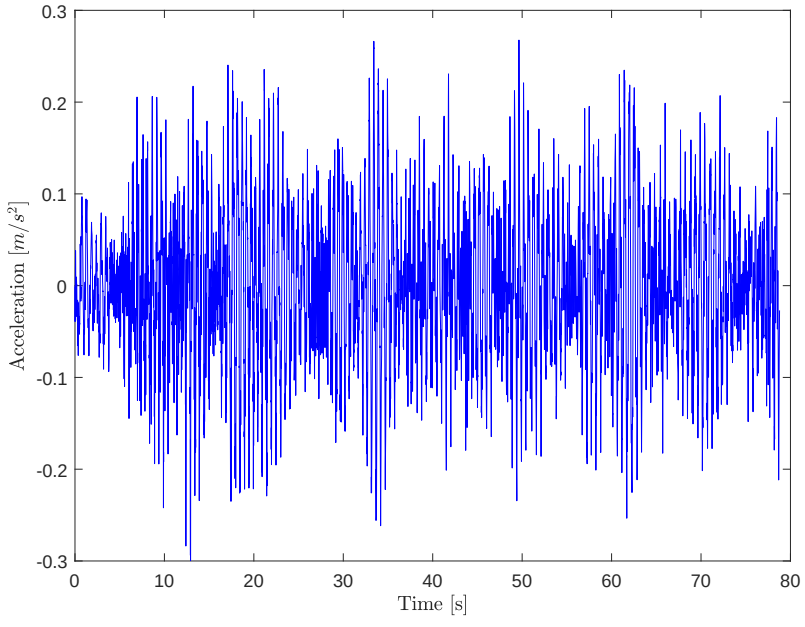

Figure 4: Accelerations register at A1. Synchronized N pedestrian group traffic (experimental)

where $y_0(x)$ is the parabola of the cable funicular curve, q is the distributed load per unit of horizontal length, H is the horizontal force, L is the length of the cable (distance between supports) and h is the unevenness between supports. The maximum descent of the cable is a design parameter, called sag, that is obtained from the parameters (q, H) by the expression:

$$f = y_0(x_{max}) = \frac{qL^2}{8H}; \quad x_{max} = \frac{L}{2} - \left(\frac{h}{L}\right)\left(\frac{H}{q}\right) \tag{2}$$

f being the sag value.

3.2 Modal analysis

The Raileigh-Ritz method[3] is used for the modal analysis of the structure. Mathematical functions that meet the boundary conditions are assumed as vibration mode shapes:

$$\phi_j(x) = \text{sin}\left(\frac{j\pi x}{L}\right) \tag{3}$$

where $\phi_j(x)$ is the vibration mode shape j.

$mode$	$f_j\,(Hz)$	ξ_j (%)
2	0.87	0.57
1	1.04	0.39
3	1.41	0.23
4	1.75	0.29
4	2.26	0.43

Table 3: Natural frequencies and modal damping factors

It is immediate to calculate the generalized masses associated with the vibration mode shapes:

$$M_j = \int^L \mu\phi_j(x)\phi_j(x)dx = \frac{\mu L}{2}; \; j = 1, \ldots, m \tag{4}$$

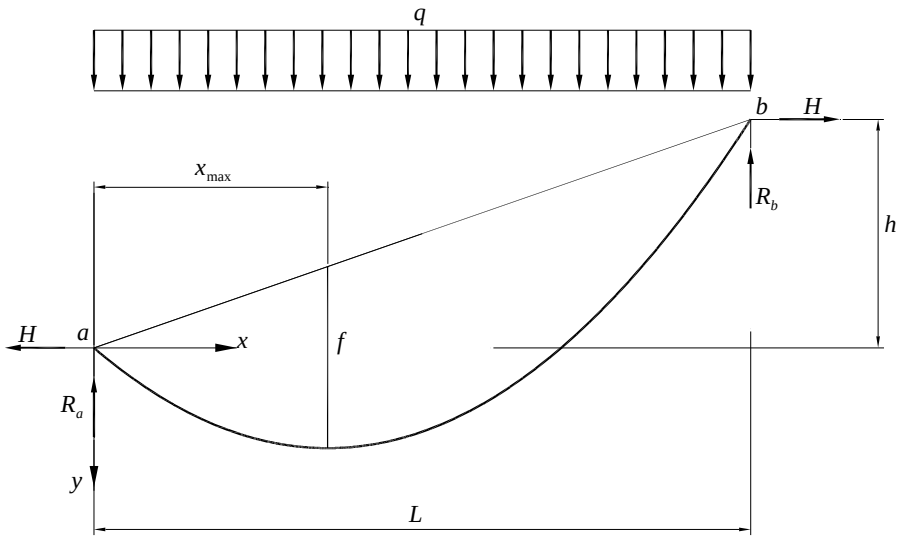

Figure 5: Static deformation

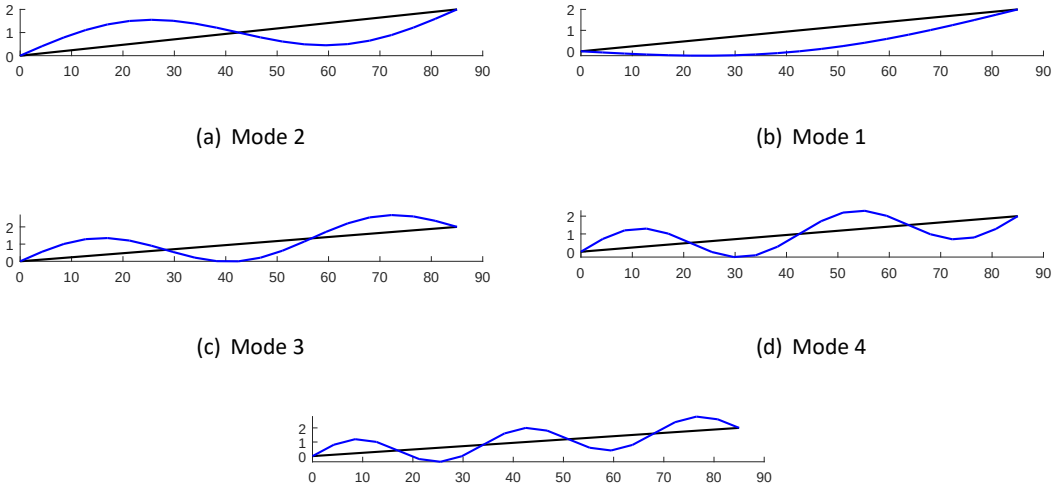

(a) Mode 2

(b) Mode 1

(c) Mode 3

(d) Mode 4

(e) Mode 5

Figure 6: Vertical vibration mode shapes

And calculate the modal mass and modal stiffness matrix:

$$\boldsymbol{M} = \begin{bmatrix} M_1 & & \\ & \ddots & \\ & & M_m \end{bmatrix}; \ \boldsymbol{K_T} = \begin{bmatrix} K_1 & & \\ & \ddots & \\ & & K_m \end{bmatrix}; \ K_j = \omega_j^2 M_j \ (j = 1, \ldots, m) \tag{5}$$

3.3 Dynamic analysis

A dynamic equation is obtained from cable analysis in deformed configuration, taking the static deformed ($y_0(x)$) as reference. It is convenient to formulate the problem in the state space. First, the damping matrix is established:

$$\boldsymbol{C} = \begin{bmatrix} C_1 & & \\ & \ddots & \\ & & C_m \end{bmatrix};\ C_j = 2\xi_j\omega_j M_j\ (j = 1, \ldots, m) \tag{6}$$

where $\boldsymbol{C}$ is the modal damping matrix of the system and ξ_j is the modal damping factor associated with the vibration mode j.

Once the damping matrix is known, the dynamic system in the space-time domain is defined:

$$\begin{aligned} \dot{\boldsymbol{x}} &= \boldsymbol{A_c} \cdot \boldsymbol{x} + \boldsymbol{B_c} \cdot \boldsymbol{u} \\ \dot{\boldsymbol{y}} &= \boldsymbol{C_c} \cdot \boldsymbol{x} + \boldsymbol{D_c} \cdot \boldsymbol{u} \end{aligned} \tag{7}$$

where $\boldsymbol{x}$ is the state vector, $\boldsymbol{y}$ is the output vector of the system, $\boldsymbol{u}$ is the input vector, $\boldsymbol{A_c}$ is the system matrix, $\boldsymbol{B_c}$ is the input matrix, $\boldsymbol{C_c}$ is the output matrix, and $\boldsymbol{D_c}$ the direct transmission matrix. They are related to the matrices of the previous section through the expressions:

$$\begin{aligned} &\boldsymbol{x} = \begin{bmatrix} \boldsymbol{q} \\ \dot{\boldsymbol{q}} \end{bmatrix};\ \boldsymbol{y} = \ddot{\boldsymbol{q}} \\ &\boldsymbol{A_c} = \begin{bmatrix} \boldsymbol{0} & \boldsymbol{I} \\ -\boldsymbol{M^{-1}} \cdot \boldsymbol{K_T} & -\boldsymbol{M^{-1}} \cdot \boldsymbol{C} \end{bmatrix};\quad \boldsymbol{B_c} = \begin{bmatrix} \boldsymbol{0} \\ \boldsymbol{M^{-1}} \end{bmatrix} \\ &\boldsymbol{C_c} = \begin{bmatrix} -\boldsymbol{M^{-1}} \cdot \boldsymbol{K_T} & -\boldsymbol{M^{-1}} \cdot \boldsymbol{C} \end{bmatrix} \qquad \boldsymbol{D_c} = \begin{bmatrix} \boldsymbol{M^{-1}} \end{bmatrix} \end{aligned} \tag{8}$$

where $\boldsymbol{q}$ is the generalized coordinates of the system.

The vertical vibrations of the structure with respect to the static deformation are obtained by modal superposition, the accelerations are:

$$\ddot{y}_i(x_i, t) = \sum_{j=1}^{m} \phi_j(x_i)\ddot{q}_j(t);\ i = 1, \ldots, n \tag{9}$$

where $\ddot{y}_i(x_i, t)$ is the vertical acceleration at x_i, with x_i being the longitudinal coordinate of node i and n the total number of nodes, all of them equally spaced.

3.4 Pedestrian group

A pedestrian is simulated as a bipedal walking model with two DOFs, as shown in figure 7. The human body is modeled as a lumped mass m_h at the center of mass (COM) and the two legs are described as two massless, linear springs of equal rest length L_0 with stiffness k_{leg} and damping c_{leg}[9, 10, 11, 12]. The pedestrian is assumed to remain in contact with the structure surface at all times.

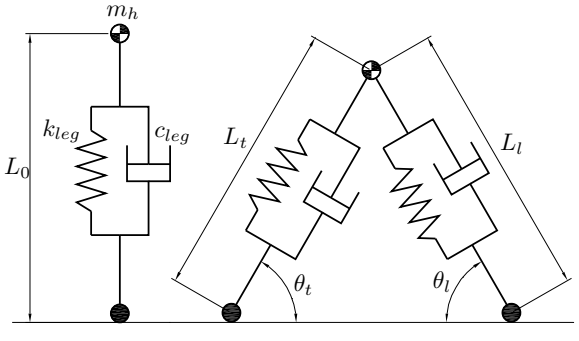

Figure 7: Simple human model

The motion of the COM is described by the generalized coordinate (z, u), where z and u denote the vertical and horizontal displacements of the COM. L_l and L_t are the length of two legs, the subscripts

"l" and "t" indicate the leading and trailing legs, respectively. The dynamic equation of the pedestrian system in matrix form is as in (10).

$$\boldsymbol{M}\ddot{\boldsymbol{U}} + \boldsymbol{C}\dot{\boldsymbol{U}} + \boldsymbol{K}\boldsymbol{U} = \boldsymbol{F}(t) \tag{10}$$

where $\boldsymbol{M}$, $\boldsymbol{C}$, $\boldsymbol{K}$, $\boldsymbol{U}$, $\dot{\boldsymbol{U}}$, $\ddot{\boldsymbol{U}}$ and $\boldsymbol{F}(t)$ are the mass, damping and stiffness matrices, the displacement, velocity, acceleration and force vectors, respectively. For the present case, the mass, damping, stiffness matrices, and the force vector, which can be expressed as

$$\begin{aligned}
\boldsymbol{M} &= \begin{bmatrix} m_h & 0 \\ 0 & m_h \end{bmatrix} \\
\boldsymbol{C} &= \begin{bmatrix} c_{t,v} + c_{l,v} & 0 \\ 0 & c_{t,h} + c_{l,h} \end{bmatrix} \\
\boldsymbol{K} &= \begin{bmatrix} k_{t,v} + k_{l,v} & 0 \\ 0 & k_{t,h} + k_{l,h} \end{bmatrix} \\
\boldsymbol{F}(t) &= \begin{bmatrix} -m_h g & F_{ctrl}(t) \end{bmatrix}^T \\
\boldsymbol{U} &= \begin{bmatrix} z & u \end{bmatrix}^T
\end{aligned} \tag{11}$$

in which

$$\begin{aligned}
c_{l,v} &= \tfrac{\alpha c_{leg} v_l \sin(\theta_l)}{\dot{z}}; & k_{l,v} &= k_{leg}\left(1 - \tfrac{L_0}{L_l}\right)\left(1 - \tfrac{y_l}{z}\right) \\
c_{t,v} &= \tfrac{(1-\alpha) c_{leg} v_t \sin(\theta_t)}{\dot{z}}; & k_{t,v} &= k_{leg}\left(1 - \tfrac{L_0}{L_t}\right)\left(1 - \tfrac{y_t}{z}\right) \\
c_{l,h} &= \tfrac{\alpha c_{leg} v_l \cos(\theta_l)}{\dot{u}}; & k_{l,h} &= k_{leg}\left(1 - \tfrac{L_0}{L_l}\right)\left(1 - \tfrac{x_l}{u}\right) \\
c_{t,h} &= \tfrac{(1-\alpha) c_{leg} v_t \cos(\theta_t)}{\dot{u}}; & k_{t,h} &= k_{leg}\left(1 - \tfrac{L_0}{L_t}\right)\left(1 - \tfrac{x_t}{u}\right)
\end{aligned} \tag{12}$$

where

$$\begin{aligned}
v_l &= (\dot{z} - \dot{y}_l)\sin\theta_l - \dot{u}\cos\theta_l \\
v_t &= (\dot{z} - \dot{y}_t)\sin\theta_t + \dot{u}\cos\theta_t \\
\alpha(t) &= \tfrac{L_t(t) - L_t(0)}{L_0 - L_t(0)}
\end{aligned} \tag{13}$$

and y_l, y_t are the vertical and x_l, x_t the horizontal coordinates of both legs. The term $F_{ctrl}(t)$ is the horizontal force to be applied to keep the pedestrian moving (see equation 11).

4 NUMERICAL RESULTS AND DISCUSSION

In this section, the methodology explained above is followed and the following values are taken: $L = 85\,m$, the distance between supports; $h = 2\,m$, unevenness between supports; $g = 9.81\,m/s^2$, the acceleration due to gravity; $E = 2.1 \cdot 10^5\,MPa$, Young's Module; $a = 3.6\,m$, the width of the steel plate; $b = 0.03\,m$, the thickness of the plate; $A = a \cdot b\,m^2$, the cross section area of the plate; and $\mu = 2.4\,t/m$, the linear density of the pedestrian footbridge.

The dynamic analysis is carried out by modal superposition. Information obtained from the experimental records, natural frequency values and modal damping factors are used, as indicated in table 3.

The dynamic model is formulated in the state space by means of the equations (8). The first five vertical vibration modes ($m = 5$) are considered in the analysis.

4.1 Synchronized N pedestrian group traffic

The dynamic simulations can now be carried out, a total of six synchronized pedestrians ($N = 6$) walk along the footbridge at a pace of $f_s = 2\,Hz$. The following data is taken into account for the pedestrian group: $mh = 80 \cdot N$, is the mass; $k_{leg} = 20000 \cdot N$, the stiffness of each leg; and $c_leg = 2\xi_h\sqrt{(m_h k_{leg})}$. A maximum acceleration value of $a_{max} = 0.303\,m/s^2$ and $RMS = 0.0840\,m/s^2$ acceleration level are obtained. This means that, for a larger group, eleven synchronized pedestrians, accelerations would exceed the comfort acceleration limits established by the Eurocode.

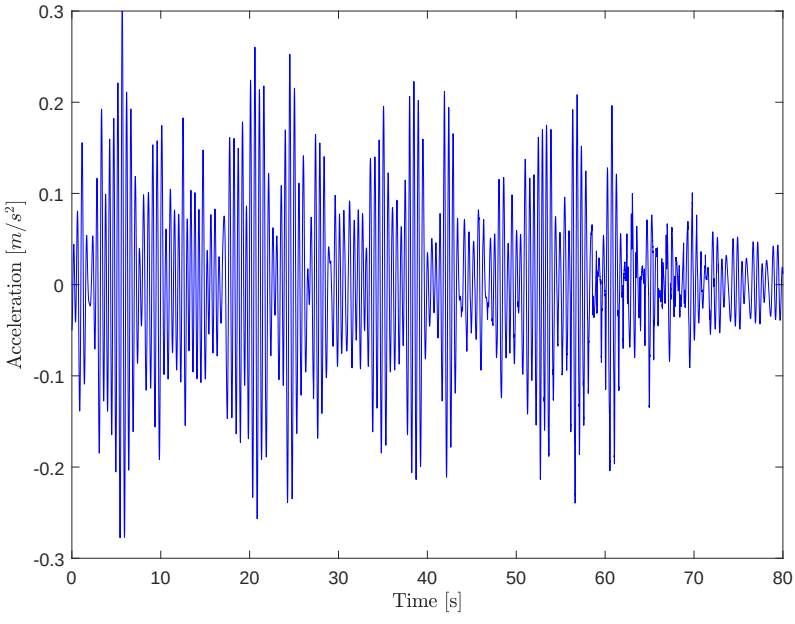

Figure 8: Accelerations register at A11. Synchronized N pedestrian group traffic (simulated)

4.2 Dynamic Load Model

The dynamic load model (**DLM2**), established by European regulations (Eurocode 1), is proposed. A dynamic analysis of the pedestrian footbridge is performed for a vertical sinusoidal load corresponding to a group of $8-15$ people. It considers an additional mass of $800\,kg$, see Annex A. The load application point is changing and the maximum acceleration level is calculated[14]. The force frequency (f_v) is taken as the natural frequency of the structure, close to $2\,Hz$, whose value is $f_v = 1.75\,Hz$, see table 3 and figure 3.

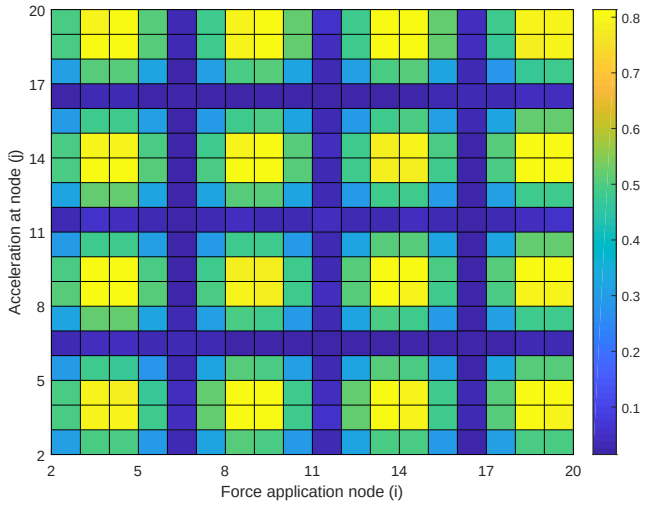

Figure 9: Dynamic Load Model (DLM2)

Figure 9 shows the maximum acceleration level at each node j (axis of ordinates) when the load acts on node i (axis of abscissa).

A maximum acceleration level of value $a_{max} = 0.8136\, m/s^2 > 0.50\sqrt{f_v}$ is obtained. This value exceeds the comfort limits established by Eurocode 1, since these are quite demanding, where $f_v = 1.75\, Hz$ is the fourth fundamental frequency of the footbridge.

5 CONCLUSIONS

Experimental acceleration records of a footbridge excited by a shaker allow us to carry out an EMA (Experimental Modal Analysis) and obtain the natural frequencies and modal damping factors. Acceleration registers due to the traffic of a group of six synchronized pedestrians at $f_s = 2\, Hz$ are compared with acceleration results of dynamic simulations proposed in this work.

Dynamic simulations use a simple mechanical model that reproduces the synchronized pedestrian group march. Structure accelerations by a group of six synchronized pedestrians are compared with experimental records. This shows that the results fit fairly well those recorded on the A11-A12 accelerometers. Maximum and minimum values and vibration level, based on RMS, are calculated.

The dynamic load model DLM2, established by the Eurocode, are also carried out. Several dynamic analyses are carried out where the node application of the dynamic load is varied. Accelerations are calculated in all the nodes of the spatial discretization. It is relatively easy to exceed the Eurocode acceleration limit levels. These limits, set by this regulation for the comfort criterion, are very demanding, as has been verified.

Finally, the dynamic analysis with a pedestrian bipedal model fits the experimental results fairly well. Therefore, an important application of the present work is excitation generated by a pedestrian mechanical model could be used for experimental modal analysis of other structures, with no need for a shaker.

ACKNOWLEDGEMENTS

The authors wishe to acknowledge the Ministerio de Economía y Competitividad of the Spanish Government, for the partial support through the RTI2018-098425 Research Project.

References

[1] H. Bachmann, Vibration Problems in Structures, Practical Guidelines, Birkhäuser: Basel, Boston, Berlin, 1997.

[2] V. Kulbach, Cable structures. Design and static analysis, Tallin: Estonian Academy Publishers, 2007.

[3] L. Meirovich, Dynamics and Control of Structures, Wiley: New York, 1990.

[4] J. Strasky, Stress Ribbon and Cable-Supported Pedestrian Bridges, Thomas Telford Ltd, London, 2006.

[5] L. Troyano, Bridge engineering. A global perspective, London: Tomas Telford Ltd, 2003.

[6] E. Caetano, A. Cunha, Experimental and numerical assessment of the dynamic behaviour of a stress-ribbon footbridge, Struct Concr 5(1) (2004) 29–38.

[7] W. Hu, E. Caetano, A. Cunha, Structural health monitoring of a stress-ribbon footbridge, Engineering Structures 57 (2013) 578–593.

[8] C. Moutinho, A. Cunha, E. Caetano, Analysis and control of vibrations in a stress-ribbon footbridge, Structural Control & Health Monitoring 18(6) (2011) 619–634.

[9] B. Whittington, D. Thelen, A simple mass-spring model with roller feet can induce the ground reactions obser ved in human walking, Journal of Biomechanical Engineering 131 (2009).

[10] M. Cacho-Pérez, A. Lorenzana, Walking model to simulate interaction effects between pedestrians and lively structures, Journal of Engineering Mechanics 143 (9) (2017).

[11] J. Qin, S. Law, Q. Yang, N. Yang, Pedestrian-bridge dynamic interaction, including human participation, Journal of Sound and Vibrationan 332 (2013) 1107–1124.

[12] S. Kim, S. Park, Leg stiffness increases with speed to modulate gait frequency and propulsion energy, Journal of Biomechanics 44 (2011) 1253–1258.

[13] P. Overschee, B. Moor, Subspace Identification for Linear Systems: Theory - Implementation - Applications, Kluwer Academic Publishers, 1996.

[14] EN 1991-2:2019 Eurocode 1: Actions on structures - Part 2: Traffic loads on bridges.

[15] B. Cleve, Numerical Computing with MATLAB, Society for Industrial and Applied Mathematics, 2004.

[16] A. Gilat, MATLAB: An Introduction With Applications, John Willey & Sons, Inc., 2005.

[17] M. Maciel, Introducción a la Optimización Numérica, Ph.D in Mathematical Sciences, Rice University, Houston, Texas, 2000.

[18] J. Nocedal, S. Wright, Numerical Optimization, Springer Series in Operations Research, 1999.

ANNEX A. EUROCODE

The application of the theory of pedestrian dynamic loading can be found in the international codes and regulations. In Eurocode 1, Part 1 “live loads on bridges”, a dynamic design load model is included that allows for svnchronization effects.

Load Model for a Pedestrian Group

Dynamic load model (**DLM2**) describes the effect of a group with a limited number of unsorted walking persons (8-15 persons). The synchronization of step frequencies and phases is taken into account by coefficient k_v.

$$Q_{gv} = 280 \cdot k_v(f_v) \cdot sin(2\pi \cdot f_v \cdot t) \tag{14}$$

where k_v is the synchronization factor.

The dynamic load of a pedestrian group should be applied as a stationary pulsating force with two components that should be considered separately. In the same way, the load should be applied on the most unfavourable position on the bridge. To allow for the influence of the pedestrian on the dynamic properties of the bridge (natural frequencies), a mass of 800 kg should be applied at the same position as the force.

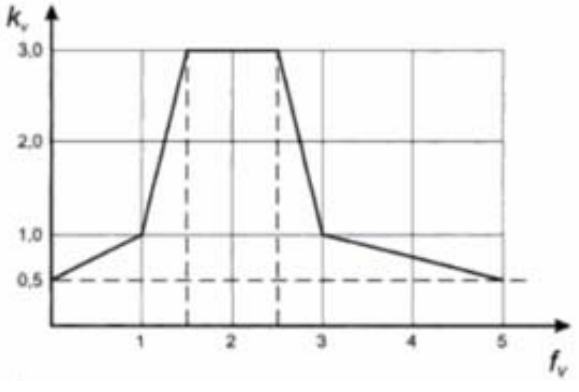

Figure 10: Dependence of k_v on natural frequency f_v

The coefficient k_v is introduced to account for random synchronized pedestrians within the group. Only the first harmonics are considered (vertical load factor 0.4) at the moment, but discussion is continuing on adding the second harmonics (vertical load factor 0.2).

Comfort Criteria and Limit Values

The human perception of vibrations is subjective and depends on individual characteristics and psychological influences. The perception is influenced by the physical factors vibration frequency, acceleration and the time period of exposure. The discomfort depends greatly on the environmental conditions and the attitude towards the vibration caused. Comfort requirements are either handled by providing natural frequency ranges to be avoided or by providing limit accelerations. Limit value for accelerations according to International Standards (Eurocode 1) is:

$$a_{V,max} = min(0.50\sqrt{f_v}, 0.70) \tag{15}$$

Composite bridge deck optimization with trajectory-based algorithms

David Martínez-Muñoz[1]; Antonio J. Sánchez-Garrido[2]; José Vicente Martí[1]; Víctor Yepes[1]

ABSTRACT

Bridge optimization can be difficult due to the large number of variables involved in the problem. In this work, the optimization of a steel-concrete composite box girder bridge has been performed considering cost as objective function. To achieve this objective, Simulated Annealing (SA) has been applied as an example of trajectory-based algorithm for the optimization of the structure. It is observed that the addition of cells to the bridge cross sections improves not only the section behavior but also the optimization results. Finally, it is observed that the proposed double composite-action design materializing slabs on the bottom flange on supports, allows eliminating the continuous longitudinal stiffeners. This method automatizes the optimization process of an initial design of a composite bridge, which has traditionally been based on the technician's own experience, allowing to reach results in a more efficient way.

Keywords: Optimization, Structures, Composite bridges, Metaheuristics, Trajectory-based algorithms.

1. INTRODUCCIÓN

Cualquier resolución de un problema se traduce en la búsqueda de una solución que permita satisfacer las necesidades planteadas con la mínima inversión de recursos posible. Además, la propuesta de solución debe contemplar y cumplir con todas las restricciones impuestas, tanto por la propia naturaleza del problema como por cualquier otro tipo de condicionantes externos. En el caso de los problemas estructurales, las necesidades del problema son diversas y las restricciones impuestas tienen relación con la resistencia de las secciones y la compatibilización de las deformaciones con el uso que se le vaya a dar al elemento objeto de diseño. A la solución propuesta, se le exige que utilice la menor cantidad de recursos posible, generalmente en términos de coste. Por tanto, un problema estructural es básicamente un problema de optimización, en el que se busca una solución que cumpla unas restricciones minimizando, en este caso, los costes de la solución. Para llegar a esta solución óptima, los técnicos realizan un proceso iterativo en el que se plantean soluciones, se comprueba si cumplen las restricciones y se comparan los costes de unas y otras. La generación de nuevas soluciones se realizan mediante una ligera modificación de las variables del elemento estructural. Como es de esperar, cuanto mayor es la experiencia del técnico, más rápido se

[1] *Instituto de Ciencia y Tecnología del Hormigón (ICITECH). Universitat Politècnica de València (ESPAÑA). damarmu1@cam.upv.es (D. Martínez-Muñoz, corresponding author); jvmartia@cst.upv.es (J.V. Martí); vyepesp@cst.upv.es (V. Yepes).*

[2] *Departamento de Ingeniería de la Construcción y Proyectos de Ingeniería Civil. Universitat Politècnica de València (SPAIN). ajsangar@doctor.upv.es (A.J. Sánchez-Garrido).*

llega a una solución óptima, ya que, normalmente, estos problemas tienen un gran número de variables haciéndolos destacar por su complejidad [1].

La tendencia actual en el campo de investigación de la optimización estructural trata de romper con esa dependencia entre la calidad de la solución y la experiencia del técnico aprovechando la capacidad computacional de los equipos informáticos. Debido a la complejidad de los problemas de optimización estructural, la exploración de todo el espacio de soluciones es imposible y por tanto, se recurre a técnicas heurísticas y metaheurísticas que, si bien no aseguran encontrar la mejor solución, han demostrado obtener buenos resultados [2, 3]. Estos métodos se han aplicado en diversos tipos de estructuras de hormigón como muros de contrafuertes [4, 5, 6], vigas de edificación [1], puentes [7, 8, 9] o incluso a la predicción de longitud de transferencia en cordones de pretensado [10]. Sin embargo, la aplicación de estos métodos a estructuras mixtas no se ha realizado de manera tan extensa tal como se indica en una revisión reciente [11]. En este estudio, además, se hace hincapié en la falta de estudio en temas como en análisis de ciclo de vida de puentes mixtos [12], tal y como se ha hecho, de manera extensa, con los puentes de hormigón [13]. esto hace destacar al campo de las estructuras mixtas como un campo con posibilidades de explotación.

La complejidad de las estructuras mixtas, en especial los puentes mixtos, puede llegar a superar a la de las estructuras de hormigón debido al gran número de variables que definen la geometría las mismas. Además, la disposición de los elementos de la sección transversal es más sensible a los esfuerzos predominantes del tablero, planteando tres geometrías básicas de las secciones transversales: cajón, vigas en I y losa mixta [14]. Este condicionante adicional, abre un gran abanico de posibilidades de cara a la aplicación de técnicas heurísticas a este tipo de estructuras, cuyo comportamiento y resultados a los problemas de optimización no son triviales. La investigación actual en este campo ha aplicado técnicas como el solver de Excel [15] o la función fmincom de Matlab® [16] para la resolución de problemas simplificados. Existen estudios aislados en los que se aplican técnicas metaheurísticas en pasarelas [17]. Para problemas más complejos la mayoría de los algoritmos aplicados a este tipo de problemas han sido de enjambre [18, 19], observándose una falta de estudio del comportamiento de los algoritmos basados en trayectorias aplicados a este tipo de estructuras.

En este artículo se plantea el problema de optimización del tablero de un puente mixto en cajón tomando como función objetivo el coste. Para llevar a cabo este problema se utiliza un algoritmo metaheurístico como es el Simulated Annealing (SA) o Recocido Simulado. Esta metaheurística se enmarca dentro de los algoritmos basados en trayectorias que realizan la búsqueda del óptimo mediante la variación de la solución inicial a soluciones próximas a esta, la descripción de la heurística se realiza en la sección 2.3. El objetivo de este trabajo es la obtención de un diseño óptimo con el fin de compararlo con otros trabajos de investigación y diseños tradicionales y añadir conocimiento al campo de la optimización de estructuras mixtas, centrándose el estudio, tanto en los aspectos de diseño, como en el comportamiento del algoritmo en este tipo de problemas.

2. DEFINICIÓN DEL PROBLEMA DE OPTIMIZACIÓN

La optimización maximiza o minimiza una función objetivo, mientras se varían las variables del problema y se comparan los resultados de esta función objetivo entre iteraciones. En la optimización de puentes, este procedimiento suele minimizar diferentes objetivos, como el coste o las emisiones entre otros. Esta búsqueda del mínimo puede realizarse considerando los objetivos por separado o

conjuntamente, lo que se denomina optimización mono o multiobjetivo, respectivamente. En este caso, el objetivo de optimización es el coste. En la ecuación 1, la función objetivo de coste se define multiplicando el coste unitario de cada material del puente por su medición. Los datos de precios que se muestran en la Tabla 1, se han obtenido del Instituto Tecnológico de la Construcción de Cataluña mediante la base de datos del BEDEC [20]. A lo largo de todo el proceso, deben cumplirse las restricciones impuestas por las normativas y recomendaciones representadas por la ecuación 2.

$$C(\vec{x}) = \sum_{i=1}^{n} p_i \cdot m_i(\vec{x}) \quad (1)$$

$$G(\vec{x}) \leq 0 \quad (2)$$

Tabla 1. Datos de precios de los materiales

Unidad	Coste (€)
m^3 de hormigón C25/30	88,86
m^3 de hormigón C30/37	97,80
m^3 de hormigón C35/45	101,03
m^3 de hormigón C40/50	104,08
m^2 de prelosa	27,10
kg de acero en barras B400S	1,40
kg de acero en barras B500S	1,42
kg de acero S275	1,72
kg de acero S355	1,85
kg de acero S460	2,01
kg de acero para conectadores	1,70

2.1. Parámetros y variables de diseño

2.1.1. Variables

Se propone la optimización de un puente mixto de acero y hormigón de tres vanos de 60-100-60 metros. Las variables del problema corresponden a la geometría, la armadura, la resistencia del hormigón y el límite elástico del acero de los elementos del puente. Para alcanzar una solución viable desde el punto de vista de su construcción, se han discretizado las variables, lo que configura un problema de optimización discreto. La discretización de las variables ha sido definida en la Tabla 2. Considerando esta discretización de variables, el número de combinaciones para el problema de optimización corresponde a $1{,}38 \cdot 10^{46}$. Debido a este gran número de combinaciones posibles, se justifica el uso de técnicas metaheurísticas para obtener el óptimo. En total, se consideran 34 variables para la definición global de este problema de optimización. Estas variables del puente se han representado en la Figura 1. Según la naturaleza de las variables, se pueden agrupar en seis categorías. La primera corresponde a las variables geométricas de la sección transversal, que son distancia superior entre alas (*b*), ángulo de alas y celdas (*αw*), espesor de la losa superior (*hs*), altura de la viga (*hb*), altura mínima de la viga de piso (*hfb*), espesor del ala superior (*tf1*), ancho del ala superior (*bf1*), altura de las celdas superiores (*hc1*) y espesor (*tc1*), espesor del alma (*tw*), altura de las celdas inferiores (*hc2*), espesor (*tc2*) y anchura (*bc2*) y espesor de la losa inferior (*hs2*).

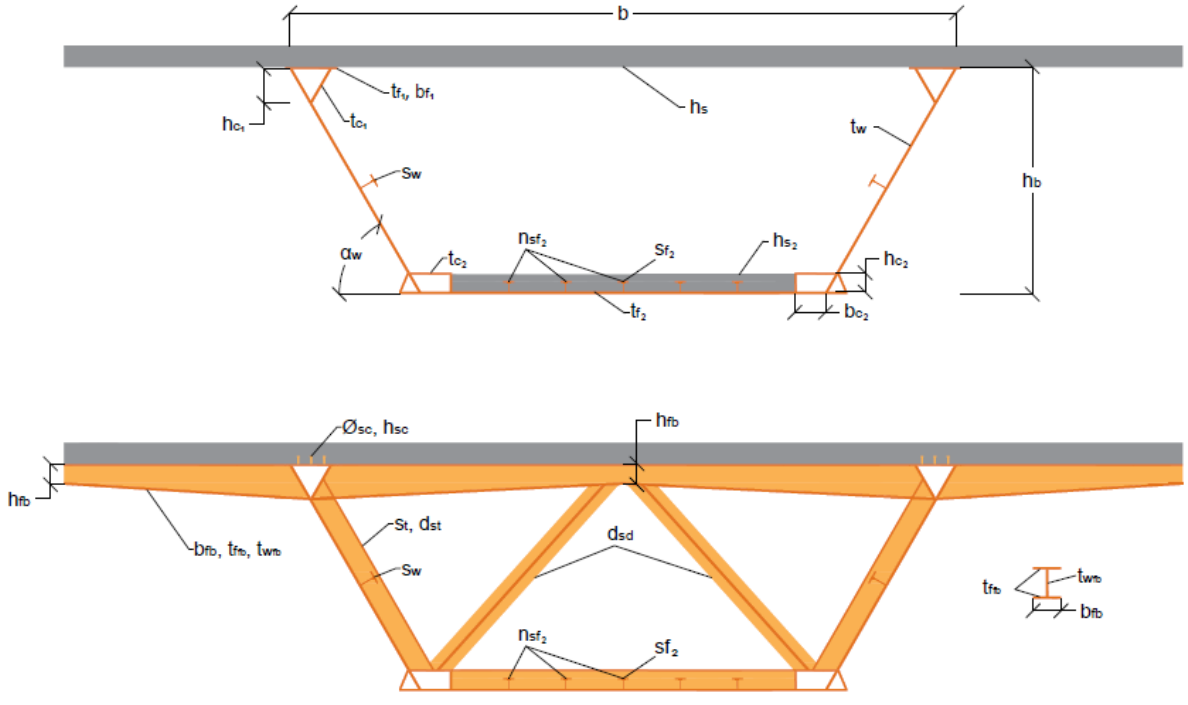

Figura 1. *Variables de la sección transversal del puente mixto.*

Los puentes mixtos aprovechan los materiales en mayor medida porque, en general, cada material que lo compone está sometido a los esfuerzos que mejor resiste. Esto sería cierto en un puente que funcionara como una viga isostática. En este caso, la losa superior de hormigón estaría comprimida en toda la longitud del puente. Esta losa superior está conectada a las alas superiores mediante conectadores. De este modo, la placa de las alas también se rigidiza, lo que evitaría el pandeo. Además, en el caso de una viga isostática, las alas inferiores estarían sometidas a esfuerzos de tracción, lo que también evita los fenómenos de inestabilidad por pandeo. Sin embargo, en el caso actual y con las cargas habituales a las que están sometidos los puentes (que son mayoritariamente de naturaleza gravitatoria), se producirán tensiones de flexión negativas en las zonas apoyadas. Esto dará lugar a una inversión de las fuerzas y, por tanto, a tracciones en la losa superior de hormigón y compresiones en el ala inferior. En este caso, para mejorar el comportamiento de la sección transversal del puente, se ha decidido materializar una losa inferior de hormigón en estas zonas, además del habitual aumento del armado de la losa superior. Para optimizar la armadura de la losa superior, se ha dividido en una armadura de base que es la mínima exigida por la normativa [21, 22, 23] a la que se le añaden dos zonas de refuerzo más en secciones de flexión negativa. Las longitudes de la losa inferior y de la zona de incremento de armadura se han descrito en el apartado 2.1.2. En consecuencia, el segundo grupo de variables corresponde a los diámetros de las barras de armado base, y del primer y segundo refuerzo (ϕ_{base}, ϕ_{r1}, ϕ_{r2}), y el correspondiente número de barras de las zonas de refuerzo de armaduras (n_{r1}, n_{r2}).

El siguiente grupo de variables corresponde a los rigidizadores. Los elementos considerados en este trabajo como rigidizadores son los perfiles medio IPE para alas (*sw*), ala inferior (*sf2*) y rigidización transversal (st). Para los rigidizadores del ala inferior, también se ha considerado como variable el número de rigidizadores (*nsf2*). Como se puede ver en la Figura 1, hay dos variables más que definen la distancia entre diafragmas (dsd) y rigidizadores transversales (dst).

Tabla 2. Variables de diseño y límites

Variables	Unidad	Límite inferior	Incremento	Límite superior	Número de valores
b	m	7	0.01	10	301
α_w	deg	45	1	90	46
h_s	mm	200	10	400	21
h_b	cm	250	1	400	151
h_{fb}	mm	400	100	700	31
t_{f_1}	mm	25	1	80	56
b_{f_1}	mm	300	10	1000	71
h_{c_1}	mm	0	1	1000	101
t_{c_1}	mm	16	1	25	10
t_w	mm	16	1	25	10
h_{c_2}	mm	0	10	1000	101
t_{c_2}	mm	16	1	25	10
b_{c_2}	mm	300	10	1000	71
t_{f_2}	mm	25	1	80	56
h_{s_2}	mm	150	10	400	26
$n_{s_{f_2}}$	u	0	1	10	11
d_{st}	m	1	0.1	5	41
d_{sd}	m	4	0.1	10	61
b_{fb}	mm	200	100	1000	9
$t_{f_{fb}}$	mm	25	1	35	11
$t_{w_{fb}}$	mm	25	1	35	11
n_{r_1}	u	200	1	500	301
n_{r_2}	u	200	1	500	301
ϕ_{base}	mm	6, 8, 10, 12, 16, 20, 25, 32			8
ϕ_{r_1}	mm	6, 8, 10, 12, 16, 20, 25, 32			8
ϕ_{r_2}	mm	6, 8, 10, 12, 16, 20, 25, 32			8
s_{f_2}	mm	De IPE 200 a IPE 600*			12
s_w	mm	De IPE 200 a IPE 600*			12
s_t	mm	De IPE 200 a IPE 600*			12
h_{sc}	mm	100, 150, 175, 200			4
ϕ_{sc}	mm	16, 19, 22			3
f_{ck}	MPa	25, 30, 35, 40			4
f_{yk}	MPa	275, 355, 460			3
f_{sk}	MPa	400, 500			2

* Siguiendo la serie estándar de perfiles IPE.

Las últimas categorías corresponden a la geometría de las variables de las vigas de piso, a las características de los conectadores, la resistencia del hormigón y el límite elástico de los aceros. Las variables de la viga de piso se definen por la anchura de la viga de piso (bfb), y los espesores de las alas (tffb) y del alma (twfb). Los conectadores se han definido por su altura (hsc) y su diámetro (φsc). Por último, el límite elástico del acero laminado (fyk), la resistencia del hormigón (fck) y el límite elástico de las barras de armado (fsk) completan la definición de las variables.

2.1.2. Parámetros

En todo problema de optimización, es necesario fijar algunas variables o propiedades para acotar el problema. Estas variables fijas se denominan parámetros y permanecen invariables durante todo el proceso de optimización. En este caso, estos parámetros corresponden a límites que se definen a algunos elementos del puente, incluyendo la dimensión, los espesores, las distribuciones de las armaduras, las condiciones ambientales externas o la densidad de los materiales entre otros. Los valores de estos parámetros se resumen en la Tabla 3.

Tabla 3. Parámetros principales del problema de optimización

Parámetros geométricos		
Ancho del puente (W)	16	m
Número de vanos	3	
Longitud del vano central	100	m
Longitud de los vanos externos	60	m
Mínimo espesor del alma ($t_{w_{min}}$)	15	mm
Mínimo espesor del ala inferior ($t_{f_{2min}}$)	25	mm
Recubrimiento	45	mm
Parámetros de los materiales		
Tamaño máximo de árido	20	mm
Módulo de deformación longitudinal del hormigón(E_{cm})	$22 \cdot ((f_{ck}+8)/10)^3$	MPa
Módulo de deformación transversal del hormigón (G_{cm})	$E_{cm}/(2 \cdot (1+0{,}2))$	MPa
Módulo de deformación longitudinal del acero (E_s)	210000	MPa
Módulo de deformación transversal del acero (G_s)	80769	MPa
Parámetros impuestos por la normativa		
Normativas	Eurocódigos[21, 22, 23, 24], IAP-11[25]	
Ambiente de exposición	XD2	
Clase estructural	S5	
Vida útil	100	años
Parámetros de carga		
Densidad del hormigón armado	25	kN/m^3
Densidad del acero	78.5	kN/m^3
Densidad del asfalto	24	kN/m^3
Espesor de la capa de asfalto	100	mm
Protecciones de tráfico	5.6	kN/m
Cargas de tráfico	Según normativa	
Gradiente térmico	Según normativa	
Carga de viento	Según normativa	

Como se ha mencionado anteriormente, este problema de optimización corresponde a un puente mixto de acero y hormigón de tres vanos de 60-100-60 metros con un ancho de tablero (W) de 16 metros sin variación de canto. En la sección transversal, se han definido cuatro celdas: dos en la parte superior de las almas y dos más en la parte inferior; como se puede ver en la Figura 1. Estas celdas permiten rigidizar estas partes del alma, creando una chapa de clase uno a tres que no necesita ser reducida según los Eurocódigos [21, 23]. Para permitir que el proceso de optimización defina si estas celdas mejoran el comportamiento estructural de la sección transversal (y en consecuencia son relevantes para obtener un mínimo de la función objetivo), la altura mínima de estas celdas se fija en cero. Los límites de todas las variables, incluyendo las alturas de las celdas (hc1, hc2), se pueden ver en la Tabla 2. Los límites de las variables se han definido siguiendo la publicación de diseño de puentes de Monleón [26]. La altura de celda(hc1 , hc2) define la altura de la viga de piso en la zona de contacto con las alas. Si la altura de la celda es menor que la altura mínima de la viga de piso (hfb), entonces se toma ese valor mínimo para la altura de la viga en esa zona. Los perfiles colocados para materializar las secciones de los diafragmas son 2L 150x15. Además, se ha considerado el uso de prelosas prefabricadas como encofrado. Hay que tener en cuenta que este elemento está diseñado para formar parte de la sección resistente. Por lo tanto, el módulo de medición del software lo resta de la cantidad total de hormigón.

El armado base tanto para la losa superior como para la inferior de hormigón se obtiene de acuerdo con la necesidad mínima de refuerzo definida en el Eurocódigo 2 [23]. La conexión entre la viga de acero y la losa de hormigón se dimensiona para resistir la tensión del hormigón considerando la anchura efectiva que viene dada por el Eurocódigo 4 [21] debida al arrastre a cortante. Dado que el

único ancho considerado como resistente (tanto en la losa de hormigón como en el ala inferior) es el efectivo, la armadura de acero de refuerzo definida se coloca sólo en ese ancho.

Para optimizar algún material en este tipo de estructuras, es habitual modificar los espesores de las almas y las alas para reducir la cuantía total de acero. En este trabajo se ha programado la variación de espesores considerando una ley teórica de flexión y cortante para una carga distribuida en toda la superficie del puente. El espesor del ala inferior se modifica a lo largo del puente, variando desde un valor mínimo *tf2min* hasta el definido como *tf2* . Esta variación corresponde a la ley teórica de flexión. En cambio, el espesor del ala varía según la ley de cortantes desde *twmin* hasta *tw*. El valor mínimo de estos espesores se ha definido según las recomendaciones de Monleón [26].

Por último, se definen las armaduras de acero y las áreas de la losa inferior. La losa inferior se coloca en tramos de flexión negativa para movilizar la doble acción mixta en estos tramos. Para definir las longitudes en las que se puede producir la flexión negativa, se ha considerado la distancia definida por el Eurocódigo 4 [21] para las tensiones de arrastre de cortante que se corresponden con un tercio de la longitud del vano. Como se ha dicho anteriormente, es necesario aumentar la armadura de la losa superior para resistir los esfuerzos de tracción producidos. En este caso de estudio, hemos considerado dos zonas de refuerzo. La primera se coloca en zonas donde la sección puede estar sometida a flexión negativa y el refuerzo de la base no puede resistir los esfuerzos. La segunda se coloca en la parte superior de los apoyos, correspondiente a un tercio de la distancia entre el apoyo y el punto de cambio de signo de la flexión de la ley teórica. Esta decisión está relacionada con la posición del centro de gravedad de la parábola, que se encuentra a un tercio de su longitud total.

2.2. Análisis estructural

Como se menciona en la sección 2, los procedimientos de optimización deben cumplir de las restricciones impuestas al problema. En la optimización de puentes, estas restricciones vienen impuestas por la normativa [21, 22, 23] y las recomendaciones [14, 26].

Las restricciones impuestas por las normativas pueden dividirse en dos grupos principales: los Estados Límite Últimos (ELU) y los Estados Límite de Servicio (ELS). El primer grupo está relacionado con la resistencia estructural de los elementos del puente sometidos a los esfuerzos debidos a las cargas actuantes. Por otra parte, los ELS está relacionado con las restricciones que garantizan la capacidad de servicio de la estructura durante su vida útil. Todas las cargas aplicadas y su combinación están definidas en la normativa [24]. La Tabla 3 resume los casos de carga que hemos considerado.

Para comprobar el ELU para todos los elementos del puente, se ha considerado tanto el análisis global como el local. Las comprobaciones consideradas para el análisis global incluyen la flexión, el cortante, la torsión y la interacción flexión-cortante. Se ha utilizado un análisis elástico lineal considerando la sección completa para obtener los pesos muertos y las tensiones. Para obtener la resistencia de la sección, se ha considerado la sección eficaz aplicando tanto las reducciones por retardo de cortante [21] como la reducción de la sección de las chapas de acero clasificadas como clase 4 [22]. Para ello se ha impuesto una precisión de 10-6 metros para el proceso iterativo. Para obtener el valor de las características mecánicas de la sección homogeneizada, se ha obtenido la relación (n) entre el módulo de deformación longitudinal del hormigón (Ecm) y del acero (Es) según la ecuación 3. La fluencia y la retracción del hormigón se han considerado según las normas [23, 21]. Además, se ha considerado un

modelo local para la comprobación de las vigas de piso, rigidizadores y diafragmas a ELU, considerando las comprobaciones de flexión, cortante, pandeo y características mecánicas mínimas.

$$n = \frac{E_s}{E_{cm}} \tag{3}$$

Los ELS considerados para el análisis son el límite de tensión para los materiales, la fatiga y las flecha máxima. No existe un límite claro para la flecha en los Eurocódigos, pero la normativa española IAP-11 [25] da un máximo de L/1000 para la combinación frecuente del valor de la flecha de la sobrecarga de uso, con L representando la longitud del vano. Este se ha impuesto como el valor máximo de la flecha. Además, se han considerado los requisitos geométricos y de factibilidad de cara a la construcción.

Se ha implementado un modelo numérico en el lenguaje de programación Python [27] para obtener las tensiones y realizar todas las comprobaciones de ELU, ELS, geométricas y de solución constructiva. Para obtener las deformaciones y tensiones, este software aplica el método de las fuerzas de empotramiento perfecto, tomando como datos de entrada las 34 variables del puente que hemos seleccionado. Este software divide cada tramo del puente en un número definido de barras. En este caso, el número total de barras es de 44, distribuidas en 12-20-12 correspondientes a los tres vanos del puente; discretizando así el puente en barras de 5 metros de longitud. Una vez obtenidas las tensiones, el programa realiza las comprobaciones estructurales y devuelve los resultados de las mediciones, el coste, las emisiones y los coeficientes de las comprobaciones. Estos coeficientes corresponden al cociente entre los valores de diseño de los efectos de las acciones (Ed) y su correspondiente valor de resistencia (Rd), tal y como se muestra en la ecuación 4. Si estos valores de coeficiente son mayores o iguales que uno, entonces la sección cumple con la restricción impuesta.

$$\frac{R_d}{E_d} \geq 1 \tag{4}$$

2.3. Algoritmo basado en trayectorias: Simulated Annealing (SA)

El Simulated Annealing (SA) o Recocido Simulado fue desarrollado por Kirkpatrick et al. [28]. Este algoritmo es una analogía basada en el comportamiento termodinámico de un grupo de átomos que forman un cristal. Esta metaheurística introduce la aceptación probabilística de las soluciones de peor calidad en el proceso de huida de los óptimos locales y dirige la búsqueda hacia mejores valores de la función objetivo. Por ello, acepta las soluciones con una probabilidad Pa. La expresión viene dada por la expresión de Boltzmann (5), donde T es un parámetro que disminuye con el tiempo yΔC es la diferencia de coste entre la solución actual y la última seleccionada por el algoritmo. En consecuencia, el algoritmo tiene de un primera fase de fijación de la temperatura inicial (T0). La definición de la temperatura inicial se realiza según el procedimiento propuesto por Medina [29], este procedimiento fija una temperatura inicial en la que la aceptación de soluciones se encuentre entre el 20 % y el 40 %. En la Figura 2 se muestra el diagrama de flujo del algoritmo.

Los parámetros de los que depende el algoritmo son la longitud de las cadenas de Markov, que representa el número de iteraciones a realizar antes de reducir la temperatura, el número de variables que cambian en cada iteración y el coeficiente de enfriamiento, que es el factor que reduce la temperatura una vez superado el número de iteraciones de la cadena de Markov. Respecto al criterio de parada, se han definido dos para este estudio. El primero es que la temperatura se haya

reducido hasta un 5 % del valor de la temperatura inicial (T0) y el segundo el número de cadenas sin mejora, que en este caso se ha fijado en 5. Respecto al resto de parámetros la longitud de la cadena de Markov se ha fijado en 1000, el número de variables en 5 y el coeficiente de enfriamiento en 0,8.

$$P_a = e^{\frac{\Delta C}{T}} \tag{4}$$

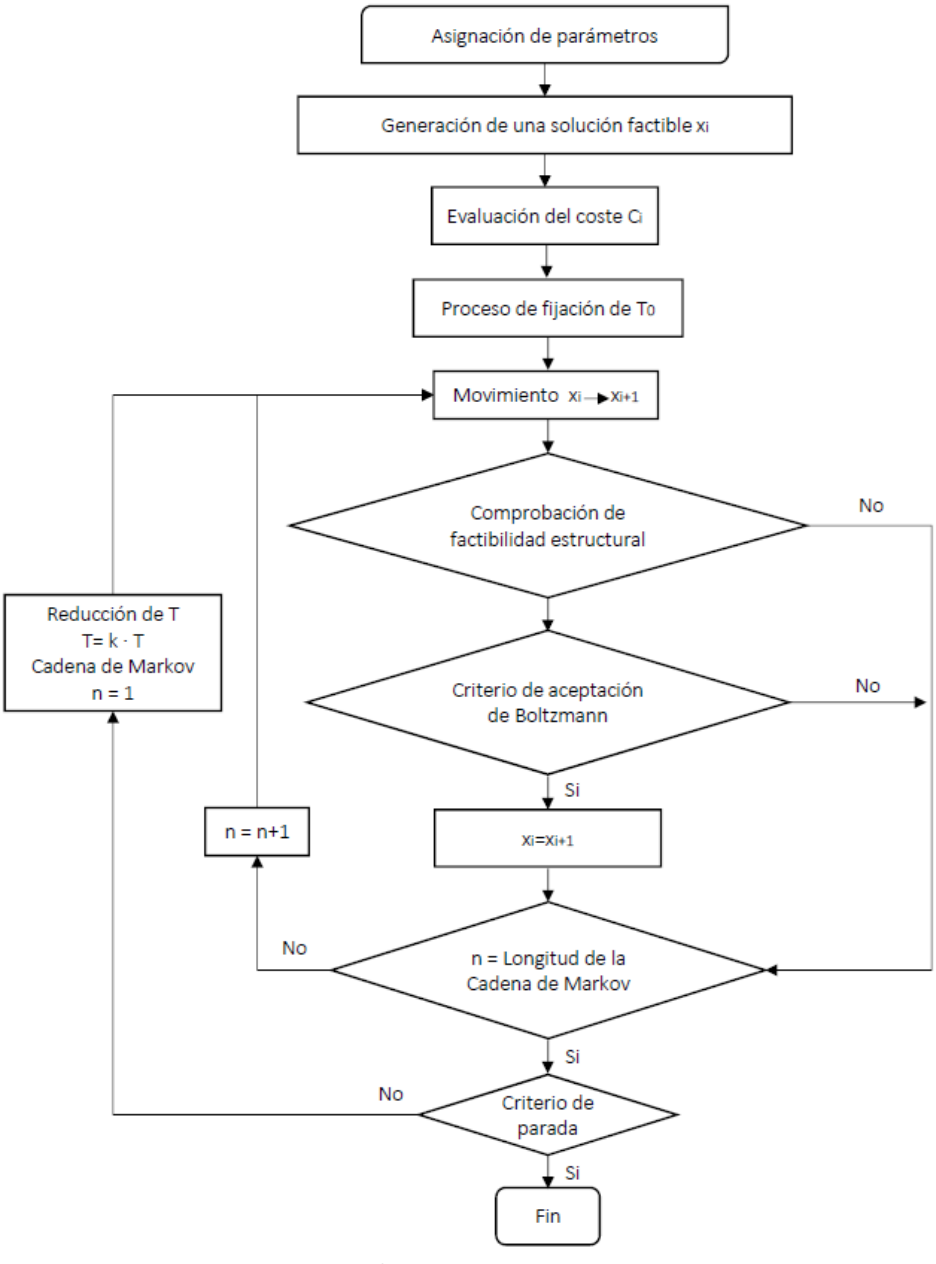

Figura 2. *Diagrama de flujo del algoritmo Simulated Annealing.*

3. RESULTADOS

Los resultados obtenidos corresponden a los valores de las variables, las cuantías de material y al coste de la solución. Para poder realizar un análisis estadístico de los resultados obtenidos se han realizado 9 corridas del algoritmo descrito en la sección 2.3 siguiendo el procedimiento de otros artículos publicados previamente en los que se resuelven problemas de optimización estructural [30]. Por tanto, en las Figuras 3, 4, 5 y 6 se muestran los resultados de las variables, mientras que en la Figura 7 se muestran los resultados obtenidos de cuantías de acero. Cabe destacar que solo se han representado los elementos más representativos de la sección.

En la Figura 3 se muestran los resultados de los valores obtenidos del canto de la viga metálica, ángulos de las almas y separación de los elementos de rigidización de la sección transversal de puente. La media de los valores de canto de la viga corresponde a un valor aproximado de 3.3 metros y varía de forma más frecuente entre los 3.2 y los 3.5 m. Respecto a los valores de la inclinación de las almas, observamos que el diseño óptimo obtenido resulta en valores de inclinación de las almas de entre 55 y 70 grados.

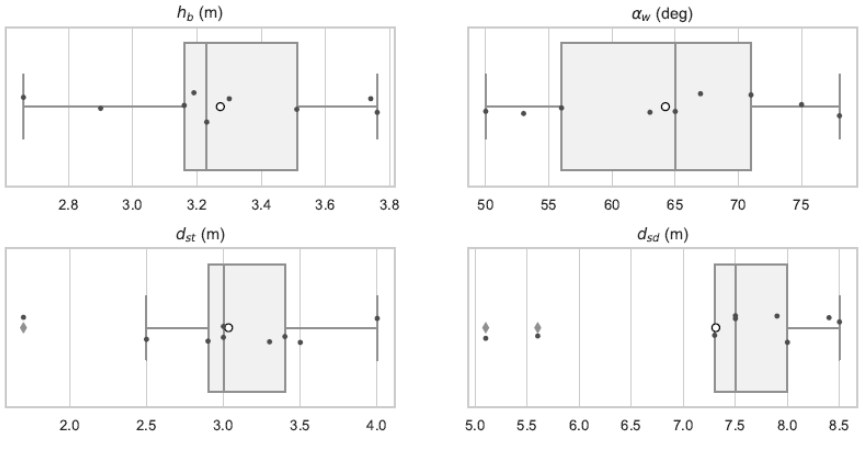

Figura 3. *Valores de las variables de la sección transversal obtenidos de la optimización.*

En la Figura 4 se observa que los valores de espesores del alma y el ala inferior siempre dan el mismo valor siendo 25 mm para las alas y 16 mm para el alma , mientras que las dimensiones de ancho y espesor del ala superior toman valores de entre 0.37 y 0.65 m y 30 y 45 mm respectivamente para un diseño óptimo con función objetivo coste.

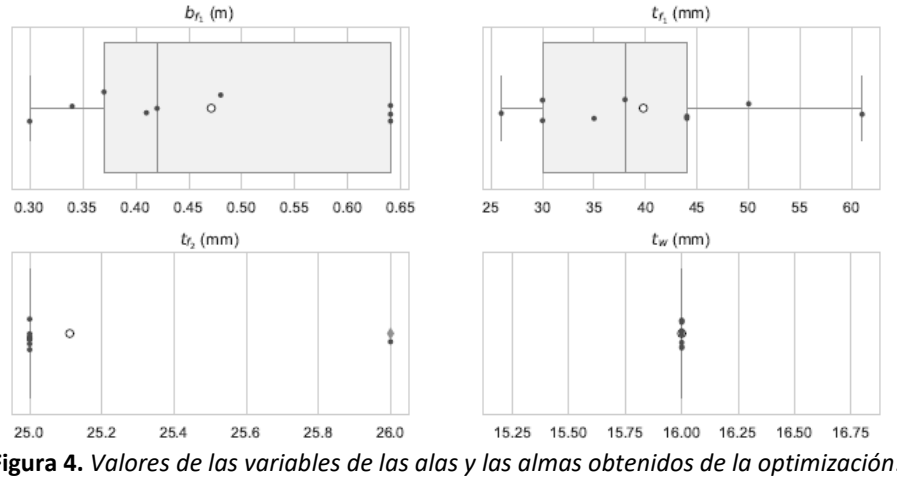

Figura 4. *Valores de las variables de las alas y las almas obtenidos de la optimización.*

Uno de los objetivos de esta investigación es la validación del diseño con celdas para la generación de un diseño óptimo. Como se ha descrito en la sección 2, se ha propuesto un diseño con celdas en la sección transversal con la intención de generar paneles de dimensiones menores que permitan evitar su reducción de sección. Los resultados obtenidos para estos elementos se muestran en la Figura 5, en las que aparecen los valores obtenidos de estos elementos para los diferentes diseños óptimos encontrados. Los parámetros de altura de ambas celdas resultan positivos en la mayoría de los casos. Además, se obtienen rangos de espesor de los paneles que conforman estos elementos.

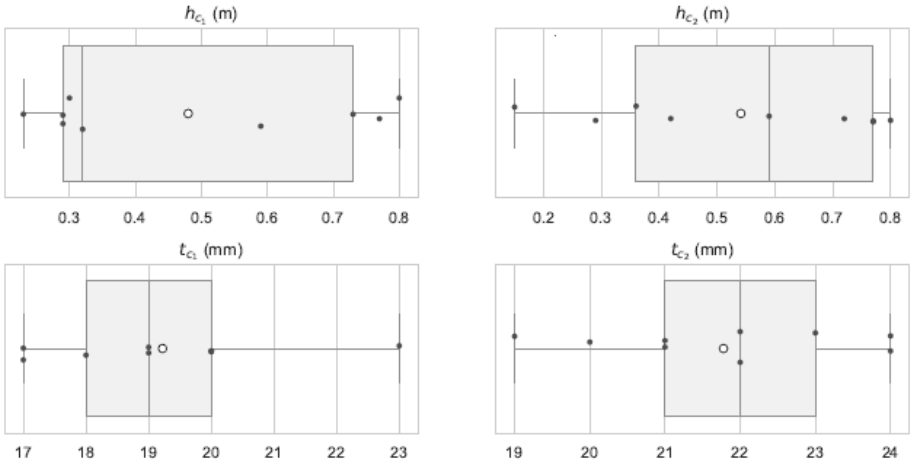

Figura 5. *Valores de las variables las celdas obtenidos de la optimización.*

Para finalizar la presentación de resultados de las variables, en la Figura 6 se muestran los valores de los elementos transversales superiores de la sección del puente que conforman las vigas de piso. Estos valores dependen directamente de la distancia superior entre almas decidida por el algoritmo y por tanto se observa una gran variación respecto a los valores obtenidos.

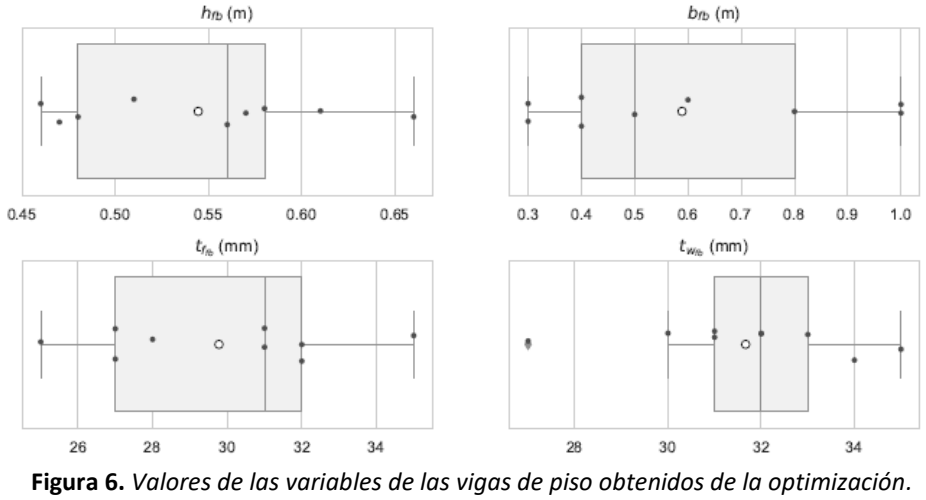

Figura 6. *Valores de las variables de las vigas de piso obtenidos de la optimización.*

Finalmente, en la Figura 7 se plasman los resultados de cuantías tanto de acero estructural como de acero en barras tomando como unidad funcional el metro cuadrado de tablero. Cabe destacar que las cuantías de acero son altas debido a que no se realiza ningún tipo de variación de canto en la estructura. Además, en la parte inferior de la figura, se muestran las trayectorias de estas cuantías a lo

largo de las iteraciones realizadas por el algoritmo. Respecto a los resultados obtenidos en relación con la resistencia de los materiales, para todas las corridas del algoritmo se obtiene el mismo valor, siendo este de 275 MPa para el límite elástico del acero estructural, 500 MPa para el acero de barras y 25 MPa de resistencia compresión del hormigón. Respecto a las dimensiones de la losa siempre se va al valor mínimo del espesor, por tanto, la medición de hormigón es la misma en todos los casos.

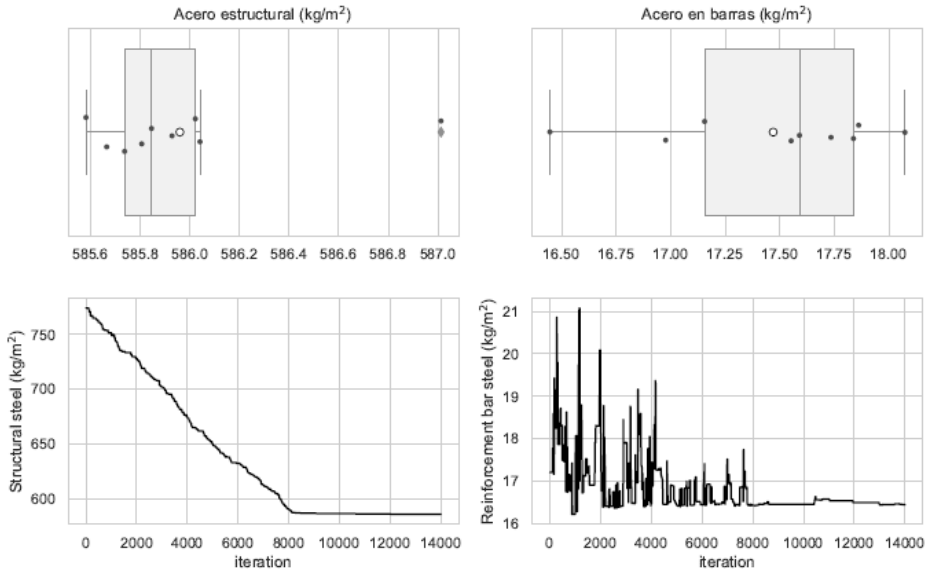

Figura 7. *Valores de las variables de las vigas de piso obtenidos de la optimización.*

4. CONCLUSIONES

En el diseño de puentes, existe una clara tendencia a considerar nuevas técnicas para obtener nuevas alternativas de diseño estructural. En consecuencia, la optimización de puentes de hormigón mediante el uso de algoritmos se ha desarrollado en gran medida. Por el contrario, los estudios de optimización de puentes mixtos de acero y hormigón son pocos y no se conoce el comportamiento de estas técnicas para este tipo de estructura. Se ha propuesto el tradicional Simulated Annealing (SA), que pertenece a los algoritmos basados en la trayectoria, como algoritmo para llevar a cabo la optimización de la estructura.

Este estudio muestra la optimización de un puente mixto en cajón mediante el uso de técnicas heurísticas. En conclusión, se ha observado que el algoritmo elimina los rigidizadores de las alas inferiores debido a la doble acción mixta de las losas de hormigón sobre los apoyos. Además, se ha considerado el uso de celdas interiores en la sección del puente, teniendo como resultado que estas celdas permiten mejorar las resistencias a los esfuerzos de la sección y reducir la distancia entre zonas no rigidizadas en las placas de acero del alma. Este trabajo permite al investigador estructural ampliar sus conocimientos sobre la optimización de puentes mixtos al considerar nuevas técnicas para obtener un diseño óptimo, y abre una puerta a la utilización de estos elementos para obtener nuevos criterios de diseño que permitan obtener alternativas de puentes mixtos más sostenibles y eficientes.

AGRADECIMIENTOS

Proyecto PID2020-117056RB-I00 financiado por MCIN/AEI/10.13039/501100011033 y por FEDER Una manera de hacer Europa.

Ayuda FPU-18/01592 financiada por MCIN/AEI/10.13039/501100011033 y por FSE invierte en tu futuro.

REFERENCIAS

[1] I. Payá-Zaforteza, V. Yepes, F. González-Vidosa, and A. Hospitaler, "On the weibull cost estimation of building frames designed by simulated annealing," Meccanica, vol. 45, no. 5, pp. 693–704, 2010.

[2] K. C. Sarma and H. Adeli, "Cost optimization of concrete structures," Journal of Structural Engineering, vol. 124, no. 5, pp. 570–578, 1998.

[3] W. Hare, J. Nutini, and S. Tesfamariam, "A survey of non-gradient optimization methods in structural engineering," Advances in Engineering Software, vol. 59, pp. 19–28, 2013.

[4] D. Martínez-Muñoz, J. V. Martí, J. García, and V. Yepes, "Embodied energy optimization of buttressed earth-retaining walls with hybrid simulated annealing," Applied Sciences, vol. 11, no. 4, p. 1800, 2021.

[5] F. Molina-Moreno, T. García-Segura, J. V. Martí, and V. Yepes, "Optimization of buttressed earth retaining walls using hybrid harmony search algorithms," Engineering Structures, vol. 134, pp. 205– 216, 2017.

[6] F. Molina-Moreno, J. V. Martí, and V. Yepes, "Carbon embodied optimization for buttressed earth retaining walls: Implications for low-carbon conceptual designs," Journal of Cleaner Production, vol. 164, pp. 872–884, 2017.

[7] T. García-Segura, V. Yepes, and D. M. Frangopol, "Multi-objective design of post-tensioned concrete road bridges using artificial neural networks," Structural and Multidisciplinary Optimization, vol. 56, p. 139–150, 2017.

[8] V. Penadés-Plà, T. García-Segura, and V. Yepes, "Accelerated optimization method for low embodied energy concrete box-girder bridge design," Engineering Structures, vol. 179, pp. 556– 565, 2019.

[9] V. Penadés-Plà, T. García-Segura, J. V. Martí, and V. Yepes, "An optimization-lca of a prestressed concrete precast bridge," Sustainability, vol. 10, no. 3, p. 685, 2018.

[10] J. R. Martí-Vargas, F. J. Ferri, and V. Yepes, "Prediction of the transfer length of prestressing strands with neural networks," Computers and Concrete, vol. 12, no. 2, pp. 187–209, 2013.

[11] D. Martínez-Muñoz, J. V. Martí, and V. Yepes, "Steel-concrete composite bridges: Design, life cycle assessment, maintenance, and decision-making," Advances in Civil Engineering, vol. 2020, p. 8823370, 2020.

[12] D. Martínez-Muñoz, J. V. Martí, and V. Yepes, "Comparative life cycle analysis of concrete and composite bridges varying steel recycling ratio," Materials, vol. 14, no. 15, 2021.

[13] V. Penadés-Plà, D. Martínez-Muñoz, T. García-Segura, I. J. Navarro, and V. Yepes, "Environmental and social impact assessment of optimized post-tensioned concrete road bridges," Sustainability, vol. 12, no. 10, 2020.

[14] I. Vayas and A. Iliopoulos, Design of steel-concrete composite bridges to Eurocodes. Boca Raton: CRC Press, 2017.

[15] Y. I. Musa and M. A. Diaz, "Design optimization of composite steel box girder in flexure," Practice Periodical on Structural Design and Construction, vol. 12, no. 3, p. 146–152, 2007.

[16] N. Lv and L. Fan, "Optimization of quickly assembled steel-concrete composite bridge used in temporary," Modern Applied Science, vol. 8, no. 4, p. 134–143, 2014.

[17] V. Yepes, M. Dasi-Gil, D. Martínez-Muñoz, V. J. López-Desfilis, and J. V. Martí, "Heuristic techniques for the design of steel-concrete composite pedestrian bridges," Applied Sciences, vol. 9, no. 16, p. 3253, 2019.

[18] A. Kaveh, T. Bakhshpoori, and M. Barkhori, "Optimum design of multi-span composite box girder bridges using cuckoo search algorithm," Steel and Composite Structures, vol. 17, no. 5, p. 703–717, 2014.

[19] A. Kaveh and M. M. M. Zarandi, "Optimal design of steel-concrete composite i-girder bridges using three meta-heuristic algorithms," Periodica Polytechnica Civil Engineering, vol. 63, no. 2, p. 317– 337, 2019.

[20] "Catalonia Institute of Construction Technology. BEDEC ITEC materials database https://metabase.itec.cat/vide/es/bedec," accessed on January 2021.

[21] CEN, Eurocode 2: Design of concrete structures. Brussels, Belgium: European Committee for Standardization,2013.

[22] CEN, Eurocode 3: Design of steel structures. Brussels, Belgium: European Committee for Standardization, 2013.

[23] CEN, Eurocode 4: Design of composite steel and concrete structures. Brussels, Belgium: European Committee for Standardization, 2013.

[24] CEN, Eurocode 1: Actions on structures. Brussels, Belgium: European Committee for Standardization, 2019.

[25] MFOM, IAP-11: Code on the actions for the design of road bridges. Madrid: Ministerio de Fomento, 2011.

[26] S. Monleón, Diseño estructural de puentes (in Spanish). València: Universitat Politècnica de València, 2017.

[27] G. Van Rossum and F. L. Drake, Python 3 Reference Manual. Scotts Valley, CA: CreateSpace, 2009.

[28] S. Kirkpatrick, C. D. J. Gelatt, and M. P. Vecchi, "Optimization by simulated annealing," Science, vol. 220, no. 4598, pp. 671–680, 1983.

[29] J. R. Medina, "Estimation of incident and reflected waves using simulated annealing," Journal of Waterway, Port, Coastal, and Ocean Engineering, vol. 127, no. 4, pp. 213–221, 2001.

[30] V. Yepes, J. V. Martí, and T. García-Segura, "Cost and CO2 emission optimization of precast prestressed concrete u-beam road bridges by a hybrid glowworm swarm algorithm," Automation in Construction, vol. 49, pp. 123–134, 2015.

NEUTROSOPHIC LOGIC APPLIED TO THE MULTI-CRITERIA EVALUATION OF SUSTAINABLE ALTERNATIVES FOR EARTH-RETAINING WALLS.

Antonio J. Sánchez-Garrido [1]; David Martínez-Muñoz [2]; Ignacio J. Navarro [1]; Víctor Yepes [2]

ABSTRACT

El diseño sostenible de las infraestructuras es uno de los aspectos clave para la consecución de los Objetivos de Desarrollo Sostenible, dada la reconocida magnitud de los impactos tanto económicos como ambientales propios del sector de la construcción. Las metodologías de decisión multicriterio permiten abordar el diseño sostenible de las infraestructuras, considerando simultáneamente la repercusión de un diseño en las distintas dimensiones de la sostenibilidad. El presente artículo propone el uso de la lógica neutrosófica para resolver uno de los principales problemas asociados con la toma de decisiones: la subjetividad de los expertos involucrados. Mediante el enfoque neutrosófico de la metodología multicriterio AHP (del inglés, Analytic Hierarchy Process) y el uso de la técnica VIKOR (del serbio, VIseKriterijumska Optimizacija I Kompromisno Resenje), se analizan los impactos económicos y ambientales asociados a cuatro diseños de muros de contención. En el presente análisis, la respuesta más sostenible a lo largo de su ciclo de vida ha resultado ser la del muro de gaviones.

Keywords: Sustainability, Retaining walls, Neutrosophic logic, AHP, Multi-criteria decision making

1. INTRODUCCIÓN

Las serias amenazas que se ciernen sobre el planeta obligan a tomar decisiones importantes de cara al futuro. La emergencia climática mundial es una realidad y desde el sector de la construcción debemos ser capaces de concebir los edificios desde una óptica responsable con la sociedad y el medio ambiente. Los Objetivos de Desarrollo Sostenible adoptados en 2015 por las Naciones Unidas marcan unas metas específicas que se deben alcanzar en 2030. Concretamente el ODS−9 consiste en "construir infraestructuras resilientes, promover la industrialización sostenible y fomentar la innovación" lo cual requiere un cambio de tendencia en las prácticas de diseño convencionales. La construcción se encuentra a nivel mundial entre las principales actividades de estrés ambiental y económico que comprometen nuestra sociedad, siendo la industria del cemento la que genera uno los mayores impactos [1]. Si bien la optimización de materiales en el diseño de las infraestructuras ha sido objeto de estudio en los últimos años [2-4], el ODS-9 supone la necesidad de incorporar en los diseños futuros conceptos complejos como la sostenibilidad o la economía circular [5] para poder alcanzar las metas propuestas para 2030.

[1] *Departamento de Ingeniería de la Construcción y Proyectos de Ingeniería Civil. Universitat Politècnica de València (SPAIN).* ajsangar@doctor.upv.es *(A.J. Sánchez-Garrido);* ignamar1@cam.upv.es *(I.J. Navarro).*

[2] *Instituto de Ciencia y Tecnología del Hormigón (ICITECH). Universitat Politècnica de València (ESPAÑA).* damarmu1@cam.upv.es *(D. Martínez-Muñoz, corresponding author);* vyepesp@cst.upv.es *(V. Yepes).*

Con la necesidad de adoptar un enfoque holístico en los problemas de diseño sostenible se recurren a técnicas de toma de decisiones multicriterio (MCDM), las cuales proporcionan un procedimiento racional a las decisiones basadas en cierta información, experiencia y juicio. Sin embargo, en los problemas de la vida real es difícil de aplicar existiendo siempre una incertidumbre en las valoraciones o en las comparaciones entre criterios que suelen ser contradictorios. Esto se complica mucho más cuando el decisor no es a título individual sino que lo forma un grupo cuyos integrantes manifiestan intereses diferentes. Zadeh [6] ya señaló que la capacidad de un individuo para emitir juicios rigurosos y precisos disminuye conforme aumenta la complejidad del problema a tratar. Es por ello que muchos de estos métodos combinan herramientas como la teoría fuzzy, el método de Montecarlo, los números Grey y, más recientemente, la teoría de conjuntos neutrosóficos (NS). Introducida por Smarandache [7] constituye la generalización más avanzada de la lógica difusa y la intuicionista, siendo bastante difícil de aplicar en el ámbito de la ingeniería real, ya que los conjuntos neutrosóficos se definen en subconjuntos reales estándar y no estándar. Solo en los últimos años, la teoría de los conjuntos neutrosóficos ha alcanzado el nivel de desarrollo suficiente como para poder utilizarse de manera práctica en problemas de ingeniería civil, llegándose a aplicar con éxito en el diseño sostenible de puentes [8] y en estructuras de edificación [9].

El presente documento propone un enfoque diferente con el que evaluar la sostenibilidad entre distintas alternativas de diseño para muros de contención, a los que se les aplicó un análisis del ciclo de vida ambiental (ACV-A) en estudios anteriores [10]. Para ello, se utilizan conjuntos neutrosóficos (NS) integrados en un proceso de jerarquía analítica grupal (NAHP-G), lo que permite captar la vaguedad e incertidumbre contenida en los juicios emitidos por los responsables de la toma de decisiones. La caracterización de las opiniones mediante números neutrosóficos triangulares (*t, i, f*) es especialmente importante cuando intervienen un número significativo de criterios, ya que a mayor número de comparaciones se diluye la atención del decisor provocando juicios que, a costa de la credibilidad, resultan menos rigurosos. La respuesta asociada a cada alternativa se obtiene según la metodología ReCiPe, que calcula la puntuación de los impactos en función de tres indicadores ambientales finales, a saber, el daño a los ecosistemas, el agotamiento de los recursos naturales y el daño a la salud humana. El proceso concluye transformando los pesos neutrosóficos a difusos, y éstos a pesos escalares obteniendo así las ponderaciones con la importancia de cada criterio. Por último, se aplica una técnica MCDM con la que agregar los diferentes criterios para evaluar la sostenibilidad de las diferentes alternativas.

Con este trabajo se pretende aumentar el conocimiento en el diseño sostenible aplicado a las estructuras de contención, proponiendo herramientas de apoyo a las técnicas de ponderación para toma de decisiones multicriterio. De la metodología se deriva que trabajar en un entorno neutrosófico permite profundizar en el campo de la subjetividad considerando las incertidumbres no probabilísticas inherentes a la vaguedad del pensamiento humano. De los resultados, se obtiene la captura de mayor información implícita en los juicios, lo que dota a la toma de decisión de robustez, rigor y más fiabilidad en comparación, por ejemplo, con el AHP convencional.

2. METODOLOGÍA

Esta sección describe una extensión neutrosófica del Proceso de Jerarquía Analítica tradicional. Siguiendo la metodología propuesta, las ponderaciones de los criterios se obtienen mediante un AHP neutrosófico de grupo. Los pasos a seguir se explican de forma secuencial a continuación.

2.1. Preliminares sobre el método AHP clásico

El proceso analítico jerárquico (AHP) es un método muy utilizado en el proceso de toma de decisiones para ayudar a seleccionar alternativas en función de ciertos criterios, normalmente jerarquizados, y muchos de los cuales son contradictorios llegando a entrar en conflicto. La técnica requiere que el decisor complete una matriz de comparación, en la que cada elemento *aij* representa cuánto más importante o preferible es la alternativa *i* con respecto a la alternativa *j*.

La matriz se completa con valores numéricos según la Escala Fundamental de Saaty [11], que permite transformar la percepción de las variables semánticas en una escala progresiva de números reales desde 1/9 a 9. Esta matriz cumple con las propiedades de reciprocidad (si *aij=x*, entonces *aji=1/x*); homogeneidad (si *i* y *j* son igualmente importantes, *aij=aji*=1, y además, *aii*=1 para todo *i*).

Para que el método AHP arroje resultados que no contengan contradicciones en las valoraciones realizadas, la matriz de comparación debe ser consistente La consistencia matemáticamente se obtiene mediante el índice de consistencia:

$$CI = (\lambda_{max} - n)/(n - 1) \quad (1)$$

donde λ_{max} es el valor propio máximo y n la dimensión de la matriz de decisión. Un valor nulo de este índice corresponde a una consistencia perfecta. Una vez obtenido *CI*, se calcula la proporción de consistencia (*CR*) siendo aceptable si no supera los valores de la Tabla 1.

$$CR = CI/RI \quad (2)$$

Tabla 1. Índice aleatorio *RI*

Número de criterios *n*	2	3	4	5	6	7	8	9	10
Índice aleatorio *RI*	0	0.58	0.90	1.12	1.24	1.32	1.41	1.45	1.49

2.2. Proceso de jerarquía analítica neutrosófica

2.2.1. Algunos conceptos de los conjuntos neutrosóficos

Los conjuntos neutrosóficos describen la variable *x* mediante un triple valor *x*= (*t, i, f*) donde "*t*" es el grado de veracidad, "*f*" es el grado de falsedad, e "*i*" es el nivel de indeterminación. La lógica neutrosófica es capaz de tratar con contradicciones que son verdaderas y falsas al mismo tiempo ya que la suma de los componentes es cualquier número entre -0 y 3+.

$$A = \{\langle x, t_A(x), i_A(x), f_A(x)\rangle | x \in X\} \quad (3)$$

$$0 \leq t_A(x) + i_A(x) + f_A(x) \leq 3 \quad (4)$$

Un número neutrosófico triangular de un solo valor $a = \langle(a_1, a_2, a_3); t_a, i_a, f_a\rangle$ en el conjunto de números reales se describe con las siguientes funciones de pertenencia [12]:

$$\mu_a(x) = \begin{cases} \dfrac{(x-a_1)}{(a_2-a_1)} \cdot t_a, & para\ a_1 \le x < a_2 \\ \dfrac{(a_3-x)}{(a_3-a_2)} \cdot t_a, & para\ a_2 \le x \le a_3 \\ 0, & de\ lo\ contrario \end{cases} \quad (5)$$

$$v_a(x) = \begin{cases} \dfrac{\left(a_2 - x + i_a \cdot (x-a_1)\right)}{(a_2-a_1)}, & for\ a_1 \le x < a_2 \\ \dfrac{\left(x - a_2 + i_a \cdot (a_3-x)\right)}{(a_3-a_2)}, & for\ a_2 \le x \le a_3 \\ 0, & de\ lo\ contrario \end{cases} \quad (6)$$

$$\lambda_a(x) = \begin{cases} \dfrac{\left(a_2 - x + f_a \cdot (x-a_1)\right)}{(a_2-a_1)}, & for\ a_1 \le x < a_2 \\ \dfrac{\left(x - a_2 + f_a \cdot (a_3-x)\right)}{(a_3-a_2)}, & for\ a_2 \le x \le a_3 \\ 0, & otherwise \end{cases} \quad (7)$$

Las operaciones aritméticas básicas entre dos números neutrosóficos triangulares de un valor $a = \langle(a_1, a_2, a_3); t_a, i_a, f_a\rangle$ y $b = \langle(b_1, b_2, b_3); t_b, i_b, f_b\rangle$ se definen como [13,14]:

Suma de dos números neutrosóficos triangulares:

$$a + b = \langle(a_1 + b_1, a_2 + b_2, a_3 + b_3); t_a + t_b - t_a t_b, i_a i_b, f_a f_b\rangle \quad (8)$$

Multiplicación de un valor constante por un número neutrosófico triangular:

$$k \cdot a = \langle(ka_1, ka_2, ka_3); 1 - (1-t_a)^k, (i_a)^k, (f_a)^k\rangle \quad (9)$$

Potencia de un número neutrosófico triangular:

$$a^k = \langle\left({a_1}^k, {a_2}^k, {a_3}^k\right); {t_a}^k, 1 - (1-i_a)^k, 1 - (1-f_a)^k\rangle \quad (10)$$

Multiplicación de dos números neutrosóficos triangulares:

$$a \times b = \langle(a_1 b_1, a_2 b_2, a_3 b_3); t_a t_b, i_a + i_b - i_a i_b, f_a + f_b - f_a f_b\rangle \quad (11)$$

División de dos números neutrosóficos triangulares:

$$a \div b = \langle\left(\frac{a_1}{b_3}, \frac{a_2}{b_2}, \frac{a_3}{b_1}\right); \frac{t_a}{t_b}, \frac{i_a - i_b}{1 - i_b}, \frac{f_a - f_b}{1 - f_b}\rangle \quad (12)$$

Siendo la operación de división es válida solo si $t_a \le t_b$, $i_a \ge i_b$, $f_a \ge f_b$, $t_b \ne 0$ e $i_b, f_b \ne 1$.

2.2.2. Obtención de la triada neutrosófica

El primer paso consiste en recopilar las matrices de comparación [A] por cada experto. Su intervención se ciñe a realizar comparaciones por pares, asignando valores en relación con la escala de Saaty, entre las categorías de impacto que constituyen los criterios de decisión inicialmente definidos. El proceso se repetirá tantas veces como sea necesario hasta que la matriz de comparación resultante sea consistente, es decir, *CR* < 0.10. Cada decisor debe completar también una matriz [SC] que contiene la certeza expresada en unidades entre 0 y 1 para cada uno de sus juicios.

Obtenidas ambas matrices, ya se puede caracterizar a cada miembro del grupo de expertos, necesario para determinar posteriormente su relevancia dentro del grupo AHP. Basándonos en el procedimiento sugerido por Sodenkamp et al. [15], se proponen las siguientes expresiones para determinar la tríada $\bar{E}_k=\langle \delta, \theta, \varepsilon \rangle$ asociada al cada experto.

La credibilidad del experto se basa en su experiencia en los campos que se evalúan. PA_k y SE_k son los años de actividad profesional y la experiencia en sostenibilidad, respectivamente, del *k* experto entre el total de *p* expertos que intervienen en la decisión; Kc_i son coeficientes ≤1 que representan el conocimiento en seis campos específicos asignando valores discretos entre 0 y 5. Más detalles sobre la parametrización de estas competencias se pueden encontrar en [9].

$$\delta_k = \left(\frac{PA_k}{\max\limits_{k=1\ldots p}\{PA_k\}} + \frac{SE_k}{\max\limits_{k=1\ldots p}\{SE_k\}} + \sum_{i=1}^{6} \frac{Kc_i}{5} \right) \Big/ 8 \tag{13}$$

La indeterminación puede obtenerse a partir del complementario de los valores de certeza c_{ij} expresados por el decisor, siendo *n* es el número de criterios a comparar.

$$\theta_k = 1 - \sum_{i,j=1}^{n} (SC_{ij}/n^2) \tag{14}$$

La incoherencia del experto se determina como la consistencia de sus juicios, medida mediante el ratio de consistencia (*CR*) de su matriz de comparación, dividida por la consistencia mínima permitida en las matrices de comparación AHP para el número *n* de elementos considerados, que en nuestro caso, para n=5 o más, CR_{lim}=0,10.

$$\varepsilon_k = CR_k / CR_{lim} \tag{15}$$

2.2.3. Construcción de la matriz de comparación AHP neutrosófica

Para reflejar la vaguedad de los juicios emitidos por los decisores, se transforman los valores de las matrices de comparación de los decisores en números neutrosóficos triangulares (NNT) del tipo $\bar{a}_{ij}$ = $=\langle (l_{ij}, m_{ij}, u_{ij}); t_{ij}, i_{ij}, f_{ij} \rangle$. Los valores (l_{ij}, m_{ij}, u_{ij}) de cada juicio se definen según la escala de Saaty entre 1/9 y 9. Los valores centrales m_{ij} corresponden a los juicios emitidos por el decisor. En este caso, los valores centrales m_{ij} también se requieren para satisfacer la comprobación de consistencia tal y como lo define Saaty. Los límites inferior y superior l_{ij} y u_{ij} dependen de la certeza del decisor asociada al juicio a_{ij}, y se obtienen como sigue:

$$l_{ij} = m_{ij} - \Delta V_{ij};\ u_{ij} = m_{ij} + \Delta V_{ij} \tag{16}$$

donde ΔV_{ij} es el número de saltos en la escala de Saaty a realizar entre el valor central m_{ij} y los correspondientes extremos. El número de saltos se hace depender de la certeza emitida por el experto como se muestra en la Tabla 2.

Tabla 2. Pasos en la escala ampliada de Saaty

Certeza a_{ij} (SC_{ij})	Saltos (ΔV_{ij}) en la escala extendida de Saaty
SC_{ij}=1	0
0.8≤ SC_{ij} <1	1
0.6≤ SC_{ij} <0.8	2
0.4≤ SC_{ij} <0.6	3
0.2≤ SC_{ij} <0.4	4
0≤ SC_{ij} <0.2	5
SC_{ij}=0	6

2.2.4. Pesos neutrosóficos

Según la técnica convencional del AHP, los pesos de cada elemento se calculan mediante el método de la media geométrica ponderada:

$$\bar{w}_i = \frac{\left(\prod_{j=1}^{n} \bar{a}_{ij}\right)^{1/n}}{\sum_{i=1}^{n}\left(\prod_{j=1}^{n} \bar{a}_{ij}\right)^{1/n}} \tag{17}$$

donde $\bar{w}_i$ es el peso neutrosófico triangular del elemento *i*, n es el número de elementos a comparar, y $\bar{a}_{ij}$ es el valor de comparación neutrosófica entre los elementos *i* y *j*. Las operaciones algebraicas necesarias para llevar a cabo el cálculo de los pesos neutrosóficos seguirán la formulación de las Eq. (8) a (12).

2.2.5. Agregación de pesos (grupo N-AHP)

Para la agregación de los pesos obtenidos por cada experto, se propone caracterizar la relevancia de cada decisor a partir de su tríada neutrosófica $\bar{E}_k$=⟨δ_k, θ_k, ε_k⟩. La relevancia de cada experto se puede obtener como la distancia entre su punto $\bar{E}_k$ y el punto de máxima fiabilidad neutrosófica ⟨1,0,0⟩ como sigue:

$$\varphi_k = \frac{1 - \sqrt{\{(1-\delta_k)^2 + {\theta_k}^2 + {\varepsilon_k}^2\}/3}}{\sum_{k=1}^{p}\left(1 - \sqrt{\{(1-\delta_k)^2 + {\theta_k}^2 + {\varepsilon_k}^2\}/3}\right)} \tag{18}$$

donde *p* es el número de expertos involucrados en la toma de decisión. Una vez obtenida la relevancia de cada experto, los pesos neutrosóficos resultantes de la agregación descrita se obtienen como:

$$W_{m,i} = \sum_{k=1}^{p} \varphi_k \cdot w_{m,i}^k \tag{19}$$

$$W_{l,i} = W_{m,i} - max_{k=1\ldots p}\ \{w_{m,i}^k - w_{l,i}^k\} \tag{20}$$

$$W_{u,i} = W_{m,i} + max_{k=1\ldots p}\ \{w_{u,i}^k - w_{m,i}^k\} \tag{21}$$

donde $W_{m,i}$, $W_{l,i}$ y $W_{u,i}$ son, respectivamente, el valor central, el límite inferior y el límite superior de los pesos neutrosóficos agregados. La figura 1 muestra de forma gráfica un peso neutrosófico típico tras un proceso de agregación como el descrito. Es importante destacar que la agregación de pesos triangulares no resulta en un peso triangular (Fig. 1).

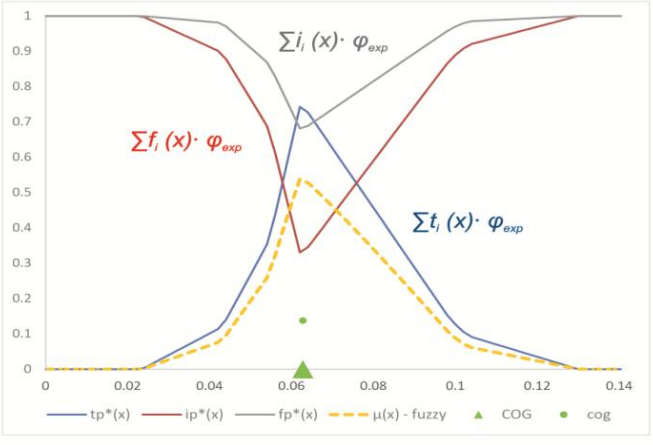

Figura 1. *Funciones de pertenencia neutrosóficas asociadas a la agregación de pesos del grupo N-AHP para cada criterio*

2.2.6. Deneutrosofización

La deneutrosofización consiste en transformar los pesos neutrosóficos agregados en números clásicos que permitan su interpretación y operabilidad matemática de forma más sencilla. Este proceso consta de dos pasos. El primero de ellos consiste en transformar los pesos neutrosóficos en pesos difusos $\hat{W}_i = \langle (W_{l,i}, W_{m,i}, W_{u,i}); \eta_i \rangle$, donde la función difusa $\eta_i(x)$ se obtiene como sigue:

$$\eta_i(x) = 1 - \sqrt{\{(1-\mu_i(x)^2) + \upsilon_i(x)^2 + \lambda_i(x)^2\}/3}\,; \quad \forall x \in [W_{l,i}\,;\, W_{u,i}] \tag{22}$$

El segundo paso consiste en transformar estos pesos difusos en pesos clásicos. Uno de los métodos más habituales para llevar a cabo dicha conversión consiste en obtener las coordenadas (CoG_x, CoG_y) del centro de gravedad (CoG) de la función difusa $\eta_i(x)$. Conocido el CoG, los pesos expresados en términos de la lógica clásica se pueden obtener como:

$$S_{\widehat{W}i} = CoG_x(\widehat{W}i) \cdot CoG_y(\widehat{W}i) \tag{23}$$

$$W_i^* = S_{\widehat{W}i} / \sum S_{\widehat{W}i} \tag{24}$$

Para facilitar el seguimiento, los pasos secuenciales de la metodología descrita se ilustran en la Fig. 2:

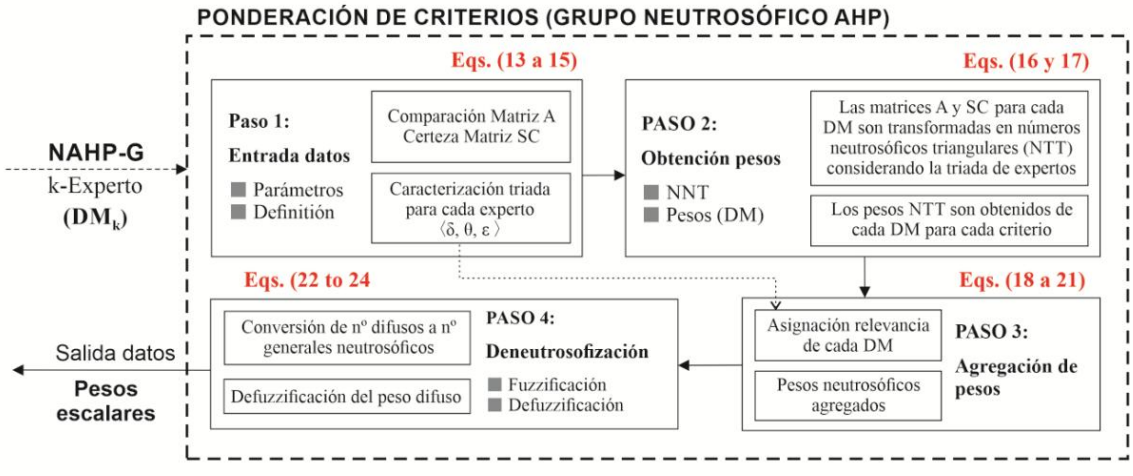

Figura 2. *Overall methodology*

2.3. Selección de la mejor alternativa

2.3.1. VIKOR

Esta técnica MCDM clasifica y determina una solución de compromiso a partir de una serie de alternativas viables en presencia de criterios conflictivos. Una vez compuesta la matriz de decisión que compone el problema, se identifica la solución ideal positiva SIP (A*) y la solución ideal negativa SIN (A-) entre los *n* criterios para cada alternativa, y se normaliza cada puntuación:

$$r_{ij}' = \left(r_i^* - r_{ij}\right)/(r_i^* - r_i^-) \tag{26}$$

A continuación se asignan las ponderaciones (wi) de cada criterio. El método VIKOR utiliza una medida basada en la unión de métricas L_1 (distancia Manhattan) y L_∞ (métrica máxima o distancia de Chebyshev), para determinar los índices S y R, respectivamente. S utiliza la métrica L_1 que tiene en cuenta la utilidad de grupo de los criterios. R utiliza la métrica L_∞, que considera el mínimo individual de cada criterio. para encontrar la máxima distancia de la alternativa a la solución ideal, es decir, el peor caso posible:

$$S_j = \sum_{i=1}^{m} w_i \left(r_i^* - r_{ij}\right)/(r_i^* - r_i^-) \tag{27}$$

$$R_j = max\left[w_i\left(r_i^* - r_{ij}\right)/(r_i^* - r_i^-)\right] \tag{28}$$

La solución de compromiso será una solución factible cerca de la solución ideal, y por tanto, con la menor distancia posible. La clasificación final se obtiene determinando la distancia relativa de cada alternativa Q_j según la ecuación:

$$Q_j = \nu \cdot \frac{(S_j - S^*)}{S^- - S^*} + (1 - \nu) \cdot \frac{(R_j - R^*)}{R^- - R^*} \tag{29}$$

donde S^*= min S_j, S^- = max S_j, R^*= min R_j, R- = max R_j, ponderado a través del factor $\nu \in [0,1]$ que determina la importancia según el balance de cada métrica. En este estudio se ha considerado v=0.5.

3. DEFINICIÓN DEL PROBLEMA

El método que integra la lógica neutrosófica en la ponderación de los criterios que se presenta aquí se aplica a un problema de toma de decisión basado en la sostenibilidad. El objetivo es discretizar entre las siguientes alternativas constructivas de muros de contención de tierras (Fig. 3):

a) Muros en ménsula de hormigón armado (CW) con puntera y talón. Realizado con hormigón HA-25/B/20/IIa fabricado en central, y vertido desde camión, y acero UNE-EN 10080 B 500 S, con una cuantía aproximada de 58 kg/m³.
b) Muros de gravedad (GW). Realizado con hormigón HM-20/P/40/I fabricado en central y vertido desde camión (60% de volumen) y bolos de piedra de 15 a 30 cm de diámetro (40% de volumen).
c) Muros de mampostería ordinaria (MW). Realizado con piedra caliza, a una cara vista, recibida con mortero de cemento industrial M-5.
d) Muros de gaviones (GM). Realizado a una cara vista, de 2000x1000x1000 mm de malla electrosoldada, de alambre de acero galvanizado de Ø4,5 mm, con una apertura de malla de 50x100 mm en las caras vistas y de 100x100 mm en ocultas; con diafragma intermedio de 1000x1000 m de malla electrosoldada; y relleno con medios mecánicos con piedra caliza, de granulometría comprendida entre 70 y 250 mm, con desgaste en el ensayo de Los Ángeles < 50.

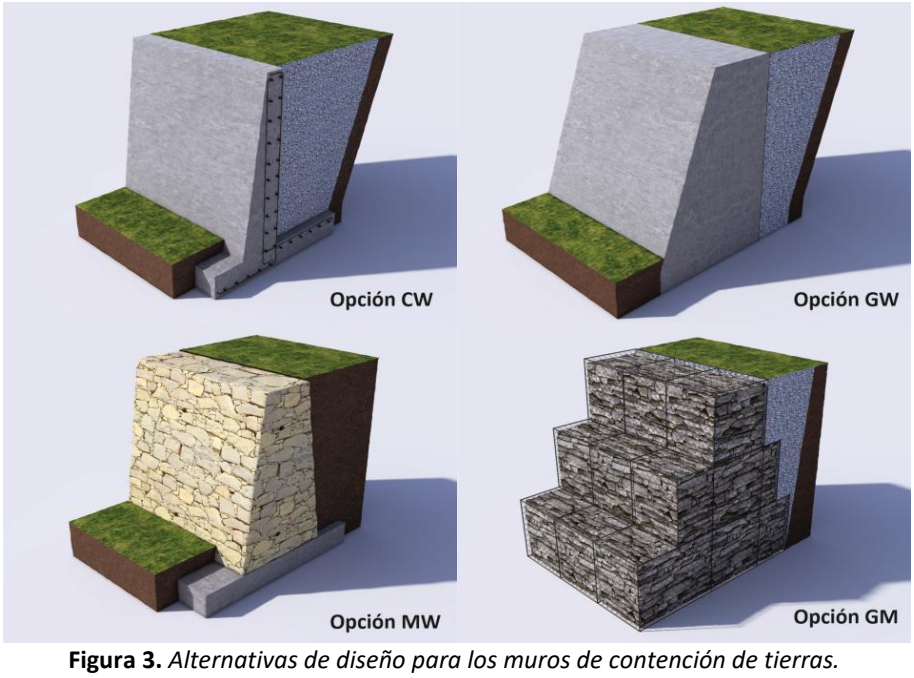

Figura 3. *Alternativas de diseño para los muros de contención de tierras.*

Los diseños CW y GW tienen como actividades comunes la excavación a cielo abierto bajo rasante, sistema de encofrado según cada tipología. Junto a las dos anteriores, la opción GM comparte como actividad el relleno en trasdós, con tierras seleccionadas procedentes de la propia excavación, y compactación en tongadas sucesivas de 30 cm de espesor máximo con bandeja vibrante de guiado manual, hasta alcanzar una densidad seca no inferior al 95% de la máxima obtenida en el ensayo Proctor Modificado. En el caso de la alternativa MW no se precisa ninguna de las actuaciones anteriores.

El ciclo de vida de los muros de contención de tierras se ha dividido en cuatro fases. La primera es la producción de todos los materiales utilizados para su construcción, incluido su transporte hasta el lugar de la obra. La segunda es la construcción, incluyendo todas las actividades realizadas para su construcción. El tercero es el uso del muro de contención de tierras durante su vida útil de 50 años según el código español para muros de contención de tierras de hormigón [12], sin actividades de mantenimiento. La cuarta es el final de la vida útil de la estructura, incluyendo todas las actividades necesarias para demoler el muro, reciclar el acero y el hormigón y crear un relleno sanitario para los restos de tierra y roca. La unidad funcional para este estudio sería un metro lineal de muro para una altura de tierras de 4.00 m.

Para abordar la sostenibilidad del ciclo de vida de los distintos diseños de muros, se propone un conjunto de seis criterios de decisión (Tabla 3). Tres de ellos están relacionados con la dimensión económica de la sostenibilidad, e implican considerar, por un lado, los costes derivados de la construcción de los muros, por otro, los costes que resultan del mantenimiento decenal y, por último, los costes de desmantelamiento de la estructura. Los resultados con los costes totales de cada etapa correspondientes a los criterios C1, C2 y C3 se recogen en la matriz de decisión de la Tabla 8.

Tabla 3. Criterios considerados en la presente evaluación de la sostenibilidad de MCDM.

Pilar de la sostenibilidad	Criterio	Descripción
Económico	C1 – Costes de construcción	Costes asociados a la producción e instalación de materiales, maquinaria y trabajadores
	C2 – Costes de mantenimiento	Valoración del montante económico que supondría mantener la construcción en los primeros diez años atendiendo a las operaciones de mantenimiento.
	C3 – Costes de final de vida	Costes asociados a la producción e instalación de materiales, maquinaria y trabajadores implicados en las actividades de demolición y/o de-construcción.
Medioambiental	C4 – Daños en los ecosistemas	Ocupación del suelo, emisión de contaminantes
	C5 – Daños en la salud humana	Emisión de contaminantes causantes de enfermedades respiratorias, cancerígenos
	C6 – Agotamiento de los recursos	Agotamiento de los recursos naturales como consecuencia de las actividades de extracción

Los impactos medioambientales se evalúan en función de la metodología, mundialmente reconocida, ReCiPe (2008) [13]. La evaluación del impacto del ciclo de vida (EICV) traduce las emisiones y las extracciones de recursos en un número limitado de puntuaciones de impacto ambiental mediante los llamados factores de caracterización. En este análisis se asume la perspectiva jerárquica como modelo de consenso más común adoptando como criterios los 3 indicadores en los que caracteriza los impactos el enfoque de punto final: daño a la diversidad del ecosistema, el daño a la salud humana y el daño a la disponibilidad de recursos.

El análisis del inventario implica la recopilación de los datos de entrada relevantes de energía y materiales necesarios para desarrollar un proceso, es decir, la construcción de un metro lineal de un muro de contención de tierras y la producción de las emisiones al medio ambiente derivadas de su ciclo de vida. Los datos de inventario (Tabla 4) se han extraído de investigaciones anteriores [6] en los que se realizaba una comparación estrictamente medioambiental entre los distintos tipos de muros. Como los resultados de esta fuente estaban traducidos a los 18 indicadores de punto medio, en este caso en estudio, se ha tenido que transformar de “midpoint” a “endpoint” con los factores de conversión de la Tabla 1.5 que figura en ReCiPe (2016) [14]. Los resultados correspondientes a los criterios C4, C5 y C6 se muestran en la matriz de decisión de la Tabla 8.

Tabla 4. Impactos de punto medio (ReCiPe) causados por cada alternativa de muro de 4 m de altura

Nº	Acrónimo	Descripción	CW	GW	MW	GM
1	ALO	Agricultural land occupation	206.02	235.21	13.37	36.57
2	GWP	Climate change	907.43	1025.58	915.08	629.23
3	FD	Fossil deplection	266.97	273.24	201.14	198.37
4	FEPT	Freshwater ecotoxicity	11.18	6.11	3.47	3.88
5	FEP	Freshwater eutrophication	0.26	0.21	0.1	0.11
6	HTP	Human toxicity	432.69	258.75	124.92	128.76
7	IRP	Ionizing radiation	145.73	100.56	74.93	59.64
8	MEPT	Marine ecotoxicity	11.19	6.18	3.51	3.99
9	MEP	Marine eutrophication	0.23	0.21	0.18	0.19
10	MD	Metal depletion	221.47	49.78	25.34	80.09
11	NLT	Natural land transformation	-0.92	-0.43	-0.74	-1
12	ODP	Ozone depletion	1.27E-04	1.20E-04	9.71E-05	9.54E-05
13	PMFP	Particulate matter formation	2.4	2.08	2.5	2.62
14	POFP	Photochemical oxidant formation	5.41	4.85	4.62	4.59
15	TAP	Terrestrial acidification	4.35	4.23	3.42	3.45
16	TETP	Terrestrial ecotoxicity	0.14	0.11	0.05	0.34
17	ULO	Urban land occupation	54.23	30.91	19.76	29.54
18	WD	Water depletion	3835.75	2473.66	1485.9	1947.02

4. RESULTADOS

4.1. Resultados del grupo neutrosófico AHP

La evaluación de la relevancia que debe tener cada uno de los seis criterios establecidos para la toma de decisión sobre la alternativa de diseño más sostenible de muros de contención se realiza mediante el método AHP. La metodología requiere que cada experto rellene una matriz de comparación [A] de 6x6, lo que implica emitir [6·(6-1)]/2 = 15 comparaciones por pares. Por su parte, la matriz de certidumbre [SC] se traducirá en un entorno neutrosófico que tiene en cuenta las incertidumbres no probabilísticas de los juicios emitidos en cada comparación. Este estudio ha contado con un seminario con tres expertos, todos ellos profesionales en activo con una experiencia de entre 2 y 19 años en arquitectura e ingeniería civil. Las Tablas 5 y 6 contienen respetivamente la matriz [A] y [SC] con los juicios emitidos por el decisor 1 (DM_1). La Tabla 7 recoge los parámetros que definen los perfiles neutrosóficos de los 3 expertos.

Tabla 5. Matriz de decisión [A] y pesos AHP perteneciente experto DM_1.

	C1	C2	C3	C4	C5	C6	$\prod aij^{(1/n)}$	w
C1	**1**	1/2	1	2	1/3	1/2	0.742	**0.105**
C2	2	**1**	3	1	1/4	1/2	0.953	**0.135**
C3	1	1/3	**1**	1/2	1/5	1/3	0.472	**0.067**
C4	1/2	1	2	**1**	1/4	1/2	0.707	**0.100**
C5	3	4	5	4	**1**	1	2.493	**0.353**
C6	2	2	3	2	1	**1**	1.698	**0.240**

Tabla 6. Matriz de certidumbre [SC] perteneciente experto DM_1.

	C1	C2	C3	C4	C5	C6
C1	**1**	0.8	0.9	0.4	0.7	0.6
C2	0.8	**1**	0.8	0.3	0.6	0.5
C3	0.9	0.8	**1**	0.5	0.7	0.6
C4	0.4	0.3	0.5	**1**	0.3	0.4
C5	0.7	0.6	0.7	0.3	**1**	0.8
C6	0.6	0.5	0.6	0.4	0.8	**1**

Tabla 7. Caracterización neutrosófica de los expertos

Parámetros	DM_1	DM_2	DM_3
Credibilidad del experto. Pertenencia a la verdad *(δ)*	**0.700**	**0.678**	**0.488**
Confianza media expresada	0.661	0.744	0.667
La certeza del experto. Pertenencia a la indeterminación *(θ)*	**0.339**	**0.256**	**0.333**
Coeficiente de coherencia de la matriz de comparación	0.044	0.016	0.031
Incongruencia del experto. Pertenencia a la falsedad *(ε)*	**0.439**	**0.163**	**0.308**

Las matrices de cada decisor se transforman en matrices triangulares de números neutrosóficos (TNN) que definen los intervalos de los juicios emitidos, según la Tabla 2, a partir de la matriz de certeza [SC] resultante de los juicios de cada experto. Siguiendo los pasos de la metodología descrita en la Subsección 2.2.3 y 2.2.4, se obtienen las ponderaciones TNN de cada decisor para cada uno de los 6 criterios. Una vez asignada la relevancia particular de la valoración de cada experto, según el apartado 2.2.5, se agregan las ponderaciones neutrosóficas individuales. Para obtener los pesos escalares, se aplica la técnica de deneutrosofización y defuzzificación conforme a las Eq. (22) a (25).

En la Fig. 4 se representa la superposición de las funciones fuzzy μ(x) comparando todos los criterios tras la deneutrosoficación. La Fig. 5 muestra también el peso escalar de cada criterio después de aplicar el método de defuzzificación [15] para los números difusos generalizados.

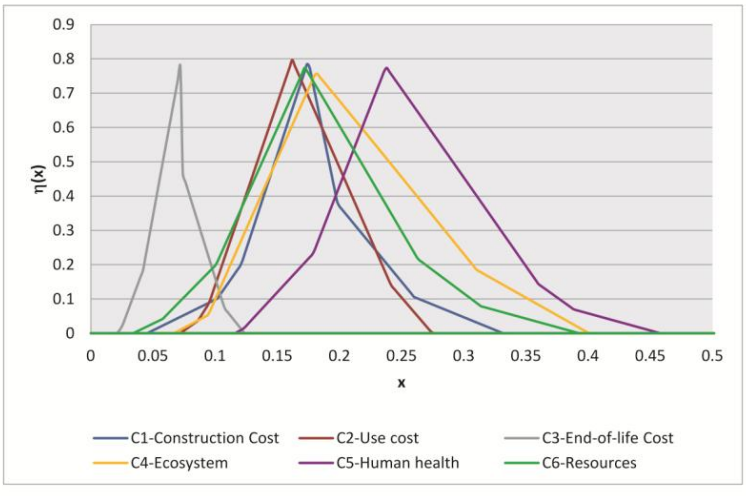

Figura 4. *Funciones fuzzy asociadas a los pesos de todos los criterios derivados de cada matriz de comparación AHP.*

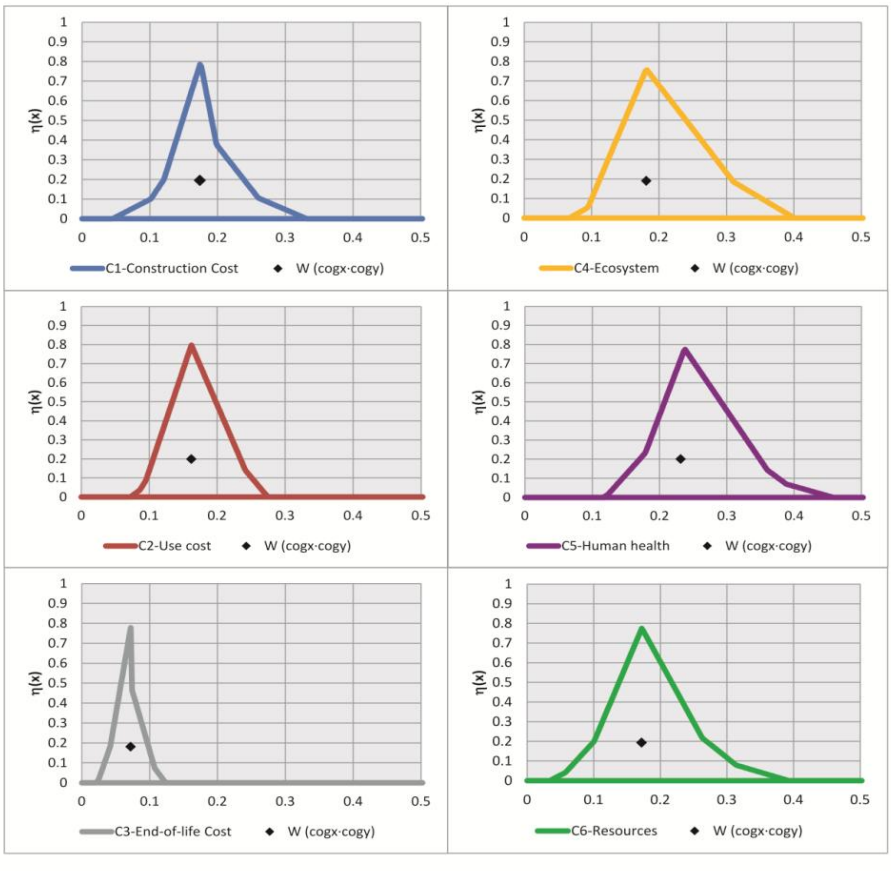

Pesos escalares *defuzzificados*

W^*_{C1}	W^*_{C2}	W^*_{C3}	W^*_{C4}	W^*_{C5}	W^*_{C6}
0.175	0.167	0.067	0.178	0.240	0.172

Figura 5. *Resultados de los pesos agregados para cada criterio tras la deneutrosofícación.*

Para contrastar las ponderaciones obtenidas, se recurre a los puntos medios de la TNN, que equivalen a la ponderación según el AHP tradicional, comparándolas como referencia con las anteriores para cada criterio (Tabla 8). Los resultados demuestran que las incertidumbres no probabilísticas influyen en las ponderaciones obtenidas, con desviaciones en los criterios más subjetivos de hasta el 7.10% si se compara con un AHP convencional. Según los juicios de los expertos, la relevancia de los impactos económicos y ambientales corresponde a una proporción de 2:3. Los pesos de los criterios, tras la deneutrosificación, han resultado en general bastante equilibrados en torno al 17%, salvo el coste del final de vida con un 6.7 %. Destaca el indicador ambiental de daños a la salud humana como el más relevante con un 24%.

Tabla 8. Ponderaciones de los 6 criterios tras la defuzzificación y comparación con el AHP convencional.

Método	**Referencia**	**C1**	**C2**	**C3**	**C4**	**C5**	**C6**
AHP	$m_{\text{criteria }(i)}$	0.175	0.162	0.073	0.181	0.237	0.172
Deneutrosoficación	$\boldsymbol{W^*_{(COGx \cdot COGy)}}$	**0.176**	**0.167**	**0.067**	**0.178**	**0.240**	**0.172**
$W^*_{(COGx \cdot COGy)}$	vs $m_{\text{criteria }(i)}$	-0.37%	-2.99%	+7.10%	+1.65%	-1.24%	+0.17%

4.2. Resultados de sostenibilidad

Incorporando las ponderaciones escalares de cada criterio obtenidas en la Tabla 7, se aplica la técnica multicriterio VIKOR para agregar las 6 categorías de impacto diferentes en una única puntuación de sostenibilidad para cada una de las opciones de diseño de muro de contención que se van a comparar. Con VIKOR, la alternativa más cercana al punto ideal se obtiene clasificando las soluciones según las Eq. (26) a (29) para seleccionar la mejor de ellas (Tabla 8), siendo mejor el valor más próximo a 0.

De la metodología se observa que aunque el muro de mampostería (MW) genera los menores impactos ambientales globales, la alternativa de muro de gaviones (GM) es la que mejor se comporta en términos de sostenibilidad debido al balance entre todos sus criterios. Esto se puede apreciar gráficamente en la Fig. 6 que muestra cómo la alternativa GM distribuye las puntuaciones de forma más uniforme sin tener la mayor en ninguno de los criterios.

Tabla 8. Resultados MCDM y selección de mejor alternativa mediante la técnica N-VIKOR.

Criterio óptimo	Valor óptimo [+] Valor pésimo [-]				**Pesos NSs**	Distancia normalizada y ponderada [1]			
	CW	**GW**	**MW**	**GM**		**CW**	**GW**	**MW**	**GM**
C1 (Min.)	867.55	806.83+	1907.77−	809.40	**0.176**	0.0097	0	0.1755	0.0004
C2 (Min.)	15.35	13.73+	286.18−	109.97	**0.167**	0.0010	0	0.1668	0.0589
C3 (Min.)	269.14+	742.46	1015.31	1213.31−	**0.067**	0	0.0338	0.0533	0.0674
C4 (Min.)	1.22E-02−	8.57E-03	6.11E-03+	6.95E-03	**0.178**	0.1781	0.0714	0	0.0244
C5 (Min.)	6.03E-05−	4.15E-05	2.50E-05+	3.10E-05	**0.240**	0.2403	0.1122	0	0.0406
C6 (Min.)	1.74E+02−	1.37E+02	9.84E+01+	1.10E+02	**0.172**	0.1719	0.0884	0	0.0258
				Distancia Manhattan	$\boldsymbol{S_j}$	0.601	0.306	0.396	0.218
				Distancia ∞	$\boldsymbol{R_j}$	0.240	0.112	0.176	0.067
	PUNTUACIÓN FINAL [1]			$\boldsymbol{Q_j}$	$\boldsymbol{v}$	**CW**	**GW**	**MW**	**GM**
				Q_{j5}	0.50	1	0.245	0.545	**0**

[1] Mejor cuanto menor distancia

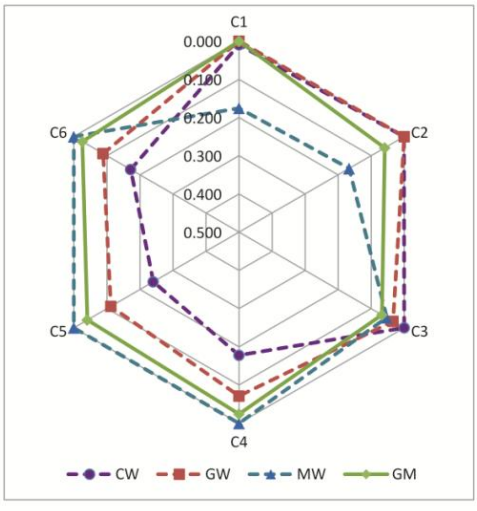

Figura 6. *Resultados de la evaluación de la sostenibilidad comparando los 4 muros.*

5. CONCLUSIONES

Los muros de contención de tierras son una de las estructuras más frecuentemente empleadas en la construcción tanto de obras civiles como de edificación. Este estudio evalúa el rendimiento de la sostenibilidad entre cuatro tipologías dispares de muros para una altura habitual de contención de tierras de 4 metros. El análisis del ciclo de vida (ACV) con un enfoque "de la cuna a la tumba" considera los impactos económicos y medioambientales asociados a las etapas de producción, construcción, uso y final de vida. Se ha supuesto una vida útil de 50 años sin necesidad de mantenimiento. Para determinar la sostenibilidad asociada a cada alternativa, comparando los resultados de un enfoque bidimensional económico-ambiental, se ha utilizado un método MCDM. Concretamente, se ha escogido la técnica VIKOR, basada en la distancia, con la que se han agregado las 6 categorías diferentes de impacto (criterios) en la evaluación final.

Para la determinación de la relevancia particular de cada criterio, se ha aplicado un AHP de grupo. Sin embargo, dada la naturaleza conflictiva de los criterios de sostenibilidad, las comparaciones por pares del AHP suelen ser complejas e inciertas. Para profundizar en las incertidumbres no probabilísticas que conllevan las técnicas de ponderación subjetiva, se ha partido de un enfoque neutrosófico para la determinación de las ponderaciones del AHP del grupo de expertos. Este procedimiento ha permitido detectar además qué criterios tienen una mayor carga de subjetividad o que generan mayores incertidumbres. En nuestro caso, el coste del final del ciclo de vida (C3) con un +7.10 % de peso respecto de un AHP convencional.

Incorporar la lógica neutrosófica a la investigación ha permitido dotar los resultados de robustez y rigor al capturar las incertidumbres no probabilísticas asociadas a la vaguedad del pensamiento humano, dando así cuenta de la valiosa información derivada de la consideración de la fiabilidad de los juicios asociada a la credibilidad, inconsistencias e indeterminaciones del decisor. Del estado del arte se deduce que, aunque la mayoría de las evaluaciones de sostenibilidad se basan en el enfoque tradicional, los investigadores están empezando a utilizar perspectivas basadas en la intuición para captar las incertidumbres no probabilísticas asociadas a la información cognitiva en los problemas complejos de toma de decisiones. Sin embargo, la teoría de los conjuntos neutrosóficos aún no se ha utilizado en las evaluaciones de sostenibilidad y mucho menos aplicado a ingeniería ni arquitectura.

AGRADECIMIENTOS

Los autores agradecen el apoyo financiero del Ministerio de Ciencia e Innovación (Proyecto: PID2020-117056RB-I00), junto con los fondos FEDER.

REFERENCIAS

[1] Worrell, E., Price, L., Martin, N, Hendriks, C., & Ozawa, L. (2001). Carbon Dioxide Emissions from the Global Cement Industry. *Annual Review of Energy and the Environment 26, 303-329.* https://doi.org/10.1146/annurev.energy.26.1.303

[2] Martínez, F.J., González-Vidosa, F., Hospitaler, A., Yepes, V. (2010). Heuristic Optimization of RC Bridge Piers with Rectangular Hollow Sections. *Computers & Structures*, *88(5-6)*, 375-386. https://doi.org/10.1016/j.compstruc.2009.11.009

[3] Payá-Zaforteza, I., Yepes, V., González-Vidosa, F., Hospitaler, A. (2010). On the Weibull cost estimation of building frames designed by simulated annealing. *Meccanica, 45(5)*, 693-704. https://doi.org/10.1007/s11012-010-9285-0

[4] Molina-Moreno, F., García-Segura; Martí, J.V., Yepes, V. (2017). Optimization of Buttressed Earth-Retaining Walls using Hybrid Harmony Search Algorithms. *Engineering Structures, 134*, 205-216. https://doi.org/10.1016/j.engstruct.2016.12.042

[5] Torres-Machí, C.; Chamorro, A., Pellicer, E., Yepes, V., Videla, C. (2015). Sustainable pavement management: Integrating economic, technical, and environmental aspects in decision making. *Transportation Research Record, 2523*, 56-63. https://doi.org/10.3141/2523-07

[6] Zadeh, L. (1973). Outline of a new approach to the analysis of complex systems and decision processes. *IEEE Transactions on Systems, Man, and Cybernetics 3*, *28–44.* https://doi.org/10.1109/TSMC.1973.5408575

[7] Smarandache, F. (1999). A *unifying field in logics, neutrosophy: Neutrosophic probability, set and logic,* p.157. Publisher: American Research Press, Rehoboth. ISBN 978-1-59973-080-6

[8] Navarro, I.J., Yepes, V., & Martí, J.V. (2020). Sustainability assessment of concrete bridge deck designs in coastal environments using neutrosophic criteria weights. *Structure and Infrastructure Engineering 16 (7), 949-967*. https://doi.org/10.1080/15732479.2019.1676791

[9] Sánchez-Garrido, A.J., Navarro, I.J., & Yepes, V. (2021). Neutrosophic multi-criteria evaluation of sustainable alternatives for the structure of single-family homes. *Environmental Impact Assessment Review 89, 106572*. https://doi.org/10.1016/j.eiar.2021.106572

[10] Pons, J.J., Penadés-Plà, V., Yepes, V., & Martí, J.V. (2018). Life cycle assessment of earth-retaining walls: An environmental comparison. *Journal of Cleaner Production 192, 411-420*. https://doi.org/10.1016/j.jclepro.2018.04.268

[11] Saaty, T.L. (1980). The Analytic Hierarchy Process; Publisher: McGraw-Hill, New York.

[12] Deli, I. & Subas, Y. (2017). A ranking method of single valued neutrosophic numbers and its applications to multi-attribute decision making problems. *International Journal of Machine Learning and Cybernetics* 8, 1309–1322. https://doi.org/10.1007/s13042-016-0505-3

[13] Ye, J. (2017). Subtraction and Division Operations of simplified neutrosophic sets. *Information* 8, 51–58. https://doi.org/10.3390/info8020051

[14] Liang, R., Wang, J. & Zhang, H. (2018). A multi-criteria decision-making method based on single-valued trapezoidal neutrosophic preference relations with complete weight information. *Neural Computing and Applications* 30, 3383–3398. https://doi.org/10.1007/s00521-017-2925-8

[15] Sodenkamp, M. A., Tavana, M., & Di Caprio, D. (2018). An aggregation method for solving group multi-criteria decision-making problems with single-valued neutrosophic sets. *Applied Soft Computing* 71, 715–727. https://doi.org/10.1016/j.asoc.2018.07.020

[16] Ministerio de Fomento (2008). Instrucción de Hormigón Estructural. EHE-08.

[17] Goedkoop, M., Heijungs, R., Huijbregts, M., De Schryver, A., Struijs, J., & Van Zelm, R. (2009). ReCiPe 2008: A life cycle impact assessment method which comprises harmonised category indicators at the midpoint and the endpoint level. The Hague: Ministerie van Volkshuisvesting, 2009.

[18] Huijbregts, M.A.J., Steinmann, Z.J.N., Elshout, P.M.F., Stam, G., Verones, F., Vieira, M., Zijp, M., Hollander, A., & Van Zelm, R. (2016). ReCiPe2016: A harmonised life cycle impact assessment method at midpoint and endpoint level, *The International Journal of Life Cycle Assessment* 22, 138-147. https://doi.org/10.1007/s11367-016-1246-y

[19] Chu, T. & Tao, C. (2002). Ranking fuzzy numbers with an area between the centroid point and original point. Computers & Mathematics with Applications *43*, 111–117. https://doi.org/10.1016/S0898-1221(01)00277-2

Numerical simulation of high-efficiency one pass welding process in thick steel plates considering hardening effects

Vukovojac, Marin[1]; Jalušić, Boris[1]; Perić, Mato[2]; Skozrit, Ivica[1]; Tonković, Zdenko[1]

ABSTRACT

In recent years, there has been a tendency to increase the efficiency of existing welding processes. This is most commonly done by achieving higher molten metal deposition rates, which is extremely important for welding steel structures of significant thickness. The buried-arc methodology allows the welding of plates up to 30 mm in thickness by only using one pass. There is a lack of data on the applicability of this relatively new welding method and is necessary to investigate this procedure experimentally and numerically. Numerical simulations are increasingly used for predicting residual stress distributions and could replace expensive experimental measurements in the future. In this paper, a prescribed temperature approach was used in order to reduce model preparation and computation time. The obtained results are compared to the previous work of authors using the constant heat flux method for simulating heat input during welding. The influence of strain hardening on residual stress distribution was considered by using bilinear isotropic and kinematic hardening models.

Keywords: structural steel, strain hardening, plasticity models, D-Arc welding, thick plates

1. INTRODUCTION

Welding is one of the cheapest and most widespread production processes of joining two or more base materials made of metal. In recent years, efforts have been made in increasing the efficiency of some of the existing welding processes. Hence, aims have been directed to reduce the consumption of additional material and/or shielding gases and increase the molten metal deposit per unit time without a major degradation of mechanical properties and weld quality. This is especially pronounced in industries such as shipbuilding, pipeline industry, heavy-duty machinery and defense industry, where the welding of parts with great thickness is a necessity. Until now, the welding of thick-walled structures was in most cases conducted in several passes. Therein, a major drawback being significant consumption of time and resources due to joint preparation, which is usually subjected to cyclic heat input. This results in local microstructure changes in the fusion zone (FZ) and heat affected zone (HAZ) of the base material (BM) and coarsening of the grains at higher heat inputs, which inevitably affects the mechanical properties of the welded joint [1]. On the other hand, there are certain welding technologies such as submerged arc welding, electron beam welding, hybrid laser-arc welding, etc.,

[1] *Chair for mechanics and strength of materials. Faculty of Mechanical Engineering and Naval Architecture (CROATIA). marin.vukovojac@fsb.hr (Corresponding author), boris.jalusic@fsb.hr (Corresponding author), ivica.skozrit@fsb.hr, zdenko.tonkovic@fsb.hr*

[2] *Bureau of Energetics and Mechanical Engineering Ltd. Bestprojekt (CROATIA). mato.peric@fsb.hr*

that are able to achieve full penetration and weld thick plates in a single pass. However, they do not give satisfactory results in respect to high amounts of time spent on joint preparation, unsatisfactory weld quality and microstructure, distortion of the weld and high heat input.

A few years ago, Japanese scientists improved the high-efficiency modified gas metal active welding (GMAW) technology implementing high current and buried arc, which enables the welding of plates up to a thickness of 30 mm in single pass. With this procedure, it is possible to achieve full penetration due to the fact that the electric arc and the molten wire tip are located under the surface level of the molten metal [2]. Perić and co-workers [3] did an experimental procedure where two plates made of low carbon steel were welded in a single pass using the aforementioned technology without weld groove preparation. Residual stresses were measured using the deep hole drilling (DHD) method after air-cooling to room temperature. Baba et al. [4] used the electron backscatter diffraction (EBSD) for microstructure observation in FZ, HAZ and BM of butt-welded low carbon steel using the same welding technology, with similar parameters and a groove angle of 25°. It was found that the grains were extremely coarse in the area adjacent to the fusion boundary while a mix of coarse and fine grains was observed in the centre of the weld.

Recently, numerical simulations have been developed and used in various industrial fields in order to replace the expensive and time-consuming experimental measurements. For that reason, they are also applied in the field of welding in order to predict residual stresses and the deformations of a welded joint. Since the welding process consists of transient and non-linear heat transfer, expansion and shrinkage, numerical simulations related to welding usually consist of both thermal and mechanical analysis, where the two can be solved simultaneously or sequentially. In other words, simultaneously means that temperature field calculus depends on the distribution of residual stresses, deformations and vice-versa, while sequential means that the solution of the thermal analysis, in the form of temperature field, is introduced as loading in mechanical analysis. Considering the manner and order of performing these simulations, there are fully coupled and sequentially coupled thermal-mechanical analysis [5]. The most common techniques for simulating the deposit of filler material are the technique of activation and deactivation sets of finite elements (element birth and death - EBD) where heat input is simulated by applying heat flux [6] (classical method) or by prescribing the weld temperature (PWT) [7] as a boundary condition. The PWT is implemented in Abaqus Welding Interface (AWI) plug-in, which enables simpler and faster modelling of welds compared to a classic method. AWI uses sequentially coupled thermal-mechanical analysis whereby the deposit of additional material is modelled by the element EBD technique. This paper is a continuation of the author's research [3] in the field of numerical modelling regarding the buried-arc welding process using the PWT method [8].

Due to the lack of data on the applicability of this method, the results of the mechanical weld material and numerical model tests of heat input by buried electric arc, experimental and numerical investigations of this procedure are of great importance.

2. NUMERICAL ANALYSIS

The starting point for the development of a numerical model is the author’s previous research presented in [3]. In this work, experimental measurements and numerical modelling of the buried-arc

welding process of two thick S355J2+N butt-welded plates were conducted. In this numerical model, the heat input was modelled using a uniformly volumetric distributed heat flux, named constant heat flux (CHF), shown in Eq. (1).

$$Q = \frac{\eta UI}{V_H} \tag{1}$$

In Eq. (1) η, U, I are heat input efficiency, welding voltage, and welding current, respectively. The total heat flux applied to the weld volume V_H is $Q = 6.27 \times 10^{10}$ $Jm^{-3}s^{-1}$.

Based on the previous author's work and the PWT method, the main goal here is to create a welding model that could be applied to more complex structures. Therein, the preparation of the model should require less time and utilization of simpler procedures, resulting in numerically less demanding computations. Due to the symmetry conditions, only half of the model was numerically modeled (right plate, Fig. 2). Assuming that the base and filler materials have the same thermal and mechanical properties, two identical material models were made using the low-alloy low-carbon steel S355J2+N temperature-dependent properties, one being defined as the base metal and the other as the weld metal. Several plasticity models were implemented in order to investigate their influence on the distribution of residual stresses. They include an elastic-ideal plastic (EIP), isotropic hardening (IH) and kinematic hardening (KH) model. For the IH and the KH, bilinear-hardening models were used. All thermal and mechanical properties of the material are given in [9]. It should be mentioned here that in the computations, the influence of phase transformations on the distribution of residual stresses and strains is not considered because it should be negligible in low carbon steels [10]. The annealing effect was taken into account and the annealing temperature was assumed to be 1000 °C, while transformation plasticity was not considered. Keeping in mind these simplifications, the total strain increment can be decomposed into three components, in the form of Eq. (2).

$$d\epsilon^{total} = \{d\epsilon^{e}\} + \{d\epsilon^{p}\} + \{d\epsilon^{th}\} \tag{2}$$

In Eq. (2), $\{d\varepsilon^{e}\}$, $\{d\varepsilon^{p}\}$, and $\{d\varepsilon^{th}\}$ are elastic, plastic, and thermal strain increments, respectively. A more detailed explanation of the numerical model was provided in the authors' previous work [11]. Fig. 1 shows a single-plate model (right plate, Fig. 2) meshed using 24,000 finite elements modelled to monitor and compare the temperature distribution over time using CHF and PWT methods with respect to the position of the thermocouples (Fig. 2). The weld is 300 mm long and the welding speed is taken as 300 mm/min, which means that every second an element of 5 mm in length with a prescribed weld temperature is inserted along the weld. Adjacent to the weld, in the HAZ, a very fine mesh was used in order to describe more precisely the nonlinearity of the process, while a coarser mesh was utilized in the rest of the model to reduce the degrees of freedom of the model and speed up the calculation process.

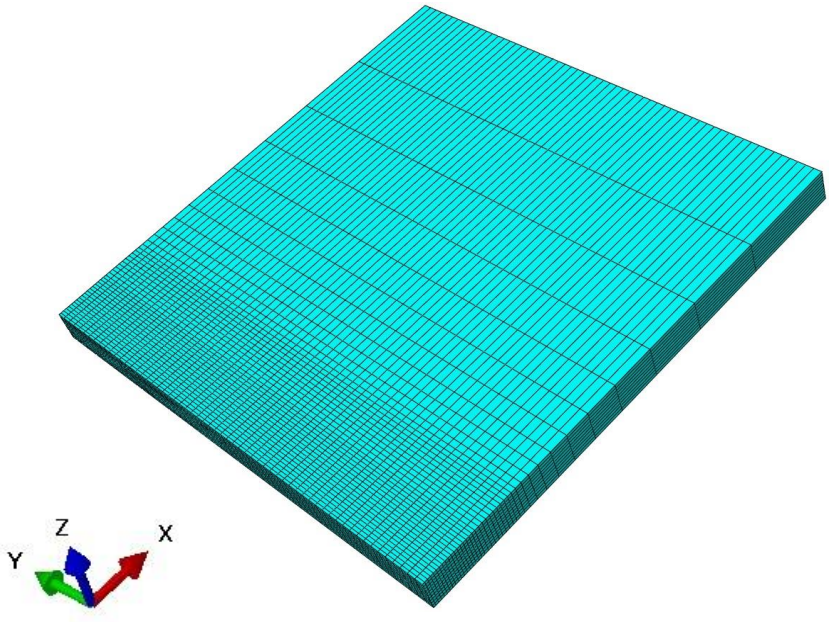

Figure 1. *Single-plate model mesh.*

In the PWT method implemented in AWI, modelling of filler metal deposition is achieved using the EBD technique in both the thermal and mechanical analysis. AWI automatically creates models for thermal and mechanical analysis, in other words, it creates steps, thermal boundary conditions, temperature fields and files related to the thermal and mechanical analysis. This enables significant time reduction needed for the "manual" preparation of the welding model. Unlike the CHF method, where the heat input simulation is performed by defining the heat flux using welding parameters, the PWT method requires the user to set a welding arc temperature, which is not so simple and straightforward because it requires an iterative determination procedure. After several iterations, 2675°C was chosen as the weld temperature value. If the model consists of only half of the intended joint, symmetry boundary condition must be included. Also, it is necessary to specify the welding speed, in other words, the length of the weld chunk that will be deposited in a unit of time as part of the EBD technique. Furthermore, the surfaces that dissipate heat by means of convection and radiation are defined. Radiation will be significant in the FZ and HAZ where temperatures are the highest, while convection will be pronounced in the remaining parts of the model. Adopted values of emissivity factor and heat transfer coefficient are $\varepsilon = 0.9$ and $h_c = 10$ Wm^{-2}. It is necessary to define cooling in the last step of the thermal analysis which extends through the thermal and mechanical analysis. Surfaces interacting with the environment are the same as those used for defining thermal boundary conditions during welding. Before AWI creates analysis files, it is necessary to specify the type of finite elements for thermal and mechanical analysis. According to Abaqus software nomenclature, DC3D8 finite elements with eight nodes were used in the thermal analysis, while C3D8I finite elements were used in the mechanical analysis. The number of finite elements used in the thermal and mechanical analysis was the same.

Since the introductory chapter states that AWI uses a sequentially coupled thermal-mechanical analysis, it is necessary to specify mechanical boundary conditions after the completion of the thermal analysis, i.e. before starting the mechanical analysis. The plates were free-welded, also without any

mechanical constraints, but they were added in the mechanical analysis to prevent the structure motion as a rigid body (Fig. 2).

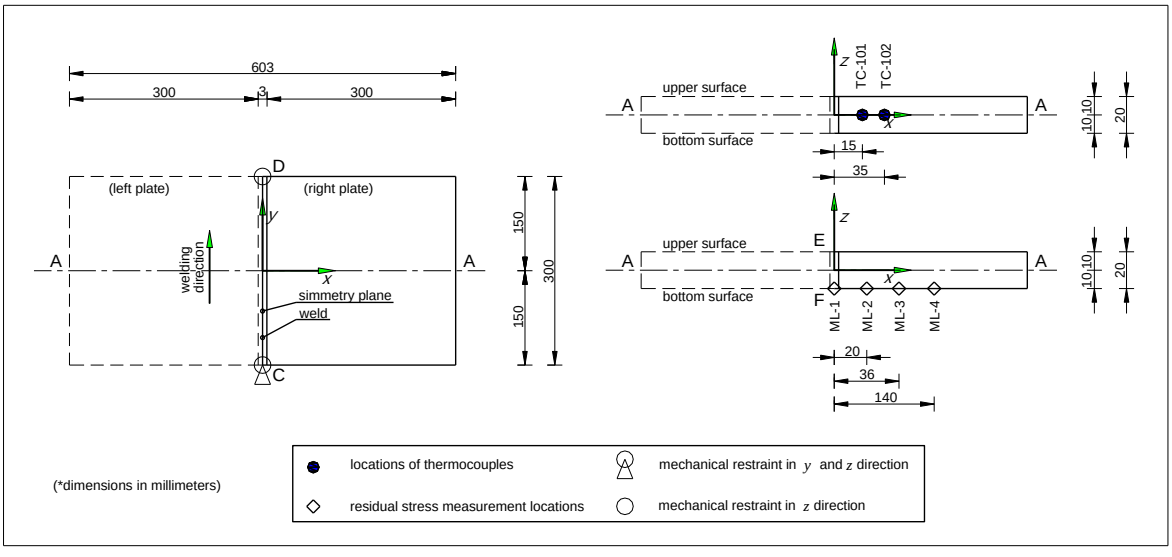

Figure 2. *Mechanical boundary conditions for the single-plate model.*

3. RESULTS

Several full analyses were made during this research and the results concerning temperature profiles, predicted residual stresses and computation time are presented in the following sections.

3.1. Temperature profiles

As shown in Fig. 3, the numerical results of the thermal analysis using the PWT method, i.e. temperature profiles for first 500 s after start of welding, are compared to the results of the thermal analysis obtained by the CHF method. As it can be seen, the achieved temperature profiles of both methods are in very good agreement with the experimental measurements from thermocouples TC-101 and TC-102.

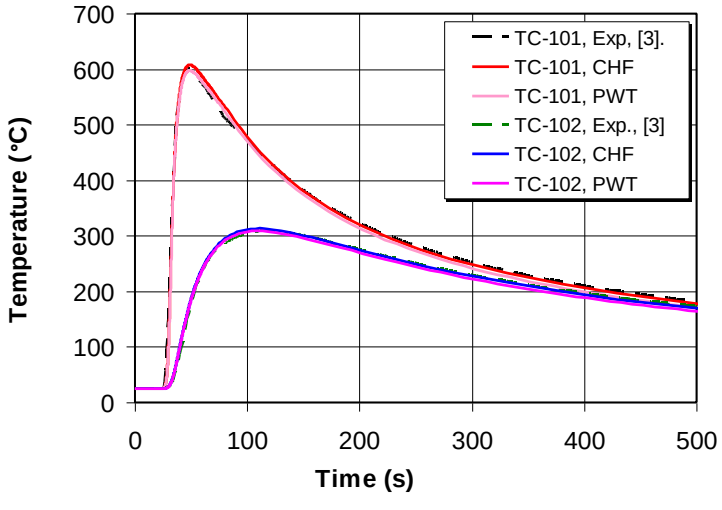

Figure 3. *Comparison of temperature profiles using both methods (Fig. 2).*

3.2. Predicted residual stresses

All the results obtained using the PWT method are compared to the full model using the CHF method with the EIP material model, which was in good agreement with the experimental measurements using the hole drilling method. When comparing longitudinal and residual stresses along line A-A at the model bottom surface (Fig. 2), which is portrayed in Figs. 4-7, it can be seen that all plasticity models produce very similar results, except for the longitudinal residual stresses in x direction in the near vicinity of the FZ and longitudinal residual stresses in y direction, along the weld line. As it can be seen in Fig. 4, the EiP model predicts lower tensile longitudinal residual stresses near the near vicinity of the FZ than the IH and KH models. Peak tensile stress value of around 386 MPa is predicted by the EiP and KH models 20 mm from the FZ, while the IH model predicts peak tensile stress values of around 395 MPa 15 mm from the FZ. All the aforementioned peak tensile stresses are higher than the yield stress of the utilized steel. Predicted distributions of longitudinal stresses along line A-A are in good agreement with the experimentally measured values at ML-1, ML-3 and ML-4 (Fig. 2).

Transversal residual stresses along line A-A (Fig. 2) are not significantly affected with the implementation of different plasticity models, as shown in Fig. 5. All stresses are tensile and the peak stress of 242 MPa is located 22 mm from the weld centreline. Predicted distributions of transversal stresses along line A-A are in good agreement with the experimentally measured values at the ML-1 and ML-4 (Fig. 2).

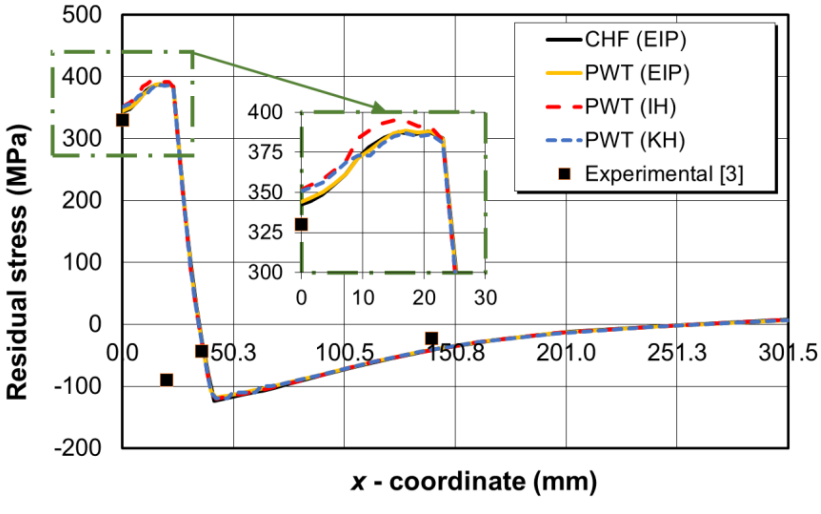

Figure 4. *Longitudinal residual stresses along section A-A (Fig. 2)*

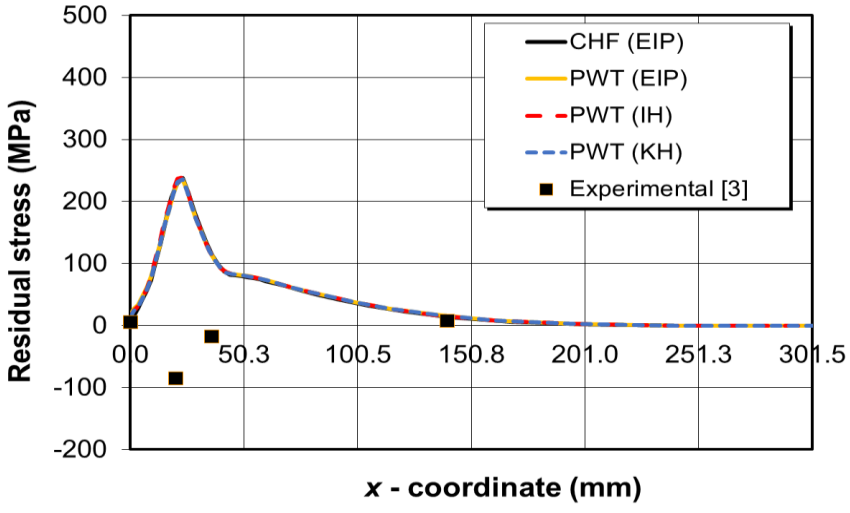

Figure 5. *Transversal residual stresses along section A-A (Fig. 2).*

Greater differences in predicted residual stresses for different plasticity models can be seen along the C-D line at the bottom model surface (Fig. 2), in the welding direction. Firstly, Fig. 6 and 7 show small differences in the predicted residual stresses at the start and end of the weld between the PWT method and CHF method. This confirms the theory that the PWT method can be successfully used in order to reduce model preparation time without significant discrepancy of predicted residual stresses. Secondly, all material models seem to over-predict residual stresses. The IH and KH seem to predict higher residual stresses than the EIP, which is in agreement with literature [12]. Both hardening models predict similar residual stress distributions at the start and end of the weld with respect to the EIP material model. Since the peak values of tensile residual stresses in the longitudinal direction present the highest risk in the exploitation of welded structures, their prediction is of highest importance. Fig. 6 shows the predicted distributions of longitudinal stresses along the weld line. At the start of the weld, all PWT models predict lower tensile stresses than the CHF model. The highest values of longitudinal residual stresses along line C-D at the model bottom surface (Fig. 2) are predicted at the half distance of total weld length.

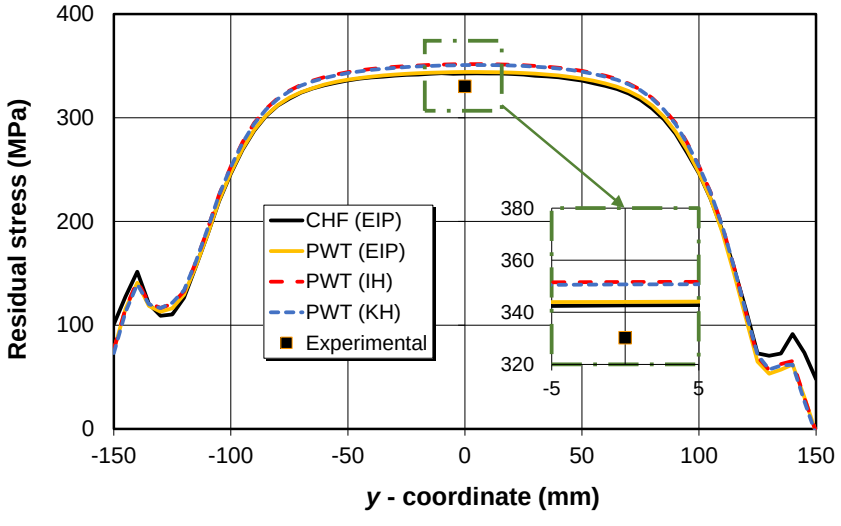

Figure 6. *Longitudinal residual stresses along section C-D.*

It can be seen that all models seem to over-predict residual stresses with respect to the experimentally measured value at ML-1 (Fig. 2). The difference between the measured and calculated residual stresses can be attributed to the introduced initial stresses during steel fabrication. A feasible procedure to eliminate initial stresses is to anneal the plates at high temperatures. Unfortunately, the annealing procedure before the start of welding was not performed in this study.The EIP model predicts a peak tensile stress value of 344 MPa, while the IH and KH models predict a peak stress of around 351 MPa. At the end of the weld, all models predict tensile stresses. Fig. 7 shows the distribution of transversal residual stresses along section C-D at the model bottom surface. At the start and end of the weld, all plasticity models predict compressive residual stresses with differences in magnitude. When closer to mid-way of the weld, residual stresses turn to tensile stresses of very small magnitude.

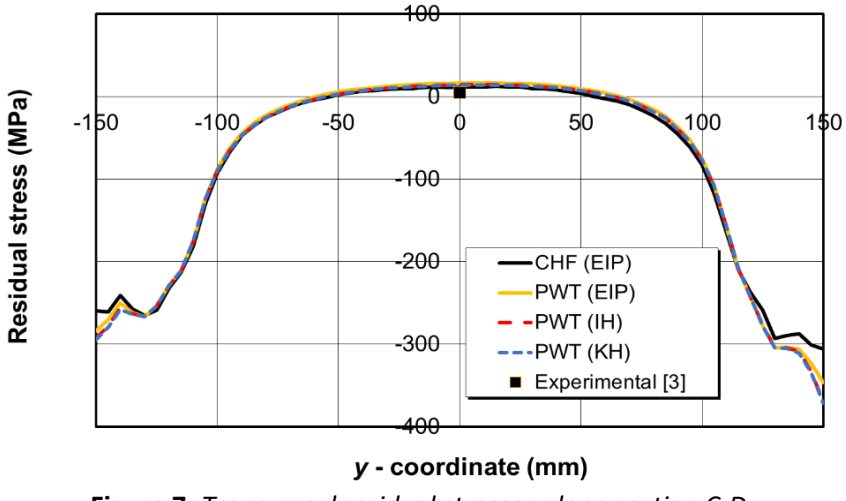

Figure 7. *Transversal residual stresses along section C-D.*

The IH and KH model predict very similar distribution of residual stresses along line A-A and C-D (Fig. 4-7), which is in contrast with the literature. This could be due to the fact that material hardening was defined using only two sets of stress-plastic strain data (linear hardening) for both the IH and KH material model. The number of welding passes could also have some influence on predicted residual stress distribution using the KH model because of multiple thermal cycles, which cause cyclic expansion and contraction of the material near the FZ.

3.3. Computation time comparison

In total, five sequentially coupled numerical analyses were conducted i.e. full numerical (FM) models using the CHF and PWT method with the EIP material model, single-plate models with the EIP material model, IH and KH by implementing symmetry boundary conditions. All of the computations were done by computer with Intel® Xeon® CPU E5-1620 v3 @ 3.50GHz and 24 GB RAM. Three out of four cores were used during the computation. Wall-clock time was compared for both thermal and mechanical analyses. Table 1 shows a comparison in wall-clock time regarding thermal analyses for the CHF and PWT methods. Thermal analysis using the PWT is 858s faster than the analysis using the CHF method, which is insignificant.

Table 1. *Wall-clock time for thermal analysis.*

Material model	Value	
	CHF	**PWT**
Elastic-ideal plastic, FM	23,996 s	23,138 s
Elastic-ideal plastic, SP	-	12,106 s
Isotropic hardening, SP	-	13,275 s
Kinematic hardening, SP	-	13,297 s

A more significant difference can be seen in the duration of mechanical analyses for both methods as is presented in Table 2. Mechanical analysis using the PWT is faster by 8,301s in comparison to the analysis using the CHF method. This difference is substantial as the goal is to use these welding simulation procedures for larger and more complex structures.

Table 2. Wall-clock time for mechanical analysis.

Material model	Value	
	CHF	**PWT**
Elastic-ideal plastic, FM	38,766 s	30,465 s
Elastic-ideal plastic, SP	-	14,001 s
Isotropic hardening, SP	-	13,089 s
Kinematic hardening, SP	-	14,705 s

As mentioned in the introductory section, model creation using the AWI plug-in saves a lot of time in the preparation of numerical models which is an additional plus when conducting a welding simulation for larger structures.

4. CONCLUSIONS

A numerical simulation of the buried-arc welding process using the PWT method and EIP material model was conducted. The results of thermal and mechanical analyses were compared to an experimentally verified numerical model using the CHF method and distributions of predicted residual stresses were in good agreement. There are some differences at the start and end of the weld which could be related to differences in simulating heat input. Strain hardening material models were also considered and the results showed there was no significant influence of strain hardening on the predicted longitudinal and transversal stresses for several reasons. The IH and KH were modelled using only two sets of stress-plastic strain data where hardening was considered only up to 10% of plastic deformation and tensile stress up to 423 MPa at 0°C. It is necessary to include more stress-plastic strain data to see the actual difference in predicted residual stresses for various hardening models, which would be the scope of further investigations. Therein, a mixed-hardening model could also be included.

The computational times of both methods were compared and data showed the PWT method implemented in the AWI plug-in is approximately 2.3 hours faster than the CHF method for the same model. Additional savings could be made by using the simmetry conditions. It is worth to mention that the AWI enables significant time reduction for numerical model preparation. The disadvantage of the AWI plug-in is the need to define the weld temperature and its dependence on the welding geometry, welding parameters, mesh, and mechanical properties of the base and filler material. It was concluded that the AWI can be a powerful tool for the welding simulation in complex structures.

ACKNOWLEDGEMENTS

This work has been supported and co-funded by the European Union through the European Regional Development Fund, Operational Programme "Competitiveness and Cohesion" 2014 – 2020 of the Republic of Croatia, project "Improvement of high-efficiency welding technology" (ImproWE, KK.01.1.1.07.0076).

REFERENCES

[1] Srinivasan, L., Deepan Bharathi Kannan, T., Sathiya, P., Biju, S. (2017). Effect of heat input, heat treatment on microstructure and mechanical properties of GTA welded aerospace material 15CDV6. *J Mater Res*, *32(7)*, *1361–1366*.

[2] Baba, H., Era, T., Ueyama, T., Tanaka, M. (2017). Single pass full penetration joining for heavy plate steel using high current GMA process. *Weld World*, *61(5)*, *963–969*.

[3] Perić, M., Garašić, I., Tonković, Z., Vuherer, T., Nižetić, S., Dedić-Jandrek, H. (2019). Numerical prediction and experimental validation of temperature and residual stress distributions in buried-arc welded thick plates. *Int J Energy Res*, *43(8)*, *3590–3600*.

[4] Baba, H., Honda, R., Era, T., Komen, H., Tanaka, M., Terasaki, H. (2020). Microstructure Observation of High-Current Buried-Arc Welded Joint. *Q J Japan Weld Soc*, *38(2)*, *11s-15s*.

[5] Yang, YP. (2021). Recent Advances in the Prediction of Weld Residual Stress and Distortion - Part 1. *Weld J*, *100(5)*, *151–170*.

[6] Perić, M., Nižetić, S., Tonković, Z., Garasić, I., Horvat, I., Boras, I. (2020). Numerical simulation and experimental investigation of temperature and residual stress distributions in a circular patch welded structure. *Energies*, *13(20)*, *1–11*.

[7] Friedrich, N., Ehlers, S. (2019). A simplified welding simulation approach used to design a fatigue test specimen containing residual stresses. *Sh Technol Res*, *66(1)*, *22–37*.

[8] Seleš, K., Perić, M., Tonković, Z. (2018). Numerical simulation of a welding process using a prescribed temperature approach. *J Constr Steel Res*, *145*, *49–57*.

[9] Perić, M., Tonković, Z., Rodić, A., Surjak, M., Garašić, I., Boras, I., et al. (2014). Numerical analysis and experimental investigation of welding residual stresses and distortions in a T-joint fillet weld. *Mater Des*, *53*, *1052–1063*.

[10] Deng, D. (2009). FEM prediction of welding residual stress and distortion in carbon steel considering phase transformation effects. *Mater Des*, *30(2)*, *359–366*.

[11] Perić, M., Seleš, K., Tonković, Z., Lovrenić-Jugović, M. (2019). Numerical simulation of welding distortions in large structures with a simplified engineering approach. *Open Phys*, *17(1)*, *719–730*.

[12] Deng, D., Zhang, C., Pu, X., Liang, W. (2017). Influence of Material Model on Prediction Accuracy of Welding Residual Stress in an Austenitic Stainless Steel Multi-pass Butt-Welded Joint. *J Mater Eng Perform*, *26(4)*, *1494–1505*.

APPLICATION OF NSGA-II TO DESIGN MULTIPLE MITIGATION DEVICES IN SLENDER STRUCTURES

Pérez Vázquez, Elena [1]; Posada Clavo, Marta [2] Magdaleno González, Alvaro[3] Lorenzana Ibán, Antolín[4]

ABSTRACT

In this paper, the multi-objective evolutionary algorithm, Non Dominated Sorting Genetic Algorithm (NSGA-II), is applied to solve the design of passive mitigation devices, commonly referred to as Tuned Mass Dampers (TMD). A common challenge is obtaining a set of optimal Pareto Points, evenly distributed along the Pareto Front.

Two usual states are used as objective functions to articulate the multi-objective optimization procedure. The Serviceability Limit States (SLS, objective number 1) can be evaluated through the accelerance frequency response functions and the Ultimate Limit States (ULS, objective number 2) is considered by evaluating the drift between storeys when undergoing, for example, a particular earthquake.

The results have shown that NSGA-II is able to obtain the Pareto Front, indicating the TMD or TMDs to install, considering those two objective functions, under the condition that the mass of the TMDs to be put is bounded.

Keywords: tuned mass damper, multi-objective optimization, genetic algorithm, ultimate limit state, serviceability.

1. INTRODUCTION

In this paper, evolutionary multi-objective optimization method is applied to assist in the design of passive mitigation devices, commonly referred to as Tuned Mass Dampers (TMDs), to obtain, complying with standards, the best safety and comfort values of slender structures.

A general multi-objective optimization problem (MOP) can be defined as shown in Eq. (1).

$$min/max\ \boldsymbol{y} = f(x) = \{f_1(\boldsymbol{x}), f_2(\boldsymbol{x}), \dots, f_m(\boldsymbol{x})\} \quad (1)$$
$$subject\ to\ \boldsymbol{x} = \{x_1, x_2, \dots, x_n\} \in X \ \ and\ \boldsymbol{y} = \{y_1, y_2, \dots, y_m\} \in Y$$

[1] *Departamento Organización Industrial y CIM. Universidad de Valladolid (SPAIN). elena@eii.uva.es (Corresponding author)*

[2] *Departamento Organización Industrial y CIM. Universidad de Valladolid (SPAIN). posada@eii.uva.es*

[3] *Departamento Construcciones Arquitectónicas, Ingeniería del Terreno y Mecánica de los Medios Continuos y Teoría de Estructuras. Universidad de Valladolid (SPAIN). alvaro.magdaleno@uva.es*

[4] *Departamento Construcciones Arquitectónicas, Ingeniería del Terreno y Mecánica de los Medios Continuos y Teoría de Estructuras. Universidad de Valladolid (SPAIN). ali@eii.uva.es*

In Eq. (1), objectives often contradict each other. In these cases, the set of solutions of a MOP consists of all decision vectors for which the corresponding objective vectors cannot be improved in any dimension without degradation in another. Each solution x^i is called pareto optimal point and their set is known as Pareto Front (PF). The PF is, thus, the set of nondominated solutions to the problem in Eq. (1). In a minimization problem, and without loss of generality, it can be stated that $x^1, x^2 \in X$, where the solution x^1 is said to dominate the solution x^2 ($x^1 \prec x^2$) when the conditions in Eq. (2) are satisfied.

$$f_j(\boldsymbol{x^1}) \leq f_j(\boldsymbol{x^2}) \; \forall \; j \in \{1,2,\dots m\} \;\; \exists \; j \in \{1,2,\dots m\} \mid f_j(\boldsymbol{x^1}) < f_j(\boldsymbol{x^2}) \tag{2}$$

Metaheuristic algorithms, and more specifically multi-objective evolutionary algorithms (MOEAs), can be applied to solve problems that contain complex restrictions [1]. A common challenge is obtaining the infinite set of optimal Pareto points in continuous MOP. However, it is impossible to calculate the complete PF in a reasonable time. Therefore, multiobjective evolutionary algorithms (MOEAs) expect to obtain an appropriate number of Pareto points uniform and smoothly distributed on the PF. In this work, a MOEA is applied to assist in the design of TMDs, installed on lively and slender structures to reduce their level of response. They can be modeled as single-degree-of-freedom (SDOF) systems, as they primarily consist of a moving mass (mt), an elastic member (kt) that joints the mass to the structure and a damper (ct). Multi-story buildings are typical slender structures. Fig. 1 shows a model for 2-story building with a TMD installed on its top floor. When appropriately tuned, TMDs are capable of drastically reducing the dynamic response of the structure in which they are installed. In general terms, the mitigation only affects the structural response in a narrow frequency band around one of the natural modes (i.e, the mode for which the TMD has been designed) drastically reducing their contribution. If the contribution of more modes needs to be mitigated, then more TMDs should be installed. There are multiple works in the literature focused on finding optimal parameters of isolated TMDs.

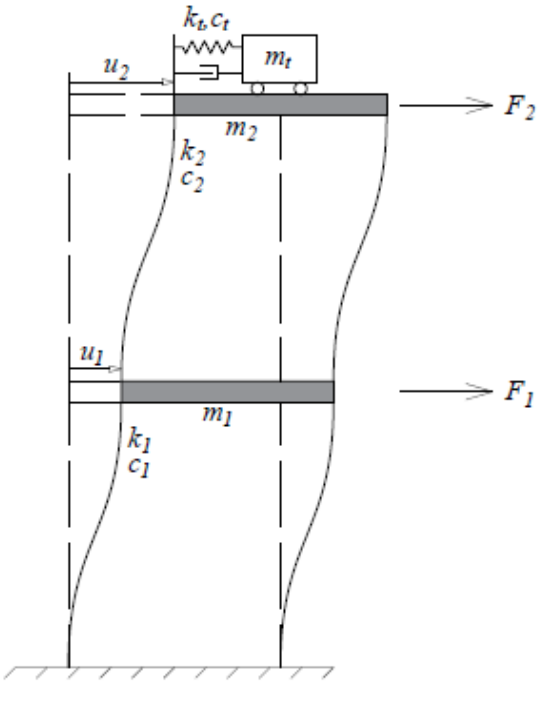

Figure 1. *2-story building with a TMD installed on its top floor*.

It is desirable for a structure to be comfortable, functional and safe at the same time, regardless the loads to which it is subjected. To meet this, some standards provide guidelines in terms of limit values for some physical magnitudes such as stresses (safety) or accelerations (comfort). In this sense, these standards make the difference between Serviceability Limit States (SLS) and Ultimate Limit States (ULS). The SLS usually defines threshold values for the acceleration response taking into consideration the perception of the occupants of the structure. The ULS focuses on the highest stresses the material can eventually develop when the structure is subjected to the worst loading scenario. In this paper, these two states are used as objective functions to articulate the MOP under study. Note that both the effectiveness of the device and its cost highly depend on the value of its moving mass, being desirable to achieve the required protection by using the minimum amount of moving mass.

A MOEA is proposed to consider both requirements at the same time. The algorithm will provide a set of TMD tuning properties (moving masses, frequencies, and damping ratios) for various scenarios. In all cases, the TMD parameters simultaneously minimize two objective functions: f_1 = JSLS (associated to SLS), and f_2 = JULS (associated with ULS). Each set of properties is represented by a point on the plane JSLS-JULS, no-dominate points draw the PF. To differentiate between solutions, some thresholds are defined for both objective functions and, based on them, the region of acceptable solutions will be separated from the region of non-acceptable ones.

Having described the 2-objective functions, one of the biggest difficulties in applying MOEAs in real-life problems is finding the proper coding process, crossover and mutation operators and the setting of parameters. We use the Non Dominated Sorting Genetic Algorithm II (NSGA-II), one of the most used nowadays MOP [2]. In NSGA-II, the nondominated solutions are saved from generation to generation in the population which has a fixed size (N) (instead of in an external archive as others MOEAs) and they are classified in successive fronts.

In MOP, determining the performance of different MOEAs is difficult because we need to compare several vectors (front) unlike only one solution. In this regard, the focus is in generate as many elements as possible of the optima Pareto front (PF), obtaining nondominated solutions uniformly smooth on the front and extreme values of objective functions, and obtaining the front in a robust way instead of occasionally [3]. To address this problem, there are several metrics [4, 5]: the Maximum Spread (MS) [3], the Normalized Spacing (SP) [6], the Hypervolume (HPV) [7], the Normalized Generational Distance (GD) [8], and cardinality metric such as the number of nondominated solutions in the front. Furthermore, it should be noted that MOEAs are stochastic, and several runs are needed to assess their performance. In each run a front is obtained, nondominated solutions of all fronts is the envelope-PF (EPF). Other metric to consider is the number of nondominated solutions in EPF (|EPF|), and how many solutions belong to the optimal Pareto front (%EPF $\in$ PF).

2. Multi-Objective Evolutionary Algorithms and their implementation.

One of the main difficulties in applying MOEAs to a real-life is the need to find the proper coding process, crossover and mutation operators and parameter settings.

2.1. Coding process and objective functions

For the particular case shown in Figure 1, it could be considered to put a single TMD (1TMD, in one of the floors and tuned to one of the modes) or two TMDs (2TMD). In the latter case the sum of their masses must equal the mass of the 1TMD case, and both can be located on floor 1, or on floor 2 or one on each floor. Each TMD is defined by its mass (M_t), stiffness (Kt), damping (Ct) and location (floor). These 4 parameters are x1, x2, x3 and x4 for the 1TMD case and x1, x2, x3, x4, x5, x6, x7 and x8 for the 2TMD case, where x1 and x2 are the masses, x3 and x3 the stifnesses and so on.

Each solution of the search space x^1 are coded by those four variables (genes) for each TMD and two objective functions. Thus, depending on the number (T) of TMD (Eq. 3):

$$\text{For T=1, } x^1 = [x_1^1, x_2^1, x_3^1, x_4^1, f_1, f_2] \qquad (3)$$
$$\text{For T=2, } x^1 = \left[x_1^1, x_2^1, x_3^1, x_4^1, x_5^1, x_6^1, x_7^1, x_{8,}^1 f_1, f_2\right]$$

With:

$x_g^1 \in \{0, M_t\}\ s.a. \sum_{g=1}^{T} x_g^1 = M$ This variable is the mass of each TMD. Note that M must be the total added mass. It is a continuous value.

$x_g^1 \in \{0, Kt\}\ \forall\ g = \{T+1, T\times 2\}$ This variable is the stiffness constant. It is a continuous value.

$x_g^1 \in \{0, Ct\}\ \forall\ g = \{(T\times 2)+1, T\times 3\}$ This variable is the viscous damping constant. It is a continuous value.

$x_g^1 \in \{1, T\}\ \forall\ g = \{(T\times 3)+1, T\times 4\}$ This variable is the floor number. It is a discrete value.

Objective function 1 f_1:. Maximum of Frequency Response Functions (JSLS)

The Frequency Response Functions (FRFs) are calculated as the magnitude of each transfer function between inputs and outputs. In this work, and for the serviceability evaluation purposes, only accelerances will be considered, i.e. the FRF with accelerations as outputs. Each point of the FRF represent the output-input ratio for every excitation frequency and the maxima is associated with the resonance phenomenon (high response levels). Assuming a wide frequency band excitation which includes several peaks, the reduction of them involves necessarily a reduction of the response.

The indicator of serviceability, JSLS, is calculated as the maximum of all FRF maxima, but only in a range of interest ($[\omega_a, \omega_B]$, see Eq. (4)). Since the objective of this indicator is to evaluate the serviceability of the structure, when deciding the values for ω_a and ω_b not only the frequency band of the excitation should be considered but also the band in which people is more sensitive to oscillations should be considered.

$$J_{SLS} = \max\left(\max\left(FRF_i(\omega)\right)\right) \qquad where\ \omega \in [\omega_a, \omega_b] \qquad (4)$$

Objective function 2 $\mathbf{f_2(x)}$: Maximum normal stress (JULS)

This indicator considers the stresses developed inside the material. The aim is to minimize this indicator not only to assure that no point of the structure reaches its yield stress but also to reduce the possibility of fatigue failure. The buildings bending in the horizontal direction is only caused by the deformation of the columns and the floors can be supposed to be rigid bodies. Regarding the strength of materials theory, the maximum stress in a column-wise element with a double-clamped-like deformed shape (typical in columns of shear buildings, see Figure 1) occurs at its ends, where the bending moment is maximum. The value of this bending moment is proportional to the shear relative displacement (or drift, δ), Eq. (5).

$$M_i = \frac{6EI_i}{L_i^2}\delta_i \;\; \delta_i = u_{i+1} - u_i \tag{5}$$

Where E is the representative Young's modulus of the material, I_i is the representative second order moment of inertia of the column and L_i is the length of the column (distance between floors). Properties I_i and L_i are defined for every floor (i) and they may change from one to another. Inside a single floor, in the case where there is a variety column sections, since they all suffer the same drift and have the same length L, the representative inertia for that floor I must be the taken as the moment of inertia of the most stressed column at its most stressed end. On the other hand, E may be the same for the whole building.

The maximum normal stress σ_i is directly related to the bending moment via the "height" h of the section where σ_i is registered (its dimension in the direction of the movement, normal to the inertia axis). For these purposes, and without loss of generality, the section is supposed to be symmetric and σ_i is defined for the i-th floor in Eq. (6).

$$\sigma_i = \frac{M_i\, h_i}{2I_i} = 3E\,\frac{h_i}{L_i^2}\delta_i = 3E\;\Delta_\mathrm{i}\;\delta_i \tag{6}$$

In this work, the ratio h_i/L_i^2 is given the name "drift to stress factor" (DSF, Δ_i) and, just like I_i and L_i, is a property of each floor. Assuming that all columns are made out of the same materials and E does not change from one floor to another, minimizing the normal stress involves minimizing the non-dimensional quantity $\Delta_\mathrm{i}\delta_i$.

Once all maximum stresses are calculated all over the simulation time, the J_{ULS} indicator to minimize is obtained as the maximum of all maxima of the absolute value of calculated stresses, whenever and wherever it occurs (Eq. 7).

$$J_{ULS} = \max_\mathrm{i}\left(\max_\mathrm{t}(|\sigma_i(t)|)\right) \tag{7}$$

Although it is not the subject of this work, the state space representation of the dynamic problem of the structure equipped with the TMDs is used in the determination of both J1 (frequency response) and J2 (time response).

An example of a solution for the 2TMD, for the case where the total mass is 0.04 kg, is [0.039, 0.001, 1.795, 4.394, 0.064, 0.015, 2, 1, 14.816, 4.841]. Note that the first TMD includes 39 grams, 1.795 N/m and 0.064 damping, being located at the second floor whereas the second one includes 1 grams, 4.394 N/m and 0.015 damping and located in floor one. Also note that these values correspond to a reduced scaled laboratory model where it is proposed to add 40 grams of mobile mass. For the same model, 60, 80, 100 and 120 grams will be added, as will be seen in the next section.

Recombination operators

Crossover and mutation operators are used to recombination process. They must maintain an adequate balance between diversity and exploiting [9]. For each of 2 solutions (x^1 and x^2) of the offspring population Q_t, the crossover operator produces 2 new solutions (x^{1*} and x^{2*}). The crossover operator usually works with a probability $p_c \in$(80%-90%). Then, x^{1*} and x^{2*} replace x^1 and x^2 in Q_t. When the crossover finishes the mutation operator will modify every i-th gene of each j-th solution (x_i^j) of Q_t with a probability $p_m \in$(1%,10%). Every mutated solution replaces the original one in Q_t.

The crossover operator implemented in the study for the continuous variables is the simulated binary crossover operator (SBX) [10]. The new solutions {x^{1*}, x^{2*}} are created as following equation with i=1,..n:

$$x_i^{1*} = 0.5\left[(1+\beta_i)x_i^1 + (1-\beta_i)x_i^2\right] \qquad (8)$$
$$x_i^{2*} = 0.5\left[(1-\beta_i)x_i^1 + (1+\beta_i)x_i^2\right]$$

In SBX a random number $u_i \in [0,1)$ are chosen for each couple of solutions. The value β_i is calculated by next equations:

$$\beta_i = (2u_i)^{1/\eta+1} \; if \; u_i \leq 0.5 \qquad (9)$$
$$\beta_i = \left(1/2(1-u_i)\right)^{1/\eta+1} \; if \; u_i > 0.5$$

Where η is a parameter to control the distance between {x^1, x^2} and {x^{1*}, x^{2*}}. Large values give high probability creating new solutions near to parents, and small value creating distant solutions, the standard value is η=2.

Genes are exchange with the one-point crossover for discrete variables, $x_i^{1*} = x_i^2 \; and \; x_i^{2*} = x_i^1$

The mutation operator used in continuous variables is the breeder genetic algorithm mutation operator BGA [11]. Given the gen x_i^j, a new value $x_i'^j$ is calculated by next equation for each gen of population with the probability p_m:

$$x_i'^j = x_i^j \pm range_i \times \delta \; with \; \delta = \sum_{k=0}^{15} \alpha_k \, 2^{-k} \qquad (10)$$

Where the + or – are selected with probability 0.5. Before mutation the value of α_k is set to 0 and it is mutated to 1 with probability (1/16). $range_i = 0.1 * (\max x_i^j - \min x_i^j)$.

The mutation operator is the classical in discrete values, that is, $x_i'^j = random(\min x_i^j, \max x_i^j)$.

3. NSGA-II and Metrics.

All evolutionary algorithms are based in Darwinian laws, selection of best individuals (selection) and exchange of their genetic material (recombination). In MOEAs, best individuals of each generation are nondominated solutions. In NSGA-II, the nondominated solutions are saved from generation to generation in the population which has a fixed size (N) (instead of in an external archive) and they are classified in successive fronts. The main steps of this algorithm are the following [2]:

1.- Set of parameters of NSGA-II, codification of solutions, crossover and mutation operators and its probabilities, stopping criterion, N population sets size.

2.- N random solutions are created (population P_t with t=0).

3.- Fitness assignment: Calculate fitness values (f_1 and f_2) of all individuals in P_t.

3.- The population is sorted based on the non-domination level. Level 1 is the best level, level 2 is the next best level, ... All nondominated solutions of P_t belong to level 1. The nondominated solutions of the rest of population belong to level 2. The process goes on until all solutions of P_t are classified in levels.

4.- Best solutions of P_t are selected to form the offspring population Q_t by the tournament crowded selection process. Two solutions of P_t are randomly chosen. The following scenarios are possible:

- Solutions belong to different levels: the solution with lowest level is the winner of the tournament and is chosen to belong to Q_t.
- Both solutions have the same level: the solution that is located in the lesser crowed region by the crowed-process (see 3.1) is the winner.

Then, other two solutions of P_t are randomly chosen. The process goes on until Q_t has N solutions.

5.- Then, Q_t is randomly divided in pairs. The crossover and mutation are applied on every pair, updating Q_t of size N. The fitness value of each new individuals in Q_t is calculated.

6.- The new population $P_t\ with\ t = t + 1$ is formed by the replacement process. Populations P_t and Q_t are combined in R_t and classified in nondominated levels as steep 3. The R_{N_1} will be solutions of level 1, being N_1 the number of solutions of level 1, R_{N_2} will be solutions of level 2, ... Then, the P_{t+1} of size N are formed. First, if $N_1 \leq N$ all solutions of $R_{N_1}$are copied in P_{t+1}. Second, if $N_2 \leq (N - N_1)$ all solutions of R_{N_2} are copied in P_{t+1}. The process goes on until a $N_k > (N - \sum_{j=1}^{k-1}(N_j))$. In this case, all solutions of R_{N_k} has not place in P_{t+1}. $(N - \sum_{j=1}^{k-1}(N_j))$ solutions of R_{N_k} are chosen by the crowded-process (see 3.1). The process returns to step 4 when the P_{t+1} is filled out.

This process goes on until a stopping criterion is achieved, in this case, a particular number of evaluations.

3.1. Crowded-process

Every x^i solution has two attributes:

- $\left(i = I_j^m\right)$ The solution (i) is ranked in position (j) in an ordered list of (l) elements in its front (k) by the objective function (m).
- $\left(d^i\right)$ The crowding distance is an estimate of the density of solutions surrounding the solution (i) in the front (k).

Then, the crowding distance is defined as:

$$d^i = d^{I_j^m} = d^{I_j^{m-1}} + \frac{f_m^{I_{j-1}^m} - f_m^{I_{j+1}^m}}{f_m^{max} - f_m^{min}} \tag{11}$$

Where m is the number of objectives, f_m^{max} is the maximum of the m-objective function value and f_m^{min} is the minimum of the m-objective function value.

The distance for boundary solutions for each objective function are $d^{I_1^m} = d^{I_l^m} = \infty$, therefore these solutions are always selected in the crowded-process. As we can see in Fig. 2, d^idepends on the density of solutions along the front. Thus, solutions isolated on the front have a crowding distance higher than other solutions located in high-density fronts. The crowded-process is used as much in the selection process as in replacement process. In both cases, the crowded-process search diversification preserving.

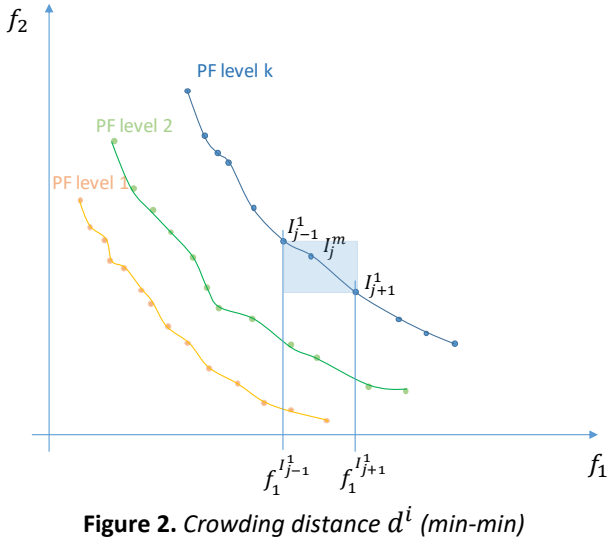

Figure 2. *Crowding distance d^i (min-min)*

3.2. Metrics

In MOP, determining the performance of different MOEAs is difficult because we need to compare several solutions (fronts) unlike only one solution. Furthermore, it should be noted that the MOEAs are stochastic, and several runs are necessary to assess their performance. On the other hand, the focus on the front will be in generate as many elements as possible of the Pareto Front (PF), or obtain nondominated solutions as near to PF as possible, and as smooth and uniform as possible along the front [3].

As we have mentioned above, we need to run the NSGA-II several times (R times). Thus, we will obtain several fronts. The front obtained in each run are joined in a set, and the dominated solutions

are deleted. All nondominated solutions are plotted, called EPF (envelope- PF). Each front and EPF will be used to analyze the performance of the NSGA-II

To address this problem, there are several metrics [4, 5]:

1.- Graphical presentation of the EPF.

2.- The Normalized Spacing (SP), [6]. This metric judges how well are distributed the solutions in the front. SP is defined as Eq. 12. The value of SP will be 0 in perfect distributed front.

$$SP = \sqrt{\frac{1}{n-1}\sum_{i=1}^{n}\left(\overline{d} - d_i\right)^2} \tag{12}$$

where d_i is the minimum distance between i solution and any solution of the front, $\overline{d}$ is the mean of minimum distances (d_i), and n is the number of nondominated solutions in the front.

There are different definitions of distance between two solutions i, j. with m function objectives. The more used is the Euclidean distance:

$$d_{ij} = \left\{\sqrt{\sum_{k=1}^{m}\left(f_k^i - f_k^j\right)^2}\right\} \tag{13}$$

When the magnitude of objective functions is significantly different, the normalized distance can be used:

$$d_{ij} = \left\{\sqrt{\sum_{k=1}^{m}\left(\frac{f_k^i - f_k^j}{f_k^{max,PF} - f_k^{min,PF}}\right)^2}\right\} \tag{14}$$

Where the maximum and minimum values of k objective function are $f_k^{max,PF}$ and $f_k^{min,PF}$. Thus, SP is defined as:

$$d_i = min_{\forall j=1\ldots n, j\neq i}\left\{\sqrt{\sum_{k=1}^{m}\left(\frac{f_k^i - f_k^j}{f_k^{max,PF} - f_k^{min,PF}}\right)^2}\right\} \quad \bar{d} = \frac{1}{n}\sum_{i=1}^{n} d_i \tag{15}$$

The average SP ($\overline{SP}$) is calculated with the R runs of NSGA-II:

$$\overline{SP} = \frac{\sum_{r=1}^{R} SP_r}{R} \tag{16}$$

3.- The Hypervolume (HPV), [7]. This metric calculates the volume covered by nondominated solutions in the front. The analysis of HPV is non-significant without the reference of the volume covered by PF. For this, in this study, the normalized hypervolume for 2-objective has been defined as Eq. 17 and Eq. 18. The reference point is (0,0) in minimization see Fig. 3. With this definition, the value of HPV is 1 when the front is the optima PF.

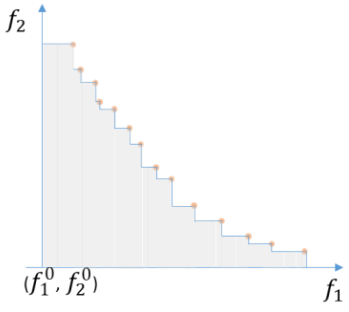

Figure 3. *Hypervolume of a PF with reference point* (f_1^0, f_2^0)

$$HPV = \sum_{i=1}^{n}\left(f_1^i - f_1^0\right)x\left(f_2^i - f_2^{i-1}\right) \Big/ \sum_{j=1}^{|PF|}\left(f_1^j - f_1^0\right)x\left(f_2^j - f_2^{j-1}\right) \quad (17)$$

$$\overline{HPV} = \frac{\sum_{r=1}^{R} HPV_r}{R} \quad (18)$$

With n, the number of nondominated solutions in the front, and R, the number of runs.

4.- The Maximum Spread (MS), [3]. MS is a widely used spread indicator. It measures the range of a front by considering the maximum extent on each objective. As in below metrics, the normalized maximum spread has been used Eq. 19 and Eq.20. When the front has the same spread than the PF, the value of MS will be 1.

$$MS = \sqrt{\frac{1}{m}\sum_{k=1}^{m}\delta_k} \quad \text{and} \quad \overline{MS} = \frac{\sum_{r=1}^{R} MS_r}{R}$$

$$with\ \delta_k = \left(\frac{max_{\forall i \in front} f_k^i - min_{\forall i \in front} f_k^i}{f_k^{max,PF} - f_k^{min,PF}}\right)^2 \quad (19)$$

$$\overline{MS} = \frac{\sum_{r=1}^{R} MS_r}{R} \quad (20)$$

5. The Normalized Generational Distance (GD), [8]. It is an estimation of the proximity of the front to the PF. The minimal distance of each solution in the front to the nearest solution of the PF is calculated, by Eq. 21. When all solutions of the front belong to the PF, the value of GD will be 0.

$$GD = \frac{\sqrt{\sum_{i=1}^{n} d_{min,i}^2}}{|PF|} \quad \text{and} \quad \overline{GD} = \frac{\sum_{r=1}^{R} GD_r}{R} \quad (21)$$

$$\text{With } d_{min,i} = min_{\forall j \in PF}\left(\sum_{k=1}^{m}\left(\frac{f_k^i - f_k^j}{f_k^{max,PF} - f_k^{min,PF}}\right)^2\right)$$

6. About cardinality metrics.

Other interesting metrics are relative to the number of solutions in the front, PF and EPF:

- |PF|, number of nondominated solutions in PF.
- |EPF|, number of nondominated solutions in EPF.
- %EPF ϵ PF, it is the number of nondominated solutions of the EPF that belong to PF.

4. Experimentation and Analysis

The value of parameters of NSGA-II used are listed below:

- Number of solutions in the population: N=250.
- Stopping criterion: maximum number of evaluations: 300.000.
- Crossover probability: 90% per solution.
- Mutation probability: 1% per gene.
- Number of runs to study statistical: 20.

In previous sections we have described two used instances and the range of each variable. The mass of TMDs have been set to 0.04, 0.06, 0.08, 0.10 and 0.12 (Kg). The NSGA-II has been run 20 times with each value of the mass.

4.1. 1TMD case.

For the instance 1TMD in a structure of 2 floor, nondominated solutions (EPF) of the 20 obtained fronts for each mass value are showed in Figure 4. The metrics are presented in table 1. In this instance although there could be four qualitatively different scenarios (depending on which floor the TMD is located on and to which mode, 1 or 2, it is tuned), the simplicity of the problem leads all solutions locate the TMD on the second floor and it is tuned to mode 1 (the most prominent one). The different solutions vary in slight changes in stiffness and damping. Note also that, as is well known, the higher the mass involved, the lower the values of the objective functions.

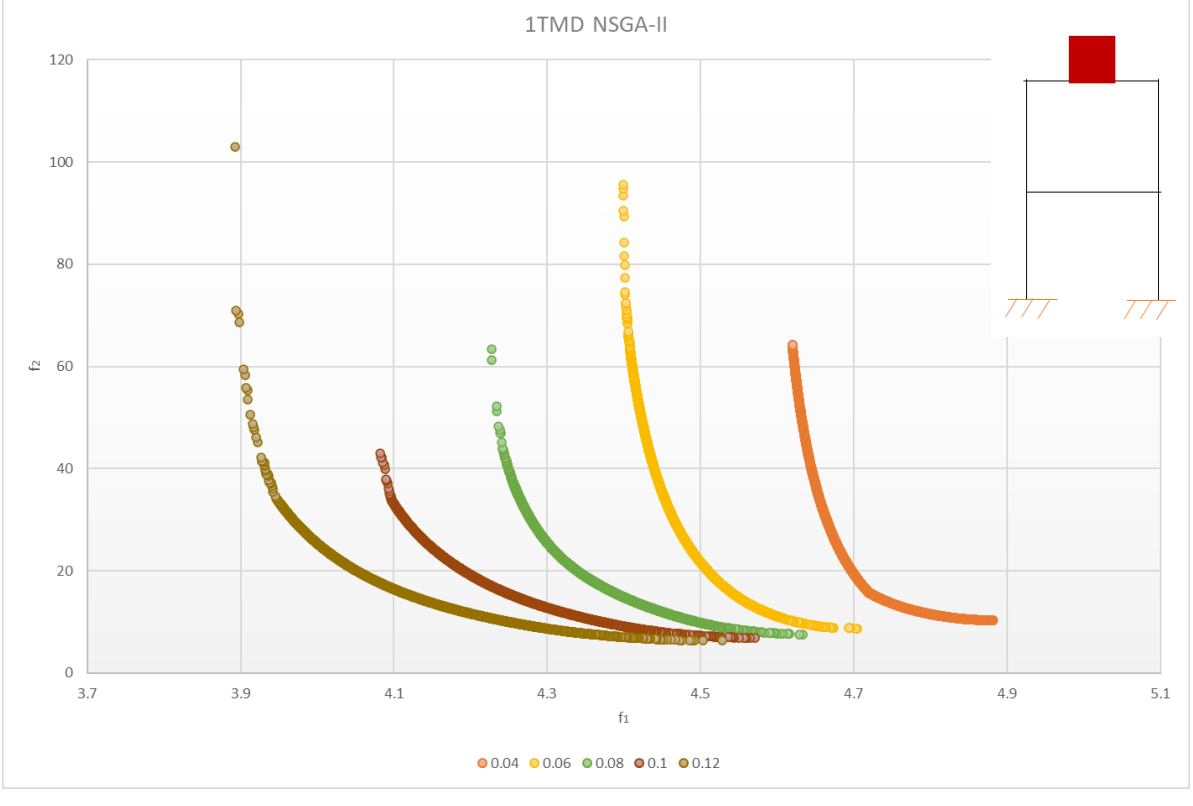

Figure 4. *EPF for 1TMD with NSGA-II. (0.04 – 0.12) from right to left*

Table 1. Metrics for NSGA-II in 1TMD for each mass value

1TMD	**0.04**	**0.06**	**0.08**	**0.10**	**0.12**
$\overline{MS}$	1.00	1.00	1.00	0.98	1.01
$\overline{HPV}$	1.00	1.00	1.00	0.95	1.02
$\overline{SP}$	0.004	0.004	0.004	0.017	0.005
$\overline{GD}$	$4.95\ 10^{-5}$	$5.38\ 10^{-5}$	$5.92\ 10^{-5}$	$4.46\ 10^{-5}$	$14.16\ 10^{-5}$
|PF|	3066	3443	3226	3332	3370
|EPF|	1961	2113	1862	2085	1891
%EPF ϵ PF	54.01%	49.38%	46.56%	51.90%	46.23%

Metrics values show the NSGA-II obtain fronts near to the PF ($\overline{\mathrm{GD}}$ ≈0), well distributed along the front ($\overline{\mathrm{SP}}$≈0), with similar volume to PF ($\overline{\mathrm{HPV}}$ ≈1) and the extreme values of f_1 and f_2 are been located ($\overline{\mathrm{MS}}$ ≈1). However, in the case 0.10 the metrics $\overline{\mathrm{SP}}$ presents an anomaly due to the nondominated solutions in front are not connected in the left part of the PF. Note, the extreme values of objective functions are difficult to locate in MOP. However, the NSGA-II has solved this challenge, but some intermediate points of the front have not been found.

4.2. 2TMD case.

In Figure 5 and Table 2 are described the results obtained for 2 masses in a structure of two floors. The 2TMD is a more complex problem than 1TMD. There are three different configurations, one mass on each floor (configuration 12), two mass on the first floor (configuration 11), and two masses on the second floor (configuration 22). The configuration 11 are discarded for the algorithm and solutions with this configuration does not belong to the front because all of them are dominated solutions. Then, the configurations 12 and 22 are present in the front, and this is the reason for the peculiar form of the front as seen in Fig.5.

Furthermore, the NSGA-II was run to check the front with two fixed configurations, once with the configuration 12, and other one with the configuration 22. The obtained fronts are showed in Fig, 6. The nondominated solutions of the two fronts shape the front of the Fig. 5. This check is intended to verify that the apparent discontinuities of the fronts are due to two different reasons. On the one hand, the TMDs can change floors and, on the other hand, even not changing floors, their parameters (mainly mass and stiffness) can be such that they tune to either mode 1 or mode 2. An inner view could clarify that for case 12 (one on each floor) always the one on the second floor is tuned to mode 1 and the one on the first floor is tuned to mode 2. However, for case 22, on the left side both TMDs are tuned to mode 1 (multi-TMD concept) while in the bottom part there is one tuned to each mode. In the symbols inserted in Fig. 6, red color indicates that the TMD is tuned to mode 1 and blue color to mode 2.

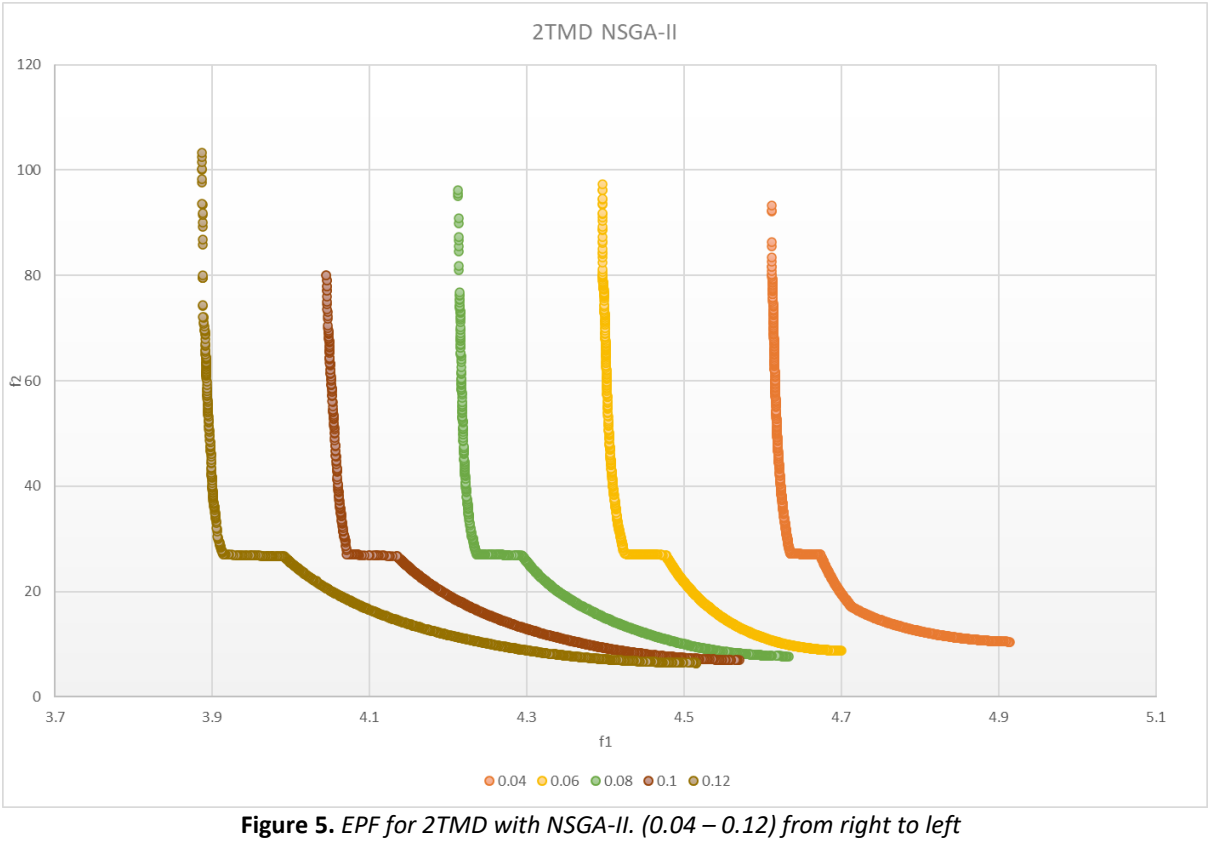

Figure 5. *EPF for 2TMD with NSGA-II. (0.04 – 0.12) from right to left*

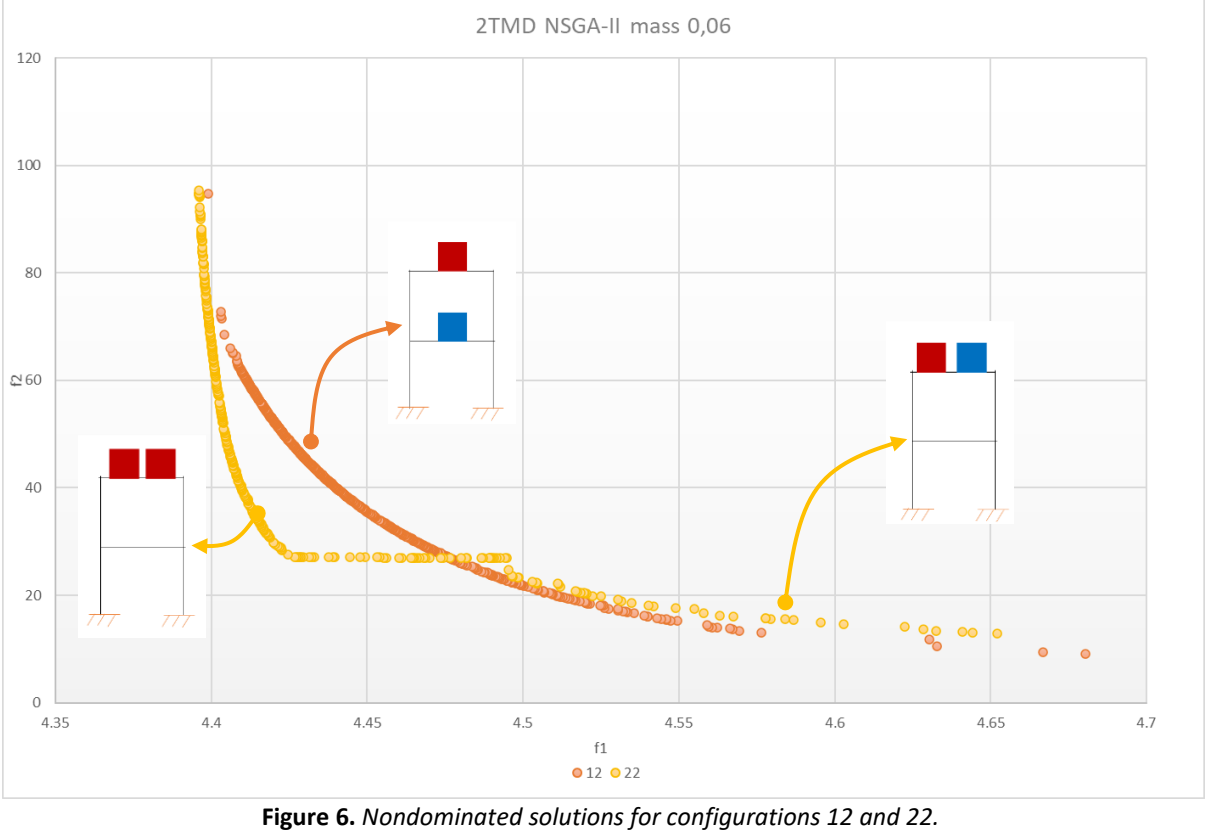

Figure 6. *Nondominated solutions for configurations 12 and 22.*

This analysis notes the importance of obtaining fronts with nondominated solutions of both configurations in every run of the NSGA-II. In table 2 is showed the percentage of run in which the (12-22) configurations are obtained on 20 runs executed. As we can see, as mass values is increasing the fronts' number with both configuration is decreasing. That is, configurations 12 and 22 are obtained in a 65% of runs, and the configuration 12 alone is obtained in the 35% of runs.

Table 2. Percentage of success.

mass	**0.04**	**0.06**	**0.08**	**0.10**	**0.12**
NSGAII	90%	85%	90%	65%	65%

In table 3 are showed metrics values for the 2TMD.

Table 3. Metrics for NSGA-II in 2TMD for each masses' value

2TMD	**0.04**	**0.06**	**0.08**	**0.10**	**0.12**
$\overline{MS}$	0.97	0.99	1.01	1.00	0.94
$\overline{HPV}$	0.94	0.98	1.04	1.00	0.87
$\overline{SP}$	0.005	0.005	0.005	0.006	0.006
$\overline{GD}$	$0.90\ 10^{-3}$	$0.76\ 10^{-3}$	$0.65\ 10^{-3}$	$1.41\ 10^{-3}$	$0.65\ 10^{-3}$
|PF|	1185	1138	1117	1291	1305
|EPF|	984	980	893	901	980
%EPF ϵ PF	73.25%	81.37%	65.71%	55.77%	59.00%

The NSGAII provides front well spread (MS), near and similar to PF (GD and HPV), well spacing (SP) and with high number of solutions |EPF| and %EPFϵ PF.

5. Conclusions

A multi-objective genetic algorithm has been proposed to solve the problem of installing several TMDs on a slender structure. In this study. the selected objectives have been minimize the maximum of Frequency Response Functions (JSLS) and the maximum normal stress (JULS). In structural engineering, analytical solutions are known for simple cases of installing optimal TMDs in a particular location and for a particular mode. The presented algorithm achieves these same solutions without the need for mathematical formulation. More demanding are the cases where the location is not known or several TMD devices can be placed. In these cases, the algorithm also offers satisfactory results, including the well-known alternative of installing two different TMDs in the same position and almost for the same mode (multi-TMD case).

Different metrics and graphical study show the nondominated solutions obtained by NSGA-II are well spread, obtaining extreme values of the objective functions. The nondominated solutions are uniformly distributed along the front and near to PF. Also, the NSGA-II has demonstrated that it is able to find solutions in the appropriated configurations.

ACKNOWLEDGEMENTS This research was partially funded by the Ministerio de Economía y Competitividad, Spanish Government, through the research project number RTI2018-098425

REFERENCES

[1] Zitzler, E., Thiele, L., Laumanns, M., Fonseca, C. M. & Da Fonseca, V. G. (2003). Performance assessment of multiobjective optimizers: An analysis and review. *IEEE Transactions on Evolutionary Computation, 7(2), 117–132. DOI: 10.1109/TEVC.2003.810758.*

[2] Deb, K., Pratap, A., Agarwal, S. & Meyarivan, T. (2002). A fast and elitist multiobjective genetic algorithm: NSGA-II. *IEEE Transactions on Evolutionary Computation, 6(2), 182-197. DOI: 10.1109/4235.996017.*

[3] Zitzler, E., Deb, K. & Thiele, L. (2000). Comparison of multiobjective evolutionary algorithms: Empirical results. *Evolutionary Computation, 8(2), 173–195. DOI: 10.1162/106365600568202.*

[4] Sarker R. & Coello C.A. (2003). Assessment Methodologies for Multiobjective Evolutionary Algorithms. *Evolutionary Optimization. International Series in Operations Research & Management Science, 48. Springer, Boston, MA. DOI: 10.1007/0-306-48041-7.*

[5] Riquelme, N., Von Lücken, C. & Baran, B. (2015). Performance metrics in multi-objective optimization. *Latin American Computing Conference (CLEI). Arequipa. (pp. 1-11). DOI: 10.1109/CLEI.2015.7360024.*

[6] Schott, J. R. (1995). Fault tolerant design using single and multicriteria genetic algorithm optimization. (PhD. thesis). Department of Aeronautics and Astronautics, Massachusetts Institute of Technology, Cambridge.

[7] Zitzler, E. & Thiele, L. (1999). Multiobjective evolutionary Algorithms: A comparative case study and the strength Pareto approach. *IEEE Transactions on Evolutionary Computation, 3(4), 257–271. DOI: 10.1109/4235.797969.*

[8] Van Veldhuizen, D. A. & Lamont, G. B. (1999). Multiobjective evolutionary algorithm test suites. Proceedings of the 1999 ACM Symposium on Applied Computing, (pp. 351–357). DOI: 10.1145/298151.298382.

[9] Goldberg, D. E. & Deb, K. (1991) A Comparative Analysis of Selection Schemes Used in Genetic Algorithms. In: Rawlins, G. (Ed.). Foundations of Genetic Algorithms, Morgan Kaufmann Publishers, San Mateo, CA, 69-93.

[10] Deb, K. & Agrawal, R. B. (1995). Simulated binary crossover for continuous search space. *Complex Systems, 9(2), 115–148*.

[11] Mühlenbein, H. & Schlierkamp, D. (1993). Predictive models for the breeder genetic algorithm. *Evolutionary computation, 1(1), 24-49. Doi: 10.1162/evco.1993.1.1.25.*

Metamodeling of the additional plate in bending in beam-to-beam steel connections.

López, Manuel [1]; Loureiro, Alfonso[2]; Gutiérez, Ruth M[3]; Reinosa, José Manuel[4]

ABSTRACT

This article focused on metamodeling the stiffness of the component additional plate in bending. This component appears in beam-to-beam bolted steel connections, when the flush end plate of the secondary beam is attached to primary beam with an additional plate welded between the flanges. The metamodel has been built using the Kriging's method with an input of seven geometrical parameters of the joint.

Keywords: kriging, metamodeling, beam-to-beam, steel joints.

1. INTRODUCTION

Over the last years wide experimental, numerical and analytical researches have been carried out in beam-to-column steel joints. Most of them relate to bi-dimensional behaviour [1-7] and some to three-dimensional [8-10]. This accumulated knowledge has been compiled in the Eurocode 3 [11], which uses the component method [12] to idealize the semirigid behaviour of the joint. However, the beam-to-beam connections [13-17] have been less studied, although they are as important as beam-to-column.

Relevant research about orthogonal beam-to-beam connections has been performed by Hawxwell D.A. and Tsvdaridis K. D. [13] who made an experimental campaign of eccentric connections with end plate in order to classify and analyse the failure mechanism. Lema L.G [14] has also investigated this beam-to-beam typology with bolted end-plates in steel platforms subject to seismic load and exceptional load induced by piping rupture.

In orthogonal beam-to-beam connections there are many ways to solve the connection. Traditionally, in welded connections the secondary is welded directly to the main beam as Figure 1a shows. If the solution is bolted the secondary beam has an end plate that is bolted to a T shape stub welded to the flanges and the web of the primary beam, as represented in Figure 1b. In both exposed cases, the flanges of the beam or the T shape stub must be cut with the cost increment that it entails.

An alternative for the exposed solutions could be to bolt the end plate of the secondary beam to a simple additional plate welded between the flanges of the primary one. In this case, notches in the

[1] *Universidad de A Coruña (SPAIN). manuellopez@udc.es (Corresponding author)*
[2] *Universidad de A Coruña (SPAIN). a.loureiro@udc.es*
[3] *Universidad de A Coruña (SPAIN). ruth.gutierrez@udc.es*
[4] *Universidad de A Coruña (SPAIN). j.reinosa@udc.es*

secondary beam flanges are avoided (Figure 1a) and welded work is also simplified compared with the connection with a T shape stub (Figure 1b), all of this ending in a cheaper solution. Figure 1c shows this configuration.

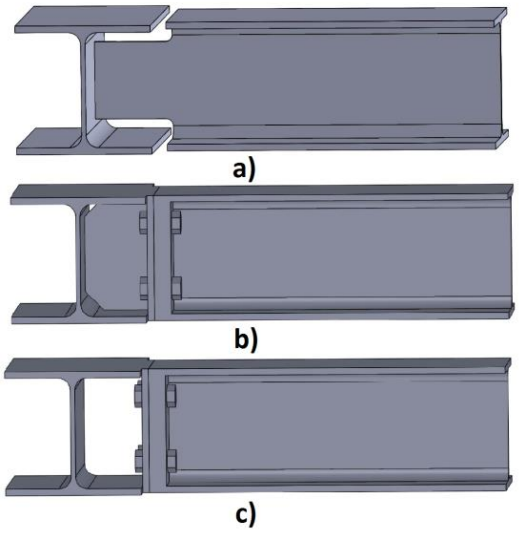

Figure 1. *Beam-to beam typology. a) Welded, b) Bolted with T shape stub and c) Bolted with additional plate.*

Lopez et al. [17] have studied this solution, where it was figured out that the additional plate in bending was the most relevant component in behaviour of the joint. This conclusion was reached after performing experimental test and an extensive parametric study with calibrated finite element models. Finally, they proposed an analytical formulation for the stiffness and resistance of the additional plate in bending.

The stiffness of the components can be modelled by traditional methods like the component method [11]. However, the expressions are complex in most of the cases. Other common solution is the use of metamodeling extracting information from experimental results or numerical models. In this field, the neural networks [18-19] have been widely used but other methods like Kriging [20] has also been used successfully in steel joints [5,21].

In this article, a metamodel of the additional plate in bending is presented and developed using Kriging's method to obtain the stiffness of the component, showing very good result. The data of the parametric study with finite elements models performed by Lopez et al. [17] was used to develop the metamodel.

2. DESCRIPTION OF THE PARMETRIC STUDY

The parametric study of finite element models was published by Lopez et al. [17] and consisted in a configuration of one primary beam with the additional plates attached by eight bolts to two secondary beams with flush end plates as Fig. 2 shows. The geometrical parameters are depicted in Fig. 3. The number of studied models were 288, as Table 1 summarized. In the study 12 different beam profiles has been used, noted that the profile of the primary beam and the secondary beam was the same. For each beam profile there were 2 horizontal distance between bolts, 2 vertical distances between bolts, 3 different thicknesses of the additional plate and 2 bolt diameters. These combinations have led to 24 cases for each beam profile.

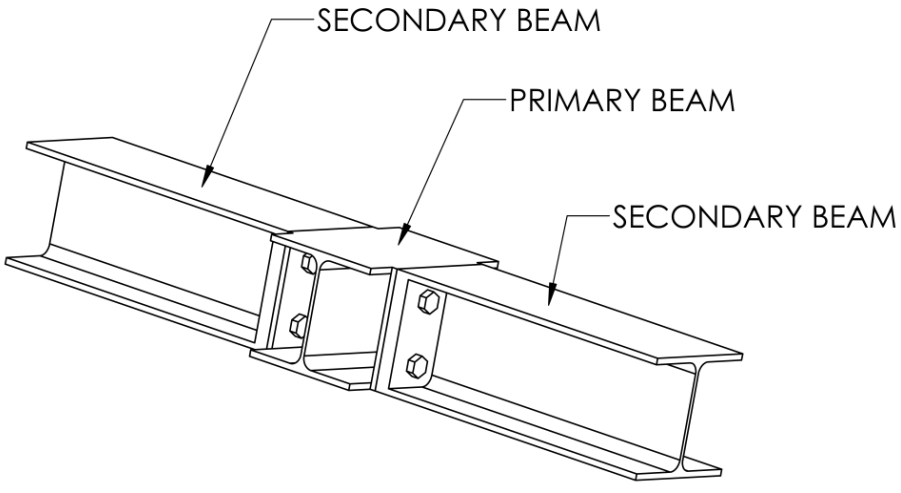

Figure 2. *3D view of the configuration.*

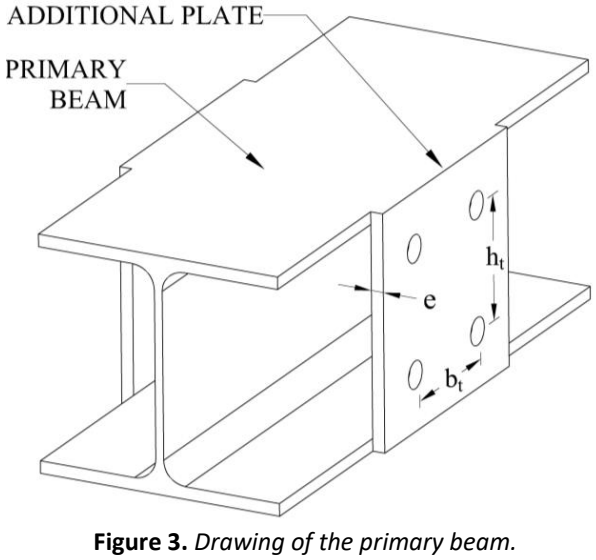

Figure 3. *Drawing of the primary beam.*

Table 1. Mechanical characterization of materials

Submodel	Profile	b_t (mm)		h_t (mm)		e(mm)			Bolt	
		b_t 1	b_t 2	h_t 1	h_t 2	e1	e2	e3	Bolt1	Bolt2
ME01	HE200A	50	100	130	100	8	10	12	10.9TR16	10.9TR20
ME02	HE240A	60	120	160	110	10	12	15	10.9TR16	10.9TR20
ME03	HE280A	70	140	200	150	10	12	15	10.9TR16	10.9TR20
ME04	HE300A	75	150	220	170	10	12	15	10.9TR16	10.9TR20

ME05	HE400A	70	200	300	250	15	18	20	10.9TR16	10.9TR20
ME06	HE450A	80	210	350	300	18	20	22	10.9TR16	10.9TR20
ME07	IPE180	50	60	120	100	8	10	12	10.9TR16	10.9TR20
ME08	IPE200	50	65	140	110	8	10	12	10.9TR16	10.9TR20
ME09	IPE240	55	70	175	150	8	10	12	10.9TR16	10.9TR20
ME10	IPE300	60	80	230	180	8	10	12	10.9TR16	10.9TR20
ME11	IPE400	60	100	320	270	10	12	15	10.9TR16	10.9TR20
ME12	IPE450	60	100	370	320	10	12	15	10.9TR16	10.9TR20

The finite element models were performed using Abaqus package. Solid elements with reduced integration and hourglass control (C3D8R) were adopted. Figure 4 shows the typical numerical model with the mesh size used.

A S275 steel properties were adopted and Von Misses yield criteria to define the inelastic response. The load of the model was performed by a displacement control having taken into account the nonlinearities of the material and geometry.

Taking the advantage of the symmetry only a quarter joint was modelled. The model was composed by: primary beam with additional plate, secondary beam with end plate, 2 bolts and the washers (see Figure 4). The parts iteration was reproduced by means of hard contact between surfaces and the friction coefficient was 0.25. The end plate of the secondary beam was modelled with 30 mm of thickness in order to avoid exerting influence on the behaviour of the additional plate.

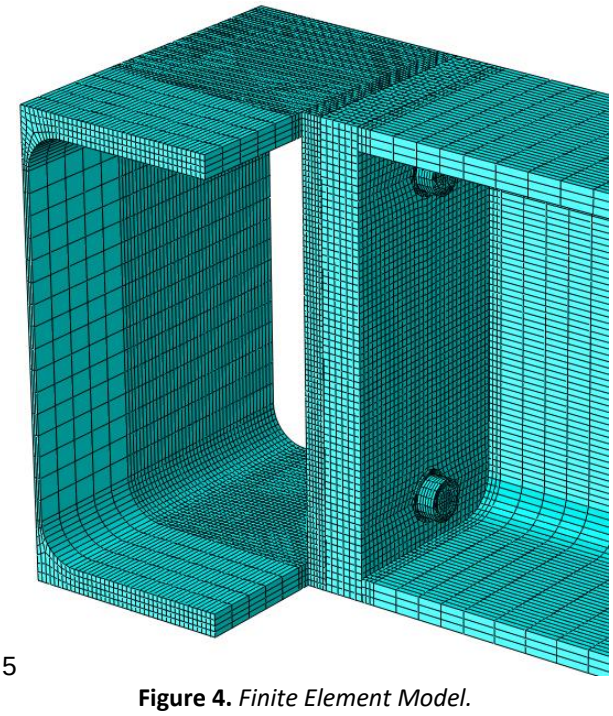

5

Figure 4. *Finite Element Model.*

3. METAMODEL

In this work the stiffness of the additional plate in bending is metamodeling using the Kriging's method, that consist in predict the response based in regression model and a radial model. DACE [20] has been used to implement the method. This Matlab application permits regression's models with constants, linear and quadratic interpolation. For radial model allows correlation models linear, exponential, Gaussian, spherical, cubic and spline. The parameters were determined minimizing the error. The geometrical parameters that have been used as input of the model were: beam height, beam width, thickness of flange, vertical distance between bolts, horizontal distance between bolts, thickness of the additional plate and bolt diameter. A linear regression model and a Gaussian correlation model have been used in the model.

As previously noted, the parametric study has 288 cases, where 192 (66%) of these cases have been used as input data to train the model and the remaining 96 cases (33%) was used to validate the model.

Figure 5 shows the comparison between finite element models and Kriging's model stiffness. Analysing these results, the average of the error was 0.43% and its standard deviation was 0.019. The maximum error was 12%. Therefore, the Kriging's model shows good accuracy predicting the stiffness of the additional plate.

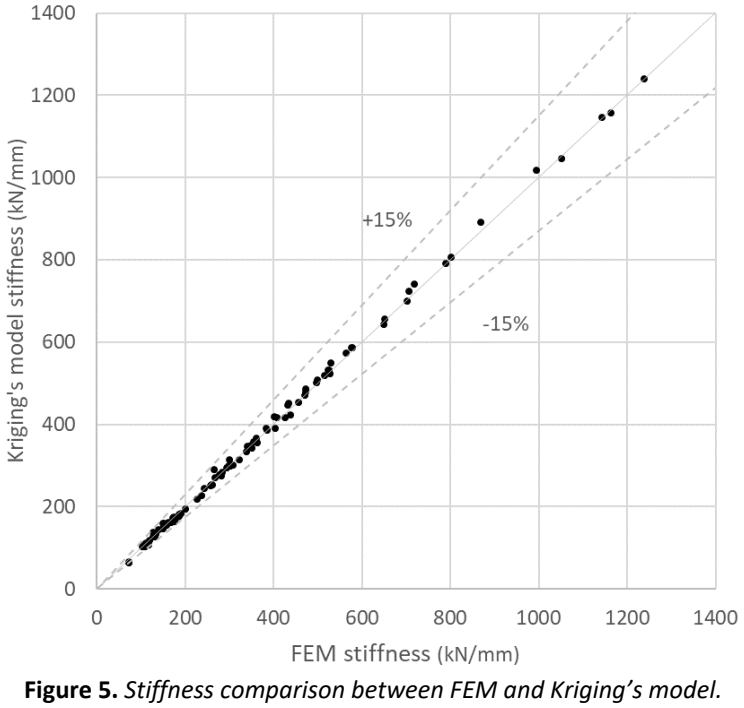

Figure 5. *Stiffness comparison between FEM and Kriging's model.*

4. CONCLUSIONS

Beam-to-beam bolted steel connections can be solved by attaching the end plate of secondary beam to the primary beam by an additional plate welded between their flanges, thus a new component appears. This component can be called additional plate in bending and it has a crucial influence in the stiffness of the connection. In order to predict the stiffness behaviour of the component, a Kriging's model has been proposed obtained very good result compared with a parametric study conducted with calibrated finite element models.

ACKNOWLEDGEMENTS

The authors would like to thank the Spanish Ministry of Science and Innovation for the financial assistance of this work by means of the project PID2020-113895GB-C31 and Programme of Human Resources from Research Galician Plan, Development and Technological Innovation of Galicia INCITE.

REFERENCES

[1] Faella C, Piluso V, Rizzano G. (2000) Structural steel semirigid connections: Theory, design and software. Boca Raton (Florida): CRC Publishers.

[2] O.S. Bursi, J.P. Jaspar. (1997) Benchmarks for finite element modelling of bolted steel connections. Journal of Constructional Steel Research 43 1-3, 17-42.

[3] Eduardo Bayo, Alfonso Loureiro, Manuel Lopez, Luís Simões da Silva. (2017) General component based cruciform finite elements to model 2D steel joints with beams of equal and different depths. Engineering Structures 152, 698-708.

[4] Sandra Jordão, L. Simões da Silva, Rui Simões.(2013) Behaviour of welded beam-to-column joints with beams of unequal depth. Journal of Constructional Steel Research 91, 42-59.

[5] Alfonso Loureiro, Manuel Lopez, J. Manuel Reinosa, Ruth Gutierrez, Eduardo Bayo. (2019) Metamodelling of stiffness matrices for 2D welded asymmetric steel joints. Journal of Constructional Steel Research 162, 105703.

[6] Alfonso Loureiro, Manuel Lopez, Ruth Gutierrez, Jose M. Reinosa (2020) Experimental evaluation, FEM and condensed stiffness matrices of 2D external welded haunched joints. Engineering Structures 205, 110110

[7] Manuel Lopez, Alfonso Loureiro, Eduardo Bayo. (2015) Shear behaviour of trapezoidal column panels. II: Parametric study and cruciform element. Journal of Constructional Steel Research 108, 70-81.

[8] Beatriz Gil, Rufino Goñi, Eduardo Bayo (2018) Initial stiffness and strength characterization of minor axis T-stub under out-of-plane bending. Journal of Constructional Steel Research 140, 208-221.

[9] A. Loureiro, M. López, R. Gutiérrez, J.M. Reinosa. (2013). Experimental and numerical analysis of E-stubs in three dimensional joints: a new analytical formulation for the stiffness calculation. Engineering Structures 53, 1–9.

[10] A. Loureiro, M. López, R. Gutiérrez, J.M. Reinosa. (2013) A new analytical formulation for the E-Stub strength calculation in three dimensional steel joints with additional plates welded to the weak axis. Engineering Structures 56, 2263-2272.

[11] CEN, Eurocode 3: Design of steel structures. Part 1.8: Design of Joints (EN 1993-1-8). 2005.

[12] Jaspart JP. (1991) Etude de la Semi-Rigidite des Noeuds Poutre-Colonne et son Influence sur la Resistance et la Stabilite des Ossatures in Acier. Ph.D. thesis. University of Liege.

[13] Daniel Allan Hawxwell, Konstantinos Daniel Tsavdaridis. (2019) Beam-to-beam eccentric end plate connections - Experimental comparison to fin plate and partial-depth end plate connections. Structures 19, 411-423.

[14] L.G. Lema. (2009) Beam-to-beam joints with bolted end-plate connections concerning steel platforms Angra 2NPP. International Nuclear Atlantic Conference – INAC 2009 Rio de Janeiro, RJ, Brazil, September 27 to October 2.

[15] Kęstutis Urbonas, Alfonsas Daniūnas (2006) Behaviour of semi-rigid steel beam-to-beam joints under bending and axial forces. Journal of Constructional Steel Research 62, 1244-1249.

[16] Alfonsas Daniūnas, Kęstutis Urbonas. (2008) Analysis of the steel frames with the semi-rigid beam-to-beam and beam-to-column knee joints under bending and axial forces. Engineering structures 30, 3114-3118.

[17] Manuel Lopez, Alfonso Loureiro, Ruth Gutierrez, Jose M. Reinosa (2021) A new analytical formulation for the stiffness and resistance of the additional plate in bending in beam-to-beam steel joints. Engineering Structures. Volume 228. 111476.

[18] Jadid, MN., Fairbairn, DR. (1996) Neural-network applications in predicting moment-curvature parameters from experimental data. *Eng Appl Artif Intel.* 9(3), 309–19.

[19] Anderson, D., Hines, EL., Arthur, SJ., Eiap, EL. (1997) Application of artificial neural networks to the prediction of minor axis steel connections. *Comput Struct*. 63(4), 685–92.

[20] Nielsen, HB., Lophaven, SN., Søndergaard J. (2002). DACE - A Matlab Kriging Toolbox. Informatics and Mathematical Modelling, Technical University of Denmark, DTU. [Computer programme].

[21] Bayo, E., Gracia, J. (2019). Stiffness modelling of 2D welded joints using metamodels based on mode shapes. J. Constr. Steel Res., 156, 242-251.

NUMERICAL MODEL FOR THE PARAMETRIC ANALYSIS OF THE IMPACT BALL-PADDLE RACQUET

Germán Castillo López[1], Felipe García Sánchez[2], José María Conde Calabrús[3]

ABSTRACT

In this study, numerical models of the ball and the paddle racquet are developed and the impact among them is explicitly analyzed. The ball has been modeled using the hyperelastic Ogden model for the rubber and an airbag element for its internal pressure. The racquet model has been completed regarding a previous work in which the model was not holes. Attempting to translate the sensation of the player to engineering variables, grip reactions and outlet angles and velocities are studied. Fail criterion is applied as a measurement of the durability of the racquet. The usefulness of the model is showed throughout the comparison of different models.

Keywords: Paddle racquet. Ogden model rubber. Airbag model ball. Holes pattern. Non-linear explicit impact analysis.

1. INTRODUCCIÓN Y OBJETIVOS

Los desafíos científico-tecnológicos que suponen las disciplinas deportivas son muy variados y de muy alto nivel. Usualmente tenemos asociados esos desarrollos a deportes de automoción de alto impacto mediático como automovilismo, motociclismo o ciclismo: una búsqueda en SCOPUS con el término "motorcycle" en el campo de título arroja 110 documentos con fecha de publicación durante 2021. Pero también los deportes de pala, entre otros, en sus distintas modalidades, han atraído el interés de los investigadores y desarrolladores, siendo especialmente relevantes los trabajos de investigación relacionados con la raqueta y la bola de tenis de S.R. Goodwill y coautores desde 2001 en adelante, entre otros:[1]–[5]. También son numerosos los trabajos dedicados al análisis de la raqueta de tenis de mesa, de entre los que citaremos, sólo como ejemplo, los publicados por M.L. Yang en 2013 [6] y por D.A. Rusell en 2018 [7].

Aparentemente el pádel atrae menos la atención de los investigadores. Es difícil encontrar trabajos sobre este tema fuera del campo de la medicina. De hecho los autores sólo tiene constancia del trabajo de F.J. Huera-Huarte [8] y algunos trabajos académicos dirigidos por el profesor M. Tur Valiente de la Universidad Politécnica de Valencia, que se han desarrollado paralelamente a los nuestros.

[1]*Dpto. Ingeniería Civil, de Materiales y Fabricación, Universidad de Málaga (España). gcastillo@uma.es (Corresponding author)*
[2]*Dpto. Ingeniería Civil, de Materiales y Fabricación, Universidad de Málaga (España). fgsanchez@uma.es*
[3]*Universidad de Málaga (España). 0619929482@uma.es*

El presente trabajo, como el publicado por los mismos autores en 2019 [9], nace de la colaboración de la empresa malagueña Grupo Shark SC con investigadores del Área de Medios Continuos y Teoría de Estructuras de la Universidad de Málaga. El objetivo es el desarrollo de un modelo numérico que permita tomar decisiones de diseño en base a criterios técnicos cuantificables. Esto supone un avance neto sobre el procedimiento de diseño actual basado en la prueba y el error.

En [9], los autores investigaron el comportamiento de la pala de pádel en su estado bruto, esto es, tal como sale del molde, en la fase previa al mecanizado de los orificios. En ese trabajo se desarrolló un modelo numérico que fue validado experimentalmente bajo la acción de cargas estáticas y dinámicas.

Para la validación dinámica se empleó uno de los impactores rígidos (acero) con los que está dotada la máquina de caída de dardo CEAST 9350 con la que se realizaron los ensayos.

En este trabajo se han incluido los orificios lo que, además de completar el modelo, permite analizar la influencia de este parámetro en el comportamiento final de la pala.

Además, siguiendo la línea de trabajo de S.R. Goodwill et al. y T.B. Allen -[2], [3], [10]- la bola se ha modelizado como una bolsa de gas (elemento airbag en el programa de resolución explícita utilizado: SOL 700 de MSC Nastran), con una presión relativa de 0.82 bar, rodeada de una superficie de goma, modelizada como un material hiperelástico con comportamiento viscoso tipo Maxwell, que permite analizar el impacto entre la bola y la pala en unas condiciones mucho más cercanas a la realidad.

De esta forma, se pretenden cuantificar aspectos esenciales de la pala como son (i) su rendimiento, (ii) el control sobre la bola, (iii) el confort del jugador y (iv) la durabilidad de la pala. Consideramos que estos aspectos son cuantificables, respectivamente, mediante (i) la relación entre las velocidades de entrada y salida de la bola, (ii) su ángulo de salida, (iii) las resultantes de fuerzas y momentos en la empuñadura y (iv) el coeficiente de seguridad del material compuesto.

2. MATERIALES

2.1. Materiales de la pala

Para todas los casos analizados en este trabajo se han tomado las características de los materiales empleados por el fabricante en la pala denominada *Marvel,* utilizadas en el trabajo publicado en 2019 [9]:

- Tejido equilibrado de vidrio $220\ \mathrm{gr/m^2}$ en la superficie mixta de golpeo (Tabla 1).
- Tejido de carbono sarga 2×2 de $3\mathrm{K}$ y $200\ \mathrm{gr/m^2}$, también en la superficie mixta de golpeo (Tabla 1).
- Trenzado (braiding) de carbono/vidrio de $40\ \mathrm{mm}$ de diámetro y $39.8\ \mathrm{gr/m}$ en el marco y la empuñadura (Tabla 2).
- Espuma EVA que conforma el núcleo de la pala ($\mathrm{E} = 1.59\ \mathrm{MPa}, \nu = 0.45$).
- Resina epoxi multipropósito para laminación por contacto manual.

Tabla 1. Propiedades mecánicas para los tejidos de fibra de carbono y vidrio.

	Lámina de tejido	
Propiedad	**Carbono**	**Vidrio**
$E_x = E_y$	32.5 GPa	12.2 GPa
E_s	2.6 GPa	1.9 GPa
ν_{xy}	0.04	0.09
$X = Y$	299 MPa	296 MPa
$X' = Y'$	414 MPa	228 MPa
S	73 MPa	222 MPa
V_f	29 %	25 %
densidad	1270 kg/m^3	1430 kg/m^3
espesor	0.39 mm	0.33 mm

Tabla 2. Propiedades de la lámina elemental de las láminas que forman el trenzado.

	Lámina unidireccional	
Propiedad	**Carbono**	**Vidrio**
E_x	59.5 GPa	20.25 GPa
E_y	5.3 GPa	4.04 GPa
E_s	2.6 GPa	1.9 GPa
ν_{xy}	0.28	0.26
X	621 MPa	590 MPa
X′	562 MPa	328 MPa
Y	40 MPa	93 MPa
Y′	246 MPa	354 MPa
S	68 MPa	216 MPa
Densidad	1270 kg/m^3	1430 kg/m^3
Espesor	0.099 mm	0.121 mm

2.2. Material de la bola

Siguiendo lo establecido en [2], [3], [10], para la bola se han empleado las propiedades hiperelásticas de un caucho incompresible cuya ley de comportamiento viene gobernada por una función de energía unitaria de deformación -W- que sigue un modelo de Ogden [11], Eq. (1), y una función de relajación de Maxwell -g(t)-, que gobierna el comportamiento viscoso, definida en forma de serie de Prony, Eq. (2).

$$W = \sum_{j=1}^{j=N} \sum_{i=1}^{i=3} \frac{\mu_j}{\alpha_j} (\lambda_i{}^{\alpha_j} - 1) + K(J - 1 - \ln J) \quad (1)$$

Donde:

- K es el módulo de compresibilidad volumétrico.
- J es el cambio unitario de volumen.
- λ_i son las deformaciones principales.

- μ_j y α_j son las constantes del material.
- N es un número, elegible, de términos que pueden ser usados para la definición de esta función. En este trabajo se han considerado tres términos.

$$g(t) = \sum_{i=1}^{i=n} G_i \, e^{-\beta_i t} \tag{2}$$

Donde:

- G_i son módulos de cortante.
- β_i factores de relajación.
- n es el número, elegible, de términos de la serie de Prony, dos en este trabajo.

Los parámetros que definen el material empleado para la bola se recogen en la tabla 3.

Tabla 3. Propiedades del caucho de la bola [10].

Caucho (Mod. Ogden)			
	Densidad	$1.15\ \mathrm{kg/m^3}$	
G	2.39 MPa	ν	0.49
μ_1	$-1.5 \cdot 10^{-2}$	α_1	-7.424
μ_2	1.552	α_2	-1.664
μ_3	2.149	α_3	3.28
G_1	$1.975 \cdot 10^{-4}$	β_1	25.675
G_2	$1.4491 \cdot 10^{-1}$	β_2	259.57

3. VALIDACIÓN DE LOS MODELOS.

El modelo de la pala ya fue validado, de forma experimental, en [9].

Dado que este modelo presenta, respecto del anterior, la incorporación de los orificios, el interés en su valoración, en este trabajo, se ha centrado en el análisis de la malla. La valoración del paso de tiempo es realizada, de forma automática, por el programa que se ha utilizado para la resolución explícita, i.e., SOL 700 de MSC Nastran; para garantizar que se cumple la condición de Courant-Friedrichs-Lewy.

Como parámetro de control se han tomado la fuerza pico en el contacto pala-bola, Fig. 1 izda., y el máximo desplazamiento en la pala, Fig. 1 dcha.

El análisis de los resultados muestra que, salvo para la malla más grosera, los resultados no están comprometidos por el tamaño de los elementos y, en consecuencia, el modelo se da por válido para cualquiera de las mallas analizadas, salvo la primera.

Buscando una solución de compromiso entre precisión de resultados y tiempo de ejecución, la malla utilizada para los resultados que se muestran en el trabajo fue la malla intermedia, con un número de elementos algo superior a 50000.

Aunque el modelo de la bola está validado por los trabajos de Goodwill et al. Y Allen [2], [3], [10], se ha realizado un análisis de malla similar al anterior. Se han seleccionado, como parámetros de control, la tensión máxima de von Mises y la deformación volumétrica máxima. Los resultados, Fig. 2, ponen de manifiesto que importantes variaciones en el número de elementos no suponen variaciones significativas en los parámetros de control.

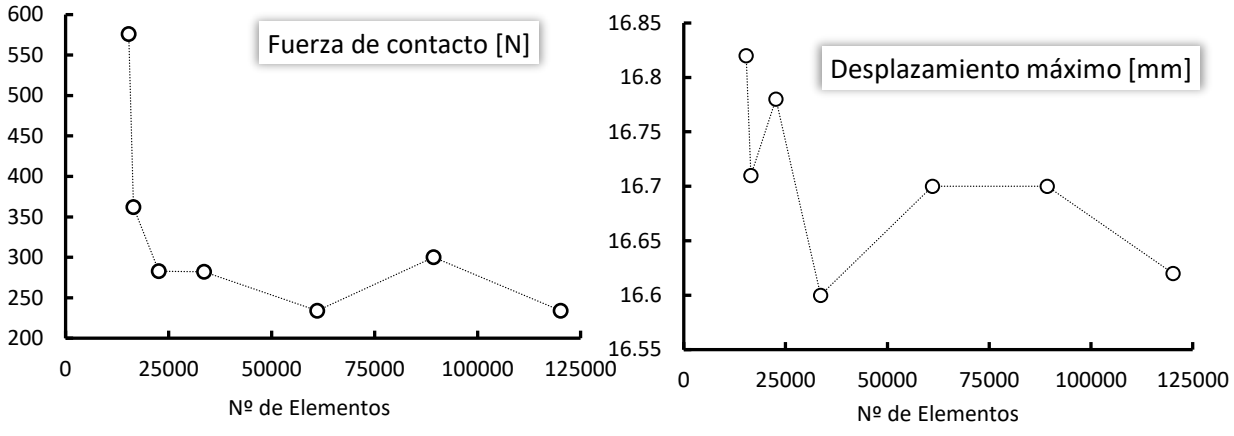

Figura 1. *Análisis de los parámetros de control con el tamaño de malla en la pala.*

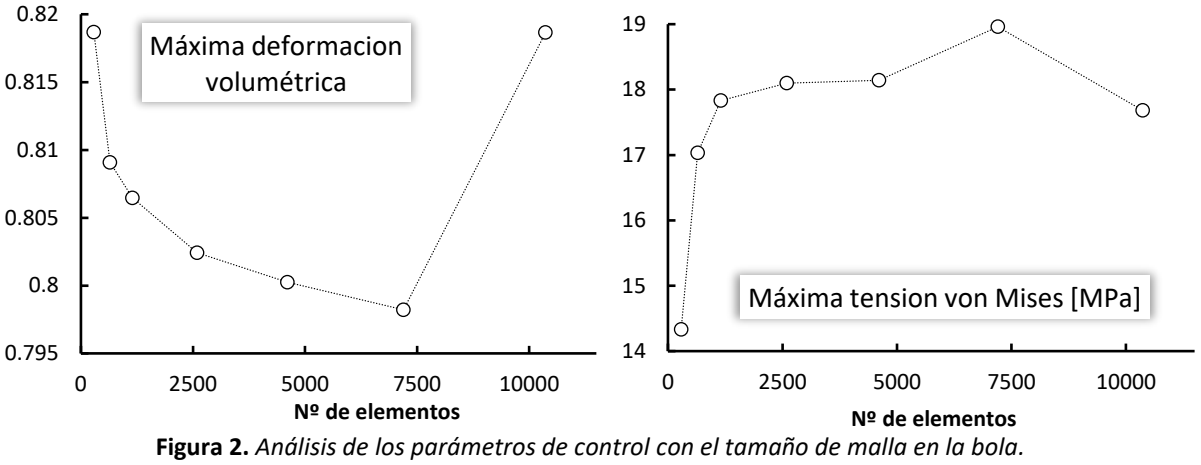

Figura 2. *Análisis de los parámetros de control con el tamaño de malla en la bola.*

4. MODELOS ANALIZADOS.

Para mostrar la utilidad del modelo desarrollado se han comparado cuatro modelos, véase Fig. 3:

- El modelo Marvel sin orificios. Que denominaremos Mb.
- El modelo Marvel definitivo. Que denominaremos Md.
- Un modelo comercial real, que será denominado Cm.
- Un modelo, sin agujeros en la zona central de la pala, analizado, desde el punto de vista aerodinámico, por F. J. Huera-Huarte en 2014 [8]: HH.

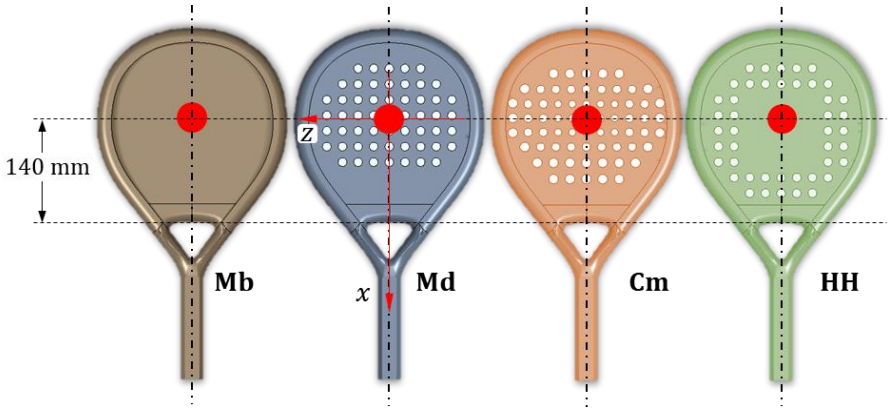

Figura 3. *Modelos analizados en este trabajo. Se indica el punto dulce y el sistema de referencia utilizado.*

Los cuatro modelos sólo se diferencian en la distribución y/o tamaño de orificios, el resto de los parámetros, geométricos y materiales son los mismos.

El modelo Mb es el que se utilizó en el trabajo publicado, por los autores de éste, en 2019 [9]. Se trata, obviamente, de un modelo más rígido al no contar con orificios, aspecto éste que se pondrá de manifiesto en los resultados. Aunque no se trata de un modelo comercializable, su valor como referencia es incuestionable.

El modelo Md es el modelo Marvel comercializado por la firma Grupo Shark SC. Tiene un total de 55 orificios de $12\ \mathrm{mm}$ de diámetro, con una distancia entre centros de $21\ \mathrm{mm} \times 21\ \mathrm{mm}$, Fig. 4 izda. Los centros de los agujeros más cercanos al corazón de la pala están a $80\ \mathrm{mm}$ del borde.

El modelo Cm, Fig. 4 centro, cuyo fabricante no puede ser revelado, se caracteriza por presentar agujeros de diferente diámetro: menores en la zona central de la pala -*punto dulce*- y mayores cerca del marco. Tiene 68 orificios de tamaños 10, 11 y $12\ \mathrm{mm}$. La distribución de orificios se define de forma que los centros de dos orificios de radios r_1 y r_2 están separados por una distancia $\mathrm{d} = \mathrm{r}_1 + \mathrm{r}_2 + 9\mathrm{mm}$. Los centros de los orificios más cercanos al corazón de la pala están separados del borde $56\ \mathrm{mm}$.

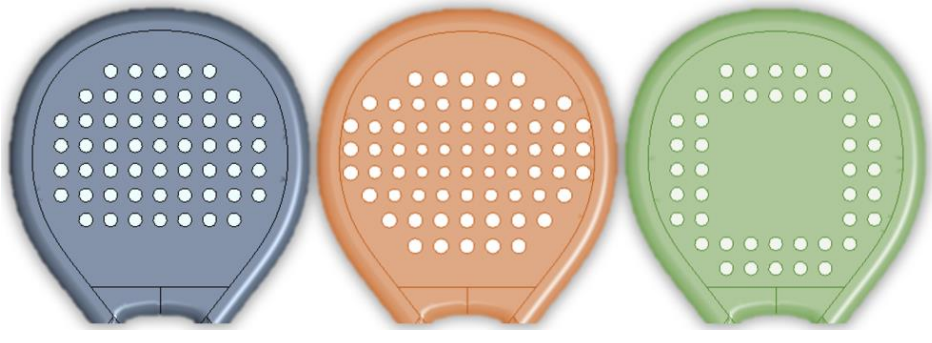

Figura 4. *Distribución de orificios en los modelos* Md *(izda),* HH *(centro) y* Cm *(dcha.).*

El modelo HH, Fig. 4 dcha., se ha incluido aquí porque F.J. Huera-Huarte [8] recomienda esta distribución de orificios, desde el punto de vista aerodinámico, frente a la usual distribución central de agujeros. Este modelo tiene 44 orificios del mismo diámetro y separación que el modelo Md. Los centros de los orificios más cercanos al corazón de la pala están separados del borde $38\ \mathrm{mm}$.

5. RESULTADOS

Se han analizado las respuestas de los cuatro modelos ante un impacto de la bola perpendicular a la pala, con una velocidad de entrada -V_{inp}- de $30\ \mathrm{m/s}$ $(108\ \mathrm{km/h})$. El impacto se produce en el punto dulce, Fig. 4. Este punto se ha situado a 140 mm del punto inferior del corazón, que es como se denomina a la forma triangular que el marco hace sobre la empuñadura, véase Fig. 3. Se han considerado restringidos todos los movimientos de la empuñadura.

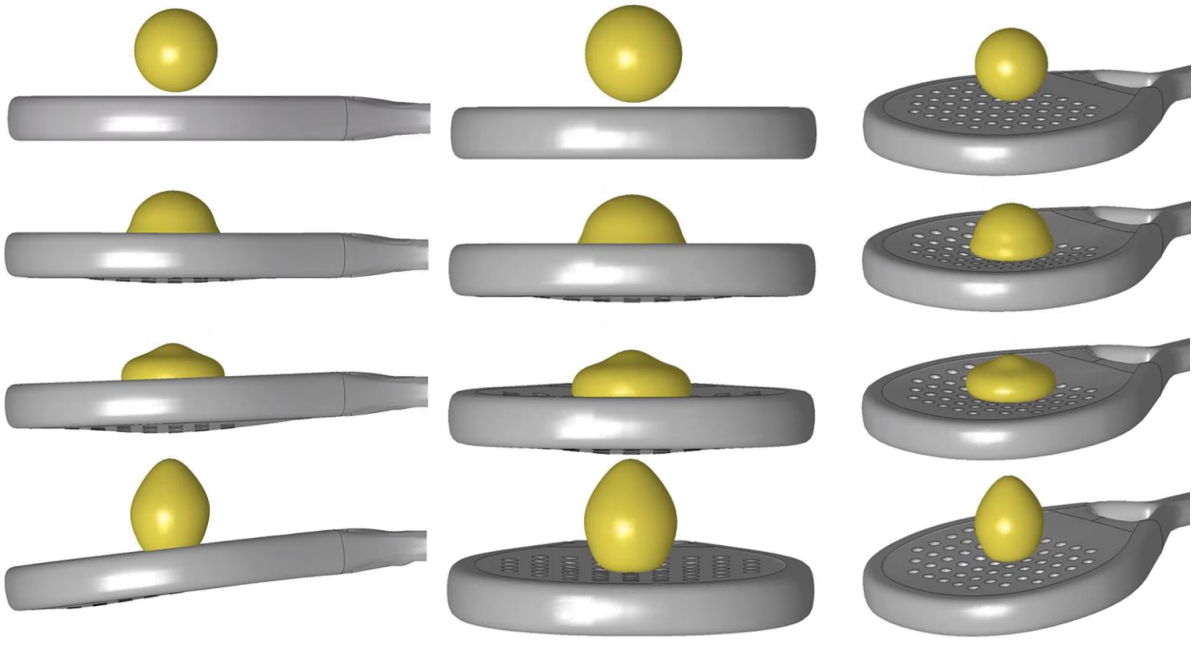

Figura 4. *Instantes de golpeo bola-pala* Md*. Vistas lateral, frontal y perspectiva.*

5.1. Parámetros de salida: velocidad y ángulo

Se ha identificado el rendimiento de la pala como la relación entre la velocidad a la que sale la bola, en la misma dirección de entrada, y la velocidad de entrada.

El control, para un golpe perpendicular como el analizado, ha sido identificado con la capacidad de la pala para devolver la bola según la misma dirección. En consecuencia, cuando más se aparte la bola de esa dirección en la salida, consecuencia de la rigidez general de la pala, menor será el control.

La tabla 4 resume los parámetros de rendimiento y control normalizados. Según se ha indicado, las componentes x e y de la velocidad de salida, véase el sistema de referencia en la Fig. 3, el factor de normalización es la velocidad de entrada -V_{inp}-. Para el ángulo de salida se ha tomado como factor de normalización el ángulo de salida de la pala Md, que es la pala que promueve esta investigación. El valor de ese ángulo ha sido $3.4°$.

En la tabla 4, se puede apreciar cómo el modelo en bruto de la pala Marvel es el que da una mayor velocidad de salida, i.e., mayor rendimiento- con menor desviación, i.e., mayor control. Este resultado es consecuencia del hecho de que sea la pala más rígida.

Tabla 4. Parámetros de salida normalizados.

Modelo	V_x/V_{inp}	V_v/V_{inp}	θ/θ_{Md}
Md	0.032	0.425	1
Mb	0.026 (18.8%↓)	0.436 (2.6% ↑)	0.786(21.4% ↓)
Cm	0.031 (≈)	0.410 (3.5% ↓)	1.006(≈)
HH	0.028 (14.3% ↓)	0.427 (≈)	0.861(13.9% ↓)

Coherentemente con lo anterior, el modelo HH, que tampoco tiene orificios, al menos, en la parte central, tiene, también, mayor control, pero la mejora de rendimiento es despreciable respecto al modelo Md.

Respecto del modelo Cm, los resultados no indican que la distribución de orificios que realiza el fabricante suponga una mejora del control, pero sí indica una caía de rendimiento.

5.2. Reacciones

Las reacciones en la empuñadura han de estar relacionadas con la confortabilidad del jugador y, de alguna manera, ha de ser una forma de medir cuanto de lesiva puede resultar determinada pala con su uso prolongado.

En este sentido, los resultados mostrados en la tabla 5, normalizados con los valores obtenidos para el modelo Md no resultan concluyentes.

Los resultados del modelo Md, utilizados en la normalización de la tabla 5 han sido $R_{Md} = 873.34\ N$, para la resultante de fuerzas y $M_{Md} = 1.18\ N \cdot m$ para el momento resultante.

Tabla 5. Momentos y fuerzas resultantes normalizados.

Modelo	R/R_{Md}	M/M_{Md}
Md	1	1
Mb	0.91 (9%↓)	0.96 (4% ↓)
Cm	1.01 (1% ↑)	0.98 (2% ↓)
HH	0.98 (2% ↓)	1.07 (7% ↑)

La disminución de reacciones en el modelo Mb indicaría que éste sería el menos hostil para el jugador siendo los resultados de fuerzas y momentos en los modelos Cm y HH contradictorios: en el primero, se produce un ligero incremento de la fuerza y un decremento del momento mientras que en el segundo ocurre lo contrario. En todo caso las diferencias no resultan significativas.

5.3. Durabilidad

Para cuantificar la afectación que, sobre la durabilidad de la pala, pueda tener la disposición (y tamaño) de los orificios, se ha calculado el coeficiente de seguridad determinando, en la superficie exterior, la que recibe el impacto de la bola, las máximas tensiones normales según las direcciones x y z (véase sistema de referencia en la Fig. 3). Con estas tensiones se calculan los esfuerzos por unidad de longitud a partir de los cuales el programa MIC-MAC [12] calcula el coeficiente de seguridad -factor R en

nomenclatura MIC-MAC- en cada una de esas direcciones. Obviamente se identifica como coeficiente de seguridad, para cada modelo, el menor de ambos.

Los factores de seguridad, normalizados con el valor obtenido para el modelo Md, aparecen en la tabla 6.

Tabla 6. Coeficiente de seguridad normalizado.

Modelo	Factor R/ Factor R_{Md}
Md	1
Mb	2.31 (130%↑)
Cm	1.05 (5% ↑)
HH	1.60 (60% ↑)

Los llamativos resultados de los modelos Mb y HH, con un factor de seguridad muy superior al modelo Marvel definitivo, es la cuantificación de un resultado esperable al tratarse de modelos sin orificios en la zona dulce. Este resultado no tendría repercusiones prácticas por tratarse de modelos no comercializables.

En el caso del modelo Cm, tampoco es sorprendente. Al tener este modelo agujeros más pequeños en torno a la zona dulce, la debilitación mecánica de esta zona ha de ser menor que en el modelo Md, en el que los orificios son mayores. En cualquier caso, la diferencia es poco significativa.

6. CONCLUSIONES Y DESARROLLOS FUTUROS

Las conclusiones mostradas en el epígrafe anterior, donde se realiza la comparación de un parámetro de diseño entre cuatro modelos diferentes, nos llevan a una conclusión definitiva respecto de la motivación de este trabajo desde su inicio: en la actualidad se ha desarrollado una herramienta numérica fiable para la evaluación de los principales aspectos de diseño relacionados con la fabricación de palas de pádel.

Mediante la herramienta desarrollada, un fabricante puede tomar decisiones de diseño: materiales de cada parte de la pala, forma y tamaño de la pala, mayor o menor presencia de orificios y distribución de éstos; en base a valores cuantificables que están directamente relacionadas con el rendimiento de la pala, su control, durabilidad y afectación mecánica sobre el brazo del palista. De esta forma un fabricante puede anticipar el comportamiento de la pala antes de comenzar su producción.

En cuanto a los desarrollos futuros cabe destacar que, en este trabajo, el modelo tomado para el comportamiento del material del núcleo -espuma EVA- ha sido un modelo de comportamiento elástico, véase epígrafe 2.1. Es conocido que las espumas en general, y la EVA en particular, tienen un comportamiento viscoelástico. Además, ante las acciones que intervienen el problema que se trata en este trabajo, con grandes velocidades de deformación, es esperable que el comportamiento sea viscoelástico no lineal.

Paralelamente al desarrollo de este trabajo, sus autores están trabajando en la caracterización viscoelástica no lineal del material del núcleo. Cuando esta caracterización esté terminada, y ese comportamiento se incorpore al modelo, tendremos un modelo aún más realista, pero, además,

estaremos en condiciones de poder afirmar cómo de acertado puede resultar la aproximación elástica lineal de la espuma al comportamiento general de la pala.

Una continuación necesaria para este trabajo es la comparación experimental de los resultados que han sido aquí obtenidos de forma numérica.

REFERENCIAS

[1] S. R. Goodwill and S. J. Haake, "Spring damper model of an impact between a tennis ball and racket," *Proc. Inst. Mech. Eng. Part C J. Mech. Eng. Sci.*, vol. 215, no. 11, pp. 1331–1341, Nov. 2001.

[2] S. R. Goodwill and S. J. Haake, "Modelling of tennis ball impacts on a rigid surface," *Proc. Inst. Mech. Eng. Part C J. Mech. Eng. Sci.*, vol. 218, no. 10, pp. 1139–1153, Oct. 2004.

[3] S. R. Goodwill, R. Kirk, and S. J. Haake, "Experimental and finite element analysis of a tennis ball impact on a rigid surface," *Sport. Eng.*, vol. 8, no. 3, pp. 145–158, 2005.

[4] T. Allen, S. Haake, and S. Goodwill, "Comparison of a finite element model of a tennis racket to experimental data," *Sport. Eng.*, 2009.

[5] N. Elliott, S. Choppin, S. Goodwill, T. Senior, J. Hart, and T. Allen, "Single view silhouette fitting techniques for estimating tennis racket position," *Sport. Eng.*, 2018.

[6] M. L. Yang, "Baseplate of table tennis racket: Allocation for material innovation and playing methods," in *Applied Mechanics and Materials*, 2013.

[7] D. A. Russell, "Acoustics of ping-pong: Vibroacoustic analysis of table tennis rackets and balls," *J. Sports Sci.*, 2018.

[8] F. J. Huera-Huarte, "Some observations on the flow physics of paddle racquets," *Proc. Inst. Mech. Eng. Part P J. Sport. Eng. Technol.*, vol. 228, no. 1, pp. 40–48, Mar. 2014.

[9] et al. Molí Díaz, Adrián Antonio, "Experimental numerical correlation of a padel racket subject to impact," in *CMMoST 2019: 5th International Conference on Mechanical Models in Structural Engineering*, 2019, pp. 351–368.

[10] T. B. Allen, "Finite element model of a tennis ball impact with a racket," Sheffield Hallam University, 2009.

[11] R. W. Ogden, *Non-linear Elastic Deformations*. 1984.

[12] Stephen W.Tsai, *Composites Design*, 4th ed. Dayton, Paris and Tokyo: THINK COMPOSITES, 1988.

ESTIMATION AND VALIDATION OF MODAL MASSES IN CONSTANT MASS-DENSITY SYSTEMS

García-Fernández, Natalia[1]; Stufano, Roberto[2]; Aenlle, Manuel[3]; Fernández, Pelayo[4]

ABSTRACT

A modal model describes the structural dynamic behaviour in terms of modal parameters: natural frequencies, damping ratios, mode shapes and modal masses. Mode shapes can be normalized in many different ways, being mass normalization and normalization to the largest component equal to unity, the techniques commonly used in FEM software. Mass normalized mode shapes contain information of both the modal mass (magnitude of the vector) and the shape of the mode (deflection shape). The modal mass in constant mass-density systems is equal to the product between the total mass of the structure, and the length of the mode shapes squared. This means that a relationship between the modal masses of the different modes exists. In this paper, a steel structure was tested by Experimental Modal Analysis (EMA) and Operational Modal Analysis (OMA). The modal masses extracted from a numerical model and those estimated from experimental results are compared and validated.

Keywords: modal mass, OMA, EMA, mode shape normalization

1. INTRODUCTION

The dynamic behavior of a structure can be expressed, in terms of modal parameters, by the frequency response function (FRF), which for proportional damped models is given by [1-7]:

$$\boldsymbol{H}(\boldsymbol{\omega}) = \sum_{r=1}^{N_M} \frac{\boldsymbol{\psi_r}\boldsymbol{\psi_r^T}}{m_r(\omega_r^2 - \omega^2 + i2\zeta_r\omega\omega_r)} \quad (1)$$

Where N_M is the number of modes, ω_r is the natural frequency, ζ_r the damping ratio, ψ_r the mode shape and m_r the modal mass, respectively, of the r-th mode. If the mass matrix $\boldsymbol{M}$ and the mode shapes $\boldsymbol{\psi}_r$ are known, the modal mass can be estimated by[1-7]:

$$m_r = \boldsymbol{\psi_r^T M \psi_r} \quad (2)$$

[1] *Department of Construction and Manufacturing Engineering; University of Oviedo (SPAIN). garciafnatalia@uniovi.es*
[2] [2]*Department of Civil, Environmental, Construction and Chemical Engineering; Polytechnic University of Bari (ITALY). r.stufano1@studenti.poliba.it*
[3] *Department of Construction and Manufacturing Engineering; University of Oviedo (SPAIN). aenlle@uniovi.es*
[4] *Department of Construction and Manufacturing Engineering; University of Oviedo (SPAIN). fernandezpelayo@uniovi.es (Corresponding author)*

where the modal mass m_r is a real scalar in un-damped and proportionally damped models.

Mode shapes can be normalized in many different ways, the most common techniques being mass normalization, normalization to the unit length of the mode shape (length scaling) and normalization to a component (usually to the largest component) equal to unity (DOF scaling). A mode shape is said to be mass normalized when the modal mass is dimensionless unity, i.e. $m = 1$. On the other hand, a mode shape is said to be un-scaled if it is not mass normalized. The mass normalized $\boldsymbol{\phi}$ and the unscaled $\boldsymbol{\psi}$ mode shapes are related by the equation [8-10]:

$$\boldsymbol{\phi} = \frac{1}{\sqrt{m}}\boldsymbol{\psi} \tag{3}$$

The modal mass is also defined as a scaling parameter for the mode shapes, i.e., it is used to convert the original unscaled mode shape vector $\boldsymbol{\psi}$ to the scaled (mass-normalized) mode shape vector $\boldsymbol{\phi}$, i.e.:

$$\boldsymbol{\phi} = \alpha\boldsymbol{\psi} \tag{4}$$

Where α is the scaling factor, which is related to the modal mass by:

$$\boldsymbol{m} = \frac{1}{\alpha^2} \tag{5}$$

In classical modal analysis, the modal masses are obtained from the experimental FRF's using some of the several identification techniques [4,5,7], which are fully described in the classical books of modal analysis [4,5,7].

Operational modal analysis (OMA) has become a very useful technique for modal identification of civil [6,11,12] and mechanical structures [6,11,12]. In OMA, the forces are unknown, and the modal masses cannot be estimated, i.e. only the un-scaled mode shapes can be identified for each mode [6,11,12]. If the modal masses are needed (structural modification, health-monitoring applications, damage detection, etc.), additional procedures to estimate the modal masses have to be used [12,13].

Several approaches to estimate modal masses in OMA have been proposed recently based on modifying the dynamic behavior of the structure by changing the stiffness and/or the mass and then performing operational modal analysis on both the original and the modified structure [13]. An alternative to the mass change method is to consider the experimental modal masses equal to those corresponding to finite element model of the structure [9]. A method to estimate the modal masses which combines the numerical and the experimental mode shapes was proposed by Aenlle and Brincker [12].

Several methods have also been proposed to estimate modal masses combining OMA and the response of the structure subject to a certain artificial excitation [14,15]. The OMAH technique was proposed in [15] where operational modal analysis is combined with mono-harmonic excitation applied by an actuator.

If the mass-density ρ of a system is constant, eq. (2) can be expressed as [8,10]:

$$m = \rho\boldsymbol{\psi}^{\boldsymbol{T}}\boldsymbol{V}\boldsymbol{\psi} \tag{6}$$

Where $\boldsymbol{V}$ is the volume matrix. If the total volume of the system is denoted as V_T, eq. (6) can also be formulated as:

$$m = M_T \frac{\boldsymbol{\psi^T V \psi}}{V_T} \tag{7}$$

Where the term:

$$L^2 = \frac{\boldsymbol{\psi^T V \psi}}{V_T} \tag{8}$$

is the length of the mode shape $\boldsymbol{\psi}$, which depends on the volume of the structure and on the mode shapes. Using Eq. (8), Eq. (7) can also be expressed as:

$$m_r = M_T \boldsymbol{L^2} \tag{9}$$

which indicates that, in constant mass-density systems, the modal mass is equal to the product between the total mass of the structure and the length squared. From eq. (9) it is derived that the modal masses of the structure are related by:

$$\frac{m_1}{L_1^2} = \frac{m_2}{L_2^2} = \cdots = \frac{m_r}{L_r^2} = \cdots = M_T \tag{10}$$

Where the subindex 'r' indicates the order of the mode.

If a structure is discretized with many finite elements of equal volume ΔV, eq. (8) can be accurately approximated by [10]:

$$L^2 \cong \frac{\Delta V \sum_{\boldsymbol{k=1}}^{\boldsymbol{N_V}} \psi_k^2}{N_V \Delta V} \tag{11}$$

Where N_V is the number of elements (number of volumes) of the structure. As the components of the mode shapes are commonly known at the nodes of the elements, eq. (11) can also be approximated by means of the expression:

$$L^2 \cong \frac{\Delta V \sum_{\boldsymbol{k=1}}^{\boldsymbol{N}} \psi_k^2}{N \Delta V} = \frac{\boldsymbol{\psi^T \psi}}{N} \tag{12}$$

Where N is the number of nodes of the model and $\boldsymbol{\psi^T \psi} = \boldsymbol{L_E^2}$ is the squared Euclidean length of the mode shape

In this paper, the modal masses of a steel structure are estimated using different techniques. A Finite element model was assembled in ABAQUS, from which the naturales frequencies, mode shapes and modal masses were extracted with a frequency analysis. The experimental modal parameters were estimated with operational modal analysis and the modal masses estimated with a method which combines experimental and numerical mode shapes [12]. Finally, the modal masses were also estimated with experimental modal analysis.

2. A STEEL STRUCTURE

2.1. Description

The structure consists of a vertical column (height $1.46\ m$) and a horizontal beam ($0.615\ m$), both with a rectangular hollow steel section $8cm \times 4cm$ and thickness $4mm$, which is fixed at the bottom of the column (see Fig. 1). The structure was weighed the total mass being $M_{Tx} = 13{,}42\ kg$

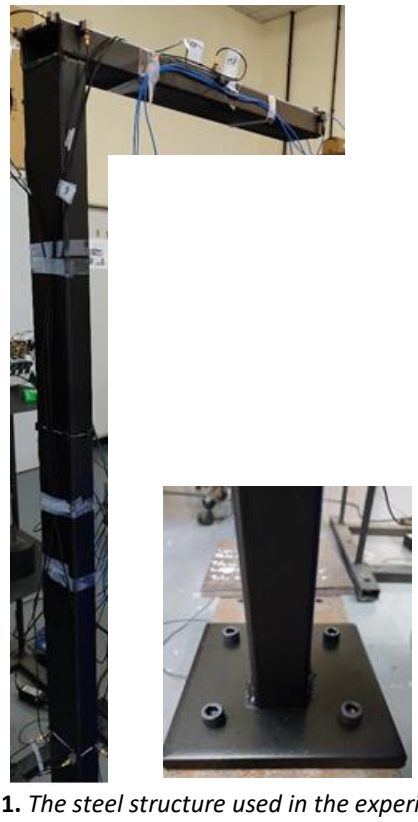

Figure 1. *The steel structure used in the experiments.*

2.2. Finite element model

A model of the structure was assembled in ABAQUS [16] and meshed with shell elements S8R (8 nodes with reduced integration) using a global size of $0.005m$ (see Figure 2). The following mechanical properties were considered for the steel: mass density $\varrho = 7850\ kg/m3$, Young's modulus $E = 210 \cdot 10^9\ N/m2$ and Poisson ratio $\nu = 0.3$. The total mass of the model is $M_{TE} = 14.59\ kg$.

The natural frequencies and the modal masses (mode shapes normalized to the largest component equal to unity) corresponding to the first 8 modes are shown in Tables 1 and 4, respectively. The mode shapes are shown in Figure 3.

Table 1. Natural frequencies (Hz)

Mode	Natural frequencies (Hz)				
	FE model	**OMA (SSI)**	**EMA**	**Error OMA [%]**	**Error EMA [%]**
1	12.53	10.945	10.938	12.65	12.71
2	20.85	18.953	18.75	9.10	10.07
3	55.74	50.995	50.781	8.51	8.90
4	55.31	54.39	54.688	1.66	1.12
5	131.98	115.485	115.625	12.50	12.39
6	198.10	179.742	180.469	9.27	8.90
7	324.78	283.539	284.572	12.70	12.38
8	502.56	464.154	465.35	7.64	7.40

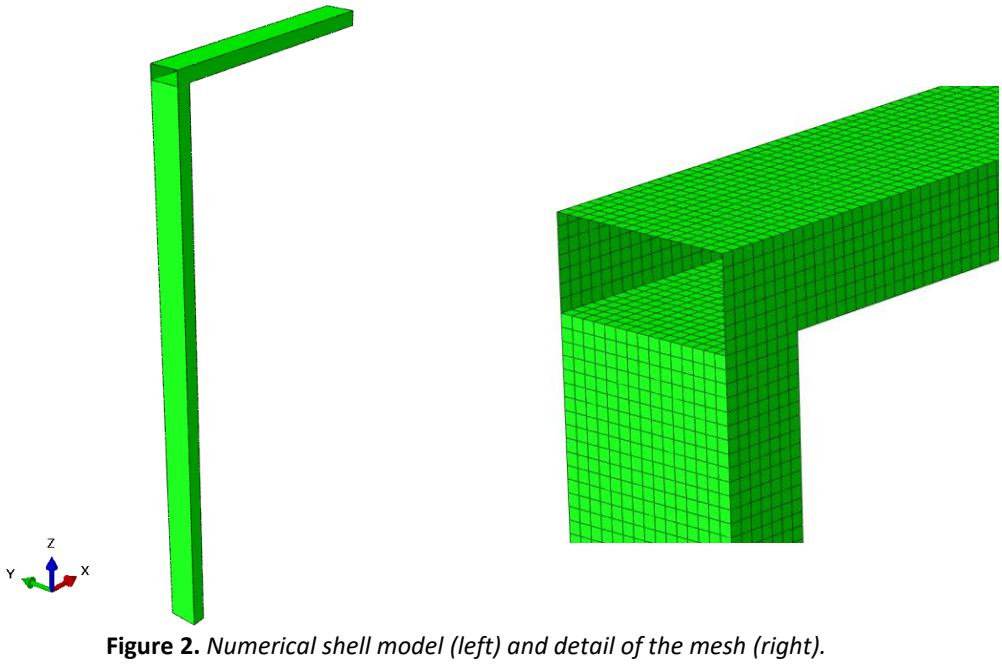

Figure 2. *Numerical shell model (left) and detail of the mesh (right).*

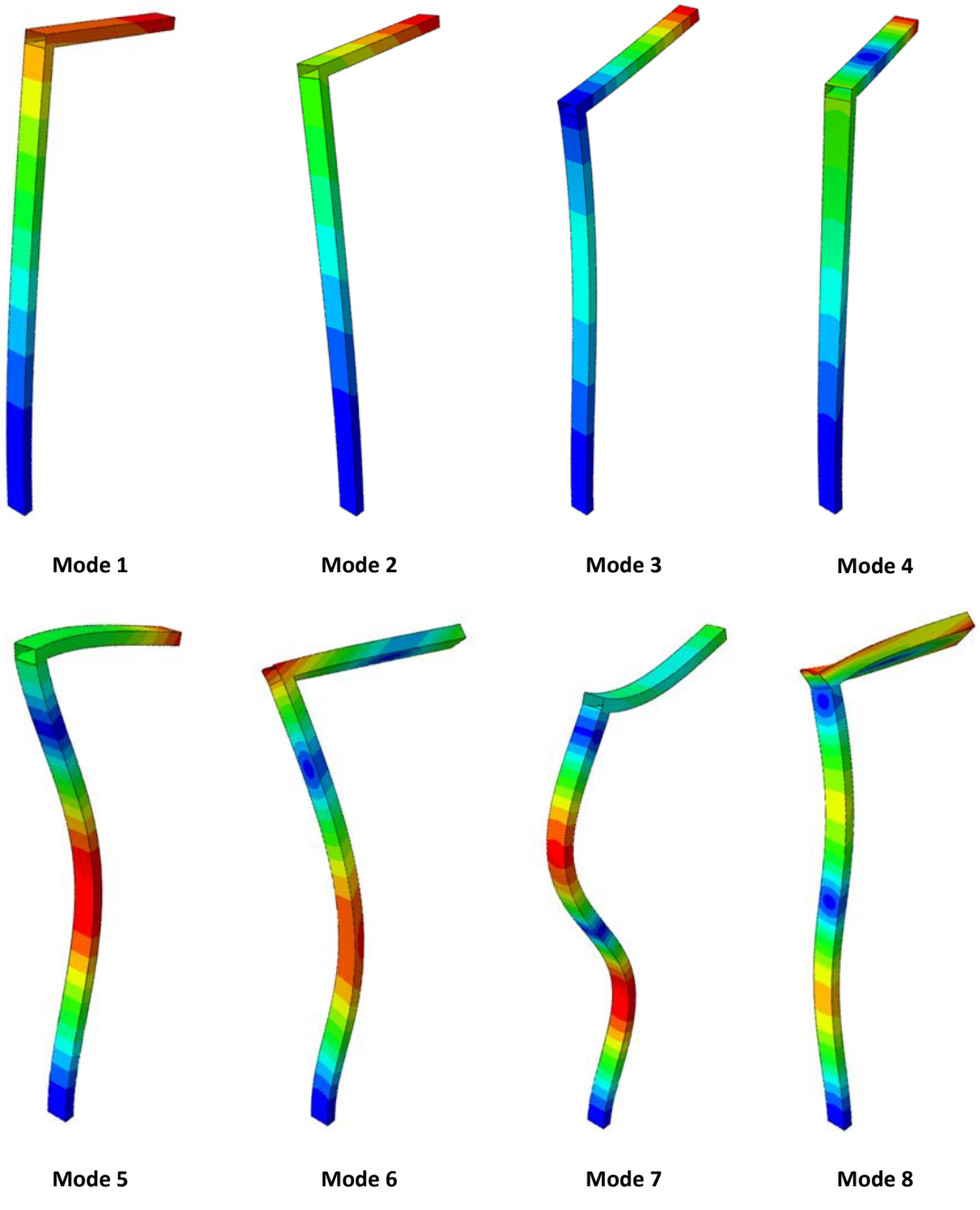

Figure 3. *Numerical mode shapes*

2.3. Operational modal analysis

The experimental modal parameters were estimated with Operational Modal Analysis (OMA). The structure was excited applying many small hits with the hands, random in time and space [6] and the responses were measured in fifteen points using twelve accelerometers (two data sets) with a sensitivity of 100 mV/g. The test setup is shown in Figure 4 where the arrows indicate the measured directions. The responses were recorded for approximately 4 minutes with a sampling frequency of 2132 Hz using a National Instruments Compact DAQ acquisition system equipped with NI9234

acceleration modules. The singular value decomposition of the experimental responses is presented in Figure 5.

The modal parameters were estimated with the stochastic subspace iteration (SSI) [6] technique. The estimated natural frequencies corresponding to the first 8 modes are presented in Table 1. The discrepancies in terms of naturals frequencies, between the numerical and the experimental model, are in the range 0-15%, whereas the modal assurance criteria (MAC) [4-7] (see Table 2) gives diagonal values over 0.9795, which indicates a good correlation in terms of mode shapes but, on the other hand, high values have been obtained out-off the diagonal.

Table 2. Modal assurance criteria (MAC)

	MAC							
Mode	1	2	3	4	5	6	7	8
1	0.9959	0.0003	0.1083	0.0005	0.1178	0.0000	0.0105	0.0000
2	0.0012	0.9960	0.0003	0.1167	0.0000	0.0051	0.0000	0.0825
3	0.1490	0.0002	0.9987	0.0001	0.1510	0.0000	0.0500	0.0000
4	0.0001	0.1590	0.0007	0.9972	0.0006	0.0893	0.0001	0.0447
5	0.1013	0.0000	0.1764	0.0000	0.9935	0.0002	0.0084	0.0000
6	0.0009	0.0039	0.0000	0.1204	0.0000	0.9927	0.0001	0.1524
7	0.0172	0.0000	0.0234	0.0000	0.0425	0.0000	0.9876	0.0001
8	0.0002	0.0700	0.0041	0.0557	0.0043	0.2200	0.0027	0.9795

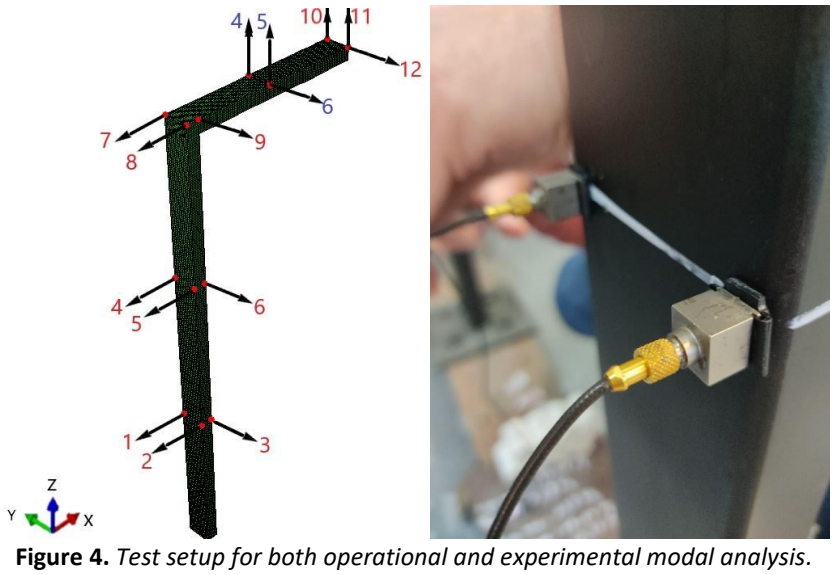

Figure 4. *Test setup for both operational and experimental modal analysis.*

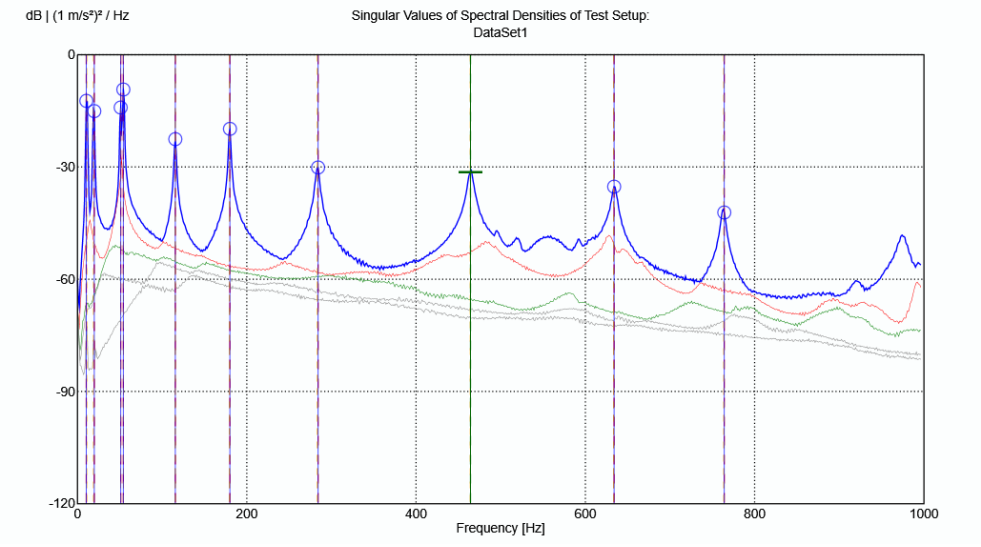

Figure 5. *Singular value decomposition of the responses.*

2.4. Experimental modal analysis

The modal parameters were also estimated with experimental modal analysis, using the same sensors, instrumentation, and test setup as those used in OMA. The structure was excited with an impact hammer applying the forces in DOF's 10, 11 and 12, respectively. The modal parameters were estimated with the Complex Mode Indication Function (CMIF) technique [4,5,7].

3. LENGTH OF MODE SHAPES

The square length L_{FE}^2 of the numerical mode shapes were obtained using eq. (12). In this paper the squared length L_x^2 of the experimental mode shapes were estimated from the expanded experimental mode shapes.

According to the structural dynamic modification theory, the experimental modal mode shapes can be expressed as a linear combination of the numerical ones [17] by means of the expression:

$$\boldsymbol{\psi_x = \phi_{FE} T} \tag{13}$$

Where $\boldsymbol{T}$ is a transformation matrix, which can be estimated by:

$$\boldsymbol{T = \phi_{FE}^{-1} \psi_x} \tag{14}$$

Due to the fact that the experimental mode shapes are only known at the measured or active DOF's, an approximation of matrix $\boldsymbol{T}$ can be obtained from the expression:

$$\boldsymbol{T = \phi_{FEa}^{+} \psi_{xa}} \tag{15}$$

Where subindex 'a' indicates active or measured. Eq. (13) can be now used to expand the experimental mode shapes to the unmeasured DOF's.

The square length L_x^2 of the experimental mode shapes were estimated using the expanded experimental mode shapes in eq. (12) The diagonal terms of matrices $\boldsymbol{L_{FE}^2}$ and $\boldsymbol{L_x^2}$ are shown in Table 3.

Table 3. Squared length of the numerical and experimental mode shapes

Mode	Square Length	
	L_{FE}^2	L_x^2
1	0.4734	0.4749
2	0.2512	0.2782
3	0.1407	0.1405
4	0.1179	0.1175
5	0.4882	0.4900
6	0.3848	0.3844
7	0.3711	0.3614
8	0.3876	0.3202

4. MODAL MASSES

The modal masses of the L steel structure, corresponding to mode shapes normalized to the largest component equal to unity, and estimated from the numerical model, from experimental modal analysis and combining experimental and numerical parameters, are shown in Table 4.

The modal masses m_{FE} corresponding to the numerical model were extracted using a frequency analysis.

Due to the fact that the total mass of the experimental structure is known, the modal masses were also estimated with eq. (9), which particularized to the experimental model results in:

$$m_{x1} = M_{Tx} L_x^2 \tag{17}$$

The modal masses were also estimated using the equation (12);

$$m_{x2} = \boldsymbol{T}^{\boldsymbol{T}} \boldsymbol{T} \tag{18}$$

where matrix $\boldsymbol{T}$ has to be estimated using mass normalized numerical mode shapes and un-scaled experimental mode shapes [17].

Due to the fact that the total mass of the numerical and the experimental models are known, eq. (18) can be improved by:

$$m_{x2} = \beta \boldsymbol{T}^{\boldsymbol{T}} \boldsymbol{T} \tag{19}$$

Where β is the ratio between the total mass of both models, i.e.:

$$\beta = M_{Tx}/M_{TE} \tag{20}$$

Which for this structure is $\beta = 0.9075$.

Finally, the modal masses were estimated from the experimental modal analysis results, using the Complex Mode Indication Function (CMIF) technique.

The errors between the different techniques are shown in Table 5.

Table 4. Modal masses (kg). Mode shapes normalized to the largest component equal to unity

Mode	Modal masses (kg)				
	m_{FE}	$m_{x1} = M_{Tx}L_x^2$	$m_{x2} = \boldsymbol{T}^T\boldsymbol{T}$	$m_{x3} = \beta\boldsymbol{T}^T\boldsymbol{T}$	$\boldsymbol{m_{x4}}$ **EMA**
1	6.9033	6.3732	6.9460	6.3035	6.25
2	3.6589	3.7333	4.0540	3.6790	3.74
3	1.7099	1.5769	1.7082	1.5502	1.47
4	2.0423	1.8854	2.0390	1.8504	1.87
5	7.1208	6.5764	7.1831	6.5187	6.57
6	5.6175	5.1591	5.6162	5.0967	5.51
7	5.4204	4.8506	5.3671	4.8706	4.93
8	5.6316	4.2968	4.6581	4.2272	4.18

Table 5. Errors (%) between modal masses

Mode	Error (%)					
	m_{FE}-m_{x1}	$m_{x2} - m_{x1}$	$m_{x3} - m_{x1}$	m_{FE}-m_{x4}	m_{x2}-m_{x4}	m_{x3}-m_{x4}
1	8.32	8.99	1.09	10.45	11.14	0.86
2	1.99	8.59	1.45	2.17	8.40	1.63
3	8.43	8.33	1.69	16.32	16.20	5.46
4	8.32	8.15	1.86	9.21	9.04	1.05
5	8.28	9.23	0.88	8.38	9.33	0.78
6	8.89	8.86	1.21	1.95	1.93	7.50
7	11.75	10.65	0.41	9.95	8.87	1.20
8	31.06	8.41	1.62	34.73	11.44	1.13

Due to the fact that the mass-density of this structure is constant, the modal masses corresponding to each mode shape are related through Eq. (10). The ratios modal mass-squared length are presented in Table 6.

The ratios m_{FE}/L_{FE}^2 are, as expected, close to the total mass $M_{TE} = 14.59\ kg$ of the numerical model, for all the modes, the discrepancies being less than 1% (see Table 7). In this case, the ratios are not exactly equal to $M_{TE} = 14.59\ kg$ because the length of the numerical mode shapes is estimated using eq. (12), which is an approximation.

The ratio m_{x1}/L_x^2 coincides with $M_{Tx} = 13.42\ kg$ because Eq. (17) was used to estimate the modal masses.

The accuracy of Eq. (18) (m_{x2}) depends on the correlation, in terms of mass, between the numerical and experimental models. Due to the fact that there is a discrepancy of approximately 10% between the total masses of both (experimental and numerical) model, it is expected to have some error in the modal masses estimated with eq. (18). It can be observed that the ratio m_{x2}/L_x^2 is very close to $M_{TE} = 14.59\ kg$ for all the modes. The maximum discrepancies between m_{x2}/L_x^2 and $M_{Tx} = 13.42\ kg$ are less than 11% for all the modes (see Table 7).

The accuracy improves with Eq. (19), where the effect of the differences in mass is corrected with parameter $\beta = \frac{M_{Tx}}{M_{TE}} = 0.9075$. Thus, the precision obtained with m_{x3}/L_x^2 is better than that obtained with m_{x2}/L_x^2, being very accurate for all the modes (errors less than 2%).

With respect to the ratio m_{x4}/L_x^2 (modal masses estimated with experimental modal analysis), the discrepancies with $M_{Tx} = 13.42\ kg$ are less than 7% for all the modes, which is less than that obtained with m_{x2}/L_x^2.

Table 6. Ratio modal mass-square length

Mode	Ratio modal mass-square length				
	m_{FE}/L_{FE}^2	m_{x1}/L_x^2	m_{x2}/L_x^2	m_{x3}/L_x^2	m_{x4}/L_x^2
1	14.5815	13.4200	14.6262	13.2733	13.1607
2	14.5658	13.4200	14.5730	13.2250	13.4442
3	14.5152	13.4200	14.5367	13.1921	12.5100
4	14.4991	13.4200	14.5138	13.1713	13.3107
5	14.5855	13.4200	14.6580	13.3022	13.4068
6	14.6002	13.4200	14.6091	13.2577	14.3328
7	14.6066	13.4200	14.8488	13.4753	13.6395
8	14.5295	13.4200	14.5486	13.2029	13.0553

Table 7. Errors (%) between the estimated ratios modal mass – squared length and the total mass of the structure

Mode	Error [%]				
	m_{FE}/L_{FE}^2 - M_{TE}	m_{x2}/L_x^2 - M_{TE}	m_{x2}/L_x^2 - M_{Tx}	m_{x3}/L_x^2 - M_{Tx}	m_{x4}/L_x^2 - M_{Tx}
1	0.06	0.25	8.99	1.09	1.93
2	0.17	0.12	8.59	1.45	0.18
3	0.51	0.37	8.32	1.70	6.78
4	0.62	0.52	8.15	1.85	0.81
5	0.03	0.47	9.23	0.88	0.10
6	0.07	0.13	8.86	1.21	6.80
7	0.11	1.77	10.65	0.41	1.64
8	0.41	0.28	8.41	1.62	2.72

5. CONCLUSIONS

- The modal masses of a lab-scaled steel structure were estimated with experimental modal analysis, with a FE model, and combining experimental mode shapes (estimated with OMA) and numerical mode shapes.

- It has been proved that the ratio modal mass-squared length of the mode shapes is constant for all the modes, and equal to the total mass of the system, in constant mass-density systems.

- The experimental mode shapes were expanded to the un-measured DOF's using the transformation matrix T. Although there are discrepancies between the numerical and the experimental models, the length L_x of the experimental mode shapes were estimated with accuracy.

- The modal masses in constant mass-density systems can be estimated accurately with eq. (17) if the total mass of the system is known.

- The ratio modal mass-squared length of the mode shapes in constant-mass density systems can be used successfully to check if the modal masses have been estimated with accuracy.

ACKNOWLEDGEMENTS

The authors would like to express their gratitude to the Spanish Ministry of Science and Innovation for the financial support through the project MCI-20-PID2019-105593GB-I00/AEI/10.13039/501100011033

REFERENCES

[1] R. W. Clough and J. Penzien, Dynamics of structures. New York: McGraw-Hill, 1993.

[2] M. Aenlle, M. Juul, and R. Brincker, "Modal Mass and Length of Mode Shapes in Structural Dynamics," Shock Vib., vol. 2020, pp. 1–16, Jun. 2020, doi: 10.1155/2020/8648769.

[3] A. K. Chopra, Dynamics of Structures. New Jersey: Prentice Hall, 1995.

[4] N. Mendes Maia and J. Montalvão Silva, Theoretical and Experimental Modal Analysis. 1997.

[5] D. J. Ewins, Modal Testing: Theory, Practice and Application. Wiley, 2000.

[6] R. Brincker and C. E. Ventura, Introduction to Operational Modal Analysis. Chichester, UK: John Wiley & Sons, Ltd, 2015.

[7] W. Heylen, S. Lammens, and P. Sas, Modal analysis theory and testing. Belgium: Katholieke Universiteit Leuven, 2007.

[8] M. Aenlle, M. Juul, and R. Brincker, "Modal Mass and Length of Mode Shapes in Structural Dynamics," Shock Vib., vol. 2020, pp. 1–16, Jun. 2020, doi: 10.1155/2020/8648769.

[9] M. Aenlle and R. Brincker, "Basic Concepts of Modal Scaling," 8th Int. Oper. Modal Anal. Conf., 2019.

[10] M. Aenlle, F. Pelayo, and R. Brincker, “Modal Mass in Classical and Operational Modal Analysis,” 8th Int. Oper. Modal Anal. Conf., 2019.

[11] Rainieri C., Fabbrocino G., (2014). “Operational Modal Analysis of Civil Engineering Structures. An introduction and a guide for applications,” New York: Springer.

[12] M. Aenlle, R. Brincker, “Modal scaling in operational modal analysis using a finite element model,” International Journal of Mechanical Sciences, vol. 76, pp. 86–101, Nov. 2013, doi: 10.1016/j.ijmecsci.2013.09.003.

[13] M. Aenlle, R. Brincker, F. Pelayo, A.F. Canteli, “On exact and approximated formulations for scaling-mode shapes in operational modal analysis by mass and stiffness change,” Journal of Sound and Vibration, vol. 331, pp. 622–637, Jan. 2012, doi: 10.1016/j.jsv.2011.09.017

[14] A. Brandt, M. Berardengo, S. Manzoni, M. Vanali, A. Cigada, “Global scaling of operational modal analysis modes with the OMAH method,” Mechanical Systems and Signal Processing, vol. 117, pp. 52–64, Feb. 2019, doi: 10.1016/j.ymssp.2018.07.017

[15] P. Guillaume, T. De Troyer, C. Devriendt, G. De Sitter, “OMAX – Operational Modal Analysis in presence of eXogenous inputs,” Proc. of the 25th IMAC. 2007.

[16] “ABAQUS UNIFIED FEA.” Dassault Systems

[17] R. Brincker, A. Skafte, M. López-Aenlle, A. Sestieri, W. D'Ambrogio, A. Canteli, “A local correspondence principle for mode shapes in structural dynamics”, Mechanical Systems and Signal Processing, vol. 45, pp. 91–104, March. 2014, doi: 10.1016/j.ymssp.2013.10.025

STUDY OF THE REINFORCEMENT IN A FOOTBRIDGE WITH VIBRATION PROBLEMS

García-Fernández, Natalia[1]; F. Pelayo[2]; López-Aenlle, Manuel[3]; Muñiz-Calvente, Miguel[4]; Álvarez-Vázquez, Adrián[5];

ABSTRACT

Footbridges are slender structures and consequently susceptible to human-induced vibrations. For this reason, structural design codes establish frequency bands to be avoided in order to prevent resonances that could cause structural damages or affect the users comfort level. The specifications established by the codes also include a safety threshold in the acceleration amplitudes for the vertical and transversal directions. In this work, the dynamic behavior of the "Pumarín-Moreda" pedestrian footbridge, located in the city of Gijón (Spain), is studied. Since the coming into service of the footbridge (1995), the users reported some discomfort during the use of the structure and, in 2014, the Gijón council executed a structural reinforcement in order to improve its dynamic behavior. In this paper, the dynamic behavior of the pedestrian footbridge before and after the reinforcement is studied, using Operational Modal Analysis (OMA) and finite element models of the structure. The results before the reinforcement show values of natural frequencies and accelerations out of the acceptable levels. On the other side, these parameters were acceptable and of maximum comfort after the reinforcement.

Keywords: Footbridge, Human-induced vibrations, Modal Analysis, Structural vibrations, Structural reinforcement.

1. INTRODUCTION

The vibration serviceability assessment is one of the criteria that must be taken into account in the design of footbridges [1]. Footbridges are often slender structures, which, due to their low mass and low damping, are highly susceptible to human induced vibrations.

In this paper, the dynamic behaviour of a pedestrian footbridge located in the city of Gijón (Spain) is studied by numerical models and operational modal analysis (OMA).

[1] *Department of Construction and Manufacturing Engineering. University of Oviedo (SPAIN). garciafnatalia@uniovi.es (Corresponding author)*
[2] *Department of Construction and Manufacturing Engineering. University of Oviedo (SPAIN). fernandezpelayo@uniovi.es*
[3] *Department of Construction and Manufacturing Engineering. University of Oviedo (SPAIN). aenlle@uniovi.es*
[4] *Department of Construction and Manufacturing Engineering. University of Oviedo (SPAIN). munizcmiguel@uniovi.es*
[5] *Department of Construction and Manufacturing Engineering. University of Oviedo (SPAIN). alvarezvadrian@uniovi.es*

This footbridge (hereafter Pumarín-Moreda footbridge) links the neighborhoods of Pumarín and Moreda in the city of Gijón (Spain) (see Figure 1) and goes over the highway and two railways. It is a steel structure (approximately symmetric) with a concrete deck 2.5 meters wide. The total length of the footbridge is 160 m and consists of 3 spans, the central span being 60 meters long. The bridge entered into service in 1995 and since then, the users reported some discomfort during the use of the structure due to excessive vibration levels in both vertical and transversal directions.

A study of the dynamic behavior of this structure, before the reinforcement, was carried by numerical and experimental techniques. A finite element model was assembled in ABAQUS and the natural frequencies and the mode shapes were extracted by a frequency analysis. The numerical results were compared with those obtained by operational modal analysis.

Figure 1. *The Pumarín-Moreda footbridge*

The footbridge was reinforced in 2014 to improve its dynamic behavior. In order to study the effect of the reinforcement, the previous numerical model was modified considering the new structural elements and a new set of natural frequencies and mode shapes were extracted. The dynamic behavior of this pedestrian footbridge located is studied comparing the modal parameters of both (before and after the reinforcement) numerical models.

2. FE MODEL BEFORE REINFORCEMENT

A finite element model of the footbridge was assembled in ABAQUS. The structure was modelled with linear shell elements (S4 and S3). The concrete and the steel were modelled as linear-elastic, and following mechanical properties were considered for concrete: Young's modulus E=25 GPa, Poisson ratio ν=0.22 and for steel E=210 GPa, Poisson ratio ν=0.3. The boundary conditions, indicated in Fig. 2, were considered fixed (translations and rotations). The natural frequencies and mode shapes, corresponding to the first ten modes, obtained with a frequency analysis, are presented in Table 1 and Fig. 3, respectively.

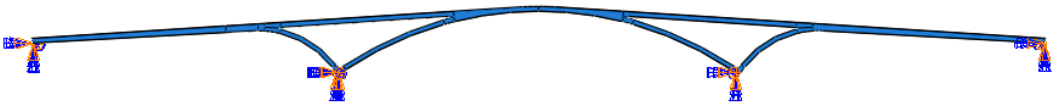

Figure 2. *Abaqus model.*

Table 1. Numerical and experimental modal parameters (L: lateral direction, V: vertical direction)

Mode_{num}	Direction	$f_{num}[Hz]$	Mode_{exp}	Direction	$f_{exp}[Hz]$	ξ_{exp} [%]	Error [%] $f_{num} - f_{exp}$
1	L	0.82	1	L	0.93	0.612	11.83
2	L	1.37	2	L	1.38	0.907	0.72
3	L	1.68	3	L	1.60	0.759	5.00
4	V	2.12	4	V	2.08	4.083	1.92
5	V	2.13	5	V	2.56	0.576	16.80
6	L	2.68	6	L	2.67	0.404	0.37
–	–	–	7	V	3.16	0.399	–
7	V	3.25	8	V	3.51	0.990	7.41
8	V	3.28	9	V	4.08	0.212	19.61
9	L	4.04	10	L	4.08	0.212	0.98
10	V	4.75	–	–	–	–	–

3. EXPERIMENTAL MODAL ANALYSIS (OMA)

The dynamic behavior of the structure was also studied by operational modal analysis under service conditions: pedestrians, runners and cyclists moving along the structure. Ten accelerometers (5 Reference sensors and 5 roving sensors) with a sensitivity of 10V/g were used to measure the acceleration response of the structure in 15 points utilizing 2 data sets. The responses were recorded with a TEAC-LX120 data acquisition system for approximately 60 minutes (in each data set) and using a sampling frequency of 50 Hz. The test setup is shown in Figure 4.

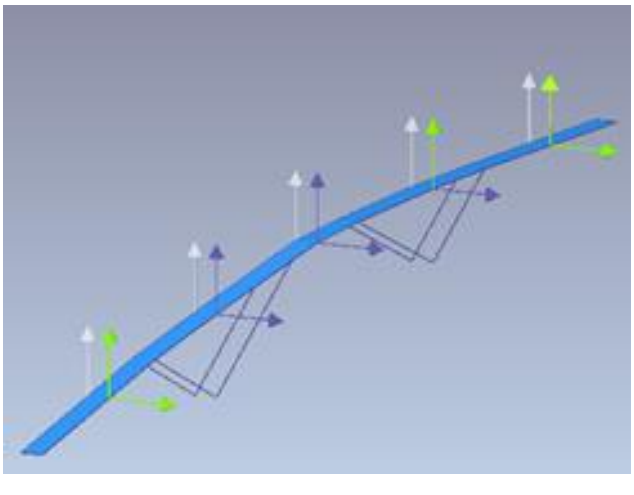

Figure 4. *Test setup.*

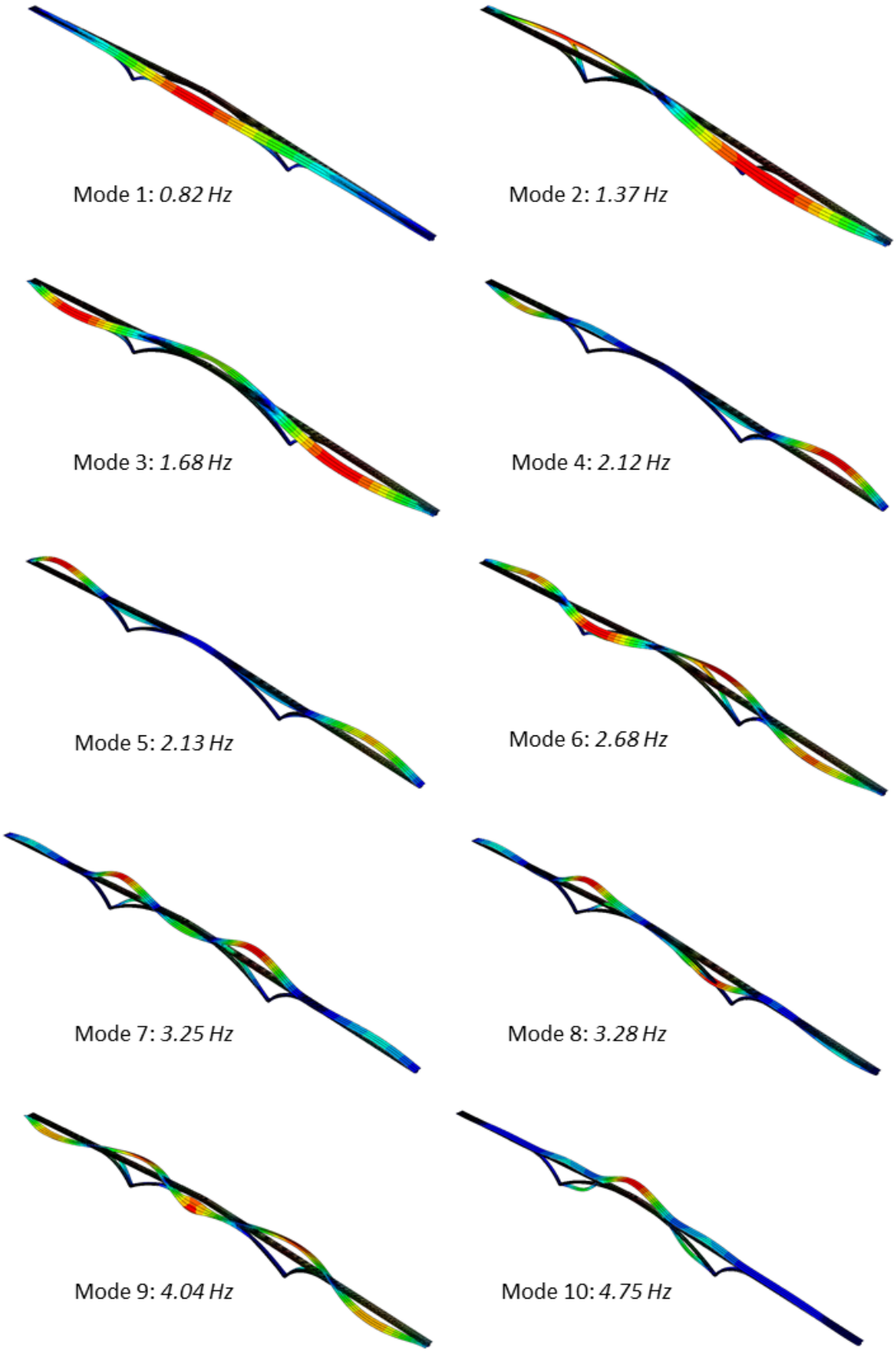

Figure 3. *Numerical mode shapes of the initial structure.*

The Singular Value Decomposition (SVD) of the experimental responses are shown in Figure 5.

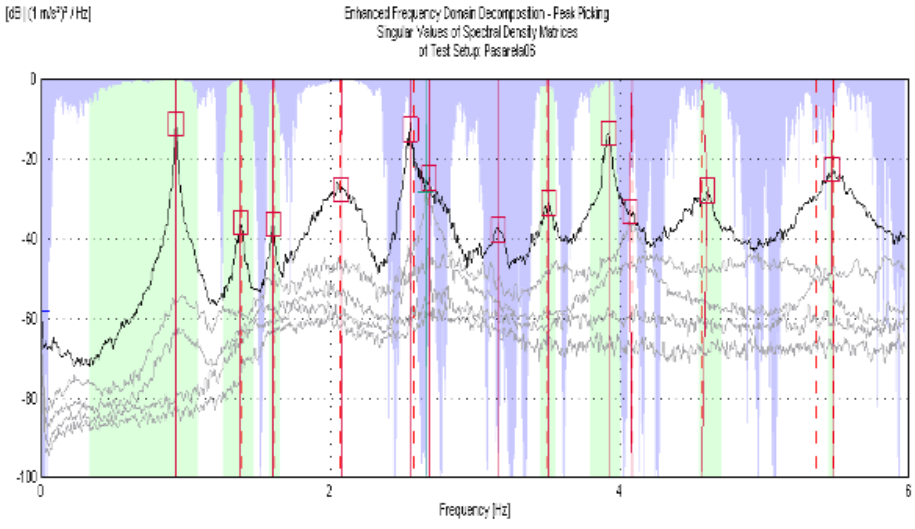

Figure 5. *Singular Value Decomposition of the responses. Structure before reinforcement*

The modal parameters were estimated using the Frequency Domain Decomposition (EFDD) technique [8] implemented in the ARTEMIS MODAL software and 8 modes were identified in the range 0−4 Hz. The natural frequencies and damping ratios are shown in Table 1. The error between experimental and numerical natural frequencies is also shown in Table 1.

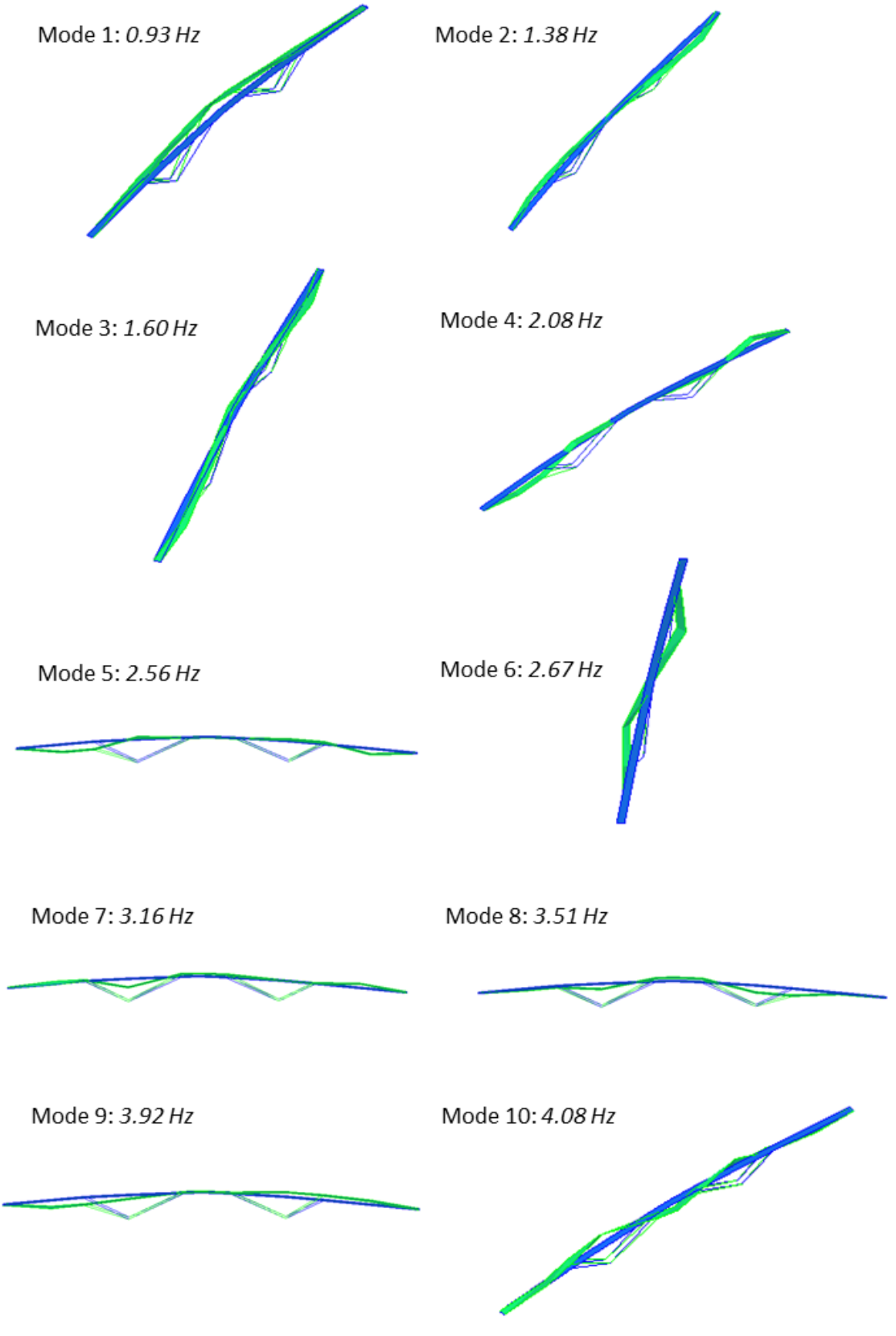

Figure 6. *Experimental mode shapes before reinforcement*

4. SERVICEABILITY LIMIT STATE (SLS) ANALYSIS

Pedestrians running or walking on footbridges can affect to the dynamic response of these structures. The running and walking frequencies are usually provided in the codes (see Table 2) and in other literature. The simplest method for preventing the risk of resonance consists of avoiding the natural frequencies in the same range of pedestrian walking frequency (Table 3). For this reason, structural design codes establish frequency bands to be avoided in order to prevent resonances.

Table 2. Pedestrian range of frequencies [2, 3].

People…	Estimated frequency range [Hz]		
	CPA	**ISO 10137**	**SETRA**
Walking	1.25 – 2.40	1.20 – 2.40	1.60 – 2.40
Running	2.00 – 3.50	2.00 – 4.00	2.00 – 3.50
Walking (2nd mode)	2.50 – 4.60	2.40 – 4.80	–

Table 3. Critical frequencies in pedestrian bridges [2, 3, 4, 5, 6].

CODE		Frequency ranges [Hz]			
		Transversal		Vertical	
		Min	**Max**	**Min**	**Max**
EAE and IAP (Spain)		0.5	1.2	1.25	4.60
EHE (Spain)		<5			
Eurocode 0 – A.2		0	2.50	0	5
SETRA (France)	maximun risk	0.5	1.1	1.7	2.1
	medium risk	0.3	0.5	1	1.7
		1.1	1.3	2.1	2.6
	low risk	1.3	2.5	2.6	5
	negligible risk	0	0.3	0	0.1
		2.5	Inf	5	Inf

If Tables 1 and 3 are compared, it is inferred that most of the natural frequencies are within the critical range recommended by the codes [2, 3, 4, 5, 6, 7]. It has been indicated with shadow in Table 3, whether there are modes with natural frequencies in the ranges that the codes suggest to avoid.

According to the Spanish codes EAE [7], EHE [5] and IAP [4], there are natural frequencies in the frequency range to be avoided. The same can be said for the EUROCODE. With respect to SETRA code [3], there are lateral and vertical modes with frequencies in the ranges corresponding to maximum risk. The codes [2, 3, 4, 5, 6, and 7] also provide values for the critical vertical and transversal accelerations and establish different comfort levels (see Table 4).

Table 4. Acceleration ranges for vertical and horizontal vibrations

CODE	Comfort	Acceleration ranges [m/s^2]	
		Vertical	Horizontal
IAP/EAE	maximum	<0.5	<0.1
	médium	0.5 to 1	0.1 to 0.3
	low	1 to 2.5	0.3 to 0.8
	not acceptable	>2.5	>0.8
SETRA	maximum	<0.5	<0.1
	medium	0.5 to 1	0.1 to 0.3
	low	1 to 2.5	0.3 to 0.8
	not acceptable	>2.5	>0.8
E5-Annex 2	aceptable (normal condition)	<0.7	<0.2
	Aceptable (exceptional)		<0.4
RPM-95	Not aceptable	>0.7	>0.4

The maximum acceleration values measured during the experimental tests in the horizontal and vertical directions were 0.553 m/s^2 and 1.047 m/s^2, respectively. These maximum values were measured under service conditions: pedestrians, runners and cyclists moving along the structure. According to Table 4, the structure is classified of low comfort attending to IAP/EAE and SETRA, whereas these acceleration values are not acceptable for the Eurocode 5 (A2). The acceleration limits that were exceed during the experimental test have been shaded in Table 4.

5. REINFORCEMENT OF THE STRUCTURE

Figure 7. *Details of the reinforcement in the pedestrian bridge.*

The structure was reinforced with four metallic "V" shaped piers (see Figures 7, 8 and 9) for design and construction (see Fig 7 and 8) decided to instal). Two located in the middle of each of the lateral spans

(A), the other two located at the position of the central supports (B). This reinforcement will improve the stiffness of the footbridge, mainly lateral vibrations.

Moreover, stiffeners (C) were located in the connection of the arches with the deck. The abutments were also modified in order to improve the torsional behaviour.

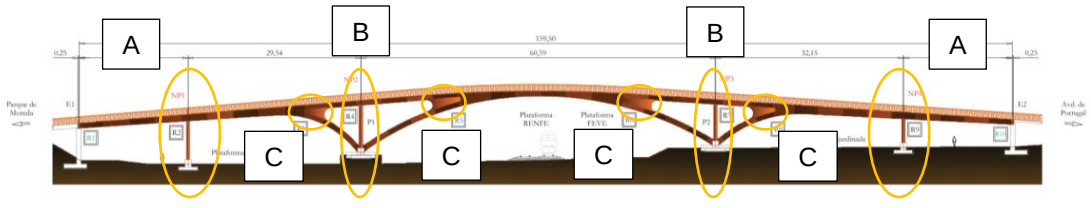

Figure 8. *Reinforced structure [10]*

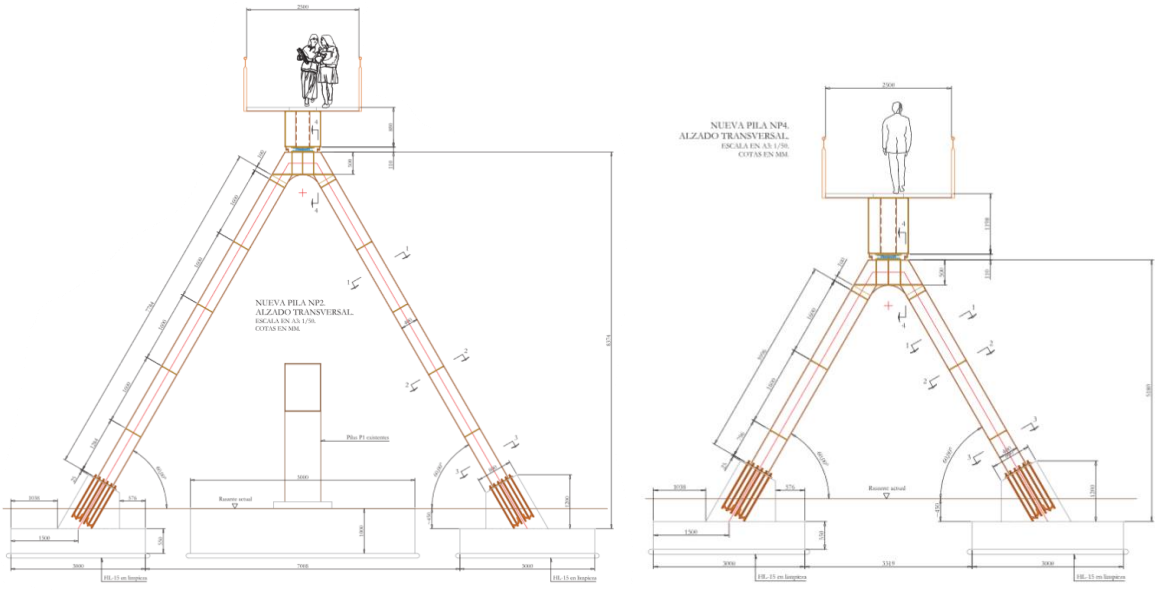

Figure 9. *"V" shaped piers [10].*

6. FE MODEL OF THE REINFORCED STRUCTURE

The dynamic behaviour of the reinforced footbridge was also studied with a second finite element model assembled in ABAQUS. The initial FE model (before reinforcement) was modified adding the V shaped piers, the stiffeners (C in Fig. 8) and changing the supports (A, B, in Fig. 8) at the abutments. The new FE model is shown in Fig. 10, where the V shaped piers were meshed with two-node linear elements (B31) and the stiffeners with Shell S4 elements. A hinge connection was considered between the V shape piers and the deck, whereas these piers were considered fixed to the ground (Fig. 12).

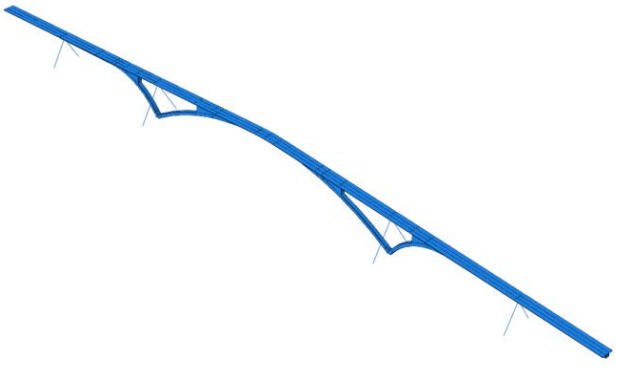

Figure 10. *ABAQUS reinforced model*

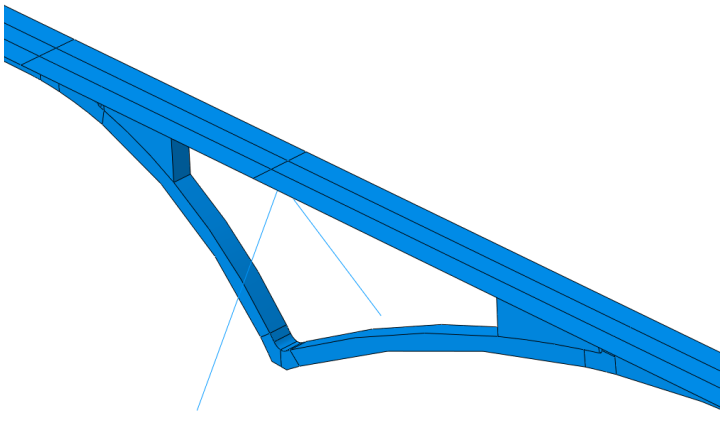

Figure 11. *Reinforcement detail*

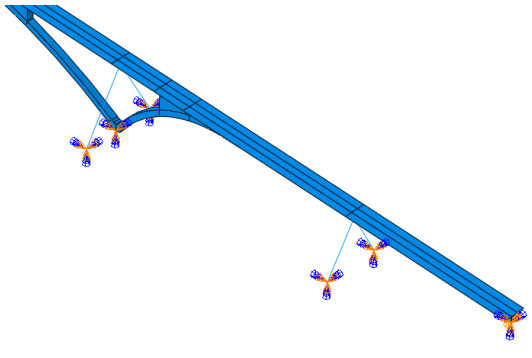

Figure 12. *Detail of the boundary conditions*

The natural frequencies corresponding to the first ten numerical modes of the reinforced model are shown in Table 5. It can be observed that all the natural frequencies have increased significantly. For example, the first lateral natural frequency has increased 94% (from 0.82 Hz to 1.59 Hz) whereas the first vertical natural frequency has increased 130% (from 2.12 Hz to 4.90 Hz). The mode shapes are presented in Figure 13.

Table 5. Natural frequencies of ABAQUS models (0 -> before reinforcement, 1 -> after reinforcement)

Mode	Direction	$f_{num0}[Hz]$	Mode	Direction	$f_{num1}[Hz]$
1	L	0.82	1	L	1.59
2	L	1.37	2	L	4.30
3	L	1.68	3	V	4.90
4	V	2.12	4	V	5.24
5	V	2.13	5	L	5.35
6	L	2.68	6	L	5.67
7	V	3.25	7	V	6.55
8	V	3.28	8	V	7.09
9	L	4.04	9	L	7.91
10	V	4.75	10	V	8.08

With regard to the lateral modes, all the natural frequencies are out of the critical ranges suggested by EAE and IAP. According to SETRA, this reinforced structure can be considered of minimum risk. As for the codes EHE and EUROCODE, there are modes with natural frequencies in the range to be avoided.

7. OPERATIONAL MODAL ANALYSIS AFTER REINFORCEMENT

The accelerations were also recorded with a mobile phone using the *iDynamics* app developed by the University of Kaiserslautem for teaching and learning purposes [11]. The maximum acceleration measured in service condition value registered in the vertical direction was 0.283 m/s^2 in the vertical direction and 0.053 m/s^2 in the lateral direction.

Table 6. Acceleration ranges for vertical and horizontal vibrations

	Maximum acceleration [m/s^2]		
	Before reinforcement	After reinforcement	Decrease [%]
Lateral	0.553	0.053	92.95
Vertical	1.047	0.283	72.97

According to the Table 4, the reinforced footbridge can be considered acceptable or of maximum comfort.

8. CONCLUSIONS

The dynamic behaviour of a footbridge in Gijón (Spain) was studied by numerical models assembled in ABAQUS and by experimental modal analysis. The analysis report that the structure has modes with natural frequencies in frequency ranges to be avoided and, also that the acceleration levels exceed the limits recommended by the codes [2, 3, 4, 5, 6].

The footbridge was reinforced in 2014 and the initial FE model was updated in order to consider all the new structural modifications (new elements and new boundary conditions) undertaken in the structure.

The natural frequencies of all the modes in the reinforced structure has increased significantly, and most of them are out of the critical frequency ranges for all the codes considered in this work.

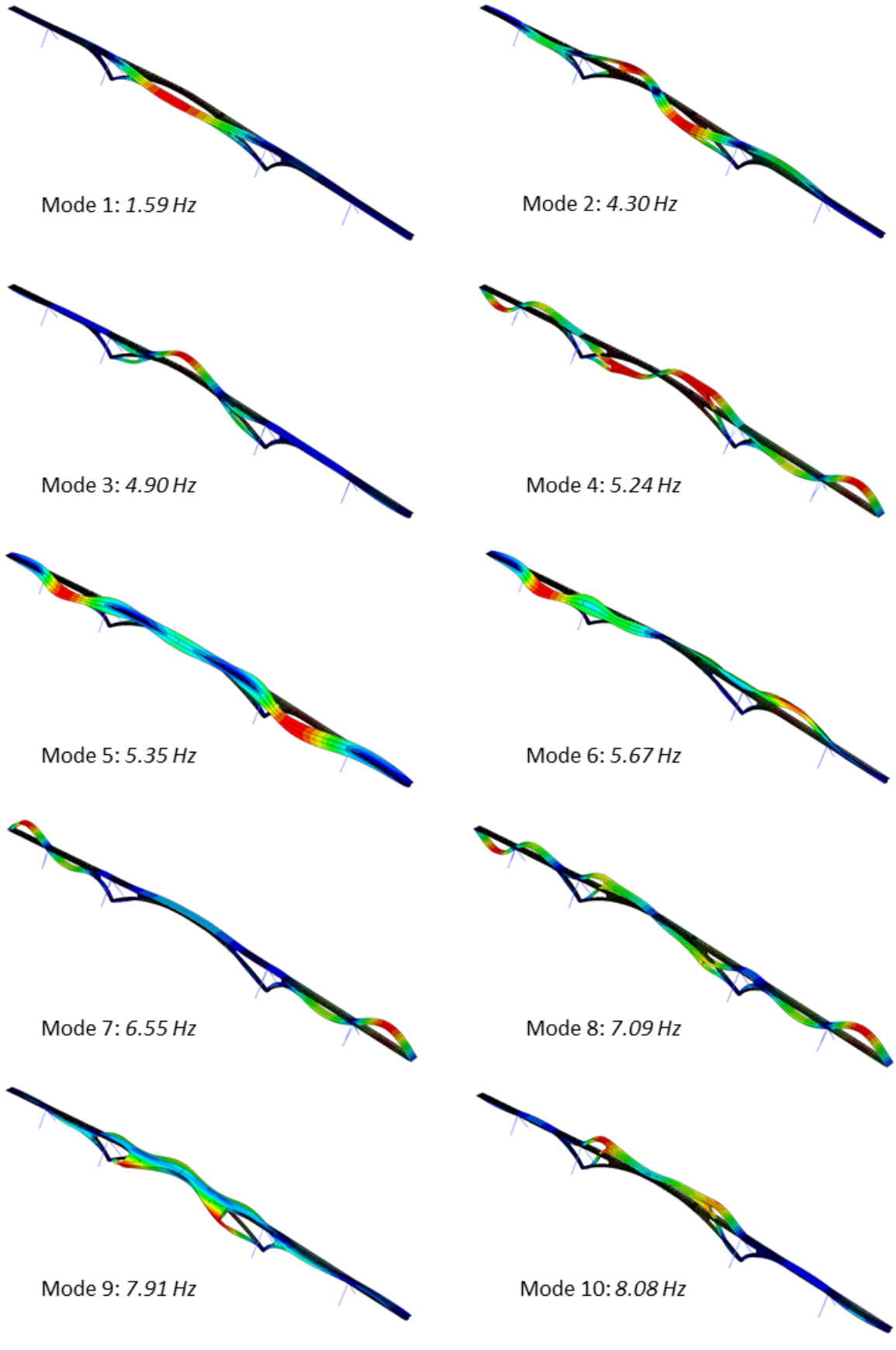

Figure 13. *ABAQUS mode shapes, reinforced structure.*

ACKNOWLEDGEMENTS

The authors would like to express their gratitude to the Spanish Ministry of Science and Innovation for the financial support through the project MCI-20-PID2019-105593GB-00/AEI/10.13039/501100011033

REFERENCES

[1] J. de Sebastián, I.M. Díaz, C.M. Casado, A.V. Poncela and A. Lorenzana. *Evaluación de la predicción de aceleraciones debidas al tránsito peatona en una pasarela en servicio.* Informes de la Construcción, 65, 531, 335-348, 2013.

[2] ISO 10137. *Bases for Design of Structures Serviceability of Buildings and Walkways against Vibrations*, International organization for standardization edition, 2007.

[3] Setra/AFGC. *Footbridges - Assessment of vibrational behaviour of footbridges under pedestrian loading,* Paris. 2006.

[4] IAP 11*. Instrucción sobre acciones a considerar en el proyecto de puentes de carretera. Centro de Publicaciones Secretaría General Técnica Ministerio de Fomento*, Madrid. 2011.

[5] EHE-08. *Instrucción de hormigón estructural. Centro de Publicaciones Secretaría General Técnica Ministerio de Fomento,* Madrid. 2008

[6] *UNE-EN 1995-2:2016.* Proyecto de estructuras de madera. Parte 2: Puentes. AENOR, 2016.

[7] Instrucción Española de Acero Estructural (EAE) 2011.

[8] R. Brincker, L-M. Zhang and P. Anderson. *Modal Identification from Ambient Response Using Frequency Domain Decomposition*, in:18th IMAC, 625-630. 2000.

[9] S. Živanović1, Diciembre, *Influence of walking and Standing Crowds on Structural Dynamic Properties*, Proceedings of the IMAC XXVII, 2009.

[10] Proyecto de remodelación y refuerzo de la pasarela de Pumarín en Gijón. LFG Estudio de Ingeniería SLP. 2013.

[11] IDynamics. Structural analysis and Dynamics. Department of Civil Engineering. University of Kaiserslautem. 2020.

Detección de daño estructural en estructuras de madera laminada mediante la actualización de modelos de elementos finitos y análisis modal

Sánchez-Ruiz, Rebeca[1]; Sancibrian, Ramón[2]; Lombillo, Ignacio[3]; Peña-Laso, Juan[4]; Gaute, Alvaro[5]

ABSTRACT

El artículo propone un procedimiento basado en la actualización de elementos finitos para obtener las variaciones de rigidez en vigas de madera laminada debido a la presencia de defectos. El módulo de elasticidad dinámico se ha obtenido a partir del análisis modal experimental, comparándolo con resultados teóricos ofrecidos por el método de elementos finitos. Para ello se realiza un procedimiento de optimización formulando una función de error que compara modos y frecuencias naturales. En una primera fase se considera que la rigidez de la viga es constante y homogénea a lo largo de toda su longitud. Cuando está hipótesis no resulta precisa y no permite reducir el error formulado, se realiza una segunda fase que considera la variabilidad de la rigidez empleando métodos de optimización basados en partículas de enjambre. Los resultados permiten reducir el error entre el modelo de elementos finitos y los resultados experimentales proporcionando la variación de la rigidez a lo largo de la viga.

K*eywords:* Laminated wood, Structural damage, Evolutionary optimization, Modal analysis.

1. INTRODUCCIÓN

La madera laminada, también conocida como Glulam, es un producto que cada vez se emplea más en construcción de estructuras de muy distinta índole (p.ej. instalaciones deportivas, aeropuertos, pasarelas, etc.). Los motivos de este creciente interés por este producto son varios, pero cabe destacar dos como los principales. En primer lugar, es un material ecológico y sostenible. El empleo de este material en construcción es una de las mejores formas de lograr un comportamiento respetuoso con el medio ambiente [1]. En segundo lugar está el aspecto estético, ya que estas estructuras generan

[1] *Departamento de Ingeniería Estructural y Mecánica. Universidad de Cantabria (España).* rebeca.sanchez@unican.es

[2] *Departamento de Ingeniería Estructural y Mecánica. Universidad de Cantabria (España).* sancibrr@unican.es *(Corresponding author)*

[3] *Departamento de Ingeniería Estructural y Mecánica. Universidad de Cantabria (España).* ignacio.lombillo@unican.es

[4] *Departamento de Puentes. WSP (España).* jupena@louisberguer.com

[5] *Departamento de Ingeniería Estructural y Mecánica. Universidad de Cantabria (España).* Alvaro.gaute@unican.es

ambientes confortables y que se amoldan mejor a los espacios naturales (ver Fig. 1). Además, hay que tener en cuenta que los avances en las tecnologías de fabricación permiten obtener productos fabricados en este material con alto rendimiento, generando geometrías curvas en vigas y columnas de gran tamaño.

Desde el punto de vista estructural, una de las principales ventajas de la madera laminada frente a la madera aserrada son sus buenas propiedades mecánicas, donde se destaca la rigidez obtenida a través de su módulo de elasticidad (MOE). Sin embargo, uno de los principales inconvenientes de este material es el desconocimiento existente en su comportamiento estructural y en la degradación que puede experimentar con el paso del tiempo. Esta degradación se traduce como una pérdida de rigidez y por tanto una variación del MOE. La madera es un material natural, lo que significa que el control sobre sus defectos es muy limitado (p.ej. la presencia de nudos, fisuras, etc.), además es marcadamente anisótropo e higroscópico y, por ese motivo, no tiene unas propiedades mecánicas tan definidas como ocurre en otros materiales. Estas diferencias no se producen solo entre especies, sino que se pueden encontrar dentro de una misma especie. Además, la madera laminada se combina con adhesivo, lo que le convierte en un material compuesto, más difícil de modelizar aún si cabe. Los procesos de deterioro (bióticos y abióticos) que afectan a este material son muy diversos [2], [3]. Las piezas individuales de material Glulam están clasificadas en clases resistentes, lo que permite un control más estricto de las propiedades logrando de este modo configuraciones con características más predecibles y una menor variabilidad de sus propiedades. Para obtener grandes dimensiones de vigas o columnas de madera laminada éstas se conectan mediante uniones denominadas *fingers*, permitiendo una unión íntima entre las tablas que forman los componentes estructurales. La presencia de estas uniones añade una mayor fuente de incertidumbre en el material.

Por los motivos expuestos anteriormente se hace necesario el desarrollo de metodologías no destructivas que puedan ser aplicadas in-situ para la detección de daño estructural en este tipo de material [4]–[7]. Varias técnicas de ensayo no destructivo han sido empleadas en madera aserrada, sin embargo, las más utilizadas a día de hoy son de carácter cualitativo, no cuantitativo. Las técnicas cualitativas consisten fundamentalmente en la inspección visual de la madera [2], [8]. Las técnicas cuantitativas se basan en ultrasonidos, resistencia a la penetración y métodos dinámicos.

Figura 1. *Pasarela peatonal construida en madera laminada en la localidad de Cieza (Cantabria).*

En este trabajo se presenta un estudio sobre el comportamiento dinámico de este tipo de material. Se ha desarrollado una metodología basada en la actualización por elementos finitos [9], [10] para la detección de daño o la variabilidad en las propiedades mecánicas basado en el comportamiento dinámico de los elementos estructurales. Para ello, se comparan los resultados experimentales con los resultados teóricos y se ajustan los parámetros mecánicos mediante optimización. En el caso de elementos dañados o con fuerte variabilidad de sus propiedades se emplea optimización por enjambre de partículas, procedimiento que ha demostrado tener una buena precisión en otros campos [11]. El procedimiento utilizado se basa en la formulación de una función objetivo que compara los modos y las frecuencias naturales. Para ello, se han realizado numerosos ensayos experimentales en elementos de madera mediante ensayo estático y análisis modal experimental en tablas simples y elementos de madera laminada (Fig. 2). Estos resultados muestran la fuerte influencia de la variabilidad de las propiedades del material y el influjo de los defectos en los parámetros modales.

2. PROGRAMA DE EXPERIMENTOS

2.1. Descripción de las vigas estudiadas

El programa de experimentos se llevó a cabo en Laboratorio de Estructuras de la Escuela Técnica Superior de Ingenieros de Caminos, Canales y Puertos de Santander. Este estudio experimental tiene por objeto el valorar la capacidad de detectar anomalías estructurales en vigas de madera laminada. En concreto el análisis se ha centrado en la variación de MOE. El estudio se ha llevado a cabo sobre elementos estructurales sencillos con el objeto de poder realizar estudios más exhaustivos en el futuro empleando elementos estructurales más complejos. En este caso se han estudiado vigas de madera simple y vigas de madera laminada denominadas de tipo Duo, de las especies forestales pino silvestre y abeto. Las vigas simples son tablas de madera aserrada, que serán utilizadas posteriormente en la fabricación de vigas de madera laminada. El objeto de estudiar este tipo de elementos es poder valorar el comportamiento dinámico de la madera sin la presencia del adhesivo ni de la interacción con otros componentes. Las vigas de madera tipo Duo consisten en dos tablas de madera unidas mediante una capa adhesivo. En este caso se trata de la viga de madera laminada más simple con la que se puede trabajar. La utilización de esta tipología permite valorar el efecto del adhesivo y la interacción entre los componentes. La tabla 1 muestra el número de vigas ensayadas de cada especie incluyendo la presencia o no de uniones *finger*.

Tabla 1. Tipología y especie de las vigas ensayadas

Tipo	Largo (m)	Ancho (m)	Alto (m)	Uniones	Pino silvestre	Abeto
Simple	1.56	0.16	0.05	Sin fingers	14	16
				Con fingers	--	---
Duo	1.55	0.17	0.07	Sin fingers	9	2
				Con fingers	3	3
				Total	26	21

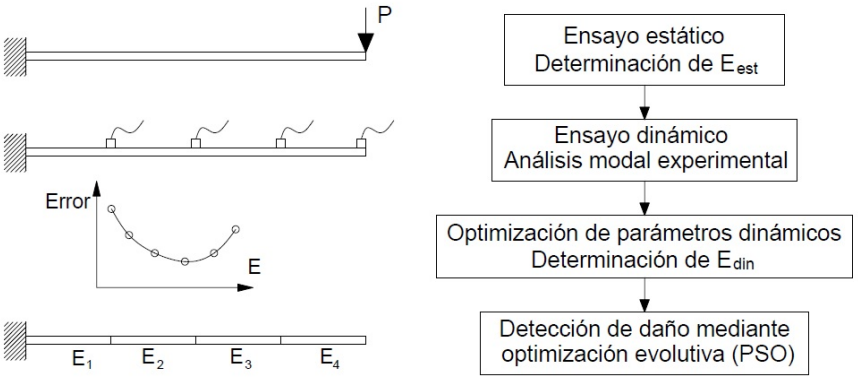

Figura 2. *Procedimiento para la obtención de la distribución de rigidez en la vigas.*

Las condiciones de contorno seleccionadas para los ensayos experimentales han sido de tipo viga empotrada-libre. La razón por la que se ha seleccionado la condición de empotramiento en un extremo de la viga es la de garantizar fielmente su reproductibilidad. En efecto, debido a la ligereza de los elementos ensayados, otras condiciones de contorno, como pueden ser biarticuladas, pueden generar problemas bajo ensayos dinámicos debido a la separación de apoyo durante la excitación.

2.2. Procedimiento de ensayo

El procedimiento de ensayo llevado a cabo en este trabajo se muestra en la Figura 2 y se divide en las 5 partes siguientes:

1. Obtención experimental del módulo de elasticidad estático. Con las condiciones de contorno establecidas anteriormente se someten las vigas a una carga puntual en su extremo libre, obteniendo la relación carga-deformación y consecuentemente el módulo de elasticidad estático (MOE_{est}) del material a flexión.
2. Ensayo modal teórico. Mediante elementos finitos se modeliza el sistema y se obtienen los cuatro primeros modos y frecuencias naturales que serán utilizados como referencia.
3. Ensayo modal experimental. Se obtienen los cuatro primeros modos y frecuencias naturales mediante ensayo modal excitando el sistema con un martillo de impacto y recogiendo la respuesta con 4 acelerómetros.
4. Obtención del módulo de elasticidad dinámico mediante optimización. Se establece una función de Error para la comparación de las frecuencias naturales y modos teóricos-experimentales. Mediante un algoritmo de optimización se busca el mínimo error, utilizando como variable de diseño el módulo de elasticidad dinámico (MOE_{din}). Para ello se considera la viga en estado sano y con un módulo de elasticidad homogéneo en todas sus dimensiones.
5. Detección de daño a través de la variación de la rigidez en la longitud de la viga. Cada viga ensayada se modeliza en elementos finitos dividiéndose en tramos. A cada tramo se le asigna una variable que representa el módulo de elasticidad dinámico. Mediante optimización, empleando un algoritmo evolutivo basado en partículas de enjambre (PSO), se reduce el error entre el modelo experimental y teórico.

Para obtener la suficiente precisión en la determinación del MOE_{din} en el análisis modal se han considerado los cuatro primeros modos y frecuencias naturales del sistema [12]. Consecuentemente se

han empleado cuatro acelerómetros (Kistler K-Beam tipo 8316A01), un martillo instrumentado para la excitación de la viga de nivel de fuerza media (2000 N) (Kister tipo 8724A). Para el procesado de datos se ha empleado el software de análisis modal Artemis©.

3. OPTIMIZACIÓN Y OBTENCIÓN DEL MÓDULO DE ELASTICIDAD DINÁMICO

Los pasos 4 y 5 del procedimiento establecido requieren la actualización de un modelo de elementos finitos mediante optimización de una función de error para obtener el módulo de elasticidad dinámico. La función de error establecida de basa en el conocido como Modal Assurance Criterion, comúnmente denominado MAC, y que responde a la siguiente formulación,

$$MAC_i = \frac{\left(\boldsymbol{\Phi}_{ti}{}^T \boldsymbol{\Phi}_{ei}\right)^2}{\left|\boldsymbol{\Phi}_{ti}{}^T \boldsymbol{\Phi}_{ti}\right|\left|\boldsymbol{\Phi}_{ei}{}^T \boldsymbol{\Phi}_{ei}\right|} \tag{1}$$

Donde $\boldsymbol{\Phi}_{ti}$ y $\boldsymbol{\Phi}_{ei}$ son las formas modales del sistema obtenidas para el modo i de forma teórica y experimental respectivamente. Por tanto, la función que mide la diferencia entre el modelo teórico y experimental es formulada de la siguiente forma,

$$F = \sum_{i=1}^{nm} \mu_i \, \Delta\omega_i + \sum_{i=1}^{nm} \nu_i \, (1 - MAC_i) \tag{2}$$

donde,

$$\Delta\omega_i = \frac{|\omega_{ti} - \omega_{ei}|}{\omega_{ei}} \tag{3}$$

representa la diferencia entre las frecuencias naturales obtenidas del modelo teórico y los resultados obtenidos experimentalmente. Los coeficientes μ_i y ν_i representan los coeficientes de ponderación y *nm* es el número de modos considerados en la comparación.

En el paso 4 del procedimiento se busca el valor del módulo de elasticidad dinámico, que considerando la viga como sana, afecta de forma homogénea a la longitud completa de la viga. Para ello se minimiza la función proporcionada la Ecuación (2), determinando el valor de E como el valor que proporciona la menor diferencia entre el modelo teórico y experimental. En este paso se ha considerado que la viga está sana, es decir, no presenta defectos importantes que afectan a su rigidez cuando la diferencia en las frecuencias naturales es menor del 5%. En caso de que alguna de las cuatro frecuencias naturales supere este valor se ha procedido a determinar la variación del módulo de elasticidad a lo largo de la longitud de la viga (paso 5). En el paso 5 se ha obtenido la variación longitudinal del módulo de elasticidad dinámico, centrándose fundamentalmente en aquellas vigas que han mostrado una diferencia mayor del 5% en las frecuencias naturales. Para ello se ha utilizado un algoritmo de optimización evolutivo, basado en la técnica optimización de partículas de enjambre (Particle Swarm Optimization, PSO). La Figura 3 muestra el modelo de elementos finitos utilizado en la optimización. Dicho modelo se ha realizado en Matlab® y consiste en 3748 elementos tetraédricos de orden cuadrático que ha sido verificado mediante un modelo analítico. El modelo de la viga se ha dividido en cuatro tramos (en diferentes colores en la figura) y a cada uno de ellos se le ha asignado un módulo de elasticidad. Es decir,

$$E = [E_1 \quad E_2 \quad E_3 \quad E_4] \tag{4}$$

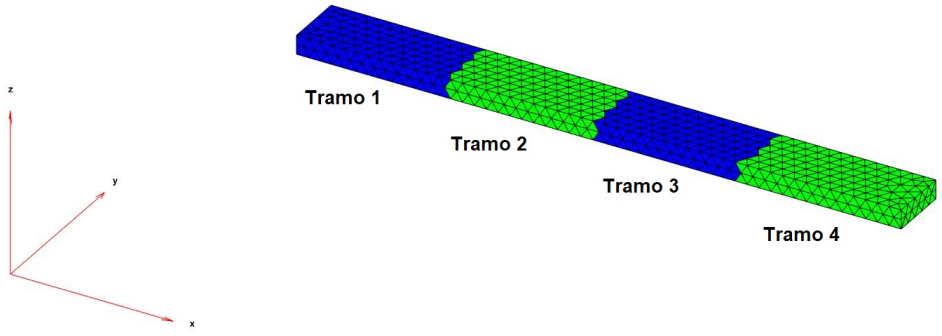

Figura 3. *Modelo de elementos finitos empleado en la optimización PSO.*

El número de tramos considerado en este trabajo se ha seleccionado en función de la variación de las propiedades estimadas a lo largo de la longitud de viga. Sin embargo, un estudio en mayor profundidad del número de tramos óptimo sería deseable, aunque este aspecto ha quedado fuera del trabajo aquí realizado. El criterio de convergencia se ha establecido en el número máximo de cincuenta iteraciones.

4. RESULTADOS

La Figura 4 muestra la disposición de la viga y los acelerómetros durante ensayos dinámicos en laboratorio. Las Tablas 2 a 4 muestra as diferencias entre el MOE_{est} y el MOE_{din} tanto en vigas sanas y dañadas en tablas simples de pino silvestre (Tabla 2), de abeto (Tabla 3), y en tablas Duo de pino silvestre (Tabla 4) y abeto (Tabla 5). Cabe destacar que el MOE_{din} es más pequeño que el MOE_{est} y esta diferencia varía entre un 12% y 20% en vigas consideradas sanas. Por otro lado, en las vigas dañadas ocurre los mismo en cuanto al menor valor del MOE_{din}, sin embargo, las diferencias presentan una mayor variabilidad. Esta variabilidad es en su mayor parte debido a los diferentes tipos de defectos que presentaban las vigas ensayadas.

Por su parte, y como se ha mencionado previamente, las vigas dañadas se sometieron a un ajuste más exhaustivo mediante la optimización por el algoritmo PSO. En este algoritmo se empleó una población de 50 individuos y se consideró la convergencia del algoritmo en la generación 30. Dado el carácter aleatorio de este procedimiento de optimización el mismo problema se ejecutó 12 veces, seleccionando como solución el caso con el menor error dado por la expresión de la Ecuación (2). La Figura 5 muestra la evolución del algoritmo hasta la solución óptima en uno de los casos considerados (viga dúo sin fingers). En la parte superior de esta figura se muestra la evolución de la función objetivo formulada en la Ecuación (2), y en la parte inferior la evolución del MOE_{din} en los cuatro tramos considerados (ver Figura 3). La Figura 6 muestra los resultados en la distribución del módulo de elasticidad dinámico en los cuatro tramos para los doce casos de ejecución en una de las vigas considerada. Se observa que la tendencia es uniforme, aunque el mejor resultado se obtuvo para un error de F = 0.000395, siendo éste el considerado como solución del problema. Finalmente, la Tabla 6 muestra la comparación de las frecuencias naturales obtenidas experimentalmente con las frecuencias obtenidas mediante simulación en elementos finitos en uno de los casos considerados. En la segunda columna se muestran los valores de las frecuencias naturales obtenidas en la simulación con un MOE_{din} constante en toda la viga,

obtenido por la optimización del paso 4. En la última columna se muestran las frecuencias obtenidas por simulación con MOE_{din} variable en los cuatro tramos. Como puede observarse, la optimización por tramos permite un ajuste mucho más preciso del modelo teórico.

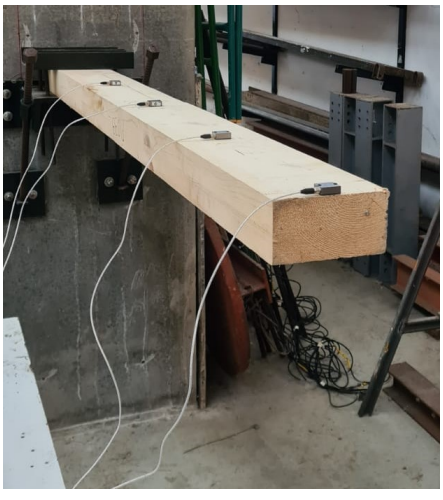

F**igura 4.** *Análisis modal experimental realizado en laboratorio.*

Tabla 2. Comparación de los valores del módulo de elasticidad estático y dinámico en la especie de pino silvestre en tabla simple.

Módulo de elasticidad	**Sano**			**Dañadas**		
	Estático (MPa)	**Dinámico (MPa)**	**Diferencia**	**Estático (MPa)**	**Dinámico (MPa)**	**Diferencia**
Valor medio	12012.0	10625.3	13.05%	8590.1	8125.0	5.72%
Desviación estándar	537.86	375.00		412.02	375.00	

Tabla 3. Comparación de los valores del módulo de elasticidad estático y dinámico en la especie abeto en tabla simple.

Módulo de elasticidad	**Sano**			**Dañadas**		
	Estático (MPa)	**Dinámico (MPa)**	**Diferencia**	**Estático (MPa)**	**Dinámico (MPa)**	**Diferencia**
Valor medio	11223.5	9312.50	20.52%	8256.40	7437.50	11.01%
Desviación estándar	431.53	646.51		1171.86	990.19	

Tabla 4. Comparación de los valores del módulo de elasticidad estático y dinámico en la especie de pino silvestre en tabla Duo.

Módulo de elasticidad	**Sano**			**Dañadas**		
	Estático (MPa)	**Dinámico (MPa)**	**Diferencia**	**Estático (MPa)**	**Dinámico (MPa)**	**Diferencia**
Valor medio	10341.86	8916.67	15.98%	9520.93	8049.00	18.29%
Desviación estándar	360.94	1124.23		660.80	505.00	

Tabla 5. Comparación de los valores del módulo de elasticidad estático y dinámico en la especie de abeto en tabla Duo.

Módulo de elasticidad	Sano			Dañadas		
	Estático (MPa)	Dinámico (MPa)	Diferencia	Estático (MPa)	Dinámico (MPa)	Diferencia
Valor medio	10199.14	9041.67	12.80%	7637.93	7029.00	8.66%
Desviación estándar	257.47	412.48		419.42	504.00	

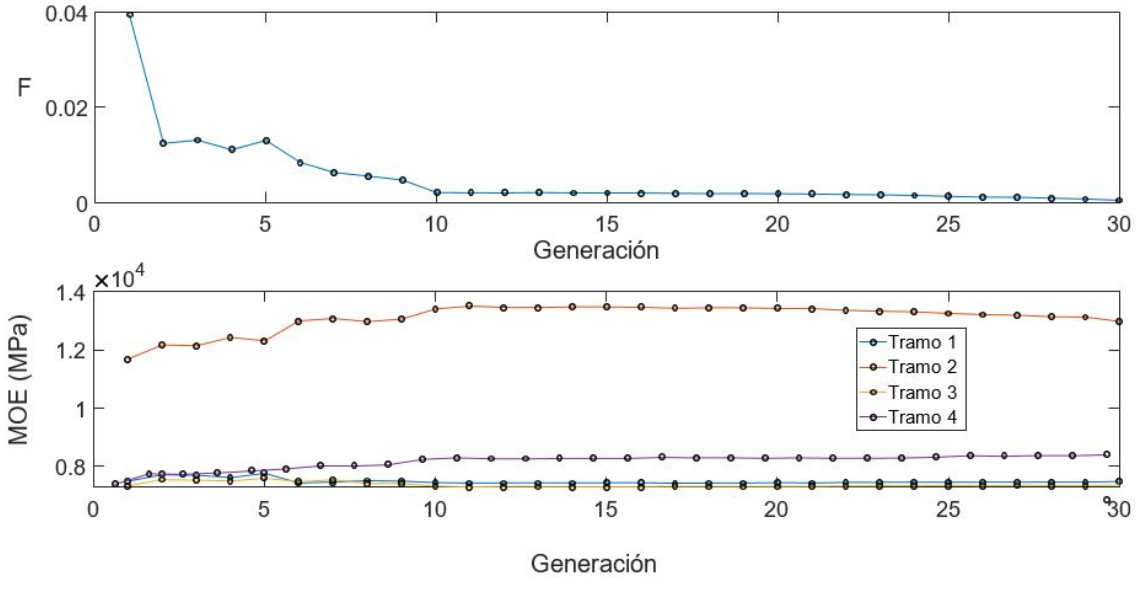

Figura 5. *Evolución del módulo de elasticidad dinámico en el algoritmo PSO.*

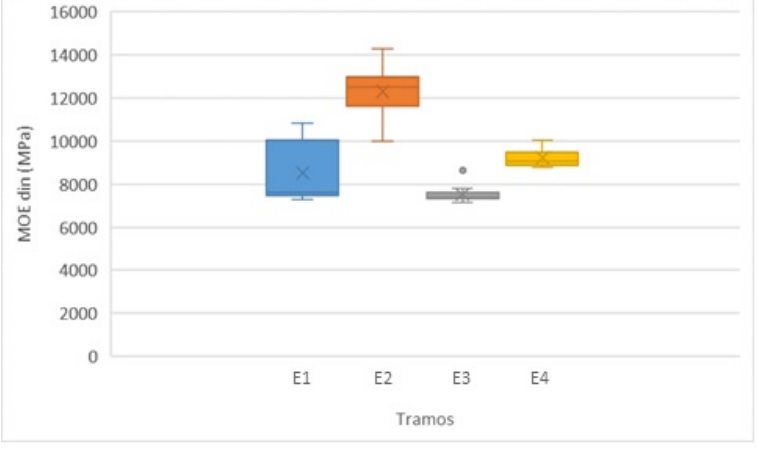

Figura 6. *Resultados del MOE_{din} en los diferentes tramos de la viga (12 casos).*

Tabla 6. Comparación de las frecuencias naturales obtenidas experimentalmente, mediante MEF con MOE uniforme, y mediante MEF con MOE variable por tramos en uno de los casos de viga dúo.

Frecuencia natural	Experimental (Hz)	Uniforme ((Hz)	4 Tramos (Hz)
F1	13.16	13.25	13.15
F2	82.70	86.30	82.66
F3	234.54	229.06	234.30
F4	448.75	446.39	449.30

5. CONCLUSIONES

En este artículo se presenta un procedimiento teórico-experimental que permite determinar el módulo de elasticidad dinámico en estructuras de madera laminada. Para ello se ha determinado en primer lugar el módulo de elasticidad estático mediante procedimientos convencionales. Este MOE_{est} sirve en este trabajo como referencia y comparación del mismo módulo en el caso dinámico. El MOE_{din} se ha obtenido experimentalmente mediante análisis modal, comparando estos resultados con los obtenidos mediante elementos finitos. En una primera fase se ha considerado que la rigidez de la viga es uniforme en toda su longitud, obteniendo buenos resultados en las vigas consideradas como sanas. En una segunda optimización se ha considerado la variación longitudinal de rigidez en la viga, y se ha obtenido esta variación mediante optimización utilizando un algoritmo PSO.

En este trabajo se han utilizado tablas simples para la fabricación de madera laminada y tablas de tipo Duo. La sencillez de estos casos permite un estudio fiable al presentar pocas fuentes de incertidumbre. Los resultados demuestran que si lo elementos no tienen defectos se puede obtener un MOE_{din} de forma sencilla. Pero en el caso en el que se presentan defectos es necesario recurrir a una optimización más compleja considerando varios tramos de rigidez variable a lo largo de la viga.

AGRADECIMIENTOS

Los autores de este trabajo desean agradecer el soporte proporcionado por la empresa YOFRA S.A. a través del convenio financiado por la Sociedad para el Desarrollo Regional de Cantabria (SODERCAN) en el marco del Programa I+C=+C 2018 – Apoyo a Proyectos de I+D.

REFERENCIAS

[1] M. Ruy, R. Gonçalves, D. M. Pereira, R. G. M. Lorensani, and C. Bertoldo, “Ultrasound grading of round Eucalyptus timber using the Brazilian standard,” *Eur. J. Wood Wood Prod.*, vol. 76, no. 3, pp. 889–898, 2018.

[2] P. Dietsch and H. Kreuzinger, “Guideline on the assessment of timber structures: Summary,” *Eng. Struct.*, vol. 33, no. 11, pp. 2983–2986, 2011.

[3] J. Parracha *et al.*, “Assessment of the density loss in anobiid infested pine using x-ray micro-computed tomography,” *Buildings*, vol. 11, no. 4, 2021.

[4] L. Acuña *et al.*, “Aplicación del resistógrafo a la obtención de la densidad y la diferenciación de

especies de madera," *Mater. Constr.*, vol. 61, no. 303, pp. 451–464, 2011.

[5] G. López, L. A. Basterra, and L. Acuña, "Infrared thermography for wood density estimation," *Infrared Phys. Technol.*, vol. 89, pp. 242–246, 2018.

[6] G. López, L. A. Basterra, G. Ramón-Cueto, and A. De Diego, "Detection of singularities and subsurface defects in wood by infrared thermography," *Int. J. Archit. Herit.*, vol. 8, no. 4, pp. 517–536, 2014.

[7] D. F. Llana, G. Íñiguez-González, J. Montón, and F. Arriaga, "In-situ density estimation by four nondestructive techniques on Norway spruce from built-in wood structures," *Holzforschung*, vol. 72, no. 10, pp. 871–879, 2018.

[8] G. Fink and J. Kohler, "Quantification of different NDT/SDT methods in respect to estimate the load-bearing capacity," *Constr. Build. Mater.*, vol. 101, pp. 1181–1187, 2015.

[9] R. Perera, S. E. Fang, and C. Huerta, "Structural crack detection without updated baseline model by single and multiobjective optimization," *Mech. Syst. Signal Process.*, vol. 23, no. 3, pp. 752–768, Apr. 2009.

[10] P. Liu, S. Huang, M. Song, and W. Yang, "Bayesian model updating of a twin - tower masonry structure through subset simulation optimization using ambient vibration data," no. 0123456789, 2020.

[11] W. Zhang, G. Li, W. Zhang, J. Liang, and G. G. Yen, "A cluster based PSO with leader updating mechanism and ring-topology for multimodal multi-objective optimization," *Swarm Evol. Comput.*, vol. 50, no. June, p. 100569, 2019.

[12] G. Kouroussis, L. Ben Fekih, and T. Descamps, "Assessment of timber element mechanical properties using experimental modal analysis," *Constr. Build. Mater.*, vol. 134, pp. 254–261, 2017.

Economic analysis about the influence of the direct connection micropile-foundation on the underpinning project costs

Pellicer-Martínez, Francisco[1]; Martínez Lirón, Vicente S.[2]; Hernández Díaz, Alejandro M.[3]; López Juárez, José A.[4]; Pérez Aracil, Jorge[5]

ABSTRACT

This work analyzes the economic repercussion of the strength of the direct connection micropile-foundation on the costs of the underpinning projects. This analysis is motivated by several recent changes in the structural codes related to the formulation that must be applied in order to calculate the bond stress in the contact zone, which is the key parameter to assess the connection strength. Firstly, an economic comparison between the underpinning costs of three buildings is performed using seven different formulations. Subsequently, a Monte-Carlo simulation, developed by using a probability distribution calibrated with experimental results, serves both as a sensibility analysis and as contrast with the results of formulations previously applied. Numerical results indicate that last changes in structural codes have increased the costs in this type of projects by 20%, and they may even reach 40% for large buildings founded on soils with thick non-resistant levels.

Keywords: Underpinning, foundation, bond stress, Monte-Carlo, grout.

1. INTRODUCCIÓN

Actualmente, el recalce de edificios mediante micropilotes es la solución más recurrida [1-3]. Su ejecución sirve para transmitir cargas a estratos profundos del terreno más resistentes [4-5]. Se pueden ejecutar de dos formas [6]. En la primera, la perforación se realiza directamente sobre la zapata y el micropilote queda unido por una superficie cilíndrica de contacto. Su ejecución es simple, pero el número de micropilotes queda limitado a las dimensiones de la zapata. En la segunda, la perforación se realiza fuera de la zapata, lo que permite la construcción de más micropilotes. En este caso, la conexión se materializa con un encepado que aglutina las cabezas de los micropilotes de forma monolítica, que se unen a la zapata existente por medio de conectores. Sin embargo, este segundo método es más complejo, costoso y menos seguro, ya que es necesaria una excavación

[1]*Departamento de Ciencias Politécnicas. Universidad Católica de Murcia (UCAM) (Spain). fpellicer@ucam.edu (Corresponding author)*
[2]*Departamento de Ciencias Politécnicas. Universidad Católica de Murcia (UCAM) (Spain). vsmartinez@alu.ucam.edu*
[3]*Dirección General de Ordenación del Territorio y Aguas, Comunidad Autónoma de Canarias (Spain). aherdiaa@gobiernodecanarias.org*
[4]*Departamento de Ciencias Politécnicas. Universidad Católica de Murcia (UCAM) (Spain) jalopez6@ucam.edu*
[5]*Departamento de Teoría de la Señal y Comunicaciones. Universidad de Alcalá de Henares (Spain) jorge.perezaracil@uha.es*

alrededor de la cimentación a recalzar. Por estos motivos, lo más habitual es realizar una conexión directa [6].

Los manuales de diseño de micropilotes indican las comprobaciones que se han de realizar. Desde aquellas dirigidas a garantizar la estabilidad de la cimentación (asiento y arranque de los micropilotes), hasta las que velan por una adecuada resistencia estructural [4, 7-16]. La mayoría de las comprobaciones estructurales están basadas en conocidos modelos resistentes que vienen desarrollados en códigos de estructuras de hormigón armado [17-19]. Sin embargo, a pesar de que la mayoría de dichos manuales de micropilotes [7-16] indican que la conexión directa debe cumplir con la correspondiente normativa de hormigón de cada país, en ellas no existe una formulación específica para evaluar la resistencia tangencial que se produce en la interfaz de contacto micropilote con la estructura existente (lechada-hormigón), denominada aquí por tensión de adherencia (τ_{adh}). Y tampoco se especifica qué comprobación estructural es la más apropiada.

Actualmente, la resistencia de la conexión directa se calcula multiplicando la superficie de contacto por un valor medio de tensión de adherencia, el cual se estima con formulaciones de otros fenómenos resistentes similares. En España, al principio se empleaba la resistencia a cortante del hormigón [21, 22]. En este sentido, algunos autores en España, basándose en nuevas versiones de la normativa americana [23], han propuesto como tensión de adherencia la resistencia a cortante del hormigón [24], resultando unos valores en el rango 0.400-0.600 MPa. Incluso un autor propuso una fórmula basada en su propia experiencia [25] acompañada de un rango de posibles valores [0.300-0.600 MPa]. En Europa, la normativa de micropilotes [8, 9] indica que hay que aplicar la comprobación a rasante en juntas de hormigonado del Eurocódigo 2 (EC2) [18], que proporciona valores entre 0.200-0.400 MPa (depende de parámetros). Volviendo a España, desde la aprobación de la Guía para el proyecto y ejecución de micropilotes en obras de carreteras (GPEMOC) [10], vigente actualmente, indica que la conexión directa tiene que cumplir con la EHE [26]. Por lo que se ha venido aplicando la formulación de rasante en juntas de hormigonado de dicha normativa. Posteriormente se aprobó la EHE-08 [19], que tiene la misma formulación para la comprobación a rasante en juntas que la EHE [26]. Las formulaciones de estas dos instrucciones [19, 26] proporcionan valores en el mismo rango que el EC2 [18]. Después de la publicación de la GPEMOC [10], un autor volvió a proponer el uso de la resistencia a cortante del hormigón basada también en las normativas americanas ACI-318 [27], volviendo al rango de valores anteriores [0.400-0.600 MPa]. Ahora en España, se acaba de aprobar el Código Estructural (CE) [28], que deroga la EHE-08, y cuya comprobación a rasante en juntas de hormigonado es la misma que la del EC2 [18]. Como contraste está la normativa americana ACI-318-19 [17], que no propone un método específico para calcular la tensión de adherencia. Sin embargo, se puede interpretar que su valor sería la resistencia nominal en juntas de hormigones ejecutados en diferentes momentos: valor constante de 0.552 MPa.

La experimentación realizada hasta el momento ha sido capaz de describir los mecanismos resistentes de la tensión de adherencia: adhesión química y rozamiento [2-3]. Los resultados indican que ambos mecanismos dependen de la rugosidad de la superficie de la perforación, y que el rozamiento está influenciado por la compresión normal que se produce por efecto Poisson una vez el micropilote entra en carga [3]. Por lo que el valor de la compresión normal dependerá del grado de confinamiento que genere la propia cimentación. Otro resultado interesante que arrojaron dos investigaciones fue que la tensión de adherencia aumenta conforme disminuye el diámetro de la perforación [3, 20]. Y, Pachla

[1], tras un exhaustivo programa de experimentación fue capaz de estimar la distribución de probabilidad de la tensión de adherencia para zapatas de distintos materiales: hormigón en masa, hormigón armado y ladrillos.

Entre las diferentes formulaciones encontradas en la bibliografía, las de las normativas EC2 [18] y el EHE-08 [19] contienen parámetros que dependen de la rugosidad de la perforación. En este sentido, la del EC2 tiene 2 parámetros: uno representativo de la adhesión química (c) y otro que sirve para estimar la fuerza de rozamiento que se genera en la conexión (μ). Este último depende de la compresión normal que se genera en la superficie de contacto (σ_n). Por su parte, la EHE-08 no contempla el efecto de la compresión en la superficie de contacto, por lo que su formulación sólo contiene un parámetro (β) que comprende ambos fenómenos resistentes: adhesión química y rozamiento. Los valores de los parámetros de ambas normativas dependen de la rugosidad de la superficie de contacto, y sus valores se establecen por el ingeniero según una descripción cualitativa incluida en las normativas (por ejemplo, la de la EC2 es: muy lisa, lisa, rugosa y dentada). Pero, como esta formulación está pensada para la tensión rasante que se genera en vigas construidas en dos fases de hormigonado, no contempla el tipo de superficie que se genera en una perforación por rotación. Por lo que se termina considerando una superficie de contacto "lisa" a la que le corresponden valores conservativos de tensión de adherencia (alrededor de 0.30 MPa).

Estos cambios normativos relativos a la formulación a emplear para evaluar la tensión de adherencia, incluido el último del CE para España [28], han reducido el valor de este parámetro resistente a casi la mitad. Esto implica una reducción de la resistencia de la conexión y, en muchos casos reales, es necesario construir un mayor número de micropilotes para reducir la carga que recibe cada conexión. El aumento de coste de los proyectos de recalces derivados de estos cambios en la tensión de adherencia viene generando incertidumbre a los ingenieros que diseñan recalces, más aún si analizan que las formulaciones que emplean no son específicas para este tipo de conexiones. En este sentido, el objetivo de este trabajo es analizar la repercusión económica del valor de la tensión de adherencia en este tipo de proyectos. Con ello se pretende mostrar las diferentes formulaciones que se han aplicado para determinar la resistencia de la conexión directa y el coste económico asociado. Para tal fin, el punto de partida es un análisis determinístico de cómo afecta la tensión de adherencia al presupuesto de tres proyectos de recalce de edificios en España, usando una muestra de siete formulaciones. Seguidamente, para generalizar los resultados, se ha realizado una simulación Monte-Carlo, aprovechando el trabajo realizado por Pachla [1]. Este análisis probabilístico completa el estudio determinístico previo, ya que compara los resultados experimentales con los de las formulaciones normativas, y posibilita conocer la probabilidad de que un determinado presupuesto sea superado dependiendo de la formulación empleada.

2. METODOLOGÍA

En primer lugar, se resume la metodología general para el diseño de recalce con micropilotes. Para este propósito, se ha realizado una revisión de los códigos, normativas, manuales y recomendaciones para el diseño y ejecución de micropilotes [4, 7-16]. Finalmente, se ha seguido la GPEMOC [10] porque las verificaciones que establece son, en esencia, las mismas que el resto de normativas internacionales, y es la que se ha aplicado en los casos de estudio. En segundo lugar, se describen las siete formulaciones para estimar la tensión de adherencia de la muestra aplicada en este trabajo. Por último, se realiza una breve descripción de la simulación Monte-Carlo.

2.1. Diseño de recalces con micropilotes

A partir del modelo estructural del edificio, se seleccionan los esfuerzos concomitantes más desfavorables sobre la cimentación, resultantes de la combinación de acciones (cargas mayoradas). Mediante un modelo de equilibrio, los esfuerzos de cada elemento de cimentación[1]se transforman en esfuerzos axiles de compresión (o de tracción, aunque esto sucede en pocos casos) sobre cada micropilote. Finalmente se selecciona el que tiene mayor carga axil (Q_m) y, por simplicidad en la ejecución, se toma como referencia para dimensionar todos los micropilotes que recalzan una misma zapata. De hecho, se procura siempre una solución simétrica, con el fin de asegurar la estabilidad del recalce en el caso de que las cargas cambien totalmente de sentido. Por este motivo, el número mínimo de micropilotes (n) a realizar por zapata es 2, teniendo todos la misma longitud, sección y armado.

La comprobación geotécnica principal es el hundimiento (o arranque) y se realiza asegurando que los micropilotes son capaces de transmitir las cargas al suelo por rozamiento del fuste (τ_f) y por punta (σ_p) (esta no se considera para la comprobación por arranque). En ésta, una vez fijado el diámetro del micropilote ($\emptyset_m$), se determina su longitud (L) con el fin de evitar el hundimiento (o arranque).

Finalmente quedarían las comprobaciones estructurales: las que evalúan la propia resistencia del micropilote, y las que comprueban la transmisión de cargas a través de las diferentes superficies de contacto entre materiales (lechada-acero y lechada-hormigón). El diámetro y armado (armadura tubular) de los micropilotes tienen que ser tales para que éste sea capaz de resistir el esfuerzo axil (Q_m). Mientras que la formulación utilizada para evaluar la resistencia en la interfaz lechada-acero depende del espesor de la zapata, de las dimensiones de la armadura tubular, y de las barras de refuerzo soldadas a la armadura tubular en la zona de la conexión. La conexión lechada-hormigón depende del diámetro de la perforación de la zapata ($\emptyset_p$), generalmente superior al del micropilote, del espesor de la zapata (h) y de la tensión de adherencia (τ_{adh}). La formulación para determinar la tensión de adherencia depende, además de la rugosidad de la superficie de contacto y de la tensión de compresión normal (σ_n), de la menor resistencia a compresión simple de los dos materiales que están en contacto (hormigón (f_{ck}) y lechada (f_{gk})). Generalmente, el hormigón de las zapatas es menos resistente que la lechada, y además no puede modificarse, por lo que se emplea en la formulación la resistencia del hormigón.

El diagrama de flujo de la Figura 1 resume los pasos seguidos en el diseño de los recalces. Primero, establecer el número de micropilotes en un dimensionamiento preliminar ($n = 2$). Para ello, se calcula la resistencia de la conexión directa (R_{ck}) para un valor de tensión de adherencia (τ_{adh}) y se compara con la carga que recibe el micropilote más cargado (Q_m). El número de micropilotes (n) se va aumentando para que así disminuya la carga que recibe el micropilote más cargado. El valor de n será el mínimo que hace que se cumpla $R_{ck} > Q_m$. Una vez fijado (n) se determina la longitud de los micropilotes (L) asegurando que la resistencia a hundimiento-arranque es superiora Q_m. La resistencia a hundimiento (R_h) se calcula multiplicando la superficie lateral del micropilote por un valor medio de rozamiento por fuste (τ_f) que depende del estrato de suelo que se atraviese (no se

[1]De aquí en adelante se particulariza para el elemento zapata, pero puede ser para una zapata corrida, o una losa de cimentación.

considera la resistencia por punta). El incremento de longitud (ΔL) que se aplica en el algoritmo es arbitrario y, para este específico caso, se ha tomado el valor de 0.50 m.

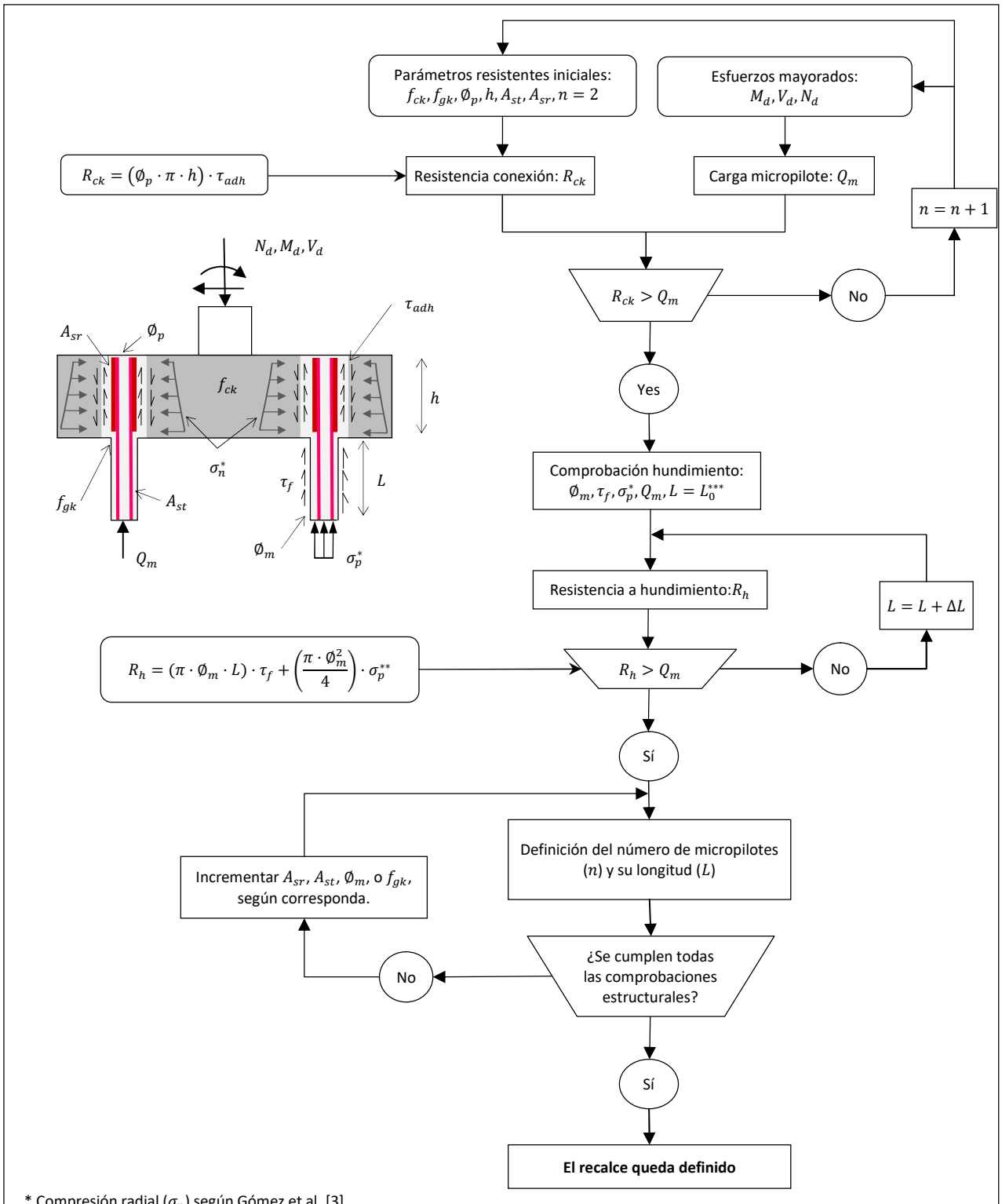

* Compresión radial (σ_n) según Gómez et al. [3].
** Se incluye en el diagrama del algoritmo, pero se ha despreciado en los cálculos ($\sigma_p = 0$).
*** La longitud comienza con L_0 = 0 m. Esta longitud se va aumentando hasta que se cumple la comprobación a hundimiento-arranque.

Figura 1. *Diagrama de flujo seguido para el diseño de recalces de edificios con micropilotes.*

Por último, se realiza el resto de comprobaciones estructurales. Primero, la resistencia en la interfaz lechada-acero, que se puede incrementar aumentando la cantidad de barras corrugadas soldadas a la armadura tubular (A_{sr}) en la zona de la conexión. A continuación, se verifica la propia resistencia del micropilote, que podría incrementarse en caso de que fuera necesario con una mayor armadura tubular (A_{st}), mejorando la calidad de la lechada, o incluso aumentando el propio diámetro del micropilote ($\emptyset_m$).

2.2. Formulaciones de tensión de adherencia

En esta sección se presentan las diferentes formulaciones que se están aplicando actualmente, o que se han aplicado en el pasado, para estimar la tensión de adherencia en la conexión directa entre micropilotes y cimentaciones existentes, y que han sido utilizadas a lo largo de este trabajo. Se ha procurado seguir un orden cronológico en su presentación, pero hay varias normativas de hormigón armado que mantienen las mismas formulaciones en varias actualizaciones consecutivas.

Una de las primeras formulaciones fue la resistencia a cortante del hormigón de la ACI-318 [23], que es la misma de las normativas de hormigón estructural españolas [21 ,22]. Se ha seleccionado la EH-08 como referencia [22]. Se calcula a partir de la resistencia a compresión simple del hormigón (f_{ck}) en kg/cm^2 (Eq. (1)). Esta resistencia esta minorada por el coeficiente de seguridad del hormigón (γ_c), obteniéndose así la resistencia de diseño a compresión simple (f_{cd}). Un valor habitual de este coeficiente de seguridad es 1.5, y es el usado aquí y en el resto de formulaciones.

$$\tau_{adh} = 0.50\sqrt{\frac{\mathrm{f_{ck}}}{\gamma_\mathrm{c}}} = 0.50\sqrt{\mathrm{f_{cd}}} \tag{1}$$

Directamente relacionada con las normativas de hormigón estructural nombradas previamente [17, 23], Rodríguez-Ortiz [24] sugirió una formulación basada en el mismo parámetro resistente (f_{cd}) en las mimas unidades (Eq. (2)). Además, recomendó un rango de valores entre 0.400-0.600 MPa. Esta formulación ha sido ampliamente utilizada en España, siendo incluso recomendada por otros autores [29].

$$\tau_{adh} = 0.5625\sqrt{\frac{\mathrm{f_{ck}}}{\gamma_\mathrm{c}}} = 0.5625\sqrt{\mathrm{f_{cd}}} \tag{2}$$

Más tarde, Oteo [25] propuso otra formulación basada también en f_{cd}(Eq. (3)), también en MPa (f_{cd}). El rango de valores que recomendó es de 0.300-0.600 MPa.

$$\tau_{\mathrm{adh}} = \frac{f_{cd}}{20} \tag{3}$$

Poco después la UNE-EN 14199 [8] fue aprobada. Esta normativa indica que la tensión de adherencia se calcula con la comprobación a rasante en juntas de hormigonado, aplicando el EC2 [23] (Eq. (4)).

$$\tau_{adh} = c \cdot f_{ctd} + \mu \cdot \sigma_n + \rho \cdot f_{yd}(\mu \sin\alpha + \cos\alpha) \leq 0.3 \cdot \left(1 - \frac{f_{ck}}{250}\right) \cdot f_{cd} \quad (4)$$

La expresión anterior se simplifica porque la unión no contiene armadura transversal ($\rho = 0$). Los parámetros c y μ dependen de la rugosidad de la superficie de contacto hormigón-lechada, y σ_n es desconocida para el caso específico de la conexión estudiada, por lo que su valor se suele despreciar ($\sigma_n = 0$). Entonces, la Eq. (4) se simplifica aun más resultando Eq. (5), cuyo factor c debe reunir los efectos resistentes de adhesión química y de rozamiento.

$$\tau_{adh} = c \cdot f_{ctd} \leq 0.3 \cdot \left(1 - \frac{f_{ck}}{250}\right) \cdot f_{cd} \quad (5)$$

El factor c puede variar desde 0.025 para superficies de contacto "muy lisas", hasta 0.5 para superficies "dentadas". Mientras que el rango de variación de μ es de 0.5 para superficies "lisas" hasta 0.9 para superficies "dentadas". f_{cd} y f_{ctd} son, respectivamente, las resistencias de diseño de compresión simple y de tracción del hormigón (MPa). Ambas reducidas por el coeficiente de minoración γ_c.

Unos años más tarde, Rodríguez-Ortiz [27] volvió a proponer casi la misma formulación que antes [24], incrementando ligeramente el coeficiente de su primera propuesta (Eq. (6)). Esta ecuación es la resistencia a cortante del hormigón que aparece en algunas normativas de hormigón americanas ACI-318 [26]. La unidades de f_{ck} vuelven a ser en kg/cm^2.

$$\tau_{adh} = 0.60 \sqrt{\frac{f_{ck}}{\gamma_c}} = 0.60\sqrt{f_{cd}} \quad (6)$$

Al año siguiente se aprueba la normativa española EHE-08 [19], que contiene una metodología específica para juntas de hormigonado sin armadura transversal de cosido en la que no se contempla la compresión normal (σ_n) (Eq. (7)).

$$\tau_{adh} = \beta \cdot \left(1.3 - 0.30 \cdot \frac{f_{ck}}{25}\right) \cdot f_{ctd} \not< 0.70 \cdot \beta \cdot f_{ctd} \quad (7)$$

El único parámetro en esta formulación relacionado con la rugosidad es β. Este parámetro, cuyo rango de variación es [0.20 – 0.80], tiene que aunar los efectos de la adhesión química y del rozamiento. El resto de parámetros resistentes son los mismos que en el EC2 [18].

Como se adelantó en la introducción, acaba de entrar en vigor el CE [28] en España, en el que la comprobación a rasante para juntas de hormigonado es la misma que en el EC2 [18]. Por tanto, todos los resultados que se obtengan con el EC2 [18] serán equivalentes a los que se obtendrían con el CE [28].

Finalmente, en la última normativa americana ACI-318-19 [17] puede considerarse la tensión de adherencia como la resistencia nominal de juntas de hormigonado (Eq. (8)), que es independiente de

la resistencia de los materiales en contacto y de la rugosidad del substrato (se puede asumir que la superficie es lisa ya que está pensada para el hormigonado sobre elementos prefabricados).

$$\tau_{adh} = 0.552 \text{ MPa} \tag{8}$$

Entre estas siete formulaciones, las de las normativas EHE-08 [19] y EC2 [18] son las únicas cuyo resultado depende de parámetros relacionados con la rugosidad de la superficie de contacto (c, μ y β). Estos valores son, en cierto modo, arbitrarios, al ser el ingeniero quien establece su valor según su experiencia previa y siguiendo las descripciones cualitativas incluidas en dichas normativas. Por lo que es necesario establecer unos valores a emplear en el presente trabajo. Para la normativa EHE-08 aquí se ha establecido $\beta = 0.3$, valor habitual en los proyectos de recalces en España cuando la superficie de contacto es la que deja una perforación por rotación. Para un hormigón de resistencia característica de 25 MPa, el valor de tensión de adherencia obtenido sería de 0.359 MPa. Ahora, si se seleccionan los parámetros del EC2 (c y μ) y se pretende obtener un mismo resultado que con la EHE-08 [19], de las posibles combinaciones de parámetros se muestran aquí dos: superficie "lisa" ($c = 0.2$) con $\sigma_n = 0.20\ MPa$, o aplicar directamente un valor de $c = 0.3$ y despreciar la compresión normal ($\sigma_n = 0\ MPa$). Este último valor de c correspondería a una rugosidad intermedia entre "lisa" y "rugosa" (según EC2 [18]). Si se cambia la resistencia del hormigón y se mantienen estas dos opciones de parámetros se obtendría resultados muy similares con ambas formulaciones. Por lo que, por simplicidad, y de aquí en adelante, la formulación EC2 [18] se aplica de forma similar a la EHE-08 [19] usando un valor del parámetro $c = 0.3$ y se desprecia la compresión normal.

2.3. Simulación Monte-Carlo

La simulación Monte-Carlo es un algoritmo ampliamente utilizado en diferentes áreas científicas [30-31]. Su uso consiste en introducir explícitamente la incertidumbre que poseen las variables de entrada de un modelo, con el fin de evaluar la repercusión en el resultado del mismo. En estructuras, se aplica generalmente con dos enfoques: i) evaluar la influencia que los parámetros de los materiales tienen sobre el resultado de la simulación de un modelo estructural [32-33], y ii) evaluar la influencia de la incertidumbre de ciertas acciones, por ejemplo, el sismo [34-35]. Aquí, se usa para evaluar la influencia que la tensión de adherencia tiene en el presupuesto final de los recalces.

Una vez seleccionadas las variables a estudiar, se definen sus funciones de distribución de probabilidad. Con ellas, se genera un conjunto de valores aleatorios para las variables que, en el caso de no ser independientes, será necesario definir la correlación entre las mismas (matriz de correlación). Para cada conjunto de parámetros se simula el modelo global de forma completa. Posteriormente, a partir de los resultados, se calculan los principales parámetros de referencia a analizar. Este proceso se ejecuta tantas veces como se requiera (usualmente en torno a 10.000 repeticiones, ver Vose [36]), obteniéndose una serie de resultados con los que se puede conocer la distribución de probabilidad de los parámetros de referencia seleccionados. Se recomienda el uso de la simulación Monte-Carlo cuando existen variables con gran incertidumbre y cuando los análisis de sensibilidad lineales no proporcionan una descripción precisa de la variación de los resultados, tal y como sucede en el problema aquí planteado.

En el trabajo de Pachla [1] se ensayan diferentes especímenes (materiales y resistencias) en los que la perforación para introducir los micropilotes se realizó mediante perforación por rotación. Por lo que la superficie de contacto se puede considerar similar a la de los recalces que habitualmente se realizan con conexión directa. Por lo tanto, se aprovechan los resultados de este trabajo previo [1] para realizar la simulación Monte-Carlo. Como sólo se analiza una variable de entrada, no es posible análisis de correlaciones. El parámetro de referencia aquí seleccionado es el presupuesto del proyecto del recalce. El procedimiento se puede resumir en las siguientes tres fases: (1) generación de valores aleatorios de tensión de adherencia, (2) diseño del recalce para cada valor de tensión de adherencia generado siguiendo el algoritmo de la Figura 1, y (3) cálculo del presupuesto del recalce.

3. CASOS DE ESTUDIO

El coste de los recalces de los tres edificios estudiados ha sido evaluado siguiendo la metodología de la Figura 1 y usando las siete formulaciones presentadas en la sección 2.2. Estos proyectos ya han sido ejecutados y se ubican en: Garrucha (A), San Juan de Terreros (B) y Alicante (C). Los casos A y B son edificios de 4 plantas cimentados sobre zapatas aisladas de hormigón armado. En el caso A, se recalzaron 9 pilares, y en el B fueron 12. En el caso C se recalzaron dos zapatas corridas de hormigón armado que soportan muros (Tabla 1). Tras el estudio de los proyectos de los tres edificios, se asumió que el hormigón en los tres casos tenía una resistencia a compresión simple de 20 MPa.

Tabla 1. Principales características de los edificios recalzados.

		A		B		C	
Tipo de cimentación		Zapata aislada		Zapata aislada		Zapata corrida	
Espesor (m)		1		0.6		0.6	
Diámetro de perforación (mm)		220					
Diámetro del micropilote (mm)		150					
Datos geotécnicos	Nivel	Capa (m)	τ_f (MPa)	Capa (m)	τ_f (MPa)	Capa (m)	τ_f (MPa)
	Estrato 1	0.0-2.20	0.0000	0.00-4.40	0.0000	0.00-5.00	0.0000
	Estrato 2	2.20-3.08	0.1470	4.40-8.00	0.0119	5.00-11.00	0.0588
	Estrato 3	3.08-3.90	0.1176	>8.00	0.1129	11.00-14.5	0.1274
	Estrato 4	> 3.7	0.0980	-		>14.5	0.0784
Cargas mayoradas sobre cada elemento estructural (kN)	Pilar/Pilar/Muro	473.7		100.0*		1176.0	
	Pilar/Pilar/Muro	785.0		199.9*		676.2	
	Pilar/Pilar/-	430.5		100.0*		-	
	Pilar/Pilar/-	726.5		799.7*		-	
	Pilar/Pilar/-	1320.4		1599.4*		-	
	Pilar/Pilar/-	716.7		799.7*		-	
	Pilar/-/-	690.2		-		-	
	Pilar/-/-	635.5		-		-	
	Pilar/-/-	1091.2		-		-	

*Esta estructura es simétrica, por lo que solo se muestran los datos de media estructura (6 pilares), pero en realidad son 12.

Tabla 2. Coste de ejecución de las principales unidades de obra a precios de 2020.

Unidad	Descripción	Armadura		Coste (€)
m	Ejecución de micropilote de 152 mm de diámetro para diferentes tiposde armadura tubular	A_{st}	73.0×6 (mm)	66.0
			88.9×7 (mm)	70.0
			88.9×9 (mm)	75.5
			101.6×9 (mm)	79.0
m	Ejecución de armadura de refuerzo soldada a la armadura tubular en la zona de conexión para incrementar el rozamiento en la interfaz lechada-acero de la armadura tubular.	A_{sr}	∅16 (mm)	10.0
			∅20 (mm)	11.0
			∅25 (mm)	12.5
m	Perforación de zapata de 220 mm de diámetro	-	-	150.0
P.A.	Transporte de los equipos de ejecución de micropilotes	-	-	3500.0

4. RESULTADOS

4.1. Comparativa de las distintas formulaciones

Los resultados de los recalces diseñados indican que el número de micropilotes a construir se reduce conforme aumenta la tensión de adherencia. Disminuir el número de micropilotes implica que éstos tengan mayor longitud para cumplir con la comprobación de hundimiento, pero esto no se traduce en una mayor longitud total (Tabla 3). Por tanto, si aumenta la tensión de adherencia, se reduce la cantidad de unidades de obra a ejecutar, reduciéndose el presupuesto del proyecto de los recalces. En términos relativos, esta reducción no es la misma para los tres edificios. Por ejemplo, pasar de la formulación del EC2 [18] a la ACI-318-19 [17] en el Edificio A supone un descenso del 42% en perforaciones, una reducción del 10% en la longitud total de los micropilotes y un ahorro del 16% del presupuesto de ejecución material (PEM). Sin embargo, para el Edificio B, estas disminuciones son del 36%, 25% y 25%, respectivamente. De forma agregada, la comparativa entre estas mismas normativas [17,18] sería del 40% (*n*), 21% ($\sum L$) y del 22% (PEM). Estas diferencias serían ligeramente superiores si se comparase la formulación del EC2 [18] con la propuesta de Rodríguez-Ortiz [27].

Una comparativa entre cargas sobre zapata y ahorro que se genera al cambiar la tensión de adherencia indica que la carga que recibe una zapata es un factor decisivo. Para visualizar esta relación se construye la Figura 2, en la que se muestran las máximas diferencias de coste en % de aplicar los valores extremos de tensión de adherencia que se han considerado: EC2 [18] y Rodríguez-Ortiz [27]. La Figura 2a indica que el número de perforaciones empieza a reducirse cuando la carga sobre la zapata es superior a 500 kN, y que será incluso mayor al 50% cuando la carga supera los 700 kN. En la misma línea, la longitud total de los micropilotes en cada elemento recalzado comienza a reducirse cuando la carga supera los 500 kN (Figura 2b). Pero, en este caso, hay algunas zapatas cuya reducción está en torno al 10% mientras que en otras es del 35-40%. La explicación de esta diferencia es el terreno. Específicamente, se debe al espesor del estrato no resistente. Cuando el espesor de este estrato es mayor, el hecho de no construir un micropilote reduce más el coste, ya que un tramo de micropilote que no va a ayudar a resistir por fuste ya no es necesario. Analizando los datos del terreno

se ve que el espesor del estrato no resistente para los Edificios B y C es de 4.40 y 5.00 metros, respectivamente. Mientras que en el Edificio A es de 2.20 metros (Tabla 1).

Tabla 3. Presupuesto de ejecución material de los proyectos de recalce de cada edificio según el valor de tensión de adherencia empleado.

	Edificio								
	A			B			C		
Tensión de adherencia (τ_{adh}) (MPa)	**n**	**$\sum$ L (m)**	**PEM (€)**	**n**	**$\sum$ L (m)**	**PEM (€)**	**n**	**$\sum$ L (m)**	**PEM (€)**
0.309 [23]	38	316.5	31,115	33	370.5	59336	16	184.0	17,324
0.328 [30]	35	308.5	30,056	30	348.0	55,736	14	168.0	16,058
0.552 [15]	22	285.0	26,245	21	277.0	44,551	9	127.5	12,880
0.566 [25]	22	285.0	26,245	21	277.0	44,551	9	127.5	12,880
0.637 [27]	20	282.5	26,087	21	277.0	44,551	8	118.5	12,191
0.667 [28]	20	282.5	26,087	18	252.0	40,712	8	118.5	12,191
0.679 [31]	20	282.5	26,087	18	252.0	40,712	8	118.5	12,191

n: número de micropilotes – número de perforaciones (unidad); $\sum$ L: longitud total de los micropilotes en cada proyecto de recalce (m); PEM: presupuesto de ejecución material de cada edificio (€).

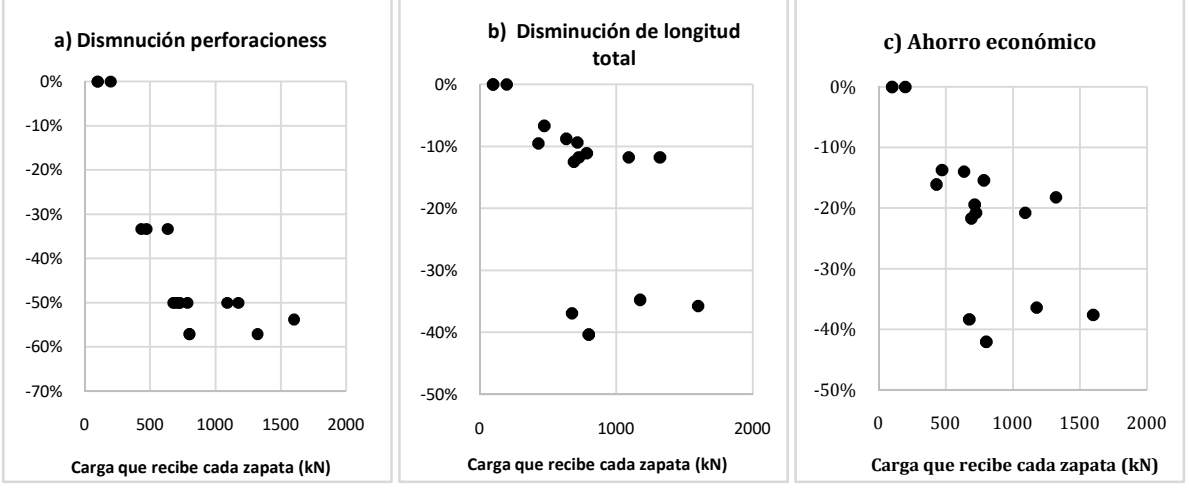

Figura 2. *a) Disminución de número de perforaciones según la carga que recibe cada zapata. b) Disminución de longitud total de micropilotes según la carga que reciben las zapatas. c) Ahorros totales por zapata según la carga que reciben.*

Los ahorros económicos por zapata pueden alcanzar el 40% (Figura 2c), teniendo un comportamiento en la gráfica similar al descenso en la longitud total de los micropilotes (Figura 2b), indicando que es ésta la variable que más afecta al PEM de los recalces. Finalmente, se observa además que hay dos zapatas cuyo recalce es independiente del valor de tensión de adherencia: dos pilares del Edificio B cuyas cargas son 100 kN y 199.9 kN (Tabla 1). Esto confirma que cuando las zapatas reciben cargas bajas (200-400 kN), no es necesaria una tensión de adherencia alta, y sería suficiente la que proporciona el EC2 [18].

4.2. Análisis probabilístico de la simulación Monte-Carlo

El trabajo realizado por Pachla [1] proporciona distribuciones de probabilidad de la tensión de adherencia para cuatro materiales diferentes (HM-15, HM-20, HA-20 y Mampostería). El hormigón de las zapatas de los tres casos de estudio es HA-20, por lo que hubo que decidir qué distribución de probabilidad emplear, o si era conveniente emplear las dos. Para ello, se realizó una breve comparativa de los parámetros media (τ_m) y desviación típica (σ) de las distribuciones para estos dos materiales HM-20 y HA-20, que son: $\tau_{m,HM}$ = 1.15 MPa y σ_{HM} = 0.19 MPa, $\tau_{m,HA}$ = 2.38 MPa y σ_{HA} = 0.32 MPa. Los valores de estos parámetros no están minorados por un coeficiente de seguridad, por lo que se dividen por el que se ha aplicado en las formulaciones previas ($\gamma_c = 1.5$). Así, los parámetros quedan: $\tau_{m,d,HM} = \tau_{m,HM}/1.5 = 0.767$ MPa y $\sigma_{d,HM} = \sigma_{HM}/1.5 = 0.129$ MPa, $\tau_{m,d,HA} = \tau_{m,HA}/1.5 = 1.587$ MPa y $\sigma_{d,HA} = \sigma_{HA}/1.5 = 0.213$ MPa. A la vista de estos parámetros, se decidió que la simulación Monte-Carlo para un hormigón HA-20 no era necesaria, ya que los valores de todas las formulaciones empleadas (Tabla 3) son muy inferiores a los que proporcionaría esta distribución (prácticamente todos estarían en el percentil del 0%). Por este motivo, sólo se utilizó la distribución HM-20, cuyos resultados además, estarían del lado de la seguridad.

La simulación Monte-Carlo se hizo generando 50.000 valores de tensión de adherencia. Para cada valor se diseñó un recalce por edificio y se calculó su presupuesto, obteniéndose las distribuciones de probabilidad representadas en forma de histograma de la Figura 4. Las cuatro distribuciones resultantes tienen un fuerte sesgo positivo y una pesada cola derecha, indicando que la mayoría de los presupuestos se concentran para valores de tensión de adherencia relativamente altos. En términos probabilísticos, para el Edificio A, el 95% de los presupuestos de menor coste se obtendrían para valores de tensión de adherencia mayores a 0.530 MPa (Figura 4a). Por lo que, los presupuestos más caros corresponden a valores de tensión de adherencia inferiores a 0.530 MPa. Para el Edificio B y C estos valores frontera serían 0.521 MPa (Figura 4b) y 0.544 MPa (Figura 4c), respectivamente. Analizando los tres edificios, 95% de los proyectos más económicos serían aquellos en los que se emplea una tensión de adherencia mayor a 0.551 MPa (Figura 4d).

Al incluir dentro de los histogramas los resultados de las siete formulaciones utilizadas previamente (Figura 4), se observa que el PEM obtenido usando la tensión de adherencia de la ACI-318-19 [17] y la EH-80 [22] están justo en el percentil del 95%, mientras que los resultados obtenidos con la formulación de Rodríguez-Ortiz [24, 27] así como la de Oteo [25] estarían por debajo de este percentil de presupuestos, entre el 85-95%, dependiendo de las características del edificio y del terreno. Por el contrario, los presupuestos más caros serían aquellos calculados con la formulación de la EHE-08 [19] y el EC2 [18], que estarían en los percentiles 99.98% y 99.99%, respectivamente. Por tanto, aplicar estas normativas para calcular la resistencia de la conexión directa arroja los presupuestos más caros para el diseño de recalces, especialmente si se sigue lo expuesto en el EC2 [18].

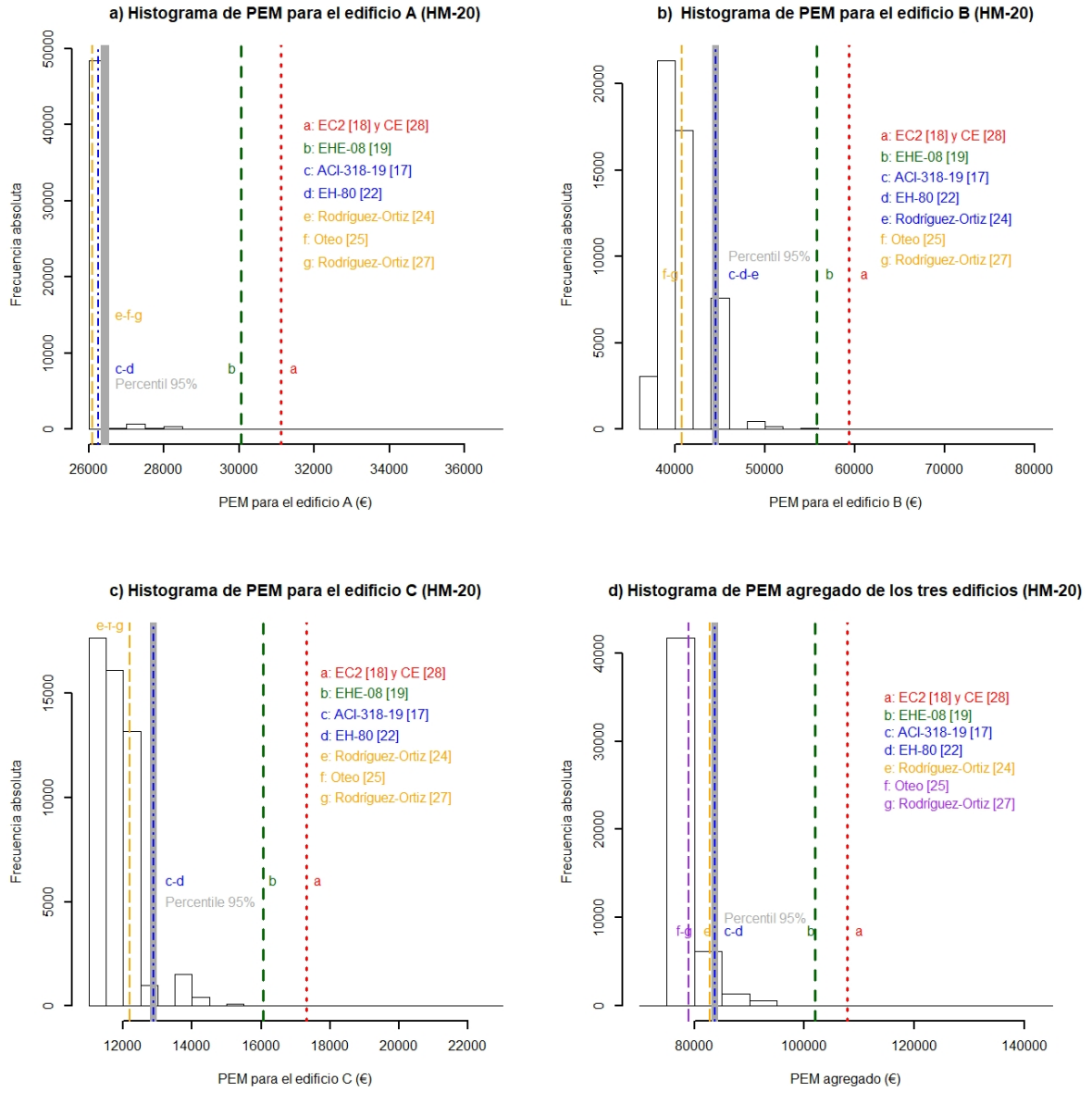

Figura 3. *Histogramas de presupuestos de recalces a partir de los resultados de la simulación Monte-Carlo. a) Edificio A. b) Edificio B. c) Edificio C. Histograma agregado (A+B+C).*

La presentación ordenada de los resultados de la simulación Monte-Carlo (PEM frente tensión de adherencia) muestra como desciende el PEM conforme aumenta el valor de tensión de adherencia empleado (Figura 5). En esta figura, también se han incluido los presupuestos obtenidos con las siete formulaciones seleccionadas (ver Tabla 3). Los cuatro gráficos presentados (Figuras 5a, 5b, 5c y 5d) indican de nuevo que los valores más restrictivos son los obtenidos si se emplea el EC2 [18] y la EHE-08 [19]. El descenso en los presupuestos es particularmente significativo al principio de la gráfica discontinua, comenzando a estabilizarse el presupuesto a partir de los valores de tensión de adherencia de la ACI-318-19 [17] y la EH-80 [22]. Para el caso específico del Edificio A (Figura 5a), no sólo se estabiliza el presupuesto, sino que a partir de un valor de 0.80 MPa, el presupuesto se incrementa al tener que aumentar la armadura tubular a lo largo de los micropilotes (A_{st}). La distribución normal de tensión de adherencia utilizada (HM-20) se muestra en el fondo de las gráficas en color azul. La línea vertical discontinua representa el percentil del 5% de la tensión de adherencia

cuyo valor es 0.558 MPa [1]. Esta línea viene a indicar las formulaciones que están dentro del conjunto cuyo percentil es igual o inferior al 5%, que son las cuatro primeras, siendo además, como ya se ha indicado previamente, la tensión de adherencia de la ACI-318-19 la que mejor se ajusta al percentil del 5%. Además, utilizar valores de tensión de adherencia superiores a 0.558 MPa no está económicamente justificado, ya que es el punto en el que los ahorros de presupuesto empiezan a ser irrelevantes. Al hilo de esto, las formulaciones propuestas por Rodríguez-Ortiz [24, 27] y Oteo [25] tendrían un coeficiente de seguridad menor, aunque aún permanecen en el lado izquierdo de la distribución. Otro interesante resultado es que siempre sería ineficiente alcanzar un valor de tensión de adherencia cercano a 1.0 MPa, ya que el coste de los presupuestos se estabiliza, y no se conseguiría ninguna mejora económica. La distribución de probabilidad para el hormigón HA-20 se ha incluido al fondo de las gráficas (sólo la cola izquierda en color gris), confirmando que los valores de las siete formulaciones empleadas estarían, aproximadamente, en el percentil del 0%.

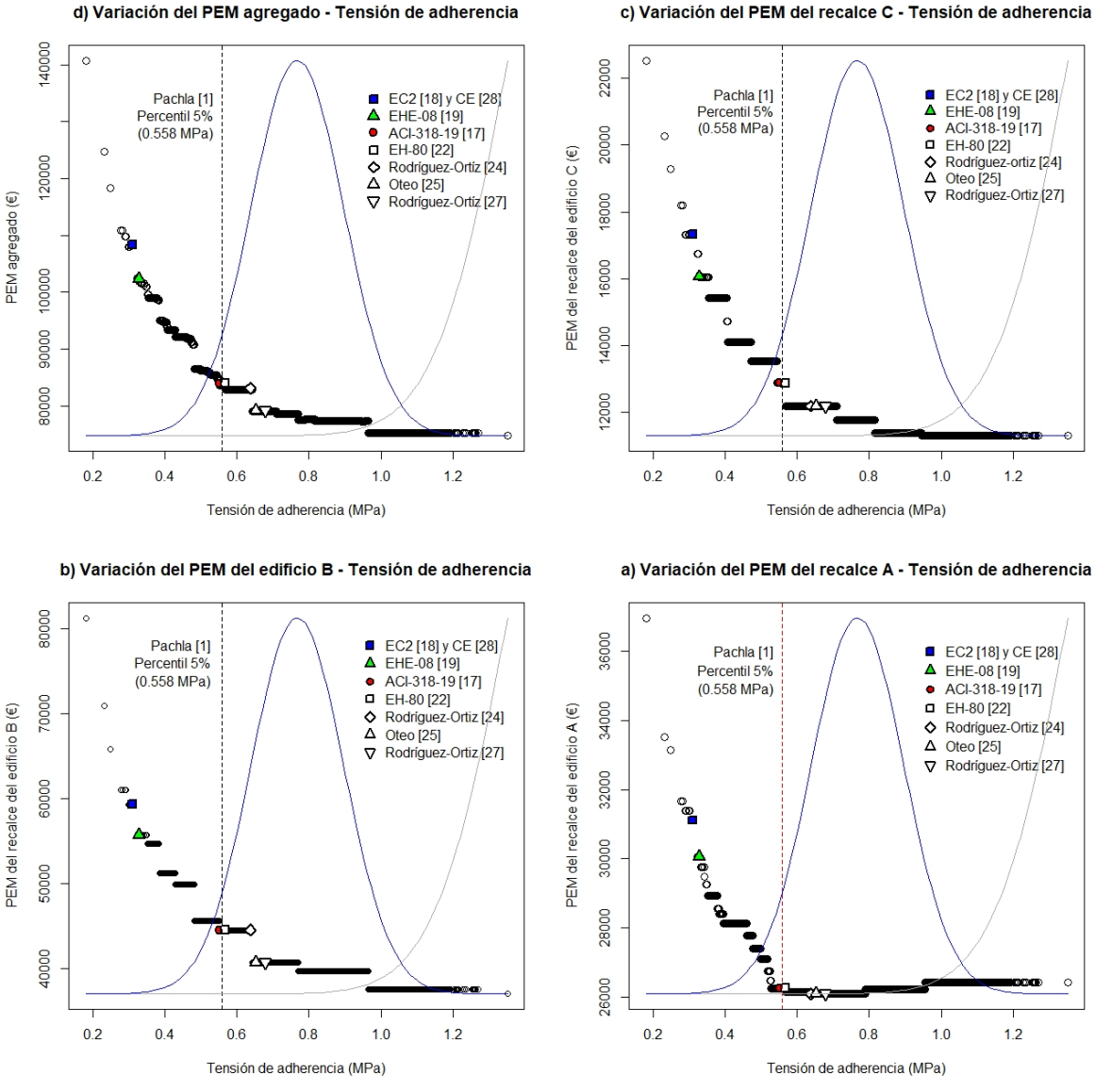

Figura 4. *Variación del PEM de los recalces respecto a la tensión de adherencia. a) Edificio A. b) Edificio B. c) Edificio C. Presupuesto agregado (A+B+C).*

5. DISCUSIÓN

La revisión bibliográfica realizada muestra que no existe una formulación específica para evaluar la resistencia en la interfaz lechada-hormigón que se genera en la conexión directa de los micropilotes a las zapatas existentes. En un principio, se ha venido utilizando la resistencia a cortante del hormigón [22, 24], y ahora, la práctica más habitual es emplear la formulación de la comprobación a rasante en juntas de hormigonado. En Europa (y España), este cambio ha reducido el valor de la tensión de adherencia a casi la mitad, lo que implica un incremento del presupuesto de los proyectos de recalces de edificios entre 20-40%. Los mayores incrementos se producen en edificios grandes que transmiten importantes cargas a la cimentación, y cuando el terreno presenta una capa superior no resistente de gran espesor (Figura 2c). Además, este cambio también supone un incremento en el tiempo de ejecución, de materiales y de residuos. Sin embargo, la normativa americana vigente ACI-318-19 [17] contiene un valor de resistencia por rasante, similar a los pasados empleados en Europa, que se podría utilizar como tensión de adherencia en micropilotes.

Tomando como referencia las siete formulaciones aplicadas, no merece la pena sobrepasar la tensión de adherencia de la normativa americana [17], ya que no supondría un ahorro sustancial en el presupuesto. La diferencia entre emplear la normativa ACI-318-19 y la formulación de Rodríguez-Ortiz [27] sería, según los resultados obtenidos de forma agregada, de tan sólo el 4%. Ahorro que no estaría justificado por el incremento del riesgo (de 4.55% a 24.03%, percentiles de la distribución de Pachla [1] utilizada en la simulación Monte-Carlo). En línea con esto, no estaría económicamente justificado querer alcanzar valores muy altos de tensión de adherencia, ya que este parámetro resistente dejaría de ser limitante en el diseño de recalces. En este sentido, si se fuera aumentando la tensión de adherencia sin restricciones, la siguiente comprobación limitante sería la resistencia en la interfaz lechada-acero. Por lo que, para cumplir esta verificación, habría que aumentar el refuerzo con barras corrugadas en la zona de la conexión, especialmente si el espesor de la zapata es pequeño. Por ejemplo, para el Edificio A, con 1.0 metro de espesor de zapata, con 3∅16 soldadas al refuerzo tubular sería suficiente hasta un valor de tensión de adherencia de 0.455 MPa. Por otro lado, para los casos B y C, el mismo refuerzo (3∅16) solo se cumpliría para una tensión de adherencia de 0.428 MPa. Por lo que, cuando se superan estos valores de tensión de adherencia, ha sido necesario aumentar el armado en la zona de conexión (Figura 4). Para grandes valores de tensión de adherencia, cercanos a 1.0 MPa, entonces la resistencia del propio micropilote no sería suficiente, y hay que aumentar la armadura tubular. Esta sería la variable que más incrementaría el presupuesto, ya que en lugar de un refuerzo puntual se haría un incremento de la armadura a lo largo de todo el micropilote. Si el aumento de armadura no respeta los recubrimientos, también habría que incrementar el diámetro del micropilote para garantizar la correcta transmisión de fuerzas [37], por lo que se aumentaría aun más el presupuesto. La última consideración sería la estabilidad por pandeo. Para este estudio en concreto, la longitud máxima que se ha obtenido es de 22 metros (τ_{adh} = 1.0 MPa), que implica una esbeltez geométrica menos a 150 por lo que, en principio, el pandeo no supondría un problema [38].

Finalmente, merece la pena discutir sobre tres aspectos clave en el diseño de los recalces. En primer lugar, recordar que se ha tomado una distribución de tensiones para hormigón en masa cuando las zapatas son de hormigón armado, por lo que el confinamiento que genera el armado no se habría tenido en cuenta y los resultados de la simulación Monte-Carlo quedarían del lado de la seguridad. En segundo lugar, considerando los resultados de la experimentación que afirman que la tensión de adherencia aumenta cuando disminuye el diámetro de la perforación, la formulación empleada no

cumple con esta premisa, ya que una de las formas de aumentar la resistencia de la conexión es aumentar el diámetro de la perforación (aumentando la superficie de contacto) manteniendo la tensión de adherencia como constante. En tercer lugar, para poder aplicar la formulación de la EC2 [18], y del nuevo CE [28], va a ser necesario definir claramente los parámetros a emplear (c, μ y sobre todo σ_n) para así evitar la incertidumbre de qué valores aplicar, y no terminar empleando valores demasiados conservadores que no estarían justificados estadísticamente según los resultados del trabajo de Pachla [1].

6. CONCLUSIONES

Los principales manuales sobre micropilotes indican que la resistencia en la conexión directa debe cumplir con los códigos de elementos de estructuras de hormigón. Sin embargo, en ellos no se encuentra ningún modelo específico para este tipo de conexión. En un principio se ha venido equiparando la tensión de adherencia con la resistencia de cortante del hormigón, y más tarde a la resistencia de rasante en las juntas de hormigonado. Este cambio supone una reducción de la tensión de adherencia en torno al 50%, y la comprobación de la resistencia de la conexión directa se ha convertido en el factor limitante habitual en los proyectos de recalces. Esta nueva situación ha provocado que sea necesario incrementar el número de micropilotes en este tipo de proyectos, que supone un coste asociado de un 20%, y que puede alcanzar un 40% según las características del edificio a recalzar y del terreno que lo sustenta. En contraposición destaca la normativa americana ACI-318-19, en la que tomando la tensión de adherencia como la resistencia a rasante en juntas de hormigonado, se volvería a aplicar valores similares a la resistencia de cortante de hormigón.

Uno de las causas de la incertidumbre que genera el uso de la comprobación a rasante en juntas de hormigonado son los parámetros contenidos en sus formulaciones, que dependen básicamente de la rugosidad de la superficie de contacto. Los micropilotes se realizan mediante rotación, resultando una superficie de contacto “lisa” y se terminan aplicando valores de parámetros que proporcionan valores de tensión de adherencia conservadores. La única forma de aumentar la resistencia sería considerar la compresión normal que aparece por efecto Poisson una vez el micropilote entra en carga, y que incrementa la componente de resistencia por rozamiento. Pero, esta compresión es difícilmente cuantificable y la única forma de considerarla es si ésta viene generada por una fuerza externa. Por tanto, se hace necesario contar con valores de estos parámetros más precisos para en el caso de los micropilotes. Más aún cuando se acaba de aprobar el Código Estructural en España, que va a generar dudas sobre qué valores son los más adecuados para no comprometer la seguridad estructural y que no generen sobrecostes excesivos.

AGRADECIMIENTOS

Este trabajo ha sido financiado por el Centro para el Desarrollo Tecnológico Industrial (CDTI), con el código: IDI-20180024

REFERENCIAS

[1] Pachla, H. (2016). Conditions of proper interaction of Low-pressure Injection Piles (LIP) with structure and soil, carrying capacity of pile anchorage in foundation. Studia Geotechnica et Mechanica, 38(4), 33-49.

[2] Veludo, J., Dias-da-Costa, D., Júlio, E.N.B.S., & Pinto, P.L. (2012). Bond strength of textured micropiles grouted to concrete footings. Engineering Structures, 35, 288-295

[3] Gómez, J., Cadden, A., Traylor, R.P., Bruce, D.A., & Eng, C. (2005). Connection Capacity between Micropiles and Concrete Footings: Interpretation of Test Results and Design Recommendations, article presented in the GEO3 Conference, November 2005, Dallas, EUA.

[4] Sabatini, J.P., Tanyu, B., Armour, T., Groneck, P., & Keeley, J. (2005). Micropile Design and Construction, Federal Highway Administration - US Department of Transportation. FHWA-NHI-05-039, Washington, D.C.

[5] Bruce, D.A., Di Millio, A.F., & Juran, I. (1995). Introduction to micropiles: an international perspective, in: Geotechnical Special Publication. (50Ed., pp. 1-26). ASCE.

[6] Echave-Rasines, J.M. (2003). Conexión de micropilotes a estructuras. Jornadas técnicas SEMSIG-AETESS. 3ª Sesión: Micropilotes, Naos Livros, p. 131-141.

[7] Bruce, D.A., Di Millio, A.F., & Juran, I. (1995). Primer on micropiles. Civil Engineering-ASCE, 65(12), 51-54.

[8] CEN. (2006). EN 14199:2006 Execution of special geotechnical works – Micropiles. European Committee for Standardization; 2006, p. 52.

[9] CEN. (2019). EN 14199:2019 Execution of special geotechnical works – Micropiles (Endorsed by AENOR in August of 2006). European Committee for Standardization; 2019, p. 65.

[10] GPEMOC. (2005). Guía para el proyecto y la ejecución de micropilotes en obras de carretera. Dirección General de Carreteras. Ministerio de Fomento. Madrid.

[11] Bruce, D.A., & Juran, I. (1997).Drilled and Grouted Micropiles: State-of-Practice Review, ADSC The International Association of Foundation Drilling, Dallas.

[12] Azuar, M.J.J., & Renault, M.J. (1986). Lex micropieux. Ministere de L'Urbanisme du Logementet des Transports. Direction des Routes. p.62. [in French].

[13] NF. P 11-12. (1992). Travaux de foundations profondes pour le bâtiment – Partie 1: Cahier des clauses techniques. Normative française. Référence DTU 13.2, p.116 [in French].

[14] H. Cyna, F. Schlosser, R. Frank, C. Plumelle, R. Estephan, F. Altamayer et al. FOREVER: Synthèse des resultants et recommandations du project national sur les micropieux (1999-2003): Presses de L'Ecole National des Ponts et Chaussées; 2004 p.347 [in French].

[15] Juran, I., Bruce, D.A., Dimillio, A., & Benslimane, A. (1999).Micropiles: the state of practice. Part II: design of single micropiles and groups and networks of micropiles. Ground Improvement, 3, 89-110.

[16] Armour, T., Groneck, P., Keeley, J., & Sharma, S. (2000). Micropile Design and Construction Guidelines - Implementation manual. Federal Highway Administration - US Department of Transportation. FHWA-SA-97-070, Washington, D.C.

[17] ACI committee 318, Building Code Requirements for Structural Concrete and Commentary (ACI 318M-19), 2019.

[18] CEN. (2010). EN 1992-1-1: Eurocode 2: Design of concrete structures (EC2) – Part 1-1: General rules and rules for buildings. Brussels: European Committee for Standardization; 2010, p. 225.

[19] EHE-08. (2008). Instrucción de Hormigón Estructural (EHE-08). Real Decreto 1247/2008, Boletín Oficial del Estado (BOE)n° 203, Madrid.

[20] Darrel, W., Gómez, J., Cadden, A.W., Traylor, R.P., & Pilkington M. (2005). Compressive Load Transfer in Micropiles through Concrete Footings: A Full Scale Test Program. Companion paper in Geo3 Conference Proceedings.

[21] Instrucción EH-73. (1973). Instrucción para el proyecto y la ejecución de obras de hormigón en masa o armado. Decreto 3062/1973. Boletín Oficial del Estado (BOE) n° 293, Madrid.

[22] Instrucción EH-80. (1980). Instrucción para el proyecto y la ejecución de obras de hormigón en masa o armado (EH-80). Real Decreto 2868/1980, Boletín Oficial del Estado (BOE) n°9, Madrid.

[23] ACI 318-02 Building Code Requirements for Structural Concrete (including Historical ACI Building Code Requirements from 1908 to 2005).

[24] Rodríguez-Ortiz, J.M. (1984). Curso de rehabilitación. Volumen 4ªEd., Colegio Oficial de Arquitectos de Madrid, Madrid, 1984.

[25] Oteo, C.S. (2007).Micropilotes. Criterios para el diseño de micropilotes, en: Jornadas Técnicas SEMSIG-AETESS 3ª Sesión. Micropilotes. Madrid.

[26] EHE. (1999). Instrucción de Hormigón Estructural (EHE). Real Decreto 2661/1998. Boletín Oficial del Estado (BOE), n° 11, Madrid.

[27] Rodríguez-Ortiz, J.M. (2007). Actuaciones y rehabilitación en construcciones históricas y singulares, en: Intervenciones en cimentación: Técnicas aplicables y patología. Jornadas Técnicas SEMSIG-AETESS 7ª Sesión.

[28] BOE. (2021). Real Decreto 470/2021. Código Estructural. Ministerio de la Presidencia, Relaciones con las Cortes y Memoria Democrática. Madrid. Nº 190 (97664-99452).

[29] Serrano-Alcudia, F. (1998). Patología de la edificación. El lenguaje de las grietas, 1ªed. Fundación Escuela de la Edificación. Madrid.

[30] Walker, W.E, Harremoës, P., Rotmans, J., van der Sluijs, J.P., van Asselt, M.B.A., Janssen, P., & Krayervon Krauss, M.P. (2003). Defining uncertainty: a conceptual basis for uncertainty management in model-based decision support. Integrated Assessment, 4(1), 5-17.

[31] Martínez-Paz, J.M, Pellicer-Martínez, F., & Colino, J. (2014). A probabilistic approach for the socioeconomic assessment of urban river rehabilitation projects. Land Use Policy, 36, 468-477.

[32] Skrzypczak, I., Słowik, M., & Buda-Ozóg, L. (2017). The application of reliability analysis in engineering practice - Reinforced concrete foundation. Procedia Engineering, 193, 144-151.

[33] Marek, P., Gustar, M., & Anagnos, T. (1999). Codified design of steel structures using Monte Carlo techniques. Journal of Constructional Steel Research, 52(1), 69-82.

[34] Nguyen, H.D., Shin, M., & Torbol, M. (2020). Reliability assessment of a planar steel frame subjected to earthquakes in case of an implicit limit-state function. Journal of Building Engineering, 32, 101782.

[35] Vazirizade, S.M., Nozhati, S., & Zadeh, M.A. (2017). Seismic reliability assessment of structures using artificial neural network. Journal of Building Engineering. 11, 230-235.

[36] Vose, D. (2008). Risk Anaysis - A quantitative guide, third ed., John Wiley and Sons.

[37] Pachla, H. (2017). Experimental verification of integrity of low-pressure injection piles structure – pile internal capacity. Studia Geotechnica et Mechanica, 39(4), 77-85.

[38] Gatto, M.P.A., & Montrasio, L. (2010). Analysis of the Behaviour of Very Slender Piles: Focus on the Ultimate Load, International Journal of Civil Engineering. 19, 145-153.

ON MODAL ANALYSIS OF PHASE-FIELD FRACTURE MODELS

Jukić, Krešimir[1]; Jarak, Tomislav[1,2]; Tonković, Zdenko[1]; Lorenzana, Antolín[2]

ABSTRACT

In this work, the modal response of a phase-field model of a damaged structure is performed and the influence of various phase-field model parameters on the dynamic response is analysed. Instead of analysing hypothetical cracks, here the crack geometries of the damaged body are predicted by a quasi-static crack propagation simulation by means of an adaptive phase-field method, performed prior to the modal analyses. The modal analyses are performed with respect to the damaged configurations obtained during the fracture simulations. The natural frequencies and corresponding mode shapes of a plate modelled as a tree-dimensional body with a crack has been inspected. Various modifications of the phase field fracture model are used in the modal analysis. The influence of element size and length scale are also studied. From the results, the recommendations for performing the modal analysis of phase-field models are drawn.

Keywords: phase-field, brittle fracture, dynamic response, modal analysis

1. INTRODUCTION

One of the major engineering design concerns is failure due to fracture. Although a brittle fracture is not as common as a ductile failure/fracture due to the predominant application of ductile engineering materials such as mild steels, it can also lead to catastrophic consequences. The analysis of brittle fracture has its roots in the work of Griffith [1]. Still, realistic complex crack topologies have to be analysed using more advanced methods, one of which is the phase-field (P-F) method. The P-F method is based on a variational approach to the Griffith's theory proposed by Francfort and Marigo [2] and an approximative crack description. It is currently one of the most promising approaches in analysing fracture/failure, since it can capture various complex phenomena, including crack initiation, propagation, branching, merging, etc., without any additional ad-hoc criteria. In the P-F method, all fracture phenomena are driven solely by the applied energy minimization principle. So far, P-F model solutions have shown a good correspondence to experimental results (see for example [3, 4]). In addition, the P-F models for brittle fracture are easily implemented into the existing FEM codes and are expandable to more complex phenomena, such as ductile fracture [5], dynamic fracture [6], or fracture due to fatigue [7].

Phase-field-based dynamic models have been used in various contributions. Usually, P-F models for predicting dynamic cracks are thermodynamically consistent and do not consider mass, i.e., kinetic energy, degradation (such as in [6, 8, 9]). However, the approximative crack description in general

[1] *University of Zagreb, Faculty of Mechanical Engineering and Naval Architecture, Croatia, kresimir.jukic@fsb.hr (Corresponding author), zdenko.tonkovic@fsb.hr*
[2] *ITAP, School of Industrial Engineering, University of Valladolid (SPAIN). tomislav.jarak@uva.es, ali@eii.uva.es*

results in a smeared distribution of damage variable, and consequently to the diffusive local loss of stiffness. This local loss of stiffness on the other hand leads to the change of wave-speed, which may affect the results in high-speed dynamic fracture processes. This motivated some authors to adopt kinetic energy degradation e.g., in [10]. In other words, kinetic energy then becomes affected by the phase field damage variable. The smeared local loss of stiffness could also affect the structural dynamic response of the obtained P-F model, thereby hindering their efficient use in structural analysis of damaged structures. Therefore, some researchers [11, 12] studied the modal parameters of the P-F models of structural elements with cracks. In those works, mass/density was degraded, depending on the phase field. Although satisfying results have been obtained, such choice is neither explained nor its effects analyzed. Rather, is seems it has been adopted in an "ad hoc" manner. At first glance there is little justification for such approach, since kinetic energy apparently is not affected by the damage variable for low-speed dynamic fracture, see e.g. [6, 8, 9]. In addition, to the best knowledge of authors, in all works dealing with the modal analysis of P-F fracture models, the P-F approach has been used only to model simple hypothetical pre-existing cracks, and damage was actually not predicted by a P-F model. Thereby, some usual techniques used for modelling the pre-existing cracks in P-F analysis are applied to model the crack geometries.

In this contribution, the modal analysis of a structure with a crack predicted by an adaptive P-F model is performed. The adaptive model is used to speed up the P-F fracture analysis, since P-F models require very dense meshes in regions around cracks. Therefore, for a realistic engineering problem, performing modal analyses of P-F models with too fine meshes could present considerable additional computational burden. This would be relevant if many such analyses would have to be performed, e.g., in monitoring and controlling a progressive fatigue damage. The influence of the approximative crack description by the phase field on the modal properties of the model with cracks is investigated. This knowledge could be valuable for developing reliable P-F models for the applications dealing structural integrity, such as failure identification and characterization. The effects of different modifications of the original P-F model, used for the prediction of fracture, on modal parameters is studied. The models with or without kinetic energy degradation are studied. Thereby, different degradation functions are considered for kinetic energy and stiffness, as well as the element deletion technique. Referent results were obtained by the model where the crack was modelled in a discrete manner, as a geometric discontinuity in the mesh (so called mesh-induced crack). The effects of mesh density and length scale on the results are also presented. In the studied example, advantages and disadvantages of different methods are demonstrated.

The rest of the work is organized as follows: in section 2 the phase-field model for brittle fracture is described, while numerical implementation is described in section 3. In section 4, the dynamic model used for the modal analysis is described, and a study of modal parameters is presented. The conclusion is given in section 5.

2. PHASE-FIELD MODEL OF BRITTLE FRACTURE

According to the variational approach of fracture, used in the Phase-Field (P-F) method, the crack propagates to the configuration of minimal total energy, and hence the entire process can be described as an energy minimization process. Formally, the total energy is given by:

$$\Psi = \Psi_{\mathrm{e}} + \Psi_f - \mathrm{P} = \int_\Omega \psi \, \mathrm{d}V + \int_\Gamma G_c \, \mathrm{d}A - \mathrm{P}, \tag{1}$$

where Ψ is the total energy, Ψ_e is the strain energy, Ψ_f is the fracture energy, while P denotes the external force potentials defined as

$$P = \int_\Omega \boldsymbol{b}\boldsymbol{u} dV + \int_{\Omega_t} \boldsymbol{t}\boldsymbol{u} dA. \tag{2}$$

In the above equations, Ψ_e and Ψ_f are defined by the deformation energy density ψ and the critical energy release rate G_c. Ω represents a n-dimensional computational domain, and Γ denotes a crack surface. As usual, $\boldsymbol{b}$ is the vector of body forces, and $\boldsymbol{t}$ represents the prescribed traction forces acting on the part of the outer boundary Ω_t.

2.1 Approximative crack description

Approximative crack description using the phase-field was firstly adopted by Bourdin [13]. He adopted a scalar field ϕ in the range from 0, which denotes undamaged healthy materially, and 1, which denotes the totally damaged material, and approximated crack surface as follows:

$$\int_\Gamma \mathrm{d}A \approx \int_\Omega \gamma \, \mathrm{d}V = \int_\Omega \frac{1}{2}\left(\frac{1}{l}\phi^2 + l(\nabla\phi)^2\right) \mathrm{d}V. \tag{3}$$

Herein, γ stands for crack surface density function, ϕ is the phase-field and l is the length-scale parameter that defines the extent of smearing of the phase-field profile. The fracture energy can then be computed by:

$$\Psi_f = \int_\Omega G_c \gamma \, \mathrm{d}V \tag{4}$$

It should be noted that the crack surface density function given in Eq. (3) is not unique, and there exist various alternative choices, such as the ones defined in [14] or [15]. However, the function defined by Eq. (3) is a common choice used in the literature because it simplifies some aspects of the model [16].

2.2 Deformation energy density function

The P-F models rely on a degradation of the strain energy, typically defined by:

$$\psi = g \cdot \psi_0^+ + \psi_0^-, \tag{5}$$

where g stands for the strain energy degradation function. ψ_0^+ is called the tensile deformation energy density and ψ_0^- is the compressive deformation energy density. The degradation of the energy density serves: 1) to simulate a loss of strength induced by the presence of crack, and 2) to allow the decrease of total energy. The degradation function is usually monotonically decreasing function bounded by one and zero. The commonly used degradation function is quadratic:

$$g(\phi) = (1-\phi)^2. \tag{6}$$

Although other degradation functions can be used, the quadratic function (6) in combination with quadratic crack surface density function defined in Eq. (3) leads to a P-F model with some significant

computational and implementation benefits, such as smaller computational costs, easier imposition of irreversibility condition on ϕ, or easier crack geometry description [16].

Energy split method is also not unique [16,17,18]. In this work, we use the so-called isotropic model in modal analysis, defined as:

$$\psi_0^+ = \psi_0, \psi_0^+ = 0, \tag{7}$$

where entire strain energy is degraded. For the crack propagation analysis, the split defined by Lo [19] is used here, which completely prevents cracking in compression. With the principal strains defined as $\varepsilon_3 \geq \varepsilon_2 \geq \varepsilon_1$, energy is defined as:

- if $\varepsilon_1 > 0$:
  $\psi_0^+ = \frac{Ev}{2(1+v)(1-2v)}(\varepsilon_1 + \varepsilon_2 + \varepsilon_3)^2 + \frac{E}{2(1+v)}(\varepsilon_1^2 + \varepsilon_2^2 + \varepsilon_3^3), \psi_0^- = 0,$ (8)
- else if $\varepsilon_2 + v\varepsilon_1 > 0$:
  $\psi_0^+ = \frac{Ev}{2(1+v)(1-2v)}(\varepsilon_3 + \varepsilon_2 + 2v\varepsilon_1)^2 + \frac{E}{2(1+v)}((\varepsilon_3 + v\varepsilon_1)^2 + (\varepsilon_2 + v\varepsilon_1)^2), \psi_0^- = \frac{E}{2}\varepsilon_1^2,$ (9)
- else if $(1-v)\varepsilon_3 + v(\varepsilon_1 + \varepsilon_2) > 0$:
  $\psi_0^+ = \frac{E}{2(1-v^2)(1-2v)}\big((1-v)\varepsilon_3 + v\varepsilon_2 + v\varepsilon_1\big)^2, \psi_0^- = \frac{E}{2(1-v^2)}(\varepsilon_1^2 + \varepsilon_2^2 + 2v\varepsilon_1\varepsilon_2),$ (10)
- else
  $\psi_0^+ = 0, \psi_0^- = \frac{Ev}{2(1+v)(1-2v)}(\varepsilon_1 + \varepsilon_2 + \varepsilon_3)^2 + \frac{E}{2(1+v)}(\varepsilon_1^2 + \varepsilon_2^2 + \varepsilon_3^3)$ (11)

2.3 Governing equations

The linear momentum balance, expressed here for the static fracture process as

$$\int_\Omega \boldsymbol{\sigma}\delta\boldsymbol{\varepsilon}dV - \int_\Omega \boldsymbol{b}\delta\boldsymbol{u}dV - \int_{\Omega_t} \boldsymbol{t}\delta\boldsymbol{u}dA = 0, \tag{12}$$

must hold at all times. Herein, $\delta\boldsymbol{u}$ and $\delta\boldsymbol{\varepsilon}$ denote variations of displacements and strains, respectively. Stresses $\boldsymbol{\sigma}$ are defined as is usual for hyperplastic materials as

$$\boldsymbol{\sigma} = \frac{\partial\psi}{\partial\boldsymbol{\varepsilon}} = g \cdot \frac{\partial\psi_0^+}{\partial\boldsymbol{\varepsilon}} + \frac{\partial\psi_0^-}{\partial\boldsymbol{\varepsilon}}. \tag{13}$$

Eq. (12), after some suitable manipulations, results in the following well-known governing equation

$$\mathrm{div}(\boldsymbol{\sigma}) = -\boldsymbol{b} \text{ in } \Omega, \quad \boldsymbol{\sigma}\cdot\boldsymbol{n} = \mathbf{t} \text{ on } \Omega_t, \tag{14}$$

where Ω_t stands for the part of the global boundary with the prescribed tractions and $\boldsymbol{n}$ is the outer normal vector to Ω_t.

The variational principle of the phase field fracture method states that the fracture process always consumes energy, which leads to the unilaterally stationary condition:

$$\delta\Psi(\boldsymbol{u},\phi) = \delta P(\boldsymbol{u}) - \delta\Psi_\mathrm{e}(\boldsymbol{u},\phi) - \delta\Psi_f(\phi) \geq 0. \tag{15}$$

After recalling the energy definitions from Eqs. (1)-(5), performing the necessary variations, and considering Eq. (12), after some mathematical manipulation and by adopting the following homogeneous boundary condition on the global boundary $\partial\Omega$

$$\nabla\phi \cdot n = 0, \text{on } \partial\Omega, \tag{16}$$

Eq. (15) reduces to the condition

$$-\left(\frac{dg}{d\phi}\psi_0^+ + \frac{G_c}{l}\phi - G_c l\Delta\phi\right)\delta\phi \geq 0 \text{ in } \Omega. \tag{17}$$

Since $\delta\phi \geq 0$ (the damage at some point can only grow in time, i.e., the phase field must be monotonous function), it follows that at every moment it must hold that

$$\frac{dg}{d\phi}\psi_0^+ + \frac{G_c}{l}\phi - G_c l\Delta\phi \leq 0 \text{ in } \Omega. \tag{18}$$

Finally, from the energy conservation condition, which must also hold at every moment of the process, it follows that:

$$\tfrac{dg}{d\phi}\psi_0^+ + \tfrac{G_c}{2\cdot l}\phi - G_c l\Delta\phi = 0 \text{ if } \dot{\phi} > 0, \tag{19}$$

meaning that the crack grows only if the equality in (20) if fulfilled. Eqs. (18) and (19), together with the irreversibility condition on the phase field, $\delta\phi \geq 0$ and $\dot{\phi} > 0$, lead to the following Kuhn-tucker loading/unloading conditions

$$\frac{dg}{d\phi}\psi_0^+ + \frac{G_c}{l}\phi - G_c l\Delta\phi \leq 0\,, \dot{\phi} > 0, \qquad \left(\frac{dg}{d\phi}\psi_0^+ + \frac{G_c}{l}\phi - G_c l\Delta\phi\right)\dot{\phi} = 0 \text{ in } \Omega. \tag{20}$$

Finally, Eqs. (14), (16) and (20) represent the governing equations of the stationary phase field fracture problem. The detailed derivation of the governing equations can be found in [16]. The phase field irreversibility is enforced here by a simple implicit enforcement method using the history field [20]. It is based on modifying the governing equation for the phase-field (20) to

$$\tfrac{dg}{\mathrm{d}\phi}H + \tfrac{G_c}{l}\phi - \mathrm{G_c}l\Delta\phi = 0, \tag{21}$$

where H is the history field, and is defined as

$$H = \max_{\tau=[0,t]} \psi_0^+(\tau). \tag{22}$$

It should be noted that the P-F models employing the history field approach are not equivalent to the original variational problem, but that they usually yield very similar results [21].

3. NUMERICAL MODELING OF FRACTURE PROCESS BY PHASE-FIELD

3.1 Finite element discretisation

The phase-field and displacement field within FEM can be described as:

$$\mathbf{u} = \mathbf{N}_{\mathrm{u}}\mathbf{v},\ \phi = \mathbf{N}_{\phi}\boldsymbol{\phi}, \tag{23}$$

where $\mathbf{u}$ stands for the displacement vector. $\mathbf{v}$ and $\boldsymbol{\phi}$ are the vectors of nodal displacements and nodal phase-field variables, respectively, while $\mathbf{N}_{\mathrm{u}}$ and $\mathbf{N}_{\phi}$ denote their corresponding shape function matrices. In this work, tetrahedron finite elements with 10 nodes are used. Variating the total energy from Eq. (1) and employing the approximations from Eq. (23) for both the trial and test functions according to the Bubnov-Galerkin principle, the following discretized equations can be obtained:

$$\int_V \mathbf{B}_u{}^{\boldsymbol{T}}\boldsymbol{\sigma}\mathrm{d}V - \int_V \mathbf{N}_u{}^{\boldsymbol{T}}\mathbf{b}\mathrm{d}V - \int_B \mathbf{N}_u{}^{\boldsymbol{T}}\mathbf{t}\,\mathrm{d}A = 0,\ \ \int_V \left(\left(\frac{dg}{\mathrm{d}\phi}H + \frac{G_{\mathrm{c}}}{l}\phi\right)\mathbf{N}_{\phi} + G_{\mathrm{c}}l\mathbf{B}_{\phi}{}^{\mathrm{T}}\nabla\phi\right)\mathrm{d}V = 0 \tag{24}$$

Herein, $\mathbf{B}_u$ is the matrix relating the strains to the nodal displacements, $\boldsymbol{\epsilon} = \mathbf{B}_u\mathbf{v}$, while $\mathbf{B}_{\phi}$ is the discrete operator relating the nodal phase-field values to the phase-field gradient, $\nabla\boldsymbol{\phi} = \mathbf{B}_{\phi}\boldsymbol{\phi}$. Note that the deformation energy density is replaced with the history field. Residuals of Eq. (26) are:

$$\mathbf{R}_u = -\int_V \mathbf{B}_u{}^{\boldsymbol{T}}\boldsymbol{\sigma}\mathrm{d}V + \int_V \mathbf{N}_u{}^{\boldsymbol{T}}\mathbf{b}\mathrm{d}V + \int_B \mathbf{N}_u{}^{\boldsymbol{T}}\mathbf{t}\,\mathrm{d}A,\quad \mathbf{R}_{\phi} = -\int_V \left(\left(\frac{dg}{\mathrm{d}\phi}H + \frac{G_{\mathrm{c}}}{l}\phi\right)\mathbf{N}_{\phi} + G_{\mathrm{c}}l\mathbf{B}_{\phi}{}^{\mathrm{T}}\nabla\phi\right)\mathrm{dV}. \tag{25}$$

3.2 Solver procedure

A staggered solver is used to solve the discretised equations [22]. The displacement fields and phase-fields are calculated separately, in two steps, in an iterative-incremental manner. In every iteration, the new displacement field is obtained by solving the equation:

$$\mathbf{v}_i^k = \mathbf{v}_i^{k-1} + \boldsymbol{K}_{uu}^{-1}\left(\mathbf{v}_i^{k-1}, \boldsymbol{\phi}_i^{k-1}\right)\cdot\mathbf{R}_u\left(\mathbf{v}_i^{k-1}, \boldsymbol{\phi}_i^{k-1}\right), \tag{26}$$

while holding the phase-field values constant. Here, k denotes the number of iterations of the current increment i. After that, a new phase-field iterative prediction is obtained as

$$\boldsymbol{\phi}_i^k = \boldsymbol{\phi}_i^{k-1} + \boldsymbol{K}_{\phi\phi}^{-1}\left(\mathbf{v}_i^k, \boldsymbol{\phi}_i^{k-1}\right)\cdot\mathbf{R}_{\phi}\left(\mathbf{v}_i^k, \boldsymbol{\phi}_i^{k-1}\right) \tag{27}$$

by using the displacements obtained in the previous step. The matrices $\mathbf{K}_{uu}$ and $\mathbf{K}_{\phi\phi}$ are defined as

$$\mathbf{K}_{uu} = \int_V \mathbf{B}_u^{\mathbf{T}}\frac{\partial\boldsymbol{\sigma}}{\partial\boldsymbol{\epsilon}}\mathbf{B}_u\mathrm{d}V,\ \ \mathbf{K}_{\phi\phi} = \int_V \left(\mathbf{N}_{\phi}^{\mathbf{T}}\left(\frac{d^2g}{\mathrm{d}\phi^2}H + \frac{G_{\mathrm{c}}}{l}\right)\mathbf{N}_{\phi} + G_{\mathrm{c}}l\,\mathbf{B}_{\phi}^{\mathbf{T}}\mathbf{B}_{\phi}\right)\mathrm{d}V. \tag{28}$$

The process is repeated until convergence criteria are met. Convergence is checked in every iteration after the phase-field step. In this work, the following convergence criteria are used:

$$\left\|\boldsymbol{\phi}_i^k - \boldsymbol{\phi}_i^{k-1}\right\|_{\infty} < f_1\,,\ \frac{\Delta\Psi_{e,i}^k}{\Delta\Psi_{e,i}^1} < f_2\,, \tag{29}$$

where $\Delta\Psi_{\mathrm{e,i}}^{k}$ stands for the change of the deformation energy computed in the displacement field step. The tolerances $f_1 = f_2 = 0.001$ are used.

3.3 Adaptive procedure

To reduce the computational cost, we used a simple adaptive remeshing procedure in the solving process. It is based on a bisection algorithm, which enables automatic refinement and coarsening of the starting tetrahedron mesh during the computation, depending on the remeshing criteria. The refinement criteria are checked for all elements. If they are satisfied for an element, the longest edge of the element are marked for splitting. Then, all neighbouring elements that possess that edge are additionally checked for remeshing. Thereby, all the neighbouring elements marked for splitting are always split during their longest edge. This process is repeated in a recursive manner, until there are no more neighbouring elements that must be split. The "longest edge" splitting rule results in meshes without large distortion, and additional smoothing of the mesh is not necessary. During the mesh refinement, a mesh hierarchy is created, with parent-children relationships being established between elements. Such hierarchy is especially useful when performing mesh coarsening. In that process, the parent element is reactivated if the children elements satisfy coarsening criteria, while the children are collapsed. During coarsening, 'hanging nodes' can appear. To avoid that problem, some additional element splitting is performed until the hanging nodes are removed. In this contribution, three simple refinement criteria are used: 1) The criterion based on the stress errors, 2) The criterion based on the phase field, 3) The criterion based on the deformation energy. The coarsening criteria are analogous to refinement criteria. This adaptive remeshing is done after every two iterations, after solving the phase-field subproblem.

3.4 Numerical simulation of fracture process

Accuracy of the proposed model is demonstrated on the example of an asymmetrically notched perforated three-point bending test specimen, presented in [23] together with experimental results. Geometry and boundary conditions (BCs) are given in Fig. 1. Material parameters are the Young's modulus $E = 20800\mathrm{MPa}$, the Poisson's coefficient $v = 0.3$, the critical energy release rate $\mathrm{G_c} = 1\,\frac{\mathrm{mJ}}{\mathrm{mm^2}}$ and the length scale parameter $l = 0.05\mathrm{mm}$. The process is controlled by the crack mouth opening, and relatively course incrementation is used. Adaptive remeshing is utilized with the minimal allowed element's edge size being $0.7l$. In the regions colored in red in Fig. 1 the Dirichlet's boundary condition ϕ=0 is prescribed at all nodes on the phase-field to prevent the initiation and growth of crack around the prescribed BCs. In addition, in those zones, remeshing is prevented.

Obtained numerical results and comparison to experimental results are shown in Fig. 2. Obviously, numerically predicted results fit experimental data well. In Fig. 3, the starting pre-defined mesh and the final adaptive mesh are depicted. The starting mesh contains 8606 elements and 14668 nodes, while the final mesh consists of 223623 elements and 318087 nodes. From the Fig. 3, it is visible that the proposed adaptive remeshing process successfully refines the mesh locally, only in the region where the growth of damage is predicted by the phase-field method.

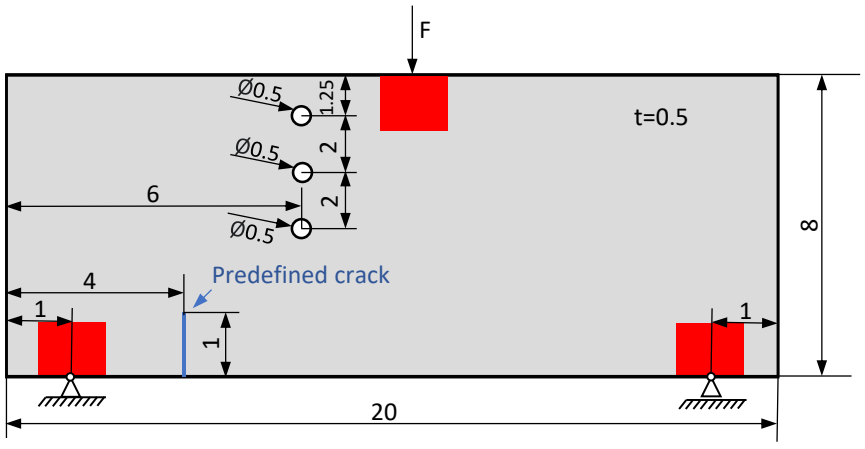

Figure 1. *Example of asymmetrically notched perforated three-point bending test specimen from [23]. All dimensions are in millimeters (mm).*

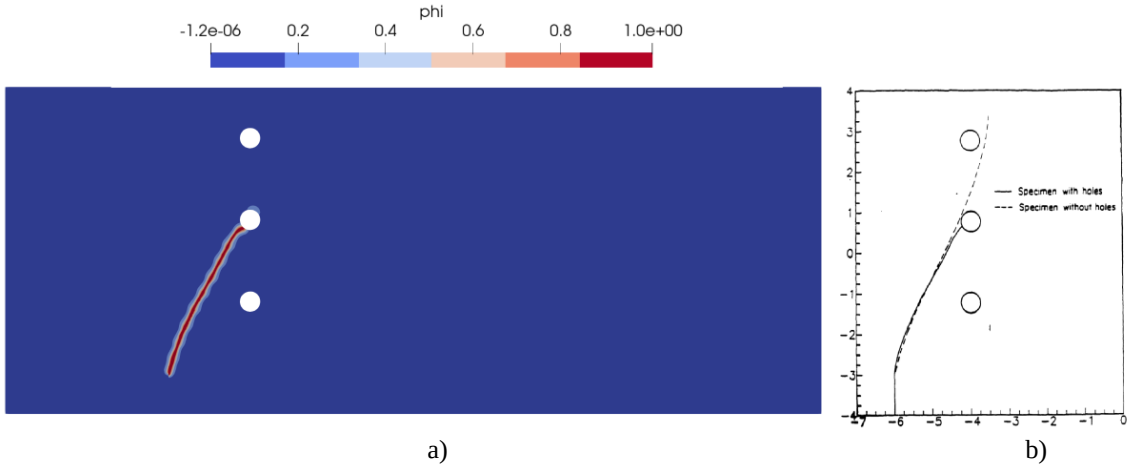

a) b)

Figure 2. *Calculated phase-field a) and experimental results b) from [23].*

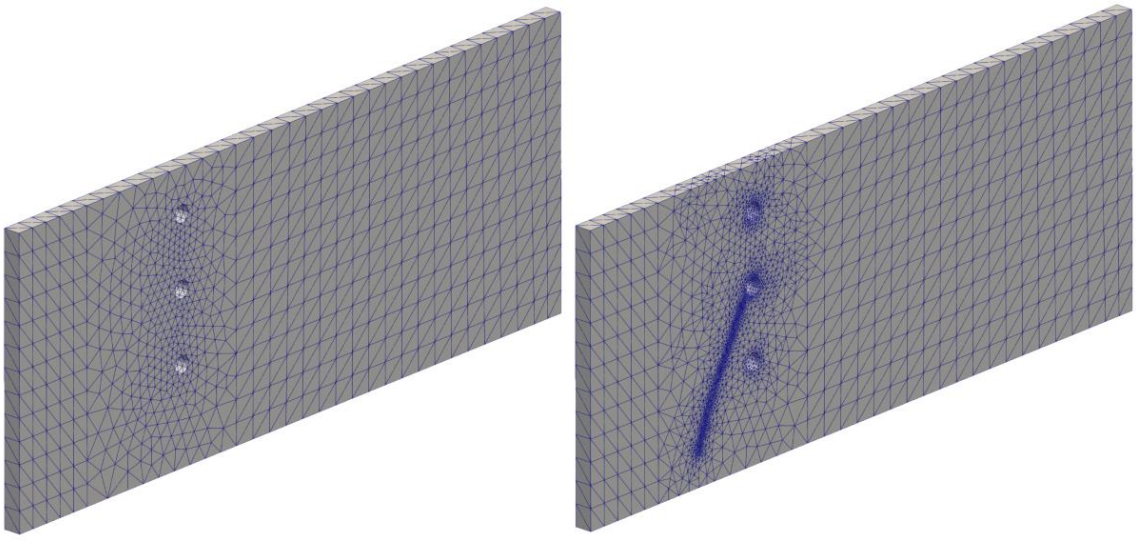

a) b)

Figure 3. *Starting mesh a), and final adapted mesh b)*

4. MODAL ANALYSIS OF THE ADAPTIVE PHASE-FIELD MODEL

4.1 Extension to dynamical problem

To extend our model to the dynamic setting, one can use the Hamiltonian principle, which states that that the following stationary condition (minimum condition) must be satisfied:

$$\delta H = \int_{t_1}^{t_2} (\delta E_k - \delta \Psi) \mathrm{d}\tau = 0 \tag{30}$$

where Ψ is the total energy as defined in eq. (1), and E_k is the total kinetic energy, defined as

$$E_k = \int_\Omega \left(\frac{1}{2} \rho \dot{\boldsymbol{u}}^2 \right) dV. \tag{31}$$

Inserting (31) into (30), recalling the definition of the total potential energy and applying the concept of the history variable, after some mathematical manipulation we can arrive to the system of governing equations consisting of Eqs. (21)-(22), defining the phase field distribution, and the equation of motion,

$$\nabla \cdot \boldsymbol{\sigma} = -\mathbf{b} + \rho \ddot{\boldsymbol{u}}. \tag{32}$$

In the existing works that deal with the modal analysis of the P-F fracture models, like [11, 12], only simple hypothetical assumed cracks are analyzed, whose geometry has been modeled by applying some standard technique for modelling the pre-existing cracks, like imposing the essential BCs on the phase field [12], or by assigning appropriate history field distribution [11]. Either way, the phase field evolution equation (here Eq. (23)) is solved first to obtain the phase field distribution, which is then inserted into the weak form of Eq. (32). In contrast to those works, we analyze the model with the crack predicted by the previously performed P-F fracture analysis and therefore, the geometry of the crack, approximated by the resulting phase field distribution, is readily available for the modal analysis.

To derive mechanical balance equations for the discretised dynamic system, one can assume the phase-field to be constant and define the stationary condition for the Hamiltonian principle by variating Eq. (30) only with respect to displacements and velocities around the state with a known phase field distribution to obtain:

$$(\delta H)|_{\boldsymbol{\phi}} = \int_{t_1}^{t_2} \left((\delta E_k)|_{\boldsymbol{\phi}} - (\delta \Psi)|_{\boldsymbol{\phi}} \right) \mathrm{d}\tau = 0. \tag{33}$$

Here, $\left(\delta(\,)\right)\big|_{\boldsymbol{\phi}}$ denotes variation around a state with a known, "frozen" phase field. Since we assume that $E_k = E_k(\dot{u})$, it can be written that

$$\delta E_k = \frac{\partial E_k}{\partial \dot{\boldsymbol{u}}} \delta \dot{\boldsymbol{u}} = \frac{\partial E_k}{\partial \dot{\boldsymbol{u}}} \frac{d}{dt}(\delta u) = \frac{d}{dt}\left(\frac{\partial E_k}{\partial \dot{\boldsymbol{u}}} \delta \boldsymbol{u} \right) - \frac{d}{dt}\left(\frac{\partial E_k}{\partial \dot{\boldsymbol{u}}} \right) \delta \boldsymbol{u}. \tag{34}$$

Then, after plugging Eq. (34) into (33), recalling that according to the Hamiltonian principle $\delta \boldsymbol{u}(t_1) = \delta \boldsymbol{u}(t_2) = 0$, assuming that the external forces acting on the system are zero (for free vibrations) (i.e., *P*=0 in Eq. (1)), and keeping in mind that $\Psi_f = \Psi_f(\boldsymbol{\phi})$, after variation one arrives at

$$(\delta H)|_{\boldsymbol{\phi}} = \int_{t_1}^{t_2} \left(-\frac{d}{dt}\left(\frac{\partial E_k}{\partial \dot{\boldsymbol{u}}}\right) \delta \boldsymbol{u} - \frac{\partial \Psi_e}{\partial \boldsymbol{\varepsilon}} \delta \boldsymbol{\varepsilon} \right) \mathrm{d}\tau = 0. \tag{35}$$

Recalling the definition of strain energy, stress and discretized strains in Eqs. (1), (13) and (24), respectively, the second term of the right-hand side of Eq. (35) can be written as

$$(\delta\Psi)|_{\boldsymbol{\phi}} = (\delta\Psi_e)|_{\boldsymbol{\phi}} = \int_\Omega \delta \mathbf{v}^{\boldsymbol{T}} \mathbf{B}^{\mathbf{T}} (\boldsymbol{\sigma})|_{\boldsymbol{\phi}} \mathrm{d}V = \int_\Omega \delta \mathbf{v}^{\boldsymbol{T}} \mathbf{B}^{\mathbf{T}} \left(\frac{\partial \boldsymbol{\sigma}}{\partial \boldsymbol{\epsilon}}\right)\Big|_{\boldsymbol{\phi}} \mathbf{B}\mathbf{v} \mathrm{d}V = \delta \mathbf{v}^{\boldsymbol{T}} \mathbf{K}_{\boldsymbol{uu}} \mathbf{v}. \tag{36}$$

After approximating displacements by Eq. (23), and considering that $\mathbf{u}(\mathbf{x}, \mathbf{t}) = \mathbf{N}_{\mathrm{u}}(\mathbf{x})\mathbf{v}(\mathbf{t})$, one can write:

$$E_k(\dot{\mathbf{v}}) = \int_\Omega \frac{1}{2} \dot{\mathbf{v}}^{\mathrm{T}} {\mathbf{N}_{\mathrm{u}}}^{\mathrm{T}} \rho \mathbf{N}_{\mathrm{u}} \dot{\mathbf{v}} \, \mathrm{d}V = \frac{1}{2} \dot{\mathbf{v}}^{\mathrm{T}} \mathbf{M} \dot{\mathbf{v}}, \;\; \mathbf{M} = \int_\Omega {\mathbf{N}_{\mathrm{u}}}^{\mathrm{T}} \rho \mathbf{N}_{\mathrm{u}} \, \mathrm{d}V, \tag{37}$$

where **M** is the mass matrix. Then, inserting Eqs. (36) and (37) into Eq. (35), one obtains:

$$\mathbf{M}\ddot{\mathbf{v}} + \mathbf{K}_{\mathbf{uu}}\mathbf{v} = \mathbf{0}. \tag{38}$$

If the solution of Eq. (40) is assumed as $\mathbf{v} = \sum_{\mathbf{i=1}}^{\mathbf{N}} \mathbf{v}_{\boldsymbol{n,i}} \mathrm{e}^{\mathrm{i}\omega_{\mathrm{i}}\mathrm{t}}$, then the first *N* natural frequencies ω_i are vibration mode shapes $\mathbf{u}_{\mathrm{n,i}}$ are obtained by solving the eigenvalue following problem:

$$\left(-\omega_i^2 \mathbf{M} + \mathbf{K}_{\mathbf{uu}}\right)\mathbf{v}_{\mathrm{n,i}} = 0, \mathrm{i} = 1,2, \ldots, \mathrm{N}. \tag{39}$$

4.2 Modifications of dynamic problem

In this work the following modifications are considered to improve dynamical properties of the model:

- Degradation of kinematic energy, leading to:

$$\mathbf{M} = \int_\Omega \mathbf{N}^{\mathrm{T}} \rho \mathbf{N} g_m \, \mathrm{d}V, \quad g_m = (1-\phi)^p \, . \tag{40}$$

  with g_m as the "mass" degradation function. Since this method can be interpreted as a mass reduction, it is expected that it will lead to higher natural frequencies than the original model.

- Modified degradation functions with threshold. Here, we consider the following modifications:

$$g_m = \begin{cases} (1-\phi)^p \text{ for } \phi \leq \phi_{\mathrm{thres}} \\ 0 \text{ for } \phi > \phi_{\mathrm{thres}} \end{cases}, \quad g = \begin{cases} (1-k)(1-\phi)^2 + \mathrm{k} \text{ for } \phi \leq \phi_{\mathrm{thres}} \\ \mathrm{k} \text{ for } \phi > \phi_{\mathrm{thres}} \end{cases}. \tag{41}$$

  Goal of this modification is to remove residual strength/ stiffness of elements that are highly damaged, but not fully damaged.

- Element deletion. This technique deletes an element if the maximal nodal value of the phase-field at its nodes is greater than 0.9. This method is somewhat similar to the so called "mesh-induced" technique for describing the crack geometry, used here to obtain referent values for our analysis.

4.3 Modal analysis of the damaged specimen

We consider the plate shown in Fig 4. The plate is modelled as a three-dimensional body. The material parameters are the Young's modulus $E = 200000\text{MPa}$, the Poisson's coefficient $v = 0.3$, the critical energy release rate $\mathrm{G_c} = 2.7\,\frac{\mathrm{mJ}}{\mathrm{mm^2}}$, length scale parameter $l = 2\mathrm{mm}$ (unless specified otherwise in the text) and density $\rho_0 = 7850 \cdot 10^{-12}\,\frac{\mathrm{t}}{\mathrm{mm^3}}$. At the beginning, a small initial crack exists at the lower edge of the plate, as illustrated in Fig. 4. It is described by the predefined history field, as in [8]. The crack propagation is predicted by the adaptive phase-field model described in Section 3. For the crack growth simulation, 100 uniform increments have been used. At the end of each increment, a modal analysis is performed. During the modal analyses, the boundary conditions shown in Fig. 4 b) are used, and the isotropic energy degradation, described by Eq. (7), is assumed in all cases.

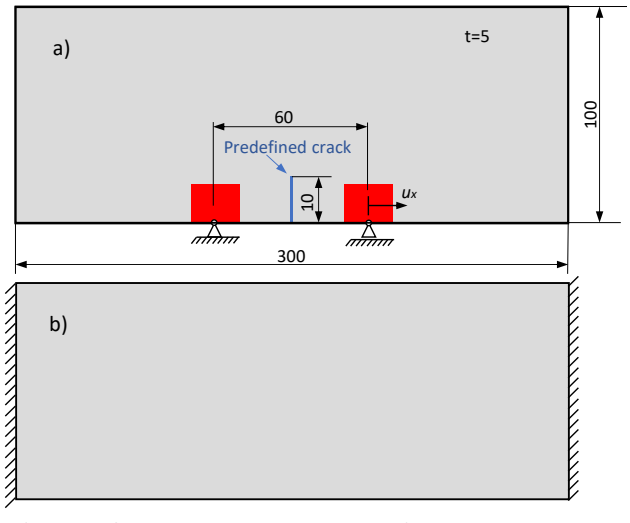

Figure 4. *Studied example: a) model for crack growth analysis. b) boundary conditions for the modal analysis. All dimensions are in millimeters (mm).*

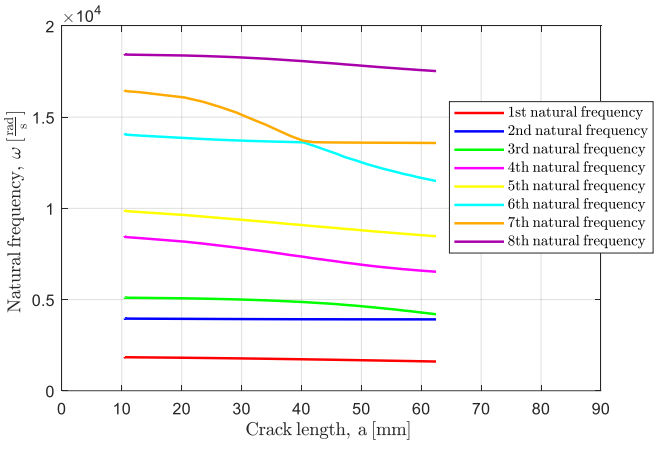

Figure 5. *Calculated natural frequencies for the model with mass degradation, with* $p = 2$

A detailed study of natural frequencies for different numerical models is performed. The convergence of natural frequencies is confirmed by a parametric study, but those results are not shown here. The obtained natural frequencies for the model with the mass degradation are shown in Fig. 5. A comparison of results obtained by different models is shown in Figs. 6 and 7. The obtained vibration modes are shown in Figs. 8 and 9.

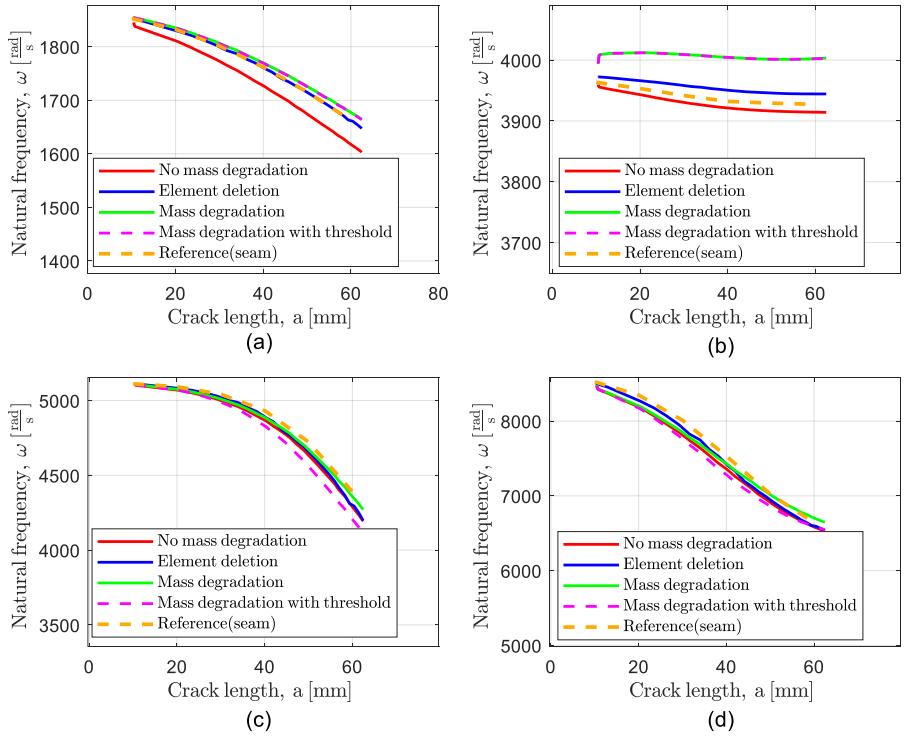

Figure 6. *Calculated natural frequencies for different models for the first four vibration modes. For models with mass degradation,* $p = 2$ *in* g_m*. For models with modified degradation function with threshold,* $\phi_{thresh} = 0.9$

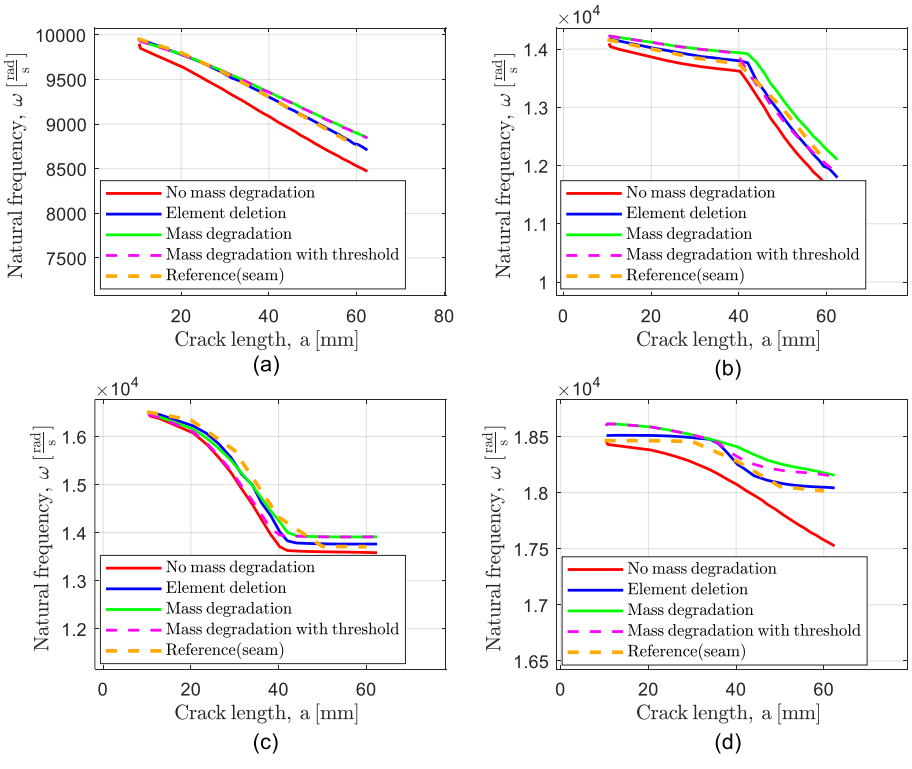

Figure 7. *Calculated natural frequencies for different models for fifth to eighth vibration modes. For models with mass degradation,* $p = 2$ *in* g_m*. For modified degradation function with threshold,* $\phi_{thresh} = 0.9$

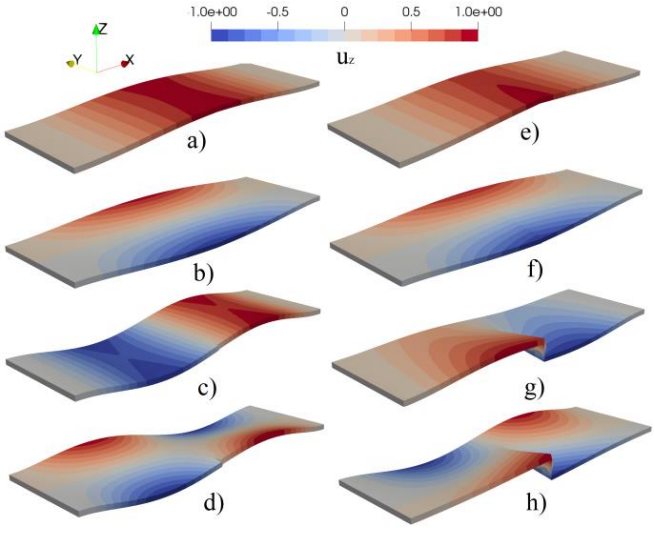

Figure 8. *Vibration mode shapes from 1 to 4 for the model with mass degradation with* $p = 2$*. Left: the crack size* $a = 10$*. Right: the crack size* $a = 60$

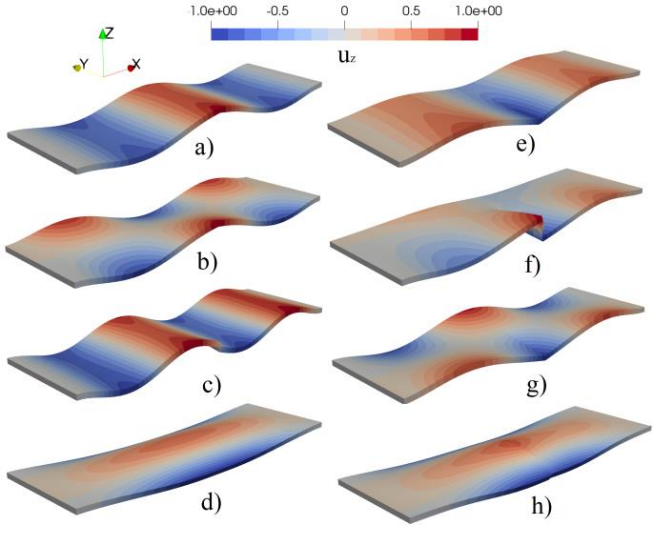

Figure 9. *Vibration mode shapes from 5 to 8 for the model with mass degradation with* $p = 2$*, Left: for crack size* $a = 10$*. Right: crack size* $a = 60$

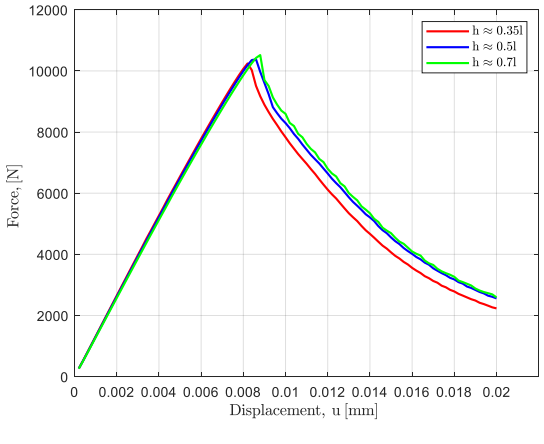

Figure 10. *Force-displacement diagrams for different minimal allowed element's edge sizes*

4.4.1 Mesh influence

The influence of finite element mesh density on calculated natural frequencies is studied. The tetrahedral mesh with three elements along the plate thickness is used at the start of the crack propagation analysis. Meshes used for the modal analyses are the result of adaptive remeshing in the P-F crack growth analyses, which were performed by defining different minimal allowed element edge size. It is to be expected that in each case a mesh would be adapted to a minimal allowed mesh resolution, i.e., to the minimal prescribed element size, around the propagating crack surface. From Fig. 10 we can observe that the force-displacement response is sensitive to the mesh density, until sufficiently fine mesh is used around the crack. However, the influence of mesh on natural frequencies is not that apparent, see Figs. 11 and 12. Therefore, one can conclude that in the P-F models modal parameters are much less sensitive to mesh density than the crack evolution.

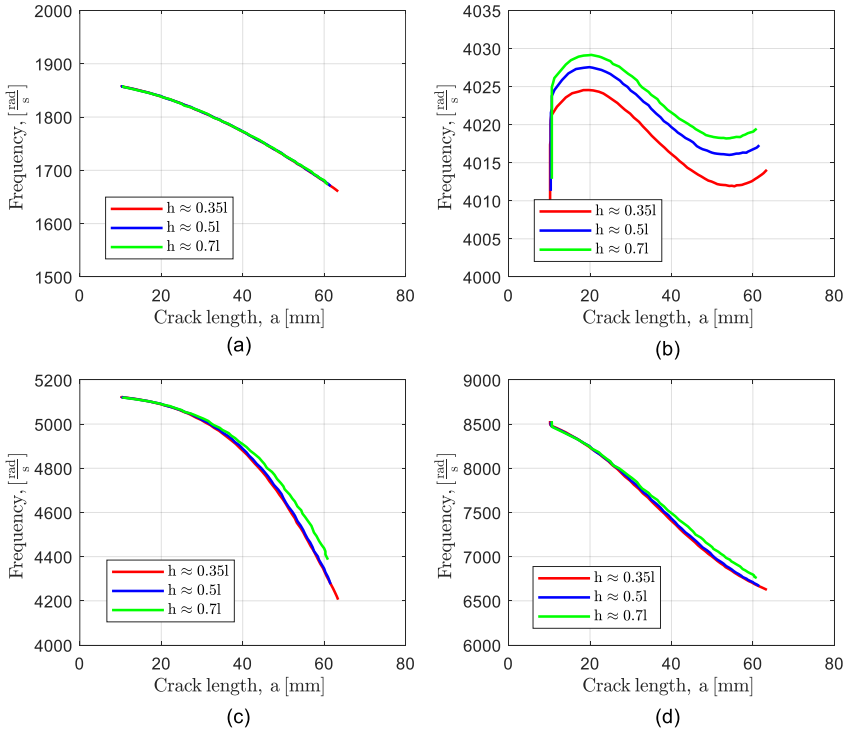

Figure 11. *Natural frequencies for different meshes, for model with mass degradation with $p = 2$. Figures a)-d) show natural frequencies 1-4, respectively.*

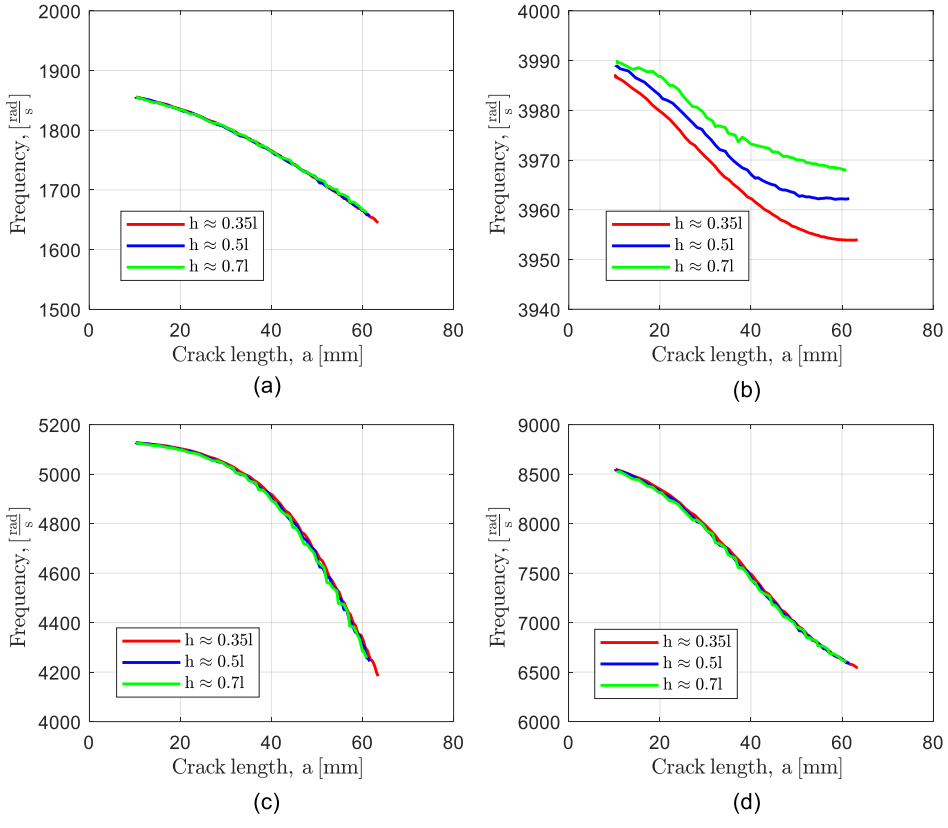

Figure 12. *Natural frequencies for different meshes, for model with element deletion. Figures a)-d) show natural frequencies 1-4, respectively*.

4.4.2 Mass degradation influence

In this subsection, the influence of mass degradation is investigated. Since P-F models lead to a local loss of stiffness, the absence of mass degradation will lead to lower natural frequencies than in the undamaged model, which can be clearly observed in Fig. 13. This effect seems to be higher if vibration modes tend to exhibit pronounced displacements, i.e., accelerations, in the zones with high phase-field values. For example, for the modes 1 and 5 the displacement fields exhibit peaks in the region around the crack (see Fig. 8) and the obtained natural frequencies are highly dependent on mass degradation at all crack lengths, see Fig. 13. In such cases the obtained values might depend more significantly on the mass degradation function. In free vibrations, changing the mass of material points that exhibit small displacements will not influence the vibration response significantly. Hence, the third mode's natural frequency at small crack lengths (see Fig. 8 left, for crack length of $a = 10mm$) is not sensitive to mass degradation parameters. This observation can also be explained by considering

$$\delta\lambda_{\mathrm{i}} = \mathbf{v}_{\mathbf{i}}^{T}(\delta\mathbf{K} - \lambda\delta\mathbf{M})\mathbf{v}_{\boldsymbol{i}}, \tag{42}$$

with $\lambda_{\mathrm{i}} = \omega_i^2$ which can be derived by the differentiation of $-\lambda_{\mathrm{i}}\mathbf{M}\mathbf{v}_i + \mathbf{K}\mathbf{v}_i = 0$, and which defines the sensitivity of eigenvalues (natural frequencies) with respect to the stiffness and mass matrix. Choosing the optimal mass degradation function might be difficult, as it seems that the effect of mass degradation is dependent on the vibration shape.

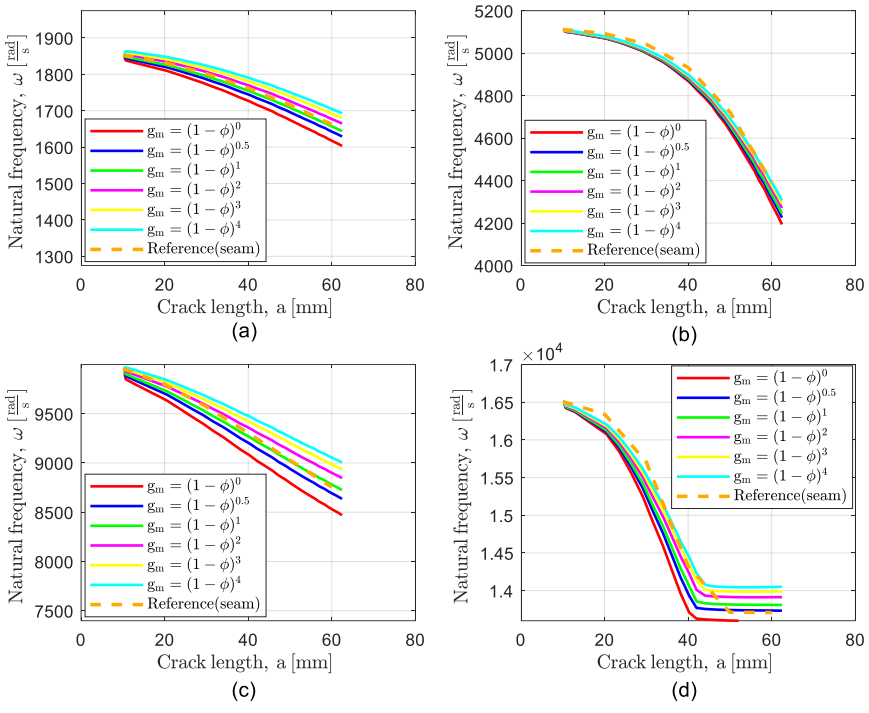

Figure 13. *Natural frequencies for model with mass degradation, for different mass degradation functions. a), b), c) and d) show 1st, 3rd, 5th and 7th natural frequency, respectively.*

4.4.3 Modified model with threshold influence

During crack growth, phase field values will sometimes exhibit values that are only a bit smaller than one. That means that some elements that are practically fully damaged will still possess some small residual strength that can influence overall response. As a result, some small stress is transmitted through the crack, and the overall stiffness of the specimen model could be higher than expected. To reduce the possibility of such an event, we introduced a modification defined by Eq. (42). The results obtained by such models are shown in Fig. 14. It can be observed that in some modes the introduction of such modification has a small influence with respect to the ordinary model ($\phi_{thres} = 1$). Exceptions are the third mode and the seventh mode (note that for large cracks the seventh mode becomes the sixth one), because in those modes the displacement fields normal to the plate plane possess large jumps in the crack zone (see Figs. 8 and 9). Hence, for the third and seventh modes the introduction of threshold modifications leads to more pronounced change in natural frequencies.

4.4.4 Length scale influence

In this section, the influence of length scale parameter value on modal response is studied. The phase-field with the infinitesimally small width of band, $l \to 0$, approximates well a crack geometry. We considered three different values of length scale, all relatively small in comparison to the model dimensions. From Fig. 15, one can see that a smaller length scale leads to natural frequencies that are closer to the referent results, as expected, and it seems that a monotonical convergence to the referent values has been achieved. It should be noted that in some P-F models the length-scale parameter is also used to calibrate material response, and therefore, it will not always be possible to choose a small enough value of length to capture well the dynamic response of the model. In that case, more radical steps should be taken, such as the element cutting techniques (see, [24]).

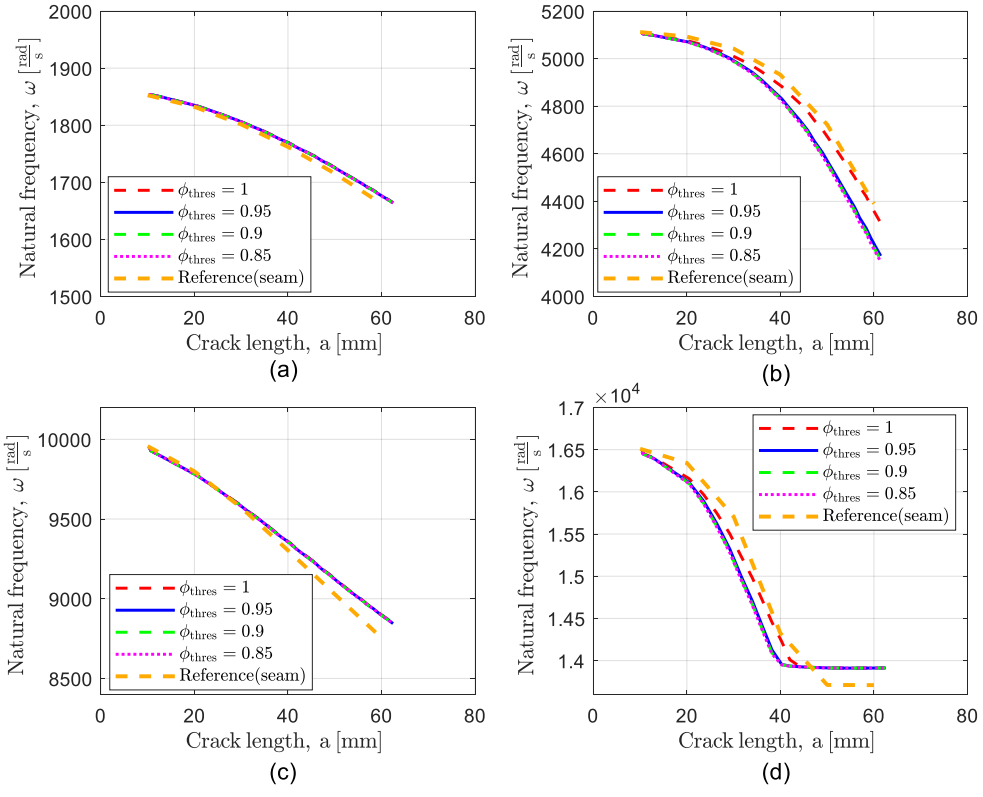

Figure 14. *Natural frequencies for model with modified degradation functions with threshold, with different values of ϕ_{thres}. a), b), c) and d) show 1st, 3rd, 5th and 7th natural frequency, respectively.*

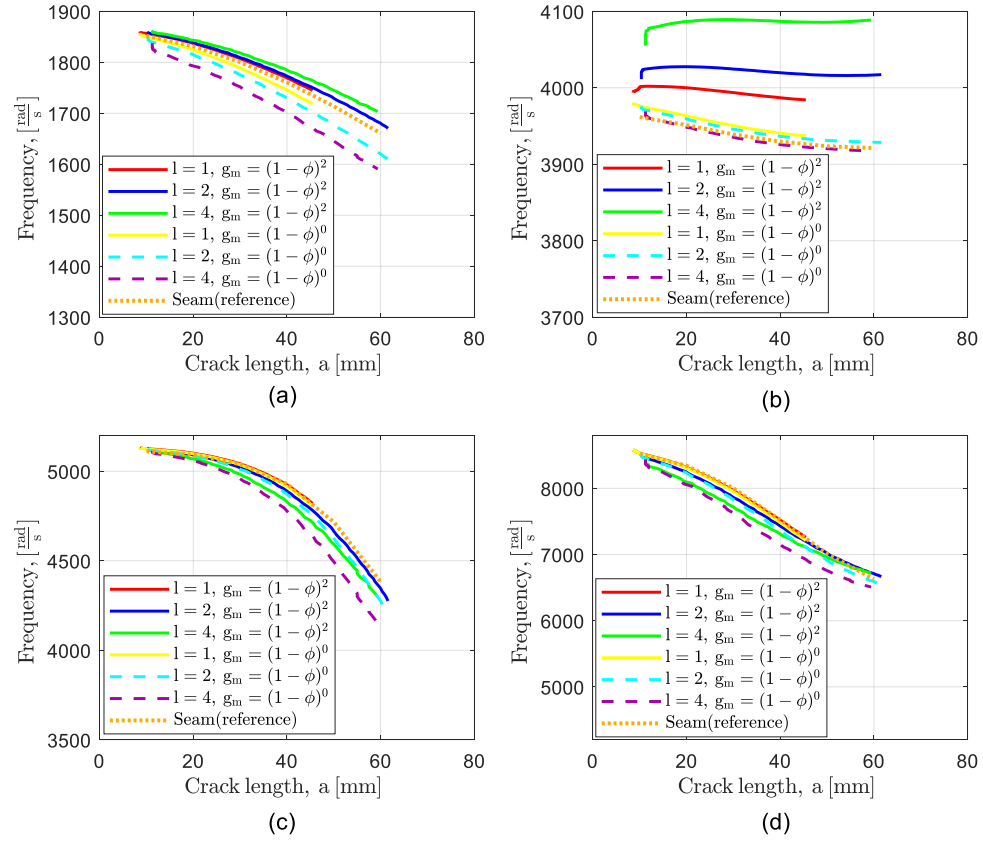

Figure 15. *Natural frequencies for different length scales (length scale is given in mm), for mass degradation models with p=0 and p=2. Figures a)-d) show natural frequencies 1-4, respectively.*

5. CONCLUSION

In this work, the modal response of the phase field model of damaged structures is studied. The influence of various aspects of the phase-field fracture models, such as mesh density, length scale parameter value, and degradation functions, on natural frequencies has been investigated. In contrast to similar papers that can be found in the literature, here the crack geometry has been predicted by applying an adaptive anisotropic phase field model prior to the modal analysis. To facilitate or improve the modal analysis, few modifications of the original P-F fracture model have been considered, such as changing the stiffness degradation functions, or introducing the mass degradation and element deletion in the modal analysis. From the results, the following can be concluded:

- The influence of mesh size around crack on natural frequencies is small, and mesh with $h = 0.5l$, with h as the minimal allowed element edge size, is sufficient. Since the second order tetrahedron element is used, this conclusion is limited to this type of finite elements.
- For most vibration modes, the reduction of length scale parameter value might lead to the exact values, under the condition that the crack pattern is well captured.
- Natural frequencies are in general sensitive to mass degradation. This sensitivity might be dependent on displacements intensity in the damaged region, expected in a vibration mode.
- The application of the modified degradation functions with a threshold can reduce the negative effect of residual strength of almost fully damaged elements on the modal response of the model. For modes that do exhibit large relative displacements between free crack surfaces, this modification can have a considerable effect.

It is to note that a more thorough research on the considered subject, encompassing various relevant verification problems, as well as a relevant experimental validation, is needed.

ACKNOWLEDGEMENTS

This work has been supported and co-funded by the European Union through the European Regional Development Fund, Operational Programme “Competitiveness and Cohesion” 2014 – 2020 of the Republic of Croatia, project “Protection of Structural Integrity in Energy and Transport” (Zacjel, KK.01.1.1.04.0056).

REFERENCES

[1] Griffith, A. A., & Taylor, G. I. (1921). VI. The phenomena of rupture and flow in solids. *Philosophical Transactions of the Royal Society of London. Series A, Containing Papers of a Mathematical or Physical Character*, *221*(582-593), 163-198.

[2] Francfort, G. A., & Marigo, J. J. (1998). Revisiting brittle fracture as an energy minimization problem. *Journal of the Mechanics and Physics of Solids*, *46*(8), 1319-1342.

[3] Pham, K. H., Ravi-Chandar, K., & Landis, C. M. (2017). Experimental validation of a phase-field model for fracture [Article]. *International Journal of Fracture*, *205*(1), 83-101.

[4] Wu, T., Carpiuc-Prisacari, A., Poncelet, M., & De Lorenzis, L. (2017). Phase-field simulation of interactive mixed-mode fracture tests on cement mortar with full-field displacement boundary conditions. *Engineering Fracture Mechanics*, *182*, 658-688.

[5] Ambati, M., Kruse, R., & De Lorenzis, L. (2016). A phase-field model for ductile fracture at finite strains and its experimental verification. *Computational Mechanics*, *57*(1), 149-167.

[6] Bleyer, J., Roux-Langlois, C., & Molinari, J.-F. (2017). Dynamic crack propagation with a variational phase-field model: limiting speed, crack branching and velocity-toughening mechanisms. *International Journal of Fracture*, *204*, 1-22.

[7] Carrara, P., Ambati, M., Alessi, R., & De Lorenzis, L. (2020). A framework to model the fatigue behavior of brittle materials based on a variational phase-field approach. *Computer Methods in Applied Mechanics and Engineering*, *361*, 112731.

[8] Borden, M. J., Verhoosel, C. V., Scott, M. A., Hughes, T. J. R., & Landis, C. M. (2012). A phase-field description of dynamic brittle fracture. *Computer Methods in Applied Mechanics and Engineering*, *217-220*, 77-95.

[9] Nguyen, V. P., & Wu, J.-Y. (2018). Modeling dynamic fracture of solids with a phase-field regularized cohesive zone model. *Computer Methods in Applied Mechanics and Engineering*, *340*, 1000-1022.

[10] Chen, C.-H., Bouchbinder, E., & Karma, A. (2017). Instability in dynamic fracture and the failure of the classical theory of cracks. *Nature Physics*, *13*(12), 1186-1190.

[11] Doan, D. H., Van Do, T., Pham, P. M., & Duc, N. D. (2019). Validation simulation for free vibration and buckling of cracked Mindlin plates using phase-field method. *Mechanics of Advanced Materials and Structures*, *26*(12), 1018-1027.

[12] Torabi, J., & Ansari, R. (2020). Numerical phase-field vibration analysis of cracked functionally graded GPL-RC plates. *Mechanics Based Design of Structures and Machines*, 1-20.

[13] Bourdin, B., Francfort, G. A., & Marigo, J. J. (2000). Numerical experiments in revisited brittle fracture. *Journal of the Mechanics and Physics of Solids*, *48*(4), 797-826.

[14] Pham, K., Amor, H., Marigo, J.-J., & Maurini, C. (2010). Gradient Damage Models and Their Use to Approximate Brittle Fracture. *International Journal of Damage Mechanics*, *20*(4), 618-652.

[15] Wu, J.-Y. (2017). A unified phase-field theory for the mechanics of damage and quasi-brittle failure. *Journal of the Mechanics and Physics of Solids*, *103*, 72-99.

[16] Wu, J.-Y., Nguyen, V. P., Nguyen, C. T., Sutula, D., Sinaie, S., & Bordas, S. P. A. (2020). Phase-field modeling of fracture. In *Advances in Applied Mechanics* (Vol. 53, pp. 1-183). Elsevier.

[17] Miehe, C., Welschinger, F., & Hofacker, M. (2010). Thermodynamically consistent phase-field models of fracture: Variational principles and multi-field FE implementations [Article]. *International Journal for Numerical Methods in Engineering*, *83*(10), 1273-1311.

[18] Amor, H., Marigo, J. J., & Maurini, C. (2009). Regularized formulation of the variational brittle fracture with unilateral contact: Numerical experiments [Article]. *Journal of the Mechanics and Physics of Solids*, *57*(8), 1209-1229.

[19] Lo, Y.-S., Borden, M. J., Ravi-Chandar, K., & Landis, C. M. (2019). A phase-field model for fatigue crack growth. *Journal of the Mechanics and Physics of Solids*, *132*, 103684.

[20] Miehe, C., Hofacker, M., & Welschinger, F. (2010). A phase field model for rate-independent crack propagation: Robust algorithmic implementation based on operator splits [Article]. *Computer Methods in Applied Mechanics and Engineering*, *199*(45-48), 2765-2778.

[21] De Lorenzis, L., & Gerasimov, T. (2020). Numerical Implementation of Phase-Field Models of Brittle Fracture. In *Modeling in Engineering Using Innovative Numerical Methods for Solids and Fluids* (pp. 75-101). Springer International Publishing.

[22] Seles, K., Lesicar, T., Tonkovic, Z., & Soric, J. (2019). A residual control staggered solution scheme for the phase-field modeling of brittle fracture. *Engineering Fracture Mechanics*, *205*, 370-386.

[23] Ingraffea, A., & Grigoriu, M. (1990). Probabilistic Fracture Mechanics: A Validation of Predictive Capability. 155.

[24] Hussein, A., Hudobivnik, B., & Wriggers, P. (2020). A combined adaptive phase field and discrete cutting method for the prediction of crack paths. *Computer Methods in Applied Mechanics and Engineering*, *372*, Article 113329.

ON THE NATURAL BOUNDARY CONDITIONS IN THE MIXED COLLOCATION METHODS FOR ELASTICITY PROBLEMS

Jalušić, Boris[1]; Jarak, Tomislav[1,2]

ABSTRACT

The mixed Meshless Local Petrov-Galerkin (MLPG) collocation method is applied for solving problems in gradient elasticity. The mixed collocation approach is utilized to lower the continuity requirements of the approximation functions in the numerical model and improve its numerical efficiency. The method utilizes a staggered solution procedure, where the original gradient elasticity problem is solved by solving two successive sub-problems governed by the second-order differential equations. Furthermore, two different staggered procedures are applied. Thereby, the solution of the first (classical) sub-problem is used as the input for the second (gradient) subproblem. Special attention is dedicated to the utilization of appropriate natural boundary conditions in the gradient subproblem. The proposed procedures are tested by the problem of a rectangular plate with a crack, where obtained numerical results are compared to available analytical solutions.

Keywords: mixed collocation methods, gradient elasticity, staggered approach, natural boundary conditions.

1. INTRODUCTION

In recent time, the increase of computing power has enabled solving complex problems in solid mechanics, as well as the application of new numerical methods such as meshless methods. One of more challenging problems is modelling problems where the material microstructure plays an important role in the deformation response of the material/structure at the macrolevel. In such cases, a preferred solution strategy is often the use of gradient methods. These theories can be described as the enhancements of classical theories, which consider the material microstructure through the higher-order spatial gradients of state variables and accompanying material parameters, called length scale parameters. It has been noted that using the meshless methods to develop numerical method for gradient elasticity could have a significant advantage due to some beneficial properties of these methods.

An overview of gradient elasticity theories, numerical formulations and the Finite Element Method (FEM) implementations are presented in [1]. The application of FEM in solving of the problems of the gradient elasticity leads to complex numerical formulations, involving complicated high-order shape

[1] *Faculty of Mechanical Engineering and Naval Architecture. University of Zagreb (CROATIA). boris.jalusic@fsb.hr (corresponding author), tomislav.jarak@fsb.hr (corresponding author)*
[2] *ITAP, School of Industrial Engineering, University of Valladolid (SPAIN). tomislav.jarak@uva.es (corresponding author)*

functions [2] or mixed approaches [3] where the satisfaction of so called LBB conditions that ensure numerical stability is far from trivial.

In contrast to FEM, in the meshless methods shape functions of an arbitrary continuity order can be derived straightforwardly, simply by adding nodes within the approximation domain, without increasing the global number of degrees of freedom. In the meshless methods nodes are not connected into elements. Thus, the approximation of unknown field variables is done without having to use pre-defined meshes consisting of adjacent elements. In addition, no mesh creation process is needed so that the user and computational burden might be lowered, especially when compared to the complicated well-defined meshes used in mesh-based methods. Furthermore, since there are no elements, the problems associated with element distortion during computations are avoided. On the other hand, meshless methods inherently have some serious drawbacks. They are plagued by high numerical costs associated with the calculation of approximation functions and their derivatives, as well as by costly and inaccurate numerical integration. Furthermore, overall accuracy can further be compromised by high errors associated with the high-order derivatives of approximation functions. This is especially visible in the solutions of gradient elasticity problems by the displacement-based (primal) methods, which are governed by high-order partial differential equations.

Some of the above-mentioned drawbacks of meshless methods are here alleviated using the collocation method [4], which does not require numerical integration, and the application of the mixed meshless paradigm [5]. The mixed approach requires more computational power for assembling the global stiffness matrix, but it lowers a necessary continuity degree of the approximation functions, i.e., lowers a derivative order in the model. In this contribution, two different collocation methods for gradient elasticity are proposed. Both are based on the mixed collocation MLPG concept [4, 5] and are of the Helmholtz type [6], where only one unknown constitutive parameter representing the material microstructure is used. Strain- (EB) and stress-based (SB) staggered procedures are applied, in which the original fourth-order equilibrium equations of gradient elasticity are solved as the uncoupled sequences of two sets of low-order differential equations [7]. The approximation of all unknown field variables is done using the interpolatory Moving Least Squares (IMLS) function [8]. Hence, the essential boundary conditions (EBCs) are imposed using a simple approach as in classical FEM. On the other hand, the natural boundary conditions (NBCs) are enforced using the direct collocation method at the discretization nodes. As numerical integration is avoided altogether, the system of discretized equations is obtained faster and in less complex manner. Due to the mixed methodology only the first derivatives of the meshless approximants are needed to assemble the discretized system of equations. In each staggered procedure, different appropriate NBCs must be applied. Thus, the focus here is the investigation of the influence of the enforced gradient NBCs on the problem solution. Hence, different sets of gradient NBCs are utilized in the EB and SB staggered procedures and the results are compared. The obtained results are presented on a representative numerical example of a rectangular plate with a crack. Furthermore, the ability of the developed methods to remove stress/strain singularities (discontinuities) around the crack tip is also tested, and results are compared with solutions from the literature [9].

The paper is organized as follows: Section 2 is related to the overview of the governing equations for the solution procedures being considered. The discretized equations of the applied mixed collocation

methods are presented in Section 3. The numerical example of a rectangular plate with a crack in gradient elasticity is analyzed in Section 4. In the last section, concluding remarks on the obtained results are given.

2. GOVERNING EQUATIONS

The gradient elasticity theory used here is a simple form that employs only one internal length parameter [10]. It can be classified as a Helmholtz-type theory since the Helmholtz operators of the state variables are utilized for describing nonlocal effects. The staggered solution procedure is applied based on the approach in [11]. Hence, the original fourth-order equilibrium equation is written as two second-order differential equations. Detailed description on the staggered procedure can be found in [12]. Two different staggered procedures are considered, based on strains and stresses, and utilized for the development of corresponding mixed colocation meshless methods. The governing equations and BCs that must be satisfied for each formulation are presented in Table 1.

Table 1. Governing equations and boundary conditions for staggered procedures

Classical problem (CP)

$\sigma^{\mathrm{c}}_{ji,j} + b_i = 0$	(1)
$\sigma^{\mathrm{c}}_{ij} = C_{ijkl}\varepsilon^{\mathrm{c}}_{kl}$	(2)
$\varepsilon^{\mathrm{c}}_{ij} = \frac{1}{2}\left(u^{\mathrm{c}}_{j,i} + u^{\mathrm{c}}_{i,j}\right)$	(3)
$u^{\mathrm{c}}_i = \bar{u}^{\mathrm{c}}_i \text{ on } \Gamma^{\mathrm{c}}_u$	(4)
$t^{\mathrm{c}}_i = \sigma^{\mathrm{c}}_{ji} n^{\mathrm{c}}_j = \bar{t}^{\mathrm{c}}_i \text{ on } \Gamma^{\mathrm{c}}_t$	(5)

Gradient problem (GP)

Strain-based procedure (EB)		**Stress-based procedure (SB)**	
$\varepsilon^{\mathrm{g}}_{ij} - l^2\varepsilon^{\mathrm{g}}_{ij,mm} = \varepsilon^{\mathrm{c}}_{ij}$	(6)	$\sigma^{\mathrm{g}}_{ij} - l^2\sigma^{\mathrm{g}}_{ij,mm} = \sigma^{\mathrm{c}}_{ij}$	(7)
$\varepsilon^{\mathrm{g}}_{ij} = \bar{\varepsilon}^{\mathrm{g}}_{ij} \text{ on } \Gamma^{\mathrm{g}}_P$	(8)	$\sigma^{\mathrm{g}}_{ij} = \bar{\sigma}^{\mathrm{g}}_{ij} \text{ on } \Gamma^{\mathrm{g}}_P$	(9)
$R^{\mathrm{g}}_{ij} = \frac{\partial \varepsilon^{\mathrm{g}}_{ij}}{\partial n^{\mathrm{g}}} = \bar{R}^{\mathrm{g}}_{ij} \text{ on } \Gamma^{\mathrm{g}}_R$	(10)	$R^{\mathrm{g}}_{ij} = \frac{\partial \sigma^{\mathrm{g}}_{ij}}{\partial n^{\mathrm{g}}} = \bar{R}^{\mathrm{g}}_{ij} \text{ on } \Gamma^{\mathrm{g}}_R$	(11)

As evident from Table 1. the solution of the gradient elasticity consists now of two separate problems, denoted here as CP and GP. Therein, CP is solved in terms of displacements using Eqs. (1) - (5), and represents the classical elasticity problem. GP can be solved either in terms of strains utilizing Eqs. (6), (8) and (10), or in terms of stresses applying Eqs. (7), (9) and (11). In the subsequent text, the upper superscript c and g denote CP or GP, respectively. It has to be stated here that the compatibility

between u_i^{c} and $\varepsilon_{ij}^{\mathrm{c}}$ given by Eq. (3) is assumed also in the EB formulation for the nonlocal displacements u_i^{g} and strains $\varepsilon_{ij}^{\mathrm{g}}$. Furthermore, the independent variables of the Helmholtz equations, Eqs. (6) and (7), are the nonlocal strains $\varepsilon_{ij}^{\mathrm{g}}$ and the nonlocal stresses σ_{ij}^{g}, and in general it is not possible to obtain the nonlocal displacements u_i^{g} from the kinematic relations once the $\varepsilon_{ij}^{\mathrm{g}}$ and σ_{ij}^{g} are obtained. The solution procedure consists of two parts: 1) CP is solved for classical displacements, and local strains and/or stresses are calculated at all nodes; 2) GP is solved for nonlocal strains (EB) or stresses (SB), using the solutions for local strains and stresses obtained in 1) as the source in the Helmholtz equations. In this contribution, the most common definitions of the gradient NBCs, here denoted as R_{ij}^{g}, are utilized. However, it is to note that for the collocation approach used here, the choice of R_{ij}^{g} could be more or less free [12]. Hence, in the EB formulation the variationally consistent BCs are utilized [12], while in the SB method the gradient EBCs for the nonlocal stress components σ_{ij}^{g} are prescribed on free boundaries [10].

3. MIXED MLPG COLLOCATION METHOD FOR STAGGERED GRADIENT ELASTICITY

A 2-D global domain Ω enveloped by the outer boundary Γ is represented by a set of nodes $\mathsf{S}=\{\mathbf{x}_I, I=1,2,\ldots,N \,|\, \mathbf{x}_I \subseteq \Omega\cup\Gamma\}$ to obtain a discretized system of equations. Therein, the total number of nodes is denoted by N. To speed up the solution process, the same nodal set is utilized in both subproblems of the staggered solution procedures. In the text, the global boundary Γ is denoted by the superscript c or g, respectively, to define what problem is being solved. The 2-D discretized homogeneous structure is presented in Fig. 1.

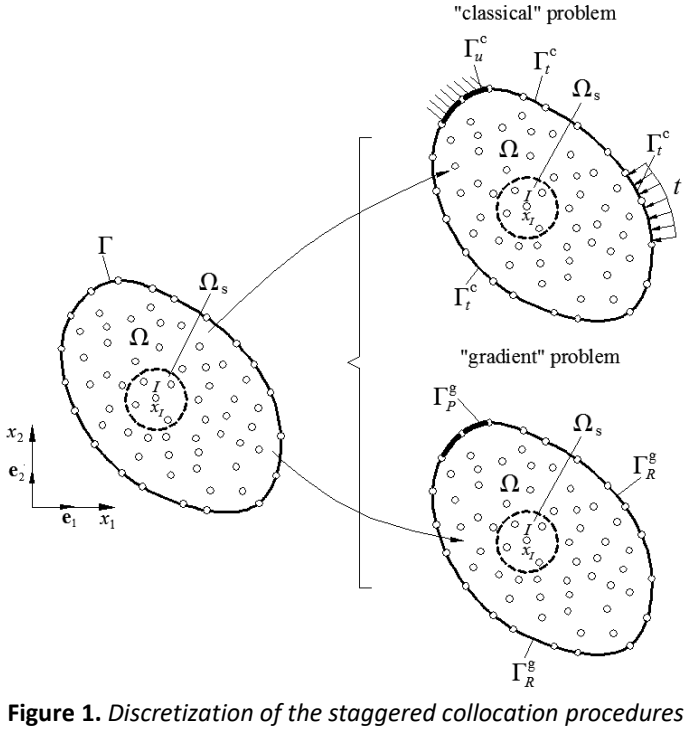

Figure 1. *Discretization of the staggered collocation procedures*

The collocation at the nodes in S may be performed by using the general MLPG paradigm. Therein, the Dirac functions are utilized as the test functions in local weak forms of governing equations [4]. In that way the set of strong-form equations is attained at the global level. The interpolatory MLS scheme is utilized in this work to approximate all unknown system variables [8]. Hence, the domain of influence Ω_s is defined around each node $\mathbf{x}_J \in \mathrm{S}$ and used for the approximation. As evident from Table 1, in both considered staggered procedures, CP is solved in the identical manner. Therefore, firstly the discretized relations for CP are going to be presented. Thereafter, main discretized equations for GP of the EB and SB procedures will be given.

3.1. Interpolary MLS function

The well-known MLS approximation scheme [4] is used for construction of nodal shape functions, and its main relations are given in this subsection. The value of the approximated function at a chosen point $\mathbf{x}$ is defined by multiplying the vector basis functions $\mathbf{p}(\mathbf{x})$ with the vector of unknown coefficients $\mathbf{a}(\mathbf{x})$,

$$f^{(h)}(\mathbf{x}) = \mathbf{p}^{\mathrm{T}}(\mathbf{x})\mathbf{a}(\mathbf{x}). \tag{12}$$

In order to determine the vector of unknown coefficients $\mathbf{a}(\mathbf{x})$, the weighted discrete L_2 error norm J, defined as

$$J(\mathbf{a}(\mathbf{x})) = \sum_{J=1}^{n} W_J(\mathbf{x})\left(\mathbf{p}(\mathbf{x}_J)\mathbf{a}(\mathbf{x}) - \hat{f}_J\right)^2, \tag{13}$$

is minimized. From the stationarity condition of J a set of linear equations is obtained and solved for unknown coefficients

$$\mathbf{a}(\mathbf{x}) = \mathbf{A}^{-1}(\mathbf{x})\mathbf{B}(\mathbf{x})\hat{\mathbf{f}}. \tag{14}$$

The value of the MLS meshless approximation function is now obtained by inserting (14) in (12) and can be written as

$$f^{(h)}(\mathbf{x}) = \sum_{J=1}^{n} \phi_J(\mathbf{x})\hat{f}_J, \tag{15}$$

where the shape function $\phi_J(\mathbf{x})$ is calculated as

$$\phi_J(\mathbf{x}) = \mathbf{p}^{\mathrm{T}}(\mathbf{x})\left[\mathbf{A}^{-1}(\mathbf{x})\mathbf{B}(\mathbf{x})\right]_J. \tag{16}$$

In the expressions (14) and (16), the momentum matrix $\mathbf{A}(\mathbf{x})$ is equal to

$$\mathbf{A}(\mathbf{x}) = \sum_{J=1}^{n} W_J(\mathbf{x})\mathbf{p}(\mathbf{x}_J)\mathbf{p}^{\mathbf{T}}(\mathbf{x}_J), \tag{17}$$

while the matrix $\mathbf{B}(\mathbf{x})$ is defined as

$$\mathbf{B}(\mathbf{x}) = \left[W_1(\mathbf{x})\mathbf{p}(\mathbf{x}_1) \quad W_2(\mathbf{x})\mathbf{p}(\mathbf{x}_2) \quad \cdots \quad W_J(\mathbf{x})\mathbf{p}(\mathbf{x}_J) \quad \cdots \quad W_n(\mathbf{x})\mathbf{p}(\mathbf{x}_n) \right]. \tag{18}$$

In general, the MLS shape functions (16) do not possess Kronecker delta property. Thus, to achieve the interpolatory properties of the approximation, the rationalized weight function $W_J(\mathbf{x})$ from [8] is utilized. The reader is referred to the cited literature for the details on the employed weight function.

3.2. Classical problem (CP)

Detailed description on solving CP can be found in previously published work of the authors on mixed collocation method [7]. Thus, here only the brief overview is given. The classical equilibrium equations may be written in terms of classical strains or displacements by inserting Eqs. (2) and (3) into Eq. (1) as

$$\frac{1}{2}C_{ijkl}\varepsilon^{c}_{kl,j} + b_i = \frac{1}{2}C_{ijkl}\left(u^{c}_{k,jl} + u^{c}_{l,jk}\right) + b_i = 0, \qquad \text{within } \Omega. \tag{19}$$

From the above equation it is evident that CP is described by the second-order partial differential equations in terms of displacements. The required continuity order of the approximation functions is here lowered by writing Eqs. (1) and (5) as the first-order equation in terms of classical strains, and then separately approximating the classical displacements and the classical strains using the same IMLS functions, leading to

$$u^{c}_i(\mathbf{x}) \approx \tilde{u}^{c}_i(\mathbf{x}) = \sum_{J=1}^{N} \phi_J(\mathbf{x})(\hat{u}^{c}_i)_J, \tag{20}$$

$$\varepsilon^{c}_{ij}(\mathbf{x}) \approx \tilde{\varepsilon}^{c}_{ij}(\mathbf{x}) = \sum_{J=1}^{N} \phi_J(\mathbf{x})(\hat{\varepsilon}^{c}_{ij})_J. \tag{21}$$

Here, ϕ_J represents the two-dimensional nodal shape function for the node $\mathbf{x}_J$, while $(\hat{u}^{c}_i)_J$ and $(\hat{\varepsilon}^{c}_{ij})_J$ are the nodal values of classical displacement and classical strain components, respectively. Depending on the position of a node, the approximations (20) and (21) are utilized to discretize Eqs. (1), (4) and (5). Thereafter, the nodal strains are eliminated from the equation system by collocating the compatibility condition (3) at the nodes, approximating displacements and strains by Eqs. (20) and (21), and replacing the nodal strains with the nodal displacements in the discretized forms of Eqs. (1) and (5). The detailed derivation of this procedure can be found in [7]. Here only the final discretized system of equations is provided. For the nodes within Ω the discretized equations can be given as

$$\sum_{J=1}^{N} \mathbf{K}_{IJ}^{\mathrm{c}} \hat{\mathbf{u}}_{J}^{\mathrm{c}} = \mathbf{R}_{I}^{\mathrm{c}}, \qquad I = 1,2,...,N, \tag{22}$$

where $\mathbf{K}_{IJ}^{\mathrm{c}} = \sum_{L=1}^{N} \mathbf{B}_{LI}^{\mathrm{c}\,\mathrm{T}} \mathbf{D} \mathbf{B}_{JL}^{\mathrm{c}}$ and $\mathbf{R}_{I}^{\mathrm{c}} = -\mathbf{b}_{I}^{\mathrm{c}}$. For the nodes on Γ_t^{c} the discretized traction boundary conditions are computed as $\bar{\mathbf{t}}_{I}^{\mathrm{c}} = \mathbf{N}_{I}^{\mathrm{c}} \mathbf{D} \sum_{L=1}^{N} \mathbf{B}_{JL}^{\mathrm{c}} \hat{\mathbf{u}}_{L}^{\mathrm{c}}$. Herein, the matrix $\mathbf{B}_{LI}^{\mathrm{c}} = \mathbf{B}_{L}^{\mathrm{c}}\left(\mathbf{x}_{I}\right)$ is the matrix of the first-order differential operator relating the nodal displacements of the node $\mathbf{x}_{L}$ to strains, computed at the node $\mathbf{x}_{I}$. It contains only the first-order derivatives of the shape functions associated with the node $\mathbf{x}_{L}$. The matrix $\mathbf{D}$ represents the elasticity matrix for isotropic linear elastic homogeneous materials, while the matrix $\mathbf{N}_{I}^{\mathrm{c}}$ is comprised of unit normal vector components. After CP is solved for $\hat{\mathbf{u}}_{J}^{\mathrm{c}}$, the nodal classical strains and stresses are computed by Eqs. (2) and (3). Thereafter, they are utilized as source terms on the right-hand side of the Helmholtz equations in GP.

3.3. Gradient problem (GP)

The solution procedure for GP is similar to the one described above and is explained in great detail in [7]. The solution is again obtained by collocating the Eqs. (6), (8) and (10) for the EB procedure, while for the SB procedure the Eqs. (7), (9) and (11) are collocated at the discretization nodes $\mathbf{x} \in \mathrm{S}$. Furthermore, the Helmholtz equations Eqs. (6) and (7) are of the second order with respect to the nonlocal strain and stress components, respectively. Therefore, analogously to CP, the nonlocal strains/stresses and strain/stress gradients can be approximated separately to lower the required continuity order in Eqs. (6) and (7).

3.3.1. Strain-based (EB) procedure

Only the main steps of the discretization procedure and final discretized equations are presented. For this procedure Eq. (6) written in terms of strains is utilized. The nonlocal strain components and their derivatives are approximated separately by the same IMLS functions, as

$$\varepsilon_{ij}^{\mathrm{g}}(\mathbf{x}) \approx \tilde{\varepsilon}_{ij}^{\mathrm{g}}(\mathbf{x}) = \sum_{J=1}^{N} \phi_{J}(\mathbf{x}) (\hat{\varepsilon}_{ij}^{\mathrm{g}})_{J}, \tag{23}$$

$$\varepsilon_{ij,k}^{\mathrm{g}}(\mathbf{x}) \approx \tilde{\varepsilon}_{ij,k}^{\mathrm{g}}(\mathbf{x}) = \sum_{J=1}^{N} \phi_{J}(\mathbf{x}) (\hat{\varepsilon}_{ij,k}^{\mathrm{g}})_{J}, \tag{24}$$

where $(\hat{\varepsilon}_{ij}^{\mathrm{g}})_{J}$ and $(\hat{\varepsilon}_{ij,k}^{\mathrm{g}})_{J}$ are the nodal values of nonlocal strains and their nodal derivatives, respectively. Here, the nodal values $(\hat{\varepsilon}_{ij,k}^{\mathrm{g}})_{J}$ are eliminated using the collocation of the compatibility conditions between the nonlocal strains $(\hat{\varepsilon}_{ij}^{\mathrm{g}})_{J}$ and their derivatives $(\hat{\varepsilon}_{ij,k}^{\mathrm{g}})_{J}$ at the nodes. In that way only the nonlocal strains $(\hat{\varepsilon}_{ij}^{\mathrm{g}})_{J}$ remain as the nodal unknowns in the discretized equations. Detailed procedure is presented in [7]. After some suitable equation manipulation, the final discretized equations for the node $\mathbf{x}_{I}$ inside Ω can be written in a compact matrix form as

$$\left(\delta_{KI} \mathbf{I}_{3} - l^{2} \sum_{J=1}^{N} \left(\mathbf{G}_{JI}^{\varepsilon} \right)^{\mathrm{T}} \mathbf{G}_{KJ}^{\varepsilon} \right) \hat{\boldsymbol{\varepsilon}}_{K}^{g} = \mathbf{F}_{I}^{\varepsilon \mathrm{g}}, \tag{25}$$

with $\mathbf{I}_3$ as the 3x3 unity matrix, and δ_{KI} as the Kronecker delta. The matrix $\mathbf{G}^{\varepsilon}_{JI}$ represents the first-order differential operator relating the nodal nonlocal strains at the node $\mathbf{x}_J$ to the gradient of nonlocal strains, computed at the node $\mathbf{x}_I$, and again contains only the first-order derivatives of the shape functions associated with the node $\mathbf{x}_J$. The source vector $\mathbf{F}^{\varepsilon g}_I = \boldsymbol{\varepsilon}^{\mathrm{c}}_I \approx \hat{\boldsymbol{\varepsilon}}^{\mathrm{c}}_I$ comprises the known nodal values of classical strains, previously calculated in CP. For the nodes on Γ^{g}_t, with prescribed gradient NBCs, $\bar{\mathbf{R}}^{\varepsilon g}_I = \mathbf{N}^{\varepsilon g}_{1I} \sum_{J=1}^{N} \mathbf{G}^{\varepsilon}_{JI} \hat{\boldsymbol{\varepsilon}}^{g}_J$. Therein, the matrix $\mathbf{N}^{\varepsilon g}_1$ contains the components of the outward unit normal vector computed at the node *I*.

3.3.2. Stress-based (SB) procedure

The discretization of the SB procedure is completely analogous to the one presented above for the EB procedure. The only difference is that the Helmholtz equation is written with respect to stresses, as visible in Eq. (7). Hence, here the nonlocal stress components and their derivatives are approximated using the same IMLS functions as

$$\sigma^{\mathrm{g}}_{ij}(\mathbf{x}) \approx \tilde{\sigma}^{\mathrm{g}}_{ij}(\mathbf{x}) = \sum_{J=1}^{N} \phi_J(\mathbf{x}) (\hat{\sigma}^{\mathrm{g}}_{ij})_J , \tag{26}$$

$$\sigma^{\mathrm{g}}_{ij,k}(\mathbf{x}) \approx \tilde{\sigma}^{\mathrm{g}}_{ij,k}(\mathbf{x}) = \sum_{J=1}^{N} \phi_J(\mathbf{x}) (\hat{\sigma}^{\mathrm{g}}_{ij,k})_J . \tag{27}$$

In the above approximations, $(\hat{\sigma}^{\mathrm{g}}_{ij})_J$ are the nodal values of nonlocal stresses and $(\hat{\sigma}^{\mathrm{g}}_{ij,k})_J$ their corresponding nodal derivatives. The derivatives $(\hat{\sigma}^{\mathrm{g}}_{ij,k})_J$ are here again eliminated from the discretized equations by collocating identical compatibility conditions as in the EB procedure, but now written using the stresses. After that, the only unknowns that are left in the discretized equations are the nonlocal stresses $(\hat{\sigma}^{\mathrm{g}}_{ij})_J$. Thus, here the discretized system of equations leads to

$$\sum_{K=1}^{N} \mathbf{K}^{\sigma g}_{KI} \hat{\boldsymbol{\sigma}}^{\mathrm{g}}_K = \mathbf{F}^{\sigma g}_I , \qquad I = 1,2,\ldots,N. \tag{28}$$

In Eq. (28), in complete analogy with the EB formulation, $\mathbf{K}^{\sigma g}_{KI} = \delta_{KI}\mathbf{I}_3 - l^2 \sum_{J=1}^{N} \left(\mathbf{G}^{\sigma}_{JI}\right)^{\mathrm{T}} \mathbf{G}^{\sigma}_{KJ}$, while the vector $\mathbf{F}^{\sigma g}_I = \boldsymbol{\sigma}^{\mathrm{c}}_I \approx \hat{\boldsymbol{\sigma}}^{\mathrm{c}}_I$ is formed by the previously calculated classical stresses in CP. The discretized NBCs are given by $\bar{\mathbf{R}}^{\sigma g}_I = \mathbf{N}^{\sigma g}_{1I} \sum_{J=1}^{N} \mathbf{G}^{\sigma}_{JI} \hat{\boldsymbol{\sigma}}^{\mathrm{g}}_J$. The matrices $\mathbf{G}^{\sigma}_{JI}$ and $\mathbf{N}^{\sigma g}_1$ are completely identical to the matrices $\mathbf{G}^{\varepsilon g}_{JI}$ and $\mathbf{N}^{\varepsilon g}_1$, respectively.

4. NUMERICAL EXAMPLE

4.1. Rectangular plate with crack

In order to verify the proposed approach, the problem of strain and stress field distributions around the crack tip is investigated. A rectangular plate with a pre-existing crack, shown in Fig. 2, is considered. The ability to remove the singularity of the stress field at the crack tip is tested for both proposed mixed staggered collocation methods. The chosen plate problem is symmetric about two axes, and therefore only one quarter of a plate is considered, as portrayed in Fig. 2. For that purpose, the appropriate symmetry BCs are utilized. The length and the height of the plate are the same and taken as $L=1\mathrm{m}$, while the material properties used are the Young's modulus $E=10000\mathrm{N/m}^2$ and the Poisson ratio $\nu=0$. As evident from Fig. 2, the pre-existing crack has the length equal to $0.2L$. The plate is subjected to the prescribed displacement of $u=0.01\mathrm{m}$ in the y direction on the upper edge ($y=L$).

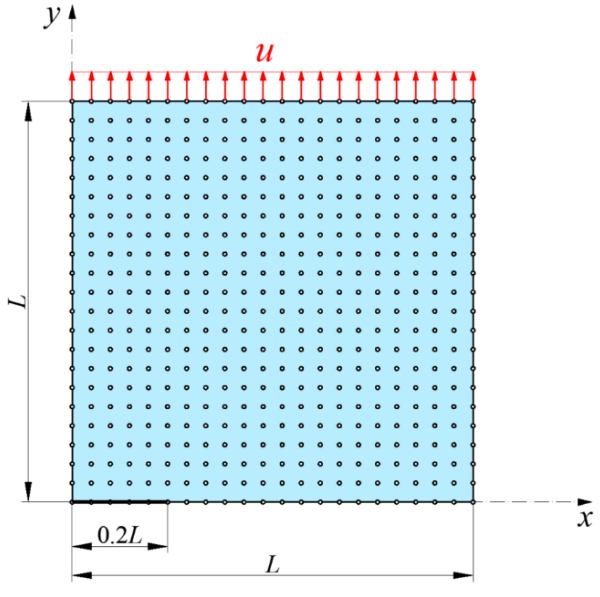

Figure 2. *Plate with a pre-existing crack*

For all numerical computations, the first-order meshless approximations functions (IMLS1) are applied. The size of the utilized nodal support domain Ω_s is equal to $r_s/h_s=1.5$. Herein, only uniform nodal discretizations are considered, where h_s is spacing between nodes in the x and y directions, respectively. The imposed BCs are concisely presented in Table 2 for both the EB and SB staggered procedures. In the EB approach, the gradient homogeneous NBCs are used along all outer sides of the plate. This has been a common choice in many gradient elasticity methods, but it is physically not always founded or justifiable, which is especially true for the considered problem [6]. As the matter of fact, it has been concluded by Lazar and Polyzos in [6] that the nonlocal staggered approach used in this work produces neither the compatible gradient elasticity solution nor the nonlocal elasticity solution as proposed by Eringen [13], but belongs to group of the so called noncompatible gradient theory, where actually the plasticity phenomena are implicitly included in the theory. In the SB approach, in addition to the homogeneous NBCs, the gradient EBCs for the nonlocal stress components are prescribed on all free boundaries, as in [10]. This means that the nonlocal stresses will satisfy the traction BCs, similar as in nonlocal elasticity theory by Eringen [6,9,13]. Due to the use of different gradient BCs, it is expected that the solutions will exhibit considerable differences than when the homogeneous BCs are imposed, which do not satisfy the traction BCs. All the obtained solutions are presented for three different values of microstructural parameter ($l=0.02\mathrm{m}$,

$l=0.04\mathrm{m}$, $l=0.06\mathrm{m}$) and 6561 uniformly distributed nodes. The attained distributions of the nonlocal hoop stresses $\sigma_{\varphi}^{\mathrm{g}}=\sigma_{y}^{\mathrm{g}}$ at $y=0$ are portrayed in Fig. 3 and Fig. 4 for each staggered formulation separately, along with the analytical solutions taken from [9]. The numerical units of all stress components depicted in distribution and subsequent contour plots are $\mathrm{N/m}^2$.

Table 2. BCs for the plate with a pre-existing crack

Classical problem (CP)	
$x=0$	$\bar{u}_x^{\mathrm{c}}=0 \quad \bar{t}_y^{\mathrm{c}}=0$
$0\le x\le 0.2L,\ y=0$	$\bar{t}_x^{\mathrm{c}}=0 \quad \bar{t}_y^{\mathrm{c}}=0$
$0.2L<x\le L,\ y=0$	$\bar{t}_x^{\mathrm{c}}=0 \quad \bar{u}_y^{\mathrm{c}}=0$
$x=L$	$\bar{t}_x^{\mathrm{c}}=0 \quad \bar{t}_y^{\mathrm{c}}=0$
$y=L$	$\bar{t}_x^{\mathrm{c}}=0 \quad \bar{u}_y^{\mathrm{c}}=0.01\mathrm{m}$

	EB procedure			**SB procedure**		
Gradient problem (GP)						
$x=0$	$\bar{R}_x^{\mathrm{g}}=0$	$\bar{R}_y^{\mathrm{g}}=0$	$\bar{R}_{xy}^{\mathrm{g}}=0$	$\bar{R}_x^{\mathrm{g}}=0$	$\bar{R}_y^{\mathrm{g}}=0$	$\bar{\sigma}_{xy}^{\mathrm{g}}=0$
$0\le x\le 0.2L,\ y=0$	$\bar{R}_x^{\mathrm{g}}=0$	$\bar{R}_y^{\mathrm{g}}=0$	$\bar{R}_{xy}^{\mathrm{g}}=0$	$\bar{R}_x^{\mathrm{g}}=0$	$\bar{\sigma}_y^{\mathrm{g}}=0$	$\bar{\sigma}_{xy}^{\mathrm{g}}=0$
$0.2L<x\le L,\ y=0$	$\bar{R}_x^{\mathrm{g}}=0$	$\bar{R}_y^{\mathrm{g}}=0$	$\bar{R}_{xy}^{\mathrm{g}}=0$	$\bar{R}_x^{\mathrm{g}}=0$	$\bar{R}_y^{\mathrm{g}}=0$	$\bar{\sigma}_{xy}^{\mathrm{g}}=0$
$x=L$	$\bar{R}_x^{\mathrm{g}}=0$	$\bar{R}_y^{\mathrm{g}}=0$	$\bar{R}_{xy}^{\mathrm{g}}=0$	$\bar{\sigma}_x^{\mathrm{g}}=0$	$\bar{R}_y^{\mathrm{g}}=0$	$\bar{\sigma}_{xy}^{\mathrm{g}}=0$
$y=L$	$\bar{R}_x^{\mathrm{g}}=0$	$\bar{R}_y^{\mathrm{g}}=0$	$\bar{R}_{xy}^{\mathrm{g}}=0$	$\bar{R}_x^{\mathrm{g}}=0$	$\bar{R}_y^{\mathrm{g}}=0$	$\bar{\sigma}_{xy}^{\mathrm{g}}=0$

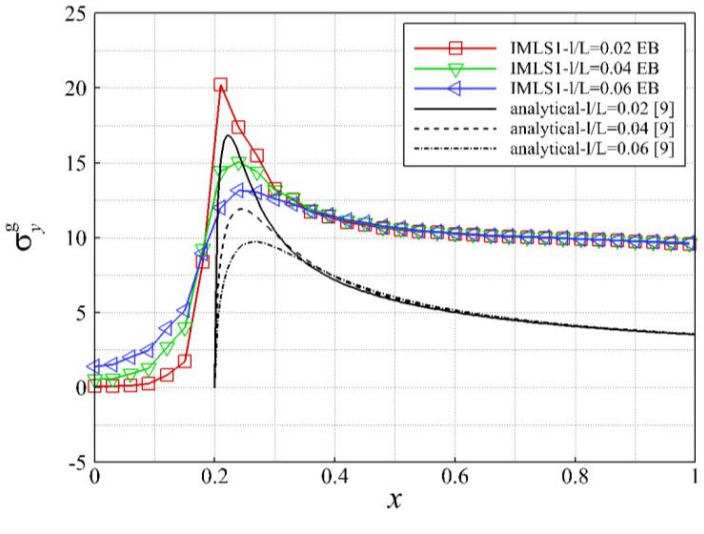

Figure 3. *Distribution of nonlocal hoop stress σ_y^{g} - EB procedure*

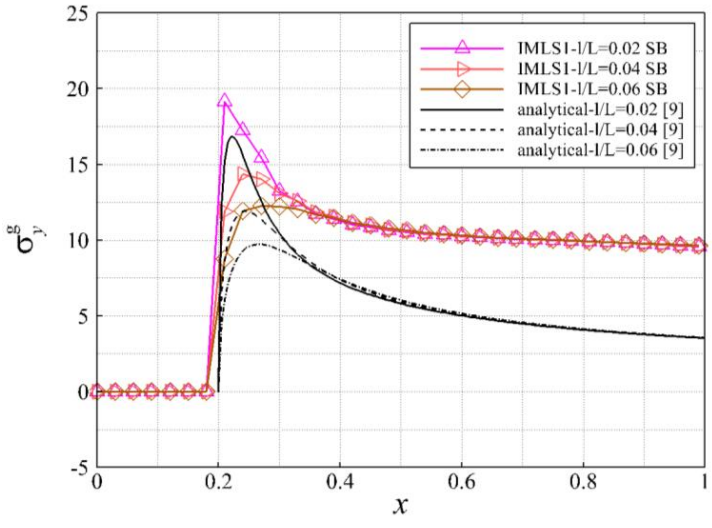

Figure 4. *Distribution of nonlocal hoop stress* σ_y^{g} *- SB procedure*

From the analysis of the obtained distribution for nonlocal hoop stresses σ_y^{g} , in both procedures, it can be seen that the use of the microstructural parameter larger than zero causes nonsingular solution at and around crack tip. It should be noted that in Fig. 3, the results obtained by using the SB formulation with the homogeneous NBCs are not shown for clarity, because in this example the results perfectly match the ones from the EB formulation. Furthermore, with the increase of the value of the microstructural parameter the values of the maximum nonlocal stresses decrease, i.e., the solutions become smoother, and the peaks tend to shift away from the crack tip, unlike in the classical fracture mechanics solution, where the stresses become infinite at the crack tip. This is in accordance with the analytical solution from [9] and has been corroborated by numerical experiments by other researchers [10]. As visible from Fig. 4, the stress distributions obtained by imposing the traction BCs in the SB formulation are in qualitative sense analogous to the analytical solutions from [9]. However, considerable quantitative differences exist, because the analytical solution in [9] has been derived for infinite plate with zero homogeneous stress BCs at infinity and at the crack tip. As mentioned in the literature, although the zero stress BCs in the analytical solution enable the non-singularity of stress distribution, the physical justification for imposing such BCs is lacking and as the matter of fact leads to the significant deviations from the Eringen solution around the crack tip, as shown in [9]. However, in the practical sense this might not be overly important, because the maximal stresses that govern the crack propagation, are predicted by all nonlocal solutions in front of the crack tip. Here it is noted that our numerical solution matches better with the Eringen's solution, probably because similar BCs, without unphysical over restrictive BCs at the crack tip, have been imposed on stresses [13]. In general, it can be stated that both EB and SB formulations remove singularities in the stress field at the crack tip, which demonstrates their efficiency. To prove this statement contour plots of the nonlocal stress components σ_x^{g} and σ_y^{g} are presented for values $l=0$ (classical solution) and $l=0.02\mathrm{m}$ in Fig. 5 - Fig. 8. Herein, the contour plot for σ_x^{g} is given for the EB procedure, while the σ_y^{g} is presented for the SB procedure.

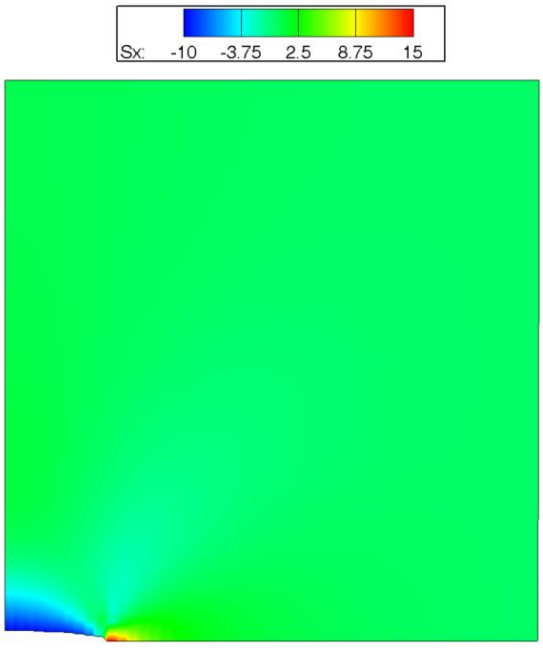

Figure 5. *Contour plot of stress σ_x^c - classical solution (l = 0)*

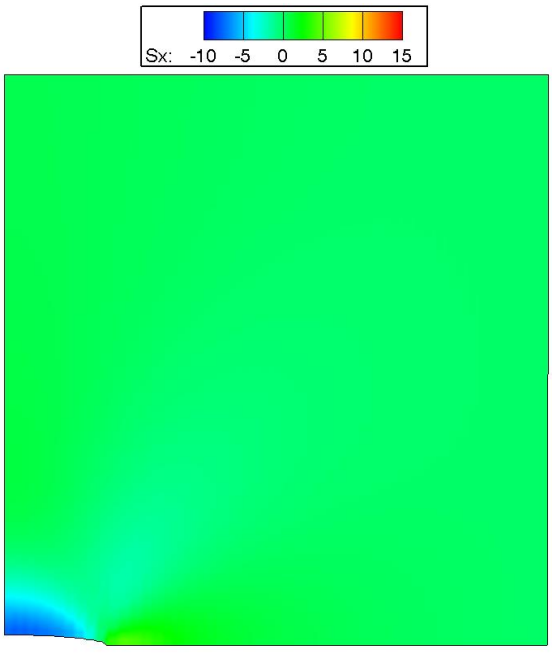

Figure 6. *Contour plot of stress σ_x^g - EB procedure (l = 0.02m)*

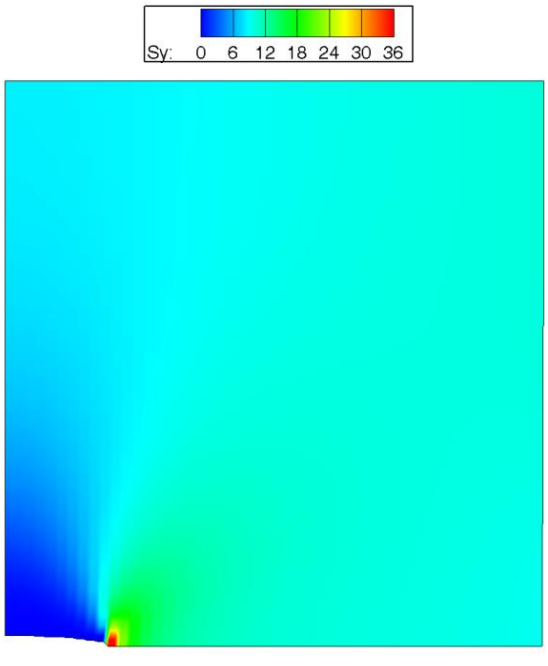

Figure 7. *Contour plot of stress σ_y^c - classical solution (l = 0)*

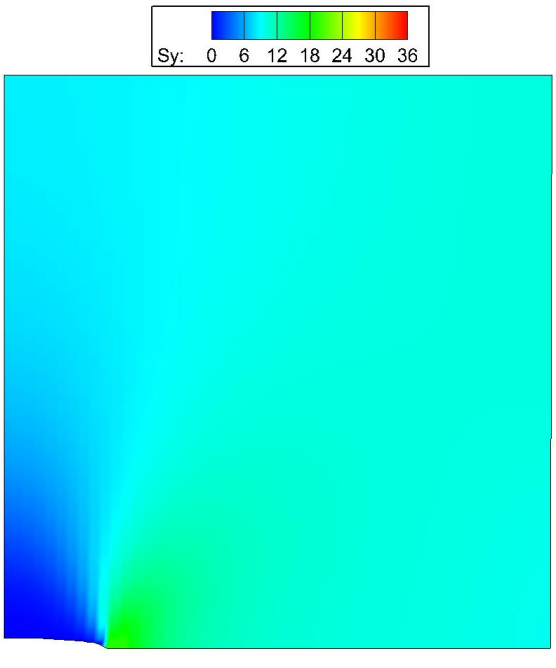

Figure 8. *Contour plot of stress σ_y^g - SB procedure (l = 0.02m)*

From the comparison of the presented gradient nonlocal stress contour plots and the classical stress plots, where the singularities are visible as red zones, it is again evident that both the EB and SB procedure remove the stress singularities at the crack tip successfully.

5. CONCLUSIONS

Two different mixed collocation methods based on the MLPG paradigm for the modelling of homogeneous structures in gradient elasticity are presented. Therein, the chosen gradient elasticity theory is of a Helmholtz type and uses only one unknown microstructural parameter. The gradient elasticity problem is solved in a staggered manner, where firstly the classical boundary value problem is solved, whose solution is then used as the input for the corresponding gradient boundary value problem described by the Helmholtz equation. Herein, two different Helmholtz equations, one written with respect to strains, and the other written in terms of stresses, are considered. In both cases, the subproblems are described by the second-order equations, instead of the original fourth-order differential equations. For the discretization, the collocation procedure of governing equations and MLS meshless approximations are utilized. Thereby, the spatial discretizations are kept the same for both the classical and gradient problem. For the approximation of all independent variables the same interpolatory MLS functions are used. By employing the mixed concept, the necessary derivative order of the approximation functions is reduced, and only the first-order derivatives of approximants are needed. In this paper, the proposed collocation methods are utilized here to compute stress fields near the crack tip. From the obtained results, it can be concluded that both considered methods are able to completely remove stress singularities at the crack tip and produce smooth stress fields around the crack tip. Furthermore, it has been shown that the application of the appropriate BCs is of extreme importance when solving this problem. Two different sets of BCs, typically encountered in the literature, are considered and different distributions of stress components have been obtained around the crack tip. Thereby, it has been noted that in the stress-based formulation it is much easier to impose the traction boundary conditions needed for satisfying the mechanical equilibrium. The obtained stress distributions are compared to the available analytical solution taken from the literature and good agreement in trends of distribution are observed. In further research, the variationally consistent boundary conditions associated with the gradient elasticity theories will be considered. In addition, the developed mixed collocation methods could also be employed in other numerical models governed by the Helmholtz equations, such as implicit gradient elasticity or damage models, the phase-field models, etc.

REFERENCES

[1] Askes, H., Aifantis, E.C. (2011). Gradient elasticity in statics and dynamics: An overview of formulations, length scale identification procedures, finite element implementations and new results, *International Journal of Solids and Structures, 48, 1962-1990.*

[2] Engel, G., Garikipati, K., Hughes, T.J.R., Larson, M.G., Mazzei, L., Taylor, R.L. (2002) Continuous/discontinuous finite element approximations of fourth-order elliptic problems in structural and continuum mechanics with applications to thin beams and plates, and strain gradient elasticity, *Computer Methods in Applied Mechanics and Engineering*, *191*, *3669-3750*.

[3] Amanatidou, E., Aravas, N. (2002). Mixed finite element formulations of strain-gradient elasticity problems, *Computer Methods in Applied Mechanics and Engineering, 191, 1723-1751.*

[4] Atluri, S.N. (2004). The Meshless Method (MLPG) for Domain & BIE Discretization, Tech Science Press, Forsyth, USA.

[5] Jalušić, B., Sorić, J., Jarak, T. (2017). Mixed Meshless Local Petrov-Galerkin Collocation Method for Modeling of Material Discontinuity. *Computational Mechanics, 59 (1), 1-19.*

[6] Lazar, M., Polyzos, D. (2015). On non-singular crack fields in Helmholtz type enriched elasticity theories, *International Journal of Solids and Structures, 62, 1-7.*

[7] Jalušić, B., Jarak, T., Sorić, J. (2020). Mixed meshless local Petrov-Galerkin (MLPG) collocation Methods for gradient elasticity Theories of Helmholtz type. *Computational Mechanics, 66 (3), 575-602.*

[8] Most, T. (2007). A natural neighbour-based moving least squares approach for the Element-free Galerkin method. *International Journal for Numerical Methods in engineering, 71(2), 224-252.*

[9] Isaksson, P., Hagglund, R. (2013). Crack-tip fields in gradient enhanced elasticity. *Engineering Fracture Mechanics, 97, 186-192.*

[10] Bagni, B., Askes, H. (2015). Unified finite element methodology for gradient elasticity. *Computers and Structures, 160, 100-110.*

[11] Ru, C. Q., Aifantis, E.C. (1993). A simple approach to solve boundary-value problems in gradient elasticity, *Acta Mechanica, 101, 59-68.*

[12] Askes, H., Morata, I., Aifantis, E.C. (2008). Finite element analysis with staggered gradient elasticity, *Computers & Structures, 86, 1266-1279.*

[13] Ari N., Eringen A. C. (1983). Nonlocal stress field at Griffith crack. *Cryst Latt Def Amorph Mat*, *10, 33–38.*

Modelling crowd-structure interaction on an ultra-lightweight FRP footbridge

Gallegos-Calderón, Christian[1];Naranjo-Pérez, Javier[2];Pulido, M. Dolores G.[3];Goicolea, José M.[4];Díaz, Iván M.[5]

ABSTRACT

Human-Structure Interaction (HSI) may influence the dynamic behaviour of Fibre Reinforced Polymer (FRP) footbridges due to the lightweight nature of composite materials. Hence, load models that account for HSI should be applied to accurately predict vibration levels on these pedestrian structures. This paper proposes a model to assess the structural response of a simply supported footbridge subjected to a weak traffic scenario (0.2 pedestrians/m^2), considering HSI and higher harmonics of pedestrians walking. The dynamic parameters of a single pedestrian, depicted as a Mass-Spring-Damper-Actuator (MSDA) system, and the modal parameters of the structure are employed to construct a coupled time-invariant crowd-structure system. The frequency-domain approach, based on a closed-loop Transfer Function (TF), considered in this study leads to a good agreement between numerical results and experimental outcomes obtained on an ultra-lightweight FRP footbridge. Thus, the proposed HSI model may be used as a first approximation to correctly estimate the dynamic response of other lightweight structures subjected to crowd-induced loads.

Keywords: FRP footbridge, dynamic response, crowd-induced load, human-structure interaction.

1. INTRODUCTION

Guidelines and codes often define non-interacting load models to represent pedestrian actions in the assessment of lightweight pedestrian structures at Vibration Serviceability Limit State (VSLS) [1–3]. Nevertheless, an unreal high estimation of the response of Fibre Reinforced Polymer (FRP) footbridges may be obtained using these load models since Human-Structure Interaction (HSI) is neglected. Moreover, higher harmonics of human actions, which are not considered in design recommendations, may excite significantly FRP structures due to the lightweight nature of composite materials [4].

A pedestrian has been usually modelled as a mechanical Mass-Spring-Damper (MSD) system together with an external harmonic force to account for interaction phenomenon on the dynamic analysis of lightweight structures [5]. Based on this idea, several approaches are available to represent a stream of pedestrians acting on a lively footbridge. For example, a HSI sub-model and a crowd sub-model, based on social forces among humans, were adopted in Ref. [6] to analyse a cable-stayed footbridge. Recently, a simplified methodology to consider vertical interaction between crowds and footbridges has been

[1] *ETSI Caminos, Canales y Puertos. Universidad Politécnica de Madrid (Spain). christian.gallegos@upm.es (Corresponding author)*
[2] *ETSI Caminos, Canales y Puertos. Universidad Politécnica de Madrid (Spain). javier.naranjo@upm.es*
[3] *Instituto de Ciencias de la Construcción Eduardo Torroja. CSIC (Spain). dpulido@ietcc.csic.es*
[4] *ETSI Caminos, Canales y Puertos. Universidad Politécnica de Madrid (Spain). jose.goicolea@upm.es*
[5] *ETSI Caminos, Canales y Puertos. Universidad Politécnica de Madrid (Spain). ivan.munoz@upm.es*

proposed in Ref. [7], obtaining charts in terms of the modal parameters of the empty structure to define a system with effective natural frequency and damping ratio. A pedestrian-to-structure mass ratio up to 30% was assumed, so the procedure may be just valid for structures made of traditional construction materials, such as concrete or steel.

The effects of HSI increases with the crowd-to-structure mass ratio [8], and human mass may easily surpass 30% of the mass associated to a specific vibration mode of an FRP footbridge. This is the case when three people, whose total mass is 218.8 kg, walked over the structure constructed at the Laboratory of Structures at *ETSI Caminos, Canales y Puertos – UPM* (see Fig. 1). As the laboratory footbridge presents a natural frequency of 7.62 Hz and modal mass of 405 kg associated to the first vertical vibration mode [4], the pedestrian-to-structure ratio is around 54%.

Figure 1. *FRP footbridge.*

This paper proposes a model to predict the structural response of a simply supported FRP footbridge subjected to weak traffic scenario, accounting for HSI and higher harmonics of pedestrians walking. After this introduction, experimental results from a test considering three pedestrians walking freely over the bridge deck are presented. Following, the model of the coupled crowd-structure system is described, and the results are compared with those obtained from the test. Finally, results from sensitivity analyses are discussed, and some conclusions of the work are drawn.

2. DYNAMIC TEST

The structure studied herein is a 10 m long simply supported footbridge (see Fig. 1), comprised of glass-FRP profiles and carbon-FRP strips manufactured by Fiberline Composites A/S [9]. The pedestrian structure was designed to meet requirements for Deflection Serviceability Limit State (SLS) and Ultimate Limit State (ULS), as reported in Ref. [10]. Due to the adopted design approach, an ultra-lightweight footbridge was obtained and excessive vertical vibrations under human actions were expected.

Three pedestrians, whose total mass was 218.8 kg, were asked to walk freely and comfortably for five minutes in a closed-loop path over the bridge deck (see Fig. 2). During the test, the acceleration response of the FRP footbridge was recorded at midspan with a sampling frequency of 1000 Hz using a high-sensitivity accelerometer attached at the bottom of the central stringer (see Fig. 3a). The collected

signal was processed using a low pass filter with a cut-off frequency of 10 Hz to account only for the contribution of the first vibration mode.

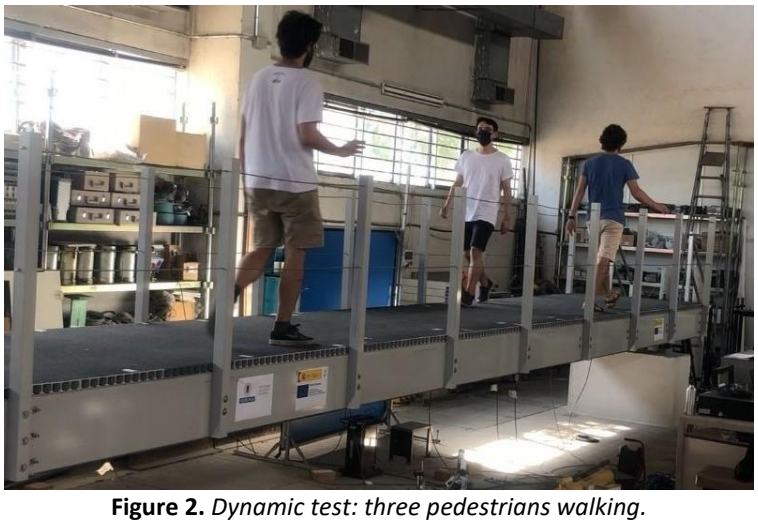

Figure 2. *Dynamic test: three pedestrians walking.*

In Fig. 3b, it is observed that the obtained maximum acceleration was 1.95 m/s^2, whereas the Maximum Transient Vibration Value (MTVV) was 1.12 m/s^2. The former is the peak value from the 1s running-root-mean square (RMS) acceleration. Multiplying the MTVV by $\sqrt{2}$, which led to 1.58 m/s^2, a minimum degree of comfort at VSLS was assigned to the FRP footbridge according to *HIVOSS* guideline [1] ($1.0\ \mathrm{m/s^2} \leq \mathrm{a_{lim}} \leq 2.5\ \mathrm{m/s^2}$).

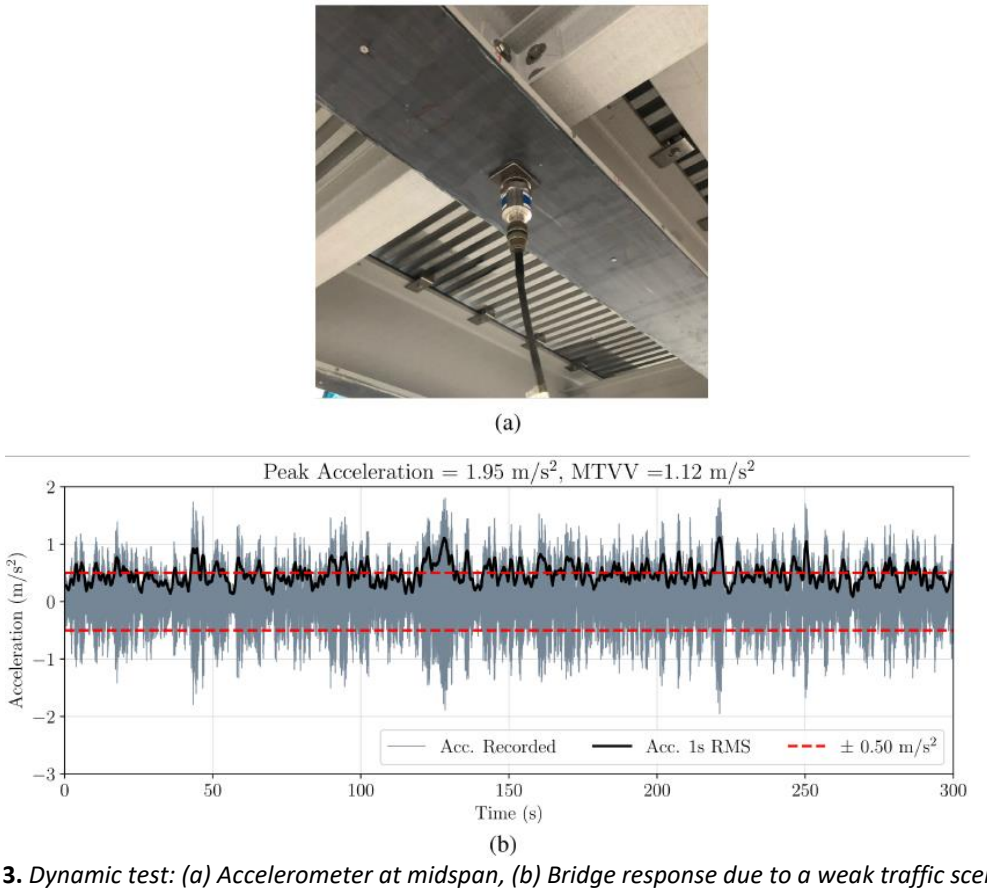

Figure 3. *Dynamic test: (a) Accelerometer at midspan, (b) Bridge response due to a weak traffic scenario.*

2.1. Numerical model neglecting interaction phenomenon

According to *prEN 1991-2* [3], the load model for a crowd of n pedestrians without considering the interaction phenomenon is

$$q_a(t) = W \cdot \cos(2\pi f_{as} t) \cdot n' \cdot \psi_w \tag{1}$$

with f_{as} being the step frequency which is assumed equal to the natural frequency of the structure, ψ_w the reduction coefficient and n' the synchronised number of pedestrians ($n' < n$) which can be calculated as

$$n' = \frac{10.8\sqrt{\zeta_s \cdot n}}{S} \tag{2}$$

where ζ_s is the damping ratio of the structure and S is the area of the deck.

Using the following values of the parameters: $f_{as} = 7.63$ Hz, $n = 3$ pedestrians, $\zeta_s = 0.0155$, $S = 15$ m^2 and $\psi_w = 0.15$, the acceleration shown in Fig. 4 was obtained employing the calibrated FE model of the structure, described in Ref. [4]. The value $\psi_w = 0.15$ is chosen in order to define the load using the fourth harmonic set in *ISO-10137* [11] ($DLF_4 = 0.06$).

Neglecting the interaction between the structure and the pedestrians, the dynamic response is very far from the actual value obtained experimentally. For this reason, the inclusion of a human model becomes essential for lightweight structures under pedestrian loads.

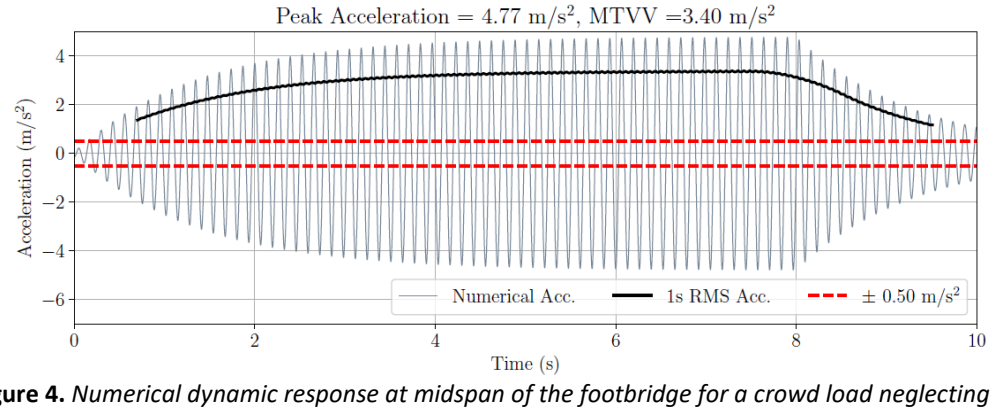

Figure 4. *Numerical dynamic response at midspan of the footbridge for a crowd load neglecting the interaction phenomenon.*

3. CROWD-STRUCTURE INTERACTION

In this section, the crowd-structure interaction model is described and implemented to obtain the acceleration of the structure under crowd loads.

3.1. Modelling

A walking pedestrian can be represented as a Mass-Spring-Damper-Actuator (MSDA) system based on the dynamic properties of the human body to account for HSI [4]. The person is defined using his/her mass (m_h), natural frequency (f_h), and damping ratio (ζ_h). Also, a harmonic force (F_a) generated by the human legs is considered in this model as a pair of action-reaction forces acting simultaneously on

both the footbridge and the human. The most intuitive approach to represent a crowd of pedestrians may be employing several MSDA systems.

Another alternative to model the crowd may be through an equivalent single-degree-of-freedom (SDOF) system defined by the parameters of a MSDA system and the number of pedestrians on a footbridge. The transfer function (TF) of this crowd-structure system between the footbridge acceleration at midspan ($\ddot{x}_s$) and the equivalent crowd driving force (F_a^{eq}) is denoted herein as GH_{CL}^{eq}. The TF is characterized by a feedback loop associated to the interaction phenomenon, and it is defined as follows for the case of a simply supported structure

$$GH_{CL}^{eq}(s) = \frac{2/\pi \cdot G_H^{eq} \cdot G_S}{1 - (2/\pi)^2 \cdot G_{HSI}^{eq} \cdot G_S} \tag{3}$$

where $s = j\omega$ is the Laplace variable, ω is the angular frequency in rad/s, $G_S(s)$ is the TF of the structural system, $G_H^{eq}(s)$ is the TF between the equivalent crowd driving force and the contact force of the pedestrians with the structure, and $G_{HSI}^{eq}(s)$ is the TF related to HSI.

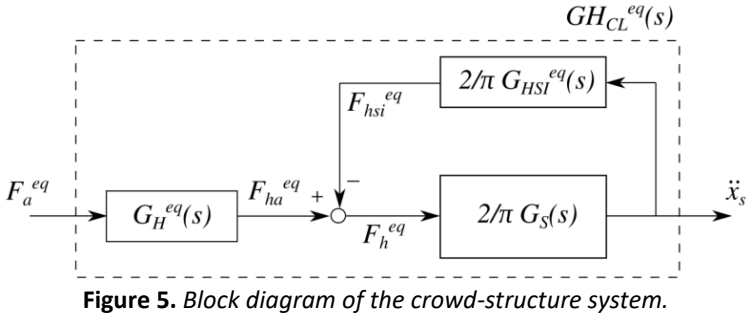

Figure 5. *Block diagram of the crowd-structure system.*

Considering the modal parameters of the first vertical vibration mode of a simply supported structure, the TF between the structure acceleration at midspan and the equivalent external force in the Laplace domain is

$$G_S(s) = \frac{s^2}{m_s\, s^2 + c_s\, s + k_s} \tag{4}$$

where m_s (kg) is the equivalent mass, $k_s = \omega_s^2 m_s$ (N/m) is the equivalent stiffness, and $c_s = 2\omega_s m_s \zeta_s$ (Ns/m) is the equivalent viscous damping of the fundamental vibration mode.

The TF between the force generated by the equivalent crowd without including the force transmitted to them due to the structure movement, and the driving force from the flow of pedestrians is as follows

$$G_H^{eq}(s) = \frac{m_h^{eq}\, s^2}{m_h^{eq}\, s^2 + c_h^{eq}\, s + k_h^{eq}} \tag{5}$$

being m_h^{eq} the equivalent mass of the crowd, and k_h^{eq} and c_h^{eq} the equivalent stiffness and viscous damping of the flow of pedestrians, respectively. These parameters are obtained as follows

$$m_h^{eq} = \sum_{i=1}^{n} m_{hi} \tag{6}$$

$$k_h^{eq} = \sum_{i=1}^{n} k_{hi} \tag{7}$$

$$c_h^{eq} = \sum_{i=1}^{n} c_{hi} \tag{8}$$

with $i = 1, 2, \cdots, n$, where n is the number of individuals within the crowd, $k_h = \omega_h^2 m_h$ (N/m) is the person stiffness, $\omega_h = 2\pi f_h$ (rad/s) is the angular natural frequency of the human, $c_s = 2\omega_s m_s \zeta_s$ (Ns/m) is the viscous damping of the pedestrian body.

Similarly to the non-interacting load models for pedestrian flows provided in *prEn 1991-2* [3], the equivalent crowd force applied at midspan of a simply supported structure is

$$F_a^{eq} = W_h \cdot GLF_r \cdot cos(2\pi f_{as}) \cdot n' \cdot S \tag{9}$$

being L the span of the footbridge, b the width of the structure, $W_h = m_h \cdot g$ (N) the weight of a person, GLF_r the generalised load factor associated to the *r*th harmonic of the walking action.

Finally, the TF between the crowd interacting force, which is the force transmitted due to the structure movement, and the structure acceleration is

$$G_{HSI}^{eq}(s) = \frac{m_h^{eq}(c_h^{eq}\, s + k_h^{eq})}{m_h^{eq}\, s^2 + c_h^{eq}\, s + k_h^{eq}} \tag{10}$$

3.2. Case study

To validate the proposed crowd-structure interaction model, the dynamic response of the FRP footbridge is obtained herein. Based on Ref. [4] and the experiment described in Section 2, the following information was employed: $m_s = 405$ kg, $f_s = 7.66$ Hz, $\zeta_s = 1.55\%$, $L = 10$ m, $b = 1.50$ m, $m_h = 0.93 \cdot 72.9$ kg, $f_h = 1.88$ Hz, $\zeta_h = 23.4\%$, $n = 3$ pedestrians, and $GLF_4 = 0.032$. Fig. 6 shows the acceleration at midspan. A clear good agreement between the MTVVs obtained via the experimental test and the numerical simulation is achieved. However, the peak value of the response presents a significant difference. This is explained by the definition of the load (see Eq. (9)), which only accounts for the fourth harmonic of the human action. Whereas for the experimental result shown in Fig. 3b, the contribution of the first three harmonics are also consider due to the low-pass filter (at 10 Hz) employed.

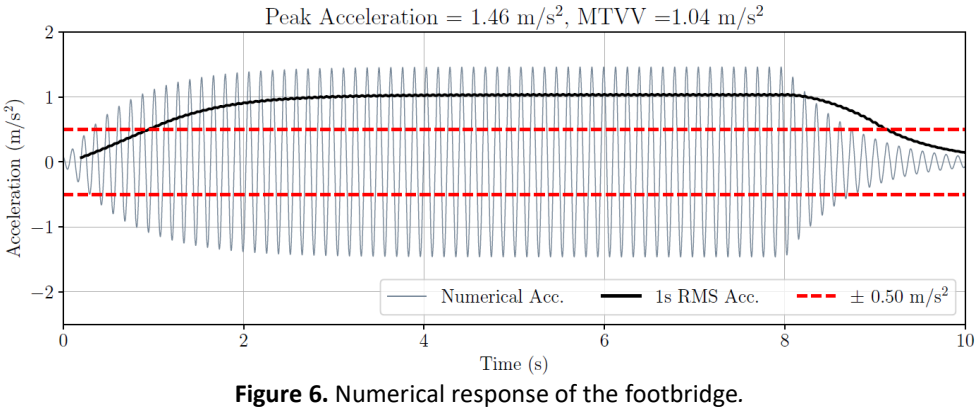

Figure 6. Numerical response of the footbridge.

4. DISCUSSION OF RESULTS

Employing the crowd-structure interaction model obtained in Section 3, two parametric analyses varying both the dynamic properties of the human body and the footbridge are conducted. The influence of every parameter on the numerical dynamic response of the FRP footbridge was investigated by considering 1000 stochastic samples generated from the following distributions:

- Uniform distributions for the three parameters of the human body (factor of the mass, frequency and damping ratio).
- Normal distribution for the mass of the footbridge.
- Weibull distribution for the frequency and damping ratio of the footbridge.

Fig. 7 shows the results of the sensitivity analysis regarding the dynamic parameters of the human body, where the most influential property on the numerical response is the damping ratio of the body, whereas the factor of the mass has the less impact.

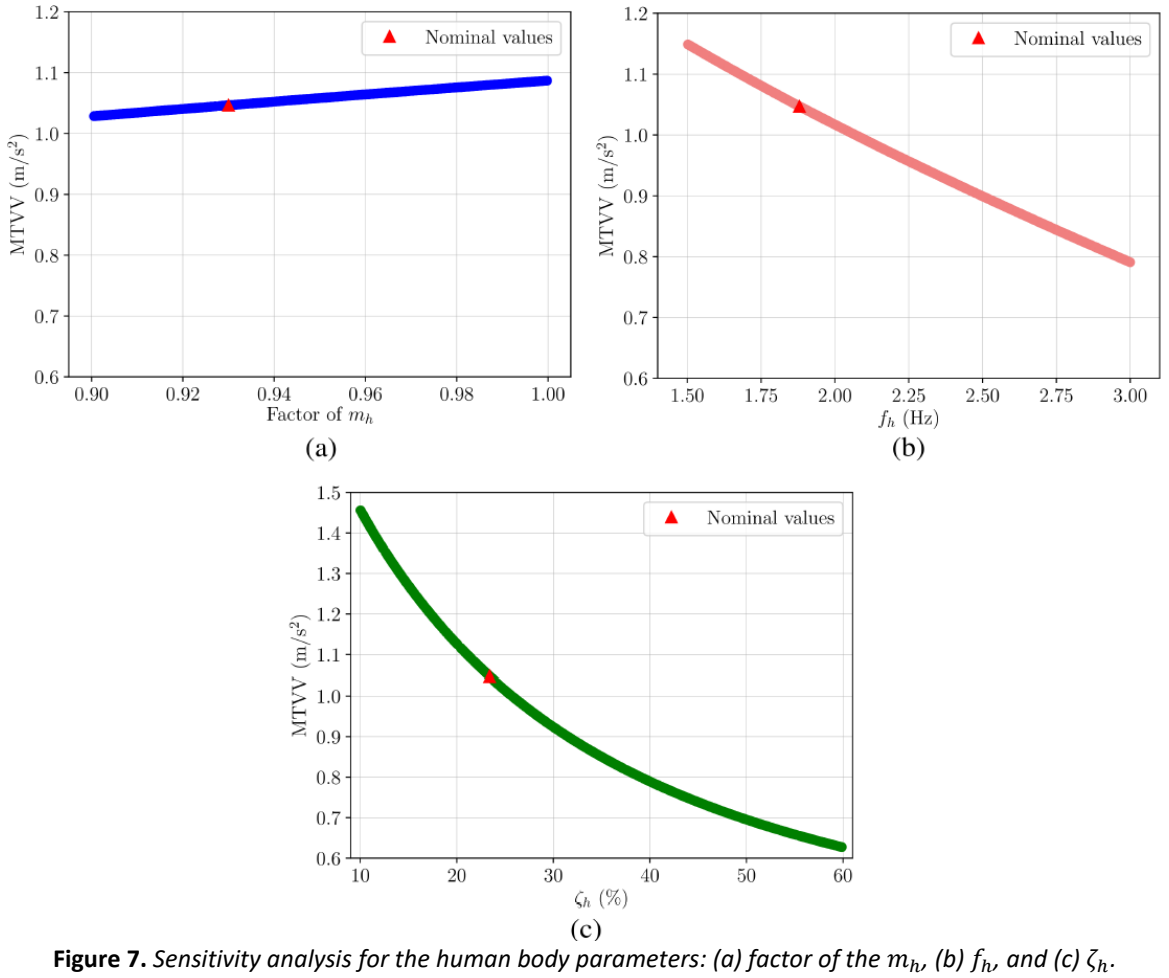

Figure 7. *Sensitivity analysis for the human body parameters: (a) factor of the m_h, (b) f_h, and (c) ζ_h.*

Regarding the footbridge parameters, it can be observed in Fig. 8 two main results. First, in contrast to the previous analysis, the damping ratio remains as the less influential parameter and, second, both mass and frequency have similar but inverse relevance. The first result is due to the large difference between the damping ratio of the human and the structure, being the first one at least ten times the

second one. The second result was the expected as more mass produces a reduction of the natural frequency when the stiffness remains constant.

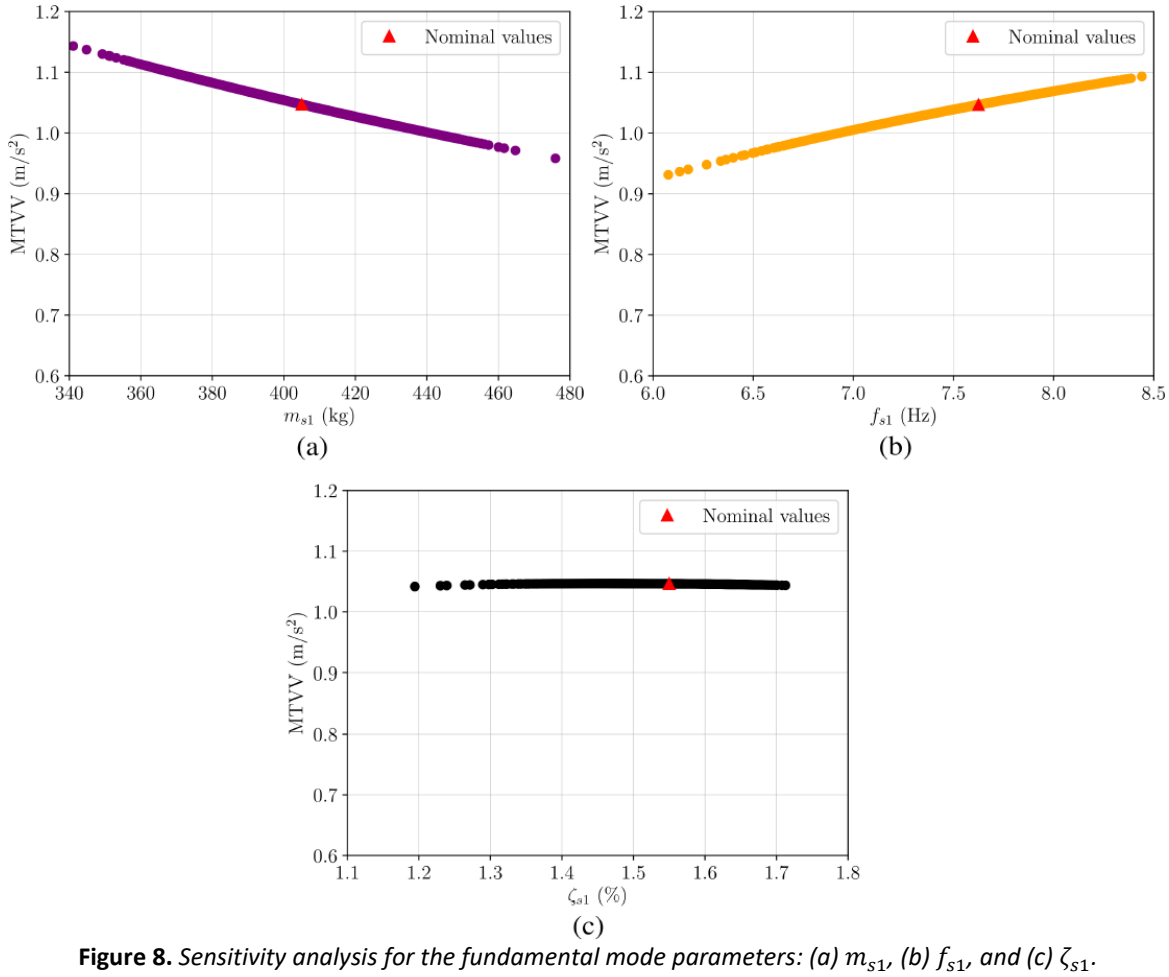

Figure 8. *Sensitivity analysis for the fundamental mode parameters: (a) m_{s1}, (b) f_{s1}, and (c) ζ_{s1}.*

4.1. Comparison of the crowd-structure interaction model with a time-domain model

The results are compared herein with a time-domain-based pedestrian-structure interaction model implemented in a modified version of the software CALDINTAV [12]. This software, developed by the Computational Mechanics Group of the Technical University of Madrid, considers the interaction phenomenon through the modification of the mass, damping and stiffness matrices of the pedestrian-structure system. Also, it accounts for a moving MSD system plus an external harmonic force (F_{ha}) to represent a walking pedestrian. The dynamic force exerted by the pedestrian is defined as follows

$$F_h(t) = W_h \sum_{r}^{n_r} VDLF_r \sin(r2\pi f_a t + \varphi_r) \tag{11}$$

with $r = 1, 2, \ldots n_r$, where n_r is the total number of harmonics considered, r is the harmonic number, $VDLF_r$ is the vertical dynamic load factor associated to the rth harmonic, and φ_r is the corresponding phase angle.

For the analysis, the parameters given in Section 3.2 were employed to define both, the structure and the pedestrians. Also, $VDLF_1 = 0.229, VDLF_3 = 0.218, VDLF_3 = 0.112, VDLF_4 = 0.034$, $\varphi_1 = 0$ rad, and $\varphi_2 = \varphi_3 = \varphi_4 = \pi/2$ rad [4]. The crowd of 3 pedestrians walking on the footbridge was simulated considering the MSD systems separated 3.30 m. Hence, it was ensured that only 3 of 10 systems were on the footbridge at a given time to obtain a stationary response.

It is observed in Fig. 9 that the MTVV is very close to the obtained using the proposed interaction model ($1.04\ \mathrm{m/s^2}$) and the peak acceleration is higher due to the contribution of the first three harmonics of the human action.

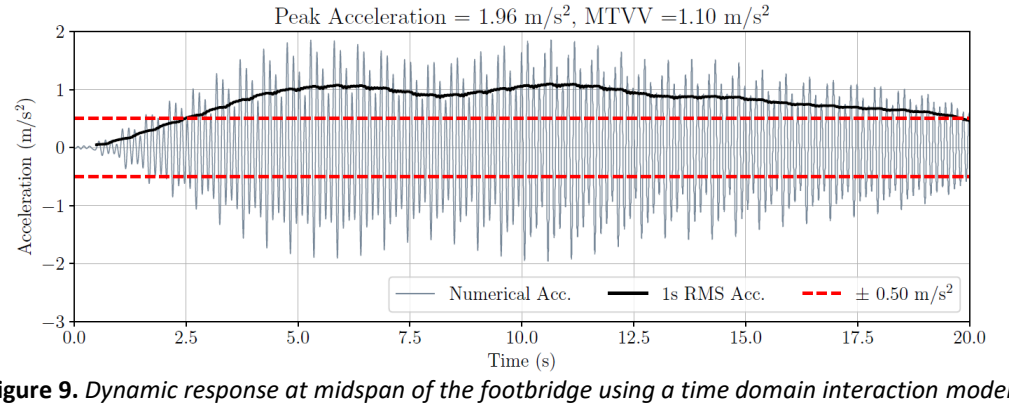

Figure 9. *Dynamic response at midspan of the footbridge using a time domain interaction model.*

Table 1 presents a summary of the MTVVs calculated using both approaches. Although good results have been obtained using the time-domain approach, to depict each person within a large crowd may not be practical in engineering offices. The modification of the mass, damping and stiffness matrices due to HSI is not straightforward and time-variant models with a very high number of DOFs may be obtained, leading to an expensive computational problem. In general, this requires expertise and advance modelling skills from the users. In this context, the frequency-domain approach considered in this study seems to be simpler to implement without excessive loss of accuracy in the results.

Table 1. Comparison of MTVVs (m/s^2)

Traffic class	Experimental	Proposed model	Time-domain model
Weak	1,12	1,04	1,10

5. CONCLUSIONS

An experiment consisting in three pedestrians walking freely has been performed in a lightweight FRP footbridge and the acceleration at midspan has been collected. Through the comparison of the results from the test with the numerical outcomes using the provisions stated in the *prEN 1991-2* [3], a poor estimation of the real behaviour was obtained as HSI was disregarded.

Hence, in the study a load model that considers HSI and a higher harmonic of walking action has been proposed to improve the prediction of the response of the lively FRP pedestrian structure subjected to a weak traffic scenario (0.2 pedestrians/m^2). The proposal is based on a closed-loop TF that uses

equivalent parameters to define a flow of pedestrians, working with a linear time invariant coupled system. The results have demonstrated that the equivalent crowd-structure interaction model gives a good assessment of the dynamic response of the footbridge at VSLS, what allows concluding that the inclusion of the dynamic properties of the human body is essential to an accurate evaluation of the dynamic behaviour of lightweight structures.

Besides, by considering HSI at the design stage of composite footbridges may be beneficial to meet vibration serviceability requirements and avoid oversizing the structural elements.

ACKNOWLEDGEMENTS

The authors acknowledge the Grant RTI2018-099639-B-I00, "Structural efficiency enhancement for bridges subjected to dynamic loading: integrated smart dampers", funded by MCIN/AEI/ 10.13039/501100011033 and by "ERDF A way of making Europe". Christian Gallegos-Calderón expresses his gratitude to the Secretariat of Higher Education, Science, Technology and Innovation of Ecuador (SENESCYT) for the PhD scholarship CZ02-000167-2018.

REFERENCES

[1] Butz C, Heinemeyer C, Keil A, Schlaich M, Goldack A, Trometer S, et al. HIVOSS: Design of footbridges guideline. Joint Research Center; 2008.

[2] CEN. Draft prEN 1990 Basis of Structural and Geotechnical Design, Annex A.2. Applications for Bridges. European Committee for Standardisation; September 2021.

[3] CEN. Draft prEN 1991-2:2021: Actions on Structures - Part 2: Traffic loads on Bridges and other Civil Engineering Works. European Committee for Standardization; September 2021.

[4] Gallegos-Calderón C, Naranjo-Pérez J, Díaz IM, Goicolea JM. Identification of a human-structure interaction model on an ultra-lightweight FRP footbridge. Appl Sci 2021;11:6654.

[5] Shahabpoor E, Pavic A, Racic V. Interaction between Walking Humans and Structures in Vertical Direction: A Literature Review. Shock Vib 2016;2016:1–22.

[6] Jiménez-Alonso JF, Sáez A, Caetano E, Magalhães F. Vertical Crowd–Structure Interaction Model to Analyze the Change of the Modal Properties of a Footbridge. J Bridg Eng 2016;21.

[7] Van Nimmen K, Pavic A, Van den Broeck P. A simplified method to account for vertical human-structure interaction. Structures 2021;32:2004–19.

[8] Živanović S, Díaz IM, Pavić A. Influence of walking and standing crowds on structural dynamic properties. IMAC XXVII Conf. Expo. Struct. Dyn., Orlando, FL: The Society for Experimental Mechanics, Inc.; 2009.

[9] Fiberline Composites A/S. General Design Certification. Middelfart, Denmark: Fiberline Composites A/S; 2018.

[10] Gallegos-Calderón C, Naranjo-Pérez J, Pulido MDG, Díaz IM. Design, construction and structural response of a lightweight FRP footbridge. IABSE Congr. Struct. Eng. Futur. Soc. Needs, Ghent, Belgium: 2021, p. 2053–61.

[11] ISO. ISO 10137 - Bases for design of structures - Serviceability of buildings and walkways against vibrations. vol. 10137. International Organization for Standardization; 2007.

[12] Goicolea JM, Nguyen K. CALDINTAV Version D1.0 Tutorial. Madrid: 2017.

SENSOR PLACEMENT OPTIMIZATION USING CONVEX L_0 NORM RELAXATIONS

Jokić, Marko[1]; Rožić, Jurica[2]

ABSTRACT

Sensor placement optimization problem is a fundamental one in vibration measurement, structural health monitoring, and so on. Many different approaches have been proposed [1], from heuristic to approximations of the original problem [2].

We present an algorithm based on a series of the convex optimizations, where each iteration simultaneously minimizes a performance criteria and a sparsity-inducing term, as well as prioritizing grouping sensors in prescribed groups [3]. In the existing algorithms [4], [3], the non-convex sparsity inducing L_0 norm is replaced by a series of weighted L_1 relaxations [5], which doesn't offer the ability of grouping the sensors. Grouping becomes important in multi-dimensional spaces to avoid eliminating a spatial coordinate from a potential sensor location. We approach grouping by using the L_2 norm alongside the relaxed L_0 norm.

Keywords: sensor placement, sensor selection, mixed L_1/L_2 norm, convex optimization, L_0 norm relaxation.

1. FORMING THE ALGORITHM

We start from the derived equation of the dynamic system discretized with finite element method (FEM):

$$\mathbf{M}\,\ddot{\mathbf{q}} + \mathbf{P}\,\dot{\mathbf{q}} + \mathbf{K}\,\mathbf{q} = \mathbf{0}, \tag{1}$$

where **M** is the mass matrix, **P** is damping matrix, **K** is stiffness matrix, and **q** is the position vector. Eq. (1) is then reformulated into a state-space system,

$$\begin{aligned} \dot{\mathbf{x}} &= \mathbf{A}\,\mathbf{x} + \mathbf{B}\,\mathbf{u}, \\ \mathbf{y} &= \mathbf{C}\,\mathbf{x}, \end{aligned} \tag{2}$$

where **A**, **B**, and **C** are the system matrices derived from **M**, **P** and **K** with state variables in **x** being displacement and velocity on all possible sensor positions. **y** is the vector of output variables of the system, and **u** is the input vector of the system. Possible sensor positions are, in this case, all FEM nodes with unconstrained relevant degrees of freedom.

[1] *Department of Applied Dynamics, University of Zagreb, Faculty of Mechanical Engineering and Naval Architecture, (CROATIA). mjokic@fsb.hr*
[2] *University of Zagreb, Faculty of Mechanical Engineering and Naval Architecture (CROATIA). jurica.rozic@fsb.hr*

Sensors used in the formulation are velocity and displacement sensors, but for real-world applications of this kind of monitoring, only acceleration sensors are a viable option. On the other hand, for the mathematical formulation of the problem is very convenient to use velocity and displacement sensors. In experiments this is solved by integrating data from acceleration sensors to simulate virtual displacement and velocity sensors.

1.1. Error minimisation

At its core, the algorithm models an observer system and minimizes its error in relation to the simulated system. Furthermore, it is augmented with additional terms for minimizing the number of sensors, as well as grouping the sensors together. The observer system is defined as:

$$\begin{aligned} \hat{\mathbf{x}} &= \mathbf{A}\,\hat{\mathbf{x}} + \mathbf{B}\,\mathbf{u} + \mathbf{L}\,(\mathbf{y} - \hat{\mathbf{y}}), \\ \hat{\mathbf{y}} &= \mathbf{C}\,\hat{\mathbf{x}}, \end{aligned} \tag{3}$$

where the cap over the variables indicates the variable belongs to the observer system, and **L** is the observer gain matrix. Observer error $\mathbf{e}$ is defined as the difference in state variables between the system and the observer system:

$$\mathbf{e} = \mathbf{x} - \hat{\mathbf{x}}, \quad \dot{\mathbf{e}} = (\mathbf{A} - \mathbf{L}\,\mathbf{C})\,\mathbf{e}, \tag{4}$$

where $\dot{\mathbf{e}}$ is time derivative of $\mathbf{e}$, but reformulated into a more appropriate format using Eq. (3). Error is in this case not a single value, but a system of values, and thus to minimize it a system norm has to be used. An H_2 system norm is used, and it forms the cost function of the optimisation process.

$$\min \quad \underbrace{||\Sigma_e(\mathbf{L})||_2}_{\substack{\mathrm{H}_2\ norm\ of \\ the\ error\ system}} \tag{5}$$

As derived in [6], the statements in Eq. (6) and Eq. (7) are equivalent:

$$\|\mathbf{H}\|_2 \leq \gamma, \tag{6}$$

There exists $\mathbf{P} \succ 0$, such that: (7.a)

$$\begin{pmatrix} -\mathbf{P} + \mathbf{C}^T\,\mathbf{C} & \mathbf{A}^T\,\mathbf{P} \\ \mathbf{P}\,\mathbf{A} & -\mathbf{P} \end{pmatrix} \prec 0, \tag{7.b}$$

$$trace(\mathbf{B}^T\,\mathbf{P}\,\mathbf{B}) < \gamma^2. \tag{7.c}$$

γ is a variable whose meaning isn't strictly defined but in this specific case it can be viewed as the upper bound on the H_2 norm of the error system. Symbols "$\succ$" and "$\prec$" are used to define that the matrix **P** in Eq. (7.a) is positive definite, and that the matrix in brackets in expression in Eq. (7.b) is negative definite. Eq. (5) is now replaced by

$$\min \quad \gamma^2, \tag{8}$$

along with its following constraints on the cost function. The new constraint in Eq. (7.b) is non-convex as it contains two variable terms: $\mathbf{P}\,\mathbf{L}$ and $\mathbf{L}^T\,\mathbf{P}$, which make it a bilinear matrix inequality. Standard procedure in solving that problem for observer systems is substituting $\mathbf{P}\,\mathbf{L}$ with $\mathbf{L}^*$, making it a linear matrix inequality problem once again. The problem with that substitution is that (in general) it only works if there are no structural constraints on the observer matrix $\mathbf{L}$, as zero and non-zero values of $\mathbf{L}^*$ and $\mathbf{L}$ must be equally distributed. Structural constraints are existent in this case, in the form of forcing sparsity on the would-be matrix $\mathbf{L}^*$. However, due to the nature of the problem of minimizing sensor count, after some columns of $\mathbf{L}^*$ are equal to zero, same corresponding columns of $\mathbf{L}$ need to be rendered zero as well, which incidentally makes the zero and non-zero values of both matrices equally distributed, therefore enabling the use of substitution $\mathbf{P}\,\mathbf{L} = \mathbf{L}^*$. With that substitution the problem becomes convex again. The cost function with additional constraints is now as follows:

$$\begin{aligned} &\min \quad \gamma^2 \\ &\text{such that:} \quad \mathbf{P} \succ 0\,, \\ &\qquad trace\,(\mathbf{B}^T\,\mathbf{P}\mathbf{B}) < \gamma^2, \\ &\qquad \begin{pmatrix} \mathbf{W}^T\,\mathbf{W} - \mathbf{P} & \mathbf{A}^T\,\mathbf{P} - \mathbf{C}^T\,\mathbf{L}^{*T} \\ \mathbf{P}\,\mathbf{A} - \mathbf{L}^{*T}\,\mathbf{C} & -\mathbf{P} \end{pmatrix} \prec 0. \end{aligned} \tag{9}$$

Matrix **W** is a weight matrix usually used to manipulate each sensor, but here it is used to either leave a sensor as is, or change its weight to zero, so it is equal to the C matrix that is used for the same purpose in this paper.

1.2. Sensor count minimization

Minimizing the sensor count, or in other words determining will a possible sensor location be utilized, is equivalent to minimizing the L_0 norm. Minimising the L_0 norm a non-convex problem. In theory it can be solved by trying out all possible combinations of sensor placement, but for practical purposes that is not feasible due to extremely high computational demands even for a modest number of sensor positions. Instead, the L_0 norm is relaxed into L_1 norm, which makes it numerically tractable. The relaxation process is described in [5]. In short, L_0 norm of each column *j:*

$$\left\| \sum_{i=1}^{n} |L_{ij}| \right\|_0 \tag{10}$$

is replaced with

$$\beta_j^{it} \sum_{i=1}^{n} |L_{ij}|, \tag{11}$$

where β_j^{it} is the weight of the *j* column, and *i* marks the iteration number. Weights are updated on each iteration to be equal to inverse of their values in the previous iteration,

$$\beta_j^{it} = \frac{1}{\varepsilon + \sum_{i=1}^{n} |L_{ij}^*|}, \tag{12}$$

therefore making the values of the columns irrelevant and only seeing them as having roughly a value of one or zero, which is basically an L_0 norm approximation. Some small value ε is introduced for numeric reasons. Term for sensor count minimization is now equal to

$$\sum_{j=1}^{n} \beta_j^{it} \sum_{i=1}^{n} |L_{ij}^*|. \tag{13}$$

It minimizes the count of L_0/L_1 norms of each $\mathbf{L}_j$ column, which approximates minimizing the total number of sensors.

1.3. Sensor grouping

Grouping of sensors is done by minimizing the sum of L_2 norms of each group of sensors, where L_2 norm of the group is L_2 norm on the sum of values of each sensor position's corresponding column in observer gain matrix $\mathbf{L}$:

$$\sum_{g} \sqrt{\sum_{j} \left(\left(\sum_{i} |L_{ij}| \right)^2 \right)}. \tag{14}$$

Sum for *i* sums all the values of a single column $\mathbf{L}_j$, sum for *j* sums the square values of forementioned column sums, and sum for *g* is the sum of L_2 norms of groups of sensors, each group containing (in this particular case) three consecutive columns *j*. The effect of that is the algorithm preferring to either use all or none of the sensors in each group. It is however not a strict constraint, so it is possible that the algorithm still uses only one or two sensors from a group.

1.4. Final cost function

Each of two additional terms from Eqs. (13) and (14) have their own factors α_1 and α_2 that are user adjustable. Their purpose is balancing the weight of each term to get the desired results. The full cost function, followed by constraints and additional formulae stands as:

$$\min \quad \underbrace{\gamma^2}_{\substack{Error \\ minimisation}} + \alpha_1 \cdot \underbrace{\sum_{j=1}^{m} \beta_j^{it} \sum_{i=1}^{n} |L_{ij}^*|}_{\substack{Sensor\ count \\ minimisation}} + \alpha_2 \cdot \underbrace{\sum_{g=1}^{m/3} \sqrt{\sum_{j=g\cdot 3-2}^{g\cdot 3} \left(\left(\sum_{i}^{n} |L_{ij}| \right)^2 \right)}}_{Sensor\ grouping} \tag{15}$$

such that $\mathbf{P} \succ 0$,

$$trag(\mathbf{B}^T\,\mathbf{PB}) < \gamma^2,$$

$$\begin{pmatrix} \mathbf{W}^T\,\mathbf{W} - \mathbf{P} & \mathbf{A}^T\,\mathbf{P} - \mathbf{C}^T\,\mathbf{L}^{*T} \\ \mathbf{P}\,\mathbf{A} - \mathbf{L}^{*T}\,\mathbf{C} & -\mathbf{P} \end{pmatrix} \prec 0,$$

$$\beta_j^{it} = \frac{1}{\varepsilon + \sum_{i=1}^{n} \left| L_{ij}^{*} \right|}.$$

2. USING THE ALGORITHM ON A BEAM STRUCTURE

While the intention of grouping three sensors together is to conveniently have each physical position contain either no sensors, or sensors in all three cartesian axes, for the purpose of testing the algorithm in its development stage it is used on a 2D problem. It's a simple problem to deal with for testing the grouping of sensors, which can then be expanded to a 3D case later.

The system used in this paper is a 2D Euler-Bernoulli beam as shown in Fig. 1.

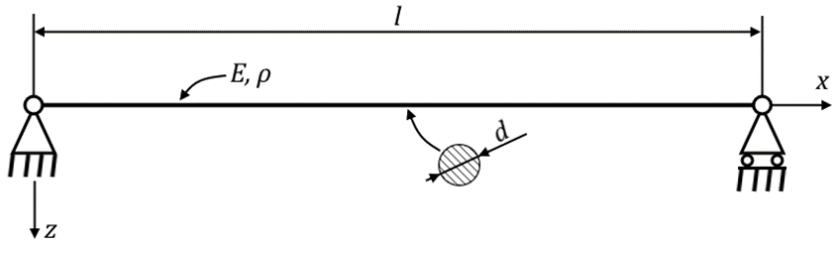

Figure 1. *Euler-Bernoulli beam used as an example*

It is discretized with 31 linear beam finite elements with degrees of freedom of deflection *w* (*z* axis) and rotation *φ* (*y* axis). The choice to use 31 finite elements is arbitrary.

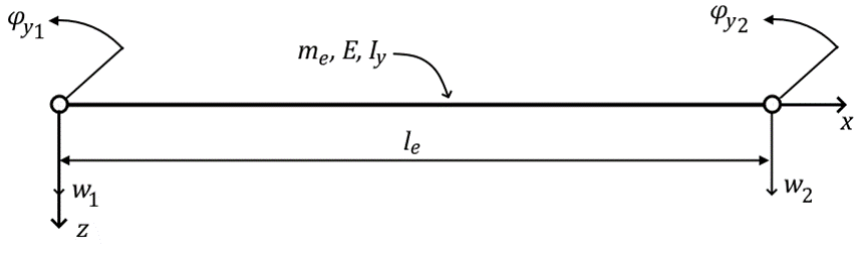

Figure 2. *Linear 2-D beam finite element*

Other noteworthy parameters used for FEM matrices are Rayleigh damping with eight most significant natural frequencies (or in other words first eight modes of vibration), and the lumped mass matrix.

3. RESULTS

Error minimization between the observer and the system yields results in the form of optimized values of the observer gain matrix $\mathbf{L}$. The diagram on Fig. 3 shows the sum of each column $\mathbf{L}_j$ on the *y* axis (each column corresponding to a single sensor), and all possible sensor locations on the *x* axis. If one imagines the edges of the visible *x*-axis as the start and end of the beam, black dots on the *x* axis can be thought of as FEM nodes, or in other words possible locations for both a displacement and velocity sensor (independently). In the case of a sensor position not being utilized, the sum of the column $\mathbf{L}_j$ is equal to zero.

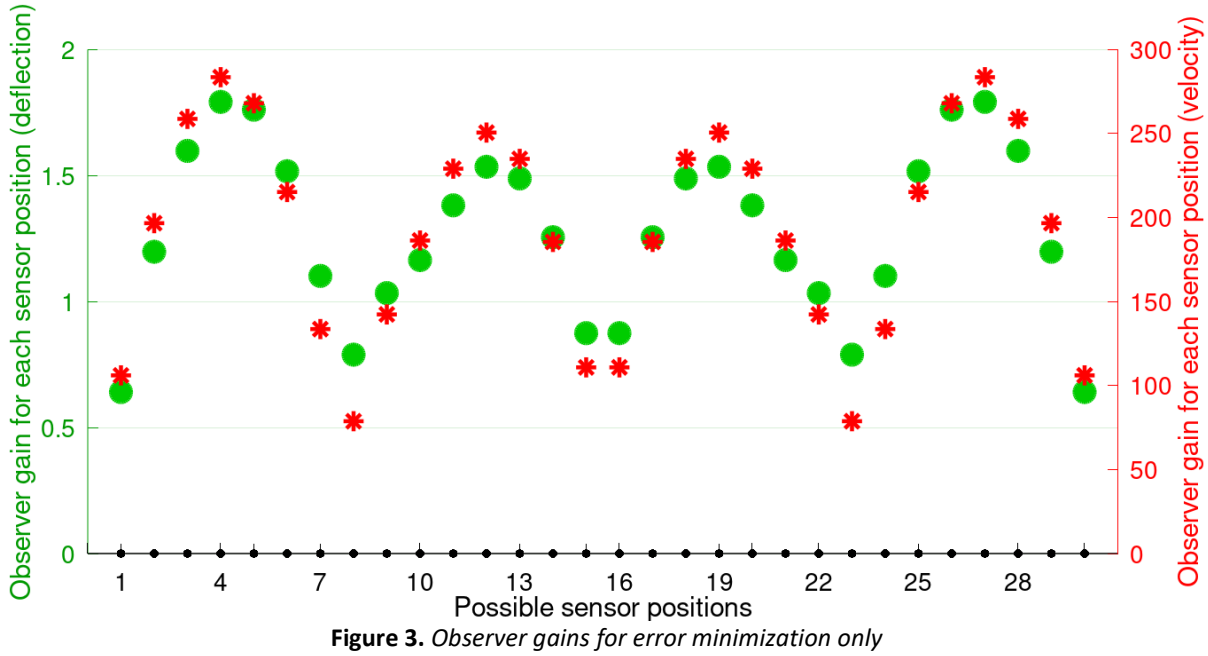

Figure 3. *Observer gains for error minimization only*

Note that all sensor locations are populated because there are no zero-value columns. With the addition of the sensor count minimization term, multiplied by the factor α_1, we observe the algorithm not utilizing all the possible sensor locations. Relationship between the factor α_1 and the utilized number of sensors is shown in the Fig. 4:

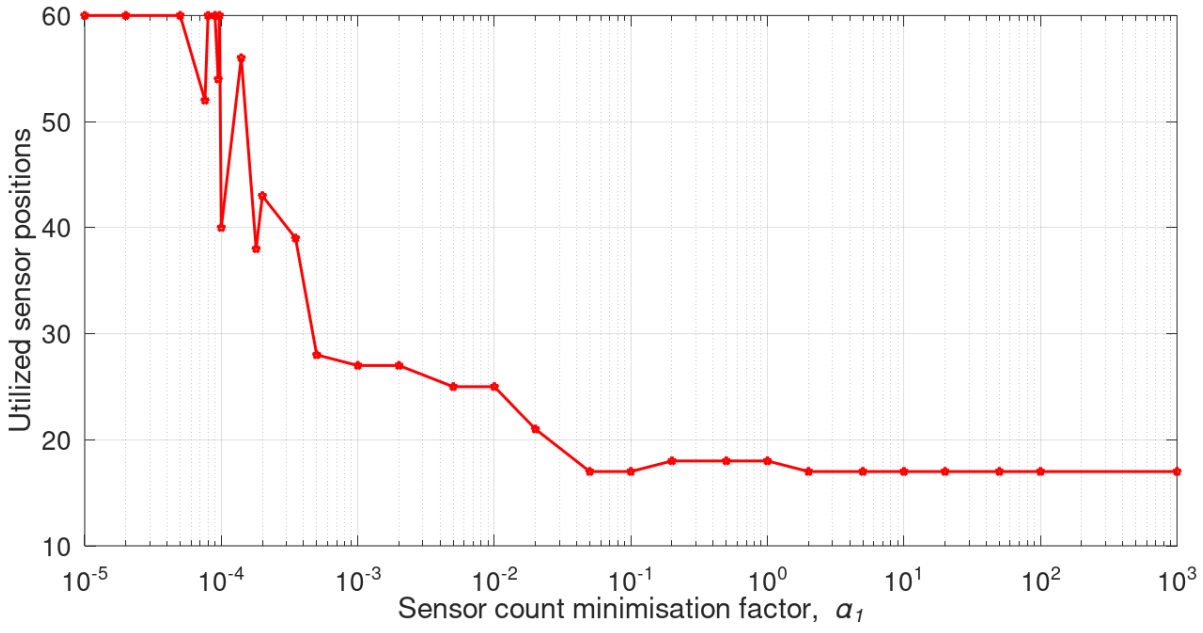

Figure 4. *Sensor count in relation to α_1 for only minimizing the error and sensor count*

Increasing α_1 decreases the number of utilized sensor positions, in a somewhat orderly fashion. Two examples of the resulting sensor locations are shown below in Fig. 4 and Fig. 5.

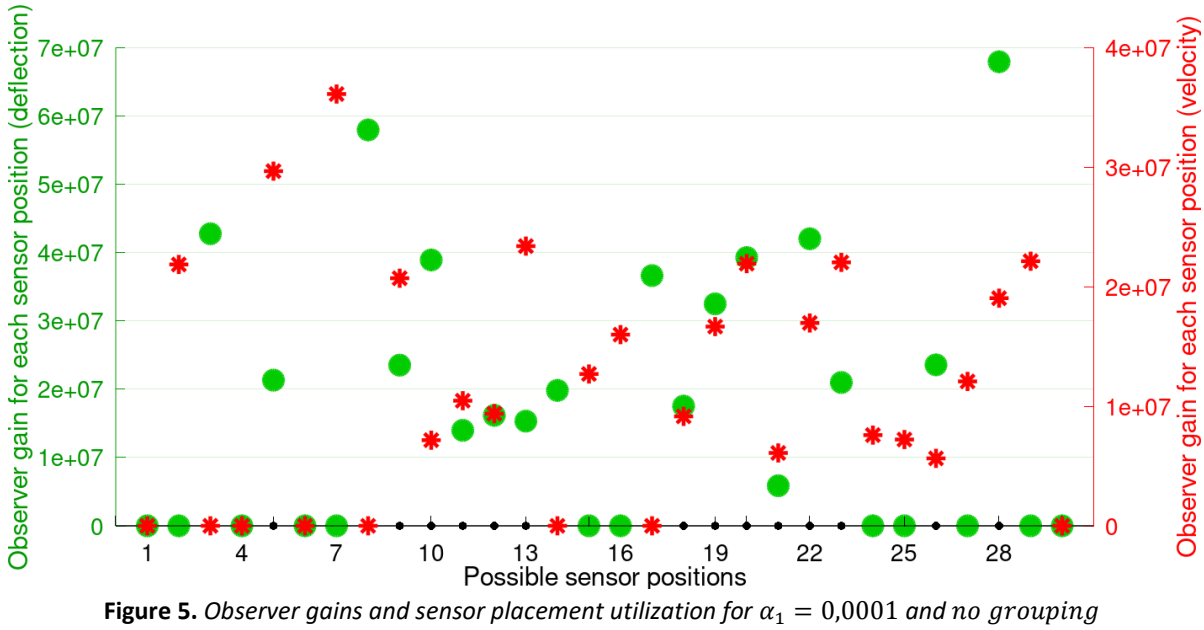

Figure 5. *Observer gains and sensor placement utilization for $\alpha_1 = 0{,}0001$ and no grouping*

Sensors that are not utilized have a corresponding value of their column equal to zero, meaning the ones that are not utilized are positioned on the *x*-axis in the diagrams.

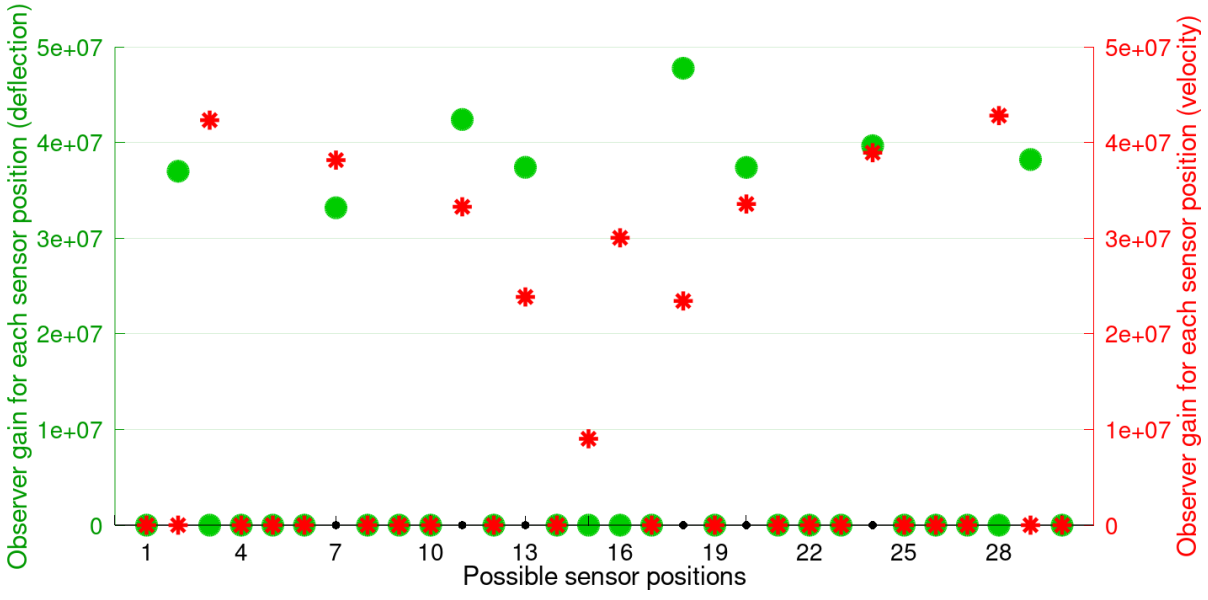

Figure 6. *Observer gains and sensor placement utilization for $\alpha_1 = 1$ and no grouping*

While the sensor count is being minimized with rising α_1, there is no clear pattern of grouping of sensors.

Finally, we add the third term with its factor α_2, which results in full cost function shown in Eq. 15. The diagram in Fig. 7 is analog to the one on Fig. 4.

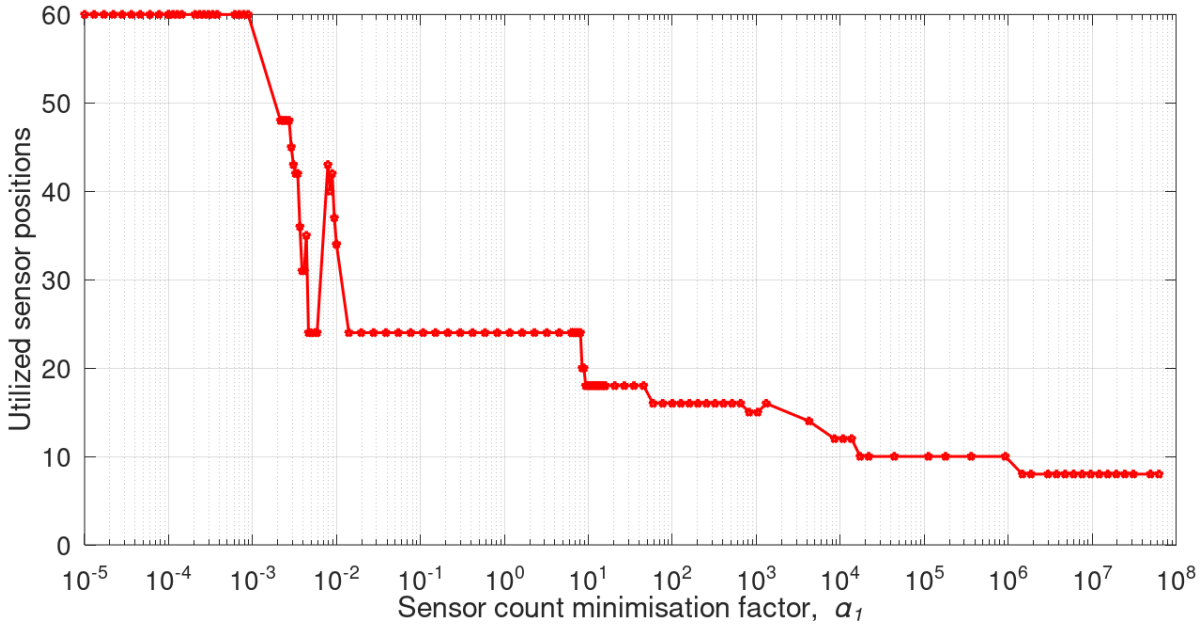

Figure 7. *Sensor count in relation to α_1 for the full cost function of the algorithm, $\alpha_2 = 1$*

Diagrams are similar in that, at first, when the algorithm starts to find solutions that don't include all sensors, the drop in utilized sensors as α_1 rises is sharp, but then it gradually slows down. The optimization that includes grouping of sensors (Fig. 7) behaves more stable, with less deviations. This is on par with what the literature predicts for group lasso algorithm [7], which is similar with the one in this paper. Next diagram compares the same α_1-sensor count relation for different α_2 values:

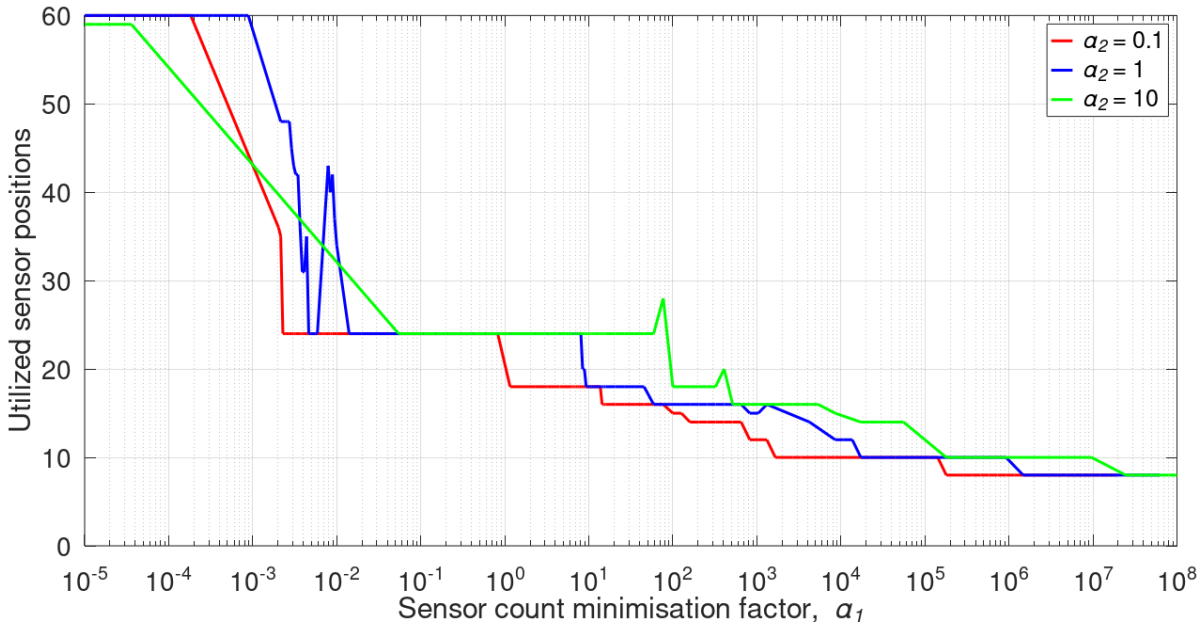

Figure 8. *Comparison of results with different α_2 values*

Factor that balances the grouping term of the cost function, α_2, does not influence the grouping of the sensors as much as it just shifts the solutions to a higher α_1 value. This was not expected, and it is not yet clear what causes such behavior; it needs further investigation beyond this paper. Lastly, we will show a few examples of sensor positions for $\alpha_2 = 1$ and varying values of α_1 (Fig. 9, 10 and 11).

Prescribed sensor groups contain three sensors each. Sensor positions are conveniently marked on every 4th position, so that each number is marking the first sensor of the group from left to right.

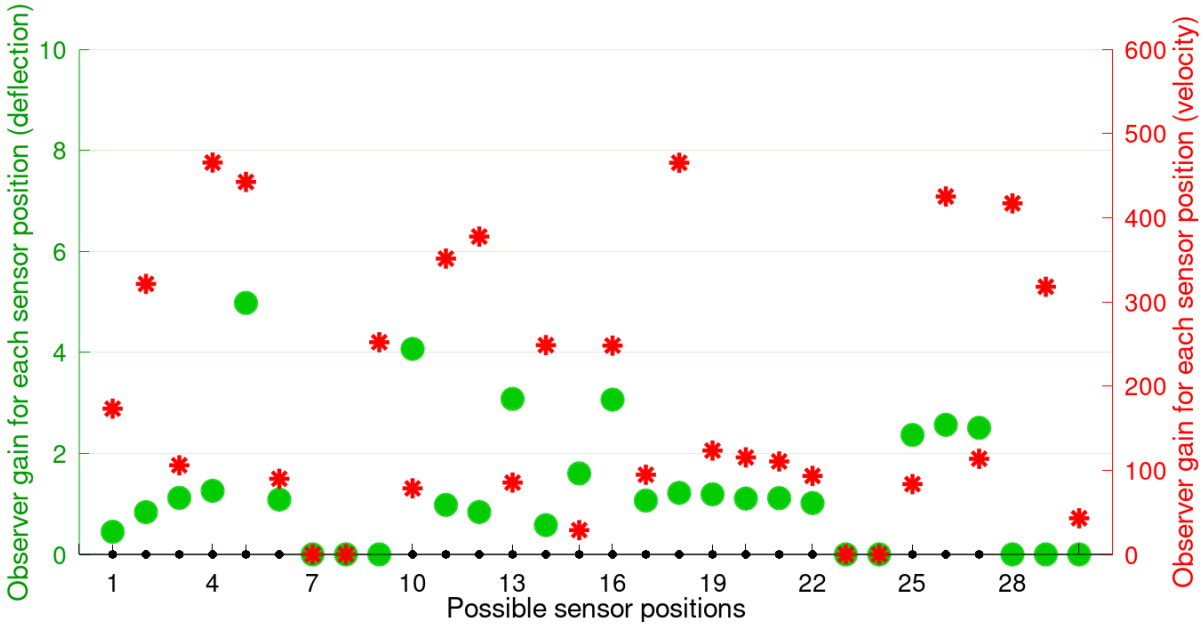

Figure 9. *Observer gains and sensor placement utilization for $\alpha_1 = 0{,}00243$ and $\alpha_2 = 1$*

While groups are not strictly populated or empty on Fig. 9, it is clear that there is a preference for doing so: 12 unpopulated sensor positions occupy only 5 groups. Also note that displacement sensor groups are not bound to velocity sensor groups, their overlapping is a product of the optimization process.

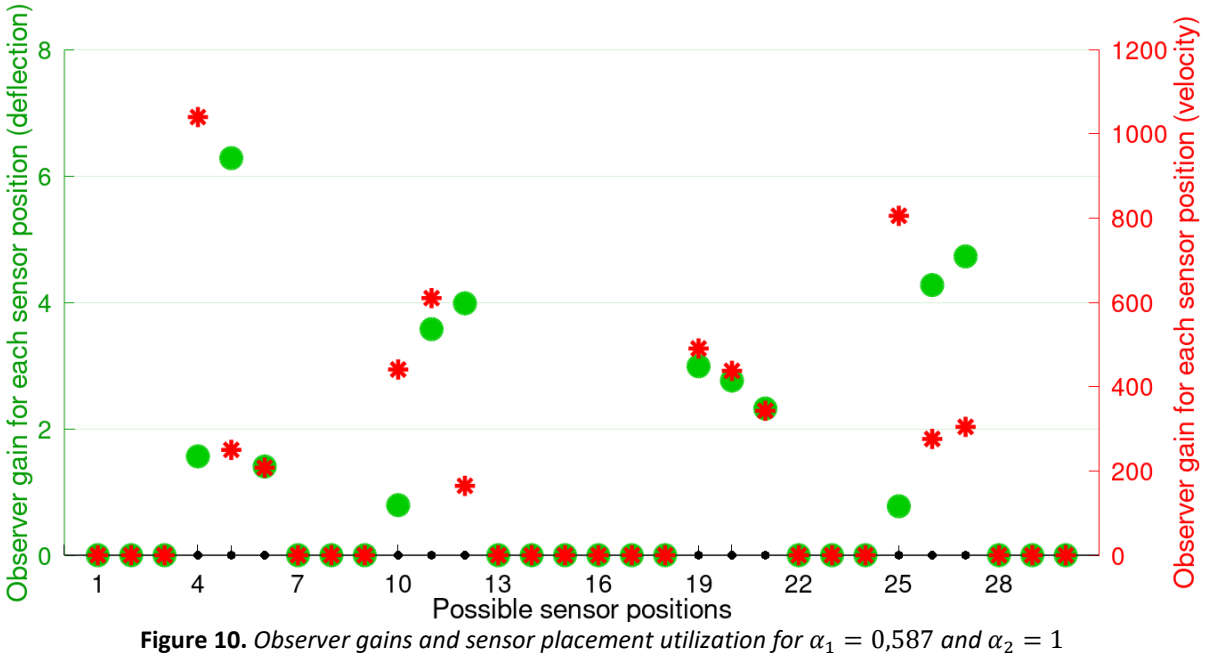

Figure 10. *Observer gains and sensor placement utilization for* $\alpha_1 = 0{,}587$ *and* $\alpha_2 = 1$

On Fig. 10 we see how all groups of sensors are either fully populated or empty. This is the ideal type of distribution and what this algorithm is intended to do. The observed tendency of the algorithm is to have longer, stable areas of dependency on α_1 where the groups of sensors are mostly or fully either populated or empty, with shorter transition areas in which there's a higher percentage of partially populated groups. When the result is aggressively pushed towards a small number of used sensors, as in Fig. 11, most groups tend to be partially populated.

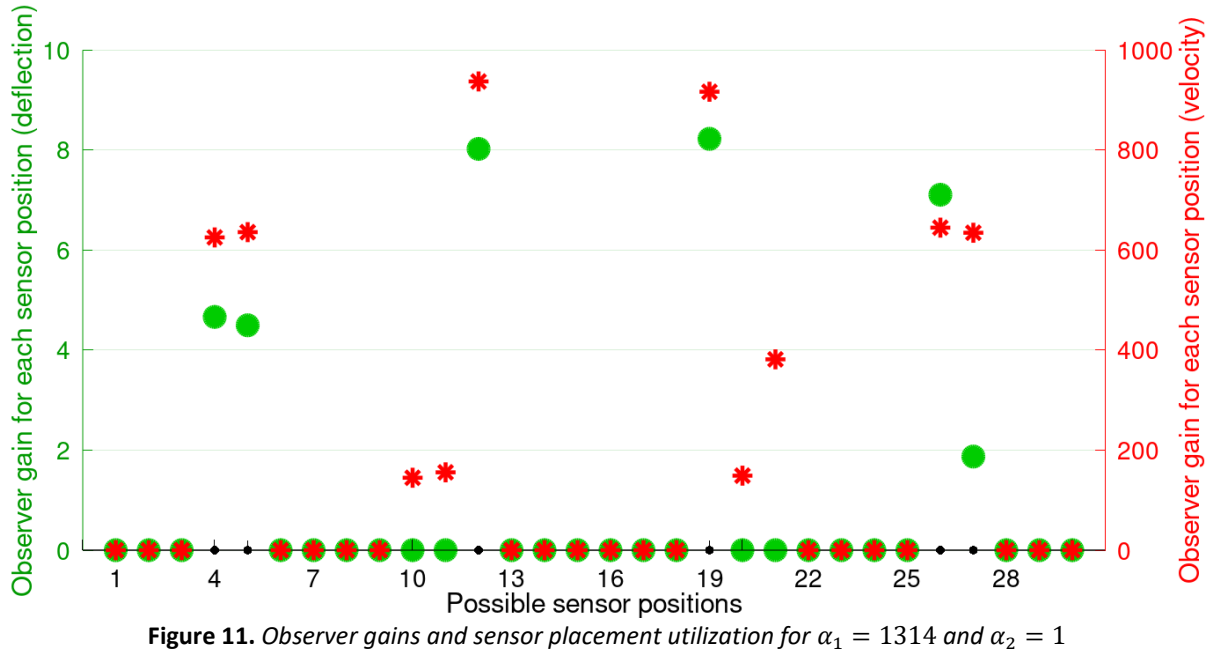

Figure 11. *Observer gains and sensor placement utilization for* $\alpha_1 = 1314$ *and* $\alpha_2 = 1$

4. CONCLUSION

The goal of the algorithm presented in this paper is to optimize the sensor quantity and placement for vibration measurement, where sensor positions are prescribed and grouped together, meaning that the whole group of sensor positions is either fully populated or fully unpopulated. The algorithm is using a procedure that could be viewed as a variation of the group lasso cost function, and it is successful in minimizing the sensor count and mostly grouping the sensors in prescribed groups. However, there are cases in which a group of sensor positions is only partially populated.

Increasing the weight of the grouping term in the cost function does not increase the grouping tendency of the algorithm. That issue needs further investigation. This is still a work in progress, and as such there will be further study and development to improve the results, and eventually validate them with experiments.

ACKNOWLEDGEMENTS

This work has been supported and co-funded by the European Union through the European Regional Development Fund, Operational Programme “Competitiveness and Cohesion” 2014 – 2020 of the Republic of Croatia, project “Protection of Structural Integrity in Energy and Transport” (Zacjel, KK.01.1.1.04.0056).

REFERENCES

[1] Tan, W., Zhang, L. (2019). Computational methodologies for optimal sensor placement in structural health monitoring: A review. *Structural Health Monitoring*, 4, 1287–1308.

[2] Joshi, S., Boyd, S. (2009). Sensor Selection via Convex Optimization. IEEE Transactions on Signal Processing, 57 (2), 451–462.

[3] Lin, F., Fardad, M., Jovanović, M. J. (2013). Design of Optimal Sparse Feedback Gains via the Alternating Direction Method of Multipliers. *IEEE Transactions on Automatic Control*, 58 (9), 2426–2431.

[4] Münz, U., Pfister, M., Wolfrum, P. (2014). Sensor and Actuator Placement for Linear Systems Based on H_2 and H_∞ Optimization. *IEEE Transactions on Automatic Control*, 59 (11), 2984–2989.

[5] Candes, M. J., Wakin, M. B., Boyd, S. P. (2008). Enhancing Sparsity by Reweighted L_1 Minimization. *Journal of Fourier Analysis and Applications*, 14, 877–905.

[6] Gahinet, P., Apkarian, P. (1994). A linear matrix inequality approach to H_∞ control. *Int. J. Robust Nonlin. Control*, vol. 4, pp. 421–448.

[7] Jenatton, R., Audibert, J.Y., Bach, F. (2010). Structured variable selection with sparsity-inducing norms. *Journal of machine learning research*, 12, 2077-2824.

Design and performance of a hysteretic dissipator

Mariella Diaferio[1]; Dora Foti[2]; Michela Lerna[3]; Maria Francesca Sabbà[4]

ABSTRACT [CALIBRI, 11PT, NEGRITA, CAPITAL LETTER, ALINEADO A LA IZQUIERDA]

In the present paper the optimal design of an energy dissipating shear panel made of aluminium and steel and the results of a nonlinear dynamic analysis of a frame equipped with the designed device are discussed. The geometrical configuration of the device is chosen in accordance with a parametric analysis performed to optimise the hysteretic behaviour of the device, and, in detail, the aim of the procedure is to maximize the plastic strain energy in the aluminium plate. Moreover, a steel frame was protected by means of the designed device and analysed numerically utilizing a finite element method. The dynamic response allows to evaluate the performance of the device showing its good dissipative behaviour, highlighted by the reduction of the global damage index and the inter-storey drifts.

Keywords: Passive control, yielding-based device, design optimization, non-linear dynamic analysis.

1. INTRODUCTION

In the field of seismic passive protection of structures an important role is played by devices able to reduce the energy entering the building. An increasing attention has been continuously paid towards the hysteretic devices during the last decades, aiming at the protection of structures affected by a seismic event. More in detail, metallic devices show a stable behaviour under cyclic loads, producing a wide hysteresis cycle which depends on the yielding limit of the material. The adoption of such anti-seismic devices would increase the stiffness of the structure, reduce the inter-story drifts and concentrate the damage in itself avoiding damage in the structural elements. Usually, such devices possess a wide dissipative capacity related to their dimensions. The limit of these kinds of Energy Dissipating Devices is that the dissipation capacity is activated only after they sustain large excursions in the inelastic field. As a consequence, the devices are ineffective for vibrations smaller than the inter-story drift that produces the yielding of the material composing the device.

A comprehensive state-of-art review of the development and implementation of metallic dampers in structural vibration control systems since the 1970s is provided in [1]. To reduce the displacement in correspondence of which the hysteresis cycles of the dissipators are activated, [2,3] proposed the use

[1] *Department of Civil, Environmental, Land, Building Engineering and Chemistry (DICATECH). Polytechnic University of Bari (ITALY).* mariella.diaferio@poliba.it
[2] *Department of Civil Engineering Sciences and Architecture (DICAR). Polytechnic University of Bari (ITALY).* dora.foti@poliba.it *(Corresponding author)*
[3] *Department of Civil Engineering Sciences and Architecture (DICAR). Polytechnic University of Bari (ITALY).* michela.lerna@poliba.it
[4] *Department of Civil Engineering Sciences and Architecture (DICAR). Polytechnic University of Bari (ITALY).* mariafrancesca.sabba@poliba.it

of low-yield steel (LYS) to build dissipators with a shear behavior. Nevertheless, the costs and the not easy availability of low-yield steel pushed the research towards alternative but similar materials, such as aluminum [4]. In fact, aluminum is characterized by a low yielding stress, lower than the LYS one, and a wide plastic field. The use of hysteretic devices has been investigated considering both far-field and near-field earthquakes [4-13]. In [4-13] hysteretic devices made with ordinary aluminum alloys have been proposed and the results of numerical and experimental investigations are shown. In [5] the use of pure aluminum for low-yield-strength Shear Panels (SPs) is proposed showing significant results. These devices allow a considerable improvement in the seismic performance of the structure in terms of rigidity, strength and ductility, with a rational control of the level of damage without having an uneconomical increase in the size of the main structural members.

The present work deals with the design of a new energy dissipating shear panel with the final aim of maximizing its hysteric energy dissipation, the objective is reached by optimizing the device dimensions. Then, the results of the numerical modelling are utilized to estimate the response of a steel frame protected by means of the "optimal" device and subjected to seven earthquakes

2. ALUMINIUM-STEEL SHEAR PANEL

The improvement of the functionality of a shear panel for seismic protection can be guaranteed either by the successful activation at low yielding limit, minimizing the deformation effects triggered by small vibrations, or by expanding the limits of the plastic wide range, i.e. increasing the shear buckling threshold, and reducing the possibility of the out-of-plane instability as well. However, the two conditions are conflicting since the first condition requires shortened panel dimensions, while the second one suggests maximizing the dimensions. Therefore, the proposal is to have a three-panel device: a central one is made of aluminum and would guarantee high energy dissipation, and two external panels, which enclose the first panel, would limit the out-of-plane possible instability. The choice was set on the S235 steel for the external plates while 1000 aluminum alloy was adopted for the central plate to take advantage of its low yielding stress and its considerably wide plastic range. The mechanical properties of the two materials are summarized in Table 1.

Table 1. Materials mechanical properties

Mechanical properties		S235	1000 Al series
f_y	Yield strength [MPa]	235	30
f_U	ultimate tensile strength [MPa]	360	90
ε_U	elongation at break [%]	26	40
E	Elastic modulus [GPa]	206	70

The central plate is manufactured with internal raised parts; able to interfere with spaces of the openings of the external steel plates, enhancing the connection strength and preventing any possible slip phenomena. The external steel plates were oriented toward the out-of-plane with their highest possible inertia. A typical configuration of the panel is presented in Figure 1.

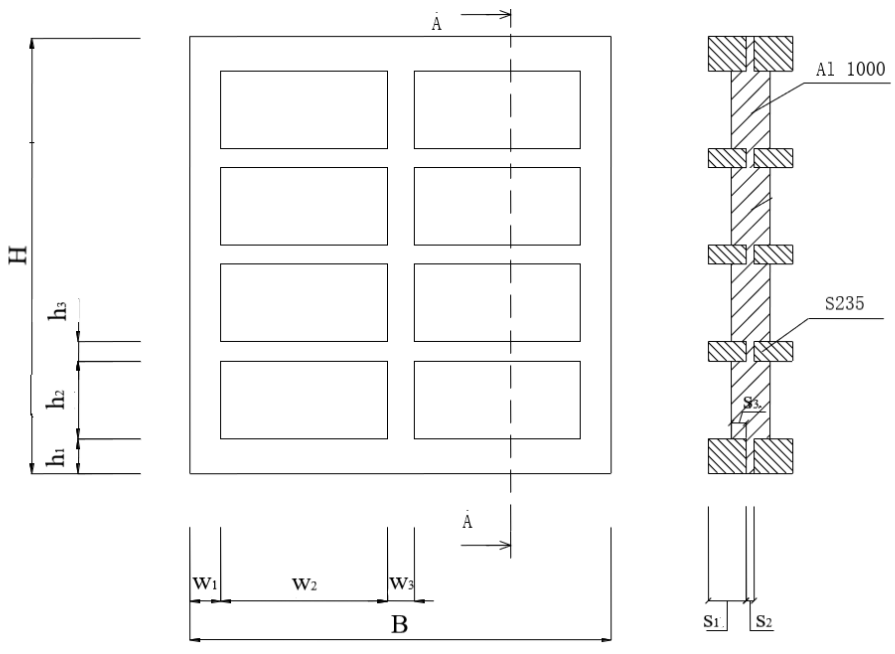

Figure 1. *Dissipator geometrical parameters for the optimization procedure.*

The geometrical details have been set by performing an optimization procedure with ANSYS software [14] in which a 20-node solid element (SOLID90) was adopted for the panel, where the lower band was fixed and the upper one left free. The adopted materials were described by bi-linear laws in agreement with the above-mentioned values in Table 1. Finally, it is worth pointing out that the assumed restraint conditions could facilitate the installation of the device which could be connected to the structure by means of bolting or welding connections along the lower and upper boundaries.

The ultimate design was obtained mainly by forcing a horizontal displacement equal to 2‰ of the inter-storey height of the frame at which the panel must be installed, which is 4 mm. Then, a 4-step optimization procedure was developed on the FE model as follows:

- The choice of the objective function to be maximized;
- The identification of the geometrical parameters of the device;
- Setting of rational ranges of variability for each parameter;
- Setting of additional constraint functions and/or boundary conditions defined in accordance with the geometrical dimensions of the structure to protect.

The plastic strain energy of the aluminum plate was chosen as an objective function; then the geometrical parameters as well as the rational ranges of variation have been set as reported in Table 2.

At the end, additional limits were set by imposing a maximum stress equal to 90 MPa and some panel dimensions, in detail the panel height was limited within the range 380-450 mm while the width range was limited within 150-600 mm. The previous limits were defined starting from the frame inside which the panel will be placed [15]. After then, many "*a priori*" configurations of the panel could be set for the optimization routine development, where different possibilities of the

openings were considered to get the best solution in terms of the highest energy dissipated by the device.

Table 2. Optimization procedure: adopted ranges of the geometrical parameters of the device.

Geometrical Parameters		**Variability range**
N_c	columns number of aluminium windows	2-6
N_r	row number of aluminium windows	1-4
w_1	peripheral vertical stiffener width [mm]	5-20
w_2	aluminium windows width [mm]	20-200
w_3	interior vertical stiffener width [mm]	5-20
h_1	external horizontal stiffener width [mm]	5-20
h_2	aluminium windows height [mm]	20-400
h_3	internal horizontal stiffener width [mm]	5-20
s_1	steel plate thickness [mm]	1-10
s_2	aluminium plate central thickness [mm]	1-4
s_3	aluminium windows projection [mm]	1-4

In Figure 2 the device realized in accordance with the results of the optimization procedure is shown. The device is characterized by 12 aluminum windows, arranged in 4 rows (Nr =4) and 3 columns (Nc =3), whose dimensions have the width equal to 40 mm and the height equal to 100 mm, and the projection equal to 2mm. The minimum thickness of the aluminum plate is equal to 3 mm. The steel stiffeners are realized by mean of a steel plate whose thickness is equal to 5 mm, moreover the vertical stiffeners width is equal to 8 mm and the horizontal stiffeners width is equal to 10 mm.

Figure 2. *Aluminum - steel dissipator with 12 windows (N_c =3, N_r =4) and w_1= 8mm, w_2=40mm, w_3=8mm, h_1=10mm, h_2=100mm, h_3=10mm, s_1=5mm, s_2=3mm, s_3=2mm.*

The optimization procedure presented in this work is intending to find the proper dimensions of the shear panels of the device characterized by thicker steel plates than the aluminum one, unlike the optimization analysis which assumed a thicker aluminum plate [5]. The choice of thicker steel plates was considered since a uniform plasticization of the aluminum plate can be guaranteed as resulted

by the analysis (Figure 3a), which would increase the dissipative capacity of the device. Finally, the Von Mises strain and the constitutive law of the proposed shear panel are presented in Figures 3a and 3b.

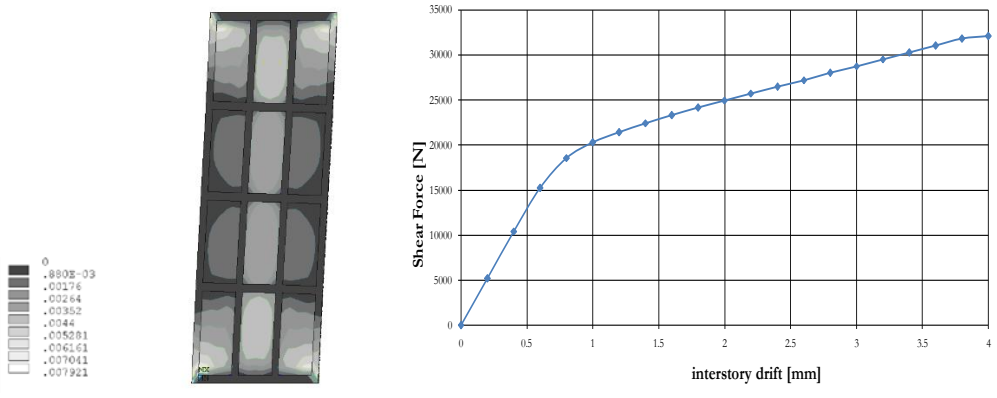

(a) (b)

Figure 3. *Aluminum - steel device: a) Von Mises strain; b) constitutive law.*

3. DYNAMIC PERFORMANCE OF THE ALUMINIUM-STEEL DEVICE

The goal of the work is to investigate the beneficial effects of one of the proposed aluminum– steel device introduced in a 2D steel frame, by performing a non-linear dynamical analysis. The software SAP 2000 Nonlinear [16] has been used to develop a numerical analysis.

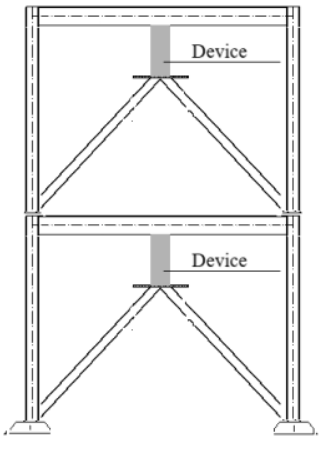

Figure 4. *2D frame with aluminum-steel devices.*

The frame equipped with the shear panel is a 2-storey steel frame consisting of IPE180 beams welded to HEB140 columns (Figure 4). The single storey is 2 m height and the columns are considered fixed at the base. Moreover, chevron type bracings are realized by HEA100 section and a welded plate is placed below the storey level allowing the installation of the anti-seismic device. The shear panels are connected to a steel panel connecting the chevron type bracing to the upper floor

by means of bolted connection along the upper and the lower edges. In detail, a plate is welded at the end of the chevrons to allow the installation of the shear panel, while at the other end the shear panel is bolted to the beam. Hence, it was assumed that the device is rigidly connected to the beam and to the chevrons.

The devices were modeled as non-linear links whose behavior is modelled in accordance with the Fig. 3b. The non-linear dynamic analysis was performed subjecting the steel frame, which was considered in two possible configurations, i.e. with ("protected frame") and without ("bare frame") aluminum-steel dissipators, to seven natural earthquakes. In particular, as shown in Figure 5, the seven earthquakes are characterized by a seismic intensity equal to 0.35 g, compatible with the response spectrum provided by Eurocode 8 [17] for soil type B, Seismic Zone 1.

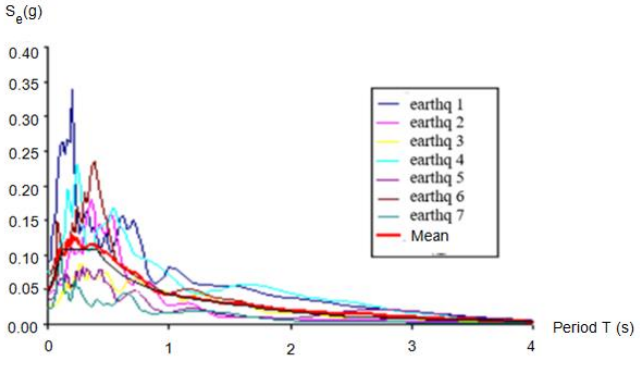

Figure 5. *Response spectrum of the examined natural earthquakes compatible with Eurocode 8 for type B soil in seismic zone 1, PGA=0.35g.*

Table 3 shows the modal frequencies of the bare and protected frames. In particular, there is a significant increase in the bending modes frequencies as a consequence of the dissipator installation.

Table 3. Modal frequencies of the bare and protected frame

Mode	Bare frame frequency [Hz]	Protected frame frequency [Hz]
I bending	3.56	10.64
II bending	12.53	29.14

The global damage index – defined as the ratio of the top displacement on the total height of the frame – is shown in Figure 6. The obtained results show that in all cases no plasticization occurs in the frames and the protected frame has a response three or four times smaller than the bare frame.

The maximum inter-storey drift index, defined as the ratio of the maximum inter-storey drift to the height of the storey, was evaluated for each of the seven earthquakes in order to emphasize the effects of the aluminum-steel dissipators. Figure 7 shows the indices evaluated at each floor. The inter-storey drifts of the protected frame for all the considered earthquakes do not exceed the limit of 0.5% that is the estimated security limit with reference to the first plasticization of the frame [15].

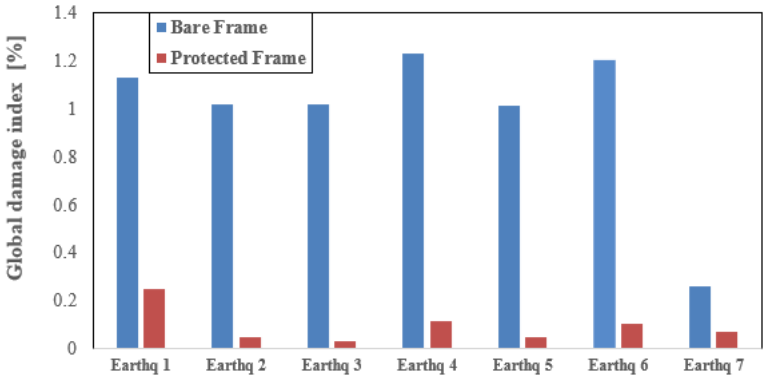

Figure 6. *Global damage index for earthquakes compatible with Eurocode 8 for type B soil in seismic zone 1, PGA=0.35g.*

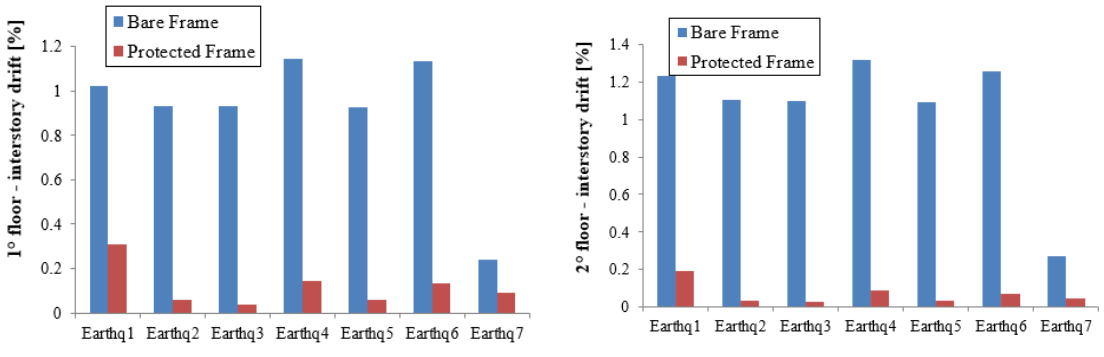

(a) (b)

Figure 7. *Maximum inter-story drift index: earthquakes compatible with Eurocode 8 for type B soils in seismic zone 1, PGA=0.35g a) 1° floor and b) 2° floor.*

4. CONCLUSIONS

In the field of anti-seismic buildings, the conception and design of an aluminum and steel hysteretic dissipator is presented. The first phase of the presented study is the definition of the geometric configuration of the device through a numerical optimization process. The proposed device has been applied to a 2D steel frame in order to evaluate the influence on the dynamic response of the structure to a series of earthquakes.

The panel design and the numerical evaluation of the dynamic properties of the aforementioned frame highlighted the efficacy of the proposed device for the protection of structures subjected to earthquakes. In detail, the performed numerical analysis allowed the evaluation of the global damage index and the inter-storey drifts at each floor and it underlined that the designed shear panel may be an effective device to be installed for the protection of structures from seismic actions.

Further studies can be conducted to deepen and improve the effectiveness of this protection device.

REFERENCES

[1] Nakashima, M., Iwai, S., Iwata, M., Takeuchi, T., Konomi, S., Akazawa, T., & Saburi, K. (1994). Energy dissipation behaviour of shear panels made of low yield steel. Earthquake engineering & structural dynamics, 23(12), 1299-1313.

[2] Nakashima, M., Akazawa, T., & Tsuji, B. (1995). Strain-hardening behavior of shear panels made of low-yield steel. II: Model. Journal of structural Engineering, 121(12), 1750-1757.

[3] Rai, D.C. and Wallace, B. J. (1998). Aluminium shear-link for enhanced seismic resistance. Earthquake Engineering and Structural Dynamics, 27(4), 315-342.

[4] De Matteis, G., Mazzolani, F.M. and Panico, S. (2007). Pure aluminium shear panels as dissipative devices in moment-resisting steel frames. Earthquake Engineering and Structural Dynamics, 36(7), 841-859.

[5] Diaferio M. (2018) Performance of seismic shear panels under near-field motions. International Journal of Engineering and Technology(UAE), 7 (2), 196 – 200.

[6] Diaferio, M., Foti, D. (2016) Mechanical behavior of buildings subjected to impulsive motions. Bulletin of Earthquake Engineering, 14 (3), 849-862.

[7] Ponzo, F.C., Di Cesare, A., Nigro, D., Vulcano, A., Mazza, F., Dolce, M., Moroni, C. (2012) Jet-pacs project: Dynamic experimental tests and numerical results obtained for a steel frame equipped with hysteretic damped chevron braces. Journal of Earthquake Engineering, 16 (5), 662-685.

[8] Foti, D., Diaferio, M., Nobile, R. (2013) Dynamic behavior of new aluminum-steel energy dissipating devices. Structural Control and Health Monitoring, 20 (7), 1106-1119.

[9] D. FOTI, M. DIAFERIO, R. NOBILE: "Optimal Design of a New Seismic Passive Protection Device Made in Aluminium and Steel", An International Journal of Structural Engineering and Mechanics, 35 n. 1:119-122, May 2010, ISSN: 1225-4568.

[10] D. FOTI, L. M. BOZZO, F. LOPEZ-ALMANSA: "Numerical Efficiency Assessment of Energy Dissipators for Seismic Protection of Buildings", Earthquake Engineering and Structural Dynamics, Wiley & Sons, Ltd., Chichester, UK, Vol. 27, pp. 543-556, 1998, ISSN: 0098-8847.

[11] D. FOTI: "On the Optimum Placement of Dissipators in a Steel Model Building Subjected to Shaking-Table Tests", The Open Construction and Building Technology Journal, vol. 8, 2014, p.142-152, ISSN: 1874-8368, DOI:10.2174/1874836801408010142

[12] D. FOTI, R. NOBILE: "Optimum Design of a New Hysteretic Dissipater", chapter 12 in Design Optimization of Active and Passive Structural Control Systems by N.D. Lagaros, V. Plevris, C.C. Mitropoulous, 2013, pp. 274-299; Ed. IGC Global USA, Hershey PA 17033 USA, DOI: 10.4018/978-1-4666-2029-2, ISBN 978-1-4666-2029-2 (hardcover) -- ISBN 978-1-4666-2030-8 (ebook) -- ISBN 978-1-4666-2031-5 (print & perpetual access), 2012.

[13] Javanmardi, A., Ibrahim, Z., Ghaedi, K., Ghadim, H. B., & Hanif, M. U. (2020). State-of-the-art review of metallic dampers: testing, development and implementation. Archives of Computational Methods in Engineering, 27(2), 455-478.

[14] ANSYS – Engineering Analysis System, ANSYS Inc., Canonsburg, PA (1998).

[15] Ponzo, F. C., Cardone, D., Di Cesare, A., Moroni, C., Nigro, D., & Vigoriti, G. (2007). Dynamic tests on JETPACS steel frame: experimental model set up. *DPC-RELUIS JETPACS Report*, (3).

[16] SAP2000 – Integrated finite element analysis and design of structures. Computers and Structures Inc.; Berkeley, CA (2008).

[17] European Code, (2005). Eurocode 8: Design of structures for earthquake resistance-part 1: general rules, seismic actions and rules for buildings. *Brussels: European Committee for Standardization.*

EXTENDING THE FATIGUE LIFE OF SLENDER STEEL FOOTBRIDGES WITH TUNED MASS DAMPERS

Jiménez-Alonso, Javier Fernando[1]; Soria, José Manuel[2]; M. Díaz, Iván[3] and Sáez, Andrés[4]

ABSTRACT

A possible effect of pedestrian-induced vibrations in slender steel footbridges is the reduction of their lifetime caused by the fatigue damage. The large number of footbridges built during the last years together with the increase of the pedestrian demand originated by the urban growth may originate a new potential scenario in which the extension of the fatigue lifecycle of these structures via the improvement of their dynamic behavior may be required. In this sense, a new necessity arises; the analysis of the performance of different retrofitting techniques when they are used to cope with this problem. Among the different alternatives, the possibility of using tuned mass dampers to achieve this objective is analyzed in this study. Thus, two feasibility analysis are performed herein: (i) to analyze under which circumstances a fatigue damage event may occur; and (ii) to avoid its occurrence via the robust design of tuned mass dampers.

Keywords: fatigue assessment; human-induced vibrations; footbridges; pedestrian traffic; tuned mass dampers.

1. INTRODUCTION

During the last decades of the previous century, the urban development of the main European cities made necessary the construction of circumferential highways to both improve the vehicle circulation and avoid traffic congestions in these urban areas. Despite the benefits, which these transportation channels have provided for the habitability and evolution of these cities, they may constitute a barrier for the remaining urban transport means [1] since these ring roads divided every urban area into two sub-regions: (i) an inner; and (ii) an outer one. For the particular case of the pedestrian mobility, multiple footbridges have been built, during the last twenty years, in order to guarantee an adequate permeability between the mentioned sub-regions.

Some common characteristics can be observed in these footbridges [2]: (i) their main span, due to the geometrical constraints generated by the lower highway, is around 40-50 m (so it is expected that their first vertical natural frequency is inside the range that characterizes the pedestrian step frequency [3]); (ii) their typology is simple with few supplementary elements (so low damping ratios are expected [3]);

[1] *Departamento de Mecánica de Medios Continuos. Universidad de Sevilla (España). jfjimenez@us.es (Corresponding author)*
[2] *Departamento de Teoría de la Señal. Universidad de Alcalá de Henares (España). jm.soria@uah.es*
[3] *Departamento de Mecánica de Medios Continuos. UPM (España). ivan.munoz@upm.es*
[4] *Departamento de Mecánica de Medios Continuos. Universidad de Sevilla (España). andres@us.es*

and (iii) their dynamic behaviour is not analysed in detail (neither numerically during their design phase nor experimentally after their construction) since high pedestrian densities are not expected on these footbridges due to their localization [3].

There are few events, reported in literature, in which these structures have shown service or failure problems. However, similarly as it has happened with other civil engineering infrastructures [4], the traffic demand on them has increased gradually during the last years, due to the great expansion experienced by the abovementioned cities (their urban centres have exceeded the peripheral barrier generated by the ring road). Thus, this changing scenario makes necessary to assess the dynamic behaviour of these footbridges under these new traffic conditions. Fig. 1 illustrates, as example, this phenomenon for the particular case of Madrid (Spain).

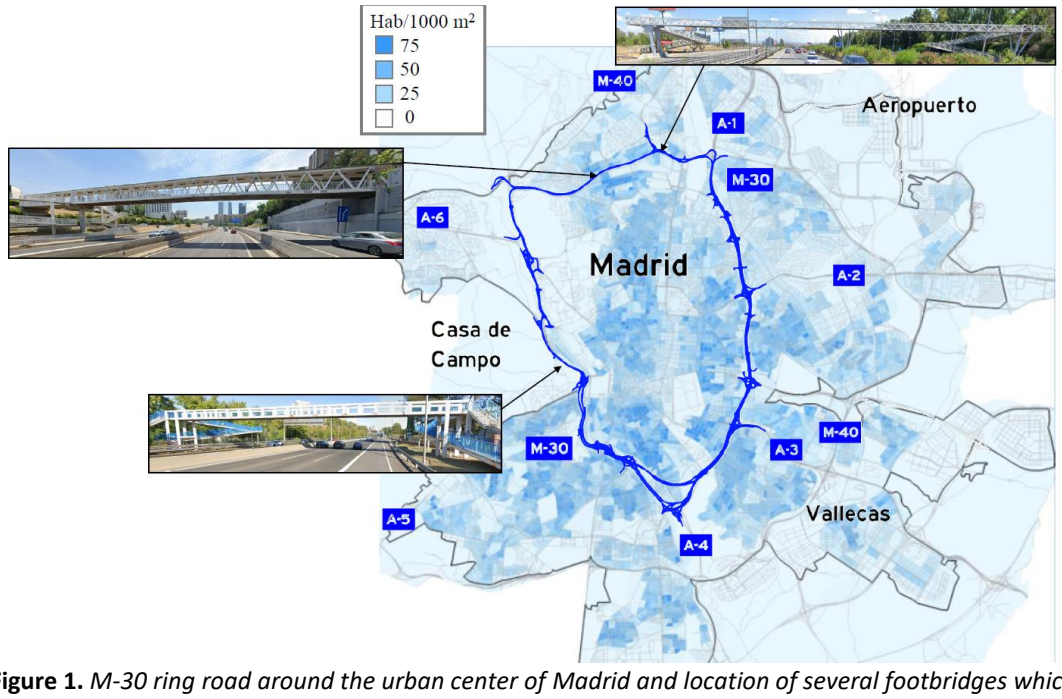

Figure 1. *M-30 ring road around the urban center of Madrid and location of several footbridges which cross over the abovementioned highway.*

As one of the main failures, that the increase of the traffic demand has originated in other civil engineering structures (for instance in steel bridges subjected to road or train loads [4]), is the fatigue damage, both the fatigue assessment of these existing footbridges under pedestrian action and the improvement of their behaviour via cost-efficient interventions [5] are interesting challenges to be tackled in the coming years.

In order to shed some light to this problem, two feasibility analysis have been performed herein. First, the possibility of the occurrence of a fatigue failure in an existing steel footbridge has been assessed via a numerical case study in which the fatigue damage of a benchmark footbridge has been computed in terms of different pedestrian intensities [6]. The uncertainty, associated with the modification of the modal properties of the footbridge during its lifecycle, has been simulated via a fuzzy approach [7]. Subsequently, the possibility of extending the lifetime of existing steel footbridges via the installation of tuned mass dampers (TMDs) has been assessed. For this purpose, a TMD has been designed, according to the motion-based design method [8], to guarantee the absence of fatigue failure in the

benchmark footbridge subjected to different pedestrian flows. Finally, some concluding remarks have been included to close the manuscript.

2. FATIGUE ASSESSMENT OF STEEL FOOTBRIDGES SUBJECTED TO PEDESTRIAN-INDUCED VIBRATIONS

According to the best of authors' knowledge, there is not currently any specific design guideline for the fatigue assessment of footbridges caused by pedestrian-induced vibrations. Thus, a practical framework has been considered herein. According to this framework, based on the so-called safe life method [9] recommended by the European code [10], the fatigue assessment of any structural element may be checked following an 8-step process [11]. These steps may be defined as (i) to select the structural element to analyse; (ii) to establish the load process (defining the traffic demand on the structure); (iii) to compute the stress history in the structural element for each load process; (iv) to perform the cycle counting (the rainflow counting method has been taken into account herein); (v) to compute the stress range, $\Delta\sigma$, spectrum from the previous cycle counting; (vi) to compute the number of cycles to failure, N_i; (vii) to evaluate the cumulated fatigue damage, D_s, according to the Palmgren-Miner's rule [9]; and (viii) to check the fulfilment of the fatigue limit state.

In order to compute either the fatigue strength or the number or cycles to failure, N_i, the S-N curves, as they are defined by European code [10], have been taken into account herein. The number of cycles to failure, N_i, may be determined as follow, in terms of the corresponding stress range, $\Delta\sigma_i$:

$$N_i = \begin{cases} 2\cdot 10^6 \cdot \left(\dfrac{\dfrac{\Delta\sigma_C}{1.35}}{\Delta\sigma_i}\right)^3 & \text{if } \Delta\sigma_i \geq \dfrac{\Delta\sigma_D}{1.35} \text{ and } \Delta\sigma_D = 0.737\Delta\sigma_C \\ 5\cdot 10^6 \cdot \left(\dfrac{\dfrac{\Delta\sigma_D}{1.35}}{\Delta\sigma_i}\right)^5 & \text{if } \dfrac{\Delta\sigma_L}{1.35} \leq \Delta\sigma_i \leq \dfrac{\Delta\sigma_D}{1.35} \text{ and } \Delta\sigma_L = 0.549\Delta\sigma_D \\ \infty & \text{if } \Delta\sigma_i \leq \dfrac{\Delta\sigma_L}{1.35} \end{cases} \quad (1)$$

where $\Delta\sigma_C$ is the reference fatigue strength at $2\cdot 10^6$ cycles; $\Delta\sigma_D$ is the constant amplitude fatigue limit; and $\Delta\sigma_L$ is the cut-off limit.

Additionally, the cumulated fatigue damage, D_s, may be determined considering the following expression:

$$D_s = \sum_{i=1}^{n_{tot}} \frac{n_i}{N_i} < D_{lim} \quad (2)$$

where n_i is the number of cyles corresponding to the stress range, $\Delta\sigma_i$; n_{tot} is the number of stress range classes; and D_{lim} is the cumulated fatigue damage limit (D_{lim}=1 according to the European code [10]).

In order to adapt the mentioned general method to the particular case of the fatigue assessment of existing footbridges, the key aspect is the definition of traffic demand (pedestrian flows) [6]. For this purpose, two different guidelines have been considered. Thus, for the definition of the vertical walking pedestrian load, the recommendations of the Synpex guidelines [3] have been considered. Additionally, for the characterization of the pedestrian flow rate, q_p, the recommendations of the Highway Capacity Manual (HCM) [12] have been taken into account. According to these traffic guidelines, the pedestrian flow rate, q_p, is defined in terms of the level of service (LOS) of the path in which the pedestrian flow moves. These guidelines define six different LOS from A (the best operating conditions, ≤ 16

P=Person/min/m) to F (the worst operating conditions, > 75 P/min/m). In order to link the pedestrian flow rate, q_p, defined by the HCM [12] with the equivalent vertical walking pedestrian load described by the Synpex guidelines [3] the following relationships are considered [13]:

$$q_p = d_p \cdot v_p \tag{3}$$

$$f_p = 0.35v_p^3 - 1.53v_p^2 + 2.93v_p \tag{4}$$

where d_p is the pedestrian density [P/m^2]; v_p is the pedestrian velocity [m/s] and f_p is the step frequency [Hz].

In this manner, the fatigue assessment of any structural element of a steel footbridge may be performed following these steps: (i) a LOS is considered in terms of the location and expected traffic on the footbridge; (ii) a train of vertical walking pedestrian loads are defined in terms of the mentioned LOS; (iii) the dynamic response of the footbridge is computed under the mentioned pedestrian action; (iv) the stress history of the considered structural element is determined based on the dynamic response; (v) the cycle counting is computed using the rainflow counting method; (vi) the stress range spectrum is determined based on the cycle counting; (vii) the number of cycles to failure is computed for each stress range of the spectrum; and (viii) the cumulated damage ratio is computed.

Finally, the random character of this process associated with both the variability of the pedestrian action and the modification of the modal properties of the footbridge during its overall lifecycle must be considered for the fatigue assessment [6]. In this sense, the recommendations of the Synpex guidelines [3] has been adopted herein for the pedestrian action; and a fuzzy approach, which is described in section 3, has been considered to simulate the variability of the modal properties.

3. ROBUST DESIGN OF TUNED MASS DAMPERS TO EXTEND THE FATIGUE LIFETIME OF STEEL FOOTBRIDGES

The motion-based design (MBD) method [8] is currently one of the most common approaches for the robust design of intelligent control systems when these damping devices are used to mitigate the pedestrian-induced vibrations in buildings and civil engineering structures. According to this method, this design problem may be formulated as an optimization problem [8], whose main objective is to find the mechanical parameters of the device that, minimizing its cost, guarantee the fulfilment of the design requirements. In this study, the fulfilment of the fatigue limit state of the structure, according to the recommendations of European code [10], is established as the design requirement to be met. Thus, the MBD method may be formulated as a constrained single-objective optimization problem as follows:

$$\text{Minimize } f(\{\theta\})$$

$$\text{Subjected to } \begin{matrix} g_{eq,j}(\{\theta\}) = g_{eq,j}^* & j = 1,2,\dots,s \\ g_j(\{\theta\}) \le g_j^* & j = 1,2,\dots,q \end{matrix} \tag{5}$$

$$\{\theta^l\} = \{\theta_i^l\} \le \{\theta\} = \{\theta_i\} \le \{\theta^u\} = \{\theta_i^u\}\ i = 1,2,\dots,n_d$$

where $f(\{\theta\})$ is the objective function, $g_{eq,j}(\{\theta\})$ is the *j-th* equality constraint, $g_{eq,j}^*$ is the threshold of the *j-th* equality constraint, s is the number of equality constraints, $g_j(\{\theta\})$ is the *j-th* inequality constraint, g_j^* is the threshold of the *j-th* inequality constraint, q is the number of inequality constraints, $\{\theta^l\}$ and $\{\theta^u\}$ are, respectively, the lower and upper bounds of the vector of design variables, $\{\theta\}$, and n_d is the total number of design variables.

For the design of TMD considering the MBD method, the following design variables are normally considered: (i) the mass ratio, $\mu = m_d/m_s$ (where m_d is the mass of the TMD and m_s is the effective

mass of the considered vibration mode of the structure); (ii) the frequency ratio, $\delta_d = f_d/f_s$ (where f_d is the natural frequency of the TMD [Hz]; and f_s is the natural frequency of the considered vibration mode of the structure [Hz]); and (iii) the damping ratio of the TMD, ζ_d; [-].

Thus, four key aspects are considered to particularize the MBD method to this problem: (i) the objective function is defined in terms of the value of the mass ratio, μ; (ii) genetic algorithms have been selected to solve the optimization problem due to the nonlinear relation between the constraints and the design variables; (iii) the numerical quantification of the uncertainty associated with the variation of the modal properties of the structure (related to the modification of the operational, environmental, degradation and damage conditions) is simulated via a fuzzy approach [7] (inequality constraints); and (iv) a design criterion (the H_∞ criterion) is set to constrain the form of the frequency response function of the controlled structure (equality constraints) [8].

In order to simulate the mentioned uncertain conditions, a fuzzy approach has been considered herein. According to this approach, the modal properties of the structure may be considered as uncorrelated fuzzy variables, $\tilde{\xi}$. Thus, the quantification of the uncertainty about a certain event may be computed by considering the possibility that a physical parameter takes a certain value. A membership function, $\tilde{\eta}_{\tilde{\xi}}$, may be assigned to each fuzzy variable. The membership function assigns to each fuzzy variable, $\tilde{\xi}$, a grade of membership ranging between 0 and 1. Thus, grade 1 (upper grade) is assigned to the nominal values, ξ_n, which means a 100 % of belief, and grade 0 (lower grade) is assigned to the maximum variability of the considered fuzzy variable, which means a 0% of belief. It is commonly considered as membership function, a triangular one, $\widetilde{\Lambda}$., which may be defined as:

$$\tilde{\eta}_{\tilde{\xi}} = \widetilde{\Lambda}(\xi_n, \alpha_l \cdot \xi_n, \alpha_u \cdot \xi_n) \tag{6}$$

where α_l is a reduction factor and α_u is an incremental factor to establish the variation range of the fuzzy variable, $\tilde{\xi}$.

Based on the associated membership functions, the α-levels, or, α-cuts, may be determined. These levels define the different grades of possibility associated with the fuzzy variables. After certain α-level is set for the different fuzzy variables, the maximum response of the system for this grade of possibility is determined via a combinatorial analysis. The sampling size for the combinational analysis is performed via a sensitivity analysis. Thus, the maximum value of the response corresponding to a certain α–level allows defining the inequality constraints for a fuzzy approach.

In this way, the formulation of the design optimization algorithm based on the H_∞ criterion may be written as:

$$\begin{gathered} \text{find } \{\theta\} = \mu \text{ optimize } f(\mu) = \mu. \\ g_{eq,1} = \delta_d - \frac{1}{1+\mu} = 0 \\ \text{Subjected to } g_{eq,2} = \zeta_d - \sqrt{\frac{3\mu}{8(1+\mu)}} = 0 \\ g_1 = \frac{D_\alpha}{D_{lim}} - 1 \leq 0 \\ 0.00 \leq \mu \leq 0.05 \end{gathered} \tag{7}$$

where D_α is the maximum cumulated fatigue damage of the structure, D_s, for the considered α-level.

4. APPLICATION EXAMPLE

Both to analyse the sensitivity of the fatigue behaviour of a steel footbridge when the traffic demand increases and to assess the performance of the TMDs as retrofit method to extend the fatigue lifetime of these structures the following application example has been carried out.

For this purpose, a numerical footbridge has been adopted here as benchmark [14]. The footbridge is a simple supported structure with a single span of 38.85 m of length. The main structural system is configured by two lateral Warren steel trusses. The trusses are curved with a vertical curvature radius of 450 m. The height of the trusses is 1.21 m and their lateral separation is 2.90 m. Both the upper and lower chords of the trusses consist of rectangular hollow section 400x200x12 mm, and the diagonal and strut elements consist of rectangular hollow section 120x120x8 mm. These trusses are braced transversally between their lower chords by strut elements. A deck of the footbridge is formed by a reinforced concrete slab of 0.10 m of thickness which rests on the strut elements configuring a composite steel-concrete section. The width of the concrete slab is 2.50 m. Fig. 2 shows the general configuration of this footbridge.

A finite element model of the footbridge was developed using a commercial package [15]. Both beam elements, BEAM188 (2 nodes per element, 6 d.o.f. in each node), and shell elements, SHELL181 (4 nodes per element, 6 d.o.f. in each node) has been considered for this purpose. The finite element model of the footbridge is composed by a mesh of 646 beam elements and 540 shell elements (Fig. 2). A linear behaviour is assumed for the constitutive law of both constitutive materials, reinforced concrete and steel. The mechanical properties adopted are: (i) for the reinforced concrete, a Young's modulus, E_c =31000 MPa, a Poisson's ratio, ν_c=0.20 and a density, ρ_c=2500 kg/m^3; and (ii) for the steel, a Young's modulus, E_s =210000 MPa, a Poisson's ratio, ν_s=0.30 and a density, ρ_s=7850 kg/m^3. A proportional damping for the structure is assumed herein. For this purpose, a damping ratio, ζ_s, about 0.4 % has been considered following the recommendations of Synpex guidelines [3].

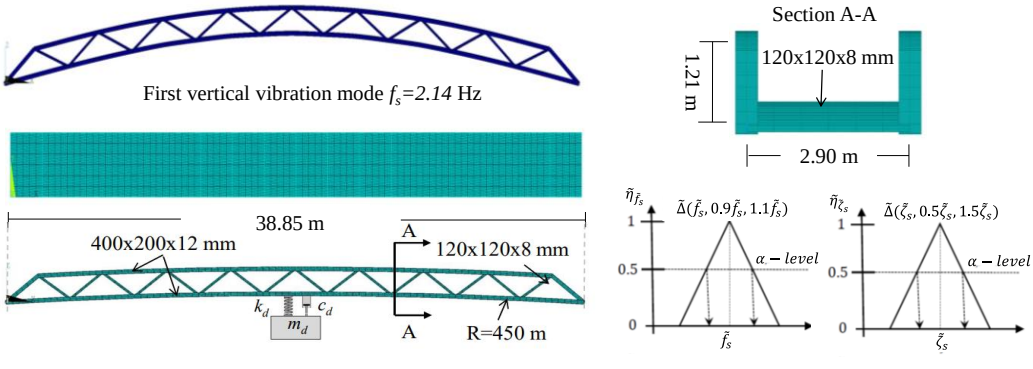

Figure 2. *Description of the benchmark footbridge, first vertical vibration mode and triangular membership functions, $\tilde{\Delta}$, of the two fuzzy variables (where $\tilde{f}_s$ is the first vertical natural frequency and $\tilde{\zeta}_s$ is the associated damping ratio) considered to simulate the uncertain conditions.*

The numerical modal parameters of the footbridge have been obtained via a numerical modal analysis. The natural frequency (f_s = 2.14 Hz) of the first vertical vibration mode (Fig. 2) and its associated modal mass (m_s=34706 kg) have been determined. As the natural frequency of this vibration mode is within the range that characterizes the vertical walking pedestrian action [3], so that it is expected that the footbridge may suffer from fatigue damage during its overall lifecycle. In order to overcome this limitation, a TMD has been installed at its mid-span and designed according to the MBD method. Additionally, the uncertainty of the modal properties of the structure has been taken into account in this study. For this purpose, both the first vertical natural frequency, f_s, and its associated damping ratio, ζ_s, are assumed as fuzzy variables which follow triangular membership functions. A variation range of ±10% and ±50% have been assumed respectively to characterize these functions (Fig. 2). As structural element to perform the fatigue assessment, the upper chord at the mid-span of the structure

has been taken into account herein. The Eurocode curve 71 is adopted as category detail for the definition of the S-N curve [10]. For computing the total number of cycles during the overall lifecycle of the footbridge the following assumptions have been performed: (i) the footbridge is "in service" during 8 hours/day; (ii) the footbridge is used for the pedestrians during 6 days/week; and (iii) the expected lifetime of the structure is about 100 years.

For our purpose two feasibility analysis have been performed. In the first analysis, the cumulated fatigue damage has been assessed in terms of the pedestrian flow and the uncertainty level. As result of this analysis, Fig. 3a shows the cumulated fatigue damage, D_s, of this footbridge in terms of the pedestrian flow and the considered α −level. In the second analysis, a TMD has been designed, according to the MBD method, to extend the fatigue lifetime of this footbridge. Fig.3b shows the mass ratio, μ, needed to avoid the occurrence of a fatigue damage event in terms of the above mentioned variables.

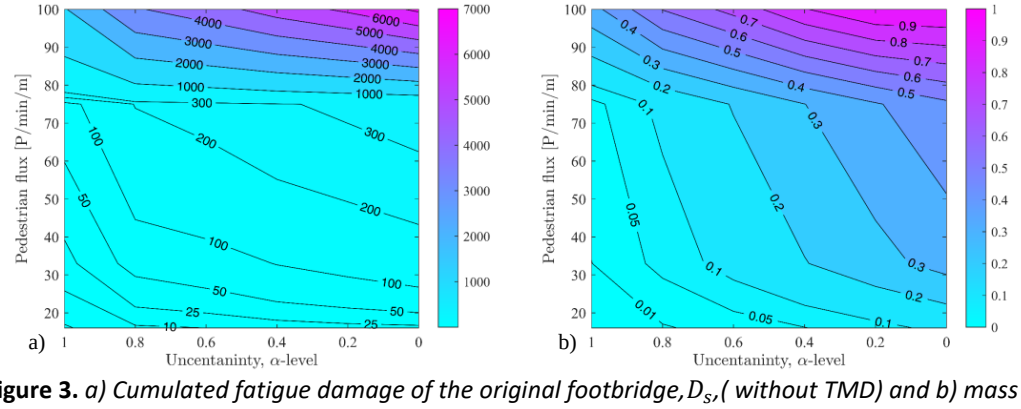

Figure 3. *a) Cumulated fatigue damage of the original footbridge, D_s, (without TMD) and b) mass ratio of the TMD, μ [%], in terms of the traffic demand (pedestrian flow) and uncertainty α-level.*

Two main conclusions can be extracted from this study: (i) the great influence that an increase of the traffic demand has on the fatigue behavior of slender steel footbridges (specially under uncertain conditions); and (ii) the good performance shown by TMDs to extend the lifetime of existing footbridges independently of the uncertain conditions considered (as mass ratio, μ, lower than 1.1 %).

5. CONCLUSIONS

In this manuscript two feasibility analysis have been performed to shed some light to two questions: (i) if an increase in the traffic demand may reduce significantly the fatigue life of existing steel footbridges; and (ii) if TMDs may be used as a cost-effective solution to extend the fatigue lifetime of these structures. For this purpose, the safe life method has been adapted for the particular case of the fatigue assessment of steel footbridges. Additionally the MBD method under uncertain conditions has been adapted for the robust design of TMDs when these vibration absorbers are employed to improve the fatigue behaviour of these structures. Finally, a numerical steel footbridge has been considered as benchmark herein. Two sensitivity analysis have been performed on this structure. First, the fatigue assessment of its upper chord in terms of the pedestrian flow rate and the uncertain conditions has been computed. Second, the mass ratio of a TMD installed in its mid-span has been evaluated, according to the MBD method, in terms of the abovementioned variables. As result of this study, both the influence of the increase of the traffic demand on the fatigue assessment of existing steel footbridges and the possibility of using TMDs as a cost-effective tool to improve the fatigue behaviour of these structures have been highlighted.

ACKNOWLEDGEMENTS

This work was partially funded by two Spanish research projects: (i) RTI2018-094945-B-C21 (Ministerio de Economía y Competitividad and the European Regional Development Fund); and (ii) SEED-SD RTI2018-099639-B-I00 (Ministerio de Ciencia, Innovación y Universidades).

REFERENCES

[1] Nugmanova, A., Arndt, W.H., Hossain, M.A., Kim, J.R. (2019). Effectiveness of Ring Roads in Reducing Traffic Congestion in Cities for Long Run: Big Almaty Ring Road Case Study. *Sustainability, 11, 4973(1-26)*.

[2] Oliveira, C.S. (2014). Fundamental Frequencies of Vibration of Footbridges in Portugal: From in Situ Measurements to Numerical Modelling. *Shock and Vibration, Article ID 925437*.

[3] Butz, C., Heinemeyer, C.H., Goldack, A., Keil, A., Lukic, M., Caetano, E., *et al*. (2007).Advanced load models for synchronous pedestrian excitation and optimised design guidelines for steel footbridges (SYNPEX). RFCS-Research Project RFS-CR-03019.

[4] Pipinato, A. (2018). Extending the lifetime of steel truss bridges by cost-efficient strengthening interventions. *Structure and Infrastructure Engineering, 14(12), 1611-1627*.

[5] Pipinato, A. (2019). Extending the Fatigue Life of Steel Truss Bridges with Tuned Mass Damper Systems. *Advances in Civil Engineering, ID 5409013, 1-16.*

[6] Pérez-Aracil, J., Hernandez-Díaz, A.M., Jiménez-Alonso, J.F., Puerta-Lopez F.J. (2018) Fatigue Assessment of a Slender Footbridge Based on an Updated Finite Element Model. *Key Engineering Materials, 774, 589-594.*

[7] Cuevas R. G., Jiménez-Alonso J.F., Martínez F., Díaz I.M. (2021). Uncertainty-based approaches for the lateral vibration serviceability assessment of slender footbridges. *Structures, 33, 3475-3485*.

[8] Jimenez-Alonso J.F., Saez A. (2018). Motion-based design of TMD for vibrating footbridges under uncertainty conditions. *Smart Structures and Systems, 21(6), 727-740*.

[9] Nussbaumer A., Borges L. & Davaine L. (2012). Fatigue design of steel and composite structures: Eurocode 3: Design of steel structures, part 1-9 fatigue; Eurocode 4: Design of composite steel and concrete structures, p.334. Ernst & Sohn.

[10] Eurocode 3: Design of steel structures - Part 1-9: Fatigue.

[11] Marques F., Moutinho C., Magalhães F., Caetano E. *et a*l. (2014). Analysis of dynamic and fatigue effects in an old metallic riveted bridge. *Journal of Constructional Steel Research, 99, 85–101.*

[12] Transportation research board. Highway Capacity Manual. National Research Council, Washington, DC 2000; 113.

[13] Bertram, J.E.A. & Ruina, A. (2001). Multiple Walking Speed–frequency Relations are Predicted by Constrained Optimization. *Journal of Theoretical Biology, 209(4), 445-453.*

[14] Setra/AFGC. (2006). Technical Guide: Footbridges–Assessment of vibrational behaviour of footbridges under pedestrian loading.

[15] Ansys Mechanical APDL 21 R1. Ansys Inc 2021 www.ansys.com (accessed September 2, 2021)

Numerical analysis of aluminium lattice structure with K-joints

Nikolić, Nina[1]; Šćepanović, Biljana[2]

ABSTRACT

A welded spatial aluminium lattice structure made of circular hollow section (CHS) profiles with uniplanar K-joints is analysed. Detailed numerical analysis of the lattice structure as a whole has been conducted in order to obtain the comprehensive results. Finite elements method (FEM) has been employed, by means of ANSYS software, with a variation of different relevant parameters, so to enlarge the insight into the static behaviour of the structure, as well as to provide a better ground basis for its design. For the high-quality FEM analysis, it is necessary to include appropriately the welds in detailed model of considered joint, because of the heat affected zone (HAZ), which is very important for aluminium as material. The HAZ is analysed herein for one of the most loaded joints. Finally, the paper aims recommendations for optimal FEM model of K-joint aluminium lattice structure in terms of time consumption vs quality and accuracy of results, that are going to be validated experimentally.

Keywords: aluminium, lattice structure, FEM analysis, K-joint, welds, HAZ, CHS.

1. INTRODUCTION

In the engineering practice, aluminium is more and more used as main structural material not only for industrial buildings, antenna towers, electrical line towers, platforms, bridges, structures in areas with extremely low temperatures etc, but also in various types of public buildings, particularly in spectacle buildings. That is mainly because of aluminium high strength and high resistance to different environmental conditions ("wear-and-tear"), as well as its aesthetics quality. Further advantages of typical aluminium structures – planar (2D) and spatial (3D) lattice structures – are light weight, low costs of transport and maintenance, as well as fast assembling. Among these structures, lattice structures made of circular hollow section (CHS) profiles have prominent role. In addition to the outstanding resistance characteristics, particularly those related to stability issues, CHS profiles provide development of attractive architectural forms. Their smooth round shape and outer surface significantly smaller than in case of open profiles, make them suitable from the aspect of aerodynamic behaviour of structure. These characteristics are also in favour of CHS profiles in case when anticorrosion protection is needed. Connections between CHS profiles in spatial (3D) aluminium lattice structures may be uniplanar (in one plane – 2D) or multiplanar (in several planes – 3D).

Connections represent not only important, but possibly critical issue in the design and construction of any type of structures, particularly those of aluminium. Beside the structural design problems, joints

[1] *Faculty of Civil Engineering. University of Montenegro (MONTENEGRO). nikolicnina1991@gmail.com*
[2] *Faculty of Civil Engineering. University of Montenegro (MONTENEGRO). biljanas@ucg.ac.me (Corresponding author)*

also influence the costs of the structure. In the case of aluminium structures, a wide choice of joining techniques is available nowadays, being able to fulfil the most different structural and non-structural requirements.

In this paper, spatial aluminium lattice structure made of CHS profiles with uniplanar K-joints, subjected to static load, is analysed. Considered K-joints are formed by direct welding of narrower CHS profiles (brace elements, having smaller radius), to the outer surface of wider CHS profiles (chord elements, with bigger radius). High stress concentration located exactly in the weld, due to discontinuous stiffness in this region, makes the joint highly critical part of the lattice structure and causes common fracture that often occurs on the surface of the chord tube. That is why special attention is devoted to adequate analysis of joints in this work.

Detailed numerical analysis of the lattice structure as a whole has been conducted in order to obtain the comprehensive results. Finite elements method (FEM) has been employed, by means of ANSYS software, with a variation of different relevant parameters, so to enlarge the insight into the static behaviour of the structure, as well as to provide a better ground basis for its design.

2. FAILURE MODES AND MODELS OF JOINTS BETWEEN CHS PROFILES

2.1. Design procedure by European Standards – EN Eurocodes

The methods and procedures of aluminium structures design in accordance with the European Standards (EN Eurocodes) are based on the principles of steel structures design, taking into account properties and specifics of aluminium and its alloys. Unlike the European Standard for steel structures design (EN 1993), the Eurocode for aluminium structures design (EN 1999) does not contain a separate part devoted to connections and joints, such as EN 1993-1-8 [1]. Design of joints in aluminium structures is only briefly elaborated within EN 1999-1-1 [2], without paying special attention to hollow section joints in lattice structures. Hence, engineers should refer to EN 1993-1-8 regarding this particular design issue. Failure modes for joints between CHS profiles, typical for lattice structures with axial forces in members, according to EN 1993-1-8, are illustrated in Figure 1 [1].

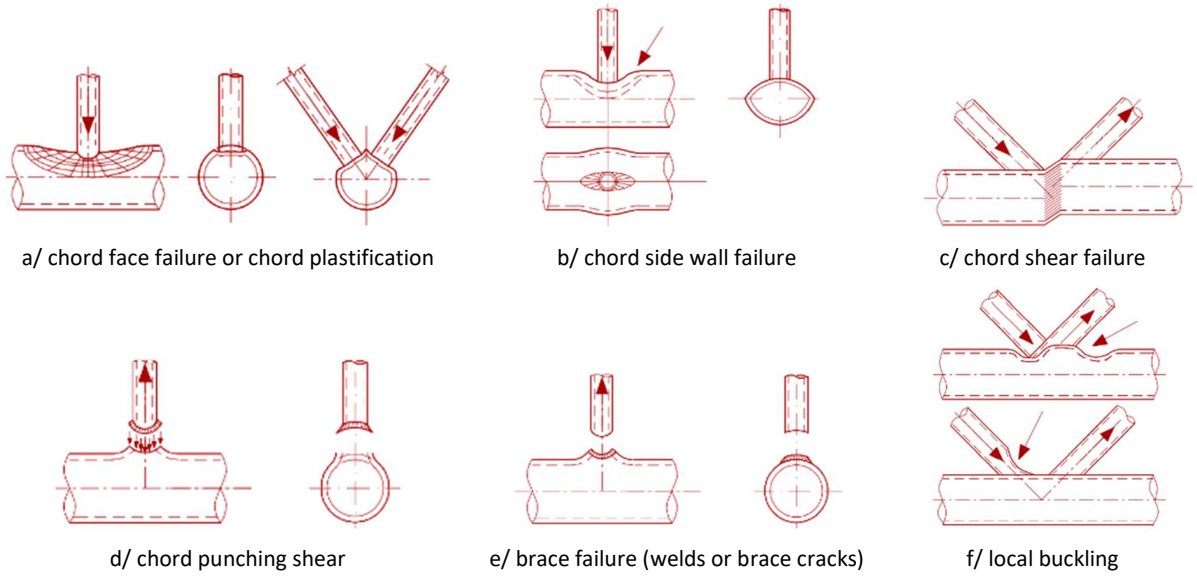

Figure 1. *Failure modes of joints between axially loaded CHS profiles, EN 1993-1-8 [1].*

If design recommendations and restrictions (for steel lattice structures made of CHS profiles), summarised in [3] and [4], are respected, the possibility of certain failure modes may be eliminated. For example, to avoid weld fracture (that may result in failure mode from Figure 1e), it is recommended to choose a "stronger" weld in relation to the connected profiles. Full penetration welds may be considered as "stronger" than the connected profiles. Partial penetration plus fillet, or fillet welds alone, usually also provide sufficient strength of a weld. Additionally, the ratio d/t (d = radius of CHS profile; t = CHS profile wall thickness) is limited by design recommendations to avoid local buckling (Figure 1f). This limitation also contributes to the elimination of local brace failure (Figure 1e) and chord side wall failure (Figure 1b). Furthermore, within the design recommendations, it turned out that the criterion for chord shear failure (Figure 1c) may be covered by the criterion for chord plastification (Figure 1a).

Eventually, the governing failure modes that should be considered for uniplanar K-joints of steel CHS profiles are *chord plastification* (Figure 1a) and *chord punching shear* (Figure 1d). For both modes, EN 1993-1-8 offers semi-empirical expressions for design resistance, based on simplified analytical models, combined with experimental data.

2.2. Analytical models

Due to the complexity of load transfer in joints between hollow tubular profiles (caused primarily by non-linear stiffness distribution along perimeter of brace CHS profiles), it is rather demanding to formulate appropriate analytical model that may realistically describe behaviour of joint elements up to the failure.

Initial analytical considerations of chord plastification in steel lattice structures date back to Togo's work in 1960s [5]. Further analyses led to two mostly used analytical models nowadays: *ring model* (for chord plastification) and *punching shear model* (for chord punching shear), both presented in [3]. Ring model [3-6], originally developed by Togo (1967), later redefined by several researchers, has good match with the experimental data for X-joints. However, it needs further adjustments for other joint types, such as K-joint. Punching shear model [3, 4, 7, 8], elaborated by Marshall (1992), served to many design recommendations. K-joints, due to their geometry, may be less susceptible to this failure mode than other joint types.

Analytical modelling of joints in steel lattice structures has been verified by experimental tests and numerical analysis. Finally, semi-empirical expressions for the joint strength have been formulated and included in design codes for steel structures [1]. It has been concluded that the chord plastification should be checked as a prime failure criterion and the chord punching shear as an additional criterion of failure in joints of steel lattice structures. In case of K-joints, the difference should be made between gap and overlap joints, i.e. K-joints having the gap between the brace members and K-joints with overlapping brace members.

Above summarised findings of the joint failure analysis of steel lattice structures presents the starting point for the corresponding analysis of aluminium structures. In the case of aluminium structures, the analysis is even more complex (due to specific material characteristics of aluminium, particularly related to welding) and still incomplete, missing both experimental and numerical data sufficient for development of comprehensive analytical formulae.

An important contribution has been done by Đuričić et al. (2017), within the research project realised at the University of Montenegro [9, 10]. Supported by the experimental and numerical data, an analytical expression for design resistance of K-joint between aluminium CHS profiles has been formulated. It is based on the expression for K-joint of steel CHS profiles, from EN 1993-1-8, accounting for aluminium softening in heat affected zone (HAZ) due to welding.

3. MODELS OF CONDUCTED NUMERICAL (FEM) ANALYSIS

Although in constant need of experimental validation, a numerical analysis nowadays, in a way, takes the precedence over the experimental testing. Being less demanding in terms of money, time and space consumption, as well as research staff requirements, numerical analysis should be used to provide as many data as possible, that are going to be efficiently verified by experiments.

So far, aluminium lattice structures have rarely been modelled entirely, as the whole structure, in order to verify certain connections. More often specific parts (e.g. joints) are singled out from the complete structure and modelled with the appropriate boundary conditions and loads. 2D models of 3D problems can be used to save the time or in lack of high-performance computing equipment (both hardware and software). However, such modelling may be inadequate in some cases, causing lower accuracy of results or even leading to incorrect conclusions. Undoubtedly, 3D models of the complete lattice structure, with adequately included geometric and material characteristics, support conditions and load, would provide the best, i.e. the most realistic result.

Hence, a numerical analysis of the aluminium lattice structure, made of CHS profiles, with welded K-joints, conducted by ANSYS software, on 3D models of the complete structure is presented in this paper, as an introductory step for the comprehensive non-linear analysis (considering material and geometric nonlinearity) that will be based on the experimental results regarding material properties as well as structural behaviour.

3.1. Geometry of modelled structure

The spatial four-side aluminium lattice cantilever structure, having square base, with the dimensions 1380 x 1380 mm, and span of 3000 mm, presented in Figure 2, has been analysed. Four identical sides of the spatial structure have welded K-joints, with direct welding of brace elements (CHS profile Ø48.3 x 4 mm) to chords (CHS profile Ø76.1 x 4 mm). The inclination angle of a side diagonal is θ = 61°.

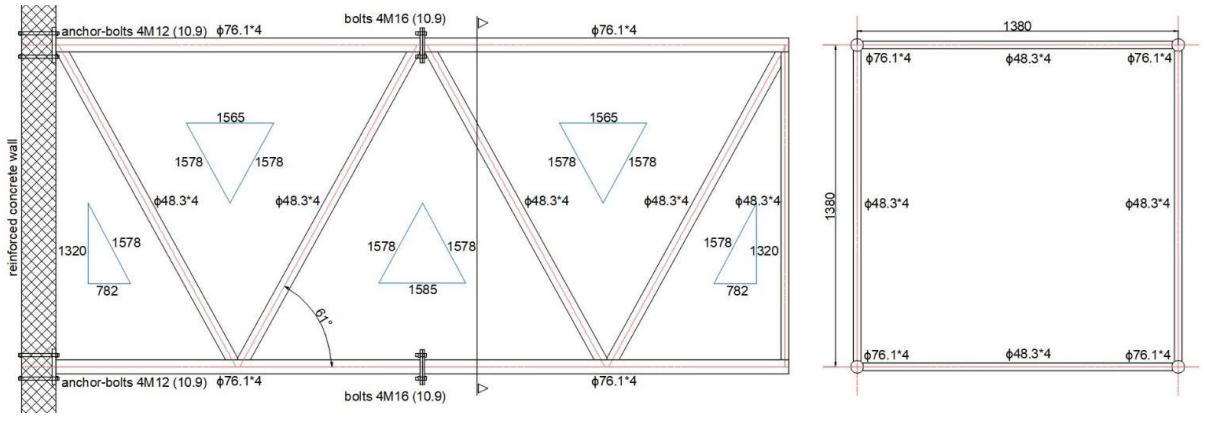

Figure 2. *General geometry of models for numerical analysis.*

Quoted general dimensions as well as horizontal position of the lattice structure are chosen in accordance with the dimensions and arrangement of experimental specimens described in [9, 10], aiming at results relation and comparison in the further research phases. Unlike experimental specimens, which were fully welded, numerical models consist of two segments, connected by means of end plates (150 x 150 x 10 mm) and bolts (4 M16, class 10.9, at each chord). That is because of the intention to analyse this type of connection in the next step of research. Lattice structure is considered to be anchored in heavy reinforced concrete wall, by means of end plates (150 x 150 x 15 mm) and anchor-bolts (4 M12, class 10.9, at each chord).

3.2. Material characteristics of the modelled structure

The material of chord and brace CHS profiles, as well as of end plates, is aluminium, while bolts are made of steel (class 10.9). The elementary characteristics of materials (E = Young's modulus of elasticity; ν = Poisson's coefficient; ρ = material density) are as follows: E_{al} = 71000 MPa, ν_{al} = 0.33, ρ_{al} = 2770 kg/m^3, E_{st} = 200000 MPa, ν_{st} = 0.3 and ρ_{st} = 7850 kg/m^3.

Parent aluminium material, with bilinear form of the stress-strain (σ-ε) diagram, has been chosen from ANSYS library. Two more types of σ-ε diagram for aluminium have been used in numerical models – for the heat affected zones (HAZ 1 and HAZ 2) that surround welds and have different material properties compared to the parent material, because of aluminium softening due to high welding temperatures, i.e. large amount of heat necessary for aluminium melting that causes significant decrease in aluminium strength. Stress-strain characteristics and diagrams of HAZ materials were evaluated in relation to the properties of the parent material, based on the experimental experience [9, 10]. Although it is expected that welding heat influences the modulus of elasticity too, in addition to the material strength, only strength reduction is analysed in this phase. The slight change of the modulus of elasticity in HAZ material will be taken into consideration upon the experimental determination. Bilinear σ-ε diagrams for three types of aluminium material are presented in Figure 3, together with the σ-ε diagram for bolts steel.

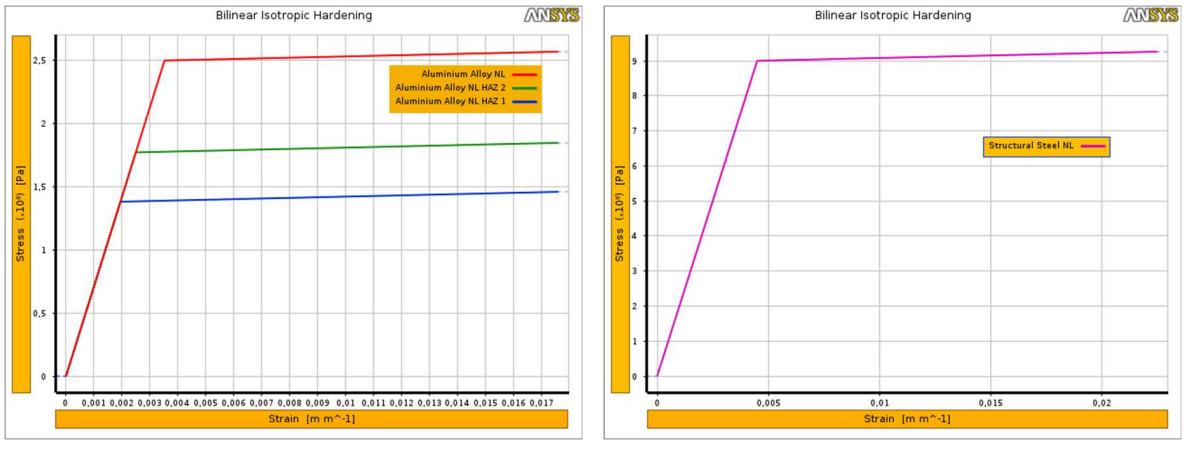

Figure 3. *Stress-strain (σ-ε) diagrams of aluminium (CHS profiles, end plates, welds) and steel (bolts).*

3.3. Applied contact geometry, support conditions, load and bolts preloading

The definition of contacts in FEM modelling by ANSYS or similar software is essential for proper and real representation of the considered problem. By defining contact surfaces, the preparation for the

analysis of interactions between the elements and nodes in the model has been done. Since contacts are significant segment of the FEM analysis, rather demanding regarding computer performances, their adequate definition may contribute to the model rationality by reduction in the amount of contact areas. For example, the washer between the bolt head and the end plate may be represented by increased head height up to the total thickness of the head and the washer, i.e. by joining them together. This does not affect either the global or the local connection behaviour.

Contact surfaces to be considered in the connection with the end plates and bolts are contact between two end plates and contacts between the bolt head or nut with the end plate. Contact surfaces which should be considered in the rest of the structure are contacts between the lattice members (chords and braces), as well as contacts of lattice members with the end plates. According to Figure 2, the lattice structure has been examined in horizontal position. The support is formed in the vertical RC wall. As the subject of this paper is not related to concrete, by appropriate contact geometry (contact of aluminium lattice structure and RC wall) has been ensured that no fracture occurs in the support zone. A frictional contact, with the appropriate friction is applied for the contact between two end plates, at the connection of two lattice segments. All the remaining contacts are modelled as bonded contacts.

Structure is loaded by concentrated forces of 15 kN, acting in joints, as shown in Figure 4.

The bolts in the connections may be numerically modelled with different parameters. The bolt package generally consists of a bolt itself (cylindrical shank with threaded portion and head), a nut and washer(s) under the bolt head and/or nut. Usually, all these components are modelled in FEM analysis software in a simplified way - as one whole body. The bolt model can be made either of solid finite elements or of beam (rod-shaped) finite elements. In the presented analysis, the bolt preload is defined in the first step, by applied static preloading force equal to the maximum preloading force according to Eurocodes [1, 2], i.e. 70% of the bolt strength value (= 110 kN for used bolts M16, class 10.9).

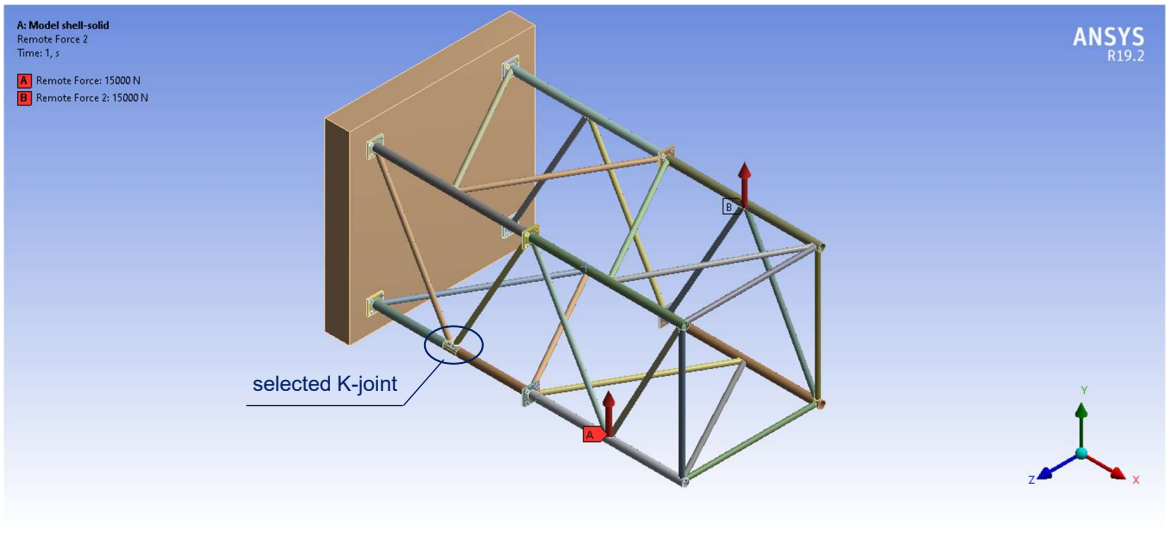

Figure 4. *ANSYS model of analysed spatial lattice structure.*

3.4. Model discretisation

Several variants of model from Figures 2 and 4 have been analysed. Different types of finite elements and mesh density have been used, in order to achieve the best possible efficiency. Four variant models and their results are going to be presented herein, with a special emphasis on HAZ modelling in one of the most loaded K-joints (noted in Figure 4), where fracture occurrence is likely to happen.

Model 1 (shell-solid) contains SHELL181 finite elements (FE) for CHS profiles and welds, SOLID186 and SOLID187 FE for end plates, and SOLID187 FE for bolts. In the selected K-joint (noted in Figure 4), where the appearance of plastification is expected, two HAZ zones are modelled as shown in Figure 5.

Model 2 (shell-beam) contains SHELL181 FE for CHS profiles and end plates, and BEAM188 FE for bolts. A discretisation into two beam elements is applied, which is minimum to realise bolt preloading.

Model 3 (solid-solid) contains SOLID186 and SOLID187 FE for CHS profiles and end plates, and SOLID187 FE for bolts.

Model 4 (solid/solsh-solid) contains SOLSH190, SOLID186 and SOLID187 FE for CHS profiles and end plates, and SOLID187 FE for bolts.

In all models FE size for CHS profiles and end plates is 10 mm. Model 1 is with the FE size of 3 mm in HAZ 1, FE size of 5 mm in HAZ 2 and FE size of 10 mm in welds. Models 3 and 4 have two layers of finite elements along the wall thickness of the CHS profiles.

Table 1 summarises general characteristics of listed models: numbers of nodes and finite elements, as well as processing time. It can be seen that Model 2 has the smallest number of nodes and finite elements, but its processing time is not the shortest. From the aspect of time consumption and computing equipment performances, Model 4 is the most efficient, and the second one is Model 1.

Table 1. General characteristics of analysed FEM (ANSYS) models

FEM (ANSYS) model	number of nodes	number of finite elements	processing time [s]
Model 1	178975	125530	11191
Model 2	83959	81658	13985
Model 3	894488	169023	24107
Model 4	429114	167203	8884

4. NUMERICAL (FEM) ANALYSIS RESULTS

This section summarises results of numerical (FEM) analysis of previously presented ANSYS models. Based on their comparison, certain advantages and disadvantages of models are underlined in order to help proper selection of numerical model(s) for use in the future research. Final validation of numerical model(s), which will be ground for the decision on the representative model(s), should be done experimentally. That is in the agenda for the next research phase.

4.1. Model 1

In Model 1, aluminium softening in welding zones has been taken into consideration by appropriate material modelling. Figure 5 displays the position of the softened zones (i.e. heat affected zones) HAZ 1 and HAZ 2 in K-joint noted at Figure 4.

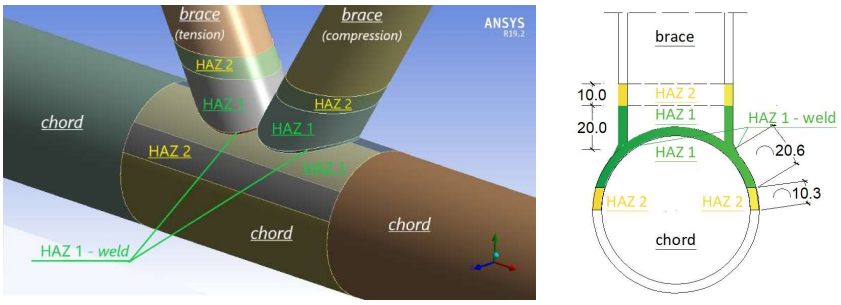

Figure 5. *Position of aluminium softening zones HAZ 1 and HAZ 2.*

Figure 6 shows Von Mises equivalent stresses for Model 1. The overall stress range for this model is 0.00145-675.43 MPa, with the maximal value in bolts. The maximal value of Von Mises equivalent stress in CHS profiles is 185.47 MPa and it is registered in the brace, at the contact with the end plate. No HAZ is modelled in the joint with endplate, but, in reality, HAZ yielding strength would be reached.

a/

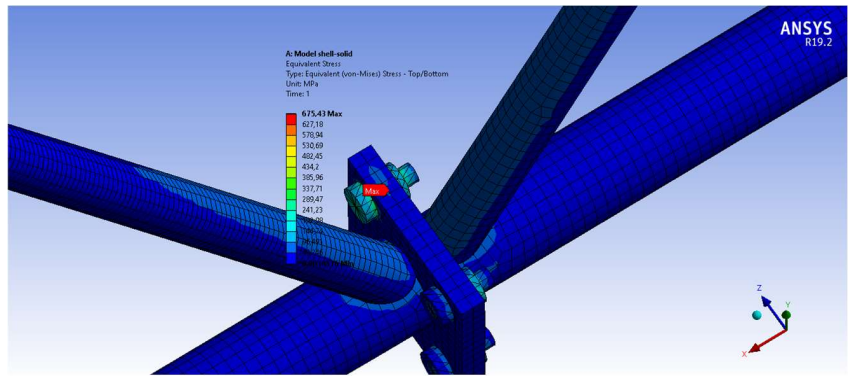

b/

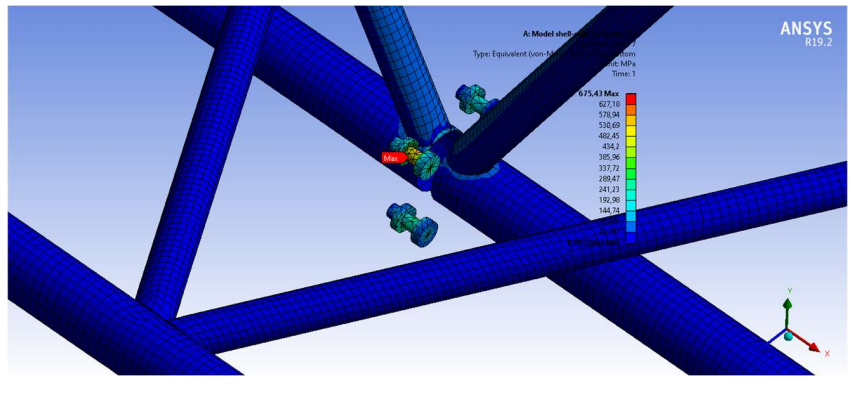

c/

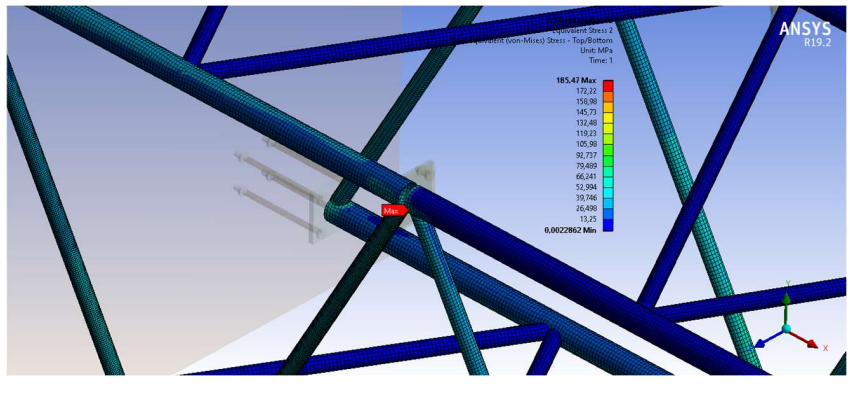

Figure 6. *Von Mises equivalent stresses for Model 1.*

Figure 7 shows Von Mises equivalent stresses for Model 1, in the selected K-joint (noted in Figure 4). The stress in the analysed K-joint of Model 1 is 145.68 MPa, i.e. reaching predefined yielding strength of HAZ 1, already at the load level of only 15 kN. In the further analysis step, material non-linearity should be accounted for.

a/

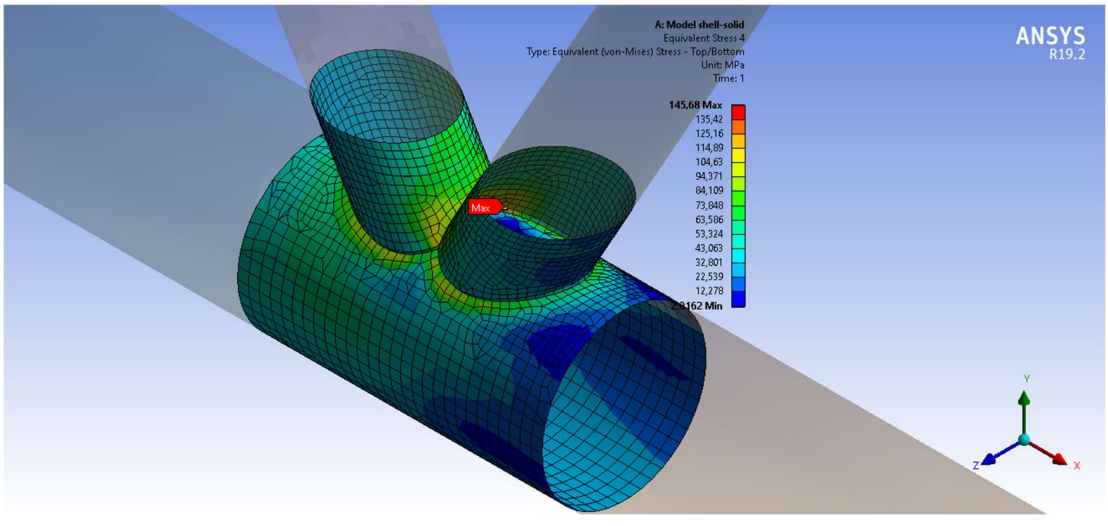

b/

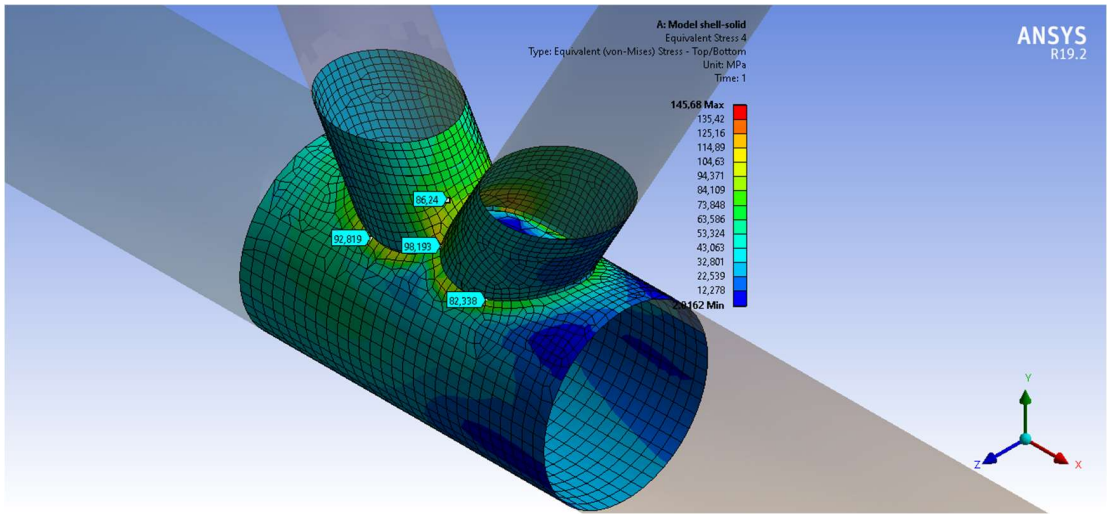

c/

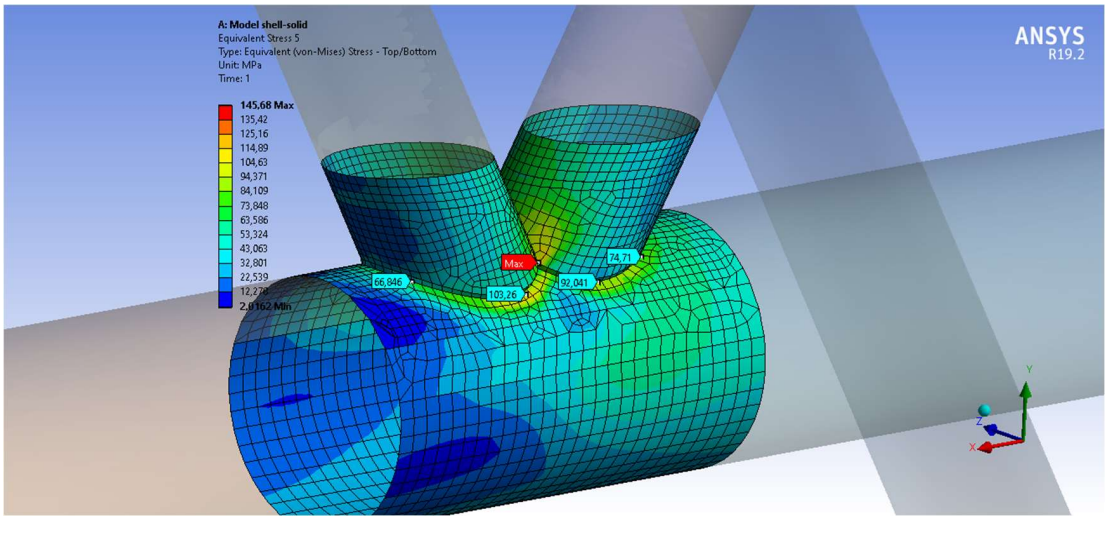

Figure 7. *Von Mises equivalent stresses in the selected K-joint (Fig. 4) of Model 1.*

The total deformation of Model 1 is 8.35 mm, at the free end (Figure 8).

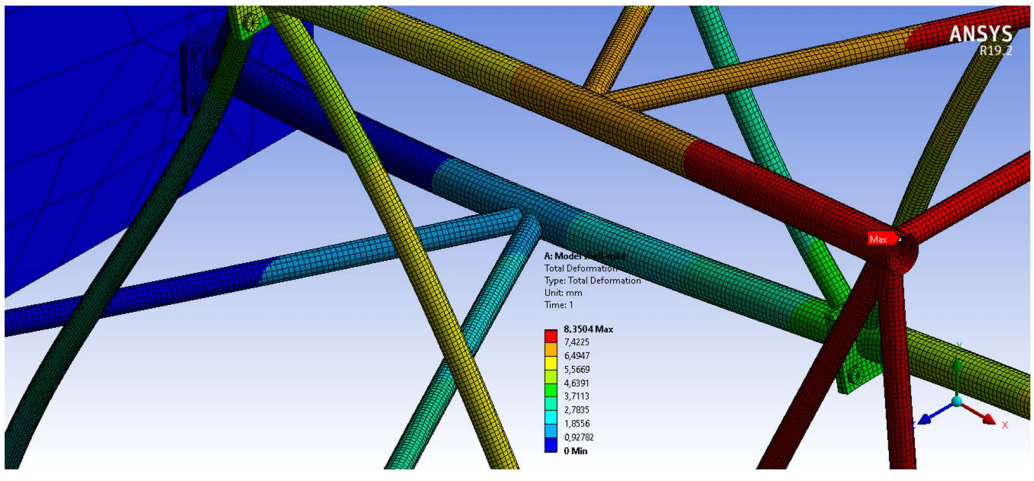

Figure 8. *Total deformation of Model 1.*

4.2. Model 2

Figure 9 shows maximum combined stresses and Von Mises equivalent stresses for Model 2. The overall stress range for this model is 0.00164-652.27 MPa, with the maximal value in bolt (maximum combined stress for beam element). The maximal value of Von Mises equivalent stress in CHS profiles is 192.1 MPa (i.e. beyond HAZ yielding strength, but HAZ is not modelled herein) and it is registered in the brace, at the contact with the chord, near the end plate.

a/

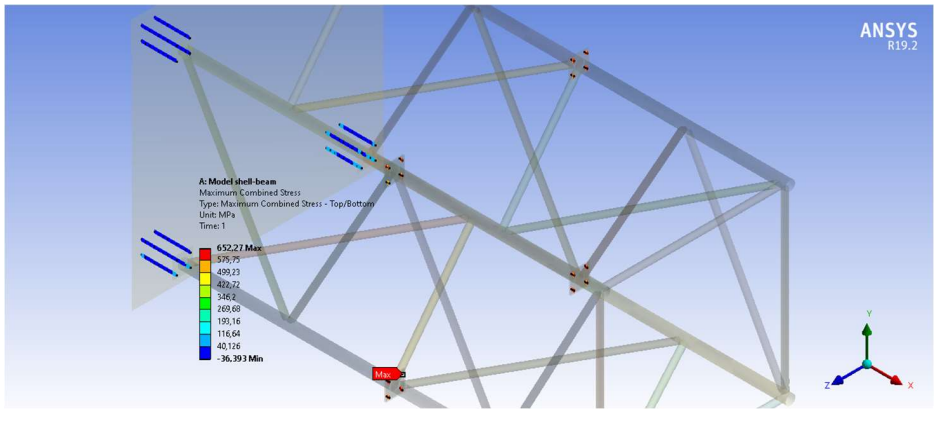

b/

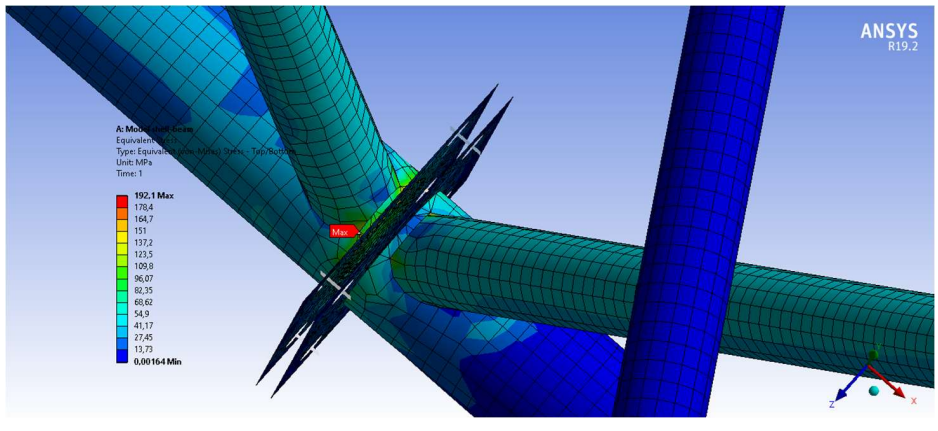

Figure 9. *Maximum combined stresses and Von Mises equivalent stresses for Model 2.*

Figure 10 shows Von Mises equivalent stresses for Model 2, in the selected K-joint (noted in Figure 4). The stress in the analysed K-joint of Model 2 is only 61.05 MPa. Obvious difference in comparison with the results of Model 1, with included HAZ zones, i.e. refined FE mesh, in this joint, as well as modelled welds in all joints, implies the significance of such details in modelling, that are particularly characteristic for aluminium.

a/

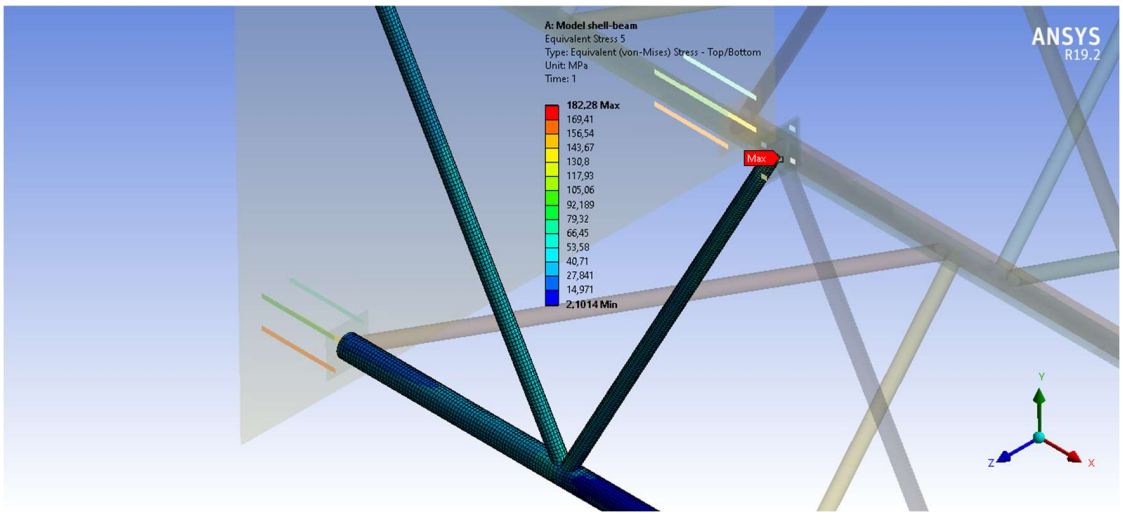

b/

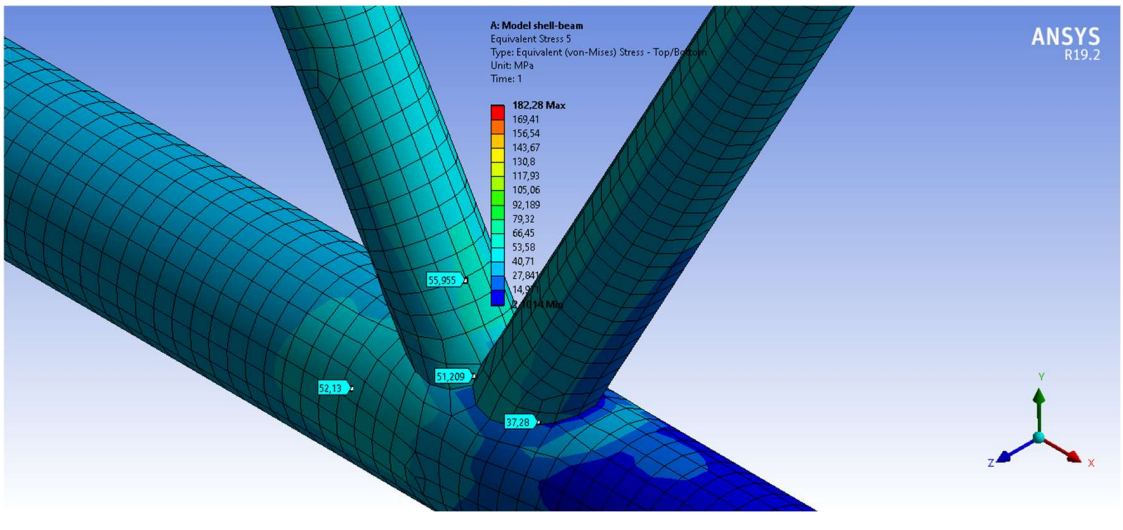

c/

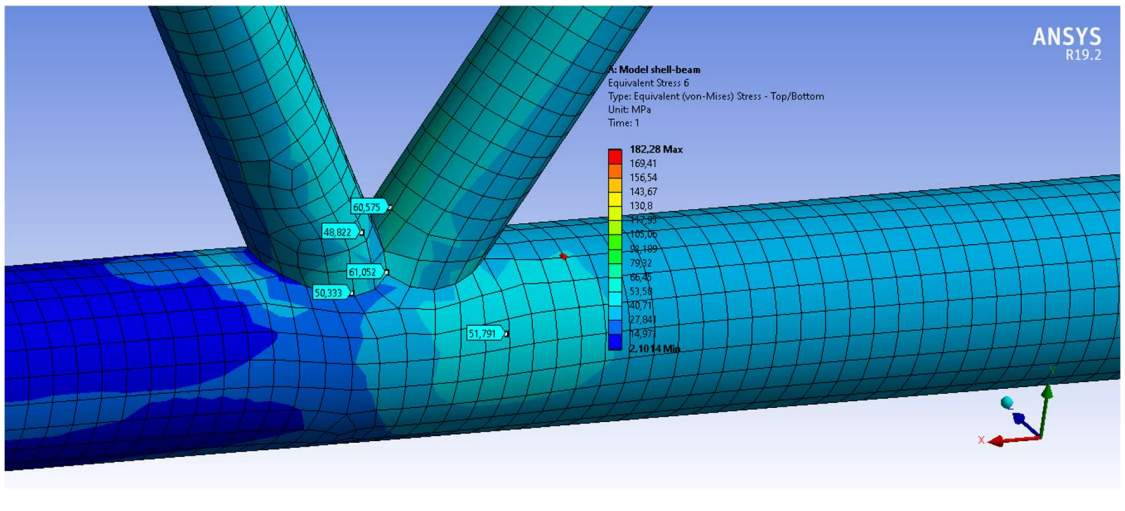

Figure 10. *Von Mises equivalent stresses in the selected K-joint (Fig. 4) of Model 2.*

The total deformation of Model 2 is 8.35 mm, at the free end (Figure 11).

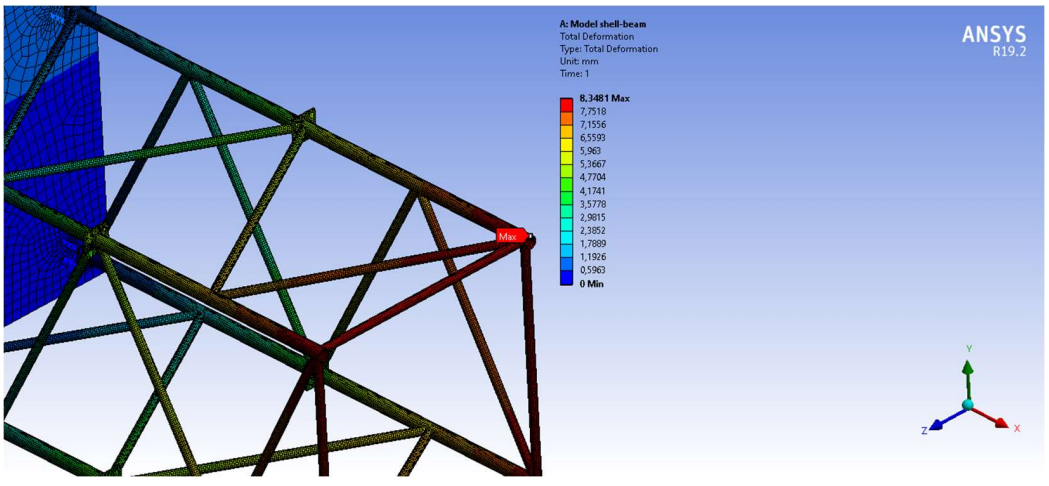

Figure 11. *Total deformation of Model 2.*

4.3. Model 3

Figure 12 shows Von Mises equivalent stresses for Model 3. The overall stress range for this model is 0.000730-540.32 MPa, with the maximal value in bolts. The maximal value of Von Mises equivalent stress in CHS profiles is 137.62 MPa (which is the approximate value of HAZ 1 yielding strength) and it is registered in the chord, in the K-joint. Bearing in mind the position of the maximal stress in the K-joint, it would most likely be in one of the HAZ zones, which are not specifically considered in this model, neither by FE mesh refinement, nor by material properties.

The total deformation of Model 3 is 8.39 mm, at the free end (Figure 14).

4.4. Model 4

Figure 13 shows Von Mises equivalent stresses for Model 4. The overall stress range for this model is 0.000715-540.38 MPa (which is approximately the same as in Model 3), with the maximal value in bolts. The maximal value of Von Mises equivalent stress in CHS profiles is 112.66 MPa (which is notably lower than in Model 3, i.e. lower than the value of HAZ 1 yielding strength) and it is registered in the brace, at the contact with chord, in the K-joint noted in Figure 4.

The total deformation of Model 4 is 8.48 mm, at the free end (Figure 15).

4.5. Models comparison

Table 2 provides an overview of the Von Mises equivalent stresses in the CHS profiles of lattice structure by models, as well as the values of the deformation of the lattice at the free end.

Based on the values of the maximum deformation at the free end of the lattice structure, it may be concluded that the deviations of models are generally small and negligible. Model 4 has slightly higher deformation, but only 1.1%.

However, when the value of the maximum stress in CHS profiles is considered, significant variations can be observed, confirming the significance of appropriate detailing in modelling. In addition, the location of the maximum stress concentration is not the same in all models.

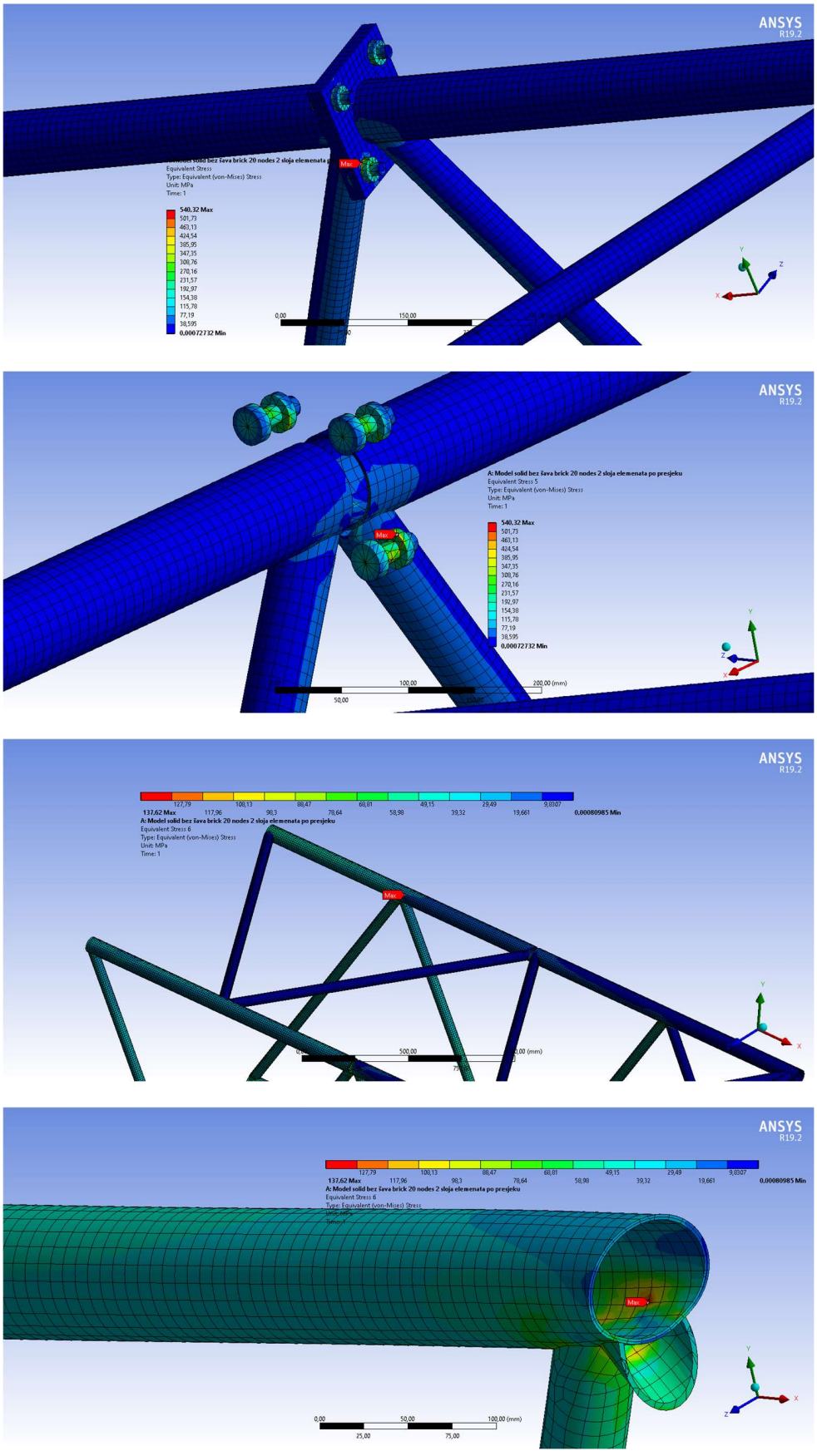

Figure 12. *Von Mises equivalent stresses for Model 3.*

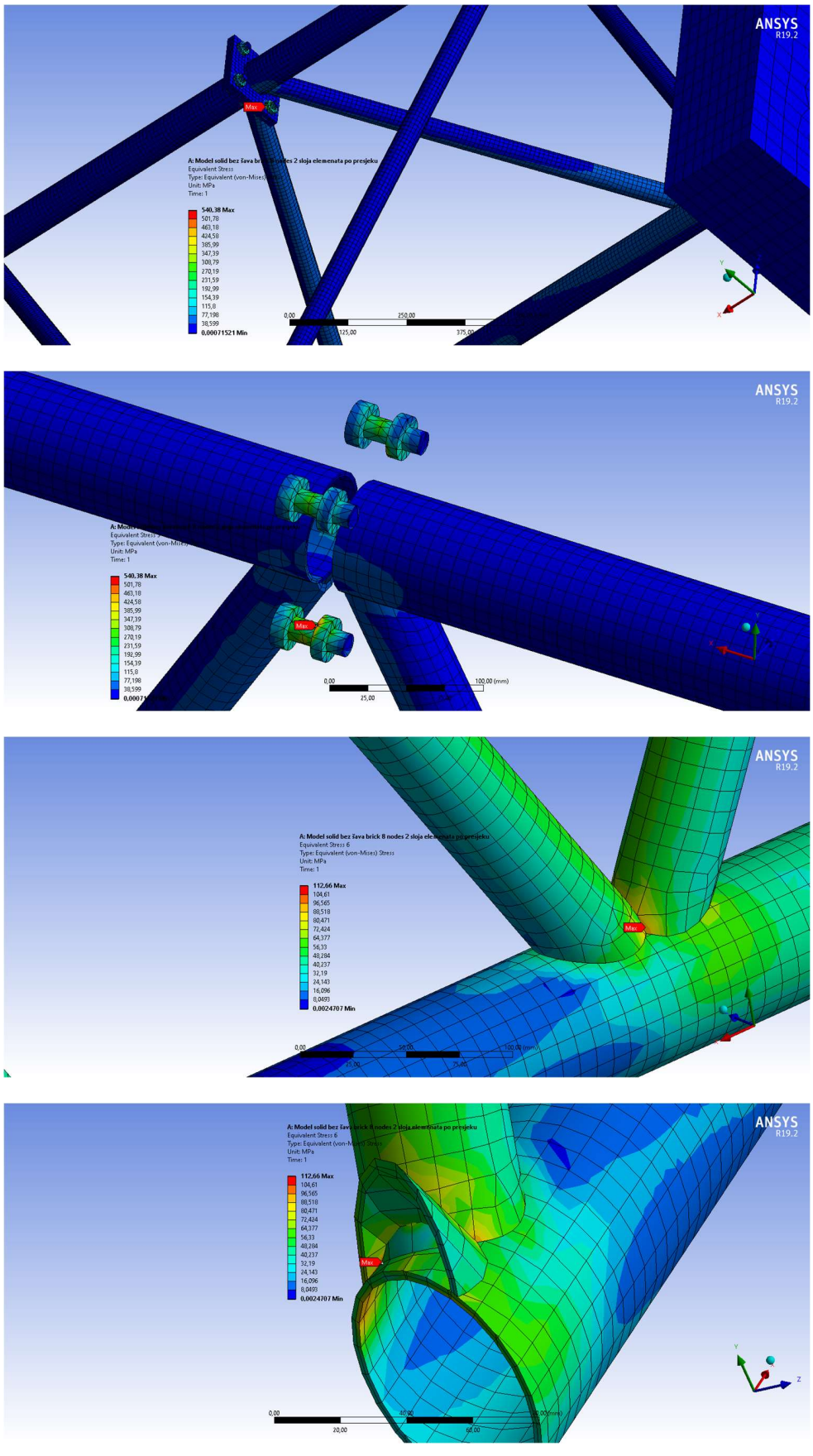

Figure 13. *Von Mises equivalent stresses for Model 4.*

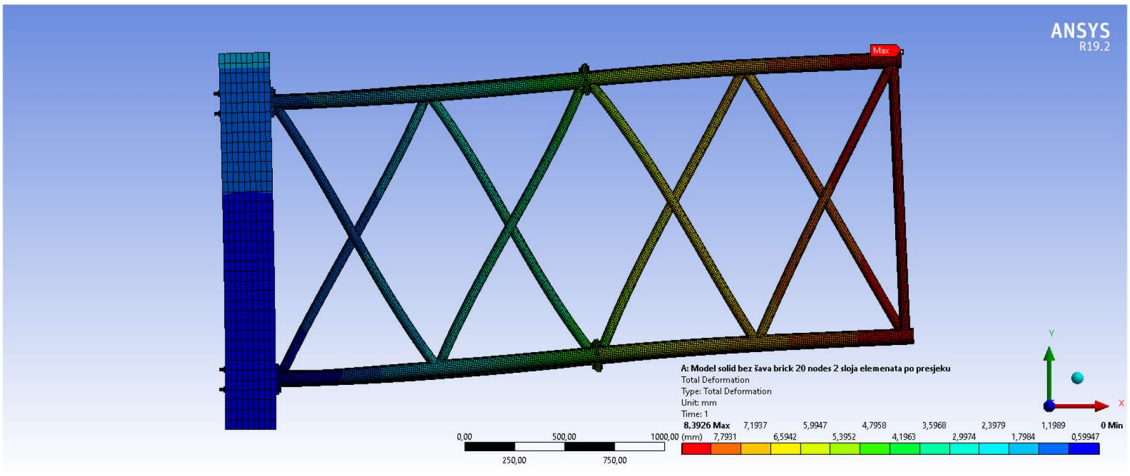

Figure 14. *Total deformation of Model 3.*

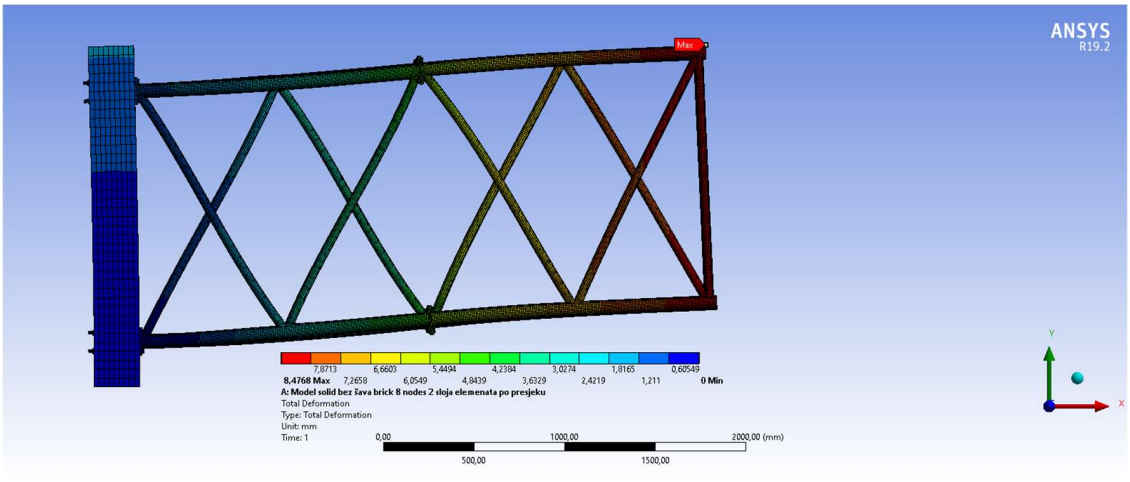

Figure 15. *Total deformation of Model 4.*

Table 2. An overview of the Von Mises equivalent stress in the CHS profiles and the value of deformation at the free end of lattice structure for analysed FEM (ANSYS) models

FEM (ANSYS) model	Von Mises equivalent stress in CHS		Deformation at the free end [mm]
	intensity [MPa]	location	
Model 1	185.47	brace, at the contact with the end plate (upper chord, Fig. 6c)	8.35
Model 2	192.10	brace, at the contact with the chord, near the end plate (lower chord, Fig. 9b)	8.35
Model 3	137.62	in the chord, in the K-joint (upper chord, Fig. 12c, 12d)	8.39
Model 4	112.66	brace, at the contact with the chord (lower chord, Fig. 13c, 13d)	8.48

As expected, a selection of FE type and size highly influenced modelling results. Further, the welds and HAZ zones modelling also has big impact on system response. Contacts between CHS profile and end plates are registered as weak and troublesome points in FEM modelling of the lattice structure. This can be attributed to the defined contacts between the shell and the solid elements in numerical analysis, so the special attention should be paid to that in the future research, especially bearing in mind that K-joints with the end plates in aluminium structures have not yet been sufficiently explored.

5. FINAL REMARKS

Aluminium is a "young" material which became the second highest used metal immediately after steel in the period since its first commercial production. In search of a material which unites functionality and cost-effectiveness, aluminium as a structural material is becoming a common choice for leading architects and engineers.

Over the last three decades, certain number of experimental and numerical studies have been conducted for uniplanar K-joints, primarily singled out of the structure, less within the structure as a whole. Research opportunities in this area are still open.

This paper contains the collection of the results of numerical analysis whose subject is the aluminium lattice structure, made of CHS profiles, with uniplanar overlapping K-joints. The aim of the study is to show the importance of analysing the behaviour of the joint through modelling and considering the global behaviour of the whole structure. Numerical analysis was performed with several various finite element meshes and options of weld and/or HAZ modelling, providing different models comparison with the intention to formulate recommendations for the future proper numerical modelling, that will be optimal considering the relation of model preciseness and time consumption. For the further consideration, it is necessary to test this type of lattice structure experimentally, in order to verify the obtained results and adopt one of numerical models (probably Model 1) as a representative FEM model.

ACKNOWLEDGEMENTS

This work (in progress) is supported by the Ministry of Science of Montenegro through the programme of the financial support for PhD researches. The first author is a grantee of that programme. The second author is the research supervisor.

REFERENCES

[1] EN 1993-1-8:2005: Eurocode 3: Design of steel structures – Part 1-8: Design of joints, CEN, 2005.

[2] EN 1999-1-1:2009: Eurocode 9: Design of aluminium structures – Part 1-1: General structural rules, CEN, 2009

[3] Wardenier, J., Packer, J.A., Zhao, X.L., Van der Vegte, G.J. (2010). Hollow sections in structural applications. CIDECT.

[4] Wardenier, J., Kurobane, Y., Packer, J.A., Van der Vegte, G.J., Zhao, X.L. (2008). Design guide for circular hollow section (CHS) joints under predominantly static loading. CIDECT.

[5] Van der Vegte, G.J. (1995). The static strength of uniplanar and multiplanar tubular T- and X-joints (PhD. thesis). Delft: Delft University of Technology.

[6] Wardenier, J. (1982). Hollow Section Joints. Delft: Delft University Press.

[7] Marshall, P.W. (1992). Design of Welded Tubular Connections. Elsevier.

[8] Marshall, P.W. (1999). Welded Tubular Connections – CHC Trusses. Structural Engineering Handbook, Ed. Chen Wai-Fah Boca Raton: CRC Press LLC.

[9] Đuričić, Đ. (2018). Experimental and Theoretical Limit States Analysis of Aluminium Lattice Structures Elements (PhD. thesis). Podgorica: University of Montenegro.

[10] Đuričić, Đ., Aleksić, S., Šćepanović, B., Lučić, D. (2017) Experimental, theoretical and numerical analysis of K-joint made of CHS aluminium profiles. *Thin-Walled Structures, 119, 58-71*.

M_{cr}-L curves for hot rolled I sections

Subotić, Petar[1]; Šćepanović, Biljana[2]

ABSTRACT

In the draft of the new version of EN 1993-1-1, a more consistent method for determining lateral torsional buckling resistance of members with hot rolled I sections is proposed. Like in the method from the current version of EN 1993-1-1, for the practical use of new method, it is necessary to calculate elastic critical lateral torsional buckling moment M_{cr} in order to determine the relative slenderness $\bar{\lambda}_{LT}$. The M_{cr} calculation done by hand can be rather time consuming and tricky. The determination of M_{cr} may be simplified by introducing graphical approach. The idea is to derive and use appropriate M_{cr}-L curves, for specific cross sections, load types and boundary conditions, that would enable easier determination of M_{cr} in engineering practice. As an example, M_{cr}-L curves, in the forms of diagrams and mathematical expressions, are derived for all IPE sections of simply supported members with length from 4 m up to 12 m, under the uniformly distributed load acting in the shear centre. An excellent match of results and significant potential of the proposed approach are proved.

Keywords: Lateral torsional buckling, elastic critical lateral torsional buckling moment, M_{cr}-L curve

1. INTRODUCTION

Structural steel members, due to their cross section plates slenderness and overall member slenderness alike, are prone to various local and global structural instability modes. For members subjected to bending, of most concern is lateral torsional buckling (LTB).

Lateral torsional buckling is a complex global structural instability phenomenon. Lateral displacement is accompanied by twisting and warping of cross section, resulting in a specific spatial deformation of member. In order to prevent the occurrence of this structural instability mode, structural members must be adequately designed.

Different methods for dealing with LTB are included in EN 1993-1-1 [1]. If the equivalent column method is going to be used, LTB resistance of members can be calculated by using either general method or alternative method for rolled sections or equivalent welded ones. Without going into theoretical aspects of before mentioned methods, from a practical point of view, for their application it is necessary to determine the value of elastic critical lateral torsional buckling moment M_{cr}. In the latest draft of the

[1] *Faculty of Civil Engineering. University of Montenegro (MONTENEGRO). petarsub@ucg.ac.me*
[2] *Faculty of Civil Engineering. University of Montenegro (MONTENEGRO). biljanas@ucg.ac.me (Corresponding author)*

new version of EN 1993-1-1 [2], significant changes are made to LTB rules. However, the key parameter for determining LTB resistance of members is still elastic critical lateral torsional buckling moment M_{cr}.

Regardless of its great practical importance, determining M_{cr} can be rather tricky and time consuming.

The aim of this paper is to present a simplified method for determining elastic critical lateral torsional buckling moment for hot rolled I section members under the uniformly distributed load. This simplified method is based on the application of M_{cr}-L curves which are unique for certain combination of member cross section, load type and boundary conditions.

2. CALCULATION OF M_{cr}

Although M_{cr} is a key parameter in determining lateral torsional buckling resistance of members, there are no guidelines or expressions in current version of EN 1993-1-1 [1] for its calculation. In some EU countries expression for M_{cr} can be found in appropriate national annexes or NCCI documents. In other countries, engineers are referred to structural stability textbooks or relevant articles.

The most commonly used expression for M_{cr} is the so called three-factor formula, Eq. (1):

$$M_{cr} = C_1 \frac{\pi^2 E I_z}{(k_z L)^2} \left\{ \sqrt{\left(\frac{k_z}{k_w}\right)^2 \frac{I_w}{I_z} + \frac{(k_z L)^2 G I_t}{\pi^2 E I_z} + \left(C_2 z_g - C_3 z_j\right)^2} - \left(C_2 z_g - C_3 z_j\right) \right\} \quad (1)$$

where:

C_1 is the factor that takes mainly into account the shape of the bending moment diagram,

C_2 is the factor that takes mainly into account the point of the load application,

C_3 is the factor that takes mainly into account the type of the cross section,

z_g is the distance between the shear centre and the point of load application,

z_j is the factor of the cross section asymmetry,

k_z, k_w are the effective length factors (k_z refers to rotation restrictions and k_w refers to warping restrictions at end cross sections),

I_z, I_w, I_t are the second moment of area about the minor axis of the cross section, warping constant and St. Venant torsional constant, respectively,

L is member length,

E, G are modulus of elasticity and shear modulus, respectively.

In this approach, the main problem is to define the values of factors C_1, C_2 and C_3 correctly. This is by no means a straightforward and easy task. Namely, factors C_i do not exclusively reflect one single influence parameter (bending moment diagram, load position, cross section shape, torsional properties etc.), but

more of them. For example, factor C_1 takes into account bending moment diagram but it is also dependent on torsional properties of the cross section. For this reason, in before mentioned national annexes, NCCI documents and relevant publications, different values for C_i factors can be found.

This can pose a problem for an engineer in practice because choosing a "correct" value for C_i factors among different recommendations is by no means easy. Bearing in mind that the C_i factors directly influence the value of M_{cr} and therefore the resistance of member to lateral torsional buckling, special attention is required in this design step.

In the latest draft of the new version of EN 1993-1-1 [2], rules for lateral torsional buckling have changed. The new method is based on the work made by Taras [3]. By developing LTB specific Aryton-Perry formulation for mechanical model and precisely calibrated imperfection factor, better consistency and precision is achieved. In accordance with this new proposed method, the reduction factor χ_{LT} should be calculated as follows:

$$\chi_{LT} = \frac{f_m}{\Phi_{LT} + \sqrt{{\Phi_{LT}}^2 - f_m {\bar{\lambda}_{LT}}^2}} \tag{2}$$

with

$$\Phi_{LT} = 0{,}5\left(1 + f_m\left(\left(\frac{\bar{\lambda}_{LT}}{\bar{\lambda}_z}\right)^2 \alpha_{LT}\left(\bar{\lambda}_z - 0{,}2\right) + {\bar{\lambda}_{LT}}^2\right)\right) \tag{3}$$

where:

f_m is the factor which takes into account the shape of bending moment between lateral restraints,

α_{LT} is the imperfection factor for LTB curves,

$\bar{\lambda}_{LT}$ is non-dimensional slenderness for LTB,

$\bar{\lambda}_z$ is non-dimensional slenderness for flexural buckling about the minor axis of the cross section.

While the theoretical and somewhat practical aspect of determining lateral torsional buckling resistance of members in [2] have changed in regard to the current version [1], M_{cr} still remains the key parameter for calculating members LTB resistance.

As in the current version of EN 1993-1-1 so in the draft of the new one, there are no guidelines on how to determine M_{cr}. Thus, the problem stated above still lingers on.

For this reason, H. Snijder, I. Balaž and R. Stroetmann, for the Working group 1 of CEN/TC250/SC3, have created a technical report called Elastic critical buckling of members, Part 1-103 [4]. This document is meant to be used with pr EN 1993-1-1 [2]. In this document for the first time there are clear guidelines and expressions on how to calculate M_{cr}, i.e. how to determine C_i factors as well as other parameters influencing M_{cr} and appearing in the expression for its calculation.

The general expression for M_{cr}, Eq. (4), is also in the form of so called three-factor formula, basically being equivalent to the expression given by Eq. (1), although written in a slightly different manner:

$$M_{cr} = \mu_{cr} \frac{\pi\sqrt{EI_z GI_t}}{L} \tag{4}$$

with:

$$\mu_{cr} = \frac{C_1}{\beta_z}\left[\sqrt{1 + k_{wt}^2 + \left(C_2\zeta_g - C_3\zeta_j\right)^2} - \left(C_2\zeta_g - C_3\zeta_j\right)\right] \tag{5}$$

$$k_{wt} = \frac{\pi}{\beta_w L}\sqrt{\frac{EI_w}{GI_t}} \tag{6}$$

$$\zeta_g = \frac{\pi z_g}{\beta_z L}\sqrt{\frac{EI_z}{GI_t}} \tag{7}$$

$$\zeta_j = \frac{\pi z_j}{\beta_z L}\sqrt{\frac{EI_z}{GI_t}} \tag{8}$$

where:

μ_{cr} is non-dimensional critical moment,

k_{wt} is non-dimensional torsion parameter,

ζ_g is relative non-dimensional coordinate of the point of load application related to shear centre,

ζ_j is relative non-dimensional cross section mono symmetry parameter,

β_z and β_w are effective length factors.

The values for C_i factors are given in Tables 5.1 to 5.4 in before mentioned report [4]. A wide variety of different boundary and loading conditions, including cantilevers, is covered. Also, values of effective length factors β_z and β_w, for different boundary conditions, are provided in the report [4]. Proposed method, together with the values of C_i factors, is based on the work done by Kolekova and Balaž [5].

If the calculation is done by hand i.e. without specialized software determining M_{cr}, the use of Eq. (4), together with the adjoining Eqs. (5)-(8), is time consuming and prone to errors. For this reason, a simplified method is proposed and presented in the following section.

3. M_{cr}-L CURVES

The basic idea behind M_{cr}-L curves is to give structural engineering practitioners a quick and easy tool for assessing and determining M_{cr} for a specific load type, support conditions, member length and cross

section. As an example, in this paper M_{cr}-L curves are derived for all IPE sections subjected to uniformly distributed load which acts in the shear centre (consequently $z_g = 0$ and both effective length factors $\beta_z = \beta_w = 1$). For IPE section, being double symmetric, $z_j = 0$. Simply supported members were analysed.

At first, the exact values of M_{cr} are determined by Eqs. (4)-(8) for different member lengths. Analysed member length for each cross section is in the range from 4 m to 12 m, with the increment of 0,1 m. For each cross section, this gives 81 values for M_{cr}, as shown in Fig. 1 for the profile IPE 200.

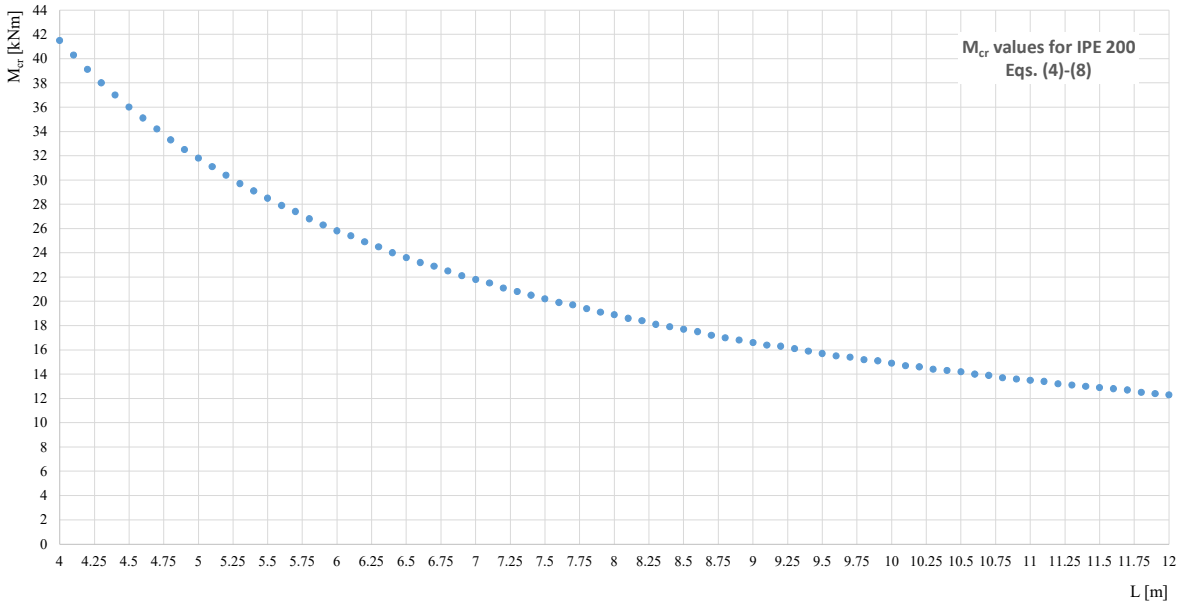

Figure 1. *An example of deriving M_{cr}-L curve for IPE 200 – the first step: calculation of exact M_{cr} values by Eqs. (4)-(8).*

Cross sections properties (I_z, I_t and I_w) used for determining M_{cr} are summarised in Table 1. Material properties E = 210 GPa and G = E/(2(1+0.3)) = 80.77 GPa were used.

Table 1. Cross section properties of analysed sections

Cross section	Value		
	I_z (cm^4)	I_t (cm^4)	I_w (cm^6)
IPE 200	142.4	6.98	12990
IPE 220	204.9	9.07	22670
IPE 240	283.6	12.88	37390
IPE 270	419.9	15.94	70580
IPE 300	603.8	20.12	125900
IPE 330	788.1	28.15	199100
IPE 360	1043	37.32	313600
IPE 400	1318	51.08	490000
IPE 450	1676	66.87	791000
IPE 500	2142	89.29	1249000
IPE 550	2668	123.2	1884000
IPE 600	3387	165.4	2846000

After calculation of the exact values of M_{cr} for one cross section (by Eqs. (4)-(8), as in Fig. 1), best fit methods were applied in order to derive mathematical expression of M_{cr}-L curve for that section. Bearing in mind that these curves are meant for engineers, the idea was to find an interpolation function as simple as possible. In this paper interpolation function is chosen as the 5th order polynomial, having coefficient of determination (R^2 value) very close to unity. Derived M_{cr}-L curves are shown in the following figures (Figs. 2-5), graphically (as drawn lines) as well as analytically (in the form of mathematical expressions).

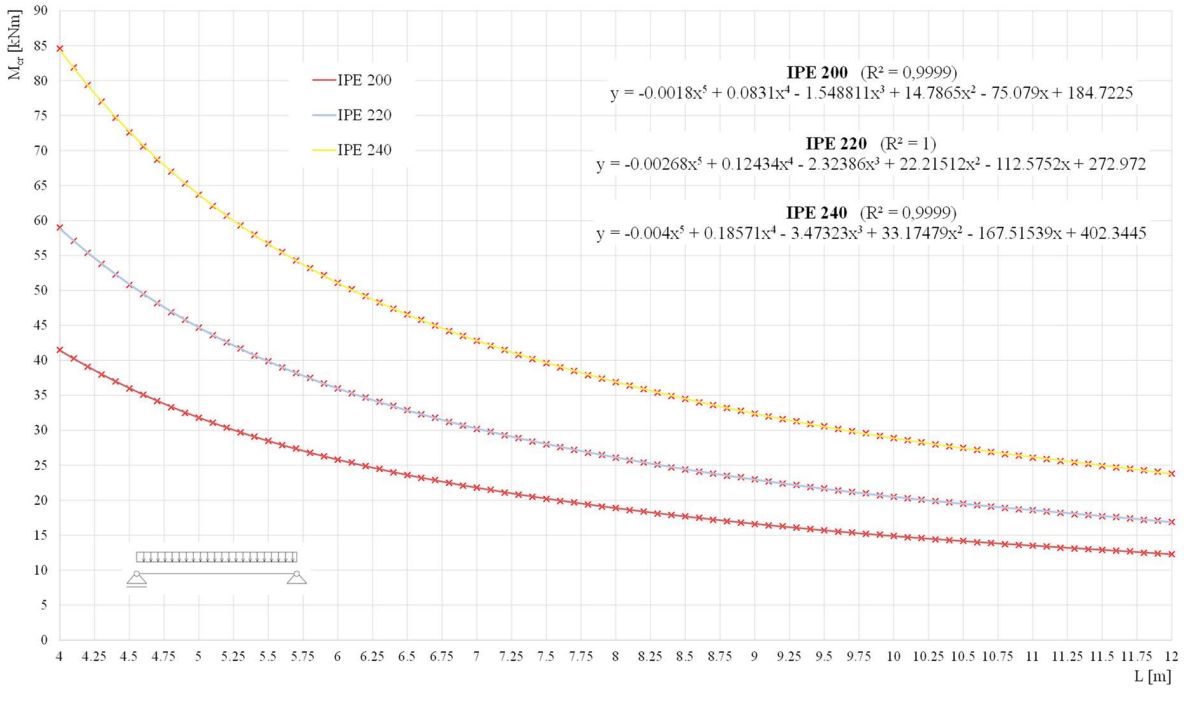

Figure 2. *M_{cr}-L curves for IPE 200, IPE 220 and IPE 240.*

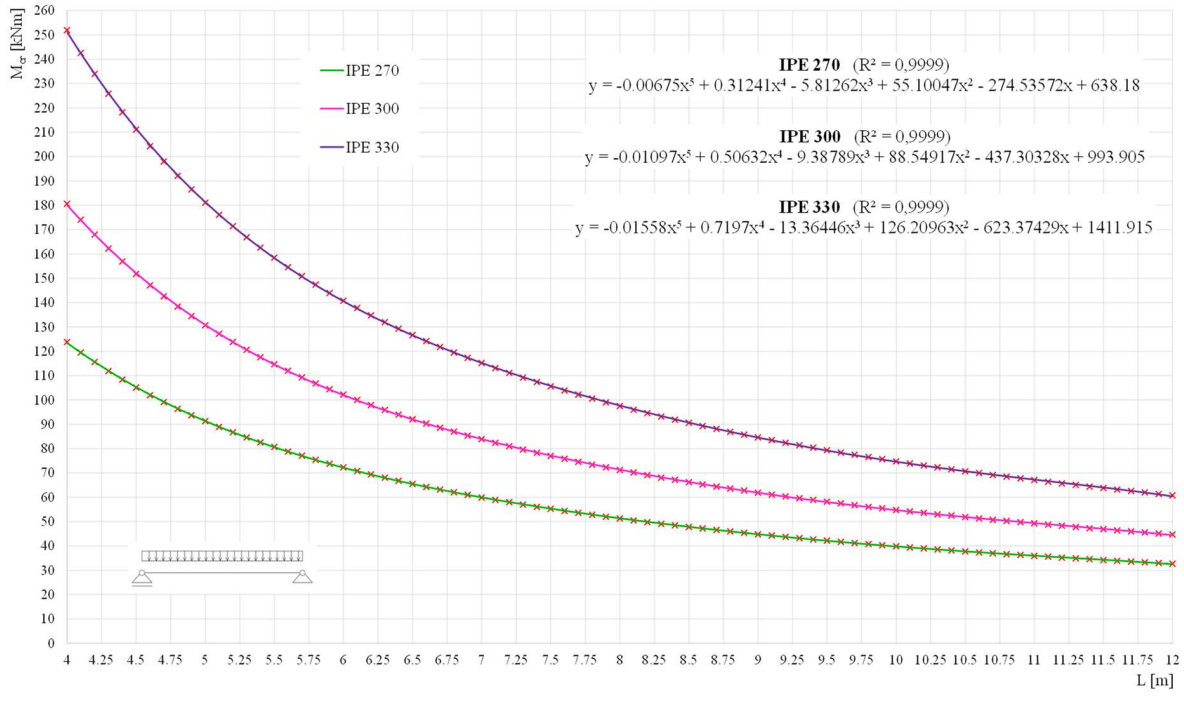

Figure 3. *M_{cr}-L curves for IPE 270, IPE 300 and IPE 330.*

Presented curves are reliable enough for the application in everyday engineering practice. The discrepancy between values of M_{cr} obtained using M_{cr}-L curves (Figs. 2-5) and calculated exact values of M_{cr} (Eqs. (4)-(8)) varies with the member length in a different way for each cross section, as it may be seen in Fig. 6, where graphs of relative difference vs member length are presented. No specific type or even trend of corelation between relative difference and member length may be noted. It may only be said that smaller sections exhibit more scattered discrepancies, while for bigger sections the specific trendlines of discrepancies are clearly formed, with tendency to be equivalent for biggest sections.

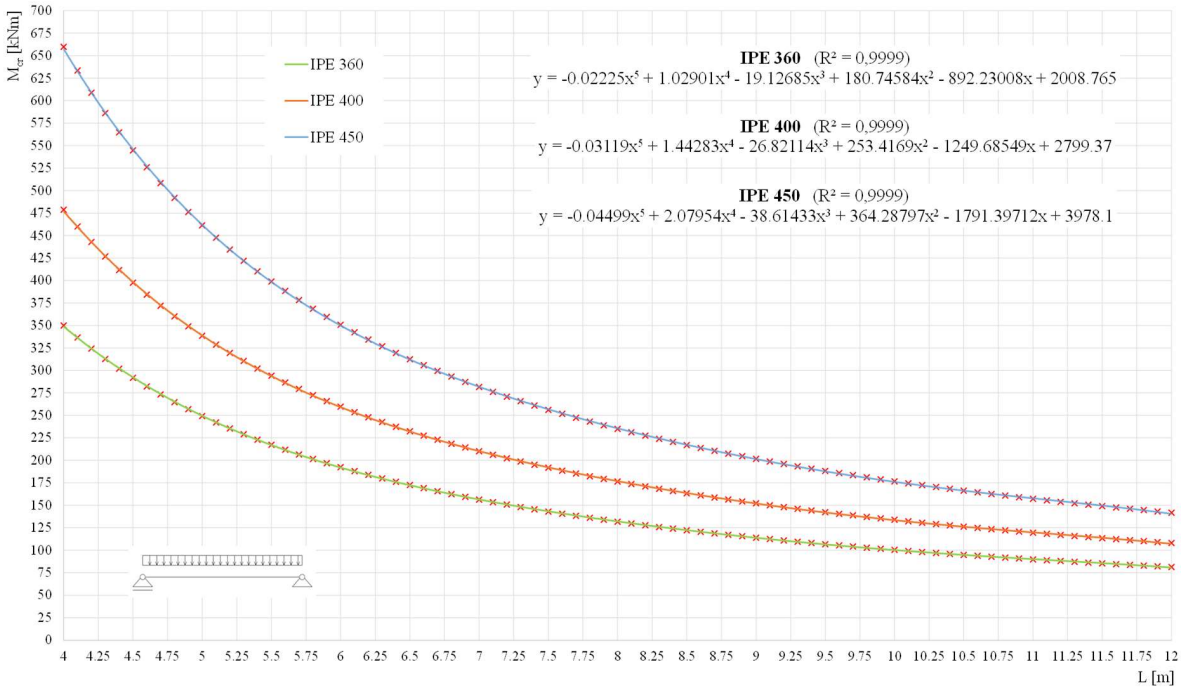

Figure 4. *M_{cr}-L curves for IPE 360, IPE 400 and IPE 450.*

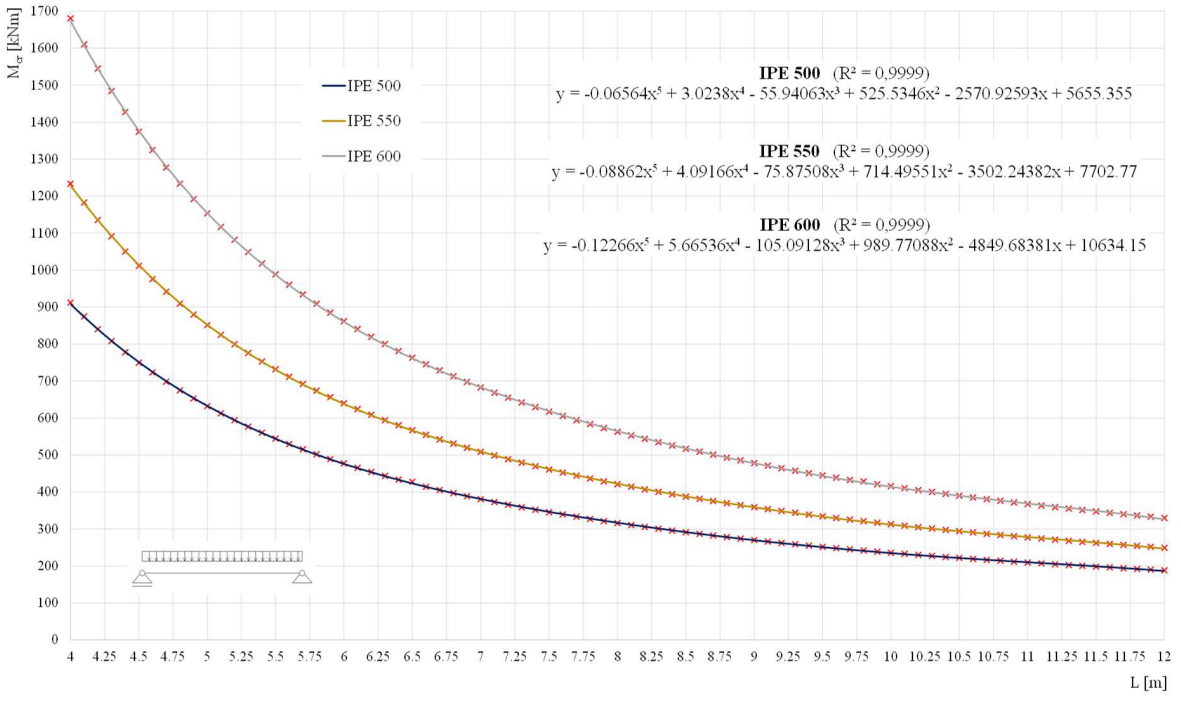

Figure 5. *M_{cr}-L curves for IPE 500, IPE 550 and IPE 600.*

The M_{cr} values obtained by M_{cr}-L curves (Figs. 2-5) are always on the safe side, i.e. lower than M_{cr} values calculated by Eqs. (4)-(8), so that relative differences in Fig. 6 are always positive. The highest discrepancy of only 3.4 %, noted for IPE 330, for max length of 12 m, speaks in favour of the simplified method accuracy and recommends its use in practice.

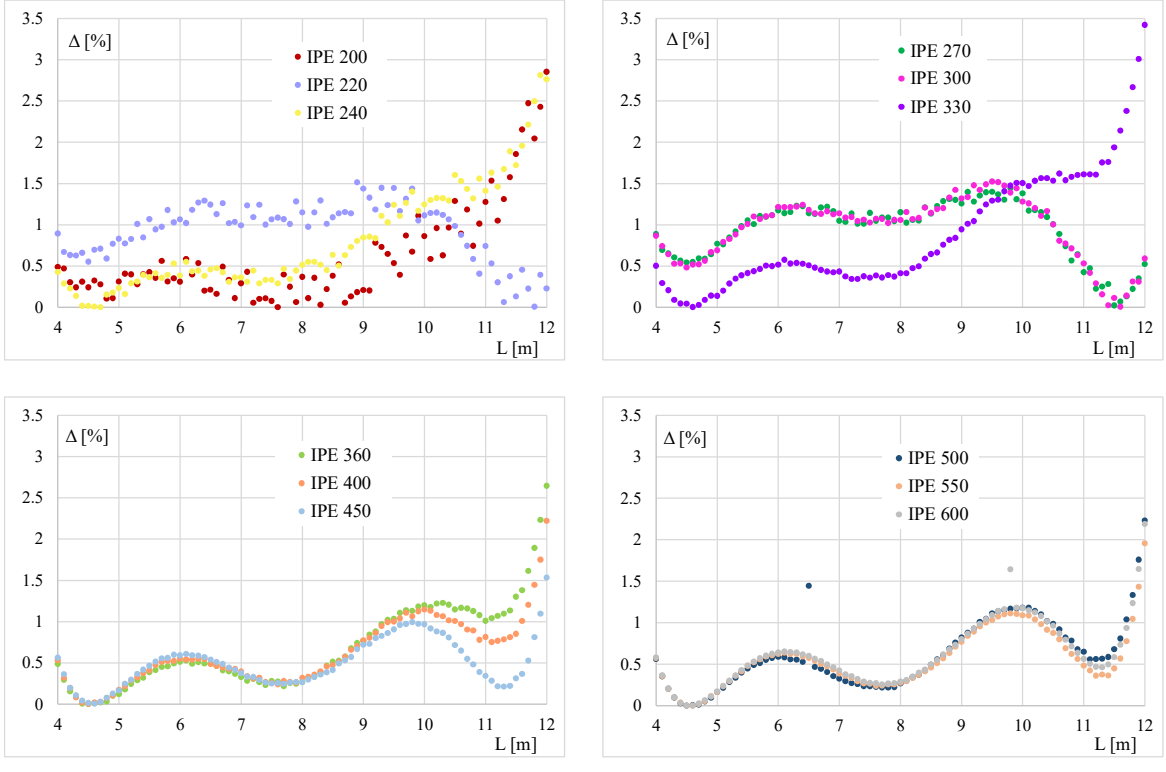

Figure 6. *Relative differences between M_{cr} values obtained by Eqs. (4)-(8) and by M_{cr}-L curves from Figs. 2-5.*

Using either analytical form of interpolation functions or a graphical approach, i.e. direct reading from diagrams, M_{cr} can be quickly and easily determined from presented M_{cr}-L curves (Figs. 2-5). The particular significance of these curves is in the predesign phase. Having M_{cr}-L curves at their disposal, the designers can now tackle lateral torsional buckling already in the predesign phase, thus making subsequent check unnecessary.

4. CONCLUSION

The determination of elastic critical lateral torsional buckling moment M_{cr} was and still is a key step in determining lateral torsional buckling resistance of steel members. Calculation of M_{cr} without specialized software is time consuming and prone to errors.

Derived M_{cr}-L curves for IPE sections provide a simplified alternative, that may be applied either graphically or analytically. These curves are a very useful tool for quick assessment or calculation of M_{cr}, thus eliminating the need for lengthy calculations.

Presented M_{cr}-L curves are reliable enough for the use in everyday engineering practice. The M_{cr} values obtained by M_{cr}-L curves are always on the safe side, i.e. lower than M_{cr} values calculated by Eqs. (4)-(8). The highest discrepancy of only 3.4 % confirms the accuracy of the offered approximation.

Such M_{cr}-L curves for HEA and HEB sections are under preparation.

The practicability of M_{cr}-L curves could be improved if simpler interpolation functions are used, perhaps a combination of a power function and an incomplete polynomial function. Also, further investigation is needed for different boundary and loading conditions.

In addition to the basic purpose of determining elastic critical lateral torsional buckling moment M_{cr}, the M_{cr}-L curves can also be used as a starting point in derivation of LTB resistance curves.

REFERENCES

[1] EN 1993-1-1:2005: Eurocode 3 – Design of steel structures – Part 1-1: General rules and rules for buildings, CEN, 2005.

[2] prEN 1993-1-1:2015: Eurocode 3 – Design of steel structures – Part 1-1: General rules and rules for buildings, CEN/TC 250, 2017.

[3] Taras, A. (2010). Contribution to the development of consistent stability design rules for steel members (PhD thesis). Graz: TU Graz.

[4] CEN/TR 1993-1-103: Eurocode 3 – Design of steel structures – Part 1-103: Elastic critical buckling of members, CEN/TC 250/SC 3, 2019.

[5] Kolekova, Y., Balaž, I. (2012). LTB resistance of beams influenced by plastic reserve or local buckling, 18th International Conference Engineering mechanics (pp. 639-655). Svratka.

A FAST APPROACH TO STUDY THE DYNAMIC RESPONSE OF RAILWAY BRIDGES ACCOUNTING FOR SOIL-STRUCTURE INTERACTION

Galvín, Pedro[1,2]; Romero, Antonio[1]; Moliner, Emma[3]; Connolly, David P.[4]; Martínez-Rodrigo, María D.[3]

ABSTRACT

A novel numerical methodology is presented to solve the dynamic response of railway bridges under the passage of running trains, considering soil-structure interaction. It is advantageous compared to alternative approaches because it permits, (i) consideration of complex geometries for the bridge and foundations, (ii) simulation of stratified soils, and, (iii) solving the train-bridge dynamic problem at minimal computational cost. The approach uses sub-structuring to split the problem into two coupled interaction problems: the soil-foundation, and the soil-foundation-bridge systems. In the former, the foundation and surrounding soil are discretized with Finite Elements (FE), and padded with Perfectly Match Layers (PML) to avoid boundary reflections. Considering this domain, the equivalent frequency dependent dynamic stiffness and damping characteristics of the soil-foundation system are computed. For the second sub-system, the dynamic response of the structure under railway traffic is computed using a FE model with spring and dashpot elements at the support locations, which have the equivalent properties determined using the first sub-system. This soil-foundation-bridge model is solved using complex modal superposition, considering the equivalent dynamic stiffness and damping of the soil-foundation corresponding to each natural frequency. The proposed approach is then validated using both experimental measurements and an alternative Finite Element-Boundary Element (FE-BE) methodology. A strong match is found and the results discussed.

Keywords: Railway bridge dynamics, Railway traffic, Bridge soil-structure interaction, Railroad Numerical Methods, Non-proportional damping

[1] Escuela Técnica Superior de Ingeniería, Universidad de Sevilla, Camino de los Descubrimientos s/n, ES-41092 Sevilla, Spain
[2] Laboratory of Engineering for Energy and Environmental Sustainability, Universidad de Sevilla, Camino de los Descubrimientos s/n, ES-41092 Sevilla, Spain
[3] Universitat Jaume I, Department of Mechanical Engineering and Construction, Avda. Sos Baynat s/n, ES-12071 Castellón, Spain
[4] Institute for High Speed Rail and System Integration, University of Leeds, Leeds LS2 9JT, UK
Corresponding author: pedrogalvin@us.es (Pedro Galvín)

1. INTRODUCTION

The response of railway bridges is strongly affected by soil-structure interaction (SSI), especially under resonance conditions [1]. Radiation and material soil damping influence the modal parameters and usually mitigate the structural vibration levels. However, the interaction between the sub-structure and the soil is seldom considered in numerical models when solving the dynamic problem. In order to predict realistically the vibrational response of bridges under railway traffic, or to asses the structural integrity for new operational situations, SSI should be considered. In the design of new structures this may lead to optimized alternatives and in the case of existing ones, it will permit to assess the bridge performance when facing operational challenges (e.g. increase in the speed or capacity of services) and improve model calibration procedures.

Several researchers have investigated the dynamic response of the bridge accounting for SSI. The soil surrounding the bridge foundations can be modelled applying the Boundary Element method [2] or the FE method adding non-reflecting boundaries [3]. Galvín and Domínguez [4] studied the vibrations induced by high-speed trains crossing a curvlet-type railroad underpass using a three-dimensional (3D) BE model. Báez H. et al. [5] analysed the aforementioned structures following a sub-structuring approach, and Zangeneh et al. [6] by means of a FE model. In all cases, the authors found the influence of SSI relevant. Romero et al. [1] and Romero et al. [7] studied the effect of SSI on the resonant response of railway bridges. They concluded that the bridge fundamental periods and damping ratios increase when soil interaction is taken into account. Later, Doménech et al. [8] and Martínez-Rodrigo [9] analysed SSI effects over an extensive catalogue of bridge typologies prone to experience high transverse accelerations at resonance for modern trains and high design velocities. They studied the structural response using a coupled 3D BE-FE model and concluded that incorporating SSI effects in the analysis of new simply supported (SS) bridges or in the analysis of existing ones for retrofitting purposes could be of great importance in the assessment of the Serviceability Limit Sate (SLS) associated to traffic safety. González et al. [10] studied the performance of inclined pile foundations on the seismic response of bridges. The authors computed impedance functions and kinematic interaction factors of the pile foundations and compared them with the results of two different approaches: a Winkler-type model and a BE-FE model. Zangeneh et al. [11] presented a simplified discrete model for calculating the modal parameters of the fundamental bending mode of railway beam bridges on viscoelastic supports. They proposed exact, closed-form expressions for the fundamental frequency and modal damping ratio, considering the effect of the dynamic stiffness and dissipation capacity of the foundation-soil system. Recently, Zangeneh [12] investigated the effect of the foundation mass on the fundamental modal properties of the beam bridges. Gara et al. [13] studied the effect of the foundation-soil system on the interpretation of experimental ambient vibration tests and on the calibration of numerical models. They concluded that the common practice of updating fixed base numerical models to fit experimental results should be prudently evaluated in the case of bridges where SSI is significant. In the aforementioned research, simplified foundation geometries are mostly considered due to the high computational cost of the chosen numerical approaches. However, the computational effort could be reduced to a certain extent during SSI simulations using Perfectly Matched Layers (PML) to limit the size of the soil domain [14–18]. For example, Davoodi et al. [19] studied the response of simplified geometries of different foundations using the absorbing layers provided by the PML incorporated in a

FE model. Lopes et al. [20] studied the problem of a track-tunnel-ground system using a two-and-a-half-dimensional (2.5D) FE–PML approach. Esmaeilzadeh Seylabi et al. [21] solved the wave propagation problem in the frequency-domain on a FE model applying PML to numerically simulate measured dynamic impedances of soil-pile systems. Zangeneh et al. [22] investigated the effect of dynamic SSI on the resonant response of portal frame bridges founded on a rigid base, and the parameters governing their interaction. The authors compare the results given by a simplified model with those from a full 3D FE-PML model.

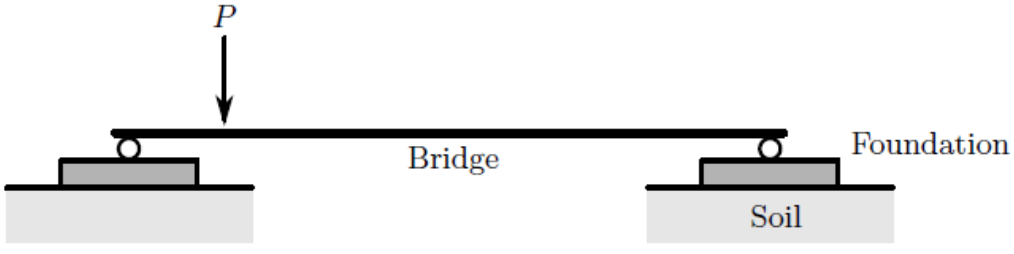

Figure 1. *Schematic representation of soil-foundation-bridge coupled system.*

Figure 1 shows a schematic representation of the railway beam-bridge coupled problem. The problem is usually divided into two sub-domains. First the bridge deck, supports and foundations are commonly represented using FEs. Then this structural domain is coupled to the soil subspace. Alternatively, if the complete problem is modelled, and therefore modal superposition is not applied, the corresponding dynamic equilibrium equations can be solved using either implicit or explicit integration schemes, in the time or frequency domains. These approaches require large amounts of computational resources and time since, in addition, it is usually required to obtain the bridge response under several train types and speeds. An alternative and faster approach is to decouple the problem and to compute the structural response as the superposition of the first modal contributions. However, this transformation is not straightforward when the soil is accounted for, due to the presence of non-proportional damping.

In this paper a general approach is proposed to solve the SSI problem in railway bridges applying modal superposition. A sub-structuring approach involving PML permits the modelling of arbitrary foundation geometries. First, the problem in Figure 1 is decoupled into i) the soil-foundation problem, and, ii) the soil-foundation-bridge interaction problem. In the first, the equivalent frequency dependent dynamic stiffness and damping characteristics of the soil-foundation system are computed using the FE-PML method. In the second, the dynamic response of the structure under railway traffic is computed using a FE model that includes spring/dashpot elements at the supports, where the equivalent properties at the bridge-foundation connection points are extracted from the first problem. This soil-foundation-bridge model is solved by modal superposition considering the equivalent dynamic stiffness and damping of the soil-foundation corresponding to each natural frequency. To do so, a model updating procedure is implemented. As the model presents non-proportional damping, the complex eigenvalue problem is solved in order to compute the natural frequencies and mode shapes.

2. NUMERICAL FORMULATION

The soil-foundation-bridge interaction problem (Figure 1) is decoupled with the aim of implementing a fast and accurate analysis tool that can be used in practice for the design and performance evaluation of these types of structures. Next, the formulation is briefly described. Detailed information is found in Reference [23].

2.1. Soil-foundation interaction problem

The dynamic stiffness of the soil-foundation system is computed applying the FE method. In order to represent the absorbing boundaries for the wave equation, PML is used [15, 24, 26].

2.2. Soil-foundation-bridge interaction problem

Figure 2 shows the soil-foundation-bridge decoupled model. Beam bridges of length L, cross-section bending stiffness EI_z, mass per unit length m_b, and structural damping ζ are discretized using two-node Bernoulli-Euler beam elements, well suited for the analysis of railway bridges in this study given the slenderness ratios and the frequency range of interest from 0 Hz to 30 Hz [8]. The spring/dashpot elements at the bridge-foundation connection points, with equivalent stiffness and damping values K_v and C_v, are obtained from the FE-PML. Therefore, the cross-interaction between the two foundations of the bridge is neglected. The bridge FE model with N dof is solved using complex modal superposition [25,26].

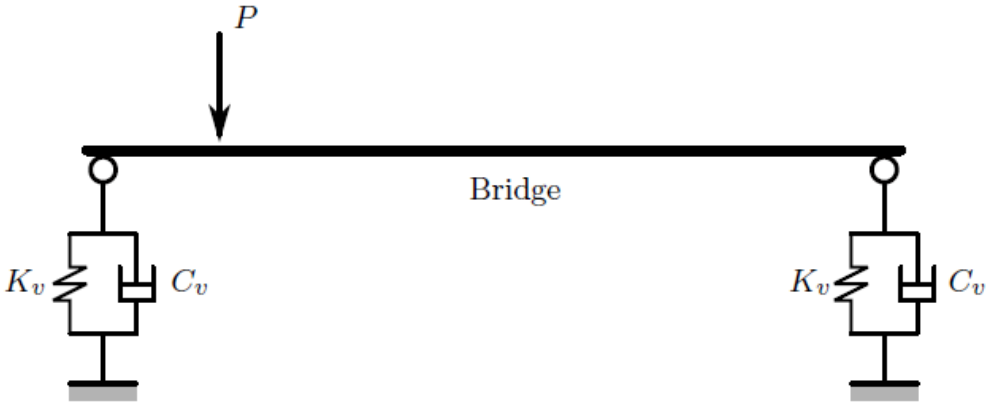

Figure 2. *Schematic representation of soil-foundation-bridge decoupled system.*

3. CASE STUDY

In this section the dynamic response of Old Guadiana bridge (Figure 3), from Madrid-Alcázar de San Juan-Jaén conventional railway line in Spain, is reproduced and compared with experimental measurements. It is a SS bridge with two identical spans of approximately 12 m of length. The deck is composed of two single track independent decks of 5.075 m width. Each deck consists of a 25 cm thickness concrete slab resting on five pre-stressed concrete beams with a 75 cm height rectangular cross-section (Figure 3.(a)). This bridge was monitored by the authors in 2019. Details of the

experimental campaign, the identified properties of the bridge and surrounding soil and the dynamic response under several train passages may be consulted in [27].

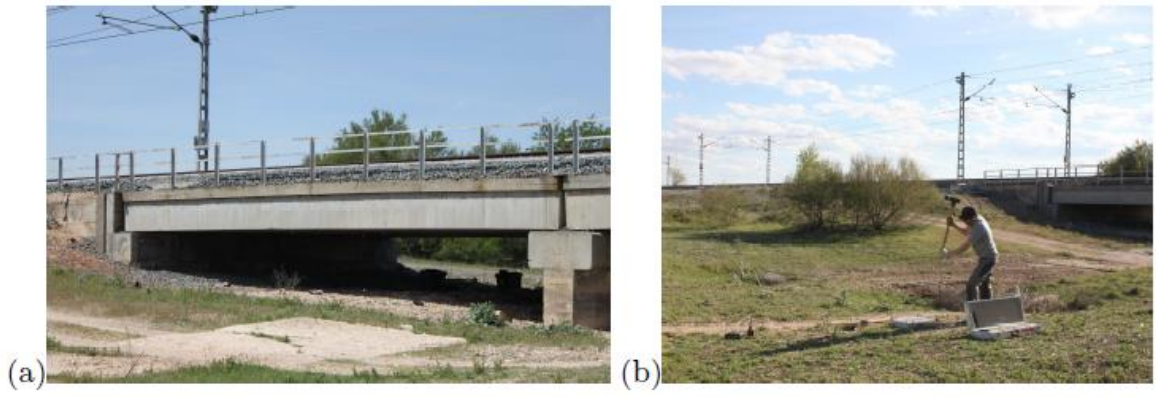

Figure 3. *(a) Old Guadiana bridge and (b) soil test set-up.*

The site has two upper soil layers with a shear wave velocity close to 300 m/s resting on a halfspace with C_s = 250 m/s (Figure 3(b) and Table 1). According to [28], the soil profile is approximated as a homogeneous stratum with average shear wave velocity V_{s30} = 303 m/s. Likewise, a material damping ratio of 7.85% is admitted. Following, the results obtained from the actual stratigraphy and the equivalent homogeneous soil are compared.

Table 1. Identified soil properties at Old Guadiana Bridge

Layer	h [m]	C_p [m/s]	C_s [m/s]	ρ [kg/m^3]
1	2	499	298	1900
2	4.5	350	207	1900
3	3.6	1300	719	1900
4	∞	500	250	1900

A first vertical bending mode with a natural frequency of 9.8 Hz is identified from ambient vibrations. The modal damping corresponding to this mode obtained under traffic conditions reaches 2.8%, which is higher than the value prescribed by standards for design purposes for this particular length and bridge typology (1.5% as per [29]). A beam model of the bridge is considered in order to show the application of the previously proposed approach. 5m x 5m rigid massless foundations are included. The value for the fundamental frequency of the beam model in the SS case is 10.06 Hz. This frequency reduces to 9.8 Hz due to SSI effects. The MAC value [30] between the experimental mode shape corresponding to the longitudinal middle section and the numerical mode shape is 0.99. As part of the initial approach, only

the contribution of this mode is taken into account as it dominates the vertical response at mid-span along the centre line. Nevertheless, the first torsion and transverse bending modes with frequencies 11.0 Hz and 12.8 Hz were also identified.

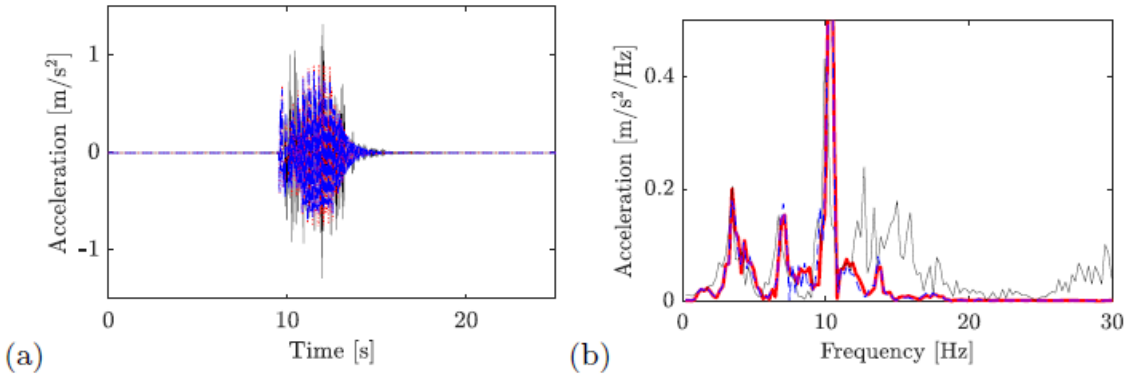

Figure 4. *Old Guadiana Bridge: (a) time history and (b) frequency content of the acceleration at the midspan induced by Renfe Altaria train with 9 coaches at v=160 km/h circulating on track 2: (black line) experimental and numerical results. The results obtained using the actual stratigraphy are plotted in blue trace, and those obtained from the equivalent homogeneous soil are represented in red.*

The response of the bridge is presented under the circulation of the Renfe Altaria train with 9 coaches crossing the bridge at v=160 km/h. Figure 4 shows the bridge acceleration response at the mid-span section, measured under the track and its comparison with the numerical predictions obtained with the proposed methodology. The agreement between numerical and experimental results is good given the simplicity of the beam model used for the deck. The response contains peaks associated with the excitation (i.e. ratio of train speed v to the characteristic distance v/d=3.38 Hz), corresponding harmonics and with the bridge lowest natural frequency. The experimental response shows certain participation of modes between 10 and 20 Hz that cannot be reproduced with the beam model. The train speed is close to a third resonance of the fundamental mode of the bridge: $v_{1,3}=f_1*d/3$ = 9.8*13.14/3*3.6=154 km/h. This justifies the dominant contribution of this mode in the frequency domain. The numerical prediction overestimates the response at the resonant frequency, which is expected because dissipation mechanisms such as vehicle-structure and track-structure interaction are not included, and are particularly relevant under these conditions. In this case, the actual stratigraphy is well represented by the equivalent homogeneous soil. The comparison between both results presents very small differences in the frequency range analysed.

4. CONCLUSIONS

A fast numerical methodology to determine the dynamic response of railway bridges under the passage of running trains including the effect of soil-structure interaction is proposed. The coupled problem is sub-structured into a soil-foundation and a soil-foundation-bridge interaction problems. In the first step, the foundation and surrounding soil are simulated via a FE-PML model. Using this approach,

equivalent frequency dependent dynamic stiffness and damping characteristics of the soil-foundation system are computed. In the second step, the dynamic response of the structure under railway traffic is calculated using a FE model that includes spring/dashpot elements at the supports, using the equivalent properties extracted from the first problem. This model is solved by complex modal superposition considering the equivalent dynamic stiffness and damping of the soil-foundation corresponding to each natural frequency. The complex modal parameters are obtained iteratively and the dynamic complex modal equations are solved using a Runge-Kutta explicit algorithm. The benefits of the proposed approach increase dramatically with the problem complexity since it allows exploiting dedicated analysis tools for addressing the soil-foundation and the superstructure domain. Using the proposed model, the experimental response of a real beam-type bridge under train loading is reproduced, capturing the frequency contributions of the first structural bending mode and the loading frequency contributions.

ACKNOWLEDGEMENTS

The authors would like to acknowledge the financial support provided by the Spanish Ministries Science and Innovation and Universities under research project PID2019-109622RB; US-126491 funded by the FEDER Andalucía 2014-2020 Operational Program; Generalitat Valenciana under research project [AICO2019/175] and the Andalusian Scientific Computing Centre (CICA).

REFERENCES

1. A. Romero, M. Solís, J. Domínguez, P. Galvín, Soil–structure interaction in resonant railway bridges, Soil Dynamics and Earthquake Engineering 47, 108 (2013). DOI http://dx.doi.org/10.1016/j.soildyn.2012.07.014. SI: José Manuel Roëesset
2. J. Domínguez, Boundary Elements in Dynamics. Computational engineering (Computational Mechanics Publications, 1993)
3. J. Lysmer, L.A. Drake, A finite element method for seismology, in Seismology: Surface Waves and Earth Oscillations, Methods in Computational Physics: Advances in Research and Applications, vol. 11, ed. by B.A. Bolt (Elsevier, 1972), pp. 181–216. DOI https://doi.org/10.1016/B978-0-12-460811-5.50009-X
4. P. Galvín, J. Dominguez, High-speed train-induced ground motion and interaction with structures, Journal of Sound and Vibration 307(3), 755 (2007). DOI https://doi.org/10.1016/j.jsv.2007.07.017.
5. HMF Báez, A. Fraile, J. Fernández, L. Hermanns, A vibration prediction model for culvert-type railroad underpasses. Engineering Structures 172 (2018), 1025–1041
6. A. Zangeneh, C. Svedholm, A. Andersson, C. Pacoste, R. Karoumi, Identification of soil–structure interaction effect in a portal frame railway bridge through full-scale dynamic testing Engineering Structures 159, 299 (2018). DOI https://doi.org/10.1016/j.engstruct.2018.01.014
7. A. Romero, P. Galvín, J. Domínguez, Comportamiento dinámico de viaductos cortos considerando la interacción vehículo-vía-estructura-suelo Revista Internacional de Métodos Numéricos para Cálculo y Diseño en Ingeniería 28(1), 55 (2012). DOI https://doi.org/10.1016/j.rimni.2011.11.004

8. A. Doménech, M. Martínez-Rodrigo, A. Romero, P. Galvín, On the basic phenomenon of soil-structure interaction on the free vibration response of beams: application to railway bridges Engineering Structures 125, 254 (2016). DOI http://dx.doi.org/10.1016/j.engstruct.2016.06.052
9. M. D Martínez-Rodrigo, P. Galvín, A. Doménech, A. Romero, Effect of soil properties on the dynamic response of simply-supported bridges under railway traffic through coupled boundary element-finite element analyses. Engineering Structures 170, 78 (2018). DOI https://doi.org/10.1016/j.engstruct.2018.02.089
10. F. González, S. Carbonari, L.A. Padrón, M. Morici, J.J. Aznárez, F. Dezi, O. Maeso, G. Leoni, Benefits of inclined pile foundations in earthquake resistant design of bridges Engineering Structures 203, 109873 (2020). DOI https://doi.org/10.1016/j.engstruct.2019.109873.
11. A. Zangeneh, J.M. Battini, C. Pacoste, R. Karoumi, Fundamental modal properties of simply supported railway bridges considering soil–structure interaction effects Soil Dynamics and Earthquake Engineering 121, 212 (2019). DOI https://doi.org/10.1016/j.soildyn.2019.03.022
12. A. Zangeneh, Dynamic soil-structure interaction analysis of high-speed railway bridges. Ph.D. thesis, KTH Royal Institute of Technology (2021)
13. F. Gara, M. Regni, D. Roia, S. Carbonari, F. Dezi, Evidence of coupled soil–structure interaction and
14. site response in continuous viaducts from ambient vibration tests, Soil Dynamics and Earthquake Engineering 120, 408 (2019). DOI https://doi.org/10.1016/j.soildyn.2019.02.005
15. U. Basu, A.K. Chopra, Perfectly matched layers for time-harmonic elastodynamics of unbounded domains: theory and finite-element implementation, Computer Methods in Applied Mechanics and Engineering 192(11), 1337 (2003). DOI https://doi.org/10.1016/S0045-7825(02)00642-4
16. U. Basu, A.K. Chopra, Perfectly matched layers for time-harmonic elastodynamics of unbounded domains: theory and finite-element implementation, Computer Methods in Applied Mechanics and Engineering 192(11), 1337 (2003). DOI https://doi.org/10.1016/S0045-7825(02)00642-4
17. U. Basu, A.K. Chopra, Perfectly matched layers for transient elastodynamics of unbounded domains, International Journal for Numerical Methods in Engineering 59(8), 1039 (2004). DOI https://doi.org/10.1002/nme.896
18. U. Basu, Explicit finite element perfectly matched layer for transient three-dimensional elastic waves, International Journal for Numerical Methods in Engineering 77(2), 151 (2009). DOI https://doi.org/10.1002/nme.2397
19. E. Kausel, J.M. de Oliveira Barbosa, Pmls: a direct approach, International Journal for Numerical Methods in Engineering 90(3), 343 (2012). DOI https://doi.org/10.1002/nme.3322
20. M. Davoodi, A. Pourdeilami, H. Jahankhah, M.K. Jafari, Application of perfectly matched layer to soil-foundation interaction analysis, Journal of Rock Mechanics and Geotechnical Engineering 10(4), 753 (2018). DOI https://doi.org/10.1016/j.jrmge.2018.02.003
21. P. Lopes, P.A. Costa, M. Ferraz, R. Calcada, A.S. Cardoso, Numerical modeling of vibrations induced by railway traffic in tunnels: from the source to the nearby buildings, Soil Dynamics and Earthquake Engineering 61-62, 269 (2014). DOI https://doi.org/10.1016/j.soildyn.2014.02.013
22. E. Esmaeilzadeh Seylabi, A. Kurtulu¸s, K.H. Stokoe, E. Taciroglu, Interaction of a pile with layered-soil under vertical excitations: field experiments versus numerical simulations, Bulletin of Earthquake Engineering 15, 3529–3553 (2017). DOI https://doi.org/10.1007/s10518-017-0099-5

23. P. Galvín, A. Romero, E. Moliner, D. P. Connolly, M.D. Martínez-Rodrigo. Fast simulation of railway bridge dynamics accounting for soil-structure interaction. Bulletin of Earthquake Engineering, 2021. http://dx.doi.org/10.1007/s10518-021-01191-0
24. A. Zangeneh, S. Francois, G. Lombaert, C. Pacoste, Modal analysis of coupled soil–structure systems, Soil Dynamics and Earthquake Engineering 144, 106645 (2021). DOI https://doi.org/10.1016/j.soildyn.2021.106645
25. D.S. Bindel, S. Govindjee, Elastic pmls for resonator anchor loss simulation, International Journal for Numerical Methods in Engineering 64(6), 789 (2005). DOI https://doi.org/10.1002/nme.1394
26. W.C. Hurty, M.F. Rubinstein, Dynamics of structures (Prentice-Hall, Inc., 1965)
27. P. Galvín, A. Romero, E. Moliner, G. De Roeck, M. Martínez-Rodrigo, On the dynamic characterisation of railway bridges through experimental testing. Engineering Structures 226, 111261 (2021). DOI https://doi.org/10.1016/j.engstruct.2020.111261
28. Eurocode 8, Eurocode 8: Design of structures for earthquake resistance–Part 1: General rules, seismic actions and rules for buildings. CEN, EN 1998-1:2004 (European Committee for Standardization, Brussels, 1998)
29. Eurocode 1, Eurocode 1: Actions on Structures - Part 2: Traffic loads on bridges. CEN, EN 1991-2 (European Committee for Standardization, Brussels, 2002)
30. R.J. Allemang, D.L. Brown, Correlation coefficient for modal vector analysis, in Proceedings of International Modal Analysis I (1982), pp. 110–116

PARAMETRIC ANALYSIS OF SERVICEABILITY LIMIT STATE VERIFICATIONS IN REINFORCED CONCRETE ELEMENTS SUBJECTED TO BENDING

Sáez Fernández, M.[1], Pereiro Barceló J.[2], Varona Moya F.B.[3]

ABSTRACT

This study is focused on the serviceability limit states (SLS) of stress limitation, cracking control and deflections of reinforced concrete (RC) beams. An initial case study is presented, in which a RC continuous beam exhibits excessive compressive stress in the concrete whilst complying with the other two SLS's and the ultimate limit state (ULS) design of reinforcement. Consequently, a massive parametric analysis of over 1,4 million RC beams was undertaken in MATLAB. More than 84% of the cases did not verify the concrete compressive stress limitation. A closer look at these problematic situations would show that a great number of them correspond to RC structures with a low strength grade concrete, manufactured with aggregate of higher quality and whose ULS design was based on a linear analysis with limited redistribution of moments. Furthermore, the excessive compressive stress in service compromises the long-term behaviour owing to the non-linear creep of concrete.

Keywords: concrete, stress limitations, cracking, deflections, parametric analysis.

1. INTRODUCCIÓN

El procedimiento de cálculo y dimensionamiento de estructuras de hormigón armado para edificaciones convencionales suele ajustarse a una secuencia claramente definida: inicialmente cada elemento de la estructura se discretiza con elementos tipo barra –con una serie de vinculaciones internas y externas– y a continuación se determinan las cargas que actúan sobre cada uno de estos elementos derivados del uso y/o función al que va a ser destinada. Seguidamente se realiza un pre-dimensionamiento, en el que en base a su principal dimensión (luz L en caso de vigas, altura H en caso de los pilares), se estiman las otras dos dimensiones que caracterizan la sección transversal (ancho b, canto h o canto útil d) siguiendo ciertos requisitos iniciales de esbeltez (d/L, h/H …) recomendados en normativas y guías de diseño como, por ejemplo, el Eurocódigo 2 en su Tabla 7.4.N [2]. Una vez configurado el modelo estructural y sus cargas asociadas, se realiza el cálculo de esfuerzos, momento a partir del cual se procede a su dimensionamiento y comprobación propiamente dichas, frecuentemente de manera iterativa hasta justificar el cumplimiento de todos los Estados Límite.

En la fase de dimensionamiento y comprobación de una pieza de hormigón armado sometida a flexión, los distintos códigos estructurales proporcionan los requisitos de verificación en rotura (ELU) y en servicio (ELS), siendo habitual iniciar el dimensionamiento mediante la definición del armado para

[1] Departamento de Ingeniería Civil. Universidad de Alicante (España). miguel.saez@ua.es
[2] Departamento de Ingeniería Civil. Universidad de Alicante (España). javier.pereiro@ua.es
[3] Departamento de Ingeniería Civil. Universidad de Alicante (España). borja.varona@ua.es (Corresponding author)

cumplir los distintos ELU y posteriormente verificar los distintos ELS efectuando las correcciones pertinentes en su caso. Tras la revisión de la bibliografía existente sobre las comprobaciones en E.L.S. [3]–[6], se observa que una amplia mayoría de ellas se centran en la verificación de las deformaciones verticales y fisuración modificando si fuera preciso el armado de la pieza para lograr reducir el ancho fisura, ya que en caso de que no se verifiquen las limitaciones de deformaciones, sería necesario recurrir a variar la geometría de la sección. En cambio, no suele ser una práctica habitual la verificación de las tensiones en servicio en el bloque comprimido de hormigón cuando el Eurocódigo 2 [2] indica que "se debe limitar con el fin de evitar fisuras longitudinales, micro fisuras o altos niveles de fluencia, que podrían producir efectos inaceptables en la función de la estructura". Adicionalmente, es un hecho ampliamente aceptado que la tensión de compresión excesiva en servicio, especialmente en condiciones cuasi-permanentes produce una fluencia no lineal, que la mayoría de los códigos de diseño no pueden predecir con precisión [5]. Por ello, algunas reglas de diseño estándar, como puede ser la adopción de una esbeltez (d/L) de 15, pueden conducir a diseños poco fiables. Paradójicamente, en algunas referencias bibliográficas [7] se recomienda literalmente no realizar la comprobación de tensiones en el hormigón.

En este artículo se realiza un caso de estudio, basado en las disposiciones del Eurocódigo 2 [2], para poner de manifiesto, que tras realizar un dimensionamiento en ELU de una pieza de hormigón armado a partir de la determinación de la armadura necesaria para resistir las acciones que actúan sobre la estructura, finalmente se comprueba que en servicio no se verifica la condición de la limitación de tensión en servicio bajo la combinación característica de carga y en cambio sí que se verifica la abertura de fisura y la deformación vertical. Tras este análisis puntual, y para mostrar el alcance del problema, se muestra el desarrollo de un análisis paramétrico masivo programado en MATLAB [1], para obtener unos gráficos de resultados que ayuden a identificar los condicionantes directores que marcan el diseño de vigas de hormigón armado.

2. CASO DE ANÁLISIS

A continuación, se procede a realizar el diseño y análisis de una viga continua de dos vanos de hormigón armado, tal y como se define en la Fig. 1 cuyo objetivo es mostrar la importancia de las verificaciones en servicio, especialmente la limitación de tensiones de compresión en hormigón. La sección transversal considerada, dispone de un ancho de 40 cm, un canto de 50 cm y un canto útil de 44 cm. La viga de hormigón armado debe soportar su peso propio además de unas cargas permanente de 5 kN/m^2 debida al peso de un forjado que sustenta con un ancho tributario de 4 m y carga muerta debida a pesos de solado, tabiquerías e instalaciones. El conjunto estructural pertenece a una edificación de viviendas, de modo que la carga variable que debe soportar es de 2 kN/m^2 (Categoría A, de acuerdo al Eurocódigo 1 [8]) y con un coeficiente de combinación casi-permanente (ψ_2) de 0,3 de acuerdo al Eurocódigo 0 [9]. Para el ancho de la sección transversal b se han considerado tres valores diferentes: 15, 20 y 30 cm.

El acero considerado para las armaduras de refuerzo tiene un límite elástico característico (f_{yk}) de 500 MPa, con un módulo de elasticidad (E_s) de 200 GPa. El criterio de armado seguido en este estudio es el definido por el Eurocódigo 2 [2]. La caracterización del hormigón se ha considerado que el mismo está realizado con áridos densos de piedra caliza, por lo que para el cálculo del módulo de elasticidad del hormigón a 28 días (E_{cm}) se ha empleado la formulación del Eurocódigo 2 y corrigiendo con un

coeficiente de 1,2 de acuerdo con el Código Modelo 2010 [10]. El coeficiente de fluencia se ha determinado empleando las ecuaciones del Anexo B del Eurocódigo 2, que son equivalentes a las proporcionadas por el Código Modelo 2010, cuando se utilice un cemento de endurecimiento normal. Para el cálculo del coeficiente de fluencia $\varphi(t,t_0)$ se consideran los siguientes parámetros: edad de diseño t = 18250 días (≈ 50 años); edad de puesta en carga t_0 = 14 días, humedad relativa del 70%. Para la determinación del perímetro expuesto y en consecuencia del valor del espesor medio, se considera que el canto del forjado es de 25 cm y se encuentra en el canto de la viga. Para la resolución de este supuesto práctico, se han considerado dos tipos de hormigón, según la Tabla 1.

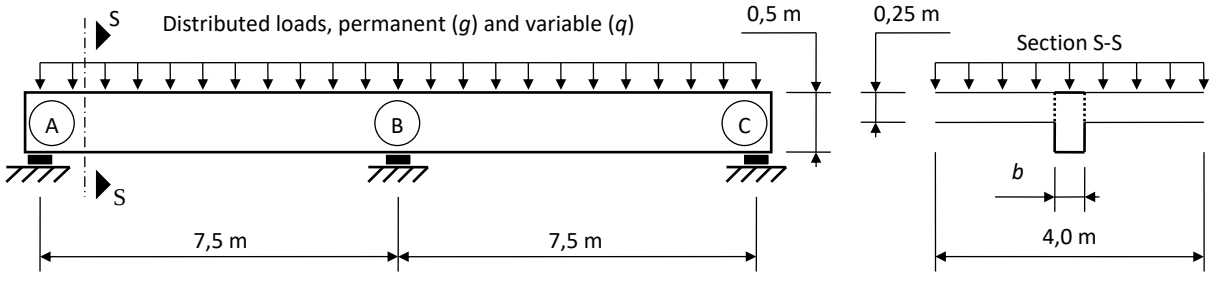

Fig. 1. Viga de hormigón armado, continua de dos vanos iguales

Tabla 1. Parámetros de diseño considerados en el diseño

Concrete grade	Characteristic concrete compressive strength f_{ck} (MPa)	Secant modulus of elasticity, 28 days E_{cm} (GPa)	Creep coeff. $\varphi(t,t_0)$		
			b = 15 cm	b = 20 cm	b = 30 cm
C20/25	20	36,0	2,61	2,55	2,47
C30/37	30	39,4	2,16	2,11	2,05

Para el diseño en ELU, sólo se considera el armado necesario por flexión, ya que, la presencia del armado a cortante prácticamente no tiene influencia para las comprobaciones de los distintos ELS posteriores. Para la determinación la armadura longitudinal en el apoyo B, se ha realizado un análisis lineal con redistribución limitada de acuerdo con el Eurocódigo 2 [2], con un coeficiente de redistribución δ = 0,8. En algunos casos es necesaria armadura de compresión para garantizar que la profundidad de la fibra neutra x_u no supere el 28,8% del canto útil d y garantizar de este modo la capacidad de rotación en rotura. Las expresiones empleadas para la determinación de las cuantías de armadura longitudinal a tracción y compresión en rotura se han tomado de [11], adoptando el diagrama rectangular para el comportamiento del hormigón a compresión, despreciando la contribución del hormigón a tracción, y un diagrama tensión – deformación del acero bi-lineal sin endurecimiento plástico para el acero de las armaduras, como se ilustra en la Fig. 2(a).

En la Tabla 2 se muestra la sección de armadura teórica necesaria tanto a tracción como a compresión ($A_{s,req}$ y $A'_{s,req}$, respectivamente) a partir de los valores de los momentos flectores tras la aplicación de la redistribución en el apoyo B (empotramiento), y en la sección de máxima flexión positiva en el vano. A partir del armado teórico, se define una armadura, definida por el número y diámetro de barras

necesarias ($A_{s,prov}$ y $A'_{s,prov}$, respectivamente). Para la verificación de los distintos ELS, no puede considerarse la redistribución de flectores realizada, de modo que para las comprobaciones en servicio se emplea el análisis lineal original tanto para la combinación característica (verificación de tensiones y deformaciones) como para la combinación cuasi-permanente (verificación de la abertura de fisura).

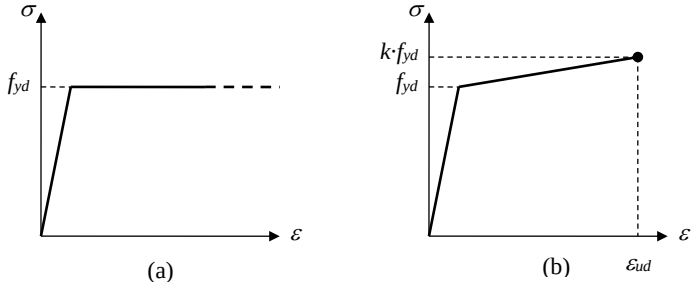

Fig. 2. Ley bi-lineal de comportamiento del acero para armaduras pasivas en ELU: (a) sin endurecimiento plástico y sin limitación de alargamiento unitario; (b) con endurecimiento plástico y limitación del alargamiento unitario.

Tabla 2. Resultados del dimensionamiento en ELU con redistribución de momentos (δ = 0,8)

	C20/25			**C30/37**		
Cross-sectional width *b*	15 cm	20 cm	30 cm	15 cm	20 cm	30 cm
Hogging M_{Ed} at B after redistribution (m·kN)	-234	-238	-248	-234	-238	-248
$A_{s,prov}$	3×Ø25	3×Ø25	5×Ø20	4×Ø16 + 2×Ø20	4×Ø16 + 2×Ø20	3×Ø25
$A'_{s,prov}$	4×Ø20	2×Ø25	3×Ø12 + 1×Ø20	1×Ø16 + 2×Ø20	3×Ø16	2×Ø8
Max. sagging M_{Ed} after redistribution (m·kN)	187	191	198	187	191	198
$A_{s,prov}$	1×Ø16 + 2×Ø25	4×Ø20	4×Ø20	4×Ø20	1×Ø16 + 2×Ø25	1×Ø16 + 2×Ø25
$A'_{s,prov}$	1×Ø10 + 2×Ø16	2×Ø10 + 1×Ø12	2×Ø8	2×Ø10	2×Ø8	2×Ø8

La combinación cuasi-permanente también es empleada para determinar el valor a corto plazo de la tensión de compresión del hormigón para comprobar el efecto no lineal a largo plazo sobre el coeficiente de fluencia si la tensión de compresión en el hormigón supera el 45 % de f_{ck}, empleando la Eq. (1) dada por el Eurocódigo 2 [2].

$$\varphi_{nl}(\infty, t_0) = \varphi(\infty, t_0) \cdot exp\left\{1{,}5 \cdot \left[\frac{\sigma_c}{f_{ck}(t_0)} - 0{,}45\right]\right\} \qquad (1)$$

donde $\varphi_{nl}(\infty,t_0)$ es el coeficiente de fluencia no lineal que remplazaría a $\varphi(\infty,t_0)$, σ_c es la tensión de compresión en el momento de puesta en carga t_0, y $f_{ck}(t_0)$ es la resistencia característica inicial del hormigón. Con la intención de simplificar, en este estudio se supone que σ_c se puede obtener considerando sólo el efecto a corto plazo de las cargas cuasi-permanentes, es decir $\varphi(t,t_0) = \varphi(t_0,t_0) = 0$. Por tanto, los valores de las tensiones a largo plazo en hormigón y armaduras, se calculan teniendo en consideración el coeficiente de homogeneización α_s para el acero con $\varphi(t,t_0)$ o $\varphi_{nl}(\infty,t_0)$ cuando sea necesario. Además, para el análisis estructural lineal basado en la teoría de elasticidad, se asume que la viga tiene una inercia constante, dado que el Eurocódigo 2 [2] permite adoptar la hipótesis de secciones no fisuradas. Bajo este supuesto, se obtienen los valores de los flectores en ELS de las Tablas 3 y 4.

Tabla 3. Resultados de las comprobaciones ELS a flexión negativa en el empotramiento B. Los valores entre paréntesis son porcentajes respecto de f_{ck} o f_{yk}

	C20/25			**C30/37**		
Anchura *b* de la sección	15 cm	20 cm	30 cm	15 cm	20 cm	30 cm
Valor caract. de M_{Ed} (m·kN)	-210	-214	-223	-210	-214	-223
Valor cuasi-perm. de M_{Ed} (m·kN)	-171	-175	-184	-171	-175	-184
Cfte. de homogeneización a corto plazo $\alpha_{s,st}$	5,56	5,56	5,56	5,08	5,08	5,08
Momento de fisura M_{cr} (m·kN)	17,9	22,3	31,5	22,4	28,2	39,9
Producto $E_c \cdot I_{cr}$ (m^2·kN)	32869	34337	38726	32087	33767	37004
Tensión característica en el hormigón $\sigma_{c,char}$ (MPa)	34,8 (174%)	31,8 (159%)	26,6 (133%)	39,0 (130%)	34,9 (116%)	29,6 (99%)
Tensión cuasi-perm. en el hormigón $\sigma_{c,qp}$ (MPa)	28,3 (141%)	25,9 (130%)	21,9 (110%)	31,7 (106%)	28,5 (95%)	24,4 (81%)
$\varphi_{nl}(t,t_0)$ / $\varphi(t,t_0)$	4,25	3,56	2,64	2,48	2,11	1,72
Cfte. de homogeneización a largo plazo $\alpha_{s,lt}$	67,3	56,1	41,8	32,3	27,7	23,0
Producto $E_c \cdot I_{cr}$ (m^2·kN)	21977	21416	23414	21113	21971	24026
Tensión característica en la armadura $\sigma_{s,char}$ (MPa)	380 (76%)	391 (78%)	386 (77%)	396 (79%)	406 (81%)	412 (82%)
Tensión cuasi-perm. en la armadura $\sigma_{s,qp}$ (MPa)	309	320	318	322	331	339
Ancho de fisura w_k (mm)	0,19	0,21	0,22	0,19	0,21	0,25

Estas tablas recogen el coeficiente de homogeneización a corto plazo $\alpha_{s,st}$ y a largo plazo $\alpha_{s,lt}$, que a su vez se emplean para la obtención del momento de fisuración M_{cr}, el producto $E_s \cdot I_{cr}$ –asociado a la rigidez a flexión– y los valores en servicio de la compresión de hormigón y de la tracción de la armadura a

tracción. En lo que respecta a la verificación de las deformaciones verticales deformación, en este primer análisis manual, se ha efectuado realizando la verificación a partir de la relación de esbeltez (luz-canto útil) indicados en el apartado 7.4.2 del Eurocódigo 2 [2], que es independiente del ancho de la sección *b* o de la resistencia característica del hormigón. Para realizar esta última verificación, se han empleado las expresiones que proporciona la norma para la comprobación de los límites de esbeltez para omitir el cálculo de deformaciones verticales, efectuando la corrección para un vano de 7,5 m y para las tensiones en el acero a largo plazo y bajo la combinación característica de carga en servicio que superan los 310 MPa en la sección de centro de vano [2].

Tabla 4. Resultados de las comprobaciones ELS en la sección a máxima flexión positiva. Los valores entre paréntesis son porcentajes respecto de f_{ck} o f_{yk}

	C20/25			**C30/37**		
Anchura *b* de la sección	15 cm	20 cm	30 cm	15 cm	20 cm	30 cm
Valor caract. de M_{Ed} (m·kN)	118	121	126	118	121	126
Valor cuasi-perm. de M_{Ed} (m·kN)	96,0	98,5	103	96,0	98,5	103
Cfte. de homogeneización a corto plazo $\alpha_{s,st}$	5,56	5,56	5,56	5,08	5,08	5,08
Momento de fisura M_{cr} (m·kN)	16,7	21,3	30,3	21,3	27,1	39,2
Producto $E_c \cdot I_{cr}$ (m^2·kN)	26740	29542	32019	28029	28581	31037
Tensión característica en el hormigón $\sigma_{c,char}$ (MPa)	23,7 (119%)	20,6 (103%)	17,1 (85%)	25,4 (85%)	22,3 (74%)	18,1 (60%)
Tensión cuasi-perm. en el hormigón $\sigma_{c,qp}$ (MPa)	19,3 (97%)	16,8 (84%)	14,1 (71%)	20,7 (69%)	18,2 (61%)	14,9 (50%)
$\varphi_{nl}(t,t_0)$ / $\varphi(t,t_0)$	2,17	1,80	1,47	1,43	1,27	1,08
Cfte. de homogeneización a largo plazo $\alpha_{s,lt}$	37,0	31,1	25,8	20,7	18,7	16,3
Producto $E_c \cdot I_{cr}$ (m^2·kN)	16226	17707	20921	17726	19551	23430
Tensión característica en la armadura $\sigma_{s,char}$ (MPa)	273 (55%)	265 (53%)	271 (54%)	260 (52%)	277 (55%)	279 (56%)
Tensión cuasi-perm. en la armadura $\sigma_{s,qp}$ (MPa)	222	216	223	212	226	230
Relación $L/d \leq$ (cf. c. 7.4.2 in [2])	19,8	20,0	19,8	20,2	19,6	21,8
d (cm) ≥	38,0	37,5	37,9	37,1	38,3	34,4
Ancho de fisura w_k (mm)	0,14	0,14	0,17	0,13	0,16	0,19

Tal y como se muestra en la Tabla 4, el canto útil de la viga (d = 44 cm) verifica el criterio de esbeltez máxima definido por el Eurocódigo 2 [2] para omitir el cálculo de deformaciones en todos los casos. En lo que respecta al control de la fisuración se ha empleado el método de cálculo de abertura de fisura del Eurocódigo 2 [2] para la determinación del ancho de fisura (mostrados en las Tablas 3 y 4) y cuyos valores son inferiores a 0,3 mm recomendado para entornos en los que puede producirse corrosión por carbonatación, por cloruros o por cloruros de agua marina. Sin embargo, la verificación de tensiones en servicio en hormigón muestra resultados controvertidos, especialmente en la sección de empotramiento B. Los valores más elevados de la tensión de compresión en el hormigón se alcanzan para un hormigón C20/25: hasta el 174 % de f_{ck} o 141 % de f_{ck} bajo la combinación característica o casi-permanente respectivamente. Incluso para un hormigón C30/37 y para un ancho de sección (b=30 cm) son muy cercanos al 100 % de f_{ck} bajo la combinación característica de carga.

A la vista de los resultados en las Tablas 3 y 4 –especialmente en la Tabla 3– deben abordarse algunas cuestiones. La primera ya fue identificada por [12]: la redacción ambigua del apartado 7.2.2 del Eurocódigo 2 [2] cuando se indica que "…puede ser apropiado limitar la tensión de compresión…", sin dejar claro si se trata de una obligación o no. Para áreas expuestas a ambientes de clases de exposición por cloruros el límite recomendado para la tensión de compresión es del 60 % de f_{ck} bajo la combinación característica. Por tanto, ¿significa que para otros ambientes de exposición es seguro permitir que las tensiones del hormigón superen el 60 % de f_{ck}?. La segunda causa tiene que ver con el comportamiento no lineal de la fluencia a través de la Eq. (1). Algunos autores (e.g., [5]), sostienen que los efectos de la fluencia no se pueden predecir con precisión si la tensión de compresión del hormigón supera el 60% de f_{ck}. De hecho, la Eq. (1) de Eurocódigo 2 [2] es muy similar a la ecuación proporcionada en el Código Modelo 2010 [10], la cual sólo sería válida para el rango de tensiones de compresión entre el 40 % y 60 % de f_{ck}. Por último, también debe considerarse que, bajo cargas permanentes sostenidas en el tiempo, la resistencia del hormigón disminuye debido a la formación de microgrietas, pudiendo disminuir un 20 % en hormigón fabricado con cemento normal [10].

3. ANÁLISIS PARAMÉTRICO

Tras la resolución del caso práctico anterior, y bajo la sospecha que el estado tensional del hormigón pueda resultar elevado para distintos tipos de edificaciones, bajo distintos tipos de modelos estructurales (forjados por vigas descolgadas), con distintas propiedades geométricas y mecánicas, se ha realizado un análisis paramétrico empleando para ello programación con MATLAB [1]. Este análisis ha generado, dimensionado y comprobado soluciones estructurales perfectamente viables en la realidad (por geometría y carga), llevando a cabo el análisis de aproximadamente millón y medio de vigas de hormigón armado mediante la variación de 12 parámetros que intervienen en el diseño.

3.1. Parámetros de diseño

Los distintos parámetros que se han considerado para abordar el análisis paramétrico han sido los que se recogen en la Tabla 5. El motivo de empleo de las variables de la Tabla 5 para abordar el análisis paramétrico es debido a la influencia que las mismas tienen sobre la obtención de las distintas verificaciones en ELS. Las características mecánicas de los materiales constituyentes del elemento a

estudiar tienen una notable influencia en la respuesta tensional de la pieza y por tanto en la aparición de fisuras y su abertura y en la deformación vertical.

Tabla 5. Variables empleadas para el análisis paramétrico

Parámetro 1: **Clase resistente del hormigón**						
Clase resistente	C20/25	C25/30	C30/37	C35/45	C40/50	
f_{ck} [MPa]	20	25	30	35	40	
Parámetro 2: **Tipo de árido**						
Tipo de árido	Calizo denso		Silíceo	Calizo	Arenisca	
Factor corrector	1,2		1	0,9	0,7	
Parámetro 3: **Humedad relativa del ambiente**						
HR [%]	40			70		
Parámetro 4: **Acero pasivo**						
Designación acero pasivo	B400 S / B400 SD		B500 S / B500 SD		B600 S / B600 SD	
Límite elástico (f_{yk}) [MPa]	400		500		600	
Parámetro 5: **Luz de Vano**						
L [m]	4	5	6	7	8	9
Parámetro 6: **Canto de la viga**						
h [m]	L/20		L/17	L/14	L/11	
Parámetro 7: **Ancho de la viga**						
b [m]	0,3·h		0,4·h	0,5·h		
Parámetro 8: **Ancho tributario del forjado**						
w [m]	0,6·L		0,8·L	1·L		
Parámetro 9: **Canto del forjado y peso propio**						
e_f [mm]	250		300	350		
Peso Propio [kN/m^2]	3		4	5		
Carga muerta [kN/m^2]	2		2	2		
Parámetro 10: **Sobrecarga de uso y factor de simultaneidad**						
Categoría de uso	A		B	C	D	
Sobrecarga de uso [kN/m^2]	2,0		3,0	4,0	5,0	
Factor de simultaneidad (ψ_2)	0,3		0,3	0,6	0,6	
Parámetro 11: **Condiciones de contorno**						
Vinculaciones externas (Fig. 3)	Biapoyado		Empotrado-Apoyado	Bi-empotrado	Rigidez Rotacional	
Parámetro 12: **Factor de Redistribución**						
δ	1		0,9	0,8	0,7	

Otros parámetros considerados:

- Recubrimiento de la armadura (d'): 40 mm.
- Tipo de cemento: Endurecimiento normal.
- Tiempo de puesta en carga: 14 días
- Tiempo de curado: 28 días
- Tiempo a largo plazo: 18250 días (≈50 Años)
- Módulo de deformación longitudinal del acero pasivo: E_s = 200 GPa

El módulo de deformación longitudinal depende de la resistencia característica y del tipo de árido con el que se fabrica el hormigón. Para el acero debe considerarse su módulo de elasticidad, así como la variedad de calidades de acero pasivo que puede emplearse en la construcción y/o fabricación de vigas de hormigón armado. Para la verificación de las comprobaciones en ELS a largo plazo, es necesario considerar el comportamiento reológico del hormigón, estando este comportamiento controlado por las variables de humedad relativa del ambiente en el que se encuentra expuesto el elemento en estudio, el tipo de cemento con el que se fabrica el hormigón, tiempo de puesta en carga, tiempo de curado y tiempo (vida útil) para el que se lleva a cabo el análisis.

Un segundo grupo de variables, que intervienen para llevar a cabo las verificaciones de los distintos ELS son la geometría de la sección; canto (h), ancho (b) y recubrimiento mecánico de la viga (d'), la luz de la pieza (L), el canto del forjado (e_f) que influye, tal y como se ha mencionado en el apartado anterior, en la determinación del área expuesta de la viga para la determinación de la retracción y fluencia de la pieza. Las condiciones de contorno que se han considerado conforme a la Fig. 3; son los tres casos canónicos que pueden considerarse para una viga (biapoyada, empotrada – apoyada y bi-empotrada), así como un caso de rigidez rotacional para simular cualquier viga que forme parte de un entramado estructural más complejo. La rigidez rotacional de cada extremo se ha modelizado el caso de una viga que pueda resultar más desfavorable para el análisis de verificación de los ELS. Para este caso tras efectuar el análisis numérico de pórticos de tres alturas y cuatro vanos, en los que, tras variar la luz de los vanos y la sección de las vigas, se ha observado que la viga más desfavorable corresponde a la viga extrema de la primera planta. A partir de los resultados obtenidos para cada uno de los pórticos se ha determinado la rigidez rotacional de cada uno de los nudos extremos a través de una expresión que permite correlacionar la geometría de la sección transversal de la viga (a través de la inercia bruta) y la luz de la viga.

El tercer grupo de parámetros que influyen en este análisis, son las cargas que actúan sobre la viga, considerándose el peso propio de la viga a partir de sus dimensiones, el peso propio del forjado, que depende a su vez del canto (como se recoge en la Tabla 5) y del ancho tributario del mismo que transmite la carga sobre la viga. En todos los casos, al tratarse de vigas descolgadas, el espesor del forjado no podrá ser superior al canto de la viga. En todos los casos se ha considerado una carga muerta de 2,0 kN/m^2, para tener en cuenta la carga muerta que supone los solados, compartimentación e instalaciones habituales en edificación. Las cargas variables debidas a la sobrecarga de uso y su correspondiente factor de simultaneidad que se han considerado en cada caso, se ha realizado a partir de los Eurocódigos 0 [9] y 1 [8].

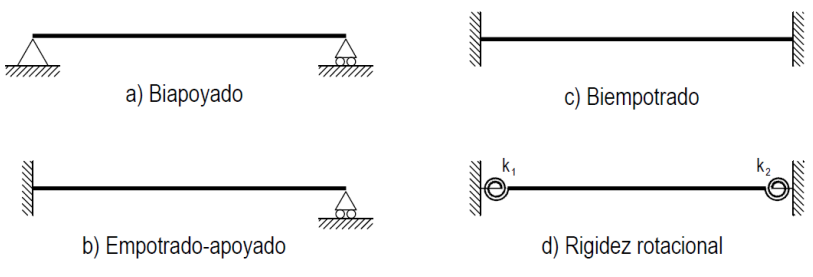

Fig. 3. Condiciones de contorno viga

Por último, dado que el Eurocódigo 2 [2] permite realizar un cálculo elástico lineal con redistribución limitada para el dimensionamiento en ELU, se han considerado para el factor de redistribución cuatro valores que abarcan la gama de valores permitidos para la relación entre el momento redistribuido y el momento flector elástico (δ).

3.2. Proceso de análisis

El proceso de análisis masivo de vigas descolgadas de un entramado de edificación ha consistido en los procesos siguientes que se describen brevemente en los siguientes apartados:

- Generación de combinaciones de los doce parámetros relacionados anteriormente.
- Dimensionamiento en ELU frente a las acciones de flexión.
- Análisis en servicio para la determinación en cada una de las secciones de cálculo en las que se ha dividido cada una de las vigas.
- Generación de fichero combinado con los datos de entrada (parámetros), y resultados asociados a cada una de las combinaciones generadas.

3.2.1. Generación de combinaciones

A partir de los parámetros de diseño iniciales, se han generado los casos compatibles empleando para ello un algoritmo que de forma automática efectúa la combinación, pero a la vez realiza la verificación de si el caso es factible o no. Para ello, analiza la compatibilidad de los distintos parámetros y verifica que la capacidad resistente de la sección sea compatible con la solicitación que actúa sobre ésta atendiendo a criterios de agotamiento de las bielas de compresión debido al cortante y de agotamiento por flexión para secciones con cuantías máxima de armadura de tracción y/o compresión. Todo ello se ha realizado bajo los criterios de comprobación que recoge el Eurocódigo 2 [2]. El algoritmo programado, también evita la generación de casos sin sentido, tales como aplicar redistribución a una viga isostática, etc. El número total de casos para el caso de una viga de canto es de 1.468.098.

Tanto para la tarea de dimensionamiento en ELU como de verificación de los distintos estados límite de servicio, cada viga (combinación) a su vez, se ha dividido en 100 secciones de cálculo, a partir de las cuales se extraen los resultados en servicio más desfavorables para cada uno de los casos analizados.

3.2.2. Dimensionamiento en ELU

A partir del fichero de combinaciones, el algoritmo, para cada viga, efectúa la combinación persistente de acciones, y su caso aplica la redistribución correspondiente, todo ello, en consonancia con las condiciones de contorno fijadas para cada una de las vigas. A partir de los valores pésimos de flectores positivos y negativos, se efectúa un armado de refuerzo a tracción y/o compresión, considerando para las armaduras de tracción y compresión el armado mínimo en base a las cuantías geométricas y mecánicas mínimas que indica el Eurocódigo 2 [2]. Los armados se han dispuesto tabulados de forma creciente para que los mismos sean compatibles con las secciones analizadas. A partir de la armadura de cálculo necesaria para cada sección el algoritmo efectúa un reparto de las armaduras de montaje (armado mínimo) y de refuerzo, acorde con las leyes de flectores que solicitan la pieza, considerando criterios de montaje en obra.

3.2.3. Análisis en servicio

Una vez se dispone de la distribución de la armadura a lo largo de la longitud de la pieza, se procede a efectuar cada una de las comprobaciones en servicio que indica el Eurocódigo 2 [2]. Para ello, inicialmente, se obtienen los valores de los esfuerzos flectores en cada una de las secciones de cálculo para la combinación característica y casi-permanente, que se emplean para la obtención de las tensiones en hormigón y acero a corto y a largo plazo respectivamente, la abertura de fisura y la deformación vertical, siguiendo los procesos que se indican a continuación:

- Tensiones en hormigón y acero a corto plazo.

Los valores de las tensiones en hormigón y acero a corto plazo se obtienen a través de un análisis elástico y lineal considerando la Ley de Navier, la sección homogeneizada bruta o fisurada según el caso, empleando para ello el valor del módulo de elasticidad que indica el Eurocódigo 2 [2] y el coeficiente de homogeneización acero/hormigón y considerando nula la resistencia a tracción del hormigón.

Para la determinación de las tensiones en los materiales de la sección de hormigón armado, y en cada una de las secciones de cálculo, se ha determinado la profundidad de la fibra neutra, elongación de la fibra superior y curvatura empleando para ello los parámetros de las secciones homogeneizadas o fisuradas considerando si la solicitación de flexión en la sección en estudio ha superado o no el momento de fisuración.

- Abertura de fisura a corto plazo.

A partir de la ley de flectores de la combinación casi-permanente de acciones que solicitan la viga, de la geometría de la viga y características mecánicas de los materiales, se efectúa el análisis de la abertura de fisura en cada una de las secciones de cálculo, considerando la formulación del Eurocódigo 2 [2].

- Deformación vertical a corto plazo.

Para aprovechar la potencia de cálculo que ofrece MATLAB [1], se han obtenido los valores de la deformación vertical en cada una de las secciones de cálculo empleando para ello la integración doble de la curvatura a través de métodos numéricos junto con teoremas energéticos, empleando para ello la Eq. (2).

$$y_a = \int_0^L \chi_m \cdot M^1 \cdot dx \tag{2}$$

donde:

y_a: Flecha alcanzada por la viga en una sección $x = a$.

L: Luz de la viga considerada.

χ_m: Curvatura en cada sección, tomando el valor medio ponderado mediante criterio del Eurocódigo 2 [2].

M^1: Ley de momentos flectores producida por una carga puntual unitaria en la sección de estudio, y considerando la viga como isostática.

- Tensiones en hormigón y acero a largo plazo.

Para la determinación de las tensiones a largo plazo, se sigue el mismo procedimiento que en el caso de corto plazo, pero empleando el módulo efectivo del hormigón a largo plazo y considerando el efecto de la fluencia en cada una de las secciones, que a su vez incluye el modelo de fluencia no-lineal cuando las tensiones bajo la combinación de cargas casi-permanente superan el 45% de f_{ck}.

- Abertura de fisura a largo plazo.

Empleando los datos de las tensiones bajo la combinación de cargas casi-permanente y el módulo efectivo del hormigón a largo plazo y siguiendo el mismo procedimiento que en caso de corto plazo, se determina la abertura de fisura a largo plazo en cada una de las secciones de cálculo.

- Deformación vertical a largo plazo.

La deformación vertical o flecha a largo plazo se obtiene como suma de la deformación generada por la combinación casi-permanente de cargas a largo plazo considerando el efecto de la fluencia a través del módulo efectivo del hormigón y la deformación que supone la retracción. Esta última flecha, a su vez se ha obtenido determinando la curvatura que se origina debido a la retracción en cada una de las secciones a largo plazo, considerando únicamente que la retracción tiene lugar en la zona no fisurada de la sección de hormigón. Finalmente, la deformación vertical en cada una de las secciones de cálculo, se obtiene mediante integración doble de la curvatura.

4. RESULTADOS ANÁLISIS PARAMÉTRICO

Tras el proceso de cálculo, se guardan los datos correspondientes a los parámetros de entrada y los siguientes resultados:

Valores a corto plazo:

- $\sigma_{c,st}$: Máxima tensión de compresión a corto plazo en hormigón en una de las secciones de cálculo, bajo la combinación característica de carga.
- $\sigma_{s,st}$: Máxima tensión de tracción a corto plazo en armadura pasiva en una de las secciones de cálculo, bajo la combinación característica de carga.
- w_{st}: Máxima abertura de fisura a corto plazo ocurrida en la pieza de hormigón analizada, en combinación casi-permanente de carga
- f_{st}: Máxima deformación vertical a corto plazo en la pieza de hormigón armado, bajo la combinación característica de carga.

Valores a largo plazo:

- $\sigma_{c,lt}$: Máxima tensión de compresión a largo plazo en hormigón en una de las secciones de cálculo, bajo la combinación característica de carga.

- $\sigma_{s,lt}$: Máxima tensión de tracción a largo plazo en armadura pasiva en una de las secciones de cálculo, bajo la combinación característica de carga.
- w_{lt}: Máxima abertura de fisura a largo plazo ocurrida en la pieza de hormigón analizada, bajo la combinación casi-permanente de carga.
- f_{st}: Máxima deformación vertical a corto plazo en la pieza de hormigón armado, bajo la combinación característica de carga.

Sobre los resultados obtenidos, y como primer tanteo de sensibilidad sobre el cumplimiento de los distintos estados límite de servicio indicados en el Eurocódigo 2 [2], se ha procedido a realizar diversos filtros que, en primera instancia, pongan de manifiesto el número de casos en los que no se verifican las comprobaciones de los estados límite de servicio tras haber realizado un dimensionamiento en rotura acorde con la normativa, y tras analizar un total de 1.468.098 casos distintos. En la Tabla 6 se especifican los datos de incumplimiento de los ELS analizados.

Tabla 6. Incumplimiento de ELS tras dimensionamiento masivo en ELU de vigas de HA.

Comprobación ELS	**Casos en los que no se verifican ELS**	
	Corto Plazo	**Largo Plazo**
Límite elástico del acero	0%	0%
80% del límite elástico del acero	19,5%	25,9%
Resistencia característica del hormigón	34,2%	----
60% de la resistencia característica del hormigón	84,4%	----
Abertura de fisura	7,6%	9%
Flecha	1,6%	9,9%

De este primer análisis, llama la atención el elevado número de casos en los que se rebasa el límite tensional propuesto por la normativa para la tensión de compresión en el hormigón. A partir de la cantidad de datos disponibles para su estudio, es necesario proceder a la agrupación de los mismos para analizar conjuntos de datos coherentes que permitan abordar el análisis de la potencial influencia de cada uno de los parámetros estudiados sobre las tensiones en los materiales constituyentes de la sección de hormigón armado, así como poder visualizar en un gráfico la importancia que cada parámetro puede tener en el comportamiento estudiado (tensiones, abertura de fisura y flechas). Para ello, se han generado una serie de gráficos de dispersión en 3D, en los que en eje "*x*" se muestra el valor de la esbeltez de la pieza (*d/L*), en el eje "*y*" se muestra el parámetro de carga relativa (P_r) tal y como se define en la Eq. (3) y el eje "*z*" se muestra la ratio (expresada en porcentaje) de máxima tensión de compresión en hormigón frente al valor de resistencia característica del hormigón.

$$P_r = \frac{(g+q)\cdot w + 25\cdot 10^{-6}\cdot b\cdot h}{b\cdot f_{ck}}\cdot 10^3 \qquad (3)$$

Considerando que los materiales constituyentes del hormigón empleados en la práctica constructiva actual para la construcción de forjados de edificación, son el acero pasivo B-500 S, junto con el hormigón de resistencia característica de 25 MPa, se muestran a continuación una serie de gráficos, que pueden ayudar a comprender la influencia de cada uno de los parámetros analizados en la verificación de los distintos estados límite de servicio que indica el Eurocódigo 2 [2] para vigas de hormigón armado.

A su vez, y en consonancia con el caso práctico resuelto al inicio del artículo, se ha adoptado una viga empotrada-apoyada para el análisis de los distintos parámetros que tienen influencia en las tensiones, exponiendo varios casos en los que se varían algunos de los parámetros empleados en el análisis.

4.1. Análisis de vigas empotradas – apoyadas por tipo de hormigón

Realizado el filtrado de datos para vigas cuyas condiciones de vinculación extremas son de empotramiento – apoyo libre, armadas con acero de límite elástico de 500 MPa, hormigón realizado con árido calizo denso, ancho de sección de b=0,30·h y sin considerar redistribución, se han obtenido los ratios de tensión frente a la resistencia característica, abertura de fisura y deformación vertical que se recogen en las Figs. 4, 5 y 6 en función de la resistencia característica del hormigón.

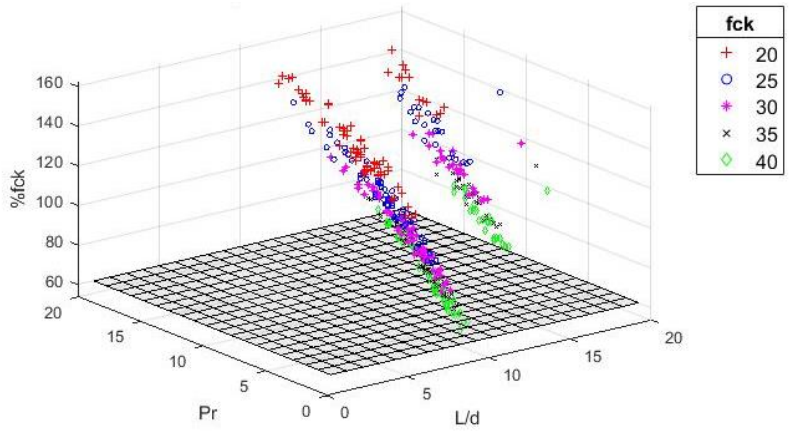

Fig. 4. Ratios de tensión de compresión en hormigón. Caso viga empotrada-apoyada, f_{yk} = 500 MPa, árido calizo denso, ancho de sección 0,3·h y sin redistribución. Análisis por tipo de hormigón.

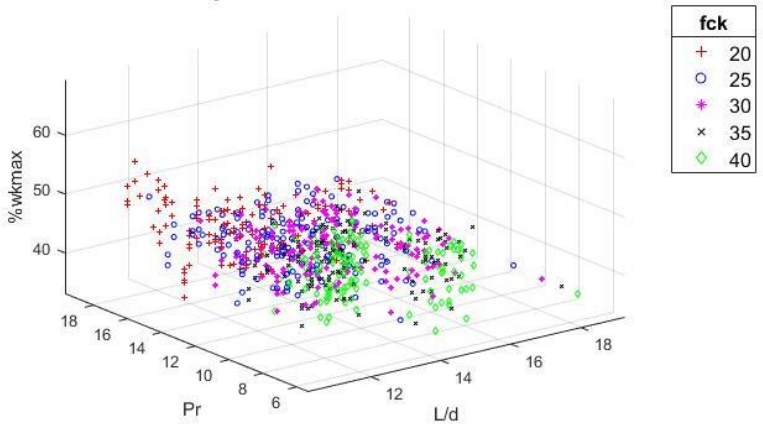

Fig. 5. Ratios de abertura de fisura. Caso viga empotrada-apoyada, f_{yk} = 500 MPa, árido calizo denso, ancho de sección 0,3·h y sin redistribución. Análisis por tipo de hormigón.

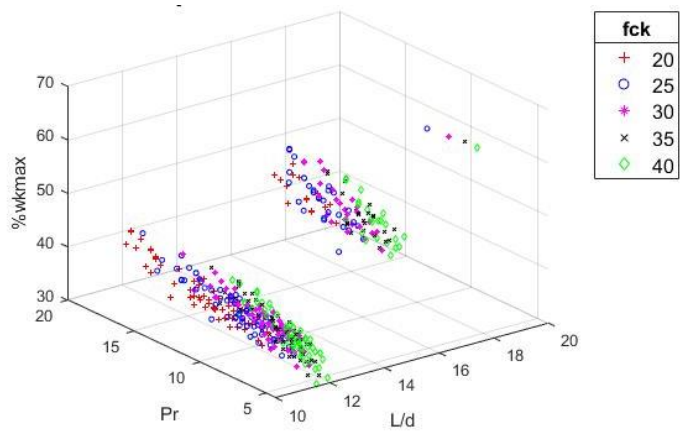

Fig. 6. Ratios de deformación vertical. Caso viga empotrada-apoyada, f_{yk} = 500 MPa, árido calizo denso, ancho de sección 0,3·*h* y sin redistribución. Análisis por tipo de hormigón.

Tras observar la información que transmite la gráfica de la Fig. 4 y, considerando las condiciones de contorno bajo las que se ha efectuado el análisis (viga empotrada-apoyada y sin realizar redistribución), fácilmente se deduce que la sección con mayor solicitación será la correspondiente al empotramiento, de dónde la ley de momentos flectores decrece de forma proporcional al cuadrado de la distancia. De la gráfica se observa que el valor de la ratio más desfavorable ($\sigma_{c,st}/f_{ck}$ = 162,5%) corresponde a un hormigón de resistencia característica de 20 MPa (tipo de hormigón habitual en edificaciones de los años 60 -70), con una esbeltez (*L*/*d*) de 15,2 de modo que considerando una luz media de 4,5 m, se obtendría una sección de unos 37 cm. de canto y 12 cm de ancho. A partir de la carga relativa, y asumiendo una separación entre pórticos equivalente a la luz de la viga se obtendría una carga total en servicio de unos 7 kN/m^2. Si adoptamos un hormigón de una calidad superior, manteniendo las mismas condiciones de esbeltez y carga, se observa que si bien el nivel tensional se reduce considerablemente del 162 % al 95 %, todavía queda por encima del umbral del 60 % marcado por el Eurocódigo 2 [2]. En cambio, las comprobaciones en servicio correspondientes a abertura de fisura (Fig. 5) y deformación vertical (Fig. 6), se verifican en la totalidad de los casos.

4.2. Análisis de vigas empotradas – apoyadas por tipo de árido

La interpretación de los resultados de este apartado se ilustra a través de las Figs. 7, 8 y 9.

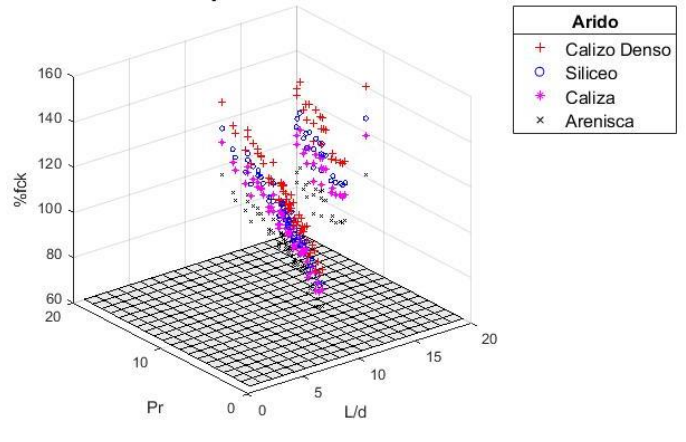

Fig. 7. Ratios de tensión de compresión en hormigón. Caso viga empotrada-apoyada, f_{ck} = 25 MPa, f_{yk} = 500 MPa, ancho de sección 0,3·*h* y sin redistribución. Análisis por tipo de árido.

En este caso, se han extraído los resultados para vigas cuyas condiciones de vinculación extremas son de empotramiento – apoyo libre, realizadas con un hormigón de resistencia característica de 25 MPa, armadas con acero de límite elástico de 500 MPa, ancho de sección de $b = 0{,}3 \cdot h$ y sin considerar redistribución. Los resultados obtenidos correspondientes a las ratios de tensión frente a la resistencia característica, abertura de fisura y deformación vertical, que se recogen en las Figs. 7, 8 y 9, corresponden a los distintos tipos de árido que pueden emplearse para la fabricación del hormigón.

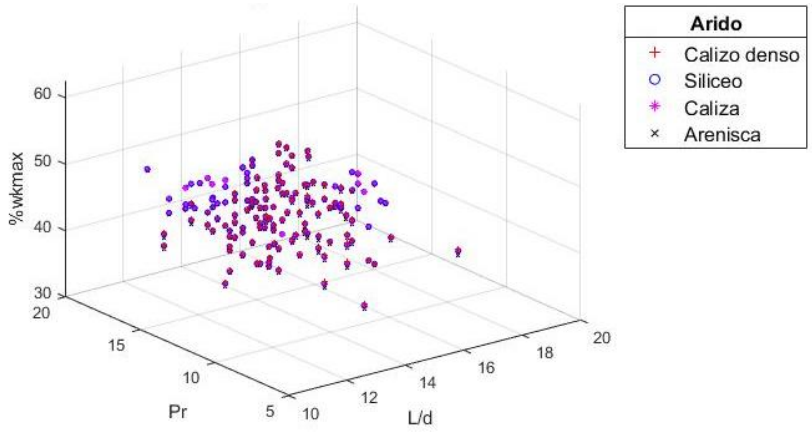

Fig. 8. Ratios de abertura de fisura. Caso viga empotrada-apoyada, f_{ck} = 25 MPa, f_{yk} = 500 MPa, ancho de sección $0{,}3 \cdot h$ y sin redistribución. Análisis por tipo de árido.

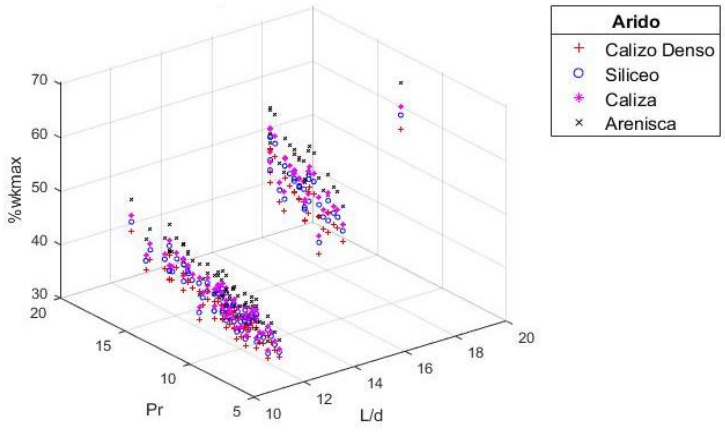

Fig. 9. Ratios de deformación vertical. Caso viga empotrada-apoyada, f_{ck} = 25 MPa, f_{yk} = 500 MPa, ancho de sección $0{,}3 \cdot h$ y sin redistribución. Análisis por tipo de árido.

Al realizar el análisis tomando como parámetro variable el tipo de árido, se observa que, para el mismo grado resistente del hormigón, se obtiene un mayor nivel tensional en piezas realizadas con áridos más resistentes tal y como se desprende de la Fig. 7. Así, por ejemplo, para el caso en el que se alcanza la mayor tensión que corresponde a un hormigón C25/30 fabricado con árido calizo denso se alcanza una ratio de tensión de 146,5 %, bajando dicha ratio al 109 % en caso de emplear para la fabricación un árido de menor compacidad como es el caso de árido procedente de roca arenisca, superando por tanto la limitación a nivel tensional que establece el Eurocódigo 2 [2]. Las verificaciones correspondientes

para la abertura de fisura y deformación vertical se cumplen satisfactoriamente, tal y como queda de manifiesto en las Figs. 8 y 9.

4.3. Análisis de vigas empotradas – apoyadas por factor de redistribución (δ)

Para analizar la influencia del factor de redistribución sobre las ratios de tensiones, fisuración y deformaciones verticales, se han seleccionado los resultados para vigas cuyas condiciones de vinculación extremas son de empotramiento – apoyo libre, realizadas con un hormigón de resistencia característica de 25 MPa y fabricado con árido calizo denso, armadas con acero de límite elástico de 500 MPa, ancho de sección b = 0,30·h. Los resultados obtenidos de las ratios de tensión frente a la resistencia característica, abertura de fisura y deformación vertical que se recogen en las Figs. 10, 11 y 12, en función del factor de redistribución considerado.

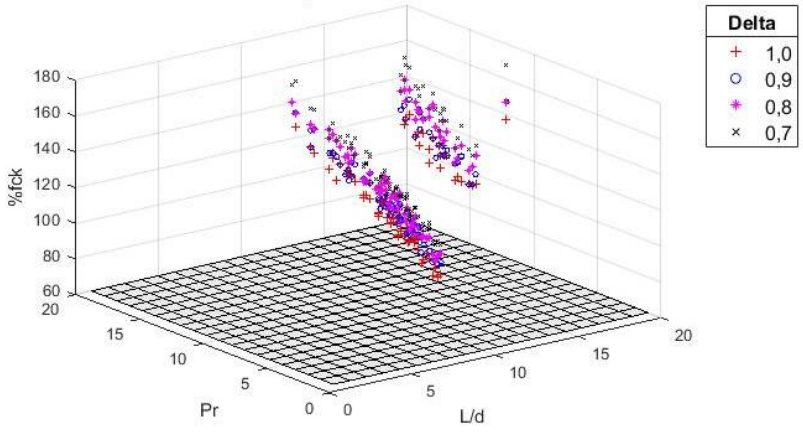

Fig. 10. Ratios de tensión de compresión en hormigón. Caso viga empotrada-apoyada, f_{ck} = 25 MPa, árido calizo denso, f_{yk} = 500 MPa, ancho de sección 0,3·h. Análisis por factor de redistribución.

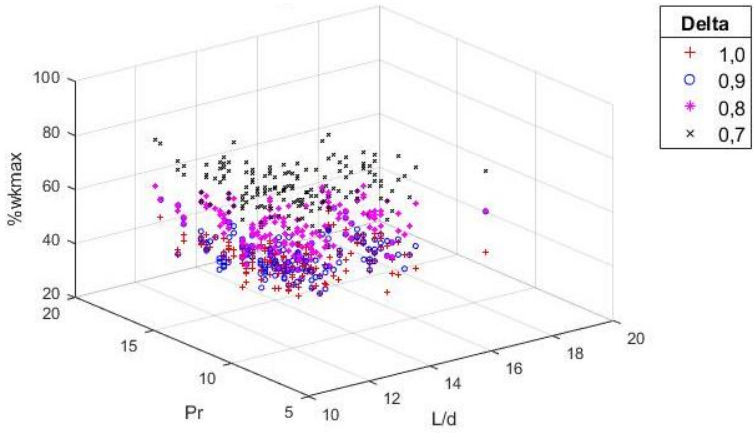

Fig. 11. Ratios de abertura de fisura. Caso viga empotrada-apoyada, f_{ck} = 25 MPa, árido calizo denso, f_{yk} = 500 MPa, ancho de sección 0,3·h. Análisis por factor de redistribución.

Si se realiza el estudio tomando como referencia el factor de distribución δ, se observa que, para el mismo grado resistente del hormigón, se obtiene un mayor nivel tensional en vigas en las que se ha realizado un dimensionamiento tomando un factor δ más bajo (mayor redistribución) tal y como se muestra en la Fig. 10. Así, por ejemplo, para el caso en el que se alcanza la mayor tensión que

corresponde a un hormigón C25/30 fabricado con árido calizo denso y con una sección dimensionada considerando un factor de redistribución de 0,7 se alcanza una ratio de tensión de 172,5%, bajando dicha ratio al 164,6% y 146,5% en caso de considerar los factores de redistribución de 0,8 y 1 respectivamente, superando en todos los casos por tanto la limitación a nivel tensional que establece el Eurocódigo 2 [2]. En otro caso más, las verificaciones correspondientes para la abertura de fisura y deformación vertical se cumplen, tal y como queda de manifiesto en las Figs. 11 y 12.

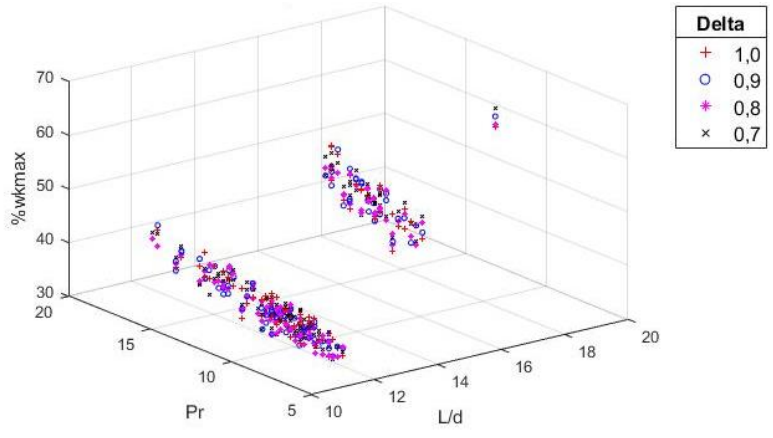

Fig. 12. Ratios de deformación vertical. Caso viga empotrada-apoyada, f_{ck} = 25 MPa, árido calizo denso, f_{yk} = 500 MPa, ancho de sección 0,3·h. Análisis por factor de redistribución.

El análisis de los resultados representados en las Figs. 4, 7 y 10 se resume en la Fig. 13, donde se comprueba claramente que con el hormigón más habitual empleado en edificación (fck = 25 MPa) se superaría el umbral del 60% de la resistencia característica del hormigón (f_{ck}) en la práctica totalidad de escenarios analizados en este estudio.

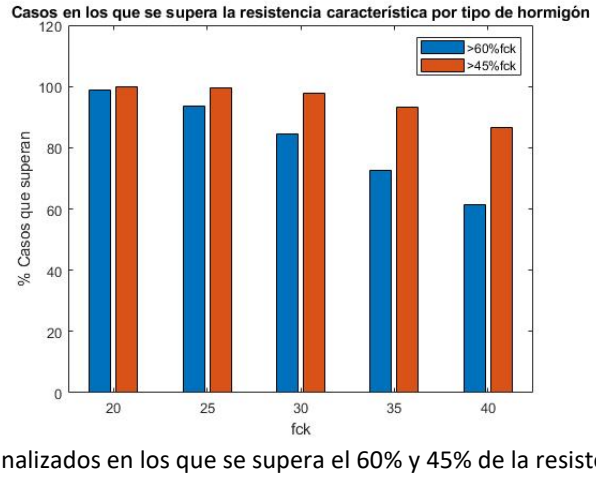

Fig. 13. Casos del total analizados en los que se supera el 60% y 45% de la resistencia característica del hormigón .

Con hormigones de mayor resistencia (el más habitual podría ser el de f_{ck} = 30 MPa) el porcentaje de casos que superan el 60% de f_{ck} se reduciría a menos del 80%. Sin embargo, el problema radicaría ahora en que incluso por debajo de dicho umbral, cuando el hormigón superase el 45% de f_{ck} sería entonces necesario que el software de análisis estructural incorporara una corrección por fluencia no lineal junto con un nuevo modelo constitutivo del hormigón para análisis a largo plazo de aquellas secciones de

hormigón armado de la viga en la que se produce esta situación. Desafortunadamente, la gran mayoría de softwares de dimensionamiento de hormigón estructural que se emplean a nivel de oficina de proyecto actualmente no cuentan con esta característica, lo que potencialmente añade un grado de incertidumbre en el pronóstico que estos programas realicen del comportamiento diferido en servicio de los edificios.

5. CONCLUSIONES

Este trabajo ha presentado un estudio paramétrico sobre el comportamiento en servicio de una cantidad masiva de escenarios de diseño de hormigón estructural en edificación, bajo condiciones reales de proyecto. Las conclusiones principales son las siguientes:

- Los resultados analizados de forma agregada en la discusión no alcanzan el 1 % de los casos estudiados. Aun así, el resumen global (Tabla 6 y Fig. 13) sí que corresponde a la práctica totalidad de la población estudiada

- Los altos niveles de tensión de compresión en vigas de hormigón armado, que superan en numerosas ocasiones la limitación tensional indicada por la normativa [2], se producen para el caso de hormigones de menor resistencia característica, fabricados paradójicamente con un árido de mayor calidad y cuyas secciones se han diseñado adoptando un análisis lineal con redistribución considerando un mayor valor de redistribución de momentos flectores.

- La conclusión más relevante es que, al realizar un dimensionamiento a flexión de vigas de hormigón armado según los criterios del Eurocódigo 2 [2], en un gran número de casos podría no llegar a verificarse el ELS de limitación de tensiones y, en cambio, sí se cumplirían las exigencias referentes a la verificación de abertura de fisura y deformaciones verticales y los Estados Límite Últimos (ELU).

- Las comprobaciones de servicio asociadas a la fisuración y la flecha, podrían no obstante estar comprometidas dado que el exceso de compresión en servicio en el hormigón puede producir una evolución no lineal de su comportamiento reológico, por lo que surgiría la necesidad de afianzar el grado de precisión de los modelos ofrecidos para ello en los distintos reglamentos de diseño e incorporar modelos constitutivos con fluencia no lineal a los programas informáticos de dimensionamiento estructural empleados por las consultoras y proyectistas.

REFERENCIAS

[1] "Matlab." [Online]. Available: https://es.mathworks.com/products/matlab.html.

[2] European Committee for Standarisation, *Eurocode 2. Design of concrete structures - Part 1-1: General rules and rules for buildings*. European Union, 2010, p. 225.

[3] H. Barros, C. Ferreira, and J. Figueiras, "Serviceability design of reinforced concrete members – Closed form solution," *Eng. Struct.*, vol. 49, pp. 600–605, Apr. 2013, doi: 10.1016/j.engstruct.2012.12.010.

[4] C. G. Karayannis and C. E. Chalioris, "Design of partially prestressed concrete beams based on

the cracking control provisions," *Eng. Struct.*, vol. 48, pp. 402–416, Mar. 2013, doi: 10.1016/j.engstruct.2012.09.020.

[5] G. L. Balázs *et al.*, "Design for SLS according to fib Model Code 2010," *Struct. Concr.*, vol. 14, no. 2, pp. 99–123, Jun. 2013, doi: 10.1002/suco.201200060.

[6] A. Marí, L. Torres, E. Oller, and C. Barris, "Performance-based slenderness limits for deformations and crack control of reinforced concrete flexural members," *Eng. Struct.*, vol. 187, pp. 267–279, May 2019, doi: 10.1016/j.engstruct.2019.02.045.

[7] A. W. Beeby and R. S. Narayanan, *Designers' guide to EN1992-1-1 and EN1992-1-2. Eurocode 2: Design of concrete structures.* London: Thomas Telford Ltd., 2010.

[8] European Committee for Standarisation, *Eurocode 1. Actions on structures - Part 1-1: General actions - Densities, self weight, imposed loads for buildings*. European Union, 2009, p. 44.

[9] European Committee for Standarisation, *Eurocode 0. Basis of structural design*. European Union, 2010, p. 116.

[10] International Federation for Structural Concrete (fib), *fib Model Code for Concrete Structures 2010*. Berlin: Ernst & Sohn, 2013.

[11] F. B. Varona, L. García-Andión, and J. A. López-Juárez, "Linear analysis with limited moment redistribution and cross-section ductility criteria in EHE-08," *Hormigón y Acero*, vol. 61, no. 257, pp. 81–90, Jan. 2010, [Online]. Available: https://www.researchgate.net/publication/277714403_El_analisis_lineal_con_redistribucion_limitada_y_los_criterios_de_ductilidad_de_las_secciones_en_la_EHE-08.

[12] M. Jędrzejczak and K. Klempka, "Limitation of Stresses in Concrete According to Eurocode 2," *MATEC Web Conf.*, vol. 117, p. 00067, Jul. 2017, doi: 10.1051/matecconf/201711700067.

Parametric structural analysis of reinforced lightweight concrete beams for buildings

Vives, Ismael[1]; Tenza, Antonio José[2]; Varona, Francisco de Borja[3]

ABSTRACT

Lightweight aggregate concrete (LWC) is an alternative to conventional concrete due to its versatility and its interesting thermal and acoustic insulation properties. In addition, lighter structural self-weight reduces the concrete volume in columns and foundations providing cost savings due to the reduction of steel reinforcement quantities. However, the reduction of concrete density leads to an increase in cement consumption to keep the required concrete compressive strength of beams and floor slabs. The present work aims to evaluate whether LWC is an economically and environmentally appropriate alternative considering the above factors. For this purpose, the design equations are presented and applied to a case study and a subsequent massive parametric analysis. From the results it can be concluded that LWC seems to constitute a sustainable alternative for densities not smaller than 1800 kg/m3. Lighter densities might have a positive effect but would require specific studies involving more parameters.

Keywords: lightweight concrete, expanded clay, dosage, structural parametric analysis.

1. INTRODUCCIÓN

A veces la necesidad de disminuir el peso de un elemento estructural no es tan importante como mantener o controlar la pérdida de resistencia, especialmente en estructuras pesadas tales como los edificios altos y puentes donde el peso de la estructura es uno de los principales problemas que afrontan los diseñadores estructurales.

El hormigón con árido ligero (*lightweight aggregate concrete*, LWC), debido a sus propiedades, es un material muy versátil y se presenta como una alternativa al hormigón de peso normal (*normal weight concrete*, NWC). Gobiernos y empresas han estado buscando minimizar el impacto ambiental durante años y las especiales funciones que ofrece el LWC son prometedoras de cara a los retos que afronta una sociedad sostenible [1].

El Eurocódigo 2 limita la densidad seca al horno del LWC a un máximo de 2000 kg/m^3 [2]. Éste se puede obtener con una proporción de áridos ligeros artificiales (*lightweight aggregates*, LWA) sustituyendo a los áridos de peso normal (*normal weight aggregates*, NWA). Es posible diseñar LWC con un amplio espectro de densidades para propósitos estructurales tales como reducir las cargas muertas y/o por motivos de aislamiento. Desde el punto de vista económico, usar LWC en edificios

[1] *Departamento de Ingeniería Civil. Universidad de Alicante (ESPAÑA). ismael.vives@ua.es*
[2] *Departamento de Ingeniería Civil. Universidad de Alicante (ESPAÑA). ajt.abril@ua.es*
[3] *Departamento de Ingeniería Civil. Universidad de Alicante (ESPAÑA). borja.varona@ua.es (Corresponding author)*

altos puede reducir considerablemente los costes totales a través de la reducción de cantidades de armaduras, reducción de las cargas permanentes y ahorro en el volumen de hormigón de la estructura portante de pilares y cimentaciones. El LWC tiene además menor módulo de elasticidad lo cual puede alargar el período de vibración natural y tiene más deformabilidad [3]. Además, el LWC mejora el aislamiento térmico y acústico [4,5], el coste de mantenimiento del edificio, bajando el impacto ambiental debido al incremento de la eficiencia energética ahorrando así consumo de energía [6,7].

Hay varias aplicaciones exitosas del LWC en construcciones civiles que indican su superioridad en algunas propiedades tales como su capacidad sísmica, resistencia a agrietamiento, buena durabilidad, resistencia a fuego, o beneficios económicos [8]. Sin embargo, el uso de LWC puede afectar negativamente al grado resistente del hormigón fabricado [9,10], i.e., podría no ser del todo compatible con elevados grados de resistencia del hormigón para niveles bajos de densidad. Además, y como consecuencia de este último apunte, puede conllevar un incremento del consumo de cemento para controlar la resistencia de proyecto. Este incremento en el consumo de cemento podría parecer, a priori, una alternativa económica y medioambientalmente inapropiada [11] y el presente trabajo se propone examinar en qué grado podría ser cierto dicho paradigma.

En primer lugar, se presentan las ecuaciones de diseño derivadas de las reglas específicas que establece el Eurocódigo 2 [2] para el proyecto con hormigón ligero estructural. A continuación, estas ecuaciones de diseño para Estado Límite Último (*Ultimate Limit State*, ULS) se aplican en un caso práctico de estudio, que pretende ilustrar los efectos positivos y menos positivos del uso del LWC en una situación potencialmente posible en una estructura de edificación. A continuación, se presenta una metodología de análisis paramétrico masivo para poder extraer conclusiones o recomendaciones acerca de cuál sería el rango de densidades de LWC que podrían tener efectos beneficiosos de cara a la sostenibilidad en el proyecto y ejecución de estructuras de edificación.

2. BASES DE CÁLCULO Y ECUACIONES DE DISEÑO EN ELU

Esta sección presenta, en primer lugar, las expresiones que se pueden usar para el diseño de vigas de hormigón armado de árido ligero sometidas a flexión (Estado Límite Último (ELU) de agotamiento por solicitaciones normales). Después, dichas expresiones se generalizan para su uso en análisis lineal elástico con redistribución limitada para obtener los momentos flectores de diseño y fuerzas cortantes en modelos estáticamente indeterminados (p.e., vigas continuas y forjados).

2.1. Expresiones para cálculo en ELU

Con respecto al cálculo estructural de LWC la norma europea EN 1992-1-1 (Eurocódigo 2) [2] admite la posibilidad de usar una versión modificada del diagrama parábola-rectángulo (Fig. 1), simplemente ajustando la deformación última en rotura en flexión con la Eq. (1).

$$\varepsilon_{lcu2} = \eta_1 \, \varepsilon_{cu2} \tag{1}$$

donde ε_{cu2} es la deformación última en compresión de hormigón de peso normal (NWC) que se puede suponer igual a 0,0035 con hormigón de resistencia normal, i.e., si la resistencia a compresión característica no sobrepasa 50 MPa. El término η_1 de la Ec. (1) se puede calcular a través de la Eq. (2):

$$\eta_1 = 0.4 + 0.6\frac{\rho}{2200} \tag{2}$$

donde ρ es la densidad seca al horno del LWC, en kg/m^3. El diagrama parábola rectángulo se muestra en la Fig. 1 donde el grado de la parábola es 2 para hormigón LWC de resistencia normal. El valor de la deformación ε_{lc2} en el diagrama es el mismo que para el NWC, i.e., ε_{lc2} = 0,002. Además de la modificación en la deformación ε_{lcu2} con respecto al NWC, otra diferencia en el caso del LWC es que el coeficiente que tiene en cuenta los efectos a largo plazo de carga mantenida en su resistencia a compresión (α_{lcc}) tiene el valor recomendado de 0,85 comparado con el valor recomendado de 1 para el caso del NWC. Así, la resistencia a compresión de diseño para el LWC para verificaciones de estado límite último (ELU) viene dada en la Eq. (3):

$$f_{lcd} = \alpha_{lcc}\frac{f_{lck}}{\gamma_c} \tag{3}$$

donde f_{lck} es la resistencia característica a compresión del LWC y γ_c es el coeficiente parcial de seguridad que tiene un valor recomendado de 1,5.

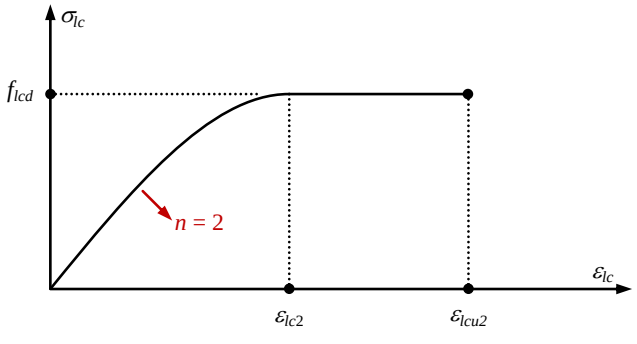

Figura 1. *Diagrama parábola-rectángulo para hormigón ligero de resistencia normal.*

Para encontrar ecuaciones de diseño compactas, se usa integración numérica para saber el área y profundidad del centroide del diagrama parábola-rectángulo. En la Fig. 2 se muestra una sección rectangular armada de LWC. Nótese que, en concordancia con el Eurocódigo 2 [2], si se ignora el endurecimiento plástico de las barras de acero en el diseño (Fig. 3(a)), no hay necesidad de comprobar la deformación de tracción de la armadura longitudinal de tracción (A_{s1}). Por tanto, si la sección estuviera sometida a flexión pura, el comportamiento de tensión-deformación del LWC en compresión siempre completaría el diagrama parábola-rectángulo de la Fig. 1.

Las soluciones analíticas para la integración numérica del diagrama parábola-rectángulo de la Fig. 1 en un área rectangular de ancho *b* y profundidad x_u (profundidad del eje neutro) se dan en la Eq. (4):

$$\sigma_{lc} = \begin{cases} f_{lc2}\left(\varepsilon_{lc}/\varepsilon_{lc2}\right)\left(2 - \varepsilon_{lc}/\varepsilon_{lc2}\right) & \text{si } \varepsilon_{lc} \le \varepsilon_{lc2} \\ f_{lc2} & \text{si } \varepsilon_{lc2} < \varepsilon_{lc} \le \varepsilon_{lcu2} \end{cases} \tag{4-i}$$

$$N_{lcd} = \lambda_{LWC}\ f_{lcd}\ b\ x_u = f_{lcd}\ b\ x_u \left[1 - \frac{1}{3}\left(\frac{\varepsilon_{lc2}}{\varepsilon_{lcu2}}\right)\right] \tag{4-ii}$$

$$k\ x_u = x_u \left[\frac{\frac{1}{2} - \frac{1}{12}\left(\frac{\varepsilon_{lc2}}{\varepsilon_{lcu2}}\right)^2}{1 - \frac{1}{3}\left(\frac{\varepsilon_{lc2}}{\varepsilon_{lcu2}}\right)}\right] \tag{4-iii}$$

donde N_{lcd} es la fuerza de compresión resultante desarrollada por el LWC y el producto $k\,x_u$ posiciona la profundidad de la fuerza N_{lcd} (ver Fig. 2), necesaria para obtener el brazo de palanca con respecto a la armadura de tracción A_{s1}. De esa forma es posible determinar diagrama equivalente del tipo 'bloque rectangular' para el LWC, sabiendo los valores de la fuerza en el hormigón y la profundidad del centroide, dadas en la Tabla 1 para diferentes clases de densidad compatibles con aplicaciones estructurales.

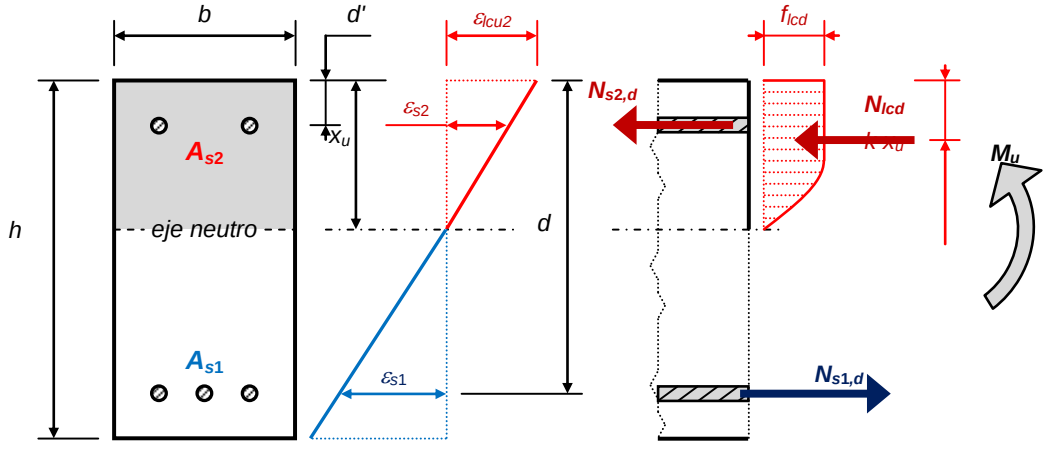

Figura 2. *Sección rectangular de LWC armado sometida a flexión pura.*

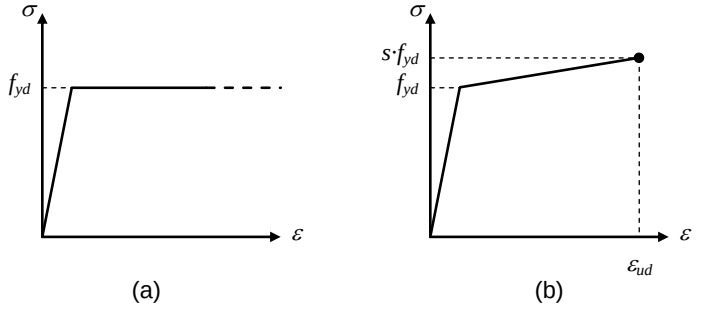

Figura 3. *Distribución bi-lineal de tensión-deformación para el acero de armado en ELU: (a) sin endurecimiento plástico ni limitación de deformación a tracción; (b) con endurecimiento plástico y con limitación de deformación a tracción.*

Tabla 1. Resultados de la integración numérica del diagrama parábola-rectángulo para varias densidades de LWC.

Clase de densidad	**1.0**	**1.2**	**1.4**	**1.6**	**1.8**	**2.0**
Densidad seca al horno (kg/m^3)	801-1000	1001-1200	1201-1400	1401-1600	1601-1800	1801-2000
Peso específico del hormigón armado (kN/m^3)	11,5	13,5	15,5	17,5	19,5	21,5
η_1	0,67	0,73	0,78	0,84	0,89	0,95
ε_{lcu2} (‰)	2,35	2,55	2,74	2,93	3,12	3,31
λ_{LWC}, Eq. (4-ii)	0,72	0,74	0,76	0,77	0,79	0,80
k, Eq. (4-iii)	0,39	0,39	0,40	0,40	0,41	0,41

Nótese que los valores para la clase de densidad 2.0 casi coinciden con los valores clásicos del diagrama parábola-rectángulo del NWC. De hecho, la profundidad de la fuerza de compresión resultante en el hormigón (N_{lcd}) podría tomarse como 0,4 veces la profundidad del eje neutro independientemente de la clase de densidad. Es la fuerza resultante N_{lcd} la que viene más afectada por la densidad del LWC, con una caída del 10% para la clase de densidad 1 con respecto al hormigón convencional. Además, cabe destacar que el valor de f_{lcd} usado en el cálculo de N_{lcd} es un 15% menor que el de un hormigón convencional, debido al coeficiente α_{cc} que tiene en cuenta las cargas de larga duración. Combinando ambos efectos, la respuesta a compresión del LWC en una viga con sección rectangular sometida a flexión pura podría ser casi un 40% menor que en una viga análoga de NWC. Para una sección rectangular de hormigón armado fabricado con árido ligero, las ecuaciones de equilibrio interno se dan en la Eq. (5):

$$\text{Equilibrio de fuerzas:} \quad 0 = \lambda_{LWC}\ f_{lcd}\ b\ x_u + A_{s2}\ \sigma_{s2} - A_{s1}\ f_{yd} \tag{5-i}$$

$$\text{Equilibrio de momentos:} \quad M_{Ed} = \lambda_{LWC}\ f_{lcd}\ b\ x_u \left(d - 0.4\ x_u\right) + A_{s2}\ \sigma_{s2}\left(d - d'\right) \tag{5-ii}$$

donde M_{Ed} es el flector de diseño para ELU; A_{s2} y A_{s1} son las áreas de compresión y tracción de armado, respectivamente (ver Fig. 2); b y d son el ancho y canto útil de la sección, respectivamente; x_u es la profundidad del eje neutro en el momento del fallo; d' es la profundidad del refuerzo a compresión; λ_{LWC} es el coeficiente asociado a la fuerza resultante de compresión del bloque de tensiones comprimido equivalente, que depende de la clase de densidad (ver Tabla 1); f_{yd} es la resistencia de cálculo de la armadura (ver Fig. 3); y ε_{s2} es la tensión de la armadura comprimida A_{s2}.

Resolviendo las ecuaciones de equilibrio interno es posible desarrollar las siguientes expresiones para cálculo en ELU, Eq. (6) y Eq. (7):

$$\text{Si } M_{Ed} \le M_{0.45d,LWC} \quad \Rightarrow \quad \begin{cases} A_{s2} \text{ no se requiere} \\ A_{s1} = \dfrac{\lambda_{LWC}\ f_{lcd}\ b\ d}{0.8\ f_{yd}}\left(1 - \sqrt{1 - \dfrac{1.6\ M_{Ed}}{\lambda_{LWC}\ f_{lcd}\ b\ d^2}}\right) \end{cases} \tag{6}$$

$$\text{Si } M_{Ed} > M_{0.45d,LWC} \quad \Rightarrow \quad \begin{cases} A_{s2} = \dfrac{M_{Ed} - M_{0.45d,LWC}}{\sigma_{s2}\left(d - d'\right)} \\ A_{s1} = A_{s2}\,\dfrac{\sigma_{s2}}{f_{yd}} + 0.45\,\lambda_{LWC}\,\dfrac{f_{lcd}}{f_{yd}}\,b\,d \end{cases} \tag{7}$$

La distinción entre la Ec. (6) y la Ec. (7) depende del flector de cálculo M_{Ed} con respecto de $M_{0.45d,LWC}$ que puede entenderse como una especie de momento frontera o momento límite. Dicho momento es la resistencia a flexión de una sección rectangular sometida a flexión pura que no requiere armadura de compresión, en la que la fibra neutra se sitúa a una profundidad exactamente igual al 45% del canto útil *d*. Para flectores superiores a $M_{0.45d,LWC}$ la sección sin armadura de compresión A_{s2} tendría una profundidad de eje neutro x_u por encima de 0,45*d*, que es el límite establecido por el Eurocódigo 2 para tener suficiente capacidad de rotación en el momento del fallo. El valor del flector $M_{0.45d,\,LWC}$ se puede calcular mediante la Eq. (8):

$$M_{0.45d,LWC} = 0.369\,\lambda_{LWC}\;f_{lcd}\;b\,d^2 \tag{8}$$

Para resolver la Eq. (7) se necesita el valor de la tensión ε_{s2} y se puede calcular usando la Eq. (9):

$$\sigma_{s2} = \eta_1\left(1 - 2.22\frac{d'}{d}\right)\cdot 700\text{ MPa} \le f_{yd} \tag{9}$$

Esta ecuación es una consecuencia de la hipótesis de Navier y las ecuaciones de compatibilidad de deformación que definen la distribución de deformaciones en la Fig. 2, asumiendo que el módulo de deformación longitudinal del acero es 200 GPa y que la profundidad del eje neutro es x_u = 0,45*d*. Como es bien sabido, el incremento del momento flector de cálculo para ser soportado por una sección de hormigón armado requiere considerar la contribución de la armadura de compresión en el equilibrio interno para mantener la profundidad del eje neutro y la capacidad de rotación inalteradas. Por tanto, la anotación "no se requiere" en la Eq. (6) significa que la armadura a compresión (A_{s2}) no es necesaria para el equilibrio interno de la sección, independientemente de una mínima cantidad de armadura que evidentemente sería menester para considerar necesidades de ejecución, control de la retracción, armaduras de piel o sostén longitudinal para la armadura de cortante. Desafortunadamente, como se verá en la siguiente sección, el límite $x_u \le 0{,}45d$ necesitaría una posterior revisión debido a que para clases de densidad inferiores el requerimiento de capacidad de rotación en el momento de la rotura es mayor que para el NWC.

2.2. Análisis lineal elástico con redistribución limitada en hormigón ligero estructural

En el Eurocódigo 2 [2] es posible la redistribución de flectores mediante análisis lineal elástico para vigas y forjados –no en pilares y muros– siempre que la sección en el instante del agotamiento tenga suficiente capacidad rotacional. Una simplificación aproximada para verificar la capacidad de rotación limita la profundidad del eje neutro a valores más restrictivos que 0,45*d*. En el caso de hormigón ligero de resistencia normal (con $f_{lck} \le 50$ MPa), el flector resultante del análisis lineal elástico puede multiplicarse por el factor δ, dado en la Eq. (10):

$$\delta \geq 0.44 + \frac{1.25\, x_u}{d}\left(0.6 + \frac{0.0014}{\varepsilon_{lcu2}}\right) = 0.44 + \frac{1.25\, x_u}{d}\left(0.6 + \frac{0.4}{\eta_1}\right) \qquad \text{(10-i)}$$

$$\frac{x_u}{d} \leq \xi_{\max} = \frac{\delta - 0.44}{1.25\left(0.6 + \frac{0.4}{\eta_1}\right)} \qquad \text{(10-ii)}$$

Además, el factor δ no puede ser menor que 0,8 en el caso de armaduras Clase A, o inferior a 0,7 en el resto de casos. Nótese cómo la Eq. (10-ii) ahora define la profundidad máxima permitida del eje neutro en el momento del fallo como una función del factor de redistribución δ usado en el análisis global para comprobaciones de ELU. Asumamos que los resultados de un análisis lineal elástico se usan para el cálculo en ELU de una viga continua en flexión pura. En tal caso, el modelo es estáticamente indeterminado y δ = 1. Si la viga estuviera hecha con NWC, el coeficiente η_1 sería igual a 1 y el cociente (x_u / d) se limitaría al valor $\xi_{\max}$ = 0,448 (que se acerca bastante a la limitación 0,45d tratada al final de la sección anterior). Sin embargo, si se usa LWC, el coeficiente η_1 ya no es igual a 1, de modo que el valor $\xi_{\max}$ en la Eq. (10-ii) debería calcularse específicamente para cada clase de densidad. Los valores de la profundidad máxima relativa del eje neutro ($\xi_{\max}$) se dan en la Tabla 2 como una función del factor de redistribución δ (valores de 1, 0,9, 0,8 y 0,7) y de la clase de densidad. Los resultados de la Tabla 2 para $\xi_{\max,\delta=1}$ significan que el conjunto de ecuaciones Eq. (6), Eq. (7) y Eq. (8), que corresponden a análisis lineal elástico sin redistribución (δ = 1), serían únicamente compatibles con la clase de densidad 2.0 o incluso 1.8, pero sin suficiente precisión y del lado de la inseguridad. Por tanto, se necesita un nuevo conjunto de expresiones para tener en consideración las diferentes clases de densidad y factores de redistribución.

Tabla 2. Valores de la profundidad relativa máxima del eje neutro para análisis lineal elástico con redistribución limitada de LWC para vigas y forjados.

Clase de densidad	1.0	1.2	1.4	1.6	1.8	2.0	NWC
$x_u / d \leq \xi_{\max,\delta=1}$	0,375	0,390	0,403	0,415	0,427	0,438	0,448
$x_u / d \leq \xi_{\max,\delta=0.9}$	0,308	0,320	0,331	0,341	0,351	0,360	0,368
$x_u / d \leq \xi_{\max,\delta=0.8}$	0,241	0,250	0,259	0,267	0,275	0,282	0,288
$x_u / d \leq \xi_{\max,\delta=0.7}$	0,174	0,181	0,187	0,193	0,198	0,203	0,208

Volviendo a las ecuaciones de equilibrio interno es posible obtener una metodología general con expresiones precisas, empezando por aquellas situaciones en las que el momento de cálculo tiene valores de bajos a moderados y el análisis de la sección podría no considerar –sin pérdida de seguridad– la contribución de la armadura de compresión. El área a tracción requerida para la armadura (A_{s1}) viene dada por la Eq. (11):

$$A_{s1} = \frac{\lambda_{LWC}\ f_{lcd}\ b\, d}{0.8\ f_{yd}}\left(1 - \sqrt{1 - \frac{1.6\, M_{Ed}}{\lambda_{LWC}\ f_{lcd}\ b\, d^2}}\right) \qquad \text{si } M_{Ed} \leq M_{thr} \qquad \text{(11)}$$

donde M_{thr} es el momento límite a partir del cual la sección de LWC necesitaría armadura específica de compresión (el subíndice 'thr' viene del inglés *threshold* o umbral a partir del cual se requiere armadura de compresión). Dicho momento límite puede calcularse mediante la Eq. (12):

$$M_{thr} = \Phi_1 \; f_{lcd} \; b \, d^2 \qquad \text{with } \Phi_1 = \lambda_{LWC} \; \xi_{\max} \left(1 - 0.4 \, \xi_{\max}\right) \tag{12}$$

Para flectores de cálculo M_{Ed} mayores que el momento umbral M_{thr} deben disponerse ambas armaduras de compresión y tracción, según la Eq. (13):

$$\text{Si } M_{Ed} > M_{thr} \quad \Rightarrow \quad \begin{cases} A_{s2} = \dfrac{M_{Ed} - M_{thr}}{\sigma_{s2} \left(d - d'\right)} \\ A_{s1} = A_{s2} \, \dfrac{\sigma_{s2}}{f_{yd}} + \Phi_2 \, \dfrac{f_{lcd}}{f_{yd}} b \, d \end{cases} \qquad \text{con } \Phi_2 = \lambda_{LWC} \; \xi_{\max} \tag{13}$$

Un aspecto importante en el control de la profundidad del eje neutro a través de la contribución de la armadura comprimida es si el acero comprimido agota su límite elástico o no. Por consiguiente, debe apuntarse que la Eq. (9) ya no es válida, porque estaba específicamente asociada con la posición límite de la profundidad del eje neutro en x_u = 0,45d que corresponde al NWC –aunque podría ser casi compatible con clases de densidad 2.0 y 1.8– y un análisis lineal elástico sin redistribución (δ = 1). De lo contrario, es obligatorio redefinir el análisis de la compatibilidad de deformaciones para las diferentes distribuciones de deformación límite $x_u = \xi_{\max} d$ para obtener la deformación ε_{s2} y la tensión σ_{s2} (con E_s = 200 GPa). Esto se resuelve y presenta en la Eq. (14), que ahora sustituye a la Eq. (9).

$$\sigma_{s2} = \eta_1 \left(1 - \frac{d'}{\xi_{\max} \, d}\right) \cdot 700 \text{ MPa} \le f_{yd} \tag{14}$$

Para comparar el impacto del factor de redistribución y la clase de densidad en el cálculo, los valores de los coeficientes Φ_1 y Φ_2 se muestran en la Tabla 3, que de este modo puede usarse junto con las Eq. (11), Eq. (12) y Eq. (13).

Tabla 3. Valores de los coeficientes Φ_1 y Φ_2.

Clase de densidad		**1.0**	**1.2**	**1.4**	**1.6**	**1.8**	**2.0**	**NWC**
δ = 1	Φ_1	0,229	0,243	0,256	0,268	0,278	0,288	0,298
	Φ_2	0,269	0,288	0,305	0,321	0,336	0,350	0,363
δ = 0,9	Φ_1	0,194	0,206	0,217	0,228	0,237	0,246	0,254
	Φ_2	0,221	0,236	0,250	0,264	0,276	0,287	0,298
δ = 0,8	Φ_1	0,156	0,166	0,176	0,184	0,192	0,199	0,206
	Φ_2	0,173	0,185	0,196	0,206	0,216	0,225	0,233
δ = 0,7	Φ_1	0,116	0,124	0,131	0,137	0,144	0,149	0,154
	Φ_2	0,125	0,133	0,142	0,149	0,156	0,162	0,168

Por otro lado, la tensión de la armadura comprimida a usar en la Eq. (13) se resuelve a través de la Eq. (14) para diferentes ratios (d' / d) como se muestra en la Tabla 4, en función de la clase de densidad y

el factor de redistribución. En la Tabla 4 se consideró una armadura con un límite elástico característico de 500 MPa, con un factor de seguridad de γ_s = 1,15 como se recomienda en el Eurocódigo 2, de ahí el valor de 435 MPa.

Tabla 4. Tensión de la armadura comprimida (en MPa) como función de la clase de densidad, el factor de redistribución δ y el ratio (*d'* / *d*).

Clase de densidad		1.0	1.2	1.4	1.6	1.8	2.0	NWC
d'/*d* = 0,05	δ = 1	408	435	435	435	435	435	435
	δ = 0,9	394	430	435	435	435	435	435
	δ = 0,8	373	407	435	435	435	435	435
	δ = 0,7	336	368	401	434	435	435	435
d'/*d* = 0,10	δ = 1	345	378	411	435	435	435	435
	δ = 0,9	318	350	382	414	435	435	435
	δ = 0,8	276	306	336	366	396	427	435
	δ = 0,7	200	228	255	282	309	336	363
d'/*d* = 0,15	δ = 1	283	313	344	374	405	435	435
	δ = 0,9	242	270	299	328	357	386	415
	δ = 0,8	178	204	230	257	283	309	335
	δ = 0,7	65	87	109	130	152	174	195
d'/*d* = 0,20	δ = 1	220	248	276	304	332	360	388
	δ = 0,9	165	191	217	242	268	294	320
	δ = 0,8	80	103	125	147	169	192	214
	δ = 0,7	-70	-54	-38	-22	-5	11	27

Valores de la relación (*d'* / *d*) en el entorno de 0,05 y 0,10 pueden corresponder a vigas de canto en la mayoría de los casos, mientras que valores entre 0,15 y 0,20 pueden darse en vigas planas y forjados. Nótese que hay numerosos ejemplos en la Tabla 4 en los cuales la armadura comprimida no alcanza el límite elástico. Es más, para clases de densidad inferiores a 1.8, la armadura comprimida estaría de hecho en tracción cuando se use un alto nivel de redistribución (δ = 0,7) y el recubrimiento de la armadura de compresión *d'* sea el 20% del canto útil *d*. Eso significa que el problema no tendría una solución práctica en esos casos y que no sería apropiado usar el nivel más alto de redistribución permitido en el Eurocódigo 2 con LWC en vigas planas y forjados.

3. CASO DE ESTUDIO

El diseño de la viga continua de hormigón armado (HA) de la Fig. 4 sirve de propósito para mostrar el impacto del hormigón ligero en el diseño de elementos de hormigón armado.

La viga tiene una sección rectangular con una profundidad *h* de 45 cm, ancho *b* de 30 cm y un canto útil *d* de 41 cm. Se asume que la armadura de compresión tiene un recubrimiento mecánico *d'* de 4 cm. La viga de HA soporta un forjado con un área tributaria de 4 m. Además de su peso propio y el del forjado, la viga de HA debe soportar una carga muerta de 2 kN/m^2 –lo cual incluye peso de instalaciones, tabiquería, techado, pavimento y acabados– además de una sobrecarga de uso de 2 kN/m^2 (categoría A en concordancia con el Eurocódigo 1 [12]. Se consideran tres valores diferentes de

ancho de sección: 15 cm, 20 cm and 30 cm. Se considera carga de ubicación alternada, lo cual significa que la sobrecarga de uso podría aplicarse en toda la longitud de la viga o sólo en uno de los vanos.

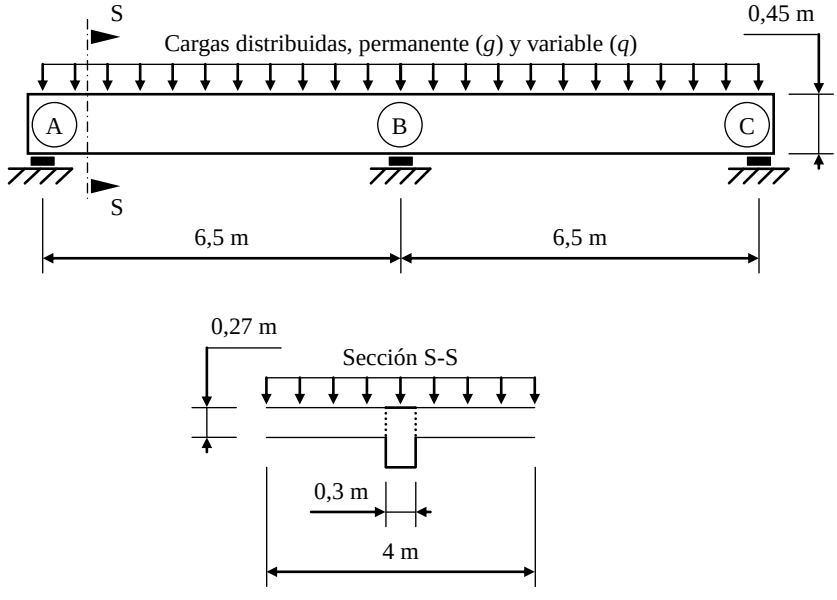

Figura 4. *Viga continua de dos vanos de hormigón armado.*

La armadura considerada para este cálculo tiene un límite elástico de 500 MPa, con un módulo de Young de 200 GPa. Para el objeto de este caso de estudio, se usan las ecuaciones de diseño presentadas en la sección previa, que están en concordancia con los coeficientes por defecto recomendados en el Eurocódigo 2 [2]. Tres densidades diferentes se consideran para este cálculo: un hormigón armado de peso normal con un peso específico de 25 kN/m^3; un LWC de clase de densidad 1.8 (con 19,5 kN/m^3); y un LWC de clase de densidad 1.2 (con 13,5 kN/m^3). La resistencia a compresión característica es $f_{ck} = f_{lck}$ = 25 MPa, para cualquier densidad. Sin embargo, el coeficiente de reducción por carga mantenida en el tiempo α_{cc} (ver Eq. (3)) tiene el valor recomendado de 1 para hormigón de peso normal y el valor de 0,85 para ambos tipos de LWC.

El análisis global de cálculo de flectores aplicado en la viga se hace con δ = 1 (sin redistribución), δ = 0,8 y δ = 0,7 para comparar cómo este factor afecta al hecho de usar hormigón ligero. En cualquier caso, nótese que las reacciones verticales transmitidas a los apoyos son las del análisis lineal elástico (δ = 1) debido a que la redistribución de momentos sólo puede usarse en los elementos horizontales de estructuras aporticadas (i.e., vigas y forjados) y no en los verticales (i.e., los pilares).

Con respecto al uso del LWC, se supone que se usa para los elementos horizontales del edificio (vigas de HA y forjados), y no en los pilares. Para el caso de forjados, en este caso se construye con vigueta y bovedilla con vigas prefabricadas (hechas con NWC, peso propio de 0,27 kN/m), relleno de bloques (1 kN/m con intereje de 70 cm) y hormigón "in situ" de peso normal o LWC (con un área de 0,0467 m^2/m para un intervalo de repetición de 70 cm). El forjado entonces pesa 3.35 kN/m^2 (hormigón "in situ" de peso normal); 3.12 kN/m^2 (hormigón "in situ" de hormigón ligero de clase de densidad 1.8); y 2.72 kN/m^2 (hormigón "in situ" con una clase de densidad 1.2). La carga vertical total transmitida a los

apoyos se da en la Tabla 5, donde se puede apreciar que la carga vertical total para ELU en los apoyos se podría reducir en un 12% en este caso particular.

Tabla 5. Influencia de la clase de densidad en el cálculo de cargas y reacciones transmitidas a los apoyos de la viga continua objeto de estudio.

	NWC	Clase 1.8	Clase 1.2
Peso específico de hormigón "in situ" (kN/m^3)	25	19,5	13,5
g_{beam} (kN/m)	3,38	2,63	1,82
Ancho tributario (m)	4	4	4
g_{floor} (kN/m)	12,40	11,53	10,05
g_{dead} (kN/m)	8	8	8
q_{live} (kN/m)	8	8	8
$p_{Ed,ULS,max}$ (kN/m)	44,09	41,92	38,83
Carga total en ELU (kN)	286,6	272,5	252,4
Ahorro (%)	N/A	4,9%	11,9%

El valor $p_{Ed,ULS,max}$ es el valor de diseño de la carga uniformemente distribuida aplicada en la viga para comprobación del ELU, con las cargas permanentes y de uso actuando con efecto desfavorable, i.e., la carga permanente total (g_{beam} + g_{floor} + g_{dead}) se multiplicaría por γ_G = 1,35 y la sobrecarga de uso (q_{live}) vendría multiplicada por γ_Q = 1,5. Los resultados asociados con el cálculo de la armadura longitudinal en las secciones críticas vienen dados en la Tabla 6 (análisis elástico lineal), Tabla 7 (redistribución de flectores con δ = 0.8) y Tabla 8 (redistribución con δ = 0.7). El efecto de la ubicación de la carga en el análisis de redistribución se muestra en la Fig. 5 y en la Fig. 6, que corresponden al diseño que usa LWC de clase de densidad 1.8.

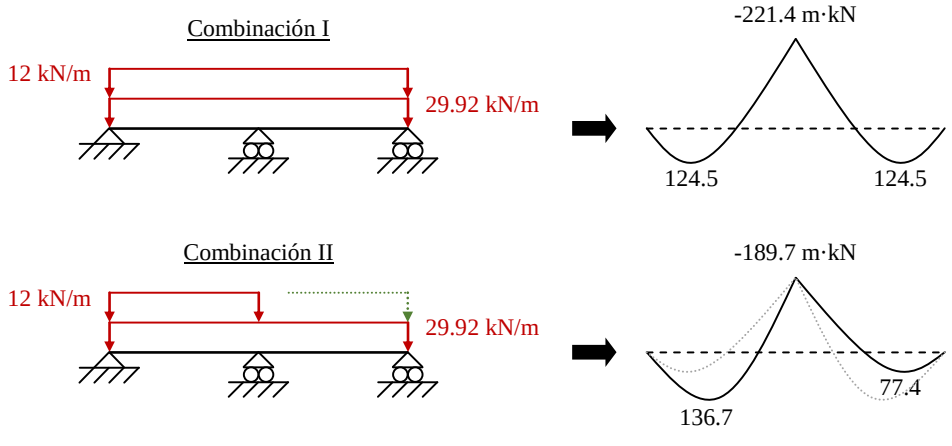

Figura 5. *Combinaciones de carga y diagramas de momentos flectores en la viga de LWC hecha con clase de densidad 1.8, con análisis lineal elástico y δ = 1.*

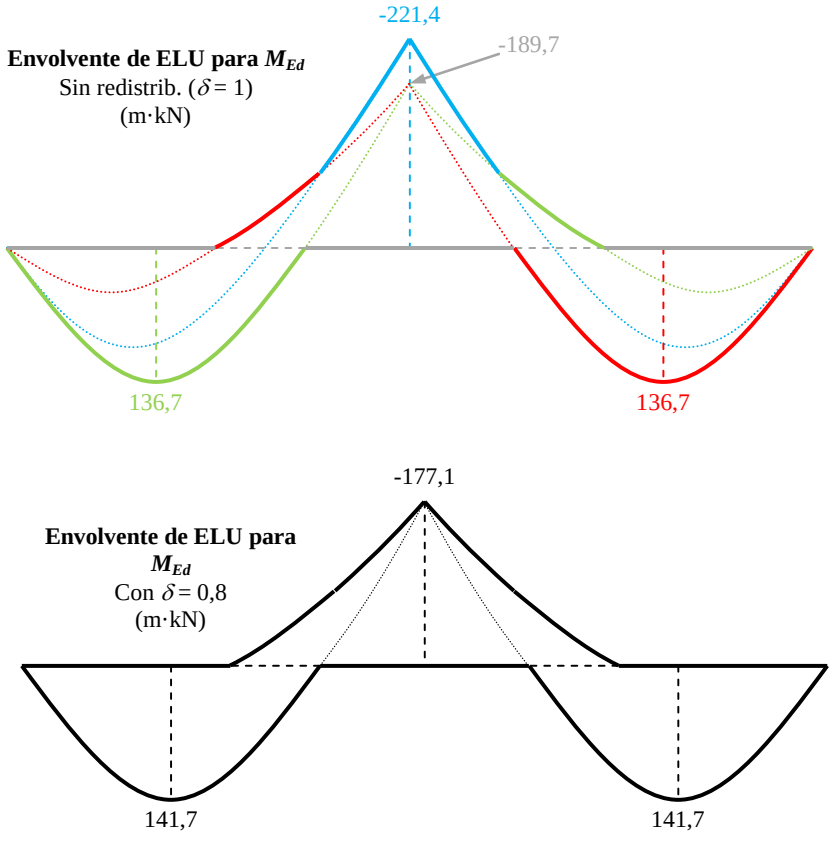

Figura 6. *Envolventes de ELU de momentos flectores en la viga de LWC hecha con densidad de clase 1.8, cuando $\delta = 1$ y cuando $\delta = 0,8$.*

Las combinaciones de carga I y II (usadas en las Tablas 6-8) se muestran en la Fig. 5 y, respectivamente, producen el máximo momento negativo en B y el valor máximo de momento flector positivo a lo largo del vano. Los diagramas de momentos flectores representados en la Fig. 5 se obtienen con análisis lineal elástico y las envolventes de cálculo de los flectores para ELU se muestran en la Fig. 6 para valores de redistribución de δ = 1 y δ = 0,8. Nótese cómo el momento flector redistribuido en B es menor que el momento original en B para la combinación II, lo cual causa un ligero incremento en el momento flector positivo para la combinación II, desde 136,7 a 141,7 (aumento del 3,7%).

Finalmente, para comparar el impacto del factor de redistribución y la clase de densidad en la reducción del acero empleado para armadura longitudinal, se hacen las siguientes suposiciones: todas las secciones sometidas fundamentalmente a flexión negativa tienen la misma armadura que la sección de B; de igual manera, las secciones sometidas preferentemente a flexión positiva tendrán la misma armadura longitudinal; finalmente, para hacer una estimación del consumo total de acero de armadura longitudinal, se supondrá que el 25% del vano está sometido predominantemente a flectores negativos. Así, sería posible tener una estimación de la cantidad de armadura longitudinal a lo largo del vano simplemente añadiendo $0,75 \cdot A_{s,total,positivos} + 0,25 \cdot A_{s,total,negativos}$, que después sería convertida a kilogramos usando la longitud de vano y la densidad del acero. Esta estimación se resume en la Tabla 9.

Tabla 6. Cálculo de armadura longitudinal para ELU en las secciones críticas sin redistribución.

	NWC	**Clase 1.8**	**Clase 1.2**
f_{ck} o f_{lck} (MPa)	25	25	25
f_{cd} o f_{lcd} (MPa)	16,67	14,17	14,17
f_{yd} (MPa)	435	435	435
M_{Ed} en B (comb. I) sin redistribución (m·kN)	-232,8	-221,4	-205,0
$M_{thr,\delta=1}$ (m·kN)	±250,2	±198,6	±173,6
Tensión σ_{s2} (MPa)	N/A	435	382
$A_{s2,req}$ (mm^2)	N/A	141,6	222,7
$A_{s1,req}$ (mm^2)	1561,9	1487,3	1347,8
$A_{s2,min}$ (mm^2) (EHE-08)	113,4	113,4	113,4
$A_{s,total,negativos}$ (mm^2)	1675,3	1628,9	1570,5
Reacción vertical en A (comb. II) (kN)	112,3	107,1	99,5
Posición de máx. positivos (m)	2,55	2,55	2,56
$M_{Ed,max.\ positivos}$ sin redistribución (m·kN)	143,1	136,7	127,5
M_{Ed} en B (comb. II) sin redistribución (m·kN)	-201,2	-189,7	-173,4
Tensión σ_{s2} (MPa)	N/A	N/A	N/A
$A_{s2,req}$ (mm^2)	N/A	N/A	N/A
$A_{s1,req}$ (mm^2)	885,0	860,9	802,5
$A_{s2,min}$ (mm^2) (EHE-08)	113,4	113,4	113,4
$A_{s,total,positivos}$ (mm^2)	998,4	974,3	915,9

Nótese que los valores anotados en la Tabla 9 corresponden a las armaduras longitudinales. El armado en las vigas de HA incluyen también armadura a cortante. En concordancia con el Eurocódigo 2 [2], la contribución del hormigón a la resistencia a cortante no puede añadirse a la resistencia a cortante aportada por los cercos, que no viene afectada por haber usado LWC. Más aún, dado que las cargas de cálculo se han reducido, podría ser posible usar mayor espaciamiento entre cercos en las secciones críticas, consumiendo así menos acero. De todas formas, no se ha considerado aquí y se supondrá que la armadura a cortante de la viga no cambia con la clase de densidad.

Si se usa un análisis elástico tradicional, según Eurocódigo 2 para cálculo en ELU, para calcular la envolvente de flectores, el impacto de la clase de densidad 1.2 en el consumo de acero es positivo, ahorrando un 7,5% en la disposición longitudinal. Hasta el momento, el hallazgo más significante de este trabajo es que los mejores y peores resultados se obtienen usando redistribución y densidad de clase 1.2, que puede llevar a una reducción del 10% en el consume de acero –con respecto al hormigón convencional NWC y el análisis lineal elástico tradicional– o a un despilfarro adicional del 25%, simplemente modificando ligeramente el factor de redistribución de δ de 0,8 a 0,7.

Tabla 7. Diseño de armaduras longitudinales para ELU en las secciones críticas con δ = 0,8.

	NWC	**Clase 1.8**	**Clase 1.2**
M_{Ed} en B (comb. I) con redistribución δ = 0,8 (m·kN)	-186,3	-177,1	-164,0
$M_{thr,\delta=0.8}$ (m·kN)	±173,4	±137,3	±118,8
Tensión σ_{s2} (MPa)	435	402	311
$A_{s2,req}$ (mm^2)	80,2	267,8	393,2
$A_{s1,req}$ (mm^2)	1179,4	1112,7	1021,8
$A_{s2,min}$ (mm^2) (EHE-08)	113,4	113,4	113,4
$A_{s,total,negativos}$ (mm^2)	1292,8	1380,5	1415,0
Posición de máx. positivos (m)	2,60	2,60	2,60
$M_{Ed,max,positivos}$ con redistribución δ = 0,8 (m·kN)	149,0	141,7	131,2
Tensión σ_{s2} (MPa)	N/A	402	311
$A_{s2,req}$ (mm^2)	N/A	29,7	107,8
$A_{s1,req}$ (mm^2)	925,8	892,5	817,9
$A_{s2,min}$ (mm^2) (EHE-08)	113,4	113,4	113,4
$A_{s,total,positivos}$ (mm^2)	1039,2	1005,9	931,3

Tabla 8. Diseño de armaduras longitudinales para ELU en las secciones críticas con δ = 0,7.

	NWC	**Clase 1.8**	**Clase 1.2**
M_{Ed} en B (comb. I) con redistribución δ = 0,7 (m·kN)	-163,0	-155,0	-143,5
$M_{thr,\delta=0.7}$ (m·kN)	±129,7	±102,5	±88,5
Tensión σ_{s2} (MPa)	372	317	234
$A_{s2,req}$ (mm^2)	241,8	447,3	634,6
$A_{s1,req}$ (mm^2)	1000,6	950,7	877,3
$A_{s2,min}$ (mm^2) (EHE-08)	113,4	113,4	113,4
$A_{s,total,negativos}$ (mm^2)	1242,3	1398,0	1511,9
Posición de máx. positivos (m)	2,68	2,60	2,60
$M_{Ed,max,positivos}$ con redistribución δ = 0,7 (m·kN)	158,5	150,7	139,6
Tensión σ_{s2} (MPa)	372	317	234
$A_{s2,req}$ (mm^2)	209,0	410,7	588,8
$A_{s1,req}$ (mm^2)	972,5	924,0	852,6
$A_{s2,min}$ (mm^2) (EHE-08)	113,4	113,4	113,4

El principal argumento que podría invalidar o llegar a poner en cuestión la conclusión anterior es el propio proceso de fabricación del LWC. Si a priori podría parecer buena idea el especificar una clase 1.2 para vigas y forjados y que el proyecto incluya el cálculo en ELU con redistribución δ = 0,8 (el 20% en el criterio tradicional de la EHE-08), debe tenerse en cuenta que, para una determinada resistencia

característica de proyecto, cuando más ligero sea el hormigón, mayor consumo de cemento demandará en su fabricación (entre otros materiales). Por otro lado, es obvio que un solo caso de estudio no basta para generalizar conclusiones. Ello motiva el análisis paramétrico que se presenta en un apartado posterior.

Tabla 9. Estimación del acero usado como armadura longitudinal (en kg) en el vano de 6,5 m (los valores entre paréntesis son reducciones o incrementos con respecto al hormigón normal NWC sin redistribución).

	NWC	**Clase 1.8**	**Clase 1.2**
$\delta = 1$	59,6	58,1 *(-2,5%)*	55,1 *(-7,5%)*
$\delta = 0{,}8$	56,3	56,1 *(-5,8%)*	53,7 *(-9,9%)*
$\delta = 0{,}7$	61,1 *(+2,5%)*	68,9 *(+15,7%)*	74,4 *(+25%)*

4. DOSIFICACIÓN DEL HORMIGÓN

El hormigón ligero estructural (LWC) introduce una dimensión adicional en el diseño de mezclas de hormigón. Como se mencionó previamente, la reducción de la densidad del hormigón reduce considerablemente la resistencia del hormigón y por tanto es necesario aumentar el contenido de cemento para recuperar la resistencia deseada y mantener así la f_{ck} (f_{lck} en el caso de los LWC).

Siguiendo la metodología para mezclas de hormigón ligero propuesta por ACI 211.2 [13], convertida a unidades del sistema internacional según las ecuaciones propuestas en [14], se obtienen los siguientes resultados para las tres de las densidades buscadas, 1.6, 1.8 y 2.0 t/m^3 según se indica en la Tabla 10.

Tabla 10. Dosificaciones para tres clases de densidad de LWC y NWA.

Clase de densidad	**1.6**	**1.8**	**2.0**	**2.2**
Cemento (kg/m^3)	442	419	396	335
Agua (l)	229	229	229	224
Árido grueso (kg/m^3)	185	465	746	1043
Árido ligero (kg/m^3)	225	147	69	0
Densidad LWAC (kg/m^3)	1591	1770	1950	2348

Dichos resultados se han obtenido para los siguientes valores de densidad seca: cemento de clase resistente 32.5 de 3.15 t/m^3; fracción 5/11 de árido grueso con una densidad de 2.65 t/m^3; fracción 0/4 de árido fino con una densidad 2.65 t/m^3. El árido ligero escogido para el análisis es en fracción gruesa de tamaño 4/12 y con una densidad de 0,48 t/m^3 (asimilable al árido comercial Arlita Leca MS [15]). Asimismo, se ha considerado un 2% de aire ocluido, un módulo de finura de la arena de 2.7 y árido grueso de tamaño máximo 11 mm. Siendo 32.5 Mpa la resistencia del cemento.

5. ANÁLISIS PARAMÉTRICO

Para mostrar la interrelación de las diferentes variables que pueden afectar al diseño, se estudia ahora una viga continua de dos vanos, pero para un ámbito mucho más amplio de los parámetros de diseño. Estos son los siguientes:

- Densidad del hormigón: las siete clases de la Tabla 2 y la Tabla 3.
- La longitud del vano: siete valores diferentes que van de 4 m a 7 m, a intervalos de 0,5 m.
- La anchura tributaria de forjado soportado por la viga: seis valores posibles que van de 3,5 m a 6 m, a intervalos de 0,5 m.
- Sobrecarga de uso: cuatro alternativas posibles de 2, 3, 4 y 5 kN/m^2.
- Resistencia a la compresión del hormigón: tres posibles grados, 20, 25 y 30 MPa.
- Recubrimiento mecánico del hormigón (hasta el centro de las armaduras longitudinales): cuatro valores posibles que van de 3,5 cm a 5 cm, a intervalos de 0,5 cm.
- Factor de redistribución δ: siete valores diferentes que van de 1 a 0,7, a intervalos de 0,05.

Se mantiene el mismo sistema de forjado de viguetas con bovedilla del ejemplo estudiado anteriormente, con un canto de forjado de 27 cm. Asimismo, el límite elástico del acero (500 MPa) y la carga permanente (acabados, particiones, instalaciones, etc., 2 kN/m^2) son también los mismos.

En lo que respecta a las dimensiones de la sección transversal de la viga, se distinguen dos tipologías:

- Vigas planas, embebidas en el forjado y, consiguientemente, con un canto impuesto de 27 cm. En este caso se estudian siete posibles alternativas con anchos de entre 40 y 70 cm a intervalos de 5 cm.
- Vigas descolgadas o de canto, con cantos totales de entre 35 y 55 cm a intervalos de 5 cm y anchuras de 25, 30 y 35 cm.

El número de diseños posibles es 691.488 con tipología de viga plana y de 1.481.760 con tipología de viga descolgada. Ello hace un total de casi 2,2 millones de modelos a estudiar. El análisis paramétrico de todos estos casos ha sido programado en MATLAB, con los siguientes resultados de salida:

- Volumen de hormigón vertido in situ en los forjados y vigas, pudiendo ser convencional (NWC) de alguna de las clases de densidad consideradas para hormigón ligero (LWC). De esta manera, conocidas las propuestas de dosificación (mediante la tipología seguida en la Tabla 10), es posible obtener el impacto en consumo de cemento.
- Máxima carga de diseño transmitida a los pilares en ELU.
- Peso del armado longitudinal de las vigas de hormigón armado (convencional o ligero).

Se presentan a continuación los resultados más relevantes de este análisis paramétrico.

5.1. Cuantía de armadura de refuerzo

Para visualizar los resultados del estudio paramétrico se muestra un resumen de algunos casos significativos en las siguientes figuras.

Como se observa en la Fig. 7a, con redistribución desde 0% a 15% se observa una ligera disminución de la cuantía de armaduras conforme disminuye la densidad del hormigón, pero a partir de dicho valor las cuantías de los hormigones más ligeros superan ampliamente a los menos ligeros.

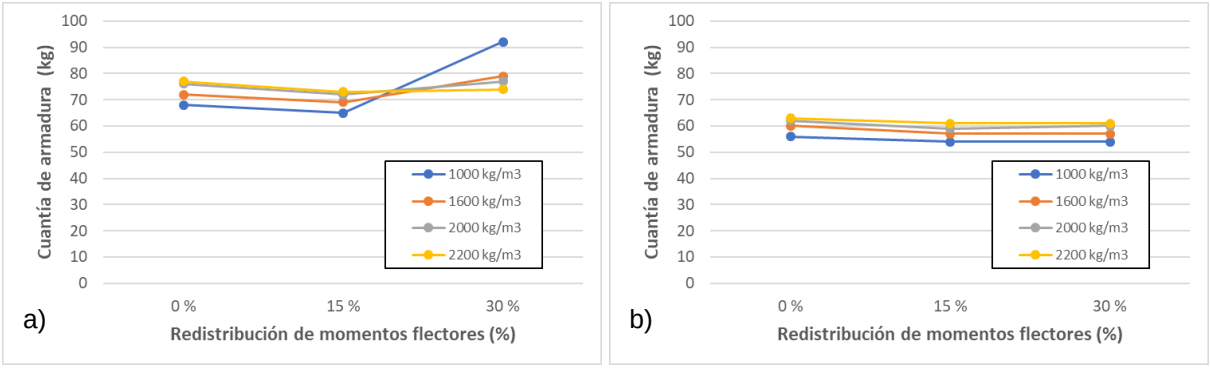

Fig. 7. *Cuantía de armadura (kg) para a) 40 cm y b) 50 cm de canto de viga, variando la densidad del hormigón (de 1000 a 2200 kg/m^3) y el grado de redistribución. Obtenido para viga de canto, vano de 5 m, recubrimiento de 40 mm, ancho de 35 cm, área tributaria de 5 m, resistencia del hormigón 25 MPa y sobrecarga de uso 2 kN/m².*

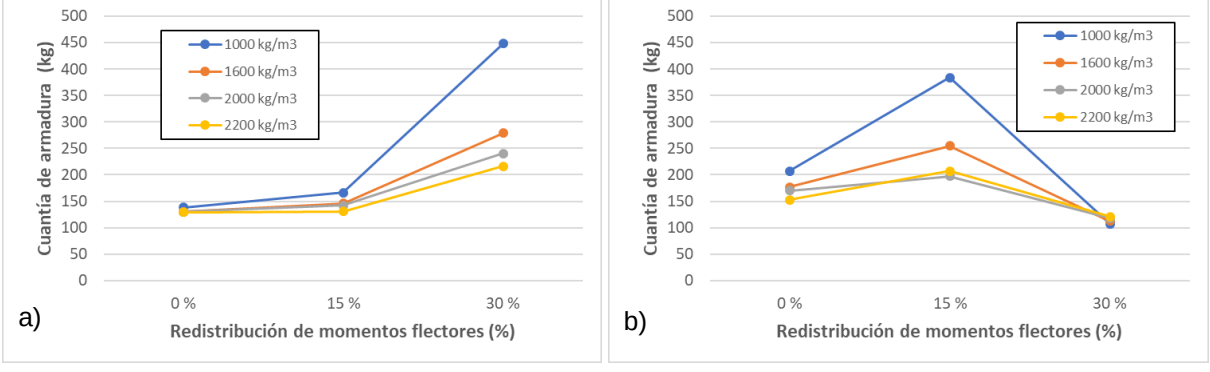

Fig. 8. *Cuantías de armadura (kg) para diferentes redistribuciones de momentos (%) y diferentes densidades de hormigón (kg/m³). Fijado recubrimiento en a) 35 mm y b) 50 mm. Obtenido para viga plana, vano de 5 m ancho en 40 cm, área tributaria 5 m, resistencia del hormigón 25 MPa, sobrecarga de uso 2 kN/m².*

En la Fig. 7a se observa que menores densidades de hormigón implican menores cuantías de armadura, pero dicha situación se prolonga sólo hasta redistribuciones pequeñas (menores del 15%). A partir del 15% de redistribución las cuantías de armadura aumentan para los hormigones más ligeros. La necesidad de cuantía de armadura es creciente para todas las densidades.

Al aumentar el canto hasta 50 cm, como se observa en la Fig. 7b, la tendencia es más acorde con el comportamiento de un hormigón convencional. Las cuantías disminuyen conforme aumenta la redistribución, en líneas generales. Asimismo, a menor densidad de hormigón menor cuantía de armadura para cualquier porcentaje de redistribución de momentos. Se observa una tendencia hacia el ahorro en cuantías de acero conforme aumenta el canto de la sección, favorable cuanto menor sea la densidad del hormigón.

Para el caso de vigas planas obtenemos, siguiendo un procedimiento similar, las cuantías de acero que se recogen en la Fig. 8a. Se observa para todas las densidades un incremento de la cuantía de

armadura conforme aumenta la redistribución de momentos, siendo dicho incremento más pronunciado cuanto mayor sea dicha redistribución. La cuantía de armadura es mayor cuanto menor sea la densidad del hormigón.

Para este caso, Fig. 8b, no se observa una tendencia clara a lo largo del intervalo de porcentajes de redistribución, siendo la cuantía mínima la obtenida para la máxima redistribución (30%). La tendencia es la misma para las diferentes densidades. No hay una regla clara para elegir la densidad que menor cuantía obtenga, ya que las densidades menores se comportan peor a bajas redistribuciones (menor del 15%) y ligeramente mejor a la redistribución máxima (30%). Se observa un claro incremento de las cuantías conforme aumentamos el recubrimiento (de 35 mm a 50 mm), como era de esperar debido a la pérdida de brazo mecánico.

5.2. Cuantía de cemento

Para los ejemplos analizados en el punto anterior de vigas de canto y vigas planas, se ha determinado la cantidad de cemento conociendo el volumen de hormigón in situ obtenido del análisis paramétrico.

En la Tabla 10 queda patente que se incrementa la cantidad de cemento por m^3 un 19% cuando se diseña un hormigón con una clase de densidad 2.0 (2000 kg/m^3) respecto al hormigón normal de 2200 kg/m^3, del 32% en el hormigón de densidad 1800 kg/m^3 y del 49% en hormigón de densidad 1600 kg/m^3.

Al tratarse el análisis paramétrico, la comparación en cuanto a la cuantía de cemento, se mantiene constante la geometría del hormigón en las diferentes densidades estudiadas, este rango de incremento de cemento (del 19% al 49% de aumento de cemento al diseñar LWC más ligeros y manteniendo la resistencia característica) es aplicable a toda la casuística. Sin embargo, este sobrecoste económico y medioambiental por la mayor demanda de cemento por m^3 puede ser compensado cuantificando la estructura completa, ya que la menor carga total sobre pilares que implica el uso de hormigones menos densos conlleva una disminución del volumen de hormigón en elementos comprimidos: pilares, muros y fundamentalmente en cimentaciones.

En la Fig. 9, se observa la cuantía de cemento y cuantía de acero necesaria por m^3, en función de la clase de densidad del hormigón. En la Fig. 9a para dos casos de vigas descolgadas y en la Fig.9b para dos casos de vigas planas.

6. CONCLUSIONES

Del estudio paramétrico realizado en el presente trabajo se pueden extraer las siguientes conclusiones basadas en los ejemplos analizados (vigas de canto y vigas planas).

Para las vigas de canto se observa una mejoría apreciable cuanto mayor es el canto de la viga, obteniéndose los máximos ahorros de armadura cuanto menor es la densidad y mayor la redistribución de momentos. Para las vigas planas el uso de densidades de hormigón inferiores a la del hormigón normal supone un incremento de la cuantía de armadura, salvo en circunstancias puntuales, para cualquier nivel de redistribución de momentos.

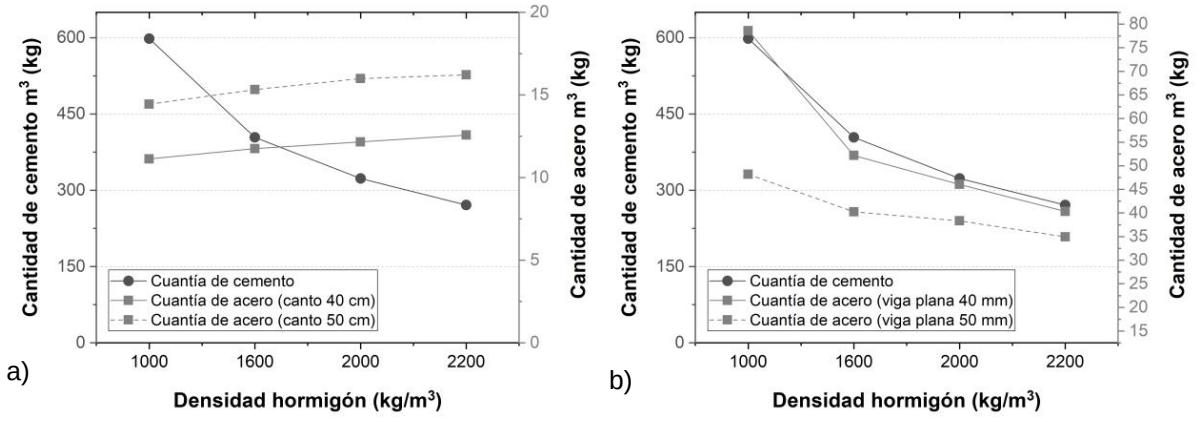

Fig. 9. *Cuantía de cemento y acero (kg) por m^3 para una redistribución de momentos del 15% y diferentes densidades de hormigón (kg/m³). Obtenido para b) viga plana fijado recubrimiento en 40 mm y 50 mm y b) canto de viga 40 cm y 50 cm. Teniendo en cuenta que el ejemplo es para una viga de vano de 5 m, ancho en 40 cm, área tributaria 5 m, resistencia del hormigón 25 MPa, sobrecarga de uso 2 kN/m².*

Tanto para vigas de canto como vigas planas se obtienen mejorías claras en cuanto a la reducción de la carga que se transmite a los apoyos, siendo menor dicha carga cuanto menor es la densidad del hormigón. Estos valores están en el orden del 15% para los hormigones más ligeros.

Se concluye que para vigas planas el uso de hormigones ligeros no es beneficioso ya que implica un aumento de las cuantías de armaduras, que unido al mayor requerimiento de cemento resultan en una solución estructural económica y medioambientalmente más cara.

En las vigas de canto la formulación no es tan perjudicial con el hormigón ligero en términos de eficiencia estructural, lo cual permite encontrar soluciones económica y medioambientalmente mejores que para el hormigón de densidad normal.

En futuras líneas de investigación se pretende extender el alcance del análisis paramétrico a la estructura del edificio en su conjunto. De esta manera, se obtendría una estimación del impacto global de consumo de cemento para averiguar si compensaría un exceso en la estructura de forjados y vigas con una reducción previsible en la estructura portante de pilares y pantallas.

REFERENCIAS

[1] Chen, Y.X.; Wu, F.; Yu, Q.; Brouwers, H.J.H. Bio-based ultra-lightweight concrete applying miscanthus fibers: Acoustic absorption and thermal insulation. Cem. Concr. Compos. 2020, 114, 103829, doi:10.1016/j.cemconcomp.2020.103829

[2] British Standards Institution Eurocode 2: Design of Concrete Structures - Part 1-1 : General Rules and Rules for Buildings; 2010.

[3] Tang, C.-W. Effect of presoaking degree of lightweight aggregate on the properties of lightweight aggregate concrete. Comput. Concr. 2017, 19, 69–78, doi:10.12989/cac.2017.19.1.069.

[4] Real, S.; Bogas, J.A.; Glória, G.M.; Ferrer, B. Thermal conductivity of structural lightweight aggregate concrete. Mag. Concr. Res. 2016, doi:10.1680/jmacr.15.00424.

[5] Mastali, M.; Kinnunen, P.; Isomoisio, H.; Karhu, M.; Illikainen, M. Mechanical and acoustic properties of fiber-reinforced alkali-activated slag foam concretes containing lightweight

structural aggregates. Constr. Build. Mater. 2018, 187, 371–381, doi:10.1016/j.conbuildmat.2018.07.228.

[6] Real, S.; Gomes, M.G.; Moret Rodrigues, A.; Bogas, J.A. Contribution of structural lightweight aggregate concrete to the reduction of thermal bridging effect in buildings. Constr. Build. Mater. 2016, doi:10.1016/j.conbuildmat.2016.06.018.

[7] Lee, Y.H.; Chua, N.; Amran, M.; Yong Lee, Y.; Hong Kueh, A.B.; Fediuk, R.; Vatin, N.; Vasilev, Y. Thermal Performance of Structural Lightweight Concrete Composites for Potential Energy Saving. Crystals 2021, 11, 461, doi:10.3390/cryst11050461.

[8] Zhang, Y.; Aslani, F. Compressive strength prediction models of lightweight aggregate concretes using ultrasonic pulse velocity. Constr. Build. Mater. 2021, 292, 123419, doi:10.1016/j.conbuildmat.2021.123419.

[9] Bogas, J.A.; Gomes, M.G.; Real, S.; Pontes, J. A new structural sand lightweight concrete mix design. Constr. Mater. Struct. 2014, 411–419, doi:10.3233/978-1-61499-466-4-411.

[10] Rashad, A.M. Lightweight expanded clay aggregate as a building material – An overview. Constr. Build. Mater. 2018, 170, 757–775.

[11] Pelisser, F.; Barcelos, A.; Santos, D.; Peterson, M.; Bernardin, A.M. Lightweight concrete production with low Portland cement consumption. J. Clean. Prod. 2012, 23, 68–74, doi:10.1016/j.jclepro.2011.10.010.

[12] British Standards Institution Eurocode 1: Actions on Structures - Part 1-1 : General actions – Densities, self-weight, imposed loads for buildings; 2009.

[13] American Concrete Institute Standard practice for selecting proportions for structural lightweight concrete ACI 211.2-98; American Concrete Institute: Michigan, 1998

[14] Abdullah, M.; Al-Mattarneh, H.M.A.; Mohammed, B.S. Equations for mix design of structural lightweight concrete. European Journal of Scientific Research. 2009, Vol. 31, No 1, 132-141.

[15] Weber Weber (Arlita Leca) Available online: https://www.arlita.es/sites/default/files/2017-07/Weber_Guia_tecnica_Arlita_Leca.pdf

Mechanical behavior of TRM masonry panels previously damaged by high temperatures

Torres, Benjamín[1]; Varona, Francisco de Borja[1]; Baeza, F. Javier[1]; Estevan, Luis[1]; Ivorra, Salvador[1].

ABSTRACT

Masonry walls exhibit low tensile strength and high material heterogeneity, which makes them especially vulnerable against accidental loadings. There are a large number of studies, both experimentally and numerically, of the masonry behaviour under accidental loadings such as earthquakes. In this regard, the most relevant research focuses on (1) evaluating the shear strength of masonry with diagonal compression tests, (2) its behavior against in-plane cyclical loadings and (3) textile reinforced mortars TRM-based reinforcement techniques. However, there are very few studies that analyse the behavior of masonry under high temperature exposure, such as those that can occur in a fire.

This paper describes the preliminary results of an experimental tests in which masonry panels (reinforced with TRM and unreinforced) have been tested in diagonal compression, previously damaged by the fire exposure. For this, masonry panels were subjected to different temperature levels, up to a maximum of 600 °C using an electric oven.

In general, the results show that high temperatures causes a decrease in shear strength, as well as the transverse stiffness modulus. However, the walls reinforced with TRM based on carbon fiber were the ones that presented the best performance, since their mechanical properties were reduced by a smaller percentage.

Keywords: masonry panels, shear strength, high temperature, Textile Reinforced Mortars (TRM).

1. INTRODUCCIÓN.

Un buen número de las edificaciones que integran nuestro patrimonio están construidas con muros de carga, generalmente fábricas de ladrillo o muros de piedra o mampostería. Estas estructuras presentan normalmente un buen comportamiento frente las cargas gravitatorias, pero resultan sensibles a las acciones horizontales como puede ser el caso del sismo. La introducción de los materiales compuestos en el ámbito de la construcción ha permitido el desarrollo de interesantes técnicas de refuerzo durante las últimas décadas. Entre otras soluciones, resultan especialmente interesantes los TRM (del inglés *Textile Reinforced Mortars*) frente a otros sistemas como los FRP (*Fiber Reinfored Polymers*), pues presentan mejor compatibilidad con los sustratos a reforzar, son permeables al vapor del agua, tienen carácter reversible (propiedad muy importante cuando se interviene en edificaciones de valor histórico o arquitectónico) y ofrecen un mejor comportamiento

[1] *Department of Civil Engineering. University of Alicante (SPAIN). E-mail adresses: benjamin.torres@ua.es (corresponding author); borja.varona@ua.es; fj.baeza@ua.es; luis.estevan@ua.es; sivorra@ua.es.*

frente al fuego. Los TRM consisten, básicamente, en la aplicación de una o varias capas de tejidos en forma de mallas de fibras de vidrio, carbono, basalto, aramida o acero (entre otros materiales) embebidas en una matriz de mortero. La efectividad de estos sistemas ha sido probada con éxito para el refuerzo de muros [1], el confinamiento de columnas [2] o la intervención en bóvedas [3], entre otras aplicaciones.

Uno de los parámetros más importantes de las fábricas de ladrillo desde el punto de vista de su respuesta frente a las acciones horizontales es su resistencia a cortante. Para estimar esta resistencia suele trabajarse con muros a pequeña escala que se ensayan en laboratorio a compresión diagonal. En los últimos años se han publicado interesantes trabajos en los que se evalúa la capacidad de refuerzo que pueden ofrecer los TRM en estas circunstancias [4–6]. En estas investigaciones se comprueba, en líneas generales, que estos sistemas proporcionan notables incrementos de resistencia y mejoran sustancialmente la ductilidad de los muros, aspecto de vital importancia en caso de edificaciones expuestas a la acción del sismo. Desde el punto de vista de la monitorización de los ensayos, se ha comprobado como las técnicas de correlación digital de imagen pueden ofrecer una elevada precisión en los resultados y aportar información de gran interés relacionada con los patrones de fisuración o los modos de rotura de los muros ensayados [7].

Respecto del comportamiento de los TRM expuestos a temperaturas elevadas, la información disponible en el momento actual es escasa. Se dispone de algunas publicaciones interesantes en las que se analiza la pérdida de propiedades mecánicas de cupones ensayados a tracción [8–10] comprobándose que, en general, el material sufre importantes pérdidas de resistencia a niveles de temperatura de 400 a 600 °C, como consecuencia de la degradación de las mallas y de la pérdida de adherencia con la matriz de mortero. Por otro lado, el efecto de la adherencia del TRM sobre muros de ladrillo expuestos a temperaturas elevadas también ha sido investigado, aunque en menor medida hasta la fecha [11,12]; en estos estudios se observa que temperaturas del orden de 300 a 500 °C afectan notablemente a la capacidad de transmisión de tensiones entre el refuerzo y el sustrato de ladrillo. De todas estas investigaciones puede concluirse que, aunque los TRM se perciben erróneamente como soluciones resistentes al fuego en muchos casos, pueden requerir protecciones adicionales en función del uso concreto al que vayan a estar destinados.

En este trabajo se plantea el análisis de la resistencia a cortante de muros reforzados con TRM tras la exposición a temperaturas elevadas pues, analizadas las publicaciones disponibles hasta la fecha, se ha detectado una carencia importante de investigación en esta materia, por lo que se considera interesante poder ampliar el estado del conocimiento. Se propone una campaña experimental con muros de fábrica de ladrillo y sistemas comerciales de TRM con mallas de fibras de carbono. Se prevén temperaturas de exposición de hasta 600 °C, pues se ha comprobado que la capacidad mecánica de estos materiales queda seriamente comprometida a estos niveles y, además, se trata de un rango de temperaturas que pueden alcanzarse fácilmente durante el desarrollo de un incendio en el interior de una edificación.

2. METODOLOGÍA DE LA CAMPAÑA EXPERIMENTAL.

Con el objetivo de evaluar la afección que las altas temperaturas tienen sobre la mampostería y sus materiales de refuerzo TRM, se ha planteado una campaña experimental que consiste inicialmente en someter a los diferentes elementos estructurales a temperaturas de hasta 600 °C. Posteriormente, se

han ensayado mecánicamente los diferentes elementos siguiendo sus procedimientos de ensayo. De esta forma se determinará la evolución de las propiedades mecánicas y su degradación.

Se indica en este apartado los materiales empleados en la campaña experimental y la metodología de ensayos llevada a cabo.

2.1. Materiales.

Los paneles de mampostería fueron construidos con ladrillos macizos de arcilla cocida y las juntas ejecutadas con mortero de cal. Los ladrillos eran de dimensiones 230×110×55 mm^3, con densidad igual a 1550 kg/m^3 y resistencia a compresión de 15 MPa (según datos del fabricante). El mortero de cal empleado para la ejecución de las juntas de la fábrica fue del tipo Morcem Cal Muro, suministrado por el Grupo Puma. Este mortero contiene principalmente cal hidráulica natural con puzolana, áridos y aditivos. De acuerdo con el suministrador, su resistencia a compresión era igual o superior a 7.5 MPa. Con el fin de mejorar la resistencia transversal en el plano de la fábrica de ladrillo, varios muros fueron reforzados con una capa de TRM aplicada a dos caras. El mortero era del tipo Planitop HDM Restauro, reforzado con fibras de vidrio discretas de 12 mm, suministrado por MAPEI; se trataba de un mortero bi-componente predosificado de alta ductilidad, a base de cal hidráulica y eco-puzolana, con una resistencia a compresión igual o superior a 15 MPa a los 28 días. Como malla de refuerzo del TRM se empleó una malla de fibra de carbono del tipo C170 (suministrada igualmente por MAPEI), cuyas principales características se indican en la *Tabla 1*.

Tabla 1. Propiedades de la malla de refuerzo del TRM

Tipo	Material	Tamaño de malla (mm)	Peso (g/m^2)	Resistencia a tracción (MPa)	Alargamiento en rotura (%)	Módulo elástico (GPa)
C170	Carbono	10 × 10	170	> 5000	2	252 ± 2 %

2.2. Exposición a altas temperaturas.

Para evaluar la afección de las altas temperaturas sobre las propiedades mecánicas de los materiales, tanto los morteros como los cupones de TRM y los paneles de mampostería (sin reforzar y reforzados con TRM) fueron sometidos a niveles de temperatura hasta 600 °C, empleando para ello un horno eléctrico programable (Fig. 1).

Los muros fueron expuestos a temperaturas de 400 y 600 °C. Para ello, eran introducidos en el horno y se les aplicaba una curva de temperatura creciente hasta alcanzar el nivel deseado, que se mantenía durante tres horas (Fig. 2). El control de la temperatura se llevó a cabo mediante termopares. Para conocer la temperatura en el interior de los paneles –concretamente en su centro de gravedad-, se realizó un taladro de 3 mm de diámetro y 115 mm de profundidad y se insertó en su interior un termopar (Fig. 1(a)), el cual fue posteriormente rellenado con masilla refractaria capaz de soportar 1200 °C. A partir de los resultados observados, a pesar de que la temperatura del aire en el interior del horno alcanzaba los 600°C (en los muros sometidos a los niveles máximos), en el interior del panel no sobrepasaban los 400 °C (Fig. 2).

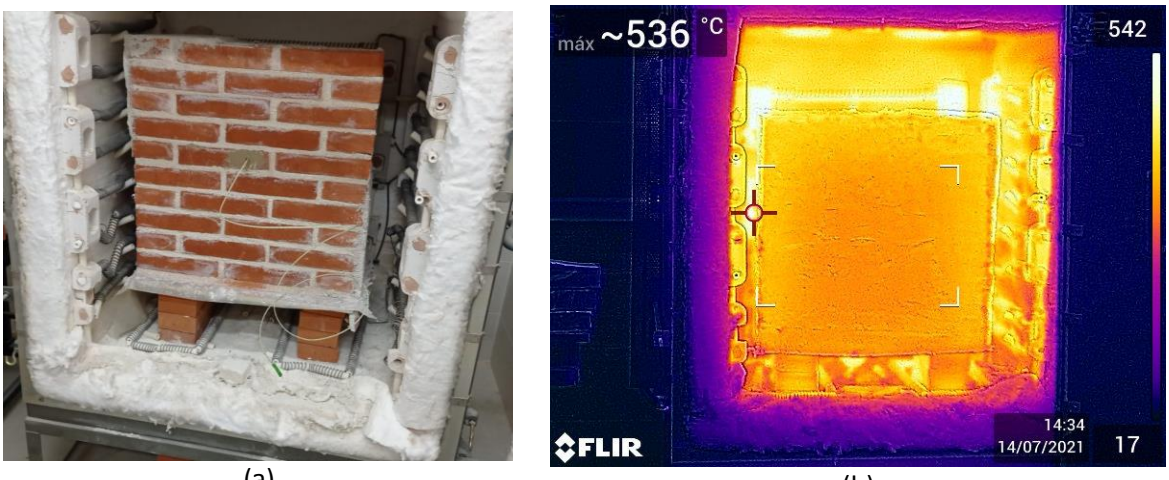

(a) (b)

Figura 1. *(a) Panel de mampostería sin reforzar en el interior del horno; (b) imagen captada con cámara termográfica, cuando la temperatura del aire del horno se encontraba a temperatura máxima de 536 °C.*

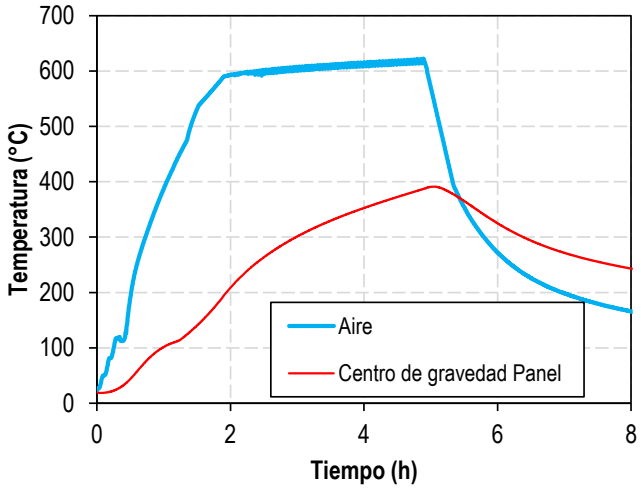

Figura 2. *Temperatura en el interior del horno y temperatura en el interior del panel de mampostería en los muros expuestos a 600 °C .*

Aproximadamente 24 horas después de los ensayos de temperatura, se procedía a realizar los ensayos mecánicos de compresión diagonal para los paneles sin reforzar y de tracción para los cupones de TRM. Los ensayos de los paneles reforzados con TRM tenían lugar a 60 días tras la aplicación del refuerzo, que a su vez se aplicaba 24 horas después del tratamiento térmico.

2.3. Ensayos mecánicos.

El comportamiento mecánico de los cupones de TRM se obtuvo de acuerdo con lo indicado en el Anejo A del código AC434 [13]. Las probetas tenían unas dimensiones de 500x100x10 mm y fueron ensayadas a temperatura ambiente y a niveles de 100, 200, 400 y 600 °C. Cada pieza se instalaba entre dos mordazas metálicas y eran ensayadas empleando una prensa eléctrica programa a una velocidad de ensayo de 0.2 mm/min. La elongación de la probeta era medida empleando un LVDT y mediante técnicas de correlación digital de imagen (Fig. 3).

(a) (b)

Figura 3. *Ensayo de tracción de cupones TRM: (a) medición mediante LVDT; (b) medición mediante sistemas de correlación digital de imagen.*

Las dimensiones de los paneles de mampostería eran 710×710×230 mm, y fueron diseñados en función del tamaño del horno empleado (Fig. 1(a)). El ensayo se realiza con el muro inclinado a 45° (en forma de rombo), sometido a una carga que introduce compresión en el sentido de la diagonal (Fig. 4).

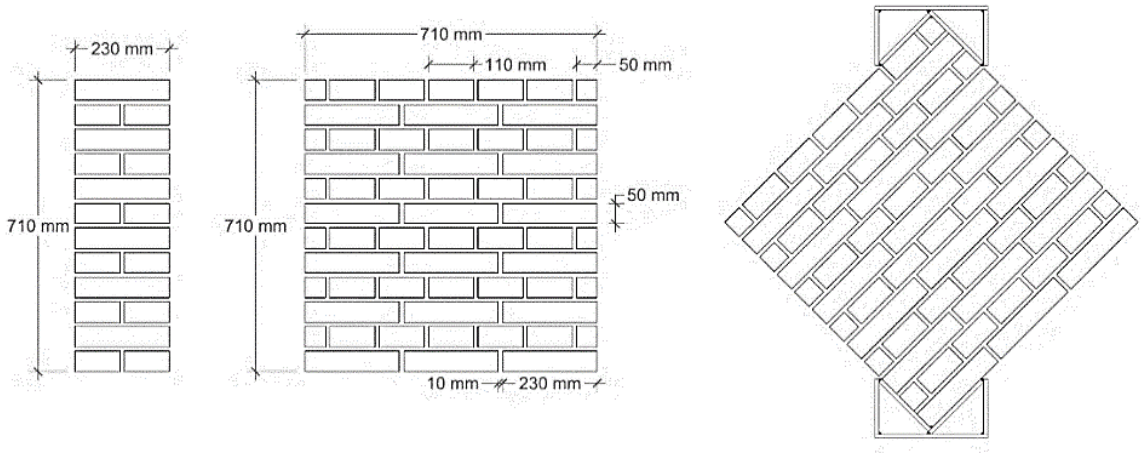

Figura 4. *Dimensiones de los paneles y configuración del ensayo de compresión diagonal.*

Figura 5. *Proceso de ejecución de los refuerzos con TRM.*

El proceso de ejecución del refuerzo TRM en las probetas de fábrica de mampostería se ilustra en la Fig. 5. Sobre la superficie humedecida de la fábrica se coloca una primera capa mortero para regularizar la superficie, con un espesor aproximado de unos 5 mm. A continuación, con el mortero fresco, se

coloca la malla de refuerzo y se aplica una ligera presión. Seguidamente, se dispone una segunda capa de mortero hasta completar un espesor total máximo de 10 mm. Por último se aplica la llana para regularizar la superficie.

Para el ensayo se siguieron las indicaciones de la norma ASTM E519 / E519M-21 [14]. El control se realizó por desplazamiento a una velocidad constante de 0.009 mm/s. Para la medida de las deformaciones se instalaron dos LVDTs situados en la misma cara y orientados según las diagonales del muro (Fig. 6(a)). La cara opuesta fue monitorizada mediante la técnica de correlación digital de imagen, para lo cual se empleó una cámara fotográfica con una resolución de 16 MP (Fig. 6(b)).

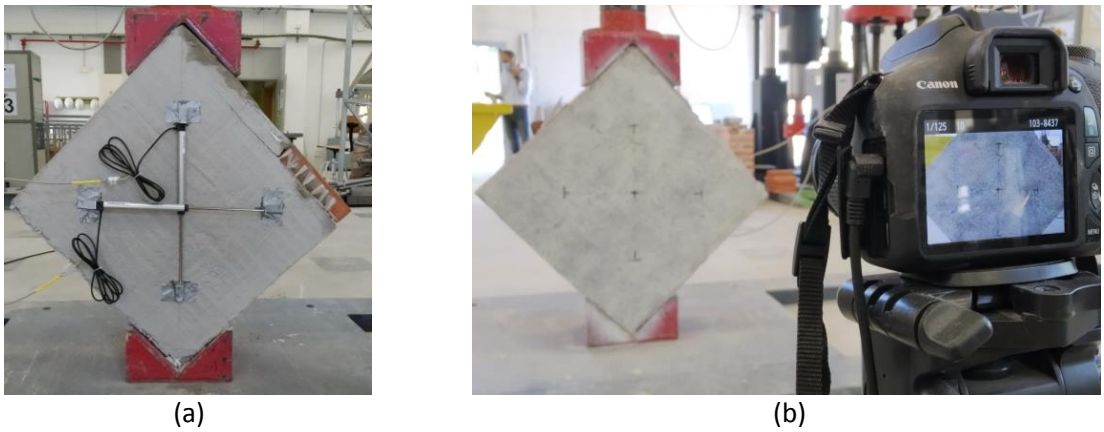

(a) (b)

Figura 6. *Control de deformaciones en los ensayos de compresión diagonal: (a) disposición de LVDTs según las diagonales del muro; (b) monitorización para correlación digital de imagen.*

Estos dispositivos permitían realizar el registro de las deformaciones para poder obtener la curva de comportamiento tensión cortante frente a distorsión angular. Las ecuaciones para el cálculo de ambos parámetros son las Ec. (1) y Ec. (2):

$$\tau = \frac{0.707\,P}{A_{net}} \tag{1}$$

$$\gamma = \frac{\Delta x + \Delta y}{g} \tag{2}$$

donde: τ es la tensión cortante (en MPa); P es el valor de la carga aplicada (en N); A_{net} es el área neta (en mm^2), conforme a la Ec. (3); γ es la distorsión angular o deformación a cortante; Δx es el acortamiento en la dirección paralela a la carga (en mm y en valor absoluto); Δy es el alargamiento en la dirección perpendicular a la carga (en mm y en valor absoluto); g es la longitud de medida en la dirección paralela a la carga (en mm), que debe ser igual a la longitud de medida en dirección perpendicular.

$$A_{net} = \left(\frac{w+h}{2}\right) t\, n \tag{3}$$

donde: w es el ancho de la probeta de ensayo (710 mm); h es la altura de la probeta de ensayo (710 mm); t es el espesor de la probeta de ensayo (230 mm); n es la fracción del área bruta del ladrillo que es macizo (en este caso la unidad, ya que se trata de ladrillos macizos).

Finalmente, el módulo de rigidez transversal *G* se calcula como el cociente entre la tensión cortante τ y la distorsión angular γ.

3. RESULTADOS Y DISCUSIÓN.

A continuación se muestran los resultados obtenidos tras los ensayos realizados en cada uno de los elementos estudiados.

3.1. Comportamiento de los morteros y los cupones de TRM.

Los morteros empleados y los cupones de TRM fueron ensayados a temperatura ambiente y a niveles variables de 100, 200, 400 y 600 °C. En la Fig. 7 se representan las resistencias residuales en valores normalizados, es decir, la relación entre la resistencia a una determinada temperatura respecto de la serie equivalente a temperatura ambiente. En el caso de los morteros se indica la resistencia a compresión, determinada según norma UNE-EN 1015-11:2000 [15]; en el caso de los cupones de TRM se indica la tensión de rotura a tracción, determinada de acuerdo a las instrucciones del código AC434 [13], tomando el valor medio de 5 probetas en cada serie.

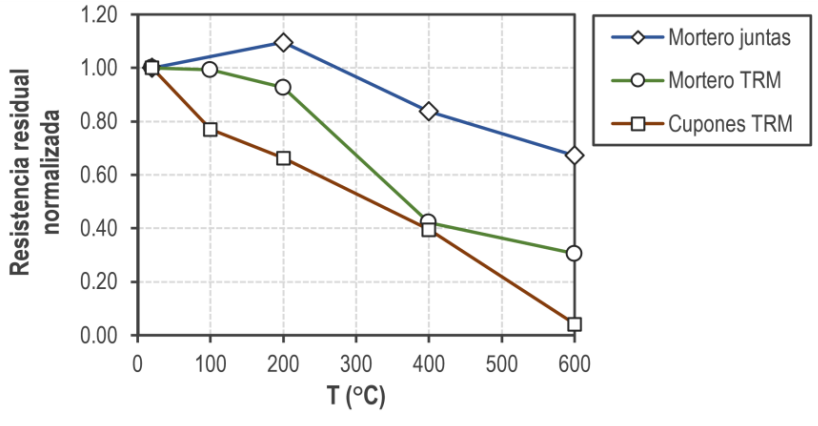

Figura 7. *Resistencia residual normalizada: resistencia a compresión en morteros y tensión de rotura a tracción en cupones de TRM.*

Como puede comprobarse, los distintos materiales estudiados conservan sus propiedades mecánicas relativamente intactas hasta niveles de temperatura del orden de 200 °C. En el caso del mortero empleado en las juntas de los muros, se observa como es el material que presenta el mejor comportamiento, presentando descensos máximos del 50% en la resistencia a compresión a 600 °C. Respecto de los TRM, se obtienen pérdidas del 60% a temperaturas de 400 °C, mientras que a 600 °C el material queda fuertemente dañado como consecuencia de la degradación de las mallas y la pérdida de adherencia con la matriz de mortero, en la línea de los resultados publicados en algunas investigaciones previas.

3.2. Comportamiento a compresión diagonal en los muros sin reforzar.

Se han realizado ensayos de compresión diagonal sobre paneles que previamente han sido dañados a temperaturas de 400 y 600 °C. Este incremento de temperatura supone una degradación de las propiedades mecánicas de la mampostería de forma que, tanto la resistencia a cortante, el módulo de rigidez transversal y la capacidad de deformación, se ven fuertemente reducidos. Esta reducción del

comportamiento mecánico viene provocada como consecuencia de la fisuración desarrollada en los paneles tras ser sometidos a 600 °C, la cual se produce no sólo siguiendo las juntas de mortero, sino también atravesando ladrillos completos (Fig. 8). Además, esta fisuración se desarrolla no sólo verticalmente sino también a lo largo del espesor del panel, aspecto que ha tenido una clara consecuencia en los modos de fallo observados durante la rotura.

Figura 8. *Fisuración observada en los paneles de mampostería tras su exposición a 600 °C.*

La Fig. 9 muestra los resultados tensión tangencial (τ) - deformación angular (γ) para tres paneles a diferentes temperaturas (20, 400 y 600 °C). Es importante destacar que las gráficas no son completas debido a que la instrumentación se ha retirado prudencialmente antes de la rotura. El motivo es que la rotura de este tipo de paneles es frágil y sin previo aviso (en los muros sometidos a altas temperaturas incluso es explosiva y a menores niveles de deformación), de forma que si no se retira la instrumentación a tiempo, se puede producir con total seguridad la rotura de los LVDTs. Por tanto, estas curvas permiten obtener el valor del módulo de rigidez transversal, pero no la máxima tensión tangencial soportada por cada panel.

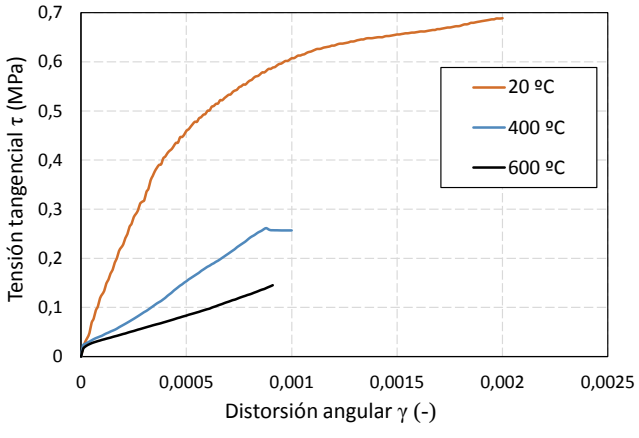

Figura 9. *Tensión tangencial - deformación angular para tres paneles sin reforzar a distintas temperaturas.*

La Fig. 10 muestra la degradación de las propiedades de la mampostería con la temperatura. Tras ser sometida a 600 °C, el módulo de rigidez transversal experimenta una reducción en torno a un 85% de su módulo de rigidez transversal a 20 °C, y una reducción de un 44% de la máxima tensión tangencial que es capaz de soportar a 20 °C.

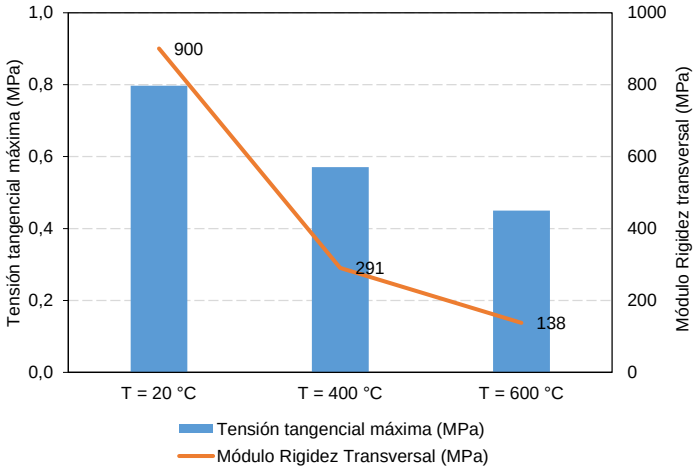

Figura 10. *Degradación de las propiedades mecánicas de la mampostería con la temperatura.*

3.3. Comportamiento a compresión diagonal en los muros reforzados con TRM.

En este apartado se presentan los resultados obtenidos en los ensayos de compresión diagonal llevados a cabo sobre paneles de mampostería reforzados con TRM tras su exposición a 600 °C. De esta forma es posible evaluar la mejora del comportamiento que supone reforzar un elemento de mampostería, que previamente ha sido dañado por el fuego. Se observa claramente que el refuerzo de un elemento de mampostería previamente dañado por el fuego mejora considerablemente su comportamiento mecánico. La Fig. 11 muestra la relación tensión tangencial (τ) - deformación angular (γ) para paneles sin reforzar a 20 y 600 °C, así como los resultados para dos paneles reforzados, uno a temperatura ambiente (20 °C) y otro reforzado tras ser expuesto a temperaturas de 600 °C. Es importante destacar que, tal y como se indicó en el apartado anterior, las curvas correspondientes a los elementos sometidos a 600 °C no son completas, pues los sensores LVDT eran retirados cuando se observaba algún indicio de rotura del panel. En los elementos sin reforzar sometidos a 600 °C la rotura se produce de forma súbita y frágil, por lo que es necesario tomar precauciones para evitar la rotura de los sensores. En el caso de los elementos reforzados tras su exposición a 600 °C, el registro de datos con los LVDT se ha realizado hasta el inicio de la delaminación del TRM, a partir de donde se observan anomalías en el registro de datos.

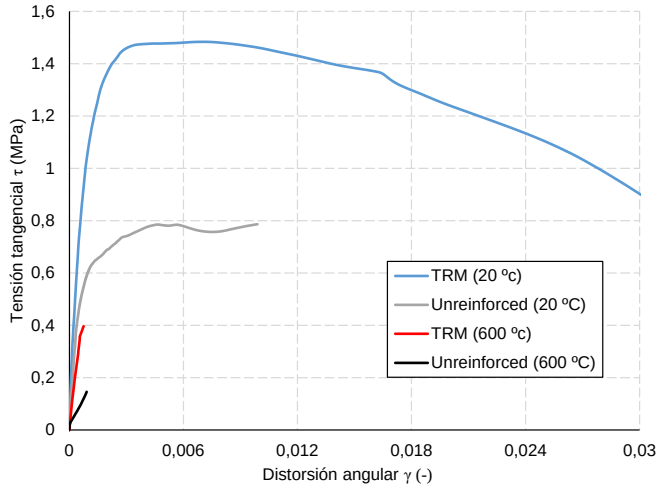

Figura 11. *Tensión tangencial - deformación angular para paneles sin reforzar y reforzados a 20 y 600 °C.*

El refuerzo con TRM hace que la mampostería dañada a fuego recupere gran parte de su módulo de rigidez transversal hasta alcanzar casi el valor del módulo original del panel a temperatura ambiente. El muro sin reforzar a 20 °C presenta un módulo de rigidez transversal de 900 MPa. Cuando se daña a temperaturas de 600 °C, sufre un descenso en este parámetro hasta alcanzar valores de 138 MPa. Tras ser expuesto a este nivel de temperaturas, el refuerzo TRM hace que el módulo incremente hasta valores de 629 MPa. En cuanto a la tensión tangencial máxima alcanzada por cada panel, se destaca que los paneles reforzados han experimentado valores máximos de 1.48 MPa para el panel reforzado que no ha sido expuesto a altas temperaturas y 0.97 MPa para el panel que ha sido reforzado tras su exposición a temperaturas de 600 °C. Este valor es superior a la tensión máxima que es capaz de alcanzar un panel sin reforzar (0.8 MPa) y sin haber sido previamente dañado por fuego. Este aspecto confirma la mejora, en términos de capacidad mecánica, del refuerzo TRM en elementos de mampostería previamente dañados por fuego. La mejora de las propiedades mecánicas se representa gráficamente en la Fig. 12 para los tres escenarios contemplados en la investigación: (i) muros sin reforzar a temperatura ambiente; (ii) muros sin reforzar expuestos a 600 °C; (iii) muros reforzados con TRM sin ser expuestos a elevadas temperaturas; (iv) muros expuestos a 600 °C y posteriormente reforzados con TRM.

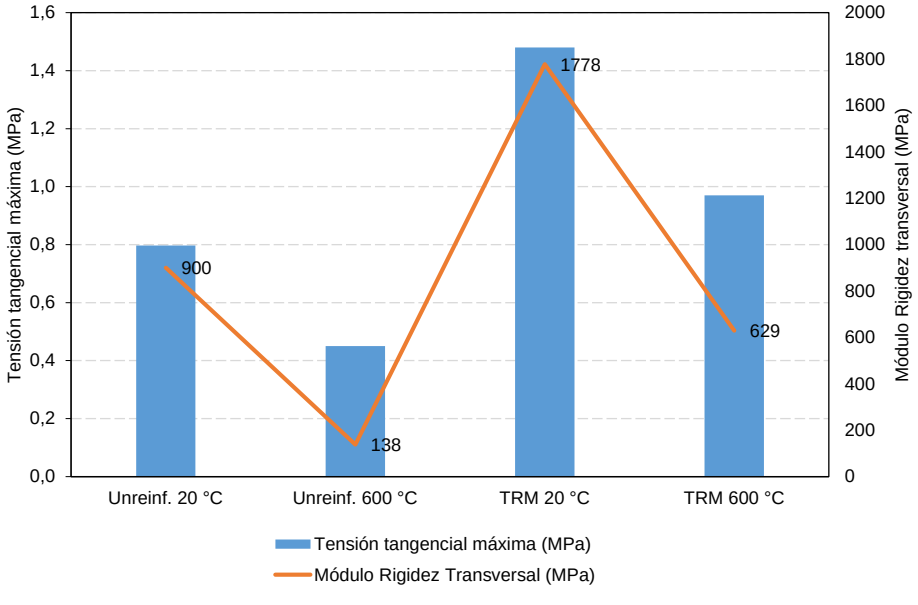

Figura 12. *Evolución de las propiedades mecánicas de los muros sin reforzar a temperatura ambiente (Unreinf. 20 °C), muros sin reforzar expuestos a 600 °C (Unreinf. 600 °C), muros reforzados sin ser dañados por altas temperaturas (TRM 20 °C) y muros expuestos a 600 °C y posteriormente reforzados con TRM (TRM 600 °C).*

En cuanto al modo de fallo, es importante destacar que en los muros expuestos a 600 °C se produce la abertura del muro por su plano medio, tanto en los muros sin reforzar como en los reforzados con TRM (Fig. 13). Este fallo viene provocado por la fisuración inicial producida por las elevadas temperaturas. También se ha observado, en el caso de los muros reforzados con TRM tras ser expuestos a altas temperaturas, la delaminación del TRM, aspecto que no ha sido observado previamente en los ensayos de compresión diagonal de elementos de mampostería a temperatura ambiente (Fig. 13.b y Fig. 13.c).

(a) (b) (c)

Figura 13. *Modos de fallo. (a) paneles sin reforzar a temperatura ambiente. (b)- Paneles reforzados con TRM a temperatura ambiente. (c)- Paneles reforzados con TRM tras la exposición a 600 °C.*

4. CONCLUSIONES.

Este artículo muestra los resultados preliminares de una campaña de ensayos experimentales realizada sobre paneles de mampostería (reforzados con TRM y sin reforzar) para caracterizar mecánicamente (evaluando la resistencia a cortante y su módulo de rigidez transversal) estos elementos cuando son dañados por elevadas temperaturas. Para ello se han realizado ensayos mecánicos sobre probetas de mortero de cal de las juntas de los paneles de mampostería, sobre probetas de mortero de aplicación de refuerzo TRM, sobre cupones de elementos de TRM y sobre paneles de mampostería, reforzados y sin reforzar. La temperatura de estudio en este trabajo ha sido de 600 °C, por (1) ser éste un nivel de temperatura que puede alcanzarse fácilmente cuando se produce un incendio y (2) por observarse un importante deterioro de las propiedades mecánicas de los diferentes materiales a este nivel de temperaturas.

En este aspecto, se ha observado que los distintos materiales estudiados conservan sus propiedades mecánicas relativamente intactas hasta niveles de temperatura del orden de 200 °C. Sin embargo, a 600 °C el mortero de las juntas ha sufrido una pérdida del 50 % de su resistencia a compresión inicial y el material de refuerzo TRM queda fuertemente dañado como consecuencia de la degradación de las mallas y la pérdida de adherencia con la matriz de mortero

En cuanto a los elementos de mampostería, la acción de elevadas temperaturas produce una degradación importante que implica una reducción drástica de su resistencia y de su módulo de rigidez transversal. De esta forma, a 600 °C el módulo de rigidez transversal ha disminuido un 85% con respecto a su valor a temperatura ambiente (138 MPa frente a 900 MPa), y un 44% para el valor de su resistencia a cortante (0.43 MPa frente a 0.8 MPa).

Tras verse dañada por temperaturas de 600 °C, la aplicación del refuerzo TRM mejora considerablemente el comportamiento mecánico de los paneles: la resistencia a cortante del muro reforzado tras la acción de altas temperaturas es un 21% mayor que el muro sin reforzar a temperatura ambiente (0.97 MPa frente a 0.8 MPa). En cuanto al módulo de rigidez transversal, este valor no se recupera por completo: El muro sin reforzar a temperatura ambiente presenta valores de 900 MPa, mientras que el muro reforzado tras ser expuesto a altas temperaturas presenta valores de 629 MPa.

Finalmente, en cuanto a los modos de fallo es importante destacar que los muros reforzados con TRM tras ser expuestos a elevadas temperaturas han sufrido la delaminación del TRM, así como la rotura del muro en su plano medio. Este aspecto no ha sido observado previamente en los elementos reforzados a temperatura ambiente.

AGRADECIMIENTOS

Los autores del presente trabajo desean mostrar su agradecimiento a MAPEI y Grupo Puma por el suministro de los materiales empleados. La investigación ha sido financiada por el Ministerio de Ciencia, Innovación y Universidades, a través del proyecto RTI2018-101148-B-100.

REFERENCIAS

[1] B. Torres, S. Ivorra, F. Javier Baeza, L. Estevan, B. Varona, Textile reinforced mortars (TRM) for repairing and retrofitting masonry walls subjected to in-plane cyclic loads. An experimental approach, Eng. Struct. 231 (2021) 111742. https://doi.org/10.1016/j.engstruct.2020.111742.

[2] L. Estevan, F.J. Baeza, D. Bru, S. Ivorra, Stone masonry confinement with FRP and FRCM composites, Constr. Build. Mater. 237 (2020) 117612. https://doi.org/10.1016/j.conbuildmat.2019.117612.

[3] E. Bertolesi, B. Torres, J.M. Adam, P.A. Calderón, J.J. Moragues, Effectiveness of Textile Reinforced Mortar (TRM) materials for the repair of full-scale timbrel masonry cross vaults, Eng. Struct. 220 (2020) 110978. https://doi.org/10.1016/j.engstruct.2020.110978.

[4] S. Babaeidarabad, F. De Caso, A. Nanni, URM Walls Strengthened with Fabric-Reinforced Cementitious Matrix Composite Subjected to Diagonal Compression, J. Compos. Constr. 18 (2014) 04013045. https://doi.org/10.1061/(asce)cc.1943-5614.0000441.

[5] L. Garcia-Ramonda, L. Pelá, P. Roca, G. Camata, In-plane shear behaviour by diagonal compression testing of brick masonry walls strengthened with basalt and steel textile reinforced mortars, Constr. Build. Mater. 240 (2020) 117905. https://doi.org/10.1016/j.conbuildmat.2019.117905.

[6] P. Meriggi, S. De Santis, S. Fares, G. de Felice, Design of the shear strengthening of masonry walls with fabric reinforced cementitious matrix, Constr. Build. Mater. 279 (2021) 122452. https://doi.org/10.1016/j.conbuildmat.2021.122452.

[7] B. Torres, F.B. Varona, F.J. Baeza, D. Bru, S. Ivorra, Study on retrofitted masonry elements under shear using digital image correlation, Sensors (Switzerland). 20 (2020). https://doi.org/10.3390/s20072122.

[8] F.D.A. Silva, M. Butler, S. Hempel, R.D. Toledo Filho, V. Mechtcherine, Effects of elevated temperatures on the interface properties of carbon textile-reinforced concrete, Cem. Concr. Compos. 48 (2014) 26–34. https://doi.org/10.1016/j.cemconcomp.2014.01.007.

[9] D.A.S. Rambo, F. de Andrade Silva, R.D. Toledo Filho, O. da Fonseca Martins Gomes, Effect of elevated temperatures on the mechanical behavior of basalt textile reinforced refractory concrete, Mater. Des. 65 (2015) 24–33. https://doi.org/10.1016/j.matdes.2014.08.060.

[10] T. Tlaiji, X.H. Vu, E. Ferrier, A. Si Larbi, Thermomechanical behaviour and residual properties of textile reinforced concrete (TRC) subjected to elevated and high temperature loading: Experimental and comparative study, Compos. Part B Eng. 144 (2018) 99–110. https://doi.org/10.1016/j.compositesb.2018.02.022.

[11] S.R. Maroudas, C.G. Papanicolaou, Effect of high temperatures on the TRM-to-masonry bond, Key Eng. Mater. 747 KEM (2017) 533–541. https://doi.org/10.4028/www.scientific.net/KEM.747.533.

[12] A. Iorfida, S. Candamano, F. Crea, L. Ombres, S. Verre, P. De Fazio, Bond behaviour of FRCM composites: Effects of high temperature, Key Eng. Mater. 817 KEM (2019) 161–166. https://doi.org/10.4028/www.scientific.net/KEM.817.161.

[13] AC434, Acceptance Criteria for Masonry and Concrete Strengthening Using Fiber-Reinforced Cementitious Matrix (FRCM) Composite Systems, ICC Evaluation Service, (2016).

[14] ASTM E519 / E519M-21, Standard Test Method for Diagonal Tension (Shear) in Masonry Assemblages, ASTM International, West Conshohocken, PA, (2021).

[15] UNE-EN 1015-11:2020, Methods of test for mortar for masonry - Part 11: Determination of flexural and compressive strength of hardened mortar, AENOR, Spanish Association for Standardisation, Madrid (Spain), (2020).

Forensic analysis taken after the collapse of a historical bell.

Ivorra Chorro, Salvador[1]; Torres Górriz, Benjamín[1]; Estevan García, Luís[1]; Bru Orts, David[1].

[1] Departamento de Ingeniería Civil. Universidad de Alicante, España. Carretera San Vicente sn 03690 San Vicente del Raspeig, Alicante.

ABSTRACT

This paper describes the analysis performed after the collapse of the historical *EL JAUME* Bell in the Cathedral of Valencia´s Micalet Bell Tower in Spain (Fig.1). When the bells were being rung during the celebration on Christmas Day 2014, a sudden collapse took place fortunately without any casualties.

After several visits to the bell tower, a forensic study was carried out to determine the causes that had originated the collapse of this historical bell, which dates back to 1429. A fractographic and metallographic analysis of the steel shaft was initially carried out. This study allowed us to know the characteristics and mechanical properties. In a second phase, a fatigue damage analysis was carried out. The remaining fatigue life was estimated from the Whöler SN curves for elements subjected to rotational bending.

Once this analysis was performed, it was concluded that the bell collapse was caused by fatigue damage in steel shaft, which theoretically should have been reached between 300000 and 400000 cycles. Specifically, damage propagation occurred due to an incorrect design of the steel shaft that caused a cross section with high stress concentration. Finally, the paper shows the remedial measures proposed in all the bells of the Micalet bell tower, whose steel shafts were designed under the same criteria and therefore, there was uncertainty about their remaining fatigue life.

Keywords: Bell, fatigue failure, cyclic loading, forensic engineering, collapse.

1. INTRODUCCIÓN.

Desde antiguas civilizaciones hasta nuestros días, los toques y avisos que se podían realizar con las campanas eran un código que los ciudadanos conocían y marcaba la vida de los pueblos. La misión de los toques de campanas ha sido fundamentalmente informativa, pero también han sido utilizadas para otros aspectos como marcar el paso del día, coordinar o delimitar el territorio [1]. Esta operación del toque de campanas ha sido realizada, a lo largo de la historia, de forma manual mediante el empleo de ballestas, cuerdas instaladas excéntricas al eje de giro de la campana para provocar su giro total o parcial. No obstante, a partir de la segunda mitad del siglo XX aparece la mecanización del toque de campanas. La mecanización consiste en el empleo de un motor que, o bien acciona el giro de la campana o bien acciona una masa golpeante mientras la campana permanece quieta.

Sin embargo, es a finales de 1980 cuando aparece la figura del campanero, voluntarios formados, profesionales no remunerados que además de tocar las campanas de forma manual, recuperan toques

antiguos, promueven restauraciones y divulgan sus actividades [2]. De esta forma, a día de hoy el toque de campanas se ha convertido en una tradición muy arraigada que se practica, habitualmente, durante las jornadas de festividades religiosas. La técnica consiste en, varios operarios o *campaners*, voltean simultáneamente varias campanas intentando compaginar los toques simultáneamente creando un lenguaje sonoro estético.

Durante el tiempo de uso de las campanas, el cual puede llegar a alcanzar varios siglos, todos sus componentes están sometidos a una serie de cargas cíclicas de naturaleza dinámica. Estos elementos, probablemente fueron diseñados bajo la hipótesis de vida infinita. Sin embargo, durante el volteo de la campana los elementos pueden iniciar a acumular daño debido a la iniciación de fisuras debidas a fatiga y su propagación [3, 4]. De hecho, la iniciación de fisuras por fatiga en acero de altas resistencias es un tema que ha recibido muchos estudios durante los últimos años. [5, 6].

El fallo y colapso de una campana, aunque resulta poco habitual (los autores del presente artículo sólo han identificado dos publicaciones científicas en la que explican en profundidad los fallos ocurridos en la *Freedom Bell* en Berlín [7], *Liberty Bell* en Filadelfia [8] and *Big Ben Bell* en Londres [8]), sus consecuencias pueden ser muy graves, ya que:

- Se trata de un elemento de grandes dimensiones y peso que voltean a varias revoluciones por minuto con respecto a un eje.

- El volteo manual implica la proximidad de los campaneros en el entorno de la campana.

- La campana se ubica frente a espacios abiertos para garantizar que las ondas se propagan con facilidad, pudiendo llegar a salir disparada de la torre.

En este contexto general, este artículo analiza el colapso de una campana histórica que data de 1429. Se trata de la campana llamada *El Jaume* con un peso total de 28.5 kN, situada en el campanario *Micalet* de la Catedral de Valencia. El colapso de la campana tuvo lugar el 25 de diciembre de 2014 durante la festividad del día de Navidad mientras se practicaba el toque manual de las mismas, afortunadamente sin producir daños personales. Tras el colapso se realizaron varias visitas al campanario y se llevó a cabo un análisis de las causas que podrían haber originado el colapso. Para ello se realizaron análisis fractográficos y metalográficos del acero del eje de la campana que fue recuperado tras el colapso, aspecto que permitió identificar el tipo y propiedades mecánicas del acero. Posteriormente se llevó a cabo un estudio del daño acumulado en el eje debido a fatiga, concluyendo que el colapso se produjo debido a un diseño incorrecto del eje, el cual provocó una sección de fuerte concentración de secciones que redujo su vida remanente a fatiga a un máximo de 400.000 ciclos. Finalmente, este artículo describe las soluciones implementadas en todas las campanas del campanario, que habían sido diseñadas bajo el mismo criterio y por tanto existía incertidumbre sobre su vida remanente a fatiga.

2. LA CAMPANA *EL JAUME* DEL CAMPANARIO *MICALET* DE LA CATEDRAL DE VALENCIA.

La catedral de Valencia se encuentra ubicada en el núcleo histórico de Valencia y su torre campanario recibe el nombre de *Micalet.* Tiene 51 metros de altura hasta la terraza y 51 metros de perímetro. Su altura total es de 63 metros y tiene forma de prisma octogonal (Figura 1.a). Su construcción se inicia en 1381 y finaliza en 1429. En la parte superior de la torre se encuentra la sala de campanas, abierta por ocho ventanales cada uno en una de sus caras. En esta sala existen un total de 11 campanas de bronce

[9]. Las tres campanas más antiguas, llamadas Catalina (1305), El Jaume (1429) y Pablo (1489) viajaron a la Exposición Universal de Sevilla en el año 1992 donde fueron declaradas como Monumento Histórico Nacional [10]. Fue entonces cuando las autoridades locales valencianas decidieron llevar a cabo un proceso de restauración de las campanas, sustituyendo algunos elementos metálicos por otros nuevos. Concretamente, los ejes metálicos que conectaban el contrapeso de madera con los rodamientos fueron sustituidos. Tras este proceso de restauración, las campanas regresaron a Valencia, fueron instaladas y continuaron funcionando.

(a)

(b)

Figura 1. *(a)- Campanario El Micalet. (b)- Campana El Jaume.*

El día 25 de diciembre de 2014, la campana llamada *El Jaume* (Figura 1.b) colapsó durante el toque manual durante la celebración del día de Navidad. La campana cayó desde una altura de cuatro metros al suelo de la sala de campanas, afortunadamente sin causar ningún herido. El peso aproximado de esta campana, incluyendo el contrapeso, herrajes, bronce y badajo es de 28.5 kN. Desde la fecha de su restauración en 1992 hasta el día de su colapso en 2014, la campana participó aproximadamente en 30 toques anuales. Cada toque tenía una duración de unos 15 minutos y la velocidad de volteo de esta campana se encuentra en torno a 35 rpm [11]. Esto hace un total, aproximadamente, de 346500 ciclos.

3. INVESTIGACIÓN DEL COLAPSO.

Tras el colapso de la campana se llevó a cabo un estudio para determinar las causas que habían originado el colapso. De la primera inspección visual, se observó que:

- Las asas de la campana (elemento de unión entre la campana y el contrapeso) estaban completamente cortadas (Figura 2.a).
- El eje de giro, en su apoyo izquierdo, estaba completamente fracturado (Figura 2.b).
- El rodamiento del eje derecho se encontraba partido (Figura 2.c).

(a)

(b)

(c)

Figura 2. *(a)-Rotura de las asas de la campana. (b)- Rotura del eje en su apoyo izquierdo. (c)- Rotura del rodamiento del eje derecho.*

La campana se encontraba en posición vertical sobre el suelo, por lo que todo parece apuntar a que la rotura se produjo en el instante en que la campana se encontraba en posición horizontal apuntando hacia el exterior de la torre.

El eje de la campana está formado por una pieza de madera de grandes dimensiones, llamado contrapeso. En la zona próxima a los apoyos, el contrapeso dispone de un cajeado hueco prismático, de dimensiones 60×60×50 mm. Sobre este hueco se inserta un elemento prismático metálico, de 650 mm de longitud y que presenta dos secciones transversales. Un primer tramo de sección cuadrada de 60×60 mm y de 550mm de longitud. Un segundo tramo, más corto, de 100 mm de longitud y de sección circular de 55 mm de diámetro. Esta parte del eje circular se inserta en el rodamiento permitiendo el giro de la campana.

Se observa que la rotura del eje en su apoyo izquierdo se ha producido justo en la sección de transición de barra de sección cuadrada a sección circular. Un dato de especial importancia es que la transición entre sección cuadrada y sección circular no presenta ningún radio de acuerdo, lo que inicialmente implica una sección de concentración de tensiones. La inspección visual de la sección de rotura (Figura

3), permitió observar cuatro zonas claramente diferenciadas (A, B, C, D), sensiblemente circulares todas ellas

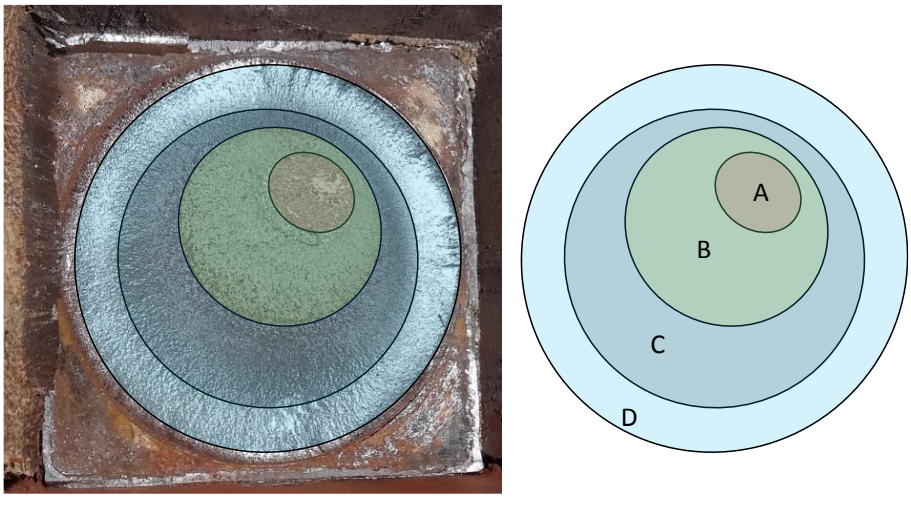

Figura 3. *Sección transversal de la rotura del eje e identificación de zonas.*

La zona A es una zona de gran rugosidad y de color brillante. Se trata de la última sección resistente cuando se produjo el colapso, por lo que la rotura de esa porción de sección se produjo de forma dúctil una vez ya plastificada. La zona B presenta menor rugosidad que la zona A y está generada por las variaciones cíclicas de tensiones de tracción y compresión por la flexión rotativa del eje. La zona C presenta un color rojizo derivado de la oxidación del acero, lo que indica que esta zona ya llevaba un cierto tiempo abierta. Finalmente, la zona D apenas presenta rugosidad debido a la fricción entre los dos extremos de una grieta, que han provocado su pulido. En esta zona es donde se inicia y propaga la rotura del eje. Este esquema de rotura es identificable al correspondiente a un eje trabajando cíclicamente a esfuerzos de tracción-compresión derivados de flexión positiva-negativa sometido a bajos esfuerzos –las revoluciones de la campana son relativamente bajas comparadas con las velocidades de trabajo de un eje de una máquina industrial- pero con concentraciones de esfuerzos severas.

A partir de lo observado, se deduce por tanto que el colapso se ha producido de la siguiente forma:

- Rotura del eje izquierdo durante el volteo de la campana, justo en la sección de transición. Todo parece indicar que la rotura ha sido debida a un fallo por fatiga del eje.
- Al producirse la rotura del eje, la campana gira con respecto al anclaje derecho.
- Este giro produce la rotura del rodamiento derecho.
- El conjunto formado por la campana y el contrapeso impactan contra el suelo produciéndose la rotura frágil de las asas.

4. ANÁLISIS METALOGRÁFICO DEL ACERO DEL EJE.

El eje metálico de la campana fue recuperado y sometido a un análisis metalúrgico, con el objetivo de determinar el tipo de acero, su estado y sus propiedades mecánicas. Se realizaron determinaciones de dureza Brinell HB y Rockwell HRb [12] y determinación de microestructura. La resistencia equivalente a partir de ensayos de dureza se obtuvo empleando las equivalencias DIN 50150 [13].

La Tabla 1 muestra los resultados de los análisis de dureza realizados. A partir de las mediciones realizadas, para cada método se han obtenido resultados con muy poca variabilidad. Se observa una mayor dispersión en las resistencias estimadas entre ambos métodos, con valores de 745 MPa estimadas mediante el método dureza Rockwell y 830 MPa con el método Brinell.

Tabla 1. Resultados de ensayos de dureza.

Ensayo de dureza	Número	Valor mínimo	Valor máximo	Valor promedio	Resistencia equivalente (MPa) [13]
Rockwell HRb	6	95	96	95.5	745
Brinell HB	6	205	220	212.5	830

Finalmente, las imágenes obtenidas del análisis fractográfico (Figura 4) mediante lupa esteroscópica muestra unas irregularidades superficiales presentes a lo largo de toda la periferia del eje en la sección de rotura. Estas irregularidades o principios de entalla pueden haber sido provocadas por impacto, seguramente provocadas con la herramienta utilizada para la inserción del eje metálico en el contrapeso. Estas irregularidades producidas en la sección de rotura han podido suponer el inicio de la propagación de las grietas asociadas a fatiga.

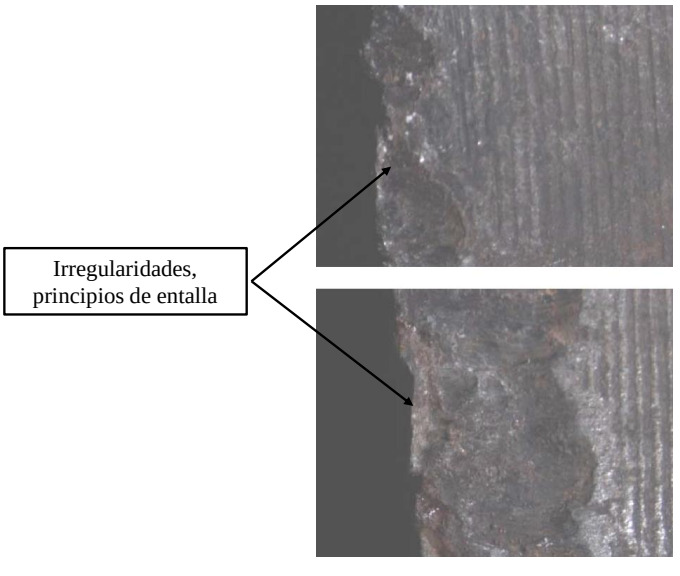

Figura 4. *Irregularidades a lo largo del perímetro de la sección circular de rotura.*

5. ESTIMACIÓN DE LA VIDA REMANENTE A FATIGA DEL EJE.

Desde un punto de vista estático, el eje de la campana puede considerarse como una viga biapoyada sometida a la acción del peso propio equivalente a 28.5 kN. Asumiendo un modelo simplificado para el conjunto, en la sección de rotura aparecen unos esfuerzos correspondientes a 1.5 kNm de momento flector y 13.9 kN de cortante. Para la sección circular, la tensión equivalente de von Mises equivale a un total de 92.6 MPa, valor muy inferior a la resistencia estimada del análisis fractográfico y cuyo valor resultó en torno a 745 MPa.

Sin embargo, el volteo de la campana produce una inversión cíclica de esfuerzos tracción-compresión. Se generan por tanto unas fuerzas de inercia H, V (Figura 5) que se transmiten a la torre a través del eje. [14] presentó estos resultados y propuso unos valores de amplificación dinámica de 1.5 para la carga vertical y 0.4 para la carga horizontal, con respecto al peso propio de la campana. Teniendo en cuenta esta consideración, la carrera de tensión von Mises amplificada dinámicamente en la sección de rotura se encuentra en torno a 139 MPa.

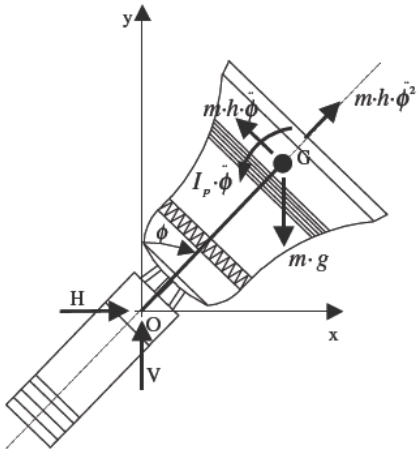

Figura 5. *Modelo simplificado de la campana y sus fuerzas de inercia. Extraído de [14].*

Para el estudio del fallo por fatiga es necesario la obtención de las curvas SN, también conocidas como curvas de Wöhler [15], las cuales permiten efectuar predicciones conservativas del comportamiento a fatiga. Sobre la base de una gran cantidad de datos experimentales sobre elementos de acero se ha podido determinar que la resistencia a la fatiga para 10^3 ciclos es de 0.9 S_u para probetas solicitadas en flexión rotativa, y que exhiben una resistencia a vida infinita, S_n = 0.5 S_u a partir de los 10^6 ciclos, donde S_u es la resistencia última del material [16].

La resistencia a vida infinita, además, se ve afectada por otros factores que tienen en cuenta el efecto de acabado superficial, tamaño, tipo de carga, temperatura y efecto concentrador de tensiones. Esta resistencia, llamada tensión de fatiga $S_n{}'$, puede obtenerse a partir de las ecuaciones (1), (2) y (3) [15]:

$$S_n{}' = K_a \cdot K_b \cdot K_c \cdot K_d \cdot K_e \cdot \left(\frac{S_n}{K_f}\right) \quad (1)$$

$$K_f = 1 + (K_t - 1) \cdot q \quad (2)$$

$$K_t = A \left(\frac{r}{d}\right)^b \quad (3)$$

Donde:

- $S_n{}'$ es la tensión de fatiga.
- K_a es el coeficiente de acabado superficial.

- K_b es el coeficiente de efecto tamaño.
- K_c es el coeficiente de tipo de carga.
- K_d es el coeficiente de temperaturas.
- K_e es el coeficiente de confiabilidad.
- S_n es la resistencia teórica a vida infinita a partir de 10^6 ciclos, $S_n = 0.9 \cdot S_u$
- K_f es el coeficiente de entalla o concentración de tensiones. A partir de los 1000 primeros ciclos, viene definido a partir de la ecuación (2).
- K_t es el factor teórico elástico, definido a partir de la ecuación (3).
- q es la sensibilidad de la muesca o entalla.
- A y b son coeficientes obtenidos a partir de [15, 16].
- r es el radio de transición en la sección de concentración de tensiones.
- d es el diámetro del eje en la sección del fallo.
- D es el diámetro equivalente a sección circular de la porción de eje de mayor sección

Para el caso que nos ocupa y a partir de las recomendaciones seguidas en [15, 16], la mayoría de los anteriores parámetros (K_a , K_b , K_c , K_d , K_e) adoptan valores muy próximos a la unidad. Sin embargo, el que representa una mayor afección sobre la tensión de fatiga es el coeficiente K_f, coeficiente de entalla el cual depende fuertemente del radio de transición entre las dos secciones transversales. La evolución del coeficiente de entalla o concentración de tensiones en función del radio de acuerdo para el eje objeto de este estudio se muestra en la Figura 6. Para valores muy reducidos –del orden de 0.01 mm-, el coeficiente K_f alcanza valores en torno a 4.7. A partir de valores de r en torno a 30 mm, el factor de concentración de tensiones se reduce a la unidad, desapareciendo este efecto de entalla.

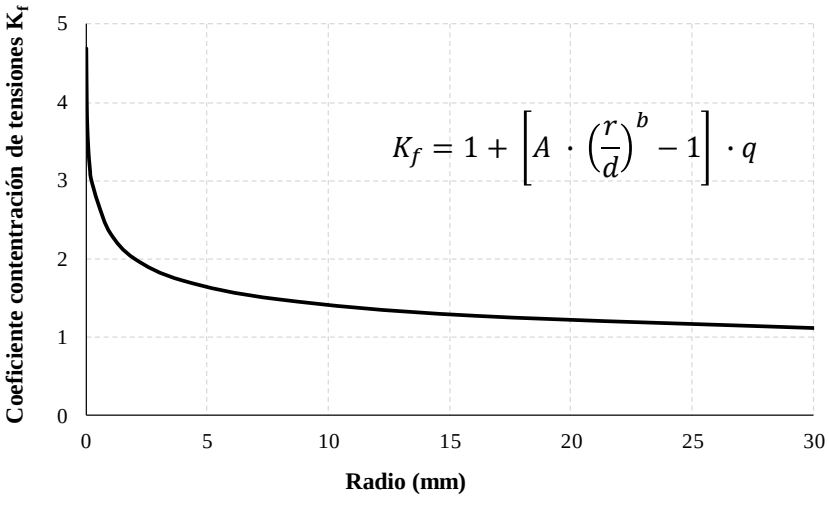

Figura 6. *Evolución del coeficiente de concentración de tensiones K_f*

La Figura 7 muestra la curva Stress S - Log (Number of cycles, N), donde se observa la curva sin considerar el efecto de concentración de tensiones, las curvas SN considerando una concentración de tensiones para un radio de transición de 0 y 2.5 mm y las tensiones de von Mises en la sección crítica del eje, amplificadas dinámicamente como se indicó en [14].

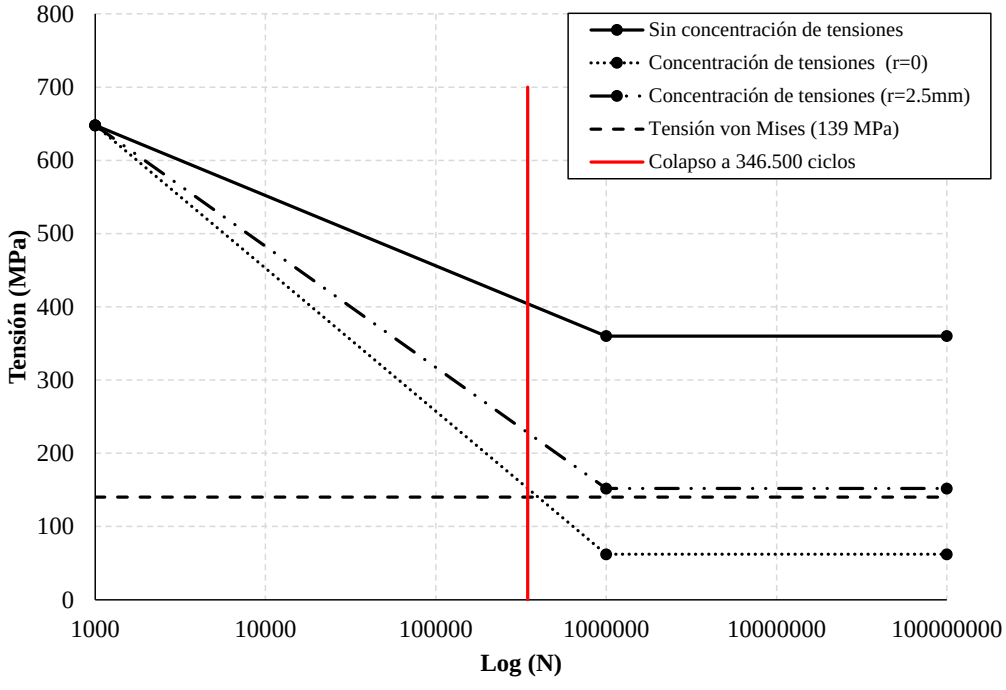

Figura 7. *Curvas SN para el eje de rotura considerando diferentes coeficientes de concentración de tensiones K_f.*

A la vista de los resultados, la rotura del eje como consecuencia del daño acumulado por fatiga ya estaba prevista en su curva de vida. La situación más desfavorable de rotura se habría producido a partir de los 355000 ciclos (cruce de la carrera de tensión de von Mises de 139 MPa con la curva SN para r=0), considerando un radio de transición de 0, es decir, una unión a 90°. De hecho, con la inspección visual se ha comprobado que el radio de transición es inexistente ya que ésta se produce en ángulo recto.

A partir del calendario anual de toques de campanas publicado anualmente en [2], la campana *El Jaume* participa aproximadamente en 30 toques anuales, con una duración de 15 minutos por toque aproximadamente. La velocidad de volteo de esta campana se encuentra en torno a 35 rpm [11] en condiciones normales de operación. Con estos datos puede estimarse que desde la fecha de su restauración en 1992 hasta el día de su colapso en 2014, la campana ha volteado alrededor de su eje unos 346500 ciclos. Por tanto, el escenario de fallo converge razonablemente bien con radios de acuerdo próximos a 0. De entre los factores que pueden haber reducido la vida útil por debajo de los 355000 ciclos calculados acelerando la rotura es la aparición de corrosión en el exterior del eje, introduciéndose en la grieta tal y como se mostró en la Figura 3.

En el caso de no existir una transición entre secciones del eje, podría concluirse que nunca se habría producido la rotura del eje ya que no existiría el efecto de concentración de tensiones (Figura 7). Tal y como se ha indicado en la Figura 6, a partir de un radio de 30 mm prácticamente desaparece el efecto concentración de tensiones, aunque podría concluirse que la rotura no se habría producido adoptando radios de transición mínimos en torno a 2.5 mm (Figura 7).

6. MEDIDAS CORRECTORAS ADOPTADAS.

Realizado el análisis del colapso de la campana El Jaume, se decidió adoptar las siguientes consideraciones para evitar nuevos colapsos en el resto de campanas, las cuales fueron rehabilitadas bajo las mismas directrices que la campana El Jaume:

- Prohibición inmediata de voltear el resto de las campanas situadas en el Micalet, que fueron restauradas en 1992 mediante el mismo procedimiento que el empleado en la campana *El Jaume*.
- Realizar una inspección de los ejes de todas las campanas, que consisten en el desmontaje completo del contrapeso de madera y ejes metálicos para someterlos a ensayos no destructivos con líquidos penetrantes y/o radiografías en la zona de cambio brusco de sección.
- Sustitución de ejes y adaptación de contrapesos que a partir de los ensayos e inspecciones realizadas, proporcionen incertidumbre en cuanto a la remanencia de su resistencia a fatiga.

Concretamente, en la campana El Jaume se aumentaron las dimensiones de los ejes metálicos para garantizar la vida remanente a fatiga. El nuevo eje metálico de la campana *El Jaume* es de 90×90 mm en la sección cuadrada y 80 mm de diámetro en la sección circular. Además se llevó a cabo una transición suave entre las secciones cuadradas y circulares del eje (Figura 8). Esta transición se ha conseguido mediante mecanización del eje. Con este mecanizado, el efecto de concentración de tensiones es muy reducido y no supone un aspecto crítico sobre la vida remanente a fatiga. Esto, unido al aumento de las dimensiones del eje, hace que el eje de la campana esté preparado para resistir las solicitaciones generadas por el volteo de la campana.

Figura 8. *Transición suave entre sección cuadrada y sección circular.*

7. CONCLUSIONES.

Este artículo describe y analiza el colapso de la campana *El Jaume* del campanario *Micalet* de la Catedral de Valencia, España. El colapso se produjo el día 25 de diciembre de 2014 durante la celebración del volteo manual de las campanas con motivo del día de Navidad, afortunadamente sin causar heridos.

La inspección visual realizada y los análisis metalúrgicos y fractográficos realizados al eje metálico de la campana permitió establecer un primer enfoque del problema. Todo indicó apuntar a que se produjo el agotamiento de la vida útil del eje de la campana debido a fatiga del material provocado por las cargas cíclicas generadas durante el volteo de la campana. En base a este primer diagnóstico, se realizó un estudio para estimar la vida remanente de fatiga empleando las curvas SN. A la vista de los resultados, se concluyó que la vida remanente a fatiga del eje de la campana se agotaría alcanzado los 355000 ciclos, mientras que el colapso de la campana se produjo a los 346500 ciclos, aproximadamente.

El diseño del eje de la campana –sustituido en 1992 con motivo de la restauración de la misma- fue uno de los motivos fundamentales que propiciaron el inicio y propagación de grietas perimetrales asociados a fatiga del material. El eje disponía de un cambio brusco de sección cuadrada a sección circular, sin transición suave entre ambas, produciendo una fuerte concentración de tensiones en esta sección. Este aspecto provocó que la tensión de fatiga a 10^6 ciclos se redujera considerablemente. Se considera altamene probable la concurrencia no de una, sino de varias grietas iniciales originadas en la periferia y en esta sección de transición.

Otro aspecto observado que también tuvo gran importancia en la iniciación de estas grietas fue la presencia de inicios de entallas perimetrales en el eje. Estas irregularidades fueron provocadas, presumiblemente, por impacto de la herramienta utilizada para la inserción y fijación del eje en el contrapeso de madera.

Basados en este diagnóstico, se establecieron una serie de medidas con el objetivo de evitar el colapso en el resto de campanas. Estas medidas consistieron en una sustitución de todos los ejes metálicos y del diseño adecuado de la transición entre secciones circulares y cuadradas para evitar una zona de fuerte concentración de tensiones que pudiera comprometer la vida remanente a fatiga de los ejes.

AGRADECIMIENTOS

Los autores quieren expresar su agradecimiento al Dr. Francesc Llop y a todo el equipo de Gremis de Campaners de la Catedral de València por su colaboración en esta investigación, así como a las empresas 2001 Técnica y Artesanía SL y Electro Recamp SL por su apoyo.

REFERENCIAS

[1] Resolución del 18 de febrero de 2019, de la Dirección General de Bellas Artes, por la que se incoa expediente de declaración de toque manual de campana como manifestación representativa del Patrimonio Cultural Inmaterial.

[2] www.campaners.com, consultada el día 11 de enero de 2015.

[3] Zhenyu Zhu, Yilin Zhu, Qingyuan Wang. Fatigue mechanisms of Wheel rim Steel under off-axis loading. Materials Science and Engineering A 773 (2020) 138731.

[4] A. Cavuto, M. Martarelli, G. Pandarese, G.M. Revel, E.P. Tomasini, Train wheel diagnostics by laser ultrasonics, Measurement 80 (2016) 99–107

[5] Y. Li, V. Aubin, C. Rey, P. Bompard, Microstructural modeling of fatigue crack initiation in austenitic steel 304L, Procedia Eng. 31 (2012) 541–549.

[6] R. Pérez-Mora, T. Palin-Luc, C. Bathias, P.C. Paris, Very high cycle fatigue of a high strength steel under sea water corrosion: a strong corrosion and mechanical damage coupling. Int. J. Fatigue 74 (2015) 156-165.

[7] D. Bettge, C-P Bork. Feilures of Berlin Freedom Bell since 1966. Engineering Failure Analysis 43 (2014) 63-76.

[8] H.J. Petroski. On the cracked bell. Journal of Sound and Vibration. Volumen 96, Issue 4, 22 October 1984, page 485-493.

[9] Francesc Llop i Álvaro. Las campanas de la Catedral de València. Universitat de València. Facultat de Geografía i Història. 2011.

[10] Decreto 217/2018 de 30 de novembre (DOGV núm. 8439 07-12-2018) (BOE núm 16 18-01-2019).

[11] Salvador Ivorra. Acciones dinámicas introducidas por las vibraciones de las campanas sobre torres-campanario. Universitat Politècnica de València. PhD, 2002.

[12] C. Barajas, J. De Vicente, J. Caja, P. Maresca, E. Gómez. Considerations to the hardness Brinell measurement using optical equipment. Manufacturing Engineering Society International Conference 2017, MESIC 2017, 28-30 June 2017, Vigo (Pontevedra), Spain. Procedia Manufacturing 13 (2017) 550–557

[13] Eulogios Santos, Julio Yenque, Oswaldo Rojas, Víctor Rosales. Notas científicas acerca del ensayo de dureza. Industrial Data 2001, (4) 2: 73-80.

[14] Ivorra S, Palomo MJ, Verdú G, Zasso A. Dynamic forces produced by swinging bells. Meccanica. 41 (1): 47-62.

[15] Robert L. Norton. Machine Design (5th Edition). Ed. Pearson, September 16, 2013.

[16] Luis A. de Vedia, Hernán Svodoba. Fatiga. Ensayos industriales. Departamento de Ingeniería Mecánica y Naval. Facultad de ingeniería. Universidad de Buenos Aires. 2002.

Structural optimization of lively composite floors with integrated constrained layer damping

Pablo Vidal Fernández[1], Carlos M. C. Renedo[1], Iván M. Díaz[1] and Jaime H. García Palacios[2]

ABSTRACT

Due current architectural trends, contemporary offices are open-plan spaces with much less weight and damping. Consequently, Vibration Serviceability Limit State (VSLS) due to human-induced vibration has become an increasing concern for structural engineers. In most of the cases, a slight increase on floor's damping will decrease considerably the vibration level. The damping strategy studied in this is work is usually known in the literature as Constrained Layer Damping or CLD. That is, a viscoelastic layer is constrained between the concrete slab and the steel beam of a lightweight composite floor.

In this paper a structural checking methodology has been developed for analyzing all the limit states which influence the final sizing of the steel-concrete composite floor elements, including a detailed analysis of the VSLS. The methodology has been implemented through an optimization algorithm which finally has found optimal structural designs with and without the viscoelastic layer implemented. Thus, it has been demonstrated that from a structural performance point of view and from the environmental impact of the floor, the integration of this damping strategy may be a cost-effective solution.

Keywords: floor vibration, vibration control, damping, structural optimization.

1. INTRODUCCIÓN

En los últimos años, la construcción de edificios tiende a ser cada vez más rápida, con grandes áreas de planta abierta y con flexibilidad en su uso final previsto. Las técnicas modernas de diseño y construcción permiten al sector de la construcción del acero satisfacer tales demandas y producir estructuras que son competitivas en términos de coste total y tiempo [1].

En busca de diseño de plantas más amplias y abiertas se están reduciendo el número de pilares y tabiques además de la eliminación de mobiliario pesado. Todo ello, sumado a la mejora en los materiales, está produciendo que los forjados sean cada vez más esbeltos, de luces mayores, ligeros y menos amortiguados [2]. Como resultado de esto, se han reducido las frecuencias naturales y la razón de amortiguamiento de los sistemas de forjado de tipología mixta con losas de chapa colaborante sobre vigas de acero. Esto ha provocado que las tipologías ligeras de forjado sean especialmente susceptibles

[1] Department of Continuous Mechanics and Theory of Structures. ETSI Caminos Canales y Puertos. Universidad Politécnica de Madrid. (SPAIN). carlos.martindelaconcha@upm.es (Renedo, Carlos M. C.)
[2] Department of Hydraulics, Energy and Environmental Engineering. ETSI Caminos, Canales y Puertos. Universidad Politécnica de Madrid. (SPAIN)

de sufrir problemas de vibraciones inducidas por humanos, que terminan afectando al confort de los usuarios del edificio. [1, 2].

Es muy habitual que esta tipología de forjados presente frecuencias naturales por debajo de los 10 Hz. Las frecuencias naturales por debajo de dicho rango son fácilmente excitables por el tercer o cuarto armónico de la carga dinámica que produce un usuario al caminar. Esto provoca que la respuesta dinámica del forjado sea de carácter resonante, alcanzando en muchas ocasiones valores de aceleración más que perceptibles. Para un usuario medio en un ambiente de trabajo usual de oficina el umbral de percepción es de 0.02-0.04 m/s2 [2].

Tradicionalmente, el Estado Límite dimensionaste en los forjados de tipología mixta, era el Estado Limite de Servicio de Deformaciones (ELSD). El ELSD restringe la flecha del forjado para evitar posible molestias, grietas o desperfectos que puedan afectar al normal funcionamiento de la estructura o a los acabados de esta. Actualmente, debido al aumento de la ligereza de la estructura y a la reducción de cargas muertas, el estado límite dimensionante ha pasado a ser en muchas ocasiones, el Estado Límite de Servicio de Vibraciones (ELSV) [1].

En un principio la comprobación del ELSV se desarrolló estableciendo un límite mínimo de la frecuencia natural del modo fundamental. Numerosas normativas, aún conservan dicha limitación en frecuencias, estableciendo valores mínimos en torno a los 4-5 Hz. Con el paso del tiempo, algunos de los forjados diseñados con este criterio comenzaron han presentado problemas de vibraciones. Así, en forjados modernos esta limitación no asegura un correcto funcionamiento del forjado. Hoy en día, la mayor parte de las guías de diseño proponen una comprobación del ELSV basada en la respuesta en términos de aceleraciones del forjado [3].

Desde el punto de vista del diseño estructural, típicamente se han desarrollado dos estrategias diferentes de cara a reducir las vibraciones, aumentar la masa y/o modificar la rigidez. El aumento de masa provoca una reducción proporcional de la vibración resonante. La modificación de la rigidez busca evitar que las frecuencias naturales de la estructura se encuentren en el rango de las frecuencias de excitación. Normalmente, la solución suele consistir en rigidizar la estructura, elevando las frecuencias naturales por encima del límite recomendado. Ambas estrategias conducen a estructuras más masivas, sobredimensionadas, poco optimizadas con un alto presupuesto y una huella de carbono más elevada [1].

Otra alternativa es la de actuar sobre la capacidad de disipación de energía de las estructuras, es decir, sobre la razón de amortiguamiento del sistema. Para hacer uso de este nuevo enfoque, los ingenieros estructurales pueden usar diferentes tecnologías [4]. Entre ellas, las que gozan de mayor aceptación actualmente en el sector son las conocidas como estrategias pasivas de disipación, pues su funcionamiento es puramente mecánico/pasivo y sus costes de mantenimiento son prácticamente nulos. Las estrategias pasivas pueden dividirse en estrategias inerciales, donde una masa inercial ejerce fuerzas contrarestadoras del movimiento, o estrategias disipativas, donde los movimientos relativos entre distintos elementos estructurales provocan disipación de energía en ciertos elementos especialmente localizados para ello.

En el presente trabajo se estudia un sistema de amortiguamiento basado en la integración de materiales de gran capacidad disipativa en la matriz estructural, como materiales viscoelásticos [2]. integrados en

forjados de tipología mixta [5]. En la técnica estudiada, una lámina muy fina (3 mm de espesor como máximo) de material viscoelástico se constriñe entre la losa de hormigón y la viga metálica para una determinada proporción de la longitud de la viga desde el apoyo, como se muestra en la Figura 1; de este modo las regiones de la viga cercanas al apoyo permanecen desconectadas a cortante con la losa debido a la presencia de la capa viscoelástica. El centro de la viga, sin embargo, permanece conectado, dotando de una mayor rigidez a flexión a las secciones más solicitadas. Al vibrar el forjado en un modo de flexión, la lámina viscoelástica sufre una deformación a cortante considerable, disipando energía por histéresis viscoelástica en forma de calor. Esta técnica de amortiguamiento es usualmente conocida como Amortiguamiento por capa constreñida o CLD (por sus siglas en inglés, Constrained Layer Damping). La primera versión de este sistema aplicado a forjados mixtos fue propuesta por ARUP en colaboración con Richard Lee Steel Decking en 2006 bajo el nombre comercial de Resotec como se muestra en la Figura 1.

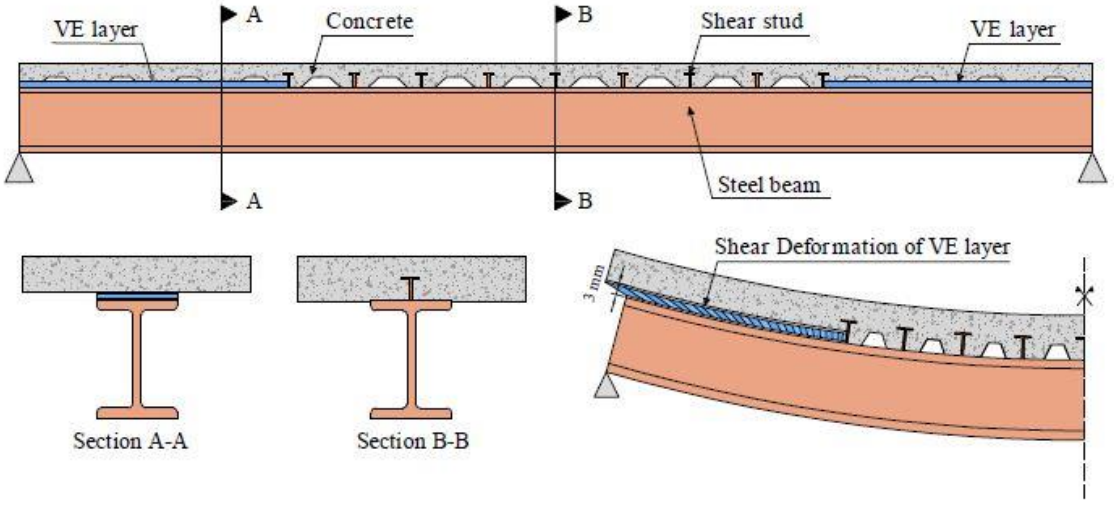

Figura 1. Viga de forjado con elastómero embebido.

Es importante recalcar que en el sistema CLD se presupone la desconexión de la viga con respecto a la losa en las regiones cercanas al apoyo, por lo que implica una pérdida de rigidez considerable en el sistema, a cambio de un aumento de la razón de amortiguamiento. Es este compromiso entre rigidez y amortiguamiento el que dota de interés y complejidad al problema, pues frecuencias más bajas se excitan más intensamente por los peatones, mientras que amortiguamientos más altos disminuyen más la respuesta dinámica [6].

Desde su creación, apenas se han desarrollado trabajos sobre las posibilidades que ofrece este sistema de amortiguamiento en el diseño de futuros forjados de tipología mixta. En el presente artículo se pretende explorar la forma de diseñar y calcular este tipo de forjados y analizar en detalle las ventajas y desventajas desde el punto de vista estructural de introducir sistemas CLD. Se presta especialmente atención a la respuesta dinámica de estos forjados y a analizar en que situaciones es útil (y rentable) usar esta tecnología.

2. OPTIMIZACIÓN ESTRUCTURAL

Se ha desarrollado una metodología para estudiar forjados mixtos con y sin tecnología CLD integrada. Dicha metodología ha sido implementada en un algoritmo de optimización de cara a obtener la solución óptima como la mejor combinación de losa de hormigón, chapa colaborante y viga. El campo de soluciones depende de estas tres variables; cada combinación diferente de variables es una solución diferente. Al ser el campo de soluciones tan extenso es necesario desarrollar un método que alcance la solución correcta con el mínimo de tiempo y recursos computacionales.

En la presente investigación se utiliza un algoritmo genético. Este algoritmo se basa en la Teoría de la Evolución de Darwin. El algoritmo lleva a cabo un cierto número de iteraciones en las cuales se evalúa un conjunto de soluciones o cromosomas conocido como población. En cada iteración se asigna a las soluciones una función de forma o aptitud. En las siguientes iteraciones las soluciones nuevas son creada mediante dos procesos: cruce entre dos soluciones de la iteración donde cada una aporta parte de su cromosoma y mutación, donde algunas partes del cromosoma son cambiadas aleatoriamente [7].

Cuanto mayor es la función de aptitud mayor es la probabilidad de que una solución transmita su cromosoma a las siguientes generaciones por medio del cruce entre soluciones. Después de múltiples iteraciones se alcanza la solución óptima global. En el transcurso del algoritmo existe el riesgo de caer en un óptimo local. Esto se debe a un bajo número de iteraciones o de diversidad genética que hacen que se obtenga la solución errónea. Por ello es importante calibrar correctamente los parámetros del algoritmo como el número de iteraciones, tamaño de población o probabilidad de mutación entre otros que hacen por un lado que el algoritmo genético no consuma demasiados recursos y por otro, que llegue a un óptimo global. En la Figura 2 se describe un esquema del algoritmo empleado, a continuación, se describen los aspectos más relevantes de dicho algoritmo.

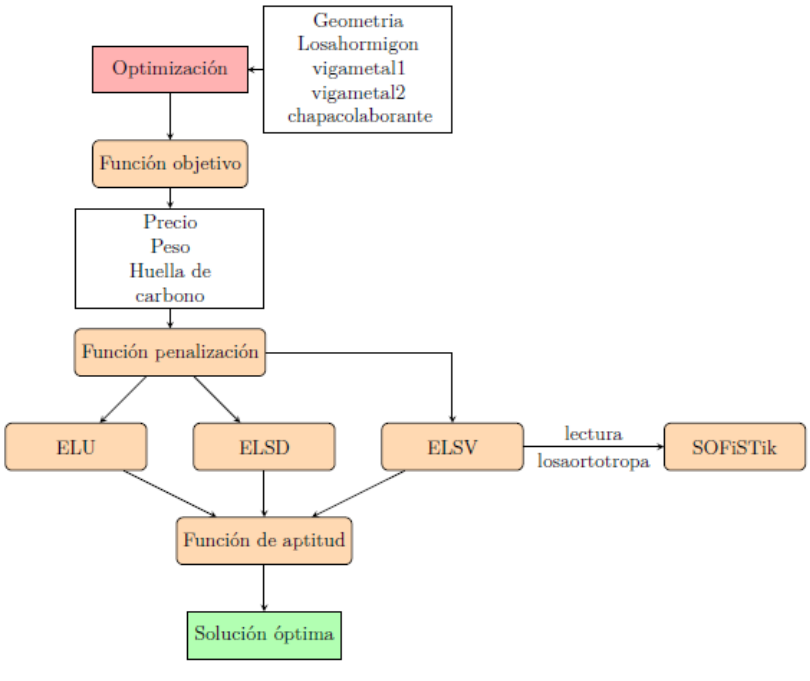

Figura 2. Esquema de la optimización estructural empleando algoritmos genéticos.

2.1. FUNCIÓN OBJETIVO

Las soluciones o cromosomas están formadas por genes que son los valores del espesor de la losa de hormigón, el perfil metálico de la viga primaria, el perfil metálico de la viga secundaria y el espesor de la chapa colaborante. La función de forma es un valor que se asigna a cada solución en función de la aptitud de esa solución frente a la optimización y está compuesta por dos funciones. La función objetivo y la función de penalización.

La función objetivo es el valor o coste que se desea optimizar. La función de penalización asigna a las soluciones coste extra o penalización si no son válidas, esto se hace para que soluciones no válidas que están cercanas a soluciones óptimas sean también consideradas por el algoritmo y de este modo sea guiado hacía la solución óptima.

Las funciones implementadas en el presente estudio son (Figura 2): el coste económico de la combinación de los diferentes materiales, el peso del forjado y la huella de carbono del forjado. La función penalización se compone del Estado Límite Último (ELU), el ELSD de la viga primaria, ELSD de la viga secundaria y del ELSV.

2.2. FUNCIÓN DE PENALIZACIÓN

Para la optimización llevada a cabo por el algoritmo genético es necesario considerar que no todas las soluciones son válidas. La función de penalización añadirá un coste extra a aquellas soluciones que no sean válidas, pero no las eliminará, gracias a esto dichas soluciones serán tenidas en cuenta a la hora de encontrar nuevas soluciones. Este coste extra se obtiene multiplicando un coeficiente k por un valor de penalización. El coeficiente k tiene un valor de 0 a 1, dependiendo del grado de cumplimiento de la restricción que son los estados límites último y de servicio de los diferentes elementos.

2.2.1. Estado Límite Último

El ELU es una de las penalizaciones que se aplican en las soluciones. Se aplicará en las vigas primarias, en las vigas secundarias y en la losa del forjado. El ELU de la viga primaria y secundaria se hace de acuerdo con el Eurocódigo 4 [8]. En la fase de construcción, la viga metálica resiste las cargas solicitantes y se comprueba la abolladura, el cortante y el momento sobre la sección de la viga metálica. En fase de servicio la sección resiste como una viga mixta y se comprueba si cumple el momento solicitante.

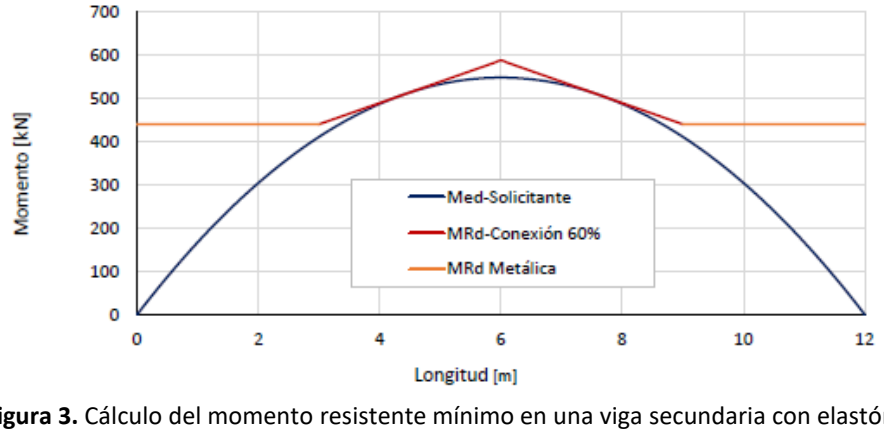

Figura 3. Cálculo del momento resistente mínimo en una viga secundaria con elastómero.

En las vigas secundarias se debe tener en cuenta la presencia del sistema CLD en fase mixta ya que reduce el momento resistente de la viga [6]. En las zonas con elastómero no se pueden colocar pernos conectadores lo que hace que el momento debe de resistirse únicamente con la sección metálica. En la zona intermedia de la viga donde hay pernos conectadores los axiles en la viga metálica y en la losa de hormigón vienen limitados por el esfuerzo de rasante, en este estudio se asume redistribución plástica del esfuerzo rasante entre los conectadores y se limita el grado de conexión al 60 % del axil máximo que resistiría la losa.

En la Figura 3 se muestra una gráfica con el momento resistente de la viga mixta donde se aprecia la zona que únicamente resiste la viga metálica en naranja. El momento resistente en el centro de vano se multiplica por un coeficiente minorador para tener en cuenta que en ningún momento la ley de momentos solicitantes parabólica sea mayor que la ley de momento resistente que crece linealmente según se van encontrando conectadores que transmiten compresiones a la losa. Este coeficiente se calcula teniendo en cuenta que el mínimo momento resistente en el centro de vano se puede obtener dibujando una recta tangente a la parábola que pase por el momento resistente de la viga metálica, tal y como se muestra en la Figura 3.

El ELU de la losa forjado se ha calculado según el Eurocódigo 4 [8]. En la fase de construcción se comprueba el momento solicitante teniendo en cuenta que solo resiste la chapa colaborante. En la fase de servicio se comprueba el momento negativo resistido únicamente con la chapa colaborante. La comprobación del momento positivo y de la rasante se realiza unificada ya que el momento obtenido a partir de la ley de rasantes es menor si se tiene en cuenta que la conexión proporcionada por las hendiduras en las grecas no es total. Con la presencia de elastómero en la viga secundaria no se colocan pernos conectadores entre viga y losa, esto conlleva que el rasante extra transmitido por el perno de la chapa colaborante a la losa de hormigón no pueda considerarse, siendo menor el momento resistente de la sección mixta chapa colaborante-losa, como muestra la Figura 4.

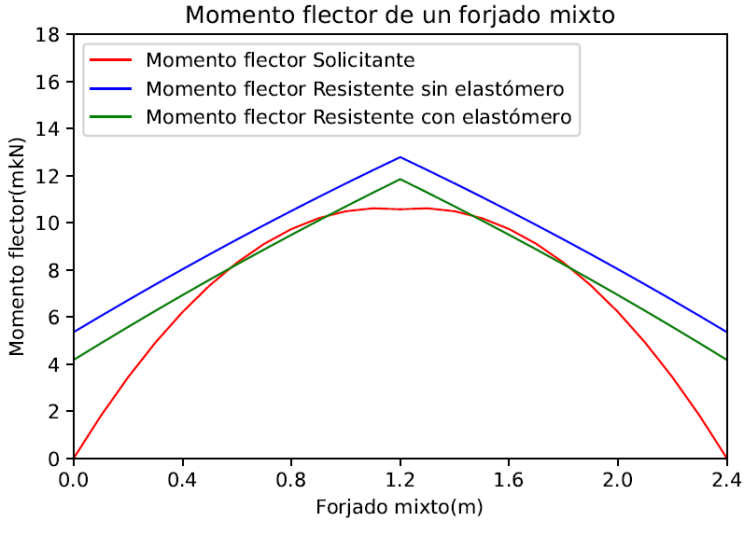

Figura 4. Cálculo del momento solicitante mínimo en un forjado mixto con una viga con elastómero.

2.2.2. Estado Límite de Servicio de Deformaciones

Las deformaciones de los elementos estructurales se calculan por medio de una integración numérica trapezoidal de la ley de curvaturas elástica por secciones. En el forjado se hacen dos comprobaciones: una comprobación de la flecha de L/180 en fase constructiva donde solo trabaja la chapa colaborante que de ser superada comenzaría a producirse el fenómeno del embalsamiento y una comprobación en fase constructiva estudiada como fase mixta con una flecha máxima del forjado de L/350.

En las vigas mixtas se comprueba que la flecha bajo la acción de la sobrecarga no supere L/350. En las vigas primarias y secundarias el ancho eficaz de la losa crece linealmente desde un valor de 6L/32 en el apoyo hasta un valor de L/4 a lo largo de un tramo equivalente a L/4, es por ello por lo que en la inercia de la viga sin elastómero y en la viga con elastómero se puede apreciar en la Figura 5 como la inercia de la viga mixta crece levemente, en la práctica, dicho valor puede considerarse constante e igual a L/4 para vigas simplemente apoyadas sometidas a cargas uniformemente distribuidas. El análisis de la viga secundaria se considera que tiene dos secciones de inercia diferentes, una sección con los valles de la chapa colaborante rellenos de hormigón y otras secciones donde solo resiste la losa de hormigón superior, algo que también puede apreciarse en la Figura 5.

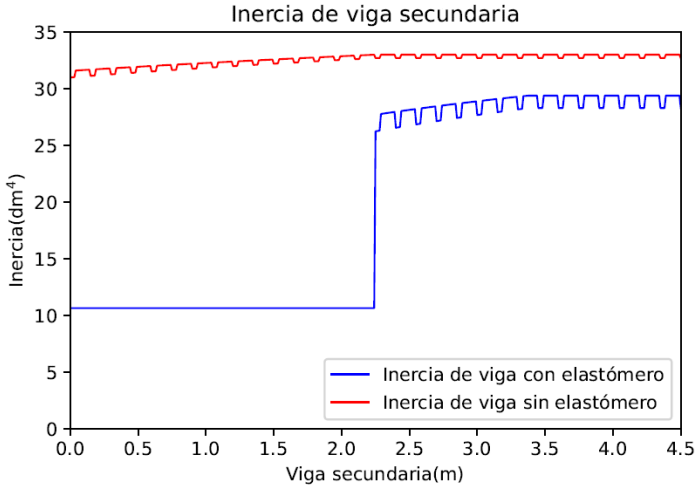

Figura 5. Inercia de una viga secundaria con y sin elastómero.

Las vigas secundarias con elastómero no tienen en los extremos de la viga pernos conectadores y es por ello por lo que en estas zonas la inercia de cálculo sólo corresponde a la inercia de la viga metálica como se muestra en la Figura 5. Las vigas secundarias con elastómero son más flexibles que las vigas sin elastómero por lo que el ELSD puede llegar a ser restrictivo en este caso. A continuación, el ELSV se trata más en detalle en un nuevo apartado.

3. ESTADO LÍMITE DE SERVICIO DE VIBRACIONES

Otra constante de penalización del algoritmo es la que depende de la aptitud del forjado respecto a las vibraciones que se pueden producir en servicio debido a las cargas inducidas por peatones al caminar sobre el forjado.

Para calcular las vibraciones en el forjado se va a utilizar un modelo computacional formado por un código en Phyton y por los resultados obtenidos del análisis modal de un modelo de elementos finitos parametrizado y programado en el software SOFiSTiK. Se va a realizar el cálculo recomendado por la AISC en el capítulo 7 que se desarrolla en los siguientes apartados [9], [10].

3.1. Modelo de SOFiSTiK y losa ortótropa equivalente para el modelado

Se ha desarrollado un modelo de elementos finitos parametrizado en el programa comercial SOFiSTiK. Con este modelo se obtendrá mediante un análisis modal los modos de vibración de la estructura y sus frecuencias propias. Se modela los elementos estructurales como una losa ortótropa sostenidas por un emparrillado de vigas primarias y secundarias metálicas que se mantienen sobre pilares comerciales HEB-600. Los pernos y el elastómero se modelizan como muelles horizontales con una rigidez muy alta en el caso de los pernos conectadores, y con una rigidez despreciable en el caso del elastómero.

El forjado mixto formado por la chapa colaborante y el hormigón se modela como una losa ortótropa [2], donde se calculan la densidad y los espesores equivalentes en función de las inercias en los ejes X e Y siguiendo la metodología propuesta en [11].

3.2. Lectura de los modos de vibración

Se ha desarrollado una subrutina llamada “ReadModes” que obtiene la aceleración máxima a la que podría ser cometido el forjado mixto por un peatón que caminase en cualquier punto de su superficie. Para obtener la aceleración se calcula la Función de Respuesta en Frecuencias (FRF) más desfavorable del forjado. Esto es aplicable si se asume que el modelo de carga de un peatón caminando sobre el forjado es el de una carga armónica e inmóvil. Esto es algo que se asume en el capítulo 7 de la guía propuesta por la AISC. La FRF empleada es una función que devuelve la respuesta dinámica armónica del forjado en un punto A (en términos de aceleración) respecto a la aplicación de una fuerza dinámica armónica de excitación en otro punto B distinto del forjado. Así, se busca la FRF entre un punto a y uno B pésima.

Para calcular la FRF entre dos puntos se utiliza la suma ponderada de las respuestas de cada modo de vibración individual. La FRF modal es la FRF para un sistema de un grado de libertad modal. Para ello se utilizan los modos de vibración anteriormente obtenidos en el programa SOFiSTiK. Previamente se eliminan los modos horizontales del forjado y aquellos modos por encima de 9 Hz por ser su aportación despreciable a la aceleración vertical.

$$\mathrm{Mod}_{\mathrm{tfre}}[\mathrm{F},\ \mathrm{f}] = \frac{(2\pi f)^2 \cdot [(2\pi F)^2 - (2\pi f)^2]}{[(2\pi F)^2 - (2\pi f)^2]^2 + (2 \cdot \xi \cdot 2\pi F \cdot 2\pi f)^2)}$$

$$\mathrm{Mod}_{\mathrm{tfim}}[\mathrm{F},\ \mathrm{f}] = \frac{(2\pi f)^2 \cdot (2 \cdot \xi \cdot 2\pi F \cdot 2\pi f)^2}{((2\pi F)^2 - (2\pi f)^2]^2 + (2 \cdot \xi \cdot 2\pi F \cdot 2\pi f)^2)} \quad (1)$$

Para calcular la FRF modal se utiliza la Ecuación (1), la primera ecuación es la parte real de la FRF y la segunda es la parte imaginaria donde F representa de frecuencia natural y f es la frecuencia de excitación y ξ es la razón de amortiguamiento. Como razón de amortiguamiento del sistema sin CLD se aplica un 2.5% de amortiguamiento cuando el forjado no dispone de elastómero, considerando así

un forjado de oficina electrónica, con falso techo y de tipología mixta, según la guía de diseño de la AISC [10]. En el caso de forjados con CLD integrado se añade un porcentaje adicional en función del porcentaje de aplicación del elastómero a lo largo de la longitud de la viga. Dicho incremento se muestra en la Figura 6 obtenida por Willford [6]. Así, una viga completamente desconectada a cortante con la losa dispondría de una razón de amortiguamiento adicional del 11%, mientras que una viga desconectada en la mitad de su longitud dispondría de un incremento del 2.7%.

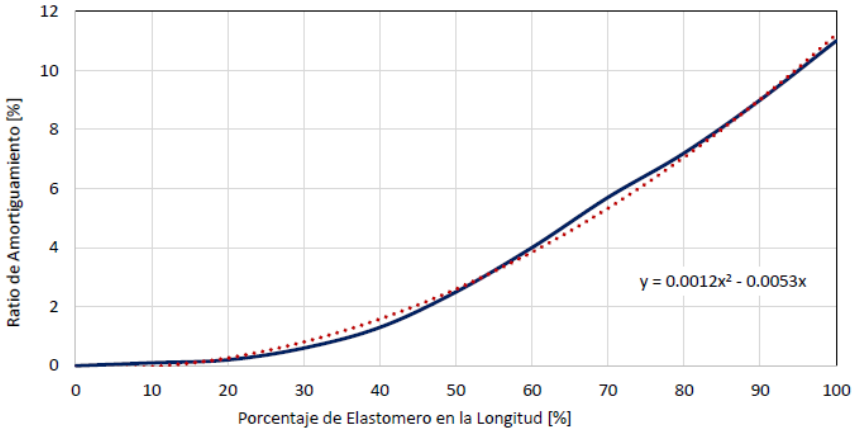

Figura 6. Razón de amortiguamiento dependiente del elastómero.

Para obtener la FRF entre dos puntos se hace el sumatorio de las multiplicaciones de las FRF modales por el valor de ese modo de vibración como muestra la Ecuación (2). En la Figura 7, la línea verde es la FRF entre dos puntos y las líneas azul y roja son las FRF modales de los dos modos principales del sistema, donde ϕ es el valor de la coordenada modal en el modo i de los puntos A y B de aplicación de la carga armónica y de respuesta, respectivamente.

$$FRF_{AB} = \sum_{i=1}^{m} (\phi_{iA}\phi_{iB}FRF_i) \tag{2}$$

La FRF se multiplica por el coeficiente dinámico en función de la frecuencia de excitación y por una carga de 700 N y se obtienen la FRF final en aceleraciones [3].

A partir de la anterior FRF, el programa selecciona el máximo valor de la aceleración en un punto A respecto a una carga armónica aplicada en B. El programa evalúa las posibles FRF consideradas a priori como pésimas. Estas FRF se obtienen al combinar realizar combinaciones entre puntos A y B dentro de un conjunto de puntos del forjado denominados como “puntos calientes” o puntos cercanos a los antinodos de los diferentes modos de vibración. La aceleración máxima del forjado será la máxima obtenida entre todas las posibles FRF resultados de combinar todos los puntos A con los B. La aceleración máxima tiene que ser menor de 0.05 m/s^2 para que no produzca molestias a los usuarios y por lo tanto cumpla el ELSV.

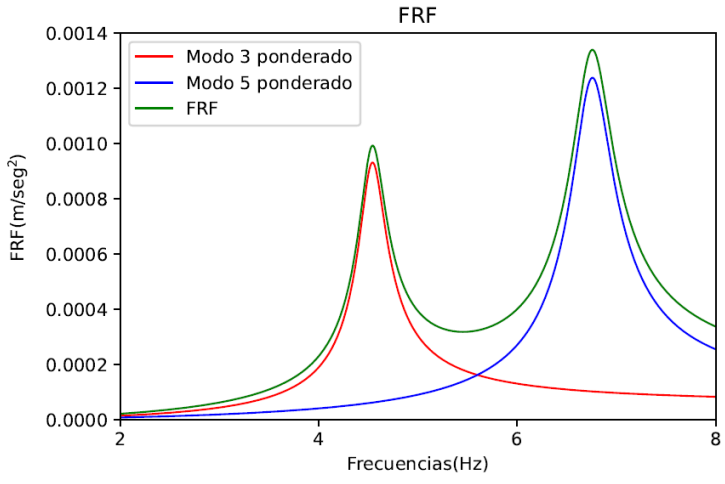

Figura 7. FRF modales y FRF entre dos puntos A y B.

4. EJEMPLO DE OPTIMIZACIÓN

En el presente estudio se ha realizado un ejemplo práctico con un forjado de un paño con vigas primarias de 9 metros y vigas secundarias de 12 m. Las vigas secundarias tienen un inter-eje de 3 metros y por lo tanto se compone de dos vigas primarias y de 4 vigas secundarias como muestra la Figura 8. Se ha asumido que la gama de chapas colaborantes a usar es Cofraplus 60 con espesores de chapa variables. Las vigas consideradas son los perfiles británicos UB de 275 MPa de resistencia, por existir en esta mayor variedad de opciones y cantos. Finalmente, el hormigón considerado es de resistencia característica 25 MPa y densidad 2400 kg/m^3.

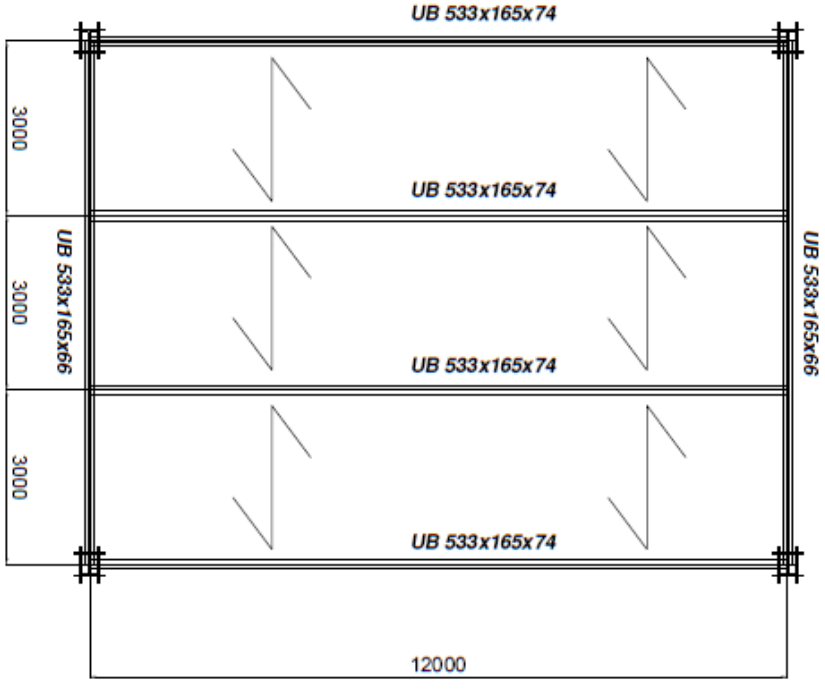

Figura 8. Esquema en planta del forjado optimizado.

4.1. Funciones objetivo y casos optimizados

Las optimizaciones del forjado realizadas se han basado en tres funciones objetivo:

- El precio de los materiales del forjado en euros donde el precio del acero es de 1.7 € /kg, el precio del hormigón es de 75 € /m3, el del elastómero es de 15 € /m, el precio de los pernos es de 7 € /m2 y el de la chapa colaborante varía entre 24 y 35 € /m^2 dependiendo de su espesor.

- El peso del forjado en kg donde la densidad del hormigón es de 2500 kg/m^3 y la del acero se considera como 7850 kg/m^3. El elastómero apenas contribuye al peso.

- La huella de carbono del forjado en kg CO_2 donde cada tonelada de acero se estima que consume 1.85 toneladas de CO_2 y cada m^3 consume 300 kg de CO_2. Es importante recalcar que estos valores son estrictamente estimativos y que un estudio más detallado y referenciado del problema debe realizarse en el futuro.

Para poder comprender mejor como influye el cumplimiento estricto del ELSV al dimensionamiento en un forjado mixto, se han procedido a optimizar para cada función objetivo los siguientes casos:

- Un forjado que no ha de cumplir el ELSV: es presumible que el forjado resultante de este diseño no cumpla el ELSV, por tener una frecuencia baja y su ligereza. Este caso nos indicará cual es el mejor modelo sin ELSV y relacionarlo con el modelo de elastómero donde el ELSV no debería ser dimensionante.

- Un forjado en el que se debe cumplir el ELSV: es de prever que en este diseño se emplee material adicional bien para aumentar la masa del forjado o su rigidez y así disminuir la respuesta vibratoria de este, permitiendo que cumpla el ELSV. En este caso se puede comparar con el caso en el que se trate el forjado con elastómero y ver si realmente se optimizan estos forjados dentro de las funciones objetivo.

- Un forjado con 50 % de CLD aplicado en sus vigas secundarias y que debe cumplir el ELSV: Este caso es el que permitirá entender cual es el verdadero efecto de introducir el sistema CLD a base de elastómeros embebidos en el diseño de un forjado mixto.

4.2. Resultados

Los resultados obtenidos a partir de las diferentes optimizaciones se muestran en la Tabla 1. En la columna resultados, el primer número corresponde al espesor de la losa de hormigón en cm por encima de la chapa colaborante. El segundo valor es la chapa grecada utilizada siendo 0, la de 0.75 mm de espesor, la 1, la de 0.88 mm, la 2, la de 1 mm de espesor y la 3, la de 1.25 mm. El tercer y cuarto número se corresponde con el perfil UB de una lista convencional de 93 perfiles, UB de la viga primaria y la viga secundaria, respectivamente. La función complemento es el valor del peso o el precio del forjado cuando la función optimizada es precio o peso respectivamente, pudiendo comparar funciones objetivos diferentes con unidades iguales. La carga muerta del forjado es la de un solado ligero, 0.85 kN/m^2 y la sobrecarga de uso es 5 kN/m^2.

Tabla 1. Tabla de resultados de las optimizaciones

Forjado 9m x 12m - 3m | 0.85 - 5 kN/m² | UB |Cofraplus 60 | f_y = 275 MPa | f_{ck} = 25 Mpa							
F. Objetivo	**ELSV**	**CLD 50%**	***f* [Hz]**	**Resultado**	**Precio €**	**Peso kg**	**kgCO₂**
Precio €	No	No	4.881	[6,0,46,46]	11174	27623	~12400
Precio €	Sí	No	4.851	[12,3,47,36]	14033	45007	~16500
Precio €	Sí	Sí	4.729	[6,0,46,47]	**11890**	28139	~13400
Peso kg	No	No	4.881	[6,0,46,46]	11174	27623	~12400
Peso kg	Sí	No	8.295	[6,0,73,77]	22253	34100	~15400
Peso kg	Sí	Sí	4.729	[6,0,46,47]	11890	**28139**	~13400
$kgCO_2$	No	No	4.881	[6,0,46,46]	11174	27623	~12400
$kgCO_2$	Sí	No	4.851	[12,3,47,46]	14033	45007	~16500
$kgCO_2$	Sí	Sí	4.729	[6,0,46,47]	11890	28139	**~13400**

En los resultados se puede apreciar como el ELSV sí es un estado determinante para el diseño del forjado estudiado ya que cuando este se aplica a la optimización aumentan las funciones objetivo un 25 % en el caso del precio, un 23 % cuando el objetivo es el peso y un 33 % en el caso de la huella de carbono. Se puede apreciar que el uso de elastómero reduce las funciones objetivo en un 15 % en el precio, un 17% la masa de la estructura y un 19 % la huella de carbono en kgCO2. Estos resultados se pueden apreciar en la Figura 9, para el caso optimizado con la función objetivo del precio en €.

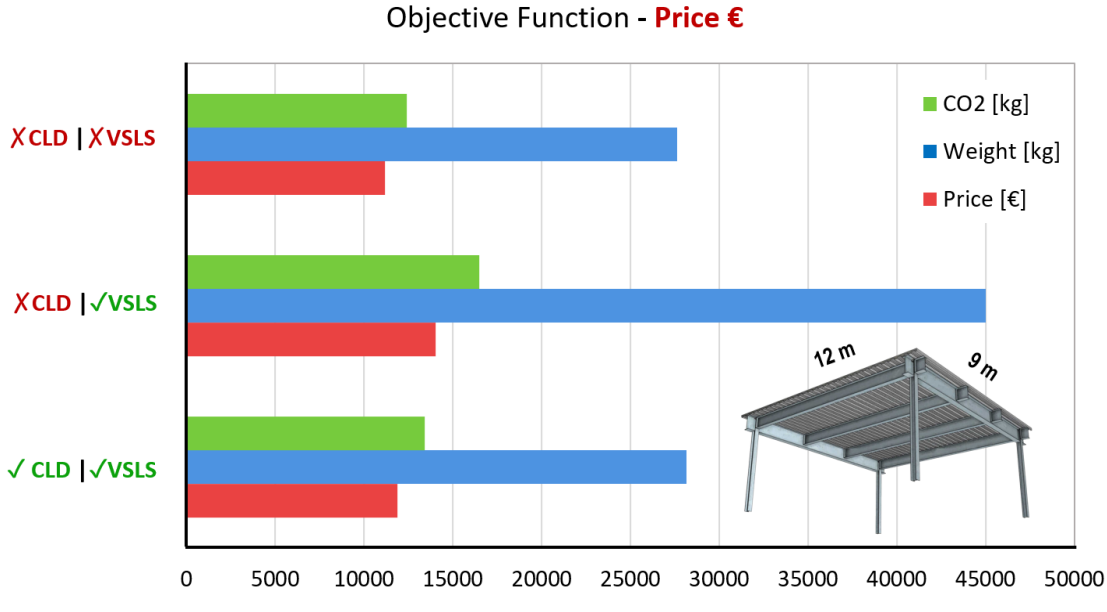

Figura 9. Resultados de la optimización estructural de un forjado mixto de 12m X 9m con y sin la comprobación de ELSV y con y sin considerar el tratamiento viscoelástico CLD estudiado.

De los resultados obtenidos pueden extraerse dos conclusiones importantes:

- Cuando la función objetivo es el precio, para mitigar las vibraciones en el caso que no dispone de elastómero se aumenta el hormigón ya que es el material más económico y un aumento de masa reduce el potencial de las vibraciones molestas. En el caso de emplear elastómero este aumento de masa proporcionado por el hormigón no es necesario pues el forjado dispone de mucho más amortiguamiento, sin embargo, es necesario aumentar ligeramente el perfil metálico para aumentar la rigidez perdida por la presencia del elastómero. Cuando el objetivo es la huella de carbono ocurre algo similar ya que es menor la huella de carbono producida por el hormigón respecto a la del acero.

- Cuando la función objetivo es el peso, para reducir el efecto de las vibraciones en el forjado sin elastómero, la estrategia óptima es aumentar la frecuencia fundamental del forjado. Para que ocurra esto, evitando aumentar la masa, se deben aumentar los perfiles de las vigas metálicas. En este caso la frecuencia del forjado se aproxima a los 9 Hz, lugar del espectro en el que el armónico de la acción peatonal es mucho menos intenso y por lo tanto se reduce la aceleración. Si se añade el elastómero se consigue reducir el efecto de las vibraciones sin tener que aumentar los perfiles metálicos.

5. CONCLUSIONES

En el presente artículo se ha desarrollado una metodología ingenieril para la optimización de forjados mixtos de chapa colaborante y losa de hormigón con la posibilidad de incluir elastómero para reducir las vibraciones. La optimización se ha realizado con un algoritmo genético que a través de diferentes iteraciones buscará soluciones óptimas hasta alcanzar la solución de menor coste. Se ha creado un código en Phyton y en SOFiSTiK para calcular los diferentes estados límites de dimensionamiento de los forjados y vigas mixtas prestando especial atención al ELSV.

Una solución está compuesta por el espesor de losa de hormigón, el espesor de chapa colaborante, el perfil de la viga primaria y el de la viga secundaria. Las soluciones deben de satisfacer los diferentes Estados Límite de diseño. Se realizan tres estudios diferentes: sin elastómero y sin considerar ELSV; sin elastómero y con ELSV y una última con elastómero y con ELSV. Los resultados obtenidos indican que el ELSV es dimensionante para el forjado estudiado, y generalmente estos parecen indicar que así ocurre cuando lo que se analiza es la influencia de un único paño (espacio entre 4 pilares) del forjado en el modelo de los elementos finitos.

Las estrategias naturales del algoritmo para reducir las vibraciones son el aumento de masa y el aumento de rigidez del forjado. Si se pretende reducir el precio del forjado, la estrategia adoptada es aumentar el volumen de hormigón, lo que aumenta la masa del sistema y reduce la aceleración de éste. Si se pretende reducir el peso, la estrategia consiste en aumenta la rigidez para aumentar la frecuencia propia del forjado a través del acero de las vigas de metal que aumentan la rigidez con menor peso. Esto se ajusta a las estrategias previamente adoptadas por los ingenieros de estructuras de cara a reducir las vibraciones. Son soluciones sobredimensionas y pobremente optimizadas, pues en ellas se emplea material para satisfacer un requisito de servicio, algo, que no es a priori deseable.

La introducción del elastómero o sistema CLD reduce las vibraciones gracias a la estrategia de incremento de amortiguamiento. Es por ello por lo que su integración provoca que el ELSV deje de ser dimensionante y los forjados resultantes son muy parecidos a los obtenidos sin elastómero y sin ELSV. Evidentemente, cuando se integra el elastómero, las vigas secundarias deben rigidizarse ligeramente de cara a su requisito resistente.

AGRADECIMIENTOS

Pablo Vidal quiere agradecer a la Universidad Politécnica por la posibilidad de realizar su investigación en el laboratorio de estructuras de la Escuela de Caminos, Canales y Puertos de Madrid. También agradecer a todo el equipo del laboratorio. Los autores agradecen la ayuda RTI2018-099639-B-I00 financiada por MCIN/AEI/ 10.13039/501100011033 y por "FEDER Una manera de hacer Europa". El trabajo ha sido financiado por el Ministerio de Ciencia, Innovación y Universidades en el Proyecto "Mejora de la eficiencia estructural de puentes sometidos a acciones dinámicas integración de amortiguadores inteligentes".

REFERENCIAS

[1] C. M. C. Renedo, I. M. Díaz, G. Palacios, H. Jaime, and S. Zivanovíc. Modelling of highlydamped composite floor beams with constrained elastomer layers. Madrid, Spain). [Floor vibration, Damping]. International Conference on Mechanical Models in Strutural Endineering., pages 1–14, 2019.

[2] P. C. M. C. Renedo, I. M. Díaz, and J. H. G. Palacios. Assessing the dynamic performance of composite floor beams with integrated constrained layer damping. (Madrid, Spain). [Dynamics; Buildings, structures & design; Control]. Structures and Buildings, pages 1–25.

[3] A. L. Smith, S. J. Hicks, and P. J. Devine. Design of Floors for Vibration: A New Approach, SCI P354. The Steel Construction Institute-SCI, Berkshire, UK, 2009.

[4] D. J. Mead, Passive Vibration Control. Southampton: John Wiley & Sons, 2000.

[5] P. Vidal Fernández, "Optimización estructural de forjados mixtos con elastómeros embebidos sometidos a vibraciones inducidas por humanos", Trabajo Fin de Máster, Madrid, 2021.

[6] M. Wilford, P. Young, and W. H. Algaard. A constrained layer damping system for composite floors. (England)[Vibration]. The Structural Engineer, pages 31–38, 2006.

[7] H. A. L. Omid Bozorg-Haddad, Mohammad Solgi. Meta-Heuristic and Evolutionary Algorithms for Engineering Optimization. WILEY, USA, 2017.

[8] Eurocódigo 4: Proyecto de estructuras mixtas de acero y hormigón. España, 2011.

[9] Z. O. Muhammad and P. Reynolds. Vibration Serviceability of Building Floors: Performance Evaluation of Contemporary Design Guidelines. (Exeter, UK) [Vibration Serviceability, Vibration Control, Damping].

[10] T. M. Murray, D. E. Allen, E. E. Ungar, and D. B. Davis. (2016). Vibrations of Steel-Framed Structural System Due to Human Activity. American Institute of Steel Construction-AISC, United States of America.

[11] T. J. Emad El-Dardiry. Modelling of the dynamic behaviour of profiled composite floors. 2005. Engineering Structures, ElSevier.

Author index

Spanish Group IABSE

ITAP

CARTIF

Ayuntamiento de Valladolid

MICHELIN

Colegio Oficial de Ingenieros Industriales de Madrid